MULTI-GROUP, MULTI-DIMENSIONAL INVESTIGATIONS OF THE POWER SPECTRAL DENSITIES OF THE GEORGIA TECH RESEARCH REACTOR AND THE FAST-THERMAL ARGONAUT REACTOR

A THESIS

Presented to

The Faculty of the Division of Graduate Studies

by

Jean-Paul A. Renier

In Partial Fulfillment

of the Requirements for the Degree

Doctor of Philosophy

in the School of Nuclear Engineering

Georgia Institute of Technology

June, 1976

MULTI-GROUP, MULTI-DIMENSIONAL INVESTIGATIONS OF THE POWER SPECTRAL DENSITIES OF THE GEORGIA TECH RESEARCH REACTOR AND THE FAST-THERMAL ARGONAUT REACTOR

APPROVED:

J. D. Clement, Chairman

G. G. Eichholz

R. W. Fink

J. L. Hammond, Jr.

L. E. Weaver

Date approved by Chairman: 5-28-74

ACKNOWLEDGMENTS

For his interest and support during the course of this research, I wish to express sincere appreciation and thanks to Dr. J. D. Clement, my thesis advisor.

I gratefully recognize the very careful review of the manuscript and the many helpful suggestions made by Dr. G. G. Eichholz.

The thesis committee members, Drs. J. D. Clement, G. G. Eichholz, R. W. Fink, J. L. Hammond, Jr., and L. E. Weaver have also helped me in this research and have provided me with invaluable professional support and encouragement throughout my studies at Georgia Tech.

I am particularly grateful to my good friend, David Y. Pitts, for his continuing interest and valuable discussions during the course of this research. Doctors Kenneth D. Kirby, David Y. Ebert, Donald N. Bridges, and Messrs. D. K. Vogt, D. Lal, J. M. Reynolds, and C. A. Sparrow provided many needed discussions and much assistance and for these I am appreciative.

I wish to thank especially Robert E. Kettner and Paul F. Schutt of the Nuclear Assurance Corporation in Atlanta for their invaluable help, many encouragements, and interest throughout this dissertation. They enabled me to bring this work to a fruitful conclusion. The interest of Steve Hill, James Burns, and Jack Rollins of the Nuclear Assurance Corporation is also appreciated.

For their help in dealing with some of the programming, I wish to thank Bill Brown of the Sperry-Univac Corporation and Jerry Segers of the

Computer Center at Georgia Tech.

I would like to acknowledge Dr. N. M. Green and Mr. R. Roussin of Oak Ridge National Laboratory for their assistance in the conversion of the XSDRN code.

The Georgia Tech Research Reactor Operations Staff and J. M. Burke of the GTRR machine shop were especially cooperative during the experimental phase of this dissertation.

Mrs. Lydia S. Geeslin and Mrs. Lyd F. Sweatt have been invaluable in the preparation and typing of the final draft of this dissertation and for this I am very appreciative. I thank Mrs. Sandy Spurgin of the Nuclear Assurance Corporation for helping in the typing of the first draft.

To my parents in Brussels, Belgium, and to my wife's parents, Mr. and Mrs. John Merritt of Atlanta, I am deeply grateful for their encouragement and guidance over this period of graduate study.

Finally, to my wife Carolyn, and our son Mark, I would like to express my deepest appreciation for their love, support, and understanding throughout this work.

TABLE OF CONTENTS

TABLE OF CONTENTS (Continued)

TABLE OF CONTENTS (Concluded)

LIST OF TABLES

LIST OF TABLES (Continued)

LIST OF TABLES (Concluded)

LIST OF ILLUSTRATIONS

LIST OF ILLUSTRATIONS (Continued)

LIST OF ILLUSTRATIONS (Continued)

LIST OF ILLUSTRATIONS (Continued)

LIST OF ILLUSTRATIONS (Concluded)

SUMMARY

In heterogeneous systems, several neutron waves may propagate simultaneously, each with different velocities, and this may cause a phenomenon of phase interference between the waves. Current techniques for the investigation of the spatial and spectral power spectral densities at high frequencies are based on one-dimensional modal approximations of the neutron flux, coupled-core theories and one-dimensional finite difference approximations to the time-dependent diffusion equations. This dissertation develops a general method for the investigation of multi-dimensional and multi-energy-group power spectral densities valid at low as well as at high frequencies, starting from the three-dimensional time-dependent P_1 approximation to the Boltzmann equation. For nuclear reactors in which there is a heterogeneous arrangement of materials, the space- and energy-dependent power spectral densities have been found to exhibit resonances at relatively high frequencies, typically above fifty cycles per second. A cascade block-tridiagonal iteration method, in which several adjacent energy groups and rows are solved simultaneously or with inner iterations, was used for the solution of the complex multi-dimensional finite difference equations. This method was combined with a complex constraint overrelaxation technique followed by rebalancing accelerations.

The model was applied to several reactors which had widely different neutron spectra: reactors containing a hard spectrum fast core, and reactors in which a thermal spectrum predominated. The space-and energy-dependent power spectral density due to the inherent volume distributed

binary fission noise was calculated for a two-dimensional configuration of the Thermal Argonaut Reactor Karlsruhe (TARK) and for the Fast-Thermal Argonaut Reactor fast assemblies loading II and IV. The frequency range was typically one to 900 cycles per second. The agreement between results of calculations of the coherence functions between neutron detectors, based upon the two-dimensional and two or three broad energy-group model, and the experimental results of the power spectral densities for TARK was approximately within 12 percent below the first minimum. The agreement between the results of the calculations of the cross-power spectral densities based upon the model and the experimental results for the Fast-Thermal Argonaut Reactor Loading II was excellent over the experimental frequency range investigated.

The power spectral densities between two neutron detectors, located at various positions, was investigated for the coupled-core configuration of the heavy water moderated and cooled, highly enriched Georgia Tech Research Reactor (GTRR). The driving sources were both inherent volume distributed binary noise, and external driven localized absorbers. For the inherent binary sources, minima in the amplitude of the coherence function were predicted at approximately 250 and 560 cycles per second. For external driven perturbations, no minima in the amplitude of the power spectral densities were found when only one localized absorber was present. In order to excite preferentially the higher modes, and minimize the contamination of the response through the high gain of the fundamental mode, two identical localized absorbers, driven 180 degrees out of phase of each other, were located in symmetrical reactor positions. For this case the model predicted one minimum in the amplitude of the cross-power spectral

density in the frequency range one to 600 cycles/sec.

An experimental investigation of the power spectral density of the full core configuration of the Georgia Tech Research Reactor was performed. The Discrete Fourier Transforms of the discrete data samples were obtained using a Fast Fourier Transformation (FFT) algorithm. The driving source was the inherent binary noise. The upper limit of the frequency range investigated was limited due to the presence of large mechanical vibrations of a safety control blade. They were induced by the D_2O coolant flow past the blade. The coolant flow induced peaks in the frequency spectrum were observed at 5.9 cps and its harmonics.

A capability to calculate multi-dimensional and multigroup power spectral densities was developed from the time-dependent three-dimensional P_1 approximation to the Boltzmann equation, and applied to fast and thermal reactors. The method was developed without any restraint on the geometry or heterogeneity of the neutronic system, and was applied over a fairly wide frequency range. In the past, accurate power spectral density and space-dependent transfer function calculations could only be performed for simplified geometries and/or a limited frequency range. The results of this work tended to point out that one-dimensional representations of heterogeneous reactors were inadequate for power spectral density investigations, and have demonstrated that solutions to multigroup space-dependent power spectral densities and transfer functions for two-dimensional representations of neutronic systems can be attained without any restrictions on the material configuration, number of energy groups, frequency range, or neutron energy spectrum. The usefulness of the method was not limited by slow convergence or divergence of the iterative process used in the solution of the frequency-dependent equations.

CHAPTER I

INTRODUCTION

Statement of Problem

The development of accurate methods and numerical solutions in the field of reactor dynamics is fundamental to the design and analysis of nuclear reactors and experiments. The field of reactor kinetics in general is based on the excitation of the neutron field by a particular disturbance and, subsequently, in the observation of the response of a reactor variable to this perturbance. Any reactor, when subjected to a spatially non-uniform perturbance, will experience spatial and spectral non-uniform changes in its neutron population.

In the earlier stages of reactor development it was satisfactory to analyze reactor dynamics with simple calculations which involved only a few space points. With the advent of large heterogeneous reactors and the modular coupled-core concept of fast reactors, spatial and spectral effects could not be ignored any more, especially at higher frequencies where the different parts of the reactor tended to decouple, and the reactor system dynamic behavior tended to become more sluggish. The problem of spatial-dependent reactor dynamics was first triggered by the well-known phenomenon of xenon spatial oscillations in the early studies of thermal reactors. Henry and Germann[1] studied the oscillations in the spatial distribution of power due to xenon buildup for a reactor of sufficient size and operating at high power density.

Large heterogeneous systems can be considered as a cluster of closely grouped interacting cores, whose overall kinetic behavior is more complex than that of a single point reactor. When the dimensions of a single-core reactor are large in comparison to the wave length of the neutron waves, its kinetic behavior can be considered as a coupled-core reactor. The coupling between cores results from the mutual exchange of neutrons which introduce phase lags due to the finite travel time between the cores. Because of those neutron time-delays between cores, a large core behaves more sluggishly than a small system in responding to transient changes in neutron population or reactivity. When reactivity is added to all sections at once, the excursions may increase faster than for the case of separate point reactors, and space-independent kinetics will underestimate the excursion. This was demonstrated by Yasinsky and Henry[2] for reactor power transients with and without spatial effects. In the cases studied, the magnitude of the power transient calculated by using space-dependent considerations ranged from three or four times greater (in a 60-cm diameter core), to more than several orders of magnitude greater (in a 240-cm diameter core) than that calculated using standard non-spatial methods. From this it was concluded that, for large reactors, the standard non-spatial methods for calculating reactor kinetics were inadequate.

Since, for the high frequency behavior of a heterogeneous reactor, the different regions tend to decouple, multi-dimensional multigroup models are a prerequisite. A considerable amount of work has been carried out to develop monoenergetic models for predicting the kinetic behavior of heterogeneous and coupled-core reactors. Assumptions had to be made

on the application of those methods to the actual reactor configuration, as "point reactor" behavior of the different parts of the reactor system, one-dimensional approximation, one-energy group assumption, and others. Although the emphasis of this study will be placed on coupled subsystems, the application to other types of reactor configurations is valid. The concept of coupled subsystems is particularly useful in the kinetics analysis of several types of reactors. Among those are the large thermal reactors, the fast reactors (fast core-blanket coupling), the fast-thermal reactors, and the modular fast reactors. From the point of view of coupling, that is, the amount of reactivity introduced by the mutual interaction of the subsystems and the time delay between them, it can range from very tightly coupled to very loosely coupled systems. The interaction between the fast core and the blanket zone of a fast reactor could be considered as that of a tightly coupled system. Higher order approximations (P_1 and higher) to the time-dependent Boltzmann must be developed. It is a well known[3,4] property that the propagation velocity of a disturbance is infinite when using the diffusion approximation: that is, any disturbance at any point in the system is felt everywhere instantly, provided the system is small enough. The use of the time-dependent P_1 equations introduces the phenomenon of retardation: it takes a finite time for the effect of a disturbance on the neutron flux to reach another part of the reactor system. It has to be observed that while the time-independent P_1 and diffusion equations are equivalent, the time-dependent P_1 equation is not equivalent to the time-dependent diffusion equation. A conference[5] in 1975 on computational methods in Nuclear Engineering

stressed the great need for computational methods and computer codes for the analysis of reactor dynamics in two and three dimensions. The objective of this investigation is to develop a foundation for studying the power spectral density between the response of neutron detectors in heterogeneous reactors in two-dimensional geometries, valid over a wide frequency range, without using either the nodal or modal techniques. Any numerical procedure to solve this problem has to have the following characteristics: 1) speed and convergence of the solution and 2) flexibility and accuracy of the model. Although the method that was developed and used in this work only applies to a "zero-power" neutronic system, it could be extended to include power feedback by incorporating a theoretical approach developed by Bridges, Clement, and Renier.[6]

Review of Space-Dependent Power Spectral Density Studies in Heterogeneous Systems

Auto-power spectral density (APSD), cross-power spectral density (CPSD), and coherence function (CHF) between the responses of neutron detectors in various reactor locations can be determined for different types of driving forces of the fluctuations of the neutron field in a reactor. A power spectral density (PSD) could be defined loosely as the AC component of the detector signal power per unit of frequency interval. For definitions of APSD, CPSD, CHF, and PSD we refer to Chapter III. Two types of driving forces have been used extensively:

1) inherent driving force due to the volume distributed fission source in each fuel region,

2) external driving force due to an external controlled neutron

source or absorber variation (e.g., pile oscillators or neutron generators). The volume distributed fission source introduces a stochastic behavior of the neutron flux through a density probability function of the fission process, similar to the distribution of Böhning. The discrete nature of the fission, capture, and leakage processes in nuclear reactors give rise to fluctuations in the fission rate. If neutrons were born independently of one another, uncorrelated by location or time of birth, the fluctuations of the neutron flux would follow a Poisson distribution. Neutrons are, however, born together, correlated as to location and time of birth, in fission events. This correlation in the fission process leads to fluctuations which are non-Poisson in character. The non-Poisson character of the fluctuations in a multiplying neutron system comes, therefore, from the fact that neutrons can be chain related. It is this non-Poisson character (usually referred to as binary noise) of the neutron flux that gives rise to finite values of the CPSD.

Compared with methods based on external controlled sources, the principal advantage of using inherent driving forces (usually referred to as noise) is that they are non-perturbing to the system. Their main disadvantage is that they require sometimes exceedingly lengthy data samples and complex and time-consuming data analysis procedures. However, the application of the Fast Fourier Transform[7,8] algorithm greatly reduces the time needed to process the lengthy data samples into discrete Fourier transform (DFT) coefficients.

The PSD of the neutron flux, seen by neutron sensitive detectors, located in different reactor locations or having different neutron energy sensitivities, will vary in large heterogeneous reactor cores. The spatial

and spectral nature of the neutron flux will therefore have to be taken into account. The zero-power power spectral density (PSD) of the neutron field fluctuations of a reactor consists basically of two terms, an overall term, due to overall statistical fluctuations of the reactor, and a space-dependent term due to space-dependent statistical fluctuations inside the reactor. In order to determine the space-dependency in a nuclear reactor core, one measures the cross-power spectral density (CPSD) or the coherence function (CHF) between two locations inside a reactor. Numerous PSD measurements have been performed in both zero- and full-power reactors, mostly to determine the reactor transfer functions. For a general review of PSD measurements and noise analysis we refer to the works of Pacilio[9] and Uhrig.[10,11] Among the major advantages of using inherent driving forces are that the investigations can be performed simultaneously over a larger frequency band as compared to most methods employing external driving forces. The frequency band of the external driving forces can however be extended with the use of pseudo-random binary sequences, as was first suggested by Balcomb, Demuth, and Gyftopoulos.[12] Since the major emphasis of this dissertation will be in the area of multi-dimensional, multi-energy group studies of heterogeneous systems at high frequencies (typically above 50 cps), we will place the emphasis on reviewing work performed in this area. Most of the calculational methods in this area are valid for external controlled forces as well as for the inherent driving forces. Quddus, Cochran, and Emon[13] performed a theoretical study of the axial propagation of plane-thermal-neutron waves in a heterogeneous system in the framework of the P_1 approximation to the

Boltzmann equation. Quddus's method used a modified form of the heterogeneous reactor theory of Feinberg and Galanin[14,15] which was based on Fermi-age theory. The two-dimensional Green's function for a line source in an infinite medium given by Morse and Feshbach[16] was used. Their analysis predicted that the phase interference between the modes of propagation in the axial direction may give rise to resonances in the frequency response. Numerical calculations were performed for a heavy-water-moderated natural uranium system in the frequency range from zero to 1500 cps. For a system with four identical fuel rods, two resonances were predicted in the transfer function. At relatively high frequencies, propagation of neutron waves in a heterogeneous case was different from the homogeneous case, due to the characteristics of the neutron waves, which were dependent on the lattice anisotropy. In a heterogeneous system, several modes are propagating simultaneously. Each mode has its own phase velocity and a phenomenon of phase interference occurs between the various modes.

In the determination of the CPSD between two detectors, resonances occur which are dependent on the heterogeneity of the reactor medium. The frequency at which those resonances occur is often called the sink frequency. The sink corresponds to a 90 degrees phase shift in the coupling transfer functions between the fuel regions. The frequency at which the heterogeneous effects occur has been shown[17] to be very much dependent on the distance between fuel regions. The sink frequency decreases with increasing distance. It is also dependent, as expected, on the nature and cross-sections of the region between fuel assemblies. There is a similarity between this neutronic heterogeneity effect in reactors and the

"positive-ion echo effect" observed by Renier et al.[18] in proportional counters, in the course of orbital electron capture studies. Since most of the positive ions are created in the electron avalanche which occurs within a few wire diameters of the center anode wire of a proportional counter, they travel as a bunch toward the cylindrical cathode walls, and their transit time for charge collection is relatively constant. When the positive-ion bunch arrives at the cathode wall, it causes emission of a secondary electron bunch, which then travels back to the center wire with essentially constant transit time, where it initiates another avalanche with the formation of another positive-ion bunch, which repeats the process. This "echo effect" is repeated with diminishing intensity at constant time intervals. The same reasoning can be applied to the neutronics behavior of a heterogeneous reactor. Since most of the fission neutrons are created in the fissioning avalanche which occurs within the fuel assembly and are thermalized in the immediate surroundings (slowing down distance), they travel as a bunch cylindrical shell to the other fuel assemblies, and their transit time is relatively constant. When the neutron bunch cylindrical shell intersects other fuel assemblies, it causes emission of a secondary neutron bunch by fissioning process, which then travels back to the original fuel assembly with essentially constant transit times, where it initiates another avalanche with the formation of another fission neutron bunch, which repeats the process. This echo effect is repeated at time intervals, which are dependent on the neutron energies. When one neutron of a neutron bunch arrives at the secondary fuel assembly, this one neutron introduces a fission neutron avalanche. The number of fission neutrons induced is dependent on, let us say, the

k_{eff} of the secondary fuel assembly, and is approximately equal to the assembly multiplication factor. One neutron induces many neutrons in a secondary bunch, which after losing neutrons in absorption and diffusion, arrives back at the primary fuel assembly. Translating this into the frequency domain, this means that when we have a 90 degree phase shift in the transfer function for neutrons of a certain energy, the round trip induces a 180 degree phase shift and, therefore, could destroy part (sink frequency) or whole (null frequency) of the frequency dependent amplitude function. We will, therefore, look for frequencies for which there is a 90 degree phase shift in the transfer function between cores, in order to expect a heterogeneous effect in determining the CPSD between two locations in a nuclear system. This can be put into a simple mathematical formulation as follows:

Assume fuel assembly 1 is located at $\bar{r}_1$, fuel assembly 2 at $\bar{r}_2$.

Place a neutron bunch source at $\bar{r}_1$: $S(\bar{r}_1)$

The flux at $\bar{r}_1$ is therefore:

$$\phi(\bar{r}_1 t) = S(\bar{r}_1 t) + \alpha_{\bar{r}_2 \to \bar{r}_1} A(\bar{r}_2) \alpha_{\bar{r}_1 \to \bar{r}_2} S(\bar{r}_1, t - \tau_{1\to2\to1})$$

where $\alpha_{\bar{r}_1 \to \bar{r}_2}$: coupling coefficient between $\bar{r}_1$ and $\bar{r}_2$

$A(\bar{r}_2)$: amplification at fuel assembly $\bar{r}_2$

$\tau_{1\to2\to1}$: time delay between assemblies for 1 round trip.

The power spectral density of the flux is therefore:

$$PSD(\bar{r}_1, \bar{r}_2, \omega) = PSD_{S_{\bar{r}_1} S_{\bar{r}_2}}(\omega) + \left|\alpha_{\bar{r}_2 \to \bar{r}_1} \alpha_{\bar{r}_1 \to \bar{r}_2}\right|^2 A(\bar{r}_1) A(\bar{r}_2)$$

$$\left|e^{-j\omega\tau}\right|^2 PSD_{S_{\bar{r}_1} S_{\bar{r}_2}}(\omega) + \alpha_{\bar{r}_2 \to \bar{r}_1} \alpha_{\bar{r}_1 \to \bar{r}_2} \left(A(\bar{r}_1) + A(\bar{r}_2)\right) e^{-j\omega\tau} PSD_{S_{\bar{r}_1} S_{\bar{r}_2}}(\omega)$$

or

$$PSD(\bar{r}_1, \bar{r}_2, \omega) = PSD_{S_{\bar{r}_1} S_{\bar{r}_2}}(\omega) \tag{1}$$

$$\times \left[1 + \left| \alpha_{\bar{r}_2 \to \bar{r}_1} \; \alpha_{\bar{r}_1 \to \bar{r}_2} \; A(\bar{r}_2) \right|^2 + 2 \, \alpha_{\bar{r}_2 \to \bar{r}_1} \, \alpha_{\bar{r}_1 \to \bar{r}_2} \cos \omega S \right]$$

We observe that the generation of a secondary neutron bunch will introduce an oscillation in the power spectra. If we assume in this example that the coupling transfer function and the time-delay distribution function are frequency-independent, then Equation (1) shows that the PSD will exhibit a dip which will recover at a slightly higher frequency.

To investigate this process, several papers on space-dependent effects, like heterogeneous effects, have been published. Hendrickson,[19] Albrecht and Seifritz[20-23] used the nodal approach of the coupled-core theory of Baldwin.[24] Hendrickson and Murphy[19] used the zero-power, two-core slab, thermal reactor model. This model has been extensively used in calculating transfer functions for Nerva[25-27] coupled-cores, and is based on a modified version of the inhour equations. In the nodal approach of Baldwin,[24] the point-reactor inhour equations were applied to each region of the reactor, and the neutronic interactions between these regions were described with an additional term added to the inhour equations, which described the coupling between those regions. Hendrickson and Murphy[19] obtained, after subtraction of the steady state equations, a set of coupled, ordinary differential equations, describing the neutronics behavior in the omega domain. They obtained an expression for the CPSD between two asymmetrical points of the reactor, and observed for

the UTR-10 coupled-core reactor (consisting of two slabs of thermal, heterogeneous, light water moderated and cooled cores, separated by 45.7 cm of graphite) heterogeneous effects at certain frequencies. Hendrickson pointed out that a most prominent characteristic of the CPSD for this system was the rapid loss and subsequent recovery of magnitude in the neighborhood of what he called the "sink" frequency. This behavior implied that there was very little correlation of the neutron density between the locations of the detectors at the sink frequency for which the CPSD was measured. No phase versus frequency values were given in their paper.

Using a transfer function approach between cores, for which point kinetics was implied, an expression for the coherence function (CHF) between "point" cores was setup by Albrecht and Seifritz.[20-23]

$$CHF(\omega) = \frac{K|S_j|^2 + K^*|S_i|^2}{|S_i|^2 + |K^2||S_j|^2}$$

where

$S_i(\omega)$: noise source for region "i"

$G(\omega)$: arbitrary nodal transfer function

$K(\omega)$: arbitrary coupling function

This expression implies that the frequency dependence of the coherence function in Albrecht's model is wholly dependent on the characteristics of the arbitrary transfer function $K(\omega)$. The coupling transfer functions were determined by using the modified inhour equations. The coupling coefficient and the time delay distribution function had to be adjusted

to the experiment. Albrecht and Seifritz applied this model to the TARK (Thermal Argonaut Reactor Karlsruhe) reactor. Their model configuration of the Argonaut reactor was a cylindrical fuel shell, where a few assemblies were symmetrically removed. The mathematical model for the space kinetics behavior of this configuration was set-up by "squeezing" this shell into two parallel slabs, separated by an equivalent distance, which was adjusted to give agreement between the calculated and the experimental sink frequency. Several time delay distribution functions were used in their calculations. They concluded that the "sink" frequency could be used to determine the mean time delay without the knowledge of the time delay distribution function itself.

The main drawbacks of the nodal models for PSD studies are:

1) calculations of the CPSD have usually to be done by adjusting the coupling coefficient to the experimental results. This is only practical for a simple geometry, such as a two core rectangular slab reactor.

2) The model did not take into account the finite dimensions of the cores. An arbitrary average distance between the cores was assumed.

3) The delay time of neutrons and the delay time distribution between cores have to be adjusted to the experiment.

4) The neutronics inside the fuel regions were not taken into account.

5) Only reactors exhibiting a very simple geometry can be studied.

6) No neutron energy structures were taken into account.

The delay in the frequency domain, as we well know, can be evaluated by $e^{-j\omega\delta_{j\to i}}$ where $\delta_{j\to i}$ is the time required for neutrons to go from core "j"

to core "i." Those delays have to be usually adjusted parametrically with the experimental PSD's. Although important parameters as the coupling coefficient could be evaluated for this simple geometry system by adjusting the theoretical calculations of the CPSD to the experimental obtained CPSD, it only can be practically done for simple systems, and assumptions.

Danofsky[28-31] and Ebert, Clement and Stacey[32-33] formulated the one-dimensional space-dependent PSD based on modal expansions. Although the application of modal expansions to one-dimensional space-dependent kinetics has been successful for simple geometries, its extension to actual configurations of reactors is practically impossible, because too many modes are required to describe actual configurations, especially when one has to extend the model to two- or three-dimensional geometries, to asymmetrical perturbances, and to multi-energy groups. The question of convergence of the modal solution must be considered, and the number of modes to be used for convergence is very much dependent on the geometry of the system and the perturbations introduced.

Carter and Danofsky[34] expanded the flux in a series of space-dependent functions, called shape functions, and time-dependent functions, called amplitude functions. A modal expansion based on variational calculus, with the functional suggested by Dougherty and Shen,[35] was applied to a one-dimensional multiregion case. A separate space-dependent calculation for all regions and for each source region was performed. In the limit, for infinite small source regions, one obtains the Green's function modes. The number of modes that one needs depends on how asymmetric the perturbation is. Having determined the space modes, the

amplitude functions can be determined based on a variational principle, as the one proposed by Dougherty and Shen. Carter and Danofsky have shown that the convergence of this variational method was superior to the Helmholtz modes.

Danofsky[28] extended this work and developed a model for the APSD and CPSD studies of an Argonaut type reactor. In his work, a modal expansion was used to describe the stochastic nature of the neutron flux. The PSD's were double series expansions of space modes. The APSD and the CPSD between two locations showed a sink of the PSD. It has to be noted that in the case of the APSD, the sink showed for a localized stochastic absorber, and in the case of the CPSD for space-dependent detector locations. The results were very sensitive to the convergence of the modal expansions.

Nagy and Danofsky[17] performed a parametric study for a one-dimensional, two-energy group representation of two infinite slabs of finite thickness. The coupling region distance was a variable, as well as the absorption and removal cross sections of the coupling media. The calculations were performed for a graphite coupling region and for a heavy water coupling medium. The sink frequency was found to be quite sensitive to the core spacing, decreasing with increasing distance. The sink frequency decreased with increasing removal and absorption cross-section of the coupling region. Ebert, Clement and Stacey[32,33] developed a one-dimensional model of the coherence function using modal expansions. They applied the model to the coupled-core Argonaut reactor and to the Solid Homogeneous Assembly (SHA) critical facility.[36] In the case of the

coupled-core Argonaut, the cylindrical fuel slabs were squeezed into two parallel infinite slabs of finite thickness. The distance between the slabs was varied so that the calculated first minimum of the PSD corresponded to the experimental determination performed by Albrecht and Seifritz.[20-23] The SHA reactor consisted of two rectangular fuel assemblies, 71.2 cm thick, separated by a 12.6 cm thick polyethylene coupling region. The agreement between experimental and predicted values of the amplitude of the coherence function of SHA was good. The multi-mode computations of the various phase angles were however very poor.

Applications

The need for better methods valid at higher frequencies has arisen from phenomena as the presence of resonances in the determination of PSD's. Resonances in the PSD were experimentally verified in reactors as TARK and UTR-10. Others were predicted using models which required many assumptions (one-dimensional configuration, one-energy group, and point-reactor approximations). Even for simple geometries, as the coupled-core Argonaut reactor, the minimum in the PSD could only be determined by varying reactor parameters, till predicted and experimental minima in the amplitude of the PSD's coincided.

Besides the inherent interest in the mathematical model and its numerical solution, there are many areas in which the multi-dimensional and multi-group PSD capability for highly heterogeneous systems are of interest. A short review follows.

1. Fast Modular Reactors[37-42]:

In order to minimize the sodium void coefficient of reactivity in

fast breeder reactors, several conceptual designs have gone to an approach where the core geometries have a large surface to volume ratio. One way to achieve this was to go to a reactor composed of modular coupled cores, in which the cylindrical core modules were surrounded each by an annular and axial blanket zones.

The advantage of such a system was a more negative sodium void coefficient and a better control over void effects in general. In addition, the spectral and spatial coupling between modules can be adjusted by changing the composition and the geometry of the fast core and the blanket.

The construction of a modular sodium-cooled fast breeder reactor would improve stability by preventing positive feedback due to sodium voiding. This is a serious problem in many current designs for large fast breeders.

In addition, in a fast reactor, the fast core section is surrounded by a blanket core, which in turn is surrounded by a reflector. The kinetic interactions between the different space points in the reactor are difficult to predict with existing methods, especially at the relatively high frequency end (50 cps and up) of the spectrum.

2. Combined Fast-Thermal Power Breeders[43-45]:

Avery[43] concluded that the coupling of a fast core and a thermal core within a reactor would enable the use of a beneficial characteristic of each core, i.e., the high breeding characteristics of the fast core and the long neutron lifetime of the thermal core causing longer time characteristics requirements of the control of the reactor system.

3. Thermal Reactors:

In large reactors, results of kinetic studies have shown that space effects can be important and must be included in the interpretation of reactor experiments.[46] In heterogeneous reactors, it has been shown that resonances exist in the PSD.

Multi-module or multi-core designs for reactor systems have been designed as the result of potentially improved economics and control.

4. Nuclear Rockers[25-27]:

In the now terminated nuclear rocket program, there were suggestions of coupling together several moderate thrust nuclear reactors, in order to obtain the desired thrust of the nuclear rocket, in a similar fashion as the conventional chemical rockets.

5. Fusion-Fission Hybrid Reactors:

In fusion-fission hybrids such as the one proposed by Leonard,[47] the fusion core was surrounded by a fission blanket. The reference blanket was composed of a lattice with niobium clad natural uranium fuel rods, one inch in diameter on a seven inch pitch, inside a graphite moderated thermal fission region. The presence of resonances in the PSD is likely for graphite distances of the order of 17.8 cm.

CHAPTER II

CURRENT METHODS

Nodal and Modal Methods

In order to give a general understanding of the various methods available, and the current state of the art, we will review some time-dependent mathematical models and methods available.

Time-dependent methods developed to date have indicated the need for more and more sophisticated models, both in the geometrical approximation of a reactor core (multi-dimensional heterogeneous), as in the accounting of the spectral dependency of the neutron waves (multi-group approximation).

The term coupled-cores theory circumscribes a great many different time-dependent models. Let us observe that the finite-difference approximation to the transport equation is a special case of coupled cores: indeed each mesh can be considered as a small sub-system, coupled with adjacent mesh points through leakage terms.

A number of investigations have developed time- or frequency-dependent models for the analysis of coupled core reactors and have found such reactors to be inherently less stable than single-core reactors. Coupled cores tend to be more sluggish than point reactors.

In the nodal approach, the reactor is subdivided into a finite number of small systems (nodes), neutronically coupled through reactivity

coupling coefficients, that take into account the neutron leakage to neighboring nodes.

The point-reactor model is a special case of the nodal approach, where the basic assumption is that the time- and space-dependent flux can be separated into a time-dependent function and into a space-dependent function: $\phi(x,t) = \psi(x) \cdot T(t)$.

A general discussion on the derivation of the point-reactor model was given by Henry.[48] The steady state adjoint to the transport equation is usually used as the weighting function. Since the point-reactor model assumes that the shape of the flux does not vary through a transient, it is not suitable for studying large size reactors.

The adiabatic model[49] is an extension of the point-reactor model where the spatial weighting function is being adjusted at different time intervals during a transient.

The subject of spatial and spectral coupling was first introduced in Avery's[50] analytical theory of the kinetic behavior of coupled cores. The different cores were usually defined as subregions of the reactor in which fission neutrons were born. Avery's equations describe the time change of the partial-fission neutron source S_{jk}, given the coupling coefficient k_{jk} and the partial neutron lifetime l_{jk}, which is the lifetime of neutrons which originate in core k and are expected to cause fission in core j. Avery's method can be considered as a "reactivity approach."

The derivation of Avery's equations, starting from the diffusion equation and its adjoint equation was later performed by Komata.[51]

Several methods[52] to calculate coupling coefficients between

interacting cores have been derived.

Cockrell and Perez[53] and Hopkins[54] derived a set of coupled-core kinetics equations in which an energy group structure has been retained. The set of equations obtained were similar to the monoenergetic derivation of Avery, but with a group structure. A major drawback of this approach is that the number of differential equations to be solved is $N^2G^2 + ND$, where N: number of coupled cores, G: number of energy groups, and D: number of delayed neutron groups.

If sufficient accuracy of the method is required in terms of the number of regions, a typical problem of N = 24, G = 2, and D = 6 would require the simultaneous solution of 1296 differential equations.

Shortly after Avery's work in 1958, Baldwin[24] derived a coupled reactor kinetics model for a loosely coupled-core reactor. In his model, the coupling term was introduced as an additional source to the diffusion equation, that was derived for each coupled core. This model can be categorized as the "effective source approach." All neutrons entering core j can be considered as another delayed neutron group, whose delay arises from a spatial effect. The delay time associated with the transfer of neutrons from one core to another is entered explicitly in Baldwin's approach.

In Baldwin's approach, the time-dependent equations were transformed into a steady state equation and a frequency-dependent equation (assuming small variations around the mean value), using the transformation:

$$n(\text{core},t) = n(\text{core}) + \nu(\text{core},\omega)\, e^{j\omega t}$$

Other models, where the coupling terms were introduced explicitly as an additional source to the diffusion or the inhour equations, were developed by Belleni-Morante,[55,56] Seale,[57] and others. In Schwalm's[58] approach, the set of equations were

$$\frac{dm_j^g(t)}{dt} = \frac{\beta_j(t) - \beta}{\ell_j} m_j^g(t) + \frac{1}{\ell_j} \sum_{k=1}^{N} \alpha_{jk} m_k^g(t - \tau_{jk}) + \sum_{d=1}^{D} \lambda_{jd} C_{jd}(t)$$

$$\frac{dC_{jd}(t)}{dt} = \sum_{g'} \frac{\beta_{jd}}{\ell_j} m_j^{g'}(t) - \lambda_{jd} C_{jd}(t)$$

Those equations are similar to Baldwin's equations but with a neutron group dependency. In Schwalm's work, each zone is surrounded by two neighboring zones, and they differ from the usual multi-group inhour equations through the presence of two source terms (which represent the leakage terms of the two adjacent zones) and which have a retardation time between them. Schwalm's approach required NG + ND equations. For a problem with N = 24, G = 2, and D = 6, the simultaneous solution of 192 differential equations were required.

The derivation of nodal equations from the Boltzmann equation were derived by several authors.[59-62] For a more complete review of nodal approximations we refer to review papers by Raju and Stone,[63] Köhler,[64] Dyos and Heck,[65] and others.

In concept, in the <u>modal</u> analysis method, the flux throughout the reactor is expanded into a truncated set of space functions (modes)

$H_k(\bar{r}E)$, with undetermined time-dependent coefficients $T_k(t)$, therefore:

$$\phi(\bar{r}Et) = \sum_{k=1}^{K} H_k(\bar{r}Et)\ T_k(t)$$

In the method of weighted residuals, $T_k(t)$ is obtained by substituting this expression into the time-dependent transport equation, followed by multiplying it by some appropriate weighting function, then integrating over all space, and requiring resulting weighted residuals to be zero.

Various types of space functions have been proposed. They can principally be subdivided into two main groups:

1. Natural modes[66-70] of the system, which are obtained by solving the steady state equations of the system, e.g., inhour modes, lambda modes, mu modes, and Green's function modes.

2. Arbitrarily chosen modes which are usually a selected set which are mutually orthogonal, e.g., Helmholtz modes.[71] A variant to the Helmholtz modes is the modified Helmholtz[72] modes

$$\phi^g(\bar{r}t) = \psi^g(\bar{r},t=0) + \sum_{k=1}^{K} H_k^g(\bar{r}t)\ T_k(t)$$

whose convergence is much improved over the conventional Helmholtz modes. In the cases where the higher modes are considerably excited, many expansion terms may be necessary to attain the required accuracy. Except for very simple geometries, the eigenfunctions (natural modes) are very difficult to calculate. If the space functions are arbitrarily chosen, many modes are usually needed, even for simple geometries.

The modal method is in general only adequate for simple

one-dimensional linear space-time kinetics problems. The method becomes undesirable for complex or multi-dimensional problems, and requires excessive computer time because a very large number of modes are needed for accurate results. For a complete review of modal approximations, we refer to review papers by Stacey.[73]

Space- and Energy-Dependent Transfer Function Methods

In concept, the transfer function method is used for studying the reactor dynamic characteristics by correlating the system response to a known input.

The experimental techniques for transfer function determination, using modulated sources, are numerous, and date back to the original papers of Weinberg and Schweinler.[74]

The nodal and modal methods have been extensively used for the calculation of transfer functions. Several calculational techniques were developed based on nodal, modal, and finite-difference approaches.

In Nomura's[75] work, the space-dependent transfer functions were calculated using modal expansions for one-dimensional geometries and two energy groups. Nomura pointed out that his method may also be utilized to determine subcriticality as well as fast and thermal neutron lifetimes.

In 1963, Seale[76] derived the space-dependent transfer functions starting from the time-dependent one group diffusion equations for coupled cores. For the i^{th} core, he wrote that

$$D_i \nabla^2 \phi_i(\bar{r}t) - \Sigma_{a_i} \phi_i(\bar{r}t) + S_i(\bar{r}t) = \frac{1}{v_i} \frac{\partial}{\partial t} \phi_i(\bar{r}t)$$

with

$$S_i(\bar{r}t) = (1-\beta)\,\nu\,\Sigma_{f_i}\,\Phi_i(\bar{r}t) + \sum_d \lambda_d\, C_{d_i}(\bar{r}t)$$

$$+ \sum_{\substack{j=1 \\ j\neq i}}^{M} \varepsilon_{j\to i}\,\Phi_j(\bar{r}, t-\tau_{j\to i})$$

Seale expanded the time-dependent variables as follows:

$$\Phi_i(\bar{r}t) = \Phi_i(\bar{r}) + \delta\Phi_i(\bar{r}s)\,e^{st}$$

$$C_{d_i}(\bar{r}t) = C_{d_i}(\bar{r}) + \delta C_{d_i}(\bar{r}s)\,e^{st}$$

$$s = j\omega$$

where $\delta\Phi_i(\bar{r}s)$ and $\delta C_{di}(\bar{r}s)$ were complex quantities. Inserting this into the i^{th} core diffusion equation, and subtracting the static equations, he obtained a set of coupled equations with complex variables. The time-dependent region coupling terms were taken into account through $\varepsilon_{j\to i}$. Over a region with the same characteristics, the heterogeneous terms were zero. The heterogeneous character of the problem was maintained through the coupling coefficients between the cores.

Loewe[77] applied the modal approximations to the two group neutron diffusion equations for a multi-region reactor, in order to obtain the transfer function for an arbitrarily located, localized oscillating absorber. The solution for the space-dependent transfer function was obtained using Fourier transforms, and expansions of the space-dependence in solutions to the Helmholtz modes. The analysis was done in one-dimension.

Loewe's analysis showed that there was no agreement between the space-dependent and the space-independent transfer function at relatively high frequencies, and this was attributed to space-dependent effects.

Kylstra and Uhrig[78] obtained the source transfer function for a single region, homogeneous reactor, using the modal expansion technique into the time-dependent diffusion equations with Fermi-age theory. Hopkins[54] derived a generalized multigroup point kinetics model, based on the inhour equations, and applied it to the Los Alamos Pulsed-Neutron Experiments.[79] In those experiments, oscillating deviations from the expected monotonic increase were observed in the rising portion of the passive-core neutron density response. This coupled core oscillatory behavior was largely due to delay-time effects. In pulsed neutrons experiments the phase shift interferences have also been demonstrated due to the presence of two kinds of thermal neutrons: those whose origin comes directly from the source with attenuation by absorption and leakage, and those originating from the slowing down of the fast fission neutrons which propagate faster. Under resonance condition this last contribution arrives just in phase. This is a phenomenon which arises from the non-separability of space and energy distribution of the neutrons. Perez, Booth, Denning, and Harley[80] have demonstrated this effect for an unreflected, prism-shaped, heavy water moderated, natural uranium, subcritical assembly, driven by a sinusoidally modulated source at the plane $z = 0$. Dips and resonances of the amplitude appeared due to the beating of the two waves, and they were a function of the lattice pitch. The calculations were based on the expansion of the flux response using Fourier coefficients.

Cohn, Johnson, and MacDonald[81] applied the Fourier transformation technique to the time-dependent diffusion equation, similar to the method of Seale. The frequency-dependent equations thus obtained were subsequently split into their real and imaginary parts, and were solved with the static two-dimensional diffusion code EXTERMINATOR-I.[82]

The model was applied to the heavy-water moderated and cooled Georgia Tech Research Reactor and to the NORA[83] reactor. The agreement between the calculations and the experimental values was good. However, convergence of the solution could be attained for two-dimensional geometries only at low frequencies. The convergence rate was also very slow even with the use of group rebalancing.

Poncelet[84] developed an approach for calculating the space dependent transfer functions with the added sophistication of the inclusion of feedback effects at power. The method described by Poncelet was based on two-group diffusion theory and is easily applicable to a multi-region reactor. The space-dependent reactor transfer function can be written in the form of a set of non-homogeneous, time-independent coupled diffusion type of equations.

Bridges, Clement, and Renier[85] extended the zero-power model of Cohn, Johnson, and MacDonald with the inclusion of temperature feedback. The equations derived were similar to the ones developed by Poncelet.

It has to be observed that within the linear approximation, the information about the complete set of modes is automatically obtained in the methods of Cohn, Johnson, and MacDonald,[81] Poncelet,[84] and Bridges, Clement, and Renier.[85] An extension to those methods will be

used as basis of the theoretical model presented in this work. For additional methods we refer to review papers by Hsu and Mulcahey[86] and the proceedings of several topical conferences.[87-89]

CHAPTER III

THEORETICAL APPROACH

Fundamental Relations

The system considered consists of a nuclear reactor volume in which are embedded two or more independent detectors of neutrons. The following relations are fundamental definitions and formulae used in noise analysis and transfer function techniques.

Correlation Function (CF) between the Responses of Detector 1 (det1) and Detector 2 (det2)

$$CF(\bar{r}_{det_1}, E_1, \bar{r}_{det_2}, E_2, \tau) = \lim_{T\to\infty} \frac{1}{2T} \int_{-T}^{T} D_1(\bar{r}_{det_1}, E_1, t) \cdot D_2(\bar{r}_{det_2}, E_2, t-\tau)\, dt \tag{2}$$

where

$D_1(\bar{r}_{det1} E_1 t)$ = response of detector 1 to the neutron (or gamma) flux of energy, E_1, at detector position, $\bar{r}_{det1}$, at time, t

$D_2(\bar{r}_{det2} E_2 t)$ = response of detector 2 to the neutron (or gamma) flux of energy, E_2, at detector position, $\bar{r}_{det2}$, at time, t

t = time

τ = lag time

$\bar{r}$ = three-dimensional space coordinate

Power Spectral Density (PSD) between the Responses of Detector 1 (det1) and Detector 2 (det2)

Fourier transformation of the correlation function gives:

$$PSD(\bar{r}_{det1}, E_1, \bar{r}_{det2}, E_2, \omega) = \lim_{T\to\infty} \int_{-T}^{T} CF(\bar{r}_{det1}, E_1, \bar{r}_{det2}, E_2, \tau)\, e^{-j\omega\tau}\, d\tau \quad (3)$$

where

ω = frequency

Auto Power Spectral Density (APSD) of the Response of Detector 1 (det1)

If $\bar{r}_{det1} \equiv \bar{r}_{det2}$ and $E_1 \equiv E_2$, i.e., both detector positions coincide and the detectors have the same neutron energy sensitivity,

$$APSD(\bar{r}_{det1}, E_1, \omega) = PSD(\bar{r}_{det1}, E_1, \bar{r}_{det1}, E_1, \omega) \quad (4)$$

Cross Power Spectral Density (CPSD)

If $\bar{r}_{det1} \neq \bar{r}_{det2}$ and/or $E_1 \neq E_2$

$$CPSD(\bar{r}_{det1}, E_1, \bar{r}_{det2}, E_2, \omega) = PSD(\bar{r}_{det1}, E_1, \bar{r}_{det2}, E_2, \omega)$$

Normalized Cross-Power Spectral Density (NCPSD) or Coherence Function (CHF)

$$NCPSD(\bar{r}_{det1}, E_1, \bar{r}_{det2}, E_2, \omega) = \frac{CPSD(\bar{r}_{det1}, E_1, \bar{r}_{det2}, E_2, \omega)}{\sqrt{APSD(\bar{r}_{det1}, E_1, \omega) \cdot APSD(\bar{r}_{det2}, E_2, \omega)}} \quad (5)$$

Due to the stochastic nature of the different reactions in a reactor (fission, absorption, diffusion, scattering (γ,n), $(n,2n)$, etc.), the neutron flux is varying around an average value, even if there is no externally controlled driving force.

This stochastic nature of the neutron flux can be thought of as being introduced by an inherent driving force. The source of those stochastic fluctuations in a reactor can be subdivided into two parts[90,91]:

1. The single or direct source, generated by Poissonian random reactions in the reactor, e.g., neutron absorption, etc.

2. The binary source, which comes from branching processes in the reactor, e.g., fission neutrons from induced fission and delayed neutrons. Other branching processes of minor importance are the $(n,2n)$, $(n,n'\gamma)$, (γ,n), etc. reactions. The (n,γ,n) reaction in a D_2O moderated reactor can be an important contribution to the binary stochastic source, especially at low power levels and high burnup levels of the fuel.

Saito[91] has shown that, if the fluctuations are of a Markoffian nature, the spectral matrix $\phi_{ss}(\omega)$ of the binary source is white for a "zero-power" reactor. Although the nuclear chain reactions are of a stochastic nature, their effect inside a reactor can be described by the Boltzmann equation.

Assume that we have a reaction of type z, at $\bar{r}_z$, which introduces one, two, or several neutrons, n_1, n_2, . . ., at positions $\bar{r}_{n1}$, $\bar{r}_{n2}$, . . . in a chain. Those neutrons introduce other fission chains.

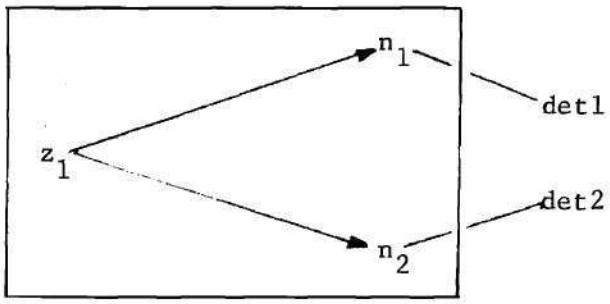

The power spectral density between detector 1 (det1) and detector 2 (det2) is

$$PSD(\bar{r}_{det1}, \bar{r}_{det2}, \omega) = PSD_{\sum_i (z_i \to det1) \cdot \sum_j (z_j \to det2)}(\omega)$$

$$= PSD_{\sum_i (z_i \to \sum_k n_k \to det1) \cdot \sum_j (z_j \to \sum_\ell n_\ell \to det2)}(\omega)$$

$$= PSD_{\left[\sum_i (z_i \to n_i \to det1) + \sum_i (z_i \to \sum_{k \neq i} n_k \to det1)\right] \cdot \left[\sum_j (z_j \to n_j \to det2) + \sum_j (z_j \to \sum_{\ell \neq j} n_\ell \to det2)\right]}$$

$$PSD(\bar{r}_{det1}, \bar{r}_{det2}, \omega) = \tag{6}$$

$$\left.\begin{aligned} & PSD_{\sum_i (z_i \to n_i \to det1)(z_i \to n_i \to det2)} \\ & + PSD_{\sum_i (z_i \to n_i \to det1)(z_i \to \sum_{\ell \neq i} n_\ell \to det2)} \\ & + PSD_{\sum_i (z_i \to \sum_{k \neq i} n_k \to det1)(z_i \to n_i \to det2)} \end{aligned}\right] \text{correlated terms}$$

(continued)

$$
\left.
\begin{aligned}
&+\mathrm{PSD}\sum_i (z_i \to m_i \to \mathrm{det}_1)\cdot\sum_{j\neq i}(z_j \to m_j \to \mathrm{det}_2)\\
&+\mathrm{PSD}\sum_i (z_i \to m_i \to \mathrm{det}_1)\cdot\sum_{j\neq i}(z_j \to \sum_{l\neq j} m_l \to \mathrm{det}_2)\\
&+\mathrm{PSD}\sum_i (z_i \to \sum_{k\neq i} m_k \to \mathrm{det}_1)\cdot\sum_{j\neq i}(z_j \to \sum_{l\neq j} m_l \to \mathrm{det}_2)
\end{aligned}
\right\}
\begin{array}{l}\text{un-}\\ \text{correlated}\\ \text{terms}\end{array}
$$

Neutron detectors can be classified into two categories:

1. Neutron absorption detectors--this type of detector cuts off the direct correlation of a neutron with neutrons in the future.

2. Fission or proton recoil neutron detectors--this type of detector keeps the binary source nature of a chain, because it does not remove any neutron from this chain.

In equation (6), the second and third terms are zero for detectors of the neutron absorption type. They are non-zero for detectors of the fission or proton recoil types. Neutrons emitted by those detectors contribute to the fission chains. Those terms represent the correlation introduced by the presence of one detector upon the other.

The fourth, fifth, and sixth terms represent the uncorrelated parts in the PSD. They are zero for cross-power spectra, and non-zero for auto-power spectra.

The first term represents the effect of the binary source (branching process). From equation (2) it can be concluded that the CPSD eliminates the contribution to the PSD of the single noise source. If there is no branching process, the PSD between two detectors would therefore be zero, while it has been shown[91] that the APSD gives a white spectrum if there is no branching process.

Saito[91] has shown that the binary noise spectrum can be rewritten as:

$$\Phi_{m_i m_i}(\bar{r}_{m_i}, E^{\hat{i}}_{m_i}, \omega) = \tag{7}$$

$$2\,\chi(\bar{r}_{m_i}, E^{\hat{i}}_{m_i}) \sum_j \frac{1}{2}\,\overline{\nu(\nu-1)}_p\, \Sigma_f(\bar{r}_{m_i}, E^j_{m_i})\, \phi(\bar{r}_{m_i}, E^j_{m_i})$$

where $\chi(E^i_{n_i})$ = neutron fission spectrum for energy $E^i_{n_i}$ at position $\bar{r}_{n_i}$

ν = number of fission neutrons per fissioning event

$\frac{1}{2}\,\overline{\nu(\nu-1)}$ = average number of prompt neutron pairs per fission

We will assume that we have neutron capture detectors, or fission neutron detectors with a sufficiently small Σ_f so that the presence of one detector will not affect the signal of another neutron detector.

The CPSD and APSD in a reactor, due to the binary stochastic source (inherent source) are

$$CPSD(\bar{r}_{det_1}, E^{det_1}, \bar{r}_{det_2}, E^{det_2}, \omega) = \tag{8}$$

$$\sum_i \sum_g T(\bar{r}_i E^g \rightarrow \bar{r}_{det_1} E^{det_1}, \omega)^* \cdot T(\bar{r}_i E^g \rightarrow \bar{r}_{det_2} E^{det_2}, \omega)$$

$$\chi^g(\bar{r}_i) \sum_{g'} \overline{\nu(\nu-1)}\, \Sigma_f^{g'}(\bar{r}_i)\, \phi^{g'}(\bar{r}_i)\, \Delta V_i$$

$$APSD(\bar{r}_{det_1}, E^{det_1}, \omega) = UNC(\bar{r}_{det_1}, E^{det_1}, \omega) \tag{9}$$

$$+ \sum_{\hat{i}} \sum_g \left| T(\bar{r}_i E^g \rightarrow \bar{r}_{det_1} E^{det_1}, \omega) \right|^2 \chi^g(\bar{r}_i) \sum_{g'} \overline{\nu(\nu-1)}\, \Sigma_f^{g'}(\bar{r}_i)\, \phi^{g'}(\bar{r}_i)\, \Delta V_i$$

where

$T(\bar{r}_i E^g \rightarrow \bar{r}_{det1} E^{det1} \omega)$ = space-, energy-, and frequency-dependent transfer function from position $\bar{r}_i$, group "g" energy, E^g, to detector location, $\bar{r}_{det1}$, group g_{det1}, energy E^{det1} at frequency ω

$T(\bar{r}_i E^g \rightarrow \bar{r}_{det1} E^{det1} \omega)^*$ = complex conjugate

ΔV_i = elementary volume of the reactor at position i

$X^g(\bar{r}_i)$ = fission spectrum at energy g, position $\bar{r}_i$

$\Sigma_f^{g'}(\bar{r}_i)$ = fission cross section at energy g', position $\bar{r}_i$

$\phi^{g'}(\bar{r}_i)$ = time-independent neutron flux at energy g', position $\bar{r}_i$

$UNC(\bar{r}_{det1} E^{det1} \omega)$ = uncorrelated part of the auto-power spectrum at detector position $\bar{r}_{det1}$, neutron energy E^{det1}, and frequency ω.

Note that the PSD between the output of neutron detectors, located in a neutronic system, is not only dependent on the neutron flux, but is also dependent on the transfer function of the detector channels.

If the PSD is determined between the responses of two pairs of two neutron detectors, namely a pair composed of detector 1 (det1) and detector 3 (det3), and a pair composed of detector 2 (det2) and detector 4 (det4) (assuming that the detectors of each pair are located in the same reactor location), then the APSD of each detector pair is obtained from the expressions:

$$APSD_{det_1}(\bar{r}_{det_1}, E^{det_1}, \omega) = CPSD_{det_1 det_3}(\bar{r}_{det_1}, E^{det_1}, \bar{r}_{det_1}, E^{det_1}, \omega)$$

$$APSD_{det_2}(\bar{r}_{det_2}, E^{det_2}, \omega) = CPSD_{det_2 det_4}(\bar{r}_{det_2}, E^{det_2}, \bar{r}_{det_2}, E^{det_2}, \omega)$$

In this case we also have

$$UNC_{det_1}(\bar{r}_{det_1}, E^{det_1}, \omega) \equiv 0 \qquad UNC_{det_2}(\bar{r}_{det_2}, E^{det_2}, \omega) \equiv 0$$

for all frequencies.

From equations (5), (8), and (9) we can, therefore, conclude that the transfer function of the detector channels is not needed only in the case of a four-detector experiment and of a coherence function (CHF) determination.

For relative PSD (between the space- and energy-dependent fluxes) measurements, only the relative frequency responses of the detector channels are needed. The usual procedure followed to determine the transfer function of the detector channels is based on the fact that the APSD of the current of the neutron chamber is constant over the frequency range investigated, when the detector is exposed to a radioactive neutron source in a non-multiplying medium.

Time- and Space-Dependent Approximation of the Transport Equation

The forward space-, time-, and energy-dependent P_1 equations, which will be taken as the basis of the mathematical approach, are derived from the Boltzmann equation:

$$\frac{1}{v(\bar{r}E)} \frac{\partial}{\partial t} \phi(\bar{r}E\Omega t) + \Omega \cdot \nabla \phi(\bar{r}E\Omega t) + \Sigma_t(\bar{r}Et)\, \phi(\bar{r}E\Omega t) \qquad (10)$$

$$= S(\bar{r}E\Omega t) + \int dE' \int d\Omega' \, \Sigma_s(\bar{r}, E'\Omega' \rightarrow E\Omega, t)\, \phi(\bar{r}E'\Omega' t)$$

With the use of the Legendre expansion, the Boltzmann equation can be

reduced to the time-, energy-, and space-dependent P_1 equations.[3,93]

$$-\nabla\Phi_1(\bar{r}Et) - \Sigma_t(\bar{r}Et)\,\Phi_0(\bar{r}Et) + \int \Sigma_{s_0}(\bar{r}, E'\rightarrow E, t)\,\Phi_0(\bar{r}E't)\,dE' \quad (11)$$

$$+ S_0(\bar{r}Et) = \frac{1}{v(\bar{r}E)}\,\frac{\partial}{\partial t}\,\phi_0(\bar{r}Et)$$

$$\nabla\Phi_0(\bar{r}Et) + 3\,\Sigma_t(\bar{r}Et)\,\Phi_1(\bar{r}Et) - 3\int \Sigma_{s_1}(\bar{r}, E'\rightarrow E, t)\,\Phi_1(\bar{r}E't)\,dE' \quad (12)$$

$$+ S_1(\bar{r}Et) = -\frac{3}{v(\bar{r}E)}\,\frac{\partial}{\partial t}\,\Phi_1(\bar{r}Et)$$

$$\beta_d(\bar{r})\int \nu\Sigma_f(\bar{r}E't)\,\Phi_0(\bar{r}E't)\,dE' - \lambda_d(\bar{r})\,C_d(\bar{r}Et) = \frac{\partial}{\partial t}C_d(\bar{r}Et) \quad (13)$$

$$S_0(\bar{r}Et) = S_0(\bar{r}Et)^{\text{prompt}} + S_0(\bar{r}Et)^{\text{delayed}} + S_0(\bar{r}Et)^{\text{external}} \quad (14)$$

Assuming that the prompt and delayed fission sources are isotropic, we can write

$$S_0(\bar{r}Et)^{\text{prompt}} = \chi(\bar{r}Et)(1-\beta(\bar{r}))\int \nu\Sigma_f(\bar{r}E't)\,\Phi_0(\bar{r}E't)\,dE' \quad (15)$$

$$S_0(\bar{r}Et)^{\text{delayed}} = \sum_d \lambda_d(\bar{r})\,\chi_d(\bar{r}Et)\,C_d(\bar{r}Et) \quad (16)$$

$$S_1(\bar{r}Et) = 0$$

where

$\phi_0(\bar{r}Et)$ = isotropic component of the directional flux

$\phi_1(\bar{r}Et)$ = anisotropic component of the directional flux

To develop the multigroup equations, the isotropic and anisotropic components of the flux are written as

$$\Phi_0(\bar{r}Et) = \Phi_0^g(\bar{r}t)\ \psi_0^g(\bar{r}Et) \quad \text{for } E_g < E \leq E_{g+1}$$

$$\Phi_1(\bar{r}Et) = \Phi_1^g(\bar{r}t)\ \psi_1^g(\bar{r}Et) \quad \text{for } E_g < E \leq E_{g+1}$$

Stacey[92] has shown that the use of spatial- and time-dependent weighting functions in defining group-averaged nuclear constants introduces several additional terms into the P_1 equations. The importance of this has not been established in our study. We will neglect those terms and assume that:

$$\Phi_0(\bar{r}Et) = \Phi_0^g(\bar{r}t)\ \delta(E_g < E \leq E_{g+1})$$

$$\Phi_1(\bar{r}Et) = \Phi_1^g(\bar{r}t)\ \delta(E_g < E \leq E_{g+1})$$

Then the forward P_1 equations (11-16) become

$$-\nabla\Phi_1^g(\bar{r}t) - \Sigma_t^g(\bar{r}t)\,\Phi_0^g(\bar{r}t) + \sum_{g'}\Sigma_{s_0}^{g'\to g}(\bar{r}t)\ \Phi_0^{g'}(\bar{r}t) \tag{17}$$

$$+ S_0^g(\bar{r}t) = \frac{1}{v^g(\bar{r})}\frac{\partial}{\partial t}\Phi_0^g(\bar{r}t)$$

$$\nabla\Phi_0^g(\bar{r}t) + 3\Sigma_t^g(\bar{r}t)\,\Phi_1^g(\bar{r}t) - 3\sum_{g'}\Sigma_{s_1}^{g'\to g}(\bar{r}t)\,\Phi_1^{g'}(\bar{r}t) \tag{18}$$

$$= -\frac{3}{v^g(\bar{r})}\frac{\partial}{\partial t}\Phi_1^g(\bar{r}t)$$

$$\beta_d(\bar{r}) \sum_{g'} \nu \Sigma_f^{g'}(\bar{r}t)\, \phi_o^{g'}(\bar{r}t) - \lambda_d(\bar{r})\, C_d(\bar{r}t) = \frac{\partial}{\partial t} C_d(\bar{r}t) \tag{19}$$

$$S_o^g(\bar{r}t) = S_o^g(\bar{r}t)^{prompt} + S_o^g(\bar{r}t)^{delayed} + S_o^g(\bar{r}t)^{external}$$

$$S_o^g(\bar{r}t)^{prompt} = \chi^g (1-\beta(\bar{r})) \sum_{g'} \nu \Sigma_f^{g'}(\bar{r}t)\, \phi_o^{g'}(\bar{r}t) \tag{20}$$

$$S_o^g(\bar{r}t)^{delayed} = \sum_d \lambda_d\, \chi_d^g(\bar{r}t)\, C_d(\bar{r}t) \tag{21}$$

It must be noted that the anisotropy of the scattering cross section, $\Sigma_{S_1}^{g'\to g}(\bar{r}t)$, is important only to the extent that the flux is anisotropic. As far as the scattering is concerned, the contribution due to $\Sigma_{S_\ell}^{g'\to g}(\bar{r}t)$ is only important as far as the flux contains a significant component of the same order. The elements of the group transfer matrix, of order ℓ, for scattering from group g' to g, are defined as:

$$\Sigma_{S_\ell}^{g'\to g} = \frac{\int_{g'} dE' \int_{g} dE\; w(E)\, \Sigma_{S_\ell}(E'\to E)}{\int_{g} w(E)\, dE}$$

Those group elements can be obtained by the use of codes such as SUPERTOG[94] or AMPX.[95] As stated in SUPERTOG, the energies at which the scattering is isotropic in the center of mass system can be obtained as follows:

$$\sum_{g'} \sigma_0^{g \to g'} = \overline{\sigma^{g \to g}}$$

$$\sum_{g'} \sigma_1^{g \to g'} = \overline{\mu \sigma^{g \to g}} = \frac{2}{3A} \sigma_t$$

where g' are all the sink energy groups to energy group g

The generation of the cross section in Chapter V shows that the scattering is not isotropic in the center of mass system for energies in the fast region. The reduction of the time-dependent Boltzmann transport equation to the time-dependent diffusion equation through the P_1 approximation requires the following assumptions:

1. Neglect $\partial \phi_1(xt)/\partial t$ (time derivative of the anisotropic flux)
2. Neglect $\partial S(xt)/\partial t$ (time-dependent sources, e.g., fission, delayed, scattering, external)
3. Isotropic sources
4. Neglect P_2 and higher scattering order.

Megreblian and Holmes[3] have shown that, assuming a time-independent source, and retaining $\partial \phi_1(xt)/\partial t$, for a one-energy group, homogeneous-material case, the P_1 approximation to the transport equation is the well known Telegraphist equation

$$\frac{3D}{v^2} \frac{\partial^2}{\partial t^2} \phi(xt) + \frac{1}{v}(1 + 3D\Sigma_a) \frac{\partial}{\partial t} \phi(xt) \tag{22}$$

$$= D\nabla^2 \phi(xt) - \Sigma_a \phi(xt) + S(x)$$

where

$$D = \frac{1}{3(\Sigma_t - \Sigma_S \mu_0)} = \frac{1}{3\Sigma_{tr}}$$

In the case of a time-dependent source, it can be shown[96] that for a one-energy group, homogeneous-material case, the P_1 equations become

$$\frac{3D}{v^2}\frac{\partial^2}{\partial t^2}\phi(xt) + \frac{1}{v}(1+3D\Sigma_a)\frac{\partial}{\partial t}\phi(xt) \tag{23}$$

$$= D\nabla^2\phi(xt) - \Sigma_a\phi(xt) + S(xt) + \frac{3D}{v}\frac{\partial}{\partial t}S(xt)$$

For the special case, for which the following assumption is made

$$\sum_{g'}\Sigma_{s_1}^{g'\to g}(x)\,\phi_1^{g'}(xt) = \sum_{g'}\Sigma_{s_1}^{g\to g'}(x)\,\phi_1^{g}(xt)$$

for any g and g', except g = g'

where

$\Sigma_{s_1}^{g'\to g}$ = anisotropic scattering from energy group g' to g

$\phi_1^{g'}(xt)$ = anisotropic part of the flux at energy group g'

We can rewrite equation (23) in energy-group form as follows:

$$\frac{3D^g}{v^{g2}}\frac{\partial^2}{\partial t^2}\phi^g(xt) + \frac{1}{v^g}(1+3D^g\Sigma_a^g)\frac{\partial}{\partial t}\phi^g(xt) \tag{24}$$

$$= D^g\nabla^2\phi^g(xt) - \Sigma_a^g\phi^g(xt) + S^g(xt) + \frac{3D^g}{v^g}\frac{\partial}{\partial t}S^g(xt)$$

where $$S^g(xt) = \chi^g\sum_{g'}\nu\Sigma_f^{g'}\phi^{g'}(xt) + \sum_{g'}\Sigma_{s_0}^{g'\to g}\phi^{g'}(xt)$$

$$+ S^g(xt)^{\text{delayed}} + S^g(xt)^{\text{external}}$$

Comparing this with the time-dependent diffusion equation,

$$\frac{1}{v^g}\frac{\partial}{\partial t}\phi^g(xt) = D^g\nabla^2\phi^g(xt) - \Sigma_a^g\phi^g(xt) + S^g(xt) \qquad (25)$$

reveals several differences:

1. an additional term involving the second time derivative of the flux, $\partial^2\phi^g(xt)/\partial t^2$

2. the alteration of the coefficient of the first derivative of the flux, $\partial\phi^g(xt)/\partial t$

3. additional terms due to the first derivative of the source introducing terms, which are dependent on the first derivative of the flux of other neutron energy groups through the source terms.

It must be observed that the coefficient $3D^g/v^g$ appears in all the terms in which a difference exists between diffusion and P_1 approximations. We can rewrite this coefficient as

$$\frac{3D^g}{v^g} = \frac{1}{v^g\Sigma_{tr}^g} = \tau_o^g \qquad (26)$$

which can be considered as the mean neutron transport time of neutrons at energy group g. The physical significance of τ_0^g is that it describes the time delay between the cause and effect at two different space points in the reactor.

It is a well known property that an instantaneous source immediately produces a perturbance at all points in space for the diffusion approximation, since the P_1 equation reduces to the diffusion equation for $\tau_0^g \equiv 0$. For the diffusion approximation, the propagation velocity of the disturb-

ance is infinite. Using the P_1 approximation, it can be shown[3,96] that the P_1 approximation exhibits the phenomenon of retardation due to the introduction of the second derivative in time of the flux. This second order derivative in time gives a wavelike behavior to the flux, while the first order derivatives in time give a residual disturbance. Mortensen and Smith[97] have shown that the P_1 approximation is more accurate than the diffusion approximation for high frequency waves. In the derivations of the P_1 equations for heterogeneous composition systems, it will be shown that several additional leakage terms are present which are dependent on $3D^g/v^g$. In order to follow the different terms of the P_1 equations, we rewrite equations (17) and (18) as follows:

$$-\alpha_1 \nabla \phi_1^g(\bar{r}t) - \alpha_2 \Sigma_t^g(\bar{r}t)\, \phi_0^g(\bar{r}t) + \alpha_3 \sum_{g'} \Sigma_{s_0}^{g' \to g}(\bar{r}t)\, \phi_0^{g'}(\bar{r}t) \tag{27}$$

$$+ \alpha_4 S_0^g(\bar{r}t) = \alpha_5 \frac{1}{v^g(\bar{r})} \frac{\partial}{\partial t} \phi_0^g(\bar{r}t)$$

$$\varepsilon_1 \nabla \phi_0^g(\bar{r}t) + 3\varepsilon_2 \Sigma_t^g(\bar{r}t)\, \phi_1^g(\bar{r}t) - 3\varepsilon_3 \sum_{g'} \Sigma_{s_1}^{g' \to g}(\bar{r}t)\, \phi_1^{g'}(\bar{r}t) \tag{28}$$

$$= -\varepsilon_4 \frac{3}{v^g(\bar{r})} \frac{\partial}{\partial t} \phi_1^g(\bar{r}t)$$

Stochastic processes introduce small variations of the flux around the mean. Therefore, we can write

$$\phi_0^g(\bar{r}t) = \phi_0^g(\bar{r}) + \delta\phi_0^g(\bar{r}t)$$

$$\phi_1^g(\bar{r}t) = \phi_1^g(\bar{r}) + \delta\phi_1^g(\bar{r}t)$$

Switching from the time domain to the frequency domain with a Fourier transformation, and using a method similar to that of Mortensen[97] and others[24,81,84,85]:

$$\Phi_0^g(\bar{r}t) = \Phi_0^g(\bar{r}) + \delta\Phi_0^g(\bar{r}\omega)\, e^{j\omega t}$$

$$\Phi_1^g(\bar{r}t) = \Phi_1^g(\bar{r}) + \delta\Phi_1^g(\bar{r}\omega)\, e^{j\omega t}$$

where $\delta\phi_0^g(\bar{r}\omega)$ and $\delta\phi_1^g(\bar{r}\omega)$ are complex variables.
They can be represented by:

$$\delta\Phi_0^g(\bar{r}\omega) = \delta\Phi_0^{Rg}(\bar{r}\omega) + j\,\delta\Phi_0^{Ig}(\bar{r}\omega)$$

$$\delta\Phi_1^g(\bar{r}\omega) = \delta\Phi_1^{Rg}(\bar{r}\omega) + j\,\delta\Phi_1^{Ig}(\bar{r}\omega)$$

After splitting the P_1 equations into their steady and stochastic parts, we obtain:

$$\varepsilon_1 \nabla\Phi_0^g(\bar{r}) + 3\varepsilon_2 \Sigma_t^g(\bar{r})\,\Phi_1^g(\bar{r}) \qquad (29)$$

$$- 3\varepsilon_3 \sum_{g'} \Sigma_{s_1}^{g'\to g}(\bar{r})\,\Phi_1^{g'}(\bar{r}) = 0$$

$$-\alpha_1 \nabla\Phi_1^g(\bar{r}) - \alpha_2 \Sigma_t^g(\bar{r})\,\Phi_0^g(\bar{r}) + \alpha_3 \sum_{g'} \Sigma_{s_0}^{g'\to g}(\bar{r})\,\Phi_0^{g'}(\bar{r}) \qquad (30)$$

$$+ \alpha_4 S_0^g(\bar{r}) = 0$$

and

$$\varepsilon_1 \nabla \delta\phi_0^g(\bar{r}\omega) + 3\varepsilon_2 \Sigma_t^g(\bar{r})\, \delta\phi_1^g(\bar{r}\omega) + 3\varepsilon_2 \phi_1^g(\bar{r})\, \delta\Sigma_t^g(\bar{r}\omega) \qquad (31)$$

$$-3\varepsilon_3 \sum_{g'} \Sigma_{s_1}^{g'\to g}(\bar{r})\, \delta\phi_1^{g'}(\bar{r}\omega) - 3\varepsilon_3 \sum_{g'} \phi_1^{g'}(\bar{r})\, \delta\Sigma_{s_1}^{g'\to g}(\bar{r}\omega)$$

$$= -\varepsilon_4 \frac{3}{v^g(\bar{r})} j\omega\, \delta\phi_1^g(\bar{r}\omega)$$

$$-\alpha_1 \nabla \delta\phi_1^g(\bar{r}\omega) - \alpha_2 \Sigma_t^g(\bar{r})\, \delta\phi_0^g(\bar{r}\omega) - \alpha_2\, \delta\Sigma_t^g(\bar{r}\omega)\, \phi_0^g(\bar{r}) \qquad (32)$$

$$+\alpha_3 \sum_{g'} \Sigma_{s_0}^{g'\to g}(\bar{r})\, \delta\phi_0^{g'}(\bar{r}\omega) + \alpha_3 \sum_{g'} \phi_0^{g'}(\bar{r})\, \delta\Sigma_{s_0}^{g'\to g}(\bar{r}\omega)$$

$$+\alpha_4\, \delta S_0^g(\bar{r}\omega) = \alpha_5 \frac{1}{v^g(\bar{r})} j\omega\, \delta\phi_0^g(\bar{r}\omega)$$

In contrast to the energy-independent case, these group-dependent equations do not yield Fick's law immediately, because of the presence of $\Sigma_{S_1}^{g'\to g}(\bar{r}t)$. In the time-independent case the usual assumptions are[98]:

$$\Sigma_{s_0}(\bar{r}E')\,\phi_0(\bar{r}E') = \Sigma_{s_0}(\bar{r}E)\,\phi_0(\bar{r}E) + (E'-E)\frac{\partial}{\partial E}\left[\Sigma_{s_0}(\bar{r}E)\,\phi_0(\bar{r}E)\right]$$

$$\Sigma_{s_1}(\bar{r}E')\,\phi_1(\bar{r}E') = \Sigma_{s_1}(\bar{r}E)\,\phi_1(\bar{r}E)$$

or

$$\int dE'\, \Sigma_{s_1}(\bar{r}, E'\to E)\,\phi_1(\bar{r}E') = \int dE'\, \Sigma_{s_1}(\bar{r}, E\to E')\,\phi_1(\bar{r}E)$$

It has been shown that, in order that those approximations hold, we require that:

1. Many collisions must occur during moderation, i.e., the moderating medium must be a heavy mass material. This condition is certainly not fulfilled in water.

2. The cross section can change only a little in one energy group interval.

We will develop the time-dependent equations based on two different approaches, depending on the following approximations:

$$1) \quad \int dE' \, \Sigma_{s_1}(\bar{r}, E' \to E) \, \phi_1(\bar{r} E' t) = \int dE' \, \Sigma_{s_1}(\bar{r}, E \to E') \, \phi_1(\bar{r} E t) \tag{33}$$

The integral is therefore independent of energy. In neutron energy-group form we have that

$$\sum_{g'} \Sigma_{s_1}^{g' \to g}(\bar{r}) \, \phi_1^{g'}(\bar{r}t) = \sum_{g'} \Sigma_{s_1}^{g \to g'}(\bar{r}) \, \phi_1^{g}(\bar{r}t) \tag{34}$$

We also have that

$$\sum_{g'} \Sigma_{s_1}^{g \to g'}(\bar{r}) = \Sigma_{s_1}^{g}(\bar{r})$$

where the g' are the sink groups for g.

We therefore have

$$\sum_{g'} \Sigma_{s_1}^{g' \to g}(\bar{r}) \, \phi_1^{g'}(\bar{r}t) = \Sigma_{s_1}^{g}(\bar{r}) \, \phi_1^{g}(\bar{r}t)$$

2) Approximation based on the assumption that $|\Sigma_{S_1}^{g'\to g}|^2 \ll |\Sigma_t^g|^2$ for any g' and g, except g = g'

If we apply assumption 1 to the steady-state P_1 equations, therefore assuming:

$$\sum_{g'} \Sigma_{S_1}^{g'\to g}(\bar{r})\,\phi_1^{g'}(\bar{r}) = \sum_{g'} \Sigma_{S_1}^{g\to g'}(\bar{r})\,\phi_1^{g}(\bar{r}) = \Sigma_{S_1}^{g}(\bar{r})\,\phi_1^{g}(\bar{r})$$

we obtain

$$\phi_1^g(\bar{r}) = -D^g(\bar{r})\,\varepsilon_1\,\nabla\phi_0^g(\bar{r})$$

where

$$D^g(\bar{r}) = \frac{1}{3\left[\varepsilon_2\Sigma_t^g(\bar{r}) - \varepsilon_3 \sum_{g'} \Sigma_{S_1}^{g\to g'}(\bar{r})\right]}$$

For the frequency-dependent equation, we get

$$\mathcal{F}\phi_1^g(\bar{r}\omega) =$$

$$-\frac{\varepsilon_1 D^g(\bar{r})}{1+\varepsilon_4 \frac{3j\omega}{v^g(\bar{r})} D^g(\bar{r})}\nabla\mathcal{F}\phi_0^g(\bar{r}\omega) - \frac{\varepsilon_1 \mathcal{F}D^g(\bar{r}\omega)}{1+\varepsilon_4 \frac{3j\omega}{v^g(\bar{r})} D^g(\bar{r})}\nabla\phi_0^g(\bar{r})$$

Combining the P_1 equations (29 and 30) gives, for the steady-state equation, the usual diffusion equation:

$$\alpha_1\varepsilon_1\nabla D^g(\bar{r})\nabla\phi_0^g(\bar{r}) - \alpha_2\Sigma_t^g(\bar{r})\phi_0^g(\bar{r}) \qquad (35)$$

$$+\sum_{g'}\alpha_3\Sigma_{S_0}^{g'\to g}(\bar{r})\phi_0^{g'}(\bar{r}) + \alpha_4 S_0^g(\bar{r}) = 0$$

and for the P_1 equations (31 and 32) in the frequency domain

$$\alpha_1 \varepsilon_1 \nabla \frac{D^g(\bar{r})}{1 + \varepsilon_4 \frac{3j\omega}{v^g(\bar{r})} D^g(\bar{r})} \nabla \delta\phi_0^g(\bar{r}\omega) \tag{36}$$

$$+\alpha_1 \varepsilon_1 \nabla \frac{\delta D^g(\bar{r}\omega)}{1 + \varepsilon_4 \frac{3j\omega}{v^g(\bar{r})} D^g(\bar{r})} \nabla \phi_0^g(\bar{r}) \quad - \alpha_2 \Sigma_t^g(\bar{r}) \delta\phi_0^g(\bar{r}\omega)$$

$$- \alpha_2 \delta\Sigma_t^g(\bar{r}\omega) \phi_0^g(\bar{r}) + \alpha_3 \sum_{g'} \left[\Sigma_{s_0}^{g' \to g}(\bar{r}) \delta\phi_0^{g'}(\bar{r}\omega) + \phi_0^{g'}(\bar{r}) \delta\Sigma_{s_0}^{g' \to g}(\bar{r}\omega) \right]$$

$$+ \alpha_4 \delta S_0^g(\bar{r}\omega) = \alpha_5 \frac{j\omega}{v^g(\bar{r})} \delta\phi_0^g(\bar{r}\omega)$$

Splitting the frequency-dependent P_1 equations into their real and imaginary parts gives:

$$\alpha_1 \varepsilon_1 \nabla D^{Rg}(\bar{r}\omega) \nabla \delta\phi_0^{Rg}(\bar{r}\omega) - \alpha_1 \varepsilon_1 \nabla D^{Ig}(\bar{r}\omega) \nabla \delta\phi_0^{Ig}(\bar{r}\omega) \tag{37}$$

$$+\alpha_1 \varepsilon_1 \nabla \frac{D^{Rg}(\bar{r}\omega)}{D^g(\bar{r})} \delta D^{Rg}(\bar{r}\omega) \nabla \phi_0^g(\bar{r}) - \alpha_1 \varepsilon_1 \nabla D^{Ig}(\bar{r}\omega) \cdot \delta D^{Ig}(\bar{r}\omega) \nabla \phi_0^g(\bar{r})$$

$$- \alpha_2 \Sigma_t^g(\bar{r}) \delta\phi_0^{Rg}(\bar{r}\omega) - \alpha_2 \phi_0^g(\bar{r}) \delta\Sigma_t^{Rg}(\bar{r}\omega)$$

$$+ \alpha_3 \sum_{g'} \Sigma_{s_0}^{g' \to g}(\bar{r}) \delta\phi_0^{Rg'}(\bar{r}\omega) + \alpha_3 \sum_{g'} \phi_0^{g'}(\bar{r}) \delta\Sigma_{s_0}^{Rg' \to g}(\bar{r}\omega)$$

$$+ \alpha_4 \delta S_0^{Rg}(\bar{r}\omega) + \alpha_5 \frac{\omega}{v^g(\bar{r})} \delta\phi_0^{Ig}(\bar{r}\omega) = 0$$

$$\alpha_1 \varepsilon_1 \nabla D^{Ig}(\bar{r}\omega) \nabla \delta\phi_o^{Rg}(\bar{r}\omega) + \alpha_1 \varepsilon_1 \nabla D^{Rg}(\bar{r}\omega) \nabla \delta\phi_o^{Ig}(\bar{r}\omega) \qquad (38)$$

$$+ \alpha_1 \varepsilon_1 \nabla \frac{D^{Rg}(\bar{r}\omega)}{D^g(\bar{r})} \delta D^{Ig}(\bar{r}\omega) \nabla \phi_o^g(\bar{r})$$

$$+ \alpha_1 \varepsilon_1 \nabla D^{Ig}(\bar{r}\omega) \delta D^{Rg}(\bar{r}\omega) \nabla \phi_o^g(\bar{r}) - \alpha_2 \Sigma_t^g(\bar{r}) \delta\phi_o^{Ig}(\bar{r}\omega)$$

$$- \alpha_2 \phi_o^g(\bar{r}) \delta\Sigma_t^{Ig}(\bar{r}\omega) + \alpha_3 \sum_{g'} \Sigma_{s_o}^{g' \to g}(\bar{r}) \delta\phi_o^{Ig'}(\bar{r}\omega)$$

$$+ \alpha_3 \sum_{g'} \phi_o^{g'}(\bar{r}) \delta\Sigma_{s_o}^{Ig' \to g}(\bar{r}\omega) + \alpha_4 \delta S_o^{Ig}(\bar{r}\omega)$$

$$- \alpha_5 \frac{\omega}{v^g(\bar{r})} \delta\phi_o^{Rg}(\bar{r}\omega) = 0$$

where $D^g(\bar{r}\omega) = D^{Rg}(\bar{r}\omega) + JD^{Ig}(\bar{r}\omega)$

$$D^{Rg}(\bar{r}\omega) = \frac{D^g(\bar{r})}{1 + \left[\varepsilon_4 \frac{3\omega}{v^g(\bar{r})} D^g(\bar{r}) \right]^2} \qquad (39)$$

$$D^{Ig}(\bar{r}\omega) = \frac{- \varepsilon_4 \frac{3\omega}{v^g(\bar{r})} D^g(\bar{r})^2}{1 + \left[\varepsilon_4 \frac{3\omega}{v^g(\bar{r})} D^g(\bar{r}) \right]^2} \qquad (40)$$

Assuming that the cross sections are frequency-independent, zero-power reactor assumption, and splitting the P_1 equations into their real and imaginary components, we get:

$$\alpha_1 \varepsilon_1 \nabla \frac{D^g(\bar{r})}{1+\left[\varepsilon_4 \frac{3\omega}{v^g(\bar{r})} D^g(\bar{r})\right]^2} \nabla \delta\phi_0^{Rg}(\bar{r}\omega) - \alpha_2 \Sigma_t^g(r)\, \delta\phi_0^{Rg}(\bar{r}\omega) \qquad (41)$$

$$+ \alpha_3 \sum_{g'} \Sigma_{s_0}^{g' \to g}(\bar{r})\, \delta\phi_0^{Rg'}(\bar{r}\omega) + \alpha_4\, \delta S_0^{Rg}(\bar{r}\omega)$$

$$+ \alpha_1 \varepsilon_1 \nabla \frac{\varepsilon_4 \frac{3\omega}{v^g(\bar{r})} D^g(\bar{r})^2}{1+\left[\varepsilon_4 \frac{3\omega}{v^g(\bar{r})} D^g(\bar{r})\right]^2} \nabla \delta\phi_0^{Ig}(\bar{r}\omega) + \alpha_5 \frac{\omega}{v^g(\bar{r})} \delta\phi_0^{Ig}(\bar{r}\omega) = 0$$

and

$$\alpha_1 \varepsilon_1 \nabla \frac{D^g(\bar{r})}{1+\left[\varepsilon_4 \frac{3\omega}{v^g(\bar{r})} D^g(\bar{r})\right]^2} \nabla \delta\phi_0^{Ig}(\bar{r}\omega) - \alpha_2 \Sigma_t^g(\bar{r})\, \delta\phi_0^{Ig}(\bar{r}\omega) \qquad (42)$$

$$+ \alpha_3 \sum_{g'} \Sigma_{s_0}^{g' \to g}(r)\, \delta\phi_0^{Ig'}(\bar{r}\omega) + \alpha_4\, \delta S_0^{Ig}(\bar{r}\omega)$$

$$- \alpha_1 \varepsilon_1 \nabla \frac{\varepsilon_4 \frac{3\omega}{v^g(\bar{r})} D^g(\bar{r})^2}{1+\left[\varepsilon_4 \frac{3\omega}{v^g(\bar{r})} D^g(\bar{r})\right]^2} \nabla \delta\phi_0^{Rg}(\bar{r}\omega) - \alpha_5 \frac{\omega}{v^g(\bar{r})} \delta\phi_0^{Rg}(\bar{r}\omega) = 0$$

or

$$\alpha_1 \varepsilon_1 \nabla D^{Rg}(\bar{r}\omega) \nabla \delta\phi_0^{Rg}(\bar{r}\omega) - \alpha_2 \Sigma_t^g(\bar{r})\, \delta\phi_0^{Rg}(\bar{r}\omega) \qquad (43)$$

$$+ \alpha_3 \sum_{g'} \Sigma_{s_0}^{g' \to g}(\bar{r})\, \delta\phi_0^{Rg'}(\bar{r}\omega) + \alpha_4\, \delta S_0^{Rg}(\bar{r}\omega)$$

$$- \alpha_1 \varepsilon_1 \nabla D^{Ig}(\bar{r}\omega) \nabla \delta\phi_0^{Ig}(\bar{r}\omega) + \alpha_5 \frac{\omega}{v^g(\bar{r})} \delta\phi_0^{Ig}(\bar{r}\omega) = 0$$

and

$$\alpha_1 \varepsilon_1 \nabla D^{Rg}(\bar{r}\omega) \nabla \delta\phi_o^{Ig}(\bar{r}\omega) - \alpha_2 \Sigma_t^g(\bar{r})\, \delta\phi_o^{Ig}(\bar{r}\omega) \tag{44}$$

$$+\alpha_3 \sum_{g'} \Sigma_{s_o}^{g' \to g}(\bar{r})\, \delta\phi_o^{Ig'}(\bar{r}\omega) + \alpha_4 \delta S_o^{Ig}(\bar{r}\omega)$$

$$+\alpha_1 \varepsilon_1 \nabla D^{Ig}(\bar{r}\omega) \nabla \delta\phi_o^{Rg}(\bar{r}\omega) - \alpha_5 \frac{\omega}{v^g(\bar{r})} \delta\phi_o^{Rg}(\bar{r}\omega) = 0$$

We observe that these equations are different from the usual form of the diffusion equation through the presence of additional leakage terms from the complementary energy.

The prompt and delayed sources can be calculated as follows:

$$\delta S_o^g(\bar{r}\omega)^{prompt} = \chi^g(\bar{r})\,(1-\beta(\bar{r})) \sum_{g'} \nu \Sigma_f^{g'}(\bar{r})\, \delta\phi_o^{g'}(\bar{r}\omega)$$

and

$$\delta S_o^g(\bar{r}\omega)^{delayed} = \sum_d \lambda_d(\bar{r})\, \chi_d^g(\bar{r})\, \delta C_d^g(\bar{r}\omega)$$

or for the prompt sources:

$$\delta S_o^{Rg}(\bar{r}\omega) = \chi^g(\bar{r})\,(1-\beta(\bar{r})) \sum_{g'} \nu \Sigma_f^{g'}(\bar{r})\, \delta\phi_o^{Rg'}(\bar{r}\omega)$$

and

$$\delta S_o^{Ig}(\bar{r}\omega) = \chi^g(\bar{r})\,(1-\beta(\bar{r})) \sum_{g'} \nu \Sigma_f^{g'}(\bar{r})\, \delta\phi_o^{Ig'}(\bar{r}\omega)$$

For the delayed sources we have

$$\delta S_o^{Rg}(\bar{r}\omega) = \sum_d \lambda_d(\bar{r})\, \chi_d^g(\bar{r})\, \delta C_d^{Rg}(\bar{r}\omega)$$

and

$$\delta S_o^{Ig}(\bar{r}\omega) = \sum_d \lambda_d(\bar{r})\, \chi_d^g(\bar{r})\, \delta C_d^{Ig}(\bar{r}\omega)$$

From the delayed equations we get

$$\chi_d^g(\bar{r})\,\delta C_d^g(\bar{r}\omega) = \frac{\beta_d(\bar{r})\,\chi_d^g(\bar{r})\sum_{g'}\nu\Sigma_f^{g'}(\bar{r})\,\delta\phi_o^{g'}(\bar{r}\omega)}{j\omega + \lambda_d(\bar{r})}$$

or

$$\chi_d^g(\bar{r})\,\delta C_d^{Rg}(\bar{r}\omega) = \frac{\beta_d(\bar{r})\,\chi_d^g(\bar{r})}{\omega^2+\lambda_d^2(\bar{r})}\left[\lambda_d(\bar{r})\sum_{g'}\nu\Sigma_f^{g'}(\bar{r})\,\delta\phi_o^{Rg'}(\bar{r}\omega) + \omega\sum_{g'}\nu\Sigma_f^{g'}(\bar{r})\,\delta\phi_o^{Ig'}(\bar{r}\omega)\right]$$

$$\chi_d^g(\bar{r})\,\delta C_d^{Ig}(\bar{r}\omega) = \frac{\beta_d(\bar{r})\,\chi_d^g(\bar{r})}{\omega^2+\lambda_d^2(\bar{r})}\left[\lambda_d(\bar{r})\sum_{g'}\nu\Sigma_f^{g'}(\bar{r})\,\delta\phi_o^{Ig'}(\bar{r}\omega) - \omega\sum_{g'}\nu\Sigma_f^{g'}(\bar{r})\,\delta\phi_o^{Rg'}(\bar{r}\omega)\right]$$

These delayed sources can therefore be incorporated into the frequency-dependent equations through additional fission terms.

It must be observed that, in the solution of the equations in the frequency domain in two dimensions, third dimensional buckling corrections are required. These buckling corrections are represented by two terms:

$$-\frac{D^g(\bar{r})}{1+\left[\epsilon_4\frac{3\omega}{v^g(\bar{r})}D^g(\bar{r})\right]^2}B_z^2\,\delta\phi_o^{Rg}(\bar{r}\omega) \quad \text{and} \quad \frac{-\frac{3\omega}{v^g(\bar{r})}D^g(\bar{r})^2}{1+\left[\epsilon_4\frac{3\omega}{v^g(\bar{r})}D^g(\bar{r})\right]^2}B_z^2\,\delta\phi_o^{Ig}(\bar{r}\omega)$$

for the real part of the frequency-dependent equation, and

$$-\frac{D^g(\bar{r})}{1+\left[\epsilon_4\frac{3\omega}{v^g(\bar{r})}D^g(\bar{r})\right]^2}B_z^2\,\delta\phi_o^{Ig}(\bar{r}\omega) \text{ and } \quad \frac{\frac{3\omega}{v^g(\bar{r})}D^g(\bar{r})^2}{1+\left[\epsilon_4\frac{3\omega}{v^g(\bar{r})}D^g(\bar{r})\right]^2}B_z^2\,\delta\phi_o^{Rg}(\bar{r}\omega)$$

for the imaginary part.

Next starting from the multigroup P_1 equation, we remove the restriction that

$$\int dE' \, \Sigma_{s_1}(\bar{r}, E' \to E, t) \, \phi_1(\bar{r} E' t) = \Sigma_{s_1}(\bar{r} E) \, \phi_1(\bar{r} E t)$$

i.e., reversibility, and we apply assumption 2.

Assuming small stochastic variations, we obtain for the steady-state part

$$\phi_1^g(\bar{r}) = D^g(\bar{r}) \left[-\varepsilon_1 \nabla \phi_0^g(\bar{r}) + 3\varepsilon_3 \sum_{g'} \Sigma_{s_1}^{g' \to g}(\bar{r}) \, \phi_1^{g'}(\bar{r}) \right]$$

and

$$-\alpha_1 \nabla \phi_1^g(\bar{r}) - \alpha_2 \Sigma_t^g(\bar{r}) \, \phi_0^g(\bar{r}) + \alpha_3 \sum_{g'} \Sigma_{s_0}^{g' \to g}(\bar{r}) \, \phi_0^{g'}(\bar{r})$$

$$+ \alpha_4 S_0^g(\bar{r}) = 0$$

We also have

$$\phi_1^{g'}(\bar{r}) = D^{g'}(\bar{r}) \left[-\varepsilon_1 \nabla \phi_0^{g'}(\bar{r}) + 3\varepsilon_2 \sum_{g''} \Sigma_{s_1}^{g'' \to g'}(\bar{r}) \, \phi_1^{g''}(\bar{r}) \right]$$

Assuming that $\left|\Sigma_{S_1}^{g' \to g}\right|^2 \ll \left|\Sigma_t^g\right|^2$ for all g' and g, except g = g', we obtain

$$\phi_1^g(\bar{r}) = D^g(\bar{r}) \left[-\varepsilon_1 \nabla \phi_0^g(\bar{r}) - 3\varepsilon_3 \sum_{g'} D^{g'}(\bar{r}) \Sigma_{s_1}^{g' \to g}(\bar{r}) \, \varepsilon_1 \nabla \phi_0^{g'}(\bar{r}) \right]$$

After elimination of $\phi_1^g(\bar{r})$ we obtain

$$\alpha_1 \varepsilon_1 \nabla D^g(\bar{r}) \nabla \phi_0^g(\bar{r}) + \alpha_1 \varepsilon_1 \varepsilon_3 \sum_{g'} \nabla D^g(\bar{r}) \, 3 \Sigma_{s_1}^{g' \to g}(\bar{r}) \, D^{g'}(\bar{r}) \nabla \phi_0^{g'}(\bar{r}) \quad (45)$$

$$-\alpha_2 \Sigma_t^g(\bar{r}) \phi_0^g(\bar{r}) + \alpha_3 \sum_{g'} \Sigma_{s_0}^{g' \to g}(\bar{r}) \phi_0^{g'}(\bar{r}) + \alpha_4 S_0^g(\bar{r}) = 0$$

We can observe that, in order to obtain the steady-state diffusion equation, the following assumption must be made

$$\sum_{g'} \Sigma_{s_1}^{g' \to g}(\bar{r}) \phi_1^{g'}(\bar{r}) = \sum_{g'} \Sigma_{s_1}^{g \to g'}(\bar{r}) \phi_1^{g}(\bar{r})$$

We subsequently get

$$\phi_1^g(r) = -\frac{1}{3\left[\Sigma_t^g(\bar{r}) - \varepsilon_3 \Sigma_{s_1}^g(\bar{r})\right]} \varepsilon_1 \nabla \phi_0^g(\bar{r})$$

and

$$\alpha_1 \varepsilon_1 \nabla \frac{1}{3\left[\Sigma_t^g(\bar{r}) - \varepsilon_3 \Sigma_{s_1}^g(\bar{r})\right]} \nabla \phi_0^g(\bar{r}) - \alpha_2 \Sigma_t^g(\bar{r}) \phi_0^g(\bar{r})$$

$$+ \alpha_3 \sum_{g'} \Sigma_{s_0}^{g' \to g}(\bar{r}) \phi_0^{g'}(\bar{r}) + \alpha_4 S_0^g(\bar{r}) = 0$$

After Fourier transformation, we obtain for the frequency-dependent P_1 equations

$$\delta\phi_1^g(\bar{r}\omega) = \frac{D^g(\bar{r})}{1 + \varepsilon_4 \frac{3j\omega}{v^g(\bar{r})} D^g(\bar{r})} \Bigg[-\varepsilon_1 \nabla \delta\phi_0^g(\bar{r}\omega) - 3\varepsilon_2 \delta\Sigma_t^g(\bar{r}\omega)\, \phi_1^g(\bar{r}) + 3\varepsilon_3 \sum_{g'} \Sigma_{s_1}^{g' \to g}(\bar{r})\, \delta\phi_1^{g'}(\bar{r}\omega) - 3\varepsilon_3 \sum_{g'} \delta\Sigma_{s_1}^{g' \to g}(\bar{r}\omega)\, \phi_1^{g'}(\bar{r}) \Bigg]$$

For a "zero-power" reactor and for binary noise, we can say that

$$\delta\Sigma_t^g(\bar{r}\omega) \equiv 0 \qquad \text{and} \qquad \delta\Sigma_s^{g' \to g}(\bar{r}\omega) \equiv 0$$

We therefore get

$$\delta\phi_1^g(\bar{r}\omega) = \frac{D^g(\bar{r})}{1 + D^g(\bar{r})\,\varepsilon_4 \frac{3j\omega}{v^g(\bar{r})}} \Bigg[-\varepsilon_1 \nabla \delta\phi_0^g(\bar{r}\omega) + 3\varepsilon_3 \sum_{g'} \Sigma_{s_1}^{g' \to g}(\bar{r})\, \delta\phi_1^{g'}(\bar{r}\omega) \Bigg] \tag{46}$$

where $$D^g(\bar{r}) = \frac{1}{3\left[\Sigma_t^g(\bar{r}) - \Sigma_{s_1}^{g \to g}(\bar{r})\right]}$$

Similarly

$$\delta\phi_1^{g'}(\bar{r}\omega) = \frac{D^{g'}(\bar{r})}{1 + \varepsilon_4 \frac{3j\omega}{v^{g'}(\bar{r})} D^{g'}(\bar{r})} \Bigg[-\varepsilon_1 \nabla \delta\phi_0^{g'}(\bar{r}\omega) + 3\varepsilon_3 \sum_{g''} \Sigma_{s_1}^{g'' \to g'}(\bar{r})\, \delta\phi_1^{g''}(\bar{r}\omega) \Bigg]$$

Again assuming that $\left|\Sigma_{S_1}^{g' \to g}\right|^2 \ll \left|\Sigma_t^g(\bar{r})\right|^2$ for all g and g', except g = g',

$$\delta\phi_1^g(\bar{r}\omega) = \frac{D^g(\bar{r})}{1 + \varepsilon_4 \frac{3J\omega}{v^g(\bar{r})} D^g(\bar{r})} \left[-\varepsilon_1 \nabla \delta\phi_0^g(\bar{r}\omega) \right.$$

$$\left. -3\varepsilon_3 \sum_{g'} \Sigma_{s_1}^{g' \to g}(\bar{r}) \frac{D^{g'}(\bar{r})}{1 + \varepsilon_4 \frac{3J\omega}{v^{g'}(\bar{r})} D^{g'}(\bar{r})} \varepsilon_1 \nabla \delta\phi_0^{g'}(\bar{r}\omega) \right]$$

We also have seen that

$$-\alpha_1 \nabla \delta\phi_1^g(\bar{r}\omega) - \alpha_2 \Sigma_t^g(\bar{r}) \delta\phi_0^g(\bar{r}\omega) + \alpha_3 \sum_{g'} \Sigma_{s_0}^{g' \to g}(\bar{r}) \delta\phi_0^{g'}(\bar{r}\omega)$$

$$+\alpha_4 \delta S_0^g(\bar{r}\omega) = \alpha_5 \frac{J\omega}{v^g(\bar{r})} \delta\phi_0^g(\bar{r}\omega)$$

Combining the two previous equations gives

$$\alpha_1 \varepsilon_1 \nabla \frac{D^g(\bar{r})}{1 + \varepsilon_4 \frac{3J\omega}{v^g(\bar{r})} D^g(\bar{r})} \nabla \delta\phi_0^g(\bar{r}\omega) \tag{47}$$

$$+ \alpha_1 \varepsilon_1 \varepsilon_3 \sum_{g'} \nabla \frac{D^g(\bar{r})}{1 + \varepsilon_4 \frac{3J\omega}{v^g(\bar{r})} D^g(\bar{r})} 3 \Sigma_{s_1}^{g' \to g}(\bar{r}) \frac{D^{g'}(\bar{r})}{1 + \varepsilon_4 \frac{3J\omega}{v^{g'}(\bar{r})} D^{g'}(\bar{r})} \nabla \delta\phi_0^{g'}(\bar{r}\omega)$$

$$-\alpha_2 \Sigma_t^g(\bar{r}) \delta\phi_0^g(\bar{r}\omega) + \alpha_3 \sum_{g'} \Sigma_{s_0}^{g' \to g}(\bar{r}) \delta\phi_0^{g'}(\bar{r}\omega)$$

$$+\alpha_4 \delta S_0^g(\bar{r}\omega) = \alpha_5 \frac{J\omega}{v^g(\bar{r})} \delta\phi_0^g(\bar{r}\omega)$$

We therefore get

$$\alpha_1 \varepsilon_1 \nabla D^g(\bar{r}\omega) \nabla \delta\phi_0^g(\bar{r}\omega) - \alpha_2 \Sigma_t^g(\bar{r}) \delta\phi_0^g(\bar{r}\omega) \tag{48}$$

$$+ \alpha_1 \varepsilon_1 \varepsilon_3 \sum_{g'} \nabla D^g(\bar{r}\omega) 3 \Sigma_{s_1}^{g' \to g}(\bar{r}) D^{g'}(\bar{r}\omega) \nabla \delta\phi_0^{g'}(\bar{r}\omega)$$

(continued)

$$+\alpha_3 \sum_{g'} \Sigma_{s_0}^{g' \to g}(\bar{r})\, \delta\phi_0^{g'}(\bar{r}\omega) \quad + \alpha_4\, \delta S_0^{g}(\bar{r}\omega) \quad - \alpha_5 \frac{j\omega}{v^{g}(\bar{r})}\, \delta\phi_0^{g}(\bar{r}\omega) = 0$$

Let us define

$$D^{g}(\bar{r}\omega) = \frac{D^{g}(\bar{r})}{1 + \varepsilon_4 \frac{3j\omega}{v^{g}(\bar{r})} D^{g}(\bar{r})} = D^{Rg}(\bar{r}\omega) + j\, D^{Ig}(\bar{r}\omega)$$

where

$$D^{Rg}(\bar{r}\omega) = \frac{D^{g}(\bar{r})}{1 + \left[\varepsilon_4 \frac{3\omega}{v^{g}} D^{g}(\bar{r})\right]^2}$$

$$D^{Ig}(\bar{r}\omega) = \frac{-\varepsilon_4 \frac{3\omega}{v^{g}} D^{g}(\bar{r})^2}{1 + \left[\varepsilon_4 \frac{3\omega}{v^{g}} D^{g}(\bar{r})\right]^2}$$

and

$$\delta\phi_0^{g}(\bar{r}\omega) = \delta\phi_0^{Rg}(\bar{r}\omega) + j\, \delta\phi_0^{Ig}(\bar{r}\omega)$$

After a few manipulations, we obtain for the real part of the frequency-dependent equation

$$\alpha_1 \varepsilon_1 \nabla D^{Rg}(\bar{r}\omega) \nabla \delta\phi_0^{Rg}(\bar{r}\omega) \quad - \alpha_1 \varepsilon_1 \nabla D^{Ig}(\bar{r}\omega) \nabla \delta\phi_0^{Ig}(\bar{r}\omega) \qquad (49)$$

$$+ 3\alpha_1 \varepsilon_1 \varepsilon_3 \sum_{g'} \nabla \Big[D^{Rg}(\bar{r}\omega)\, \Sigma_{s_1}^{g' \to g}(\bar{r})\, D^{Rg'}(\bar{r}\omega)$$

$$- D^{Ig}(\bar{r}\omega)\, \Sigma_{s_1}^{g' \to g}(\bar{r})\, D^{Ig'}(\bar{r}\omega) \Big] \nabla \delta\phi_0^{Rg'}(\bar{r}\omega)$$

(continued)

$$- 3\alpha_1 \varepsilon_1 \varepsilon_3 \sum_{g'} \nabla \Big[D^{Rg}(\bar{r}\omega) \Sigma_{s_1}^{g' \to g}(r) D^{Ig'}(\bar{r}\omega)$$

$$+ D^{Ig}(\bar{r}\omega) \Sigma_{s_1}^{g' \to g}(\bar{r}) D^{Rg'}(\bar{r}\omega) \Big] \nabla \delta\phi_o^{Ig'}(\bar{r}\omega)$$

$$- \alpha_2 \Sigma_t^g(\bar{r}) \delta\phi_o^{Rg}(\bar{r}\omega) + \alpha_3 \sum_{g'} \Sigma_{s_o}^{g' \to g}(\bar{r}) \delta\phi_o^{Rg'}(\bar{r}\omega)$$

$$+ \alpha_4 \delta S_o^{Rg}(\bar{r}\omega) + \alpha_5 \frac{\omega}{v^g(\bar{r})} \delta\phi_o^{Ig}(\bar{r}\omega) = 0$$

and for the imaginary part

$$\alpha_1 \varepsilon_1 \nabla D^{Rg}(\bar{r}\omega) \nabla \delta\phi_o^{Ig}(\bar{r}\omega) + \alpha_1 \varepsilon_1 \nabla D^{Ig}(\bar{r}\omega) \nabla \delta\phi_o^{Rg}(\bar{r}\omega) \qquad (50)$$

$$+ 3\alpha_1 \varepsilon_1 \varepsilon_3 \sum_{g'} \nabla \Big[D^{Rg}(\bar{r}\omega) \Sigma_{s_1}^{g' \to g}(\bar{r}) D^{Rg'}(\bar{r}\omega)$$

$$- D^{Ig}(\bar{r}\omega) \Sigma_{s_1}^{g' \to g}(\bar{r}) D^{Ig'}(\bar{r}\omega) \Big] \nabla \delta\phi_o^{Ig'}(\bar{r}\omega)$$

$$+ 3\alpha_1 \varepsilon_1 \varepsilon_3 \sum_{g'} \nabla \Big[D^{Rg}(\bar{r}\omega) \Sigma_{s_1}^{g' \to g}(\bar{r}) D^{Ig'}(\bar{r}\omega)$$

$$+ D^{Ig}(\bar{r}\omega) \Sigma_{s_1}^{g' \to g}(\bar{r}) D^{Rg'}(\bar{r}\omega) \Big] \nabla \delta\phi_o^{Rg'}(\bar{r}\omega)$$

$$- \alpha_2 \Sigma_t^g(\bar{r}) \delta\phi_o^{Ig}(\bar{r}\omega) + \alpha_3 \sum_{g'} \Sigma_{s_o}^{g' \to g}(\bar{r}) \delta\phi_o^{Ig'}(\bar{r}\omega)$$

$$+ \alpha_4 \delta S_o^{Ig}(\bar{r}\omega) - \alpha_5 \frac{\omega}{v^g(\bar{r})} \delta\phi_o^{Rg}(\bar{r}\omega) = 0$$

We observe that the frequency-dependent equations (43 and 44) for assumption 1, and equations (49 and 50) for assumption 2, cannot be solved with

conventional finite difference equations, based on the diffusion equations, because of the presence of complex leakage terms.

Stochastic Power Spectral Density

We have seen that

$$\mathcal{S}S_o^g(\bar{r}\omega) = \mathcal{S}S_o^g(\bar{r}\omega)^{prompt} + \mathcal{S}S_o^g(\bar{r}\omega)^{delayed} + \mathcal{S}S_o^g(\bar{r}\omega)^{external}$$

where the subscript "0" denotes that the fission neutrons, the delayed neutrons, and the external disturbance are assumed to be emitted isotropically, and where

$$\mathcal{S}S_o^g(\bar{r}\omega)^{prompt} = \chi^g(\bar{r})\,(1-\beta(\bar{r}))\sum_{g'}\nu\Sigma_f^{g'}(\bar{r})\;\mathcal{S}\phi_o^{g'}(\bar{r}\omega)$$

$$\mathcal{S}S_o^g(\bar{r}\omega)^{delayed} = \sum_d \lambda_d(\bar{r})\,\chi_d^g(\bar{r})\;C_d^g(\bar{r}\omega)$$

For a unit source at space point $\bar{r}'$ and energy group g_I, we have

$$\mathcal{S}S_o^g(\bar{r}\omega)^{external} = \chi^{g_I}\;\mathcal{S}(\bar{r}-\bar{r}')\;\mathcal{S}(g-g_I)$$

where $\delta(\bar{r}-\bar{r}') = 1$ if $\bar{r} = \bar{r}'$

$= 0$ if $\bar{r} \neq \bar{r}'$

$\delta(g-g_I) = 1$ if $g = g_I$

0 if $g \neq g_I$

Using equations (43) and (44) and (49) and (50), we will set up the approach of calculating the transfer function $T(\bar{r}E^{g} \leftarrow \bar{r}'E^{g'})$ based on assump-

tion 2. The derivation of the space-, energy-, and frequency-dependent transfer function equations based on assumption 1 is similar. We have previously derived the complex expression

$$\alpha_1 \varepsilon_1 \nabla D^g(\bar{r}\omega) \nabla \delta\phi_o^g(\bar{r}\omega) - \alpha_2 \Sigma_t^g(\bar{r}) \delta\phi_o^g(\bar{r}\omega)$$

$$+ 3\alpha_1 \varepsilon_1 \varepsilon_3 \sum_{g'} \nabla D^g(\bar{r}\omega) \Sigma_{s_1}^{g' \to g}(\bar{r}) D^{g'}(\bar{r}\omega) \nabla \delta\phi_o^{g'}(\bar{r}\omega)$$

$$+ \alpha_3 \sum_{g'} \Sigma_{s_o}^{g' \to g}(\bar{r}) \delta\phi_o^{g'}(\bar{r}\omega) + \alpha_4 \delta S_o^g(\bar{r}\omega) = \alpha_5 \frac{j\omega}{v^g(\bar{r})} \delta\phi_o^g(\bar{r}\omega)$$

If we only consider a unit source at energy-group g_I and at space-variable $\bar{r}'$, we obtain

$$\alpha_1 \varepsilon_1 \nabla D^g(\bar{r}\omega) \nabla \delta T(\bar{r}' g_I \to \bar{r} g, \omega) \tag{51}$$

$$+ 3\alpha_1 \varepsilon_1 \varepsilon_3 \sum_{g'} \nabla D^g(\bar{r}\omega) \Sigma_{s_1}^{g' \to g}(\bar{r}) D^{g'}(\bar{r}\omega) \nabla \delta T(\bar{r}' g_I \to \bar{r} g', \omega)$$

$$- \alpha_2 \Sigma_t^g(\bar{r}) \delta T(\bar{r}' g_I \to \bar{r} g, \omega) + \alpha_3 \sum_{g'} \Sigma_{s_o}^{g' \to g}(\bar{r}) \delta T(\bar{r}' g_I \to \bar{r} g', \omega)$$

$$+ \alpha_4 \sum_d \lambda_d(\bar{r}) \chi_d^g(\bar{r}) C_d(\bar{r}' g_I \to \bar{r} g, \omega)$$

$$+ \alpha_4 \chi^g(\bar{r}) (1 - \beta(\bar{r})) \sum_{g'} \nu \Sigma_f^{g'}(\bar{r}) \delta T(\bar{r}' g_I \to \bar{r} g', \omega)$$

$$+ \chi^{g_I} \delta(\bar{r} - \bar{r}') \delta(g - g_I) = \alpha_5 \frac{j\omega}{v^g(\bar{r})} \delta T(\bar{r}' g_I \to \bar{r} g, \omega)$$

We now define the following complex operators:

$$D^g(\bar{r}\omega) = \frac{D^g(\bar{r})}{1 + \varepsilon_4 \frac{3j\omega}{v^g(\bar{r})} D^g(\bar{r})}$$

$$Lk^g(\bar{r}\omega) = \alpha_1 \varepsilon_1 \nabla D^g(\bar{r}\omega) \nabla$$

$$Lk^{g'\to g}(\bar{r}\omega) = 3\alpha_1 \varepsilon_1 \varepsilon_3 \nabla D^g(\bar{r}\omega) \Sigma_{s_1}^{g'\to g}(\bar{r}) D^{g'}(\bar{r}\omega) \nabla$$

$$PF^{g'\to g}(\bar{r}\omega) = \alpha_4 \chi^g(\bar{r}) (1-\beta(\bar{r})) \nu \Sigma_f^{g'}(\bar{r})$$

$$EL^{g'\to g}(\bar{r}\omega) = Lk^{g'\to g}(\bar{r}\omega) + \alpha_3 \Sigma_{s_0}^{g'\to g}(\bar{r}) + Delayed^{g'\to g}(\bar{r}\omega)$$

$$+ PF^{g'\to g}(\bar{r}\omega)$$

Equation (51) then becomes

$$\left[Lk^g(\bar{r}\omega) + EL^{g\to g}(\bar{r}\omega) - \alpha_2 \Sigma_t^g(\bar{r}) - \alpha_5 \frac{j\omega}{v^g(\bar{r})}\right] \Im T(\bar{r}' g_I \to \bar{r} g, \omega)$$

$$+ \sum_{g'} EL^{g'\to g}(\bar{r}\omega) \Im T(\bar{r}' g_I \to \bar{r} g', \omega)$$

$$+ \chi^{g_I} \delta(\bar{r}-\bar{r}') \delta(g-g_I) = 0$$

or in matrix form

$$\left[M(\bar{r}'\bar{r}\omega)\right] \cdot \left[\Im T(\bar{r}' \to \bar{r}, \omega)\right] = - \left[\delta(\bar{r}-\bar{r}')\right] \cdot \left[\chi^I\right]$$

or

$$\left[\delta T(\bar{r}' \rightarrow \bar{r}, \omega)\right] = -\left[M(\bar{r}'\bar{r}\omega)\right]\left[\delta(\bar{r}-\bar{r}')\right]\left[\chi^{I}\right] \tag{52}$$

It will be observed that, in the numerical approximation, each element in the above matrix is a sub-matrix of size; i.e., number of mesh points in the x-direction times number of mesh points in the y-direction.

Assuming that the sensitivity of neutron detector 1 (det1) at space point $\bar{r}_{det1}$ is in energy group g_{det1} (and similarly for det2), we have for inherent binary noise, that the cross-power spectral density between detector 1 and detector 2 is:

$$CPSD^{g_{det1}\, g_{det2}}(\bar{r}_{det1}, \bar{r}_{det2}, \omega) = \tag{53}$$

$$\int_{Reactor} d\bar{r} \sum_{g} \delta T(\bar{r}g \rightarrow \bar{r}_{det1}\, g_{det1}, \omega)^{*} \cdot \delta T(\bar{r}g \rightarrow \bar{r}_{det2}\, g_{det2}, \omega)$$

$$\chi^{g}(\bar{r}) \sum_{g'} \overline{\nu(\nu-1)}\, \Sigma_f^{g'}(\bar{r})\, \phi^{g'}(\bar{r})$$

or in matrix form

$$\left[CPSD(\bar{r}_{det1}, \bar{r}_{det2}, \omega)\right] = \tag{54}$$

$$\int_{Reactor} d\bar{r} \left[\delta T(\bar{r} \rightarrow \bar{r}_{det1}, \omega)^{*}\right] \cdot \left[\delta T(\bar{r} \rightarrow \bar{r}_{det2}, \omega)\right]\left[\chi(\bar{r}) \sum_{g'} \overline{\nu(\nu-1)}\, \Sigma_f^{g'}(\bar{r})\, \phi^{g'}(\bar{r})\right]$$

or

$$\left[CPSD(\bar{r}_{det_1}, \bar{r}_{det_2}, \omega)\right] = \tag{55}$$

$$\int_{Reactor} dr \left[\left[M(\bar{r}\bar{r}_{det_1}\omega)\right]^{-1}\cdot\left[S(\bar{r}-\bar{r}_{det_1})\right]\cdot\left[\chi^{I}\right]\right]\left[\left[M(\bar{r}\bar{r}_{det_2}\omega)\right]^{-1}\cdot\left[S(\bar{r}-\bar{r}_{det_2})\right]\cdot\left[\chi^{I}\right]\right]$$

$$\left[\chi(\bar{r})\sum_{g'}\overline{\nu(\nu-1)}\,\Sigma_f^{g'}(\bar{r})\,\phi^{g'}(\bar{r})\right]$$

Only for very simple geometries in one dimension could this matrix be solved analytically. The numerical solution for two dimensional approximations will be derived in Chapter IV using a cascade block-tridiagonal iteration method combined with a constraint over-relaxation technique.

For the sake of better understanding of the stochastic behavior of a neutronic system, due to space-dependent inherent stochastic fission sources, we will derive a simplified set of equations for a case with two neutron groups (fast and thermal), no upscattering, fission introduced only by thermal neutrons, prompt fission neutrons born in fast broad-group only, no delayed neutrons.

We obtain for the fast broad group:

$$Lk^{(1)}(\bar{r}\omega)\,ST(\bar{r}'_1 \to \bar{r}_1, \omega) - \left[\alpha_2\,\Sigma_t^{(1)}(\bar{r}) + \alpha_5\frac{j\omega}{v^{(1)}}\right] ST(\bar{r}'_1 \to \bar{r}_1, \omega)$$

$$+ EL^{2\to 1}(\bar{r}\omega)\,ST(\bar{r}'_1 \to \bar{r}_2, \omega) = S(\bar{r}-\bar{r}')$$

for the thermal broad group:

$$Lk^{(2)}(r\omega)\ ST(\bar{r}'_1 \to \bar{r}_2, \omega) - \left(\alpha_2 \Sigma_t^{(2)}(\bar{r}) + \alpha_3 \frac{j\omega}{v^{(2)}}\right) ST(\bar{r}'_1 \to \bar{r}_2, \omega)$$

$$+ Lk^{1\to 2}(\bar{r}\omega)\ ST(\bar{r}'_1 \to \bar{r}_1, \omega) + \alpha_3 \Sigma_{s_o}^{1\to 2}\ ST(\bar{r}'_1 \to \bar{r}_1, \omega) = 0$$

After some manipulations, it can be shown that

$$ST(\bar{r}'_1 \to \bar{r}_1, \omega) = \left[S(\bar{r}-\bar{r}') \left(\alpha_2 \Sigma_t^{(2)}(\bar{r}) + \alpha_3 \frac{j\omega}{v^{(2)}}\right) \right. \tag{56}$$

$$-\left(\alpha_2 \Sigma_t^{(2)}(\bar{r}) + \alpha_3 \frac{j\omega}{v^{(2)}}\right) Lk^{(1)}(\bar{r}\omega)\ ST(\bar{r}'_1 \to \bar{r}_1, \omega)$$

$$+ EL^{2\to 1}(\bar{r}\omega)\ Lk^{(2)}(\bar{r}\omega)\ ST(\bar{r}'_1 \to \bar{r}_2, \omega) + EL^{2\to 1}(\bar{r}\omega) Lk^{1\to 2}(\bar{r}\omega)$$

$$\left. ST(\bar{r}'_1 \to \bar{r}_1, \omega)\right] \Big/ \left[EL^{2\to 1}(\bar{r}\omega)\ \alpha_3 \Sigma_{s_o}^{1\to 2}(\bar{r}) \right.$$

$$\left. -\left(\alpha_2 \Sigma_t^{(1)}(\bar{r}) + \alpha_3 \frac{j\omega}{v^{(1)}}\right)\left(\alpha_2 \Sigma_t^{(2)}(\bar{r}) + \alpha_3 \frac{j\omega}{v^{(2)}}\right)\right]$$

and

$$ST(\bar{r}'_1 \to \bar{r}_2, \omega) = \left[S(\bar{r}-\bar{r}')\ \alpha_3 \Sigma_{s_o}^{1\to 2}(\bar{r}) \right. \tag{57}$$

$$-\alpha_3 \Sigma_{s_o}^{1\to 2}(\bar{r})\ Lk^{(1)}(\bar{r}\omega)\ ST(\bar{r}'_1 \to \bar{r}_1, \omega) + \left(\alpha_2 \Sigma_t^{(1)}(\bar{r}) + \alpha_3 \frac{j\omega}{v^{(1)}}\right)$$

$$\left. \left(Lk^{(2)}(\bar{r}\omega)\ ST(\bar{r}'_1 \to \bar{r}_2, \omega) + Lk^{1\to 2}(\bar{r}\omega)\ ST(\bar{r}'_1 \to \bar{r}_1, \omega)\right)\right]$$

$$\Big/ \left[\alpha_3 \Sigma_{s_o}^{1\to 2}(\bar{r})\ EL^{2\to 1}(\bar{r}\omega) - \left(\alpha_2 \Sigma_t^{(1)}(\bar{r}) + \alpha_3 \frac{j\omega}{v^{(1)}}\right)\left(\alpha_2 \Sigma_t^{(2)}(\bar{r}) + \alpha_3 \frac{j\omega}{v^{(2)}}\right)\right]$$

We rewrite equations (56) and (57) as

$$ST(\bar{r}'_1 \rightarrow \bar{r}_1, \omega) = \frac{S(\bar{r}-\bar{r}')\left(\alpha_2 \Sigma_t^{(2)}(\bar{r}) + \alpha_5 \frac{J\omega}{v^{(2)}}\right) + Leak(\bar{r}'_1 \rightarrow \bar{r}_1, \omega)}{Denom^{1\rightarrow 1}(\bar{r}\omega)} \quad (58)$$

$$ST(\bar{r}'_1 \rightarrow \bar{r}_2, \omega) = \frac{S(\bar{r}-\bar{r}')\ \alpha_3 \Sigma_{s_0}^{1\rightarrow 2}(\bar{r}) + Leak(\bar{r}'_1 \rightarrow \bar{r}_2, \omega)}{Denom^{1\rightarrow 2}(\bar{r}\omega)} \quad (59)$$

where

$$Denom^{1\rightarrow 1}(\bar{r}\omega) = EL^{2\rightarrow 1}(\bar{r}\omega)\,\alpha_3 \Sigma_{s_0}^{1\rightarrow 2}(\bar{r}) - \left(\alpha_2 \Sigma_t^{(1)}(\bar{r}) + \alpha_5 \frac{J\omega}{v^{(1)}}\right)\left(\alpha_2 \Sigma_t^{(2)}(\bar{r}) + \alpha_5 \frac{J\omega}{v^{(2)}}\right)$$

$$Denom^{1\rightarrow 2}(\bar{r}\omega) = \alpha_3 \Sigma_{s_0}^{1\rightarrow 2} EL^{2\rightarrow 1}(\bar{r}\omega) - \left(\alpha_2 \Sigma_t^{(1)}(\bar{r}) + \alpha_5 \frac{J\omega}{v^{(1)}}\right)\left(\alpha_2 \Sigma_t^{(2)}(\bar{r}) + \alpha_5 \frac{J\omega}{v^{(2)}}\right)$$

$$\begin{aligned} Leak(\bar{r}'1\rightarrow\bar{r}1,\omega) = {} & -\left(\alpha_2 \Sigma_t^{(2)}(\bar{r}) + \alpha_5 \frac{J\omega}{v^{(2)}}\right) Lk^{(1)}(\bar{r}\omega)\, ST(\bar{r}'_1 \rightarrow \bar{r}_1, \omega) \\ & + EL^{2\rightarrow 1}(\bar{r}\omega)\, Lk^{(2)}(\bar{r}\omega)\, ST(\bar{r}'_1 \rightarrow \bar{r}_2, \omega) \\ & + EL^{2\rightarrow 1}(\bar{r}\omega)\, Lk^{1\rightarrow 2}(\bar{r}\omega)\, ST(\bar{r}'_1 \rightarrow \bar{r}_1, \omega) \end{aligned}$$

$$\begin{aligned} Leak(\bar{r}'1\rightarrow\bar{r}2,\omega) = {} & -\alpha_3 \Sigma_{s_0}^{1\rightarrow 2}(\bar{r})\, Lk^{(1)}(\bar{r}\omega)\, ST(\bar{r}'_1 \rightarrow \bar{r}_1, \omega) \\ & + \left(\alpha_2 \Sigma_t^{(1)}(\bar{r}) + \alpha_5 \frac{J\omega}{v^{(1)}}\right)\Big(Lk^{(2)}(\bar{r}\omega)\, ST(\bar{r}'_1 \rightarrow \bar{r}_2, \omega) \\ & \qquad + Lk^{1\rightarrow 2}(\bar{r}\omega)\, ST(\bar{r}'_1 \rightarrow \bar{r}_1, \omega)\Big) \end{aligned}$$

We also have that, for the inherent binary noise (assuming that the fast fission neutrons are born in the fast broad group)

$$PSD^{g_{det1},g_{det2}}(\bar{r}_{det1},\bar{r}_{det2},\omega) = \int_{Reactor} d\bar{r}\ \delta T(\bar{r}_1 \rightarrow \bar{r}_{det1}\ g_{det1},\omega)^{*} \quad (60)$$

$$\delta T(\bar{r}_1 \rightarrow \bar{r}_{det2}\ g_{det2},\omega)\ \ \overline{\nu(\nu-1)}\,\Sigma_f^{(2)}(\bar{r})\,\phi^{(2)}(\bar{r})$$

Let us compute the thermal-thermal and the fast-thermal CPSD's. The expression for the thermal-thermal PSD (PSD between the thermal response of detector 1 and the thermal response of detector 2) is

$$PSD^{2,2}(\bar{r}_{det1},\bar{r}_{det2},\omega) = \quad (61)$$

$$= \int_{Reactor} dr\ \delta T(\bar{r}_1 \rightarrow \bar{r}_{det1}\ 2,\omega)^{*} \cdot \delta T(\bar{r}_1 \rightarrow \bar{r}_{det2}\ 2,\omega)\ \overline{\nu(\nu-1)}\,\Sigma_f^{(2)}(\bar{r})\,\phi^{(2)}(\bar{r})$$

$$= \int_{Reactor} dr\ \Big[\delta(\bar{r}-\bar{r}_{det1})\,\delta(\bar{r}-\bar{r}_{det2})\,\alpha_3\,\Sigma_{s_0}^{1\rightarrow 2}(\bar{r}_{det1})\,\alpha_3\,\Sigma_{s_0}^{1\rightarrow 2}(\bar{r}_{det2})$$

$$+ \delta(\bar{r}-\bar{r}_{det1})\,\alpha_3\,\Sigma_{s_0}^{1\rightarrow 2}(\bar{r}_{det1})\ Leak(\bar{r}_1 \rightarrow \bar{r}_{det2}\ 2,\omega)$$

$$+ Leak(\bar{r}_1 \rightarrow \bar{r}_{det1}\ 2,\omega)^{*}\ \delta(\bar{r}-\bar{r}_{det2})\,\alpha_3\,\Sigma_{s_0}^{1\rightarrow 2}(\bar{r}_{det2})$$

$$+ Leak(\bar{r}_1 \rightarrow \bar{r}_{det1}\ 2,\omega)^{*} \cdot Leak(\bar{r}_1 \rightarrow \bar{r}_{det2}\ 2,\omega)\Big]$$

$$\overline{\nu(\nu-1)}\,\Sigma_f^{(2)}(\bar{r})\,\phi^{(2)}(\bar{r})$$

$$\Big/ \Big[Denom^{1\rightarrow 2}(\bar{r}_{det1}\,\omega)^{*} \cdot Denom^{1\rightarrow 2}(\bar{r}_{det2}\,\omega)\Big]$$

This expression is similar to the one derived by Ebert[99] although the terms, Leak ($\bar{r}1 \rightarrow \bar{r}_{det}$,2,ω), are complicated functions of local leakage, isotropic, and anisotropic leakage scattering. The meaning of the different terms is also different.

The first term is always zero for a CPSD, and non-zero for an APSD only if the detector is located in a fission region. This term is frequency-dependent through the denominator. In the case where the CPSD is determined between two detectors belonging to the same detector pair of a four-detector system, the CPSD is non-zero only if the detectors are located in a fission region. The second term is non-zero for the CPSD and APSD if detector det1 is located in a fission region and is frequency-dependent. The third term is non-zero for the CPSD and APSD if detector det2 is located in a fission region and is frequency-dependent. The fourth term is always non-zero for the CPSD and the APSD.

In a reactor with a material and geometrical symmetry, and with detectors det1 and det2 in symmetrical locations to the symmetry axis, we have

$$\text{Leak}(\bar{r}_1 \rightarrow \bar{r}_{det_1}, 2, \omega) = \text{Leak}(\bar{r}_{sym\,1} \rightarrow \bar{r}_{det_2}, 2, \omega) ,$$

where $\bar{r}_{sym}$ is a symmetrical location to $\bar{r}$,

and since

$$\text{Imaginary}\left[\text{Leak}(\bar{r}_1 \rightarrow \bar{r}_{det_1}, 2, \omega)^*\right] = -\ \text{Imaginary}\left[\text{Leak}(\bar{r}_1 \rightarrow \bar{r}_{det_1}, 2, \omega)\right]$$

we have, therefore, that $PSD^{2_{det1}\ 2_{det2}}(\bar{r}_{det1}\ \bar{r}_{det2}\ \omega)$ is real. Thus the phase is either 0 or $\pm 180^{\circ}$. This characteristic will give an idea of the relative error introduced by the numerical approximation of the model, when the reactor exhibits a material and geometrical symmetry axis, and the detectors are identical, located in symmetrical locations.

The expressions for the fast-thermal PSD (between the fast response of detector 1 and the thermal response of detector 2) are:

$$PSD^{1,2}(\bar{r}_{det1}, \bar{r}_{det2}, \omega) \tag{62}$$

$$= \int_{Reactor} d\bar{r}\ ST(\bar{r}_1 \rightarrow \bar{r}_{det1}\ 1, \omega)^* \cdot ST(\bar{r}_1 \rightarrow \bar{r}_{det2}\ 2, \omega)\ \overline{\nu(\nu-1)}\ \Sigma_f^{(2)}(\bar{r})\ \Phi^{(2)}(\bar{r})$$

$$= \int_{Reactor} d\bar{r} \Bigg[\delta(\bar{r}-\bar{r}_{det1})\ \delta(\bar{r}-\bar{r}_{det2}) \left(\alpha_2 \Sigma_t^{(2)}(\bar{r}_{det1}) - \alpha_5 \frac{j\omega}{v^{(2)}(\bar{r}_{det1})}\right)$$

$$\alpha_3 \Sigma_{s_0}^{1\rightarrow 2}(\bar{r}_{det2})$$

$$+ \delta(\bar{r}-\bar{r}_{det1}) \left(\alpha_2 \Sigma_t^{(2)}(\bar{r}_{det1}) - \alpha_5 \frac{j\omega}{v^{(2)}(\bar{r}_{det1})}\right) Leak(\bar{r}_1 \rightarrow \bar{r}_{det2}\ 2, \omega)$$

$$+ Leak(\bar{r}_1 \rightarrow \bar{r}_{det1}\ 1, \omega)^*\ \delta(\bar{r}-\bar{r}_{det2})\ \alpha_3 \Sigma_{s_0}^{1\rightarrow 2}(\bar{r}_{det2})$$

$$+ Leak(\bar{r}_1 \rightarrow \bar{r}_{det1}\ 1, \omega)^* \cdot Leak(\bar{r}_1 \rightarrow \bar{r}_{det2}\ 2, \omega)\Bigg]\ \overline{\nu(\nu-1)}\ \Sigma_f^{(2)}(\bar{r})\ \Phi^{(2)}(\bar{r})$$

$$/ \left[Denom^{1\rightarrow 1}(\bar{r}_{det1}\ \omega)^* \cdot Denom^{1\rightarrow 2}(\bar{r}_{det2}\ \omega)\right]$$

Similar conclusions can be reached for the fast-thermal PSD as for the thermal-thermal PSD. However, for reactors with a material and geometrical symmetry axis, and for the detectors in symmetrical locations, the phase is not zero.

In the case of a totally homogeneous, infinite large reactor, we have for the thermal-thermal PSD

$$PSD^{2,2}(\bar{r}_{det_1}, \bar{r}_{det_2}, \omega) =$$

$$\int_{Reactor} d\bar{r} \; \frac{\delta(\bar{r}-\bar{r}_{det_1})\,\delta(\bar{r}-\bar{r}_{det_2})\,\alpha_3\,\Sigma_{s_0}^{1\to 2}(\bar{r}_{det_1})\,\alpha_3\,\Sigma_{s_0}^{1\to 2}(\bar{r}_{det_2})}{Denom^{1\to 2}(\bar{r}_{det_1}\,\omega)^* \cdot Denom^{1\to 2}(\bar{r}_{det_2}\,\omega)}$$

$$\times\; \overline{\nu(\nu-1)}\,\Sigma_f^{(2)}(\bar{r})\,\phi^{(2)}(\bar{r})$$

and for the fast-thermal PSD

$$PSD^{1,2}(\bar{r}_{det_1}, \bar{r}_{det_2}, \omega) =$$

$$\int_{Reactor} d\bar{r} \; \Big[\delta(\bar{r}-\bar{r}_{det_1})\cdot\delta(\bar{r}-\bar{r}_{det_2})\left(\alpha_2\,\Sigma_t^{(2)}(\bar{r}_{det_1}) - \alpha_5\,\frac{j\omega}{v^{(2)}(\bar{r}_{det_1})}\right)$$

$$\alpha_3\,\Sigma_{s_0}^{1\to 2}(\bar{r}_{det_2})\;\overline{\nu(\nu-1)}\,\Sigma_f^{(2)}(\bar{r})\,\phi^{(2)}(\bar{r})\Big]$$

$$/\;\Big[Denom^{1\to 1}(\bar{r}_{det_1}\,\omega)^* \cdot Denom^{1\to 2}(\bar{r}_{det_2}\,\omega)\Big]$$

The thermal-thermal CPSD is therefore zero, and the thermal-thermal APSD is non-zero. That the thermal-thermal CPSD is zero was to be expected, because no space-dependency is expected in a total homogeneous infinite large reactor. This reactor behaves precisely like a point reactor.

The fast-thermal CPSD is non-zero, and presents the coupling between the fast and thermal broad groups. The phase of the fast-thermal CPSD is:

$$\text{arc tg} \frac{\omega}{v^{(2)}(\bar{r}_{det})\ \Sigma_t^{(2)}(\bar{r}_{det})}$$

for an infinite large, homogeneous reactor. The same conclusion was reached by Ebert and Ackermann, Nieto, and Akhtar,[100] for point reactors. The numerical solution to the multi-dimensional, multigroup PSD's due to inherent binary noise or external disturbances will be sought in Chapter IV. The numerical approximations were performed for the two approximations to the anisotropic scattering in the P_1 equations.

In Appendix A we have derived the frequency-dependent equations to the three dimensional P_1 approximation. They were found to be equivalent to the frequency-dependent equations derived from the one dimensional P_1 equations (17 and 18).

CHAPTER IV

COMPUTATIONAL APPROACH

The objective of this chapter is to describe the approach taken in solving the partial differential equations, which describe the auto-power spectral density (APSD), cross-power spectral density (CPSD), and the coherence function (CHF) for a reactor and which have been described in Chapter III.

Several authors have applied the use of Fourier transformations in solving partial differential equations for kinetic models. Johnson, MacDonald, and Cohn[81] have calculated space- and energy-dependent transfer function and noise using static diffusion codes. They encountered instability problems in the iterations scheme used in the nuclear code EXTERMINATOR-II.[82] Due to convergence problems, they could treat only two dimensional problems at low frequencies (below 40 cps). At higher frequencies, their approach produced a totally unstable iteration, and no solution could be found. Even at frequencies of the order of 40 cycles per second, a two dimensional, two neutron group, single transfer function calculation took approximately 200 to 300 outer iterations for each frequency, whereas the steady state, two dimensional problem took only approximately 30 iterations.

Bridges and Clement[101,102] applied the Fourier transformation to the solution of the space- and energy-dependent response to a pseudo-random external binary source, using a space- and energy-dependent model

with temperature feedback, developed by Bridges, Clement, and Renier.[85] While the time-independent, one dimensional, two energy group model using the Gauss-Seidel iterative procedure converged in less than 20 iterations, the numerical solution to the time-dependent numerical model (one dimensional, two energy group, single transfer function with feedback) was much more time consuming. A typical calculation required 1,500 outer iterations per frequency, at a point convergence criterion of less than 1.0E-5 and required as much as 30 minutes of Univac-1108 time.

The numerical approach taken for a two dimensional, two or three energy group, multi-transfer function calculation of the PSD, CPSD, or CHF in this work was a novel cascade multi-line block-tridiagonal method, in which several adjacent energy groups and several adjacent rows were solved simultaneously or with inner iterations. This method was combined with a complex constraint overrelaxation technique and with different types of rebalancing accelerations.

A single frequency case for a typical 70 x 20 mesh, two broad energy group PSD calculation took approximately 10 to 50 iterations per transfer function calculation and required approximately four to five minutes cpu on a U-1108 computer. It seems that this technique gave a stable convergent iteration, and it was used for frequencies of up to 900 cycles per second. It should be noted that, for the calculation of a PSD, the calculation of many different weighted transfer functions was required.

In order to reduce the computer time requirements and to accelerate convergence, the partial inverses of the block-tridiagonal matrices were saved on random IO (Input-Output) devices during the first step of

the iteration of the first space- and energy-dependent transfer function calculation at a given frequency. The partial inverses were subsequently used in all the space- and energy-weighted transfer function calculations needed in the determination of the power spectral densities at a given frequency. The partial inverses of the block-tridiagonal matrices have, therefore, to be determined only once for each given frequency.

Note that, since the frequency-dependent fluxes are complex, the real and imaginary parts can be solved simultaneously using complex numbers arithmetic or sequentially, in which case the real and imaginary parts can be looked upon as separate energy groups in the difference approximations.

In the description of the different iterative methods and the different balance acceleration techniques which were used or experimented in the determination of the power spectral densities, the simultaneous solution (real and imaginary) and the sequential solution (real, then imaginary) were implemented.

Difference Equations

In this section, the basic finite difference equations will be developed for the solution of the partial differential equations obtained in Chapter III.

A two dimensional difference solution, with a third dimensional axial buckling correction was sought. The two-dimensional reactor geometry can be an x-y, r-z, or r-θ geometry with zero, reflective, or cyclic boundaries. The five-point difference equations which were obtained are different from the five-point difference equations used in normal diffusion

theory, through the introduction of additional complex leakage terms.

A similar technique to that found in EQUIPOISE[103] and TWENTY GRAND[104] codes was used in setting up the necessary difference equations in two dimensions. Parts of the following derivations were taken from Greenspan, Kelber, and Okrent.[105] Let us take an x-y geometry in which the x-dimension was subdivided into JMAX mesh intervals (columns) of length Δx_0, Δx_1, . . ., Δx_{JMAX-1}, and the y-dimension into IMAX mesh intervals (rows) of length Δy_0, Δy_1, . . ., Δy_{IMAX-1}. We therefore have subdivided the reactor into IMAX x JMAX cells. Let us take a cell at location (I,J) (Figure 1).

Let us consider around the mesh point (I,J) the four volumes, V_1, V_2, V_3, and V_4 (see figure) and let us define $\Sigma_{I-1,J-1}$ as a nuclear constant for the region described by mesh lines I-1 and I, and by J-1 and J.

We now convert $\nabla D \nabla$ into a numerical expression following standard procedures[105] over the volume circumscribed by I-1 and I+1, and by J-1 and J+1.

$$\iiint_V \nabla_{xyz}\, D(xyz\omega) \nabla_{xyz}\, \phi(xyz\omega)\, dx\, dy\, dz =$$

$$\iiint_{V_1} + \iiint_{V_2} + \iiint_{V_3} + \iiint_{V_4}$$

We also assume a "cos $B_z z$" dependence of the flux and constant material characteristics in the z-direction. Therefore,

$$\iiint_V \nabla_{xyz}\, D(xyz\omega)\, \nabla_{xyz}\, \phi(xyz\omega)\, dx\, dy\, dz \longrightarrow$$

$$\iint_S \nabla_{xy}\, D(xy\omega)\, \nabla_{xy}\, \phi(xy\omega)\, dx\, dy$$

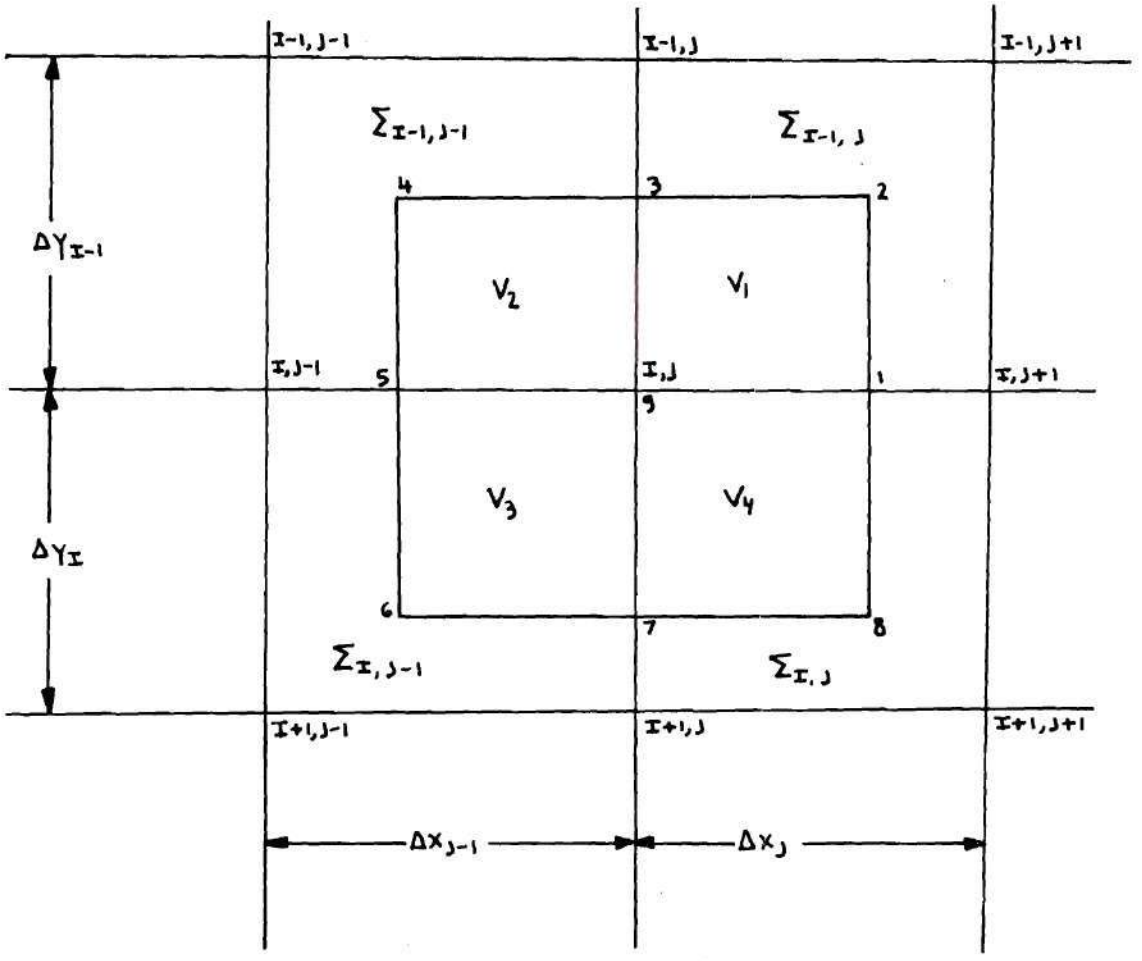

Figure 1. Mesh Cell in Rectangular Geometry

Applying Green's theorem and noting that:

$\overline{ds}$ = + ds if from outside to inside

$\overline{ds}$ = - ds if from inside to outside

$$\iint_{S_1} \nabla_{xy} D(xy\omega)\, \nabla_{xy} \phi(xy\omega)\, dx\, dy = \int_{S_{1\to 2}} D(xy\omega) \nabla_x \phi(xy\omega)\, ds_{1\to 2}$$

$$+ \int_{S_{2\to 3}} D(xy\omega) \nabla_y \phi(xy\omega)\, ds_{2\to 3} - \int_{\substack{S_{3\to 9} \\ x_{J+}}} D(xy\omega) \nabla_x \phi(xy\omega)\, ds_{3\to 9}$$

$$- \int_{\substack{S_{9\to 1} \\ y_{I+}}} D(xy\omega) \nabla_y \phi(xy\omega)\, ds_{9\to 1}$$

Applying a first order approximation in the expansion gives

$$\iint_{S_1} \nabla_{xy} D(xy\omega)\, \nabla_{xy} \phi(xy\omega)\, dx\, dy =$$

$$D_{I-1,J}\, s_{1\to 2}\, \frac{\phi_{I,J+1} - \phi_{I,J}}{2\Delta x_J} + D_{I-1,J}\, s_{2\to 3}\, \frac{\phi_{I-1,J} - \phi_{I,J}}{2\Delta y_{I-1}}$$

$$- \int_{\substack{S_{3\to 9} \\ x_{J+}}} D(xy\omega) \nabla_x \phi(xy\omega)\, ds_{3\to 9} - \int_{\substack{S_{9\to 1} \\ y_{I+}}} D(xy\omega) \nabla_y \phi(xy\omega)\, ds_{9\to 1}$$

Similar expressions can be obtained for $\iint_{S_2}$, $\iint_{S_3}$, and $\iint_{S_4}$.

Observing that the line integrals $\int_{\substack{S_{3\to 9} \\ x_{J+}}} D(xy)\nabla_x\phi(xy)\,dS_{3\to 9} = \int_{\substack{S_{9\to 3} \\ x_{J-}}} D(xy)\nabla_x\phi(xy)\,dS_{9\to 3}$ and that similar relations held for the other line integrals, we obtain the numerical equivalent in first order approximation of $\nabla D \nabla \phi$. In order to comply with the first order approximation, some restrictions on mesh spacing have to be followed. This will be more closely studied later in this chapter. For some boundary

conditions, the line integrals do not cancel each other out and the contribution of those line integrals will therefore have to be taken into account.

After a few manipulations we can write

$$\iint \nabla_{xy}\, D(xy\omega)\, \nabla_{xy}\, \phi(xy\omega)\, dx\, dy = \tag{63}$$

$$DD3_{I,J}\, \Phi_{I,J+1} + DD2_{I,J}\, \Phi_{I+1,J} + DD4_{I,J}\, \Phi_{I,J-1}$$

$$+ DD1_{I,J}\, \Phi_{I-1,J} - \left[DD3_{I,J} + DD2_{I,J} + DD4_{I,J} + DD1_{I,J}\right] \Phi_{I,J}$$

$$+ \text{Line Integrals}$$

where

$$DD3_{I,J} = D_{I-1,J}\, \frac{\Delta y_{I-1}}{2\Delta x_J} + D_{I,J}\, \frac{\Delta y_I}{2\Delta x_J} \tag{64}$$

$$DD2_{I,J} = D_{I,J-1}\, \frac{\Delta x_{J-1}}{2\Delta y_I} + D_{I,J}\, \frac{\Delta x_J}{2\Delta y_I}$$

$$DD4_{I,J} = D_{I-1,J-1}\, \frac{\Delta y_{I-1}}{2\Delta x_{J-1}} + D_{I,J-1}\, \frac{\Delta y_I}{2\Delta x_{J-1}}$$

$$DD1_{I,J} = D_{I-1,J}\, \frac{\Delta x_J}{2\Delta y_{I-1}} + D_{I-1,J-1}\, \frac{\Delta x_{J-1}}{2\Delta y_{I-1}}$$

Let us now evaluate the line integrals for the different boundaries. We assume that the boundaries are at mesh lines J = 2, J = JMAX-1, I = 2, I = IMAX-1. The lines J = 1, J = JMAX, I = 1, and I = IMAX are, therefore,

fictitious convenience mesh lines.

For example, for the right boundary (J = JMAX), we have $D_{I-1,JMAX-1} \equiv 0$, $D_{I,JMAX-1} \equiv 0$, and $D_{I+1,JMAX-1} \equiv 0$. Therefore

$$DD3_{I,JMAX-1} = 0 \tag{65}$$

$$DD2_{I,JMAX-1} = D_{I,JMAX-2} \frac{\Delta x_{JMAX-2}}{2\Delta y_I}$$

$$DD4_{I,JMAX-1} = D_{I-1,JMAX-2} \frac{\Delta y_{I-1}}{2\Delta x_{JMAX-2}} + D_{I,JMAX-2} \frac{\Delta y_I}{2\Delta x_{JMAX-2}}$$

$$DD1_{I,JMAX-1} = D_{I-1,JMAX-2} \frac{\Delta x_{JMAX-2}}{2\Delta y_{I-1}}$$

All line integrals cancel each other out except $\int_{S_{9\to3}} x_{(JMAX-1)}^{-}$ and $\int_{S_{7\to9}} x_{(JMAX-1)}^{-}$ and others.

After a few manipulations, it can be shown that those line integrals contribute to the leakage through the boundaries and that the leakage terms for $\nabla D \nabla$ are:

Right boundary leakage $(J = JMAX-1)$:

$$\sum_{I=2}^{IMAX-1} DD3_{I,JMAX-1}\ \Phi_{I,JMAX-1}$$

Left boundary leakage $(J = 2)$:

$$\sum_{I=2}^{IMAX-1} DD4_{I,2}\ \Phi_{I,2}$$

Top boundary leakage $(I=2)$:

$$\sum_{J=2}^{JMAX-1} DD1_{2,J}\ \Phi_{2,J}$$

Bottom boundary leakage $(I=IMAX-1)$:

$$\sum_{J=2}^{JMAX-1} DD2_{IMAX-1,J}\ \Phi_{IMAX-1,J}$$

Next, we convert $\Sigma\phi$ into a numerical expression, similar to the one used for $\nabla D\nabla\phi$:

$$\iint_S \Sigma(xy\omega)\,\Phi(xy\omega)\,dx\,dy = \iint_{S_1} + \iint_{S_2} + \iint_{S_3} + \iint_{S_4}$$

In first order approximation, we get

$$\iint_S \Sigma(xy\omega)\,\Phi(xy\omega)\,dx\,dy =$$

$$\left[\Sigma_{I-1,J}\,S_1 + \Sigma_{I-1,J-1}\,S_2 + \Sigma_{I,J-1}\,S_3 + \Sigma_{I,J}\,S_4\right]\Phi_{I,J}$$

or

$$\iint_S \Sigma(xy\omega)\,\Phi(xy\omega)\,dx\,dy = \left[\Sigma_{I-1,J}\,\frac{\Delta x_J\,\Delta y_{I-1}}{4}\right. \tag{66}$$

$$\left. + \Sigma_{I-1,J-1}\,\frac{\Delta x_{J-1}\,\Delta y_{I-1}}{4} + \Sigma_{I,J-1}\,\frac{\Delta x_{J-1}\,\Delta y_I}{4} + \Sigma_{I,J}\,\frac{\Delta x_J\,\Delta y_I}{4}\right]\Phi_{I,J}$$

Using the approximations described above, we will set up the proper difference equations corresponding to the differential equations of Chapter III.

Using the relations previously derived, we obtain the set of difference equations. (It has to be noted that all coefficients are space- and frequency-dependent, and all fluxes are frequency- and transfer-function dependent.)

$$LK(DD)^{R,R}_{I,J,K} - LK(DD)^{I,I}_{I,J,K} + 3\sum_{K'}\Big[LK(DE)^{R,R}_{I,J,K'\to K} - LK(DE)^{I,I}_{I,J,K'\to K}\Big] - DDS_{I,J,K}\,\Phi^{R}_{I,J,K} - DDG_{I,J,K}\,\Phi^{I}_{I,J,K} + \sum_{K'} Tr_{I,J,K'\to K}\,\Phi^{R}_{I,J,K'} + \sum_{K'} S_{I,J,K'\to K}\,\Phi^{R}_{I,J,K'} + S^{ext\,R}_{I,J,K} = -\alpha_S \frac{\omega}{v_{I,J,K}}\,\Phi^{I}_{I,J,K} \tag{67}$$

$$LK(DD)^{R,I}_{I,J,K} + LK(DD)^{I,R}_{I,J,K} + 3\sum_{K'}\Big[LK(DE)^{R,I}_{I,J,K'\to K} + LK(DE)^{I,R}_{I,J,K'\to K}\Big] - DDS_{I,J,K}\,\Phi^{I}_{I,J,K} - DDG_{I,J,K}\,\Phi^{R}_{I,J,K} + \sum_{K'} Tr_{I,J,K'\to K}\,\Phi^{I}_{I,J,K'} + \sum_{K'} S_{I,J,K'\to K}\,\Phi^{I}_{I,J,K'} + S^{ext\,I}_{I,J,K} = \alpha_S \frac{\omega}{v_{I,J,K}}\,\Phi^{R}_{I,J,K}$$

with

$$LK(DD)^{R,RI}_{I,J,K} = DD3^{R}_{I,J,K}\,\Phi^{RI}_{I,J+1,K} + DD2^{R}_{I,J,K}\,\Phi^{RI}_{I+1,J,K} + DD4^{R}_{I,J,K}\,\Phi^{RI}_{I,J-1,K} + DD1^{R}_{I,J,K}\,\Phi^{RI}_{I-1,J,K} - \Big[DD3^{R}_{I,J,K} + DD2^{R}_{I,J,K} + DD4^{R}_{I,J,K} + DD1^{R}_{I,J,K}\Big]\,\Phi^{RI}_{I,J,K}$$

$$LK(DE)^{R,RI}_{I,J,K'\to K} = DE3^{R}_{I,J,K'\to K}\,\Phi^{RI}_{I,J+1,K'} + DE2^{R}_{I,J,K'\to K}\,\Phi^{RI}_{I+1,J,K'}$$

$$+ DE4^{R}_{I,J,K'\to K}\,\Phi^{RI}_{I,J-1,K'} + DE1^{R}_{I,J,K'\to K}\,\Phi^{RI}_{I-1,J,K'} - \left[DE3^{R}_{I,J,K'\to K} + DE2^{R}_{I,J,K'\to K}\right.$$

$$\left. + DE4^{R}_{I,J,K'\to K} + DE1^{R}_{I,J,K'\to K}\right]\Phi^{RI}_{I,J,K'}$$

where

$$D^{R}_{I,J,K} = \frac{D_{I,J,K}}{1 + \left[\epsilon_4 \frac{3\omega}{V_{I,J,K}} D_{I,J,K}\right]^2}$$

$$D^{I}_{I,J,K} = \frac{-\epsilon_4 \frac{3\omega}{V_{I,J,K}} (D_{I,J,K})^2}{1 + \left[\epsilon_4 \frac{3\omega}{V_{I,J,K}} D_{I,J,K}\right]^2}$$

$$DD3^{RI}_{I,J,K} = D^{RI}_{I-1,J,K}\frac{\Delta y_{I-1}}{2\Delta x_J} + D^{RI}_{I,J,K}\frac{\Delta y_I}{2\Delta x_J} \tag{71}$$

$$DD2^{RI}_{I,J,K} = D^{RI}_{I,J-1,K}\frac{\Delta x_{J-1}}{2\Delta y_I} + D^{RI}_{I,J,K}\frac{\Delta x_J}{2\Delta y_I}$$

$$DD4^{RI}_{I,J,K} = D^{RI}_{I-1,J-1,K}\frac{\Delta y_{I-1}}{2\Delta x_J} + D^{RI}_{I,J-1,K}\frac{\Delta y_I}{2\Delta x_{J-1}}$$

$$DD1^{RI}_{I,J,K} = D^{RI}_{I-1,J,K}\frac{\Delta x_J}{2\Delta y_{I-1}} + D^{RI}_{I-1,J-1,K}\frac{\Delta x_{J-1}}{2\Delta y_{I-1}}$$

$$DS^{R}_{I,J,K'\to K} = \tag{72}$$

$$D^{R}_{I,J,K}\,\Sigma_{s_1}^{I,J,K'\to K}\,D^{R}_{I,J,K'} - D^{I}_{I,J,K}\,\Sigma_{s_1}^{I,J,K'\to K}\,D^{I}_{I,J,K'}$$

$$DS^{I}_{I,J,K'\to K} =$$

$$D^{R}_{I,J,K}\,\Sigma_{s_1}^{I,J,K'\to K}\,D^{I}_{I,J,K'} + D^{I}_{I,J,K}\,\Sigma_{s_1}^{I,J,K'\to K}\,D^{R}_{I,J,K'}$$

$$DE3^{RI}_{I,J,K'\to K} = DS^{RI}_{I-1,J,K'\to K}\frac{\Delta y_{I-1}}{2\Delta x_J} + DS^{RI}_{I,J,K'\to K}\frac{\Delta y_I}{2\Delta x_J} \qquad (73)$$

$$DE2^{RI}_{I,J,K'\to K} = DS^{RI}_{I,J-1,K'\to K}\frac{\Delta x_{J-1}}{2\Delta y_I} + DS^{RI}_{I,J,K'\to K}\frac{\Delta x_J}{2\Delta y_I}$$

$$DE4^{RI}_{I,J,K'\to K} = DS^{RI}_{I-1,J-1,K'\to K}\frac{\Delta y_{I-1}}{2\Delta x_J} + DS^{RI}_{I,J-1,K'\to K}\frac{\Delta y_I}{2\Delta x_{J-1}}$$

$$DE1^{RI}_{I,J,K'\to K} = DS^{RI}_{I-1,J,K'\to K}\frac{\Delta x_J}{2\Delta y_{I-1}} + DS^{RI}_{I-1,J-1,K'\to K}\frac{\Delta x_{J-1}}{2\Delta y_{I-1}}$$

$$DDS_{I,J,K} = \Sigma_t^{I,J,K} + D^R_{I,J,K}B_z^2$$

$$DDG_{I,J,K} = D^I_{I,J,K}B_z^2$$

where $Tr_{I,J,K'\to K}$ = isotropic scattering

$S_{I,J,K'\to K}$ = source generating neutrons in energy group K, due to reactions in group K'

In the case where we use assumption 1, as described in Chapter III, we set $DS^R_{I,J,K'\to K} \equiv 0$ and $DS^I_{I,J,K'\to K} \equiv 0$ for all I, J, K, and K'.

One-Line, One-Group Numerical Solution and Balance Accelerations

We have derived a set of difference equations, which can be written in matrix form as $[M][\phi] = [T_r][\phi] + \frac{1}{\lambda}[F][\phi] + S$.

The formal solution is: $[\phi] = (M - T_r - \lambda^{-1})^{-1}S$.

Matrix M couples points in energy at one space point and it has the transport coupling between adjacent points in space, primarily at one energy, but also from the complementary energy (using the Fourier

transformation definition, we have that the complementary energy for the real part of the flux is the imaginary part of the flux, and vice versa) through the leakage terms.

The size of the matrix $(M - T_r - \lambda^{-1} F)$ is generally far too large to be solved by a direct inversion scheme such as the Gauss reduction technique. For a typical problem of 68 mesh-points in the x-direction (JMAX), 20 mesh-points in the y-direction (IMAX), and three energy (KMAX) groups, this would give a matrix of size N by N where N = IMAX x JMAX x KMAX x 2, therefore, 8160 by 8160. The inversion would require approximately $N^3(5.4 \times 10^{11})$ complex operations. Each operation associates itself with a round-off error, and the propagation of the round-off error through the computation tends to contribute in giving a divergent solution.

In the inversion of matrix M, in general, an iterative process is used. Two very widely used techniques are the one-line, overrelaxation method and the alternating-direction method.

Johnson[81] solved a similar set of difference equations using a one-line, overrelaxation method (with the use of the code EXTERMINATOR-II[82]). The space distribution for the "J's" (x-direction) at one "I" (y-direction) and at one energy group was obtained by solving a tridiagonal matrix with diagonal dominance. The source matrix consisted of fission, scattering, external source, and the leakage terms due to $\phi_{I+1,J,K}$ and $\phi_{I-1,J,K}$. After each tridiagonal inversion for a fixed I and K, the fluxes were successfully corrected using the overrelaxation expression

$$\phi^t_{I,J,K} = \phi^{t-1}_{I,J,K} + \beta(\phi^{t*}_{I,J,K} - \phi^{t-1}_{I,J,K})$$

where t = iteration number

$\phi^{t}_{I,J,K}$ = value of $\phi_{I,J,K}$ at iteration t, after overrelaxation

$\phi^{t*}_{I,J,K}$ = computed value of $\phi_{I,J,K}$ after tridiagonal inversion and before overrelaxation

β = overrelaxation coefficient.

In this method, always the latest values for the unknown fluxes were used. Johnson[81] encountered instability problems in this iteration scheme, mainly due to poor coupling between the real and imaginary parts of the fluxes, the presence of the flux vector in the second, third, or fourth quadrant of the complex domain, and the nature of the overrelaxation expression. The behavior of the overrelaxed fluxes away from the real axis tended to introduce corrections, whose relative error tends to amplify through the iteration. Through the use of group rebalancing,[106] a more stable system was obtained. However, for two dimensional, two energy group problems, the iterations still tended to become unstable at frequencies above 40 cycles/second.

Bridges[101] also solved a similar set of difference equations, using an iteration process without overrelaxation correction. The problem solved was a one dimensional, two energy group problem with feedback. The space distribution at one energy for both the real and the imaginary part of the flux was obtained by solving a tridiagonal matrix in the complex domain. The iteration scheme for a one dimensional problem was very time consuming and required as much as 1,500 outer iterations for a single transfer function calculation with feedback at one frequency. No calculations were performed at higher frequencies (above 10 cps).

One of the causes of this very slow convergence is that, in the transfer matrix of a multi-group and multi-dimensional technique (such as the usual one-line, one-energy overrelaxation technique), the elements representing group-to-group transfer require off-diagonal elements on the side opposite to the down-transfer elements (by "down-transfer" we mean from higher energies to lower energies).

In the one-line, one-energy overrelaxation technique, the solution of a tridiagonal matrix gives the values of the fluxes simultaneously along a row at one energy; while the inscatter, outscatter, fission, external sources, leakage from adjacent rows are being handled as external coupling terms, which are held constant while the fluxes along the row are being solved. Superimposed to this, one can use many additional techniques such as group-dependent and/or space-dependent scaling which rebalances fluxes, alternating the direction of iteration, inner iterations, etc.

Since the fluxes are usually solved group by group, starting with the group of highest energy, we find that the in-transfer source into a lower group is due to the transfer from groups of higher energies (and/or the real part of the flux), for which the latest estimate (current outer iteration) of the fluxes is available, and also due to the transfer from groups of lower energy (and/or the imaginary part of the flux), for which only the fluxes of the previous outer iteration are available.

For multi-dimensional problems, we have in addition a neutron imbalance, within the energy group, due to the leakage terms in the finite difference equations. The difference equations are solved by tridiagonal or block-tridiagonal inversion in one space direction (e.g., x), usually for increasing mesh numbers of another space direction (e.g., y). The

"within" group in-transfer sources due to leakage are from lower mesh numbers of y and are based on the latest estimate of the fluxes, and from higher mesh number of y, based on the fluxes of the previous outer iteration.

We know that this can lead to a poor neutron balance and for each group and for the overall system, especially when sharp gradients (energy and/or space) of the fluxes are present. In the case of power spectral density calculations, the nature of the neutron waves, especially at higher frequencies, brings with them high gradients. While at lower frequencies, a disturbance in a part of a reactor almost instantaneously propagates through the reactor, a disturbance at higher frequencies (smaller wavelength) will undergo higher attenuations in space and, therefore, will generate higher gradients. This neutron imbalance can lead to very slow convergence, or even to instabilities of the iteration scheme.

An attempt to overcome this was first attempted by Tobias, Vondy, and Fowler.[106] Tobias included a method which forced a neutron balance between groups. Group-dependent "driving factors," D^g, were found by multiplying all the fluxes in an energy group by D^g in the difference equations. By setting one of the driving factors to one, all the other group-dependent driving factors were found by elimination between the difference equations.

In this manner, group balances were forced at each outer iteration. It must be noted, however, that at an intermediate stage during an outer iteration, these balances do not hold. Tobias et al.[106] concluded, from experimentation with this method, that this group rebalancing does not gain very much in speed of convergence for non-cell calculation, but it

was found useful for cell calculations, primarily for those in which the groups were poorly coupled. In this case, the speed of convergence was greatly improved. A similar technique was used by the two dimensional diffusion code, EXTERMINATOR-II.[82] In this code, a complete sweep for each energy group for each line was performed, using line-overrelaxation. After the completion of an outer iteration, the fluxes were rebalanced using the driving factors. As mentioned previously, this scheme did not prove successful at higher frequencies, mainly because of the neutron imbalances during the course of an outer iteration. The imbalance at a certain energy group and at a line propagates itself through all the following line iterations of the outer iteration, and this causes instabilities at higher frequencies. Also, the possibility exists of spectral neutron imbalance.

Another attempt to overcome this imbalance was the incorporation of a group-independent up-scatter scale factor as in the DTF-IV code.[107] The fluxes were multiplied with this scale factor, which is defined as:

$$f^{up} = \frac{\sum_g \sum_i V_i (Q_g + \chi^g F^{itp})}{\sum_g \sum_i V_i (Q_g + \chi^g F^{itp}) + Tr_{up,i}^{g \to g} (\phi_{gi}^{itp} - \phi_{gi}) V_i} \quad (74)$$

where Q_g = fixed source into group g

$\chi^g F^{itp}$ = fission neutron into group g, due to fluxes obtained in previous iteration itp

$Tr_{up,i}^{g \to g}$ = self-transfer into group g = $\sum_{g'=g-1}^{1} Tr_{up,i}^{g \to g'}$

V_i = volume element at mesh i

ϕ_{gi}^{itp} = flux at energy group g, mesh i, outer iteration itp.

An extension of this is the use of a group-dependent flux scaling factor. The group-dependent scale factors, with which the fluxes were multiplied during an outer iteration, were defined by

$$f_g = \frac{\sum_i V_i (Q_g + \chi^g F^{itp})}{\sum_i V_i (Q_g + \chi^g F^{itp}) + Tr_i^{g \to g} (\phi_{gi}^{itp} - \phi_{gi})} \qquad (75)$$

It should be noted that these group-dependent scaling factors did not scale the fluxes of those groups where no neutrons were born, and that they produced a balance in each group. At the completion of an outer iteration, however, the overall system is generally unbalanced, since part of the fission sources and the up-scatter sources are calculated based on the fluxes of the previous outer iterations, and the remainder on the current iteration. As was done in ANISN,[108] this suggests the need for rescaling of all groups with group-dependent scaling factors at the completion of the current outer iteration.

We performed extensive experimentation using the group rebalancing and the group-dependent scaling factor techniques in the numerical solution of the multi-dimensional power spectral densities. Although at lower frequencies, improvements in the speed of convergence of the iteration scheme were encountered, no stable iteration was obtained at higher frequencies. As we mentioned before, similar difficulties were encountered by Johnson[81] and Bridges.[101]

Another technique with which we experimented was based on an extension of a method developed by Engle.[109] While the group rebalancing technique developed by Tobias et al.[106] was based on correcting the

fluxes with a group-dependent, but space-independent driving function, the rebalancing method of Engle was based on correcting the fluxes with group-dependent and space-dependent driving factors. He implemented this in the usual discrete ordinate inner iteration (inner iterations at a neutron group are necessary in transport calculations because neutrons may scatter from any angle to any other angle, and the flux in all angles is unknown at the beginning of an iteration) of a special version of the ANISN[108] code, and demonstrated the effectiveness of group- and space-dependent scaling. As the dominance ratio (ratio of the number of particles that collided in the n^{th} iteration to the number that collide in the $(n-1)^{th}$ iteration) approached unity, the rate of convergence decreased rapidly. A fast improvement in the convergence rate of the inner iteration was encountered over the standard iteration, and even over the Chebyshev acceleration. The same method is applied in DOT-III,[110] which is a two dimensional transport code.

This method was extended to the outer iteration computations of the PSD's in order to accelerate convergence. In a manner similar to Mynatt et al.[110] and Tobias et al.,[106] let us write the balance equations. At the end of an outer iteration the balance equation for the space volume defined by mesh (I,J), for energy group K, can be written as:

$$LI^{m}_{I-1,J,K} + LI^{m}_{I+1,J,K} + LI^{m}_{I,J-1,K} + LI^{m}_{I,J+1,K} \qquad (76)$$

$$- LO^{m}_{I,J,K} - \Sigma^{R}_{I,J,K}\,\varphi^{m}_{I,J,K} + \sum_{K'} S^{m}_{I,J,K'\to K} + S^{ext}_{I,J,K} = 0$$

where

$LI^{n}_{I,J,K}$ = leakage into space volume defined by mesh (I,J), at energy group K, at the end of the n^{th} outer iteration

$LO^{n}_{I,J,K}$ = leakage out of space volume

$\Sigma^{R}_{I,J,K} = \Sigma^{a}_{I,J,K} + \sum_{K'} \Sigma_{S}^{I,J,K\to K'}$ + others

$S^{n}_{I,J,K'\to K}$ = external, fission, delayed, and scattering sources into group K, due to reactions in group K', at the end of the n^{th} outer iteration

$\phi^{n}_{I,J,K}$ = neutron flux at mesh (I,J) for neutrons of group K, at the end of the n^{th} outer iteration

$S^{ext}_{I,J,K}$ = external source at mesh (I,J) and neutron energy group K.

After multiplying the fluxes with space- and group-dependent scale factors, we obtain

$$f_{I-1,J,K}\, LI^{m}_{I-1,J,K} + f_{I+1,J,K}\, LI^{m}_{I+1,J,K} + f_{I,J-1,K}\, LI^{m}_{I,J-1,K} \quad (77)$$

$$+ f_{I,J+1,K}\, LI^{m}_{I,J+1,K} - f_{I,J,K}\, LO^{m}_{I,J,K} - \Sigma^{R}_{I,J,K}\, f_{I,J,K}\, \Phi_{I,J,K}$$

$$+ \sum_{K'} f_{I,J,K'}\, S^{m}_{I,J,K'\to K} + S^{ext}_{I,J,K} = 0$$

A set of difference equations is therefore obtained, with the scale factors $f_{I,J,K}$ as unknown. Each difference equation has the characteristics of a five-point difference equation. The solution for $f_{I,J,K}$ can be obtained similarly to methods used for the solution of the fluxes $\phi_{I,J,K}$.

At the i^{th} iteration for $f_{I,J,K}$ we can rewrite equation (77) as follows:

$$f^{i}_{I,J-1,K}\, LI^{m}_{I,J-1,K} + f^{i}_{I,J+1,K}\, LI^{m}_{I,J+1,K} - f^{i}_{I,J,K}\, LO^{m}_{I,J,K} \qquad (78)$$

$$- \sum^{R}_{I,J,K} f^{i}_{I,J,K}\, \Phi^{m}_{I,J,K} = - \sum_{K'} f^{i}_{I,J,K'}\, S^{m}_{I,J,K'\to K}$$

$$- f^{i}_{I-1,J,K}\, LI^{m}_{I-1,J,K} - f^{i}_{I+1,J,K}\, LI^{m}_{I+1,J,K} - S^{ext}_{I,J,K}$$

In order to be able to use a standard iteration technique, the $f_{I,J,K}$ in the right hand side of this equation were taken at the previous $(i-1)^{th}$ iteration. Therefore:

$$f^{i}_{I,J-1,K}\, LI^{m}_{I,J-1,K} + f^{i}_{I,J+1,K}\, LI^{m}_{I,J+1,K} - f^{i}_{I,J,K}\, LO^{m}_{I,J,K} \qquad (79)$$

$$- \sum^{R}_{I,J,K} f^{i}_{I,J,K}\, \Phi^{m}_{I,J,K} = - \sum_{K'} f^{i-1}_{I,J,K'}\, S^{m}_{I,J,K'\to K}$$

$$- f^{i-1}_{I-1,J,K}\, LI^{m}_{I-1,J,K} - f^{i-1}_{I+1,J,K}\, LI^{m}_{I+1,J,K} - S^{ext}_{I,J,K}$$

A one-group, one-line overrelaxation scheme, with $\beta = 1.0$ was attempted in order to obtain the $f_{I,J,K}$. This iteration on the scale factors was performed starting with all $f_{I,J,K} = 1.0$, and was completed after that

$$\text{Max} \left| \frac{f^{i}_{I,J,K} - f^{i-1}_{I,J,K}}{f^{i}_{I,J,K}} \right| \leq 0.001 \qquad \text{for all I, J, K.}$$

The fluxes at the end of the n^{th} outer iteration were thus corrected by

$L_{s,t}$ = summed leakage

$F_{s,t}$ = summed fission sources

S_s = summed fixed sources

h_t = fixed source scaling factor

A similar method of fixed source rescaling could be applied in the iterative process of the power spectral density calculations. We do not know, however, the relative merit of fixed source rescaling as compared to the frequency-dependent flux scaling rebalancing schemes that were described earlier.

Another acceleration method with which we experimented in the PSD calculations was based on inner iterations with or without acceleration by rebalancing at the end of an outer iteration step.

The usual one-line, one-energy overrelaxation method is based on solving a tridiagonal matrix in order to obtain the values of the fluxes along a row of points at a particular energy, while the inscatter, fission, and external sources, leakage terms from adjacent rows, are being handled as external coupling terms. After the solution of the tridiagonal matrix, the fluxes along the row and the energy group were overrelaxed. The identical method is then used to obtain the fluxes along the same row, but at a higher energy group. This process is then repeated for all energy groups. The method is then applied to the next row, etc. Always the latest values of the fluxes are used in the computation of the external coupling terms. The inner iterations acceleration consisted of performing the iteration with one of the following schemes:

1. between all energy groups, at a particular row
2. between all energy groups, and between several rows, which are

adjacent to each other.

This was done until an inner-iteration convergence criterion was met. The inner iteration criterion

$$\varepsilon_{inner} = Max \left| \frac{\Phi^{i,n}_{I,J,K} - \Phi^{i-1,n}_{I,J,K}}{\Phi^{i-1,n}_{I,J,K}} \right|$$

for any J and K at a particular I

where $\phi^{i,n}_{I,J,K}$ = flux at mesh points I,J, energy group K at inner iteration i, at outer iteration n

KMAX = maximum group number

IMAX = maximum number of rows

is considered to be the only reliable one by which the iterative process can be terminated. The inner-iteration was considered to be converged when $\varepsilon_{inner} \leqq$ 1.0E-3. However, the inner iterations were also terminated when the number was greater than an inputted number, generally 10.

Following scheme "1," we solved for the fluxes along row I = 2 at energy group 1, then along the same row I = 2, but at energy group 2, etc., and finally we solved for the fluxes along row I = 2, but at energy group KMAX. This same sequence for row I = 2 was then repeated for all the energy groups at row I = 2, until the inner-iteration criterion was met. This was then followed by finding the fluxes at row I = 3 for all energy groups following this same method of iteration, then row I = 4, etc. After IMAX rows, we have completed one outer-iteration. This method of inner-iterations following scheme "1" was found to be helping somewhat in accelerating convergence, although the convergence was still very slow in the computation of the PSD at higher frequencies.

In iteration scheme 2, we have used the same method as described above, except that the inner-iteration scheme was extended to include several adjacent rows. Figure 2 shows a schematic flow diagram of the inner-iteration, and Figure 3 the flow diagram of the outer-iterations. In experimenting with this method, it was found that, after completion of an inner-iteration scheme, the convergence could be somewhat accelerated by starting the next inner-iteration scheme at a row that was already covered in a previous inner-iteration. This method of inner-iteration following scheme "2" was found to be accelerating convergence appreciably; however, the computer time needed to achieve convergence was not necessarily reduced. At high frequencies, convergence was not always achieved, and the convergence rate was slow.

Tests of this method have shown that appreciable imbalances are being generated not only through external coupling terms from adjacent groups, but also from space points. At high frequencies, in the determination of the PSD's, high gradients of the waves were encountered, which amplified those imbalances. Attempts to achieve acceleration by reducing mesh spaces (therefore increasing the number of mesh points) by a factor of four were not successful. Further reductions were not attempted because of the increased computer time and core required.

The failure to achieve a stable iteration scheme pointed to the following changes to be made:

1. Concentrate the calculational effort on the space distribution at either one-energy in the complex domain, or at several energies in the complex domain.

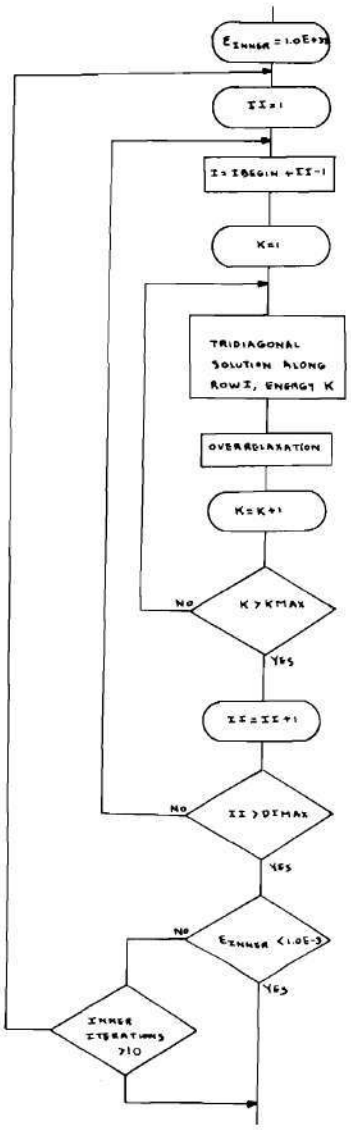

Figure 2. Inner-Iteration Flow Diagram

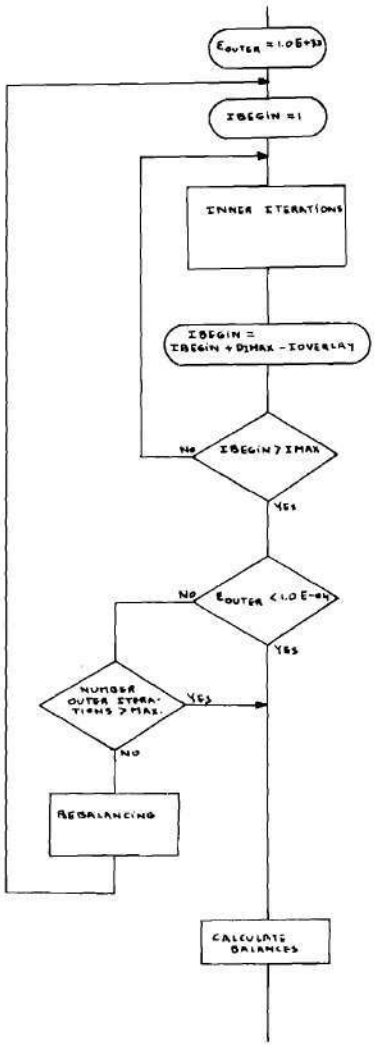

Figure 3. Outer-Iteration Flow Diagram

2. Improvement of the one-line, overrelaxation method or the alternating direction method, with or without overrelaxation.

Constraint Overrelaxation in the Complex Domain

In order to avoid complications due to bad initial flux guesses, to poor coupling between neutron groups, and the nature of the flux (complex domain), the overrelaxation formula had to be restrained similar to a method used in the code CITATION.[111] Additional restraints had to be imposed on the overrelaxation adjustment of the complex flux. After an inversion (tridiagonal or block tridiagonal) in the complex domain, the computed fluxes were adjusted through the following overrelaxation relation

$$\Phi_m = \Phi_{m-1} + \beta(\Phi_m^* - \Phi_{m-1}) \tag{80}$$

or

$$\Phi_m^R = \Phi_{m-1}^R + \beta^R(\Phi_m^{*R} - \Phi_{m-1}^R) - \beta^I(\Phi_m^{*I} - \Phi_{m-1}^I)$$

$$\Phi_m^I = \Phi_{m-1}^I + \beta^R(\Phi_m^{*I} - \Phi_{m-1}^I) + \beta^I(\Phi_m^{*R} - \Phi_{m-1}^R)$$

where ϕ_n^R = real part of corrected flux (through overrelaxation)at iteration n

ϕ_n^{*R} = real part of calculated flux at iteration n

ϕ_n^I = imaginary part of corrected flux at iteration n

ϕ_n^{*I} = imaginary part of calculated flux at iteration n

β^R = real part of the overrelaxation coefficient

β^I = imaginary part of the overrelaxation coefficient

For most of the iterations used for the determination of the space- and energy-dependent PSD's (CPSD, APSD, and CHF) in two dimensions, the β^R was started at a value of 1.5, and subsequently reduced every 20 iterations to $\beta^R = (9\beta^R + 1) \div 10$, if ϵ_n^R and ϵ_n^I were not decreasing monotonically

where

$$\epsilon_n^R = \max \left| \frac{\phi^{R,n}_{I,J,K}}{\phi^{R,n-1}_{I,J,K}} - 1 \right| \qquad \text{for any } I,J,K$$

$$\epsilon_n^I = \max \left| \frac{\phi^{I,n}_{I,J,K}}{\phi^{I,n-1}_{I,J,K}} - 1 \right| \qquad \text{for any } I,J,K$$

No significant improvement in the speed of the convergence of the iteration was found by using values of β^I different from zero. Subsequently, all runs were made with β^I kept zero.

The following relaxation with the appropriate constraints similar to the relaxation restraints of the code CITATION[111] were used, for both the real and the imaginary parts of the complex flux.

If $\frac{\Phi_m^{*R}}{\Phi_{m-1}^R} > 0$, then $\Phi_m^R = \Phi_{m-1}^R + \beta^R(\Phi_m^{*R} - \Phi_{m-1}^R) - \beta^I(\Phi_m^{*I} - \Phi_{m-1}^I)$

or $$\frac{\Phi_m^R}{\Phi_{m-1}^R} = 1 + \beta^R\left(\frac{\Phi_m^{*R}}{\Phi_{m-1}^R} - 1\right) - \beta^I\left(\frac{\Phi_m^{*I}}{\Phi_{m-1}^R} - \frac{\Phi_{m-1}^I}{\Phi_{m-1}^R}\right),$$

with the restraints that

$$\alpha \Phi_m^{*R} < \Phi_m^R < \gamma(\Phi_m^{*R} + \Phi_{m-1}^R)$$

If $\frac{\Phi_m^{*I}}{\Phi_{m-1}^{I}} < 0$, then $\Phi_m^I = -\Phi_{m-1}^I + \beta^R\left(\Phi_{m-1}^I - \Phi_m^{*I}\right) + \beta^I\left(\Phi_{m-1}^R - \Phi_m^{*R}\right)$

or $$\frac{\Phi_m^I}{\Phi_{m-1}^I} = -1 + \beta^R\left(1 - \frac{\Phi_m^{*I}}{\Phi_{m-1}^I}\right) + \beta^I\left(\frac{\Phi_{m-1}^R}{\Phi_{m-1}^I} - \frac{\Phi_m^{*R}}{\Phi_{m-1}^I}\right),$$

with the restraints that

$$\gamma\left(-\Phi_{m-1}^I + \Phi_m^{*I}\right) < \Phi_m^I < \alpha\,\Phi_m^{*I}$$

or $$\gamma\left(-1 + \frac{\Phi_m^{*I}}{\Phi_{m-1}^I}\right) < \frac{\Phi_m^I}{\Phi_{m-1}^I} < \alpha\,\frac{\Phi_m^{*I}}{\Phi_{m-1}^I} \quad .$$

Note that the calculated real and imaginary parts of the flux (ϕ_n^{*R} and ϕ_n^{*I}) were obtained simultaneously in the cascade inversion of the block tridiagonal matrix. However, for the case where β^I was kept zero, the overrelaxation of the real and imaginary parts of the flux was independent of one another.

Figure 4 shows the overrelaxation scheme for $\beta^I = 0$, $\gamma = 1$, and $\alpha = 0.5$. In this figure we have plotted ϕ_n/ϕ_{n-1} versus ϕ_n^*/ϕ_{n-1} where

ϕ_n = overrelaxed flux at iteration n

ϕ_n^* = calculated flux at iteration n after the tridiagonal or block tridiagonal inversion

This scheme applies and for the real and for the imaginary parts of the frequency-dependent flux.

It is well known that, if β^R is taken too low or too high, the iteration scheme is very slowly converging. Usually β^R was kept between

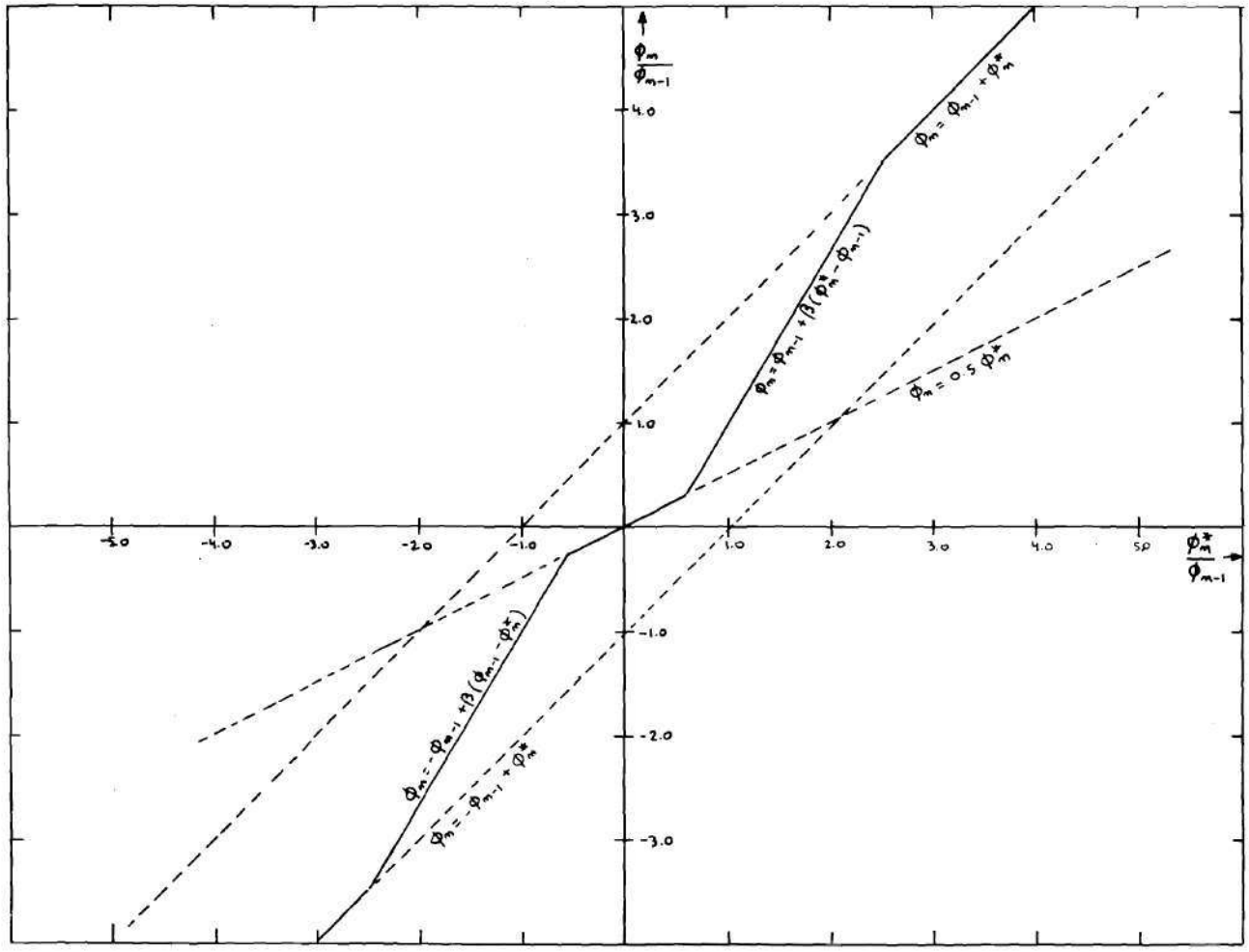

Figure 4. Complex Constraint Overrelaxation Scheme

approach taken by Bridges (solving real and imaginary parts of the flux simultaneously) indicated that the emphasis should be put on the calculations of the space points simultaneously at several energies, in the complex domain, and simultaneously for several rows.

One-Line All-Energy Groups Method with Constraint Overrelaxation

Let us rewrite the set of equations (67 and 68) in matrix form for the case of a single line overrelaxation ("I" constant) and for all energy groups.

$$\begin{bmatrix} M_{I,J=1} & & & \\ & M_{I,J=2} & & \\ & & \ddots & \\ & & & M_{I,JMAX} \end{bmatrix} \times \begin{bmatrix} \Phi_{I,J=1} \\ \Phi_{I,J=2} \\ \vdots \\ \Phi_{I,J} \\ \vdots \\ \Phi_{I,JMAX} \end{bmatrix} = \begin{bmatrix} TL_{I,J=1} & BL_{I,J=1} \\ TL_{I,J=2} & BL_{I,J=2} \\ \vdots & \vdots \\ TL_{I,J} & BL_{I,J} \\ \vdots & \vdots \\ TL_{I,JMAX} & BL_{I,JMAX} \end{bmatrix} \times \begin{bmatrix} \Phi_{I-1,J=1} \cdots \Phi_{I-1,J} \cdots \Phi_{I-1,JMAX} \\ \Phi_{I+1,J=1} \cdots \Phi_{I+1,J} \cdots \Phi_{I+1,JMAX} \end{bmatrix} + \begin{bmatrix} S_{I,J=1} \\ S_{I,J=2} \\ \vdots \\ S_{I,J} \\ \vdots \\ S_{I,JMAX} \end{bmatrix} \tag{81}$$

where $M_{I,J}$, $\Phi_{I,J}$, $TL_{I,J}$, $BL_{I,J}$, $S_{I,J}$ are sub-matrices.

Matrix M_I, represented by its sub-matrices $M_{I,J}$, is a block-

tridiagonal matrix, with a band of non-zero elements of width equal to 3 x KMAX x 2, the length of the band is equal to JMAX x KMAX x 2, the number of elements in this band is JMAX x $KMAX^2$ x 12. The number of elements (zero and non-zero) in matrix M_I is $\overline{JMAX \times KMAX \times 2}^2$. For a typical two-dimensional (JMAX=68), three group problem (KMAX=3), and for a single row (I=constant), the number of elements in the block-tridiagonal band is therefore 7,344, while the number of elements in the matrix M is 166,464.

The sub-matrices $\phi_{I,J}$ and $S_{I,J}$ are represented by:

$$\Phi_{I,J} = \begin{bmatrix} \Phi^R_{I,J,K=1} \\ \Phi^I_{I,J,K=1} \\ \\ \Phi^R_{I,J,K} \\ \Phi^I_{I,J,K} \\ \\ \Phi^R_{I,J,KMAX} \\ \Phi^I_{I,J,KMAX} \end{bmatrix} \qquad S_{I,J} = \begin{bmatrix} S^R_{I,J,K=1} \\ S^I_{I,J,K=1} \\ \\ S^R_{I,J,K} \\ S^I_{I,J,K} \\ \\ S^R_{I,J,KMAX} \\ S^I_{I,J,KMAX} \end{bmatrix}$$

The sub-matrix $TL_{I,J}$ is of size 2 x KMAX by 2 x KMAX and is represented by the elements $DD1^R_{I,J,K}$, $DD1^I_{I,J.K}$, $DE1^R_{I,J,K'\to K}$, $DE1^I_{I,J,K'\to K}$ which were previously derived (equations 71 and 72). The sub-matrix $BL_{I,J}$ is of size 2 x KMAX by 2 x KMAX and is of the same form as the above matrix except that DD1 is replaced by DD2, DE1 by DE2.

The solution of the flux along one line sweep is therefore:

$$[M_I][\Phi_I] = [TL_I \quad BL_I]\begin{bmatrix}\Phi_{I-1}\\ \Phi_{I+1}\end{bmatrix} + [S_I] \tag{82}$$

or

$$[\Phi_I] = [M]^{-1}\left[[TL_I \; BL_I]\begin{bmatrix}\Phi_{I-1}\\ \Phi_{I+1}\end{bmatrix} + [S_I]\right]$$

After the solution for the real and imaginary parts of the (JMAX x KMAX) energy-dependent complex fluxes was determined by finding the inverse of M_I through matrix factorization, they were overrelaxed as described previously. A revised source was subsequently calculated and the solution for the next line was determined.

The indicator that an iteration is convergent can be shown to be for a steady state reactor problem:

$$\varepsilon_m^{st} < \varepsilon_{m-1}^{st}$$

where

$$\varepsilon_m^{st} = \max\left|\frac{\Phi_{I,J,K}^{n} - \Phi_{I,J,K}^{m-1}}{\Phi_{I,J,K}^{m-1}}\right| = \max\left|\frac{\Phi_{I,J,K}^{m}}{\Phi_{I,J,K}^{m-1}} - 1\right| \quad \text{for any } I,J,K$$

During the calculation of a transfer function, the iterations were monitored by computing

$$\varepsilon_m^{Ampl} = \max \left| \left[\frac{\overline{\Phi_{I,J,K}^{R,m}}^2 + \overline{\Phi_{I,J,K}^{I,m}}^2}{\overline{\Phi_{I,J,K}^{R,m-1}}^2 + \overline{\Phi_{I,J,K}^{I,m-1}}^2} \right]^{1/2} - 1 \right| \qquad \text{for any I,J,K}$$

$$\varepsilon_m^{phase} = \max \left| \frac{\operatorname{arctg} \dfrac{\Phi_{I,J,K}^{I,m}}{\Phi_{I,J,K}^{R,m}}}{\operatorname{arctg} \dfrac{\Phi_{I,J,K}^{I,m-1}}{\Phi_{I,J,K}^{R,m-1}}} - 1 \right| \qquad \text{for any I,J,K}$$

The indication that an iteration was convergent was taken to be $\varepsilon_n^{Ampl} < \varepsilon_{n-1}^{Ampl}$. After the first 20 iterations were completed, if those conditions failed three times in ten iterations, then the overrelaxation coefficient β^R was subsequently reduced as explained above.

For most of the PSD calculations, the iteration was considered convergent when ε_n^{Ampl} was smaller than 1.0×10^{-4} and ε_n^{phase} was smaller than 1.0×10^{-2}.

After completion of a convergent problem, the balance equations were set up and computed for each I,J,K and the relative balance error was determined as follows:

$$EB_{I,J,K}^{Ampl} =$$

$$\max \left| \left[\frac{\left(\text{Leakage}_{I,J,K}^{R} + \text{Losses}_{I,J,K}^{R}\right)^2 + \left(\text{Leakage}_{I,J,K}^{I} + \text{Losses}_{I,J,K}^{I}\right)^2}{\left(\text{Gains}_{I,J,K}^{R} + \text{Ext. Sources}_{I,J,K}^{R}\right)^2 + \left(\text{Gains}_{I,J,K}^{I} + \text{Ext. Sources}_{I,J,K}^{I}\right)^2} \right]^{1/2} - 1 \right| \qquad \text{for any I,J,K}$$

Those quantities were obtained by back-substituting the real and imaginary parts of the complex flux and coefficients into the difference equations.

Multi-Line Cascade Block-Tridiagonal Module Method with Constraint Overrelaxation

In this section, we will put the emphasis on the numerical solution of the kinetics behavior of the multi-module reactors. However, this numerical approach can also be applied to large uniform heterogeneous reactors.

By multi-module reactor we understand spectral-coupled systems, spatially (modular) coupled systems, etc. In spectral-coupled systems, the coupling is typically between drastically different parts with drastically different energy spectra (e.g., fast core blanket, fast thermal systems), in spatially coupled systems the coupling is between multiple similar parts (e.g., multi-core fast reactor, split core GTRR, split core thermal Argonaut, etc.).

A reactivity insertion in a section of a reactor module affects other modules through the neutronic coupling, which in turn is totally dependent on the time dependent leakage terms between modules.

The interaction can be very tight coupling, as in the fast-thermal STARK[112-115] and STEK[116] reactors, the multi-modular type fast breeders, such as the Westinghouse Liquid Metal Fast Breeder Reactor Design Study,[37-40,112] or the Dounray 350 MWe Fast Breeder,[112] or relate to very loosely coupled systems, such as in the coupled rocket reactor

concepts.

Simplified coupled-reactors kinetics equations based on modified inhour equations, with an additional pseudo-delayed group, representing the leakage from one module to the others, has been formulated by Avery[50] and others.[53,54] Avery's equations describe the time-dependent change of fission neutron source population, given a coupling coefficient and a partial neutron lifetime. In Baldwin's method,[24] the coupling between modules was assumed to be small, so that the individual modules could be represented by point reactors, whose kinetic behavior could be described by inhour equations with a pseudo-delayed group, whose delay was representative of the transit times between modules.

In more tightly coupled cases, the individual modules cannot be anymore represented by individual coefficients. Plaza and Köhler[60] and others[48,51] have set up inhour type of equations (whose coefficients were calculated based on forward or adjacent fluxes) starting from the time-dependent diffusion equation. The calculation of the coupling coefficients ϵ_{kj} was dependent on the particular geometry of the system and can be best calculated by Monte Carlo methods. Plaza and Köhler derived the coupled-reactor kinetics equations using neutron transport theory. The individual modules were replaced by points, described by the inhour equations, whose coefficients were adjoint weighted. We have previously reviewed the disadvantages of those nodal approximations. The value of the nodal approach was very dependent on the accuracy with which the coupling coefficients and the transit-time function could be calculated. The spatial kinetic detail within the modules was also lost,

unless the coefficients were recomputed for each frequency.

The major disadvantages of modal approximations were discussed in Chapter II. Mainly that, practically, they can be applied only to one dimensional, very simple geometrical reactor types.

A considerable amount of work has been done in mono-energetic kinetic methods of coupled-cores, and in few-group, one dimensional modal methods for simple geometries. However, multi-group, multi-dimensional numerical solutions of coupled-core and heterogeneous reactors in the areas of kinetics and power spectral densities have received very little attention.

The use of one-line, multi-group, overrelaxation methods improved convergence at higher frequencies. In multi-module type of problems, the convergence can be greatly improved by performing multi-line, multi-group overrelaxation. The coupling matrix of part of or of a whole module is being solved simultaneous (or with inner iterations) and the leakage through the boundaries of the module is being treated through the numerical approximation of the complex expressions, $\nabla D^{g}(\bar{r}\omega)\nabla$, in the source matrix. The calculational effort is therefore being concentrated simultaneously on the whole or part of the module for several or all of the energy groups in the complex domain.

The vast improvement of multi-line over one-line numerical solutions of PSD problems at higher frequencies is due to the presence of large gradients of the flux in the complex domain and, therefore, large changes of the leakage terms across the reactor system. In other words, at higher frequencies, the kinetic transport lengths are much smaller than at lower frequencies. At low frequencies, a reactivity change in

any part of the reactor system is significantly effective in other parts of the reactor, while at higher frequencies, a reactivity change in one part is not as effective as in other parts of the reactor. The different parts of the system tend to decouple from one another at higher frequencies. It was found that subdividing the reactor into different modules and solving each module separately, with leakage terms between modules accounted for through the source matrix, reduced the building up of iteration errors during convergence, especially for highly heterogeneous systems and/or at higher frequencies.

While a one-line, all-energy-groups kinetic problem required for each iteration IMAX solutions of a block-tridiagonal matrix of band width KMAX x 3 x 2, band length KMAX x JMAX x 2, number of elements in the band JMAX x $KMAX^2$ x 12, a multi-line, all-energy-groups kinetic problem required for each iteration NIMAX x NJMAX inversions (where NIMAX is the number of I-mesh subregions of the reactor system, and NJMAX is the number of J-mesh subregions). Each inversion required the solution of a block-tridiagonal matrix of band width KMAX x DIMAX x 3 x 2, band length KMAX x DJMAX x DIMAX x 2, number of elements $KMAX^2$ x $DIMAX^2$ x DJMAX x 12 in the band.

For a typical problem of IMAX = 20, JMAX = 68, KMAX = 3, DIMAX = 5, DJMAX = 68, the number of inversions is 4, the band width is 90, and the band length 2040, number of elements in the band = 183,600. For a one-line problem, each iteration required 20 inversions, band width 18, band length 408, number of elements in the band 7,344.

It would seem that a major disadvantage of this approach would be that the number of computer operations required for each iteration, and

the directly addressable computer memory required in the case of the multi-line method is far greater than in the case of one-line numerical solutions of a kinetics problem. However, except for problems which require only a few iterations and which converge easily, the multi-line method is far superior for problems with difficult convergence and/or which require many iterations. The total number of computer operations is not necessarily more than one-line overrelaxation methods, while for certain multi-dimensional multi-group kinetic problems in the omega domain, no convergence could be obtained at relatively high frequencies using conventional methods, no significant problems with convergence were encountered with a multi-line, multi-group, constraint overrelaxation numerical approach.

Let us now set up the set of equations (67 and 68) in matrix form for a multi-line, multi-column, overrelaxation problem. For the sake of simplicity, we will derive the case for J1 = 1 and J2 = JMAX.

$$\begin{bmatrix} M_{I1\to I2,\ J=J1} & & & \\ & M_{I1\to I2,\ J=J1+1} & & \\ & & M_{I1\to I2,\ J} & \\ & & & M_{I1\to I2,\ J=J2} \end{bmatrix} \times \begin{bmatrix} \Phi_{I1\to I2,\ J=J1} \\ \Phi_{I1\to I2,\ J=J1+1} \\ \vdots \\ \Phi_{I1\to I2,\ J} \\ \vdots \\ \Phi_{I1\to I2,\ J=J2} \end{bmatrix} = \quad (83)$$

$$\begin{bmatrix} TL_{I1,\,J=J1} & BL_{I2,\,J=J1} \\ TL_{I1,\,J=J1+1} & BL_{I2,\,J=J1+1} \\ \vdots & \vdots \\ TL_{I1,\,J} & BL_{I2,\,J} \\ \vdots & \vdots \\ TL_{I1,\,J=J2} & BL_{I2,\,J=J2} \end{bmatrix} \times \begin{bmatrix} \Phi_{I1-1,\,J=J1} & \cdots & \Phi_{I1-1,\,J} & \cdots & \Phi_{I1-1,\,J=J2} \\ \Phi_{I2+1,\,J=J1} & \cdots & \Phi_{I2+1,\,J} & \cdots & \Phi_{I2+1,\,J=J2} \end{bmatrix}$$

$$+ \begin{bmatrix} LB_{I=I1,\,J1} & RB_{I=I1,\,J2} \\ LB_{I=I1+1,\,J1} & RB_{I=I1+1,\,J2} \\ \vdots & \vdots \\ LB_{I,\,J1} & RB_{I,\,J2} \\ \vdots & \vdots \\ LB_{I=I2,\,J1} & RB_{I=I2,\,J2} \end{bmatrix} \times \begin{bmatrix} \Phi_{I=I1,\,J1-1} & \cdots & \Phi_{I,\,J1-1} & \cdots & \Phi_{I=I2,\,J1-1} \\ \Phi_{I=I1,\,J2+1} & \cdots & \Phi_{I,\,J2+1} & \cdots & \Phi_{I=I2,\,J2+1} \end{bmatrix} + \begin{bmatrix} S_{I1\to I2,\,J=J1} \\ S_{I1\to I2,\,J=J1+1} \\ \vdots \\ S_{I1\to I2,\,J} \\ \vdots \\ S_{I1\to I2,\,J=J2} \end{bmatrix}$$

where

$$\Phi_{J}^{I1\to I2} = \begin{bmatrix} \Phi_{J}^{I=I1} \\ \Phi_{J}^{I=I1+1} \\ \vdots \\ \Phi_{J}^{I} \\ \vdots \\ \Phi_{J}^{I=I2} \end{bmatrix} \qquad S_{J}^{I1\to I2} = \begin{bmatrix} S_{J}^{I=I1} \\ S_{J}^{I=I1+1} \\ \vdots \\ S_{J}^{I} \\ \vdots \\ S_{J}^{I=I2} \end{bmatrix}$$

Matrices $M_{\substack{I1\to I2\\J1\to J2}}$ are composed by their sub-matrices, $M_{\substack{I1\to I2\\J}}$, which in turn are represented by their sub-matrices $M_{I,J}$.

Matrix $M_{\substack{I1\to I2\\J1\to J2}}$ is a block-tridiagonal matrix, with a band width of 3 x (I2-I1+1) x KMAX x 2; band length (I2-I1+1) x (J2-J1+1) x KMAX x 2; number of elements in the band $KMAX^2$ x $(I2-I1+1)^2$ x (J2-J1+1) x 12. The solution of the flux in the complex domain for a multi-line module problem is, therefore:

$$\left[M_{\substack{I1\to I2\\J1\to J2}}\right]\times\left[\Phi_{\substack{I1\to I2\\J1\to J2}}\right] = \left[TL_{\substack{I1\\J1\to J2}} \quad BL_{\substack{I2\\J1\to J2}}\right]\times\begin{bmatrix}\Phi_{\substack{I1-1\\J1\to J2}}\\ \Phi_{\substack{I2+1\\J1\to J2}}\end{bmatrix} + \left[LB_{\substack{I1\to I2\\J1}} \quad RB_{\substack{I1\to I2\\J2}}\right]\begin{bmatrix}\Phi_{\substack{I1\to I2\\J1-1}}\\ \Phi_{\substack{I1\to I2\\J2+1}}\end{bmatrix} + \left[S_{\substack{I1\to I2\\J1\to J2}}\right] \tag{84}$$

or

$$\left[\Phi_{\substack{I1\to I2\\J1\to J2}}\right] = \left[M_{\substack{I1\to I2\\J1\to J2}}\right]^{-1}\times\left[\left[TL_{\substack{I1\\J1\to J2}} \quad BL_{\substack{I2\\J1\to J2}}\right]\times\begin{bmatrix}\Phi_{\substack{I1-1\\J1\to J2}}\\ \Phi_{\substack{I2+1\\J1\to J2}}\end{bmatrix} + \left[LB_{\substack{I1\to I2\\J1}} \quad RB_{\substack{I1\to I2\\J2}}\right]\times\begin{bmatrix}\Phi_{\substack{I1\to I2\\J1-1}}\\ \Phi_{\substack{I1\to I2\\J2+1}}\end{bmatrix} + \left[S_{\substack{I1\to I2\\J1\to J2}}\right]\right] \tag{85}$$

It would seem that the inversion of matrix $M_{\substack{I1\to I2\\J1\to J2}}$, although block-tridiagonal would be very time consuming, and would not fit in even large-

scale computers, even if it was stored in its block-tridiagonal compact form. But, in the determination of the complex flux at a given frequency the inverses of the individual matrices $M_{\substack{I1\rightarrow I2 \\ J1\rightarrow J2}}$ only have to be determined once in the first iteration. During this first iteration, the partial inversion of the different matrices $M_{\substack{I1\rightarrow I2 \\ J1\rightarrow J2}}$ are found by matrix factorization and saved on a disk or drum file using a random access routine NTRAN on a super-scale U-1108 computer system. For each subsequent iteration, the partial inverses of the different matrices $M_{\substack{I1\rightarrow I2 \\ J1\rightarrow J2}}$ are read from a random IØ device and used in the iteration.

During the first iteration at a certain frequency, the matrices $M_{\substack{I1\rightarrow I2 \\ J1\rightarrow J2}}$ are split into an upper block-tridiagonal and a lower block-tridiagonal matrix.

Let the elements of matrix [M] be represented by $m_{i,j}$

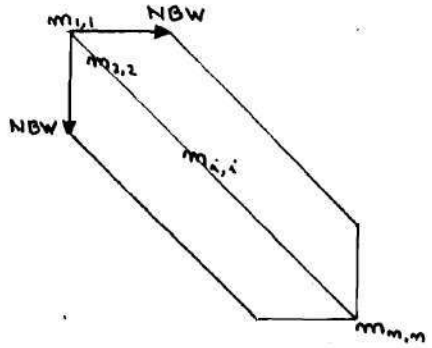

where NBW is half the bandwidth

It can be shown[117] that a matrix M can be factorized into an upper matrix U and a lower matrix L, if all the principal minors of M are non-singular. The factorization into an upper and into a lower block-tridiagonal matrix will fail if $l_{ii}=0$ for any i. During the computation,

the values of l_{ii} were therefore closely monitored. If any of them were zero, in which case [M] would be singular, the iteration was aborted. Let L be a lower block-tridiagonal matrix, with elements l_{ij}, and U be an upper block-tridiagonal matrix, with elements u_{ij}. It can be shown[117] that the elements of matrix L and of matrix U, which satisfies the relation M = LU, are determined by

$$l_{ij} = m_{ij} - \sum_{k=1}^{j-1} l_{ik} u_{kj} \quad \text{for } i \geq j \tag{86}$$

$$u_{ij} = \frac{m_{ij} - \sum_{k=1}^{i-1} l_{ik} u_{kj}}{l_{ii}} \quad \text{for } i < j \tag{87}$$

We also know that (in matrix form):

$$M\phi = S \quad \text{or}$$

$$\phi = M^{-1} S = (LU)^{-1} S = U^{-1} L^{-1} S$$

and $LU\phi = S$

Let us define $U\phi = Z$.

If relation (86) and relation (87) are followed, we then obtain

$$LZ = S$$

$$U\phi = Z$$

The inversion of an upper or lower block-tridiagonal matrix is straightforward and can be obtained by the relation

$$z_i = \frac{s_i - \sum_{k=1}^{i-1} l_{ik} z_k}{l_{ii}} \tag{88}$$

for i going from 1 to n (in increasing order)

and

$$\phi_k = \frac{z_k - \sum_{j=k+1}^{n} u_{kj}\,\phi_j}{u_{kk}} \qquad (89)$$

for k going from n to 1 (in decreasing order).

At the beginning of the first iteration of a transfer function problem at a particular frequency, the elements l_{ij} of the lower block-tridiagonal matrix L were determined using relation (86), and the elements u_{ij} of the upper block-tridiagonal matrix U were determined using relation (87).

Those lower matrices L and upper U matrices were saved on a random IO access device using the random access routine NTRAN. It has to be noted that all arithmetic for u_{ij} and l_{ij} was done in double precision in order to reduce the truncation errors during the iteration process. This was then followed by the determination of the variables z_i using relation (88), followed by the determination of the unknown fluxes ϕ_k^* for each module using relation (89). Those unknown complex fluxes were subsequently constrained overrelaxed as explained previously. This was followed by the determination of the errors ε^A and ε^{phase}. Subsequently, for the second and following outer iterations, only the variables z_i and ϕ_k^*, followed by constraint overrelaxation were obtained for each module using the l_{ij} and u_{ij} matrices that were stored by random IO access in the first iteration. Determination of the z_i and ϕ_k^* only took approximately

five percent of the CPU computer time necessary for setting up the L or U matrices. Using the multi-line, multi-column method not only saved computer time for difficult problems through a drastic reduction in the number of iterations required for convergence, but also enabled us to obtain a convergent solution for highly heterogeneous problems at relatively high frequencies. It was found in the course of this investigation that the module method gave convergent solutions in cases where the one-line method was non-convergent, or very slowly convergent, even by the use of the one-line multi-energy method in the complex domain; however, the danger of an accumulation of round-off errors could be increased. Pivotal switching would be available to reduce this type of error. At the end of each successful iteration (convergence with ϵ^{Ampl} below given values), the relative balance error was determined and found to be less than 1.0E-04 for all the cases run in this dissertation. One can conclude that the accumulation of round-off errors was not significant, while the iteration was vastly accelerated.

In the numerical determination of the CPSD, using relation

$$CPSD(\bar{r}_{det_1}, E^{det_1}, \bar{r}_{det_2}, E^{det_2}, \omega) = \tag{90}$$

$$\sum_i \sum_g T(\bar{r}_i E^g \rightarrow \bar{r}_{det_1} E^{det_1}, \omega)^* \cdot T(\bar{r}_i E^g \rightarrow \bar{r}_{det_2} E^{det_2}, \omega)$$

$$\cdot \chi^g(\bar{r}_i) \sum_{g'} \overline{\nu(\nu-1)} \Sigma_f^{g'}(\bar{r}_i) \phi^{g'}(\bar{r}_i) \Delta V_i$$

we observe that a convergent iteration process is necessary for each transfer function calculation. A transfer function calculation is

necessary for each mesh quadrant ΔV_i and energy group "g", where a source is present. In the case of inherent binary sources this means that a transfer function is needed for each ΔV_i and each energy group, g, where $\chi^g(r_i) \neq 0$, $\Sigma_f^g(r_i) \neq 0$, and $\phi^{g'}(r_i) \neq 0$ for g' from group 1 to group G(=KMAX).

The elements m_{ij} of the module matrices $M_{\substack{I1\to I2 \\ J1\to J2}}$ remain the same for all space-dependent transfer functions at a particular frequency. Subsequently, the matrices L and U have only to be determined once for each frequency, at the beginning of the first iteration step of the first transfer function calculation. A full convergent iteration was, however, necessary for each transfer function determination using relations (88) and (89), by random accessing the values l_{ij} and u_{ij} of the matrices L and U of the module matrices $M_{\substack{I1\to I2 \\ J1\to J2}}$. The values of the kinetic fluxes ϕ_k^* were subsequently constraint-overrelaxed for each module, at each iteration step, for each transfer function calculation at a particular frequency.

There is still the question of the large amount of computer memory required to solve this kinetic problem using module matrices. We have seen that each module matrix $M_{\substack{I1\to I2 \\ J1\to J2}}$ was a block-tridiagonal matrix with $KMAX^2 \times (I2-I1+1)^2 \; (J2-J1+1) \times 12$ elements in the block-multidiagonal band. For a typical problem, the band contained 183,600 elements. If the calculations were performed in double-precision arithmetic, this problem would require 367,200 computer words for the l_{ij} and u_{ij} elements only. This is far greater than most scientific computers could handle. In order to circumvent this problem, a special cascade factorization scheme was

developed in order to obtain the solution to a module, namely, the l_{ij} and u_{ij} elements of the matrices L and U of the module matrices, and the associated z_i and ϕ_k^* values of the unknowns. This cascade factorization required $KMAX^2$ x $(I2-I1+1)^2$ x 5 x 2 (or 36,000) double-precision locations.

A similar technique could be employed for three dimensional kinetic problems in the omega domain, although super-scale computers as the U-1110 or the large IBM 370 would be required.

The code TDPSD (Two Dimensional Power Spectral Density) that was developed for the two dimensional multi-group power spectral density calculations performed in this dissertation used a programming technique called "flexible dimensioning." This enabled one to run a problem of any size and complexity as far as the number of rows, number of columns, number of energy groups, number of different materials and compositions was concerned. It also assured that all available locations were used. The only restriction was that the total storage requirement must be smaller than the maximum available user core. The use of variable dimensioning, therefore, did not limit the size of any one parameter.

CHAPTER V

GENERATION OF CROSS SECTIONS FOR THE FAST-THERMAL AND THERMAL ARGONAUT REACTORS

Multi-group, two dimensional numerical calculations of the power spectral density function (PSD) and the coherence function (CHF) were performed using the previously described methods for an externally unperturbed TARK reactor (Thermal Argonaut Reactor Karlsruhe) and the STARK reactor (Schnell-Thermischen Argonaut Reaktor Karlsruhe) for fast assemblies loading II and IV. Those numerical calculations were compared with measurements performed on those reactors and found to be in good agreement.

Brief Description of the STARK Coupled-Core Reactor

The STARK[44,112-115] reactor is a 10 watt research reactor located in Karlsruhe, Germany. This reactor has a fast neutron spectrum zone surrounded by a natural uranium zone, which in turn is surrounded by a thermal Argonaut fuel driver zone. The basic configuration is shown in Figures 5, 6, and 7.

The STARK reactor consists mainly of six regions:

1. A fast region consisting of an array of 37 vertical stainless steel square drawers, fixed to a 10 cm stainless steel bottom grid plate. Those drawers are easily accessible for loading and unloading from the top of the reactor and are filled with horizontal platelets, which are made up of core material. Combinations of different types of platelets

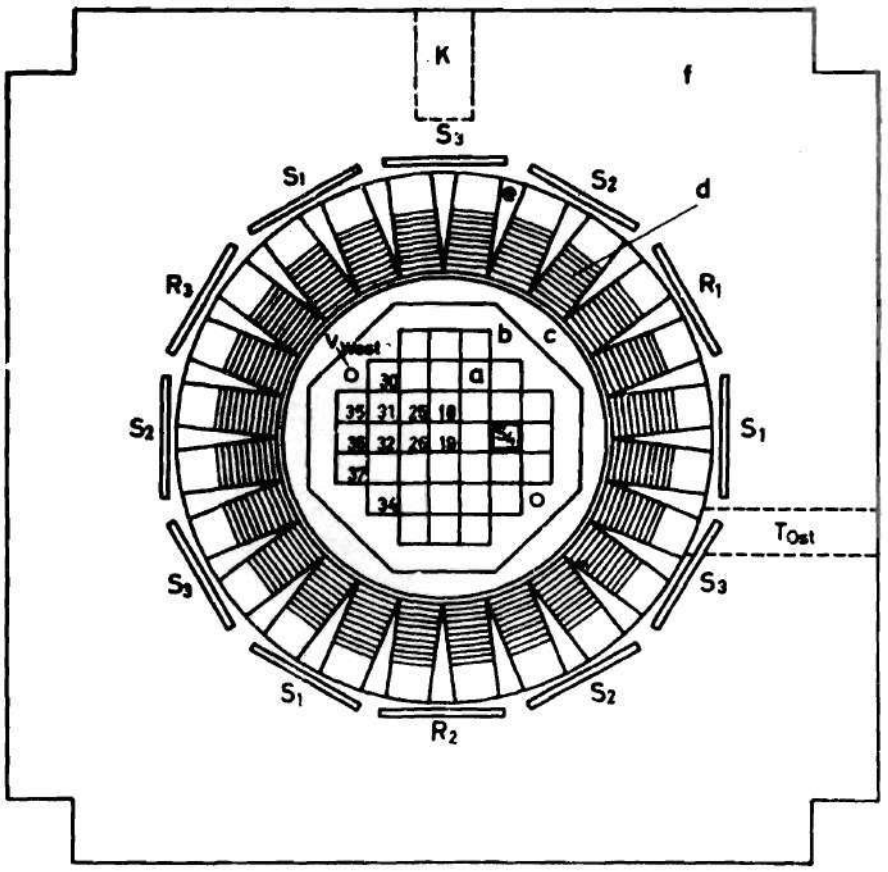

a - Fast region
b - Natural uranium blanket
c - Graphite insert
d - Thermal region (fuel elements)
e - Thermal region (graphite fillings)
f - Graphite reflector

R_1, R_2, R_3 - Control plates
S_1, S_2, S_3 - Safety plates
S_4 - Shutdown rod in the fast region
V_{West} - Vertical channel in the uranium blanket
K, T_{Ost} - Experimental channels in the graphite reflector

Figure 5. Horizontal Schematic Diagram of STARK

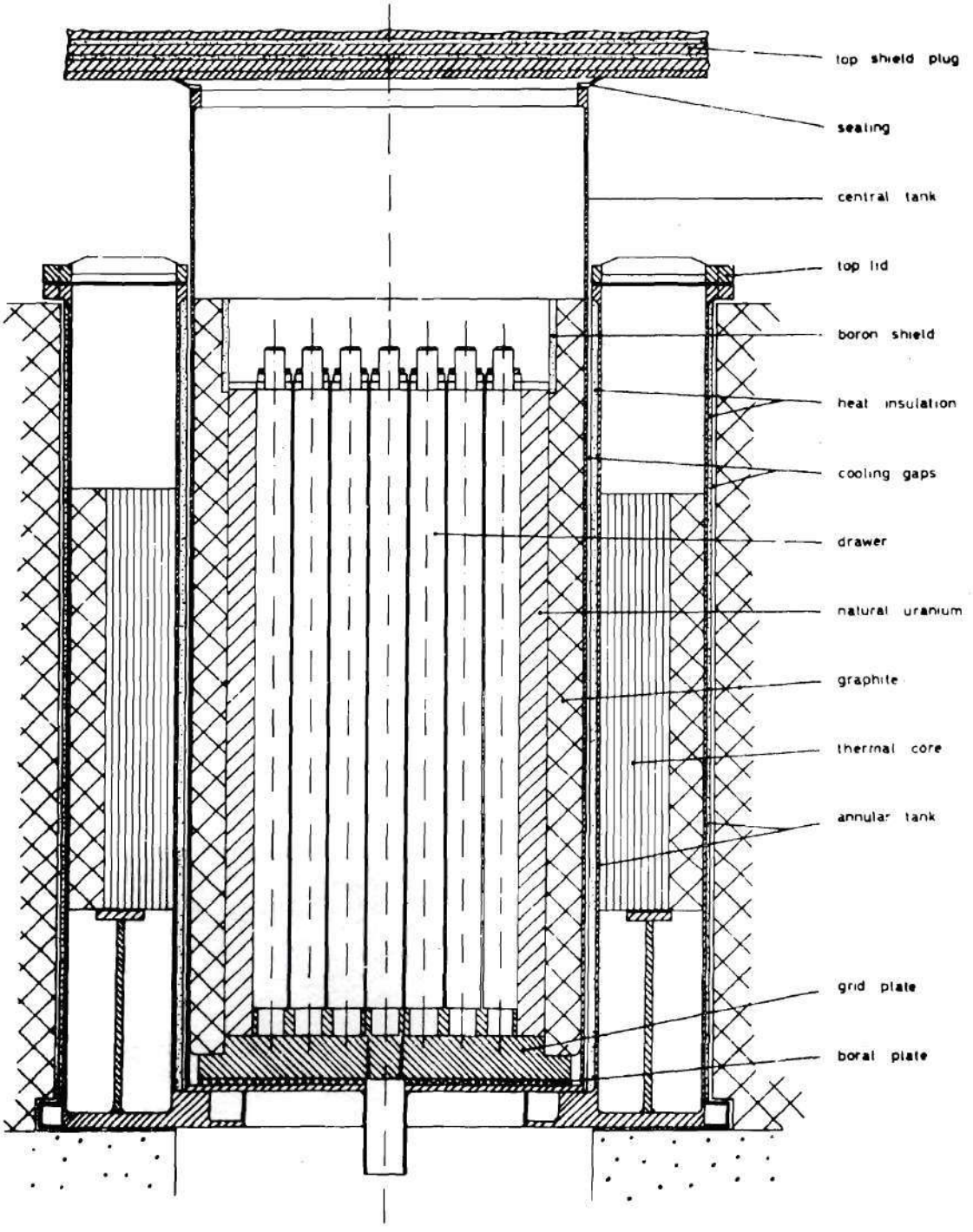

Figure 6. Vertical Section Core Region STARK

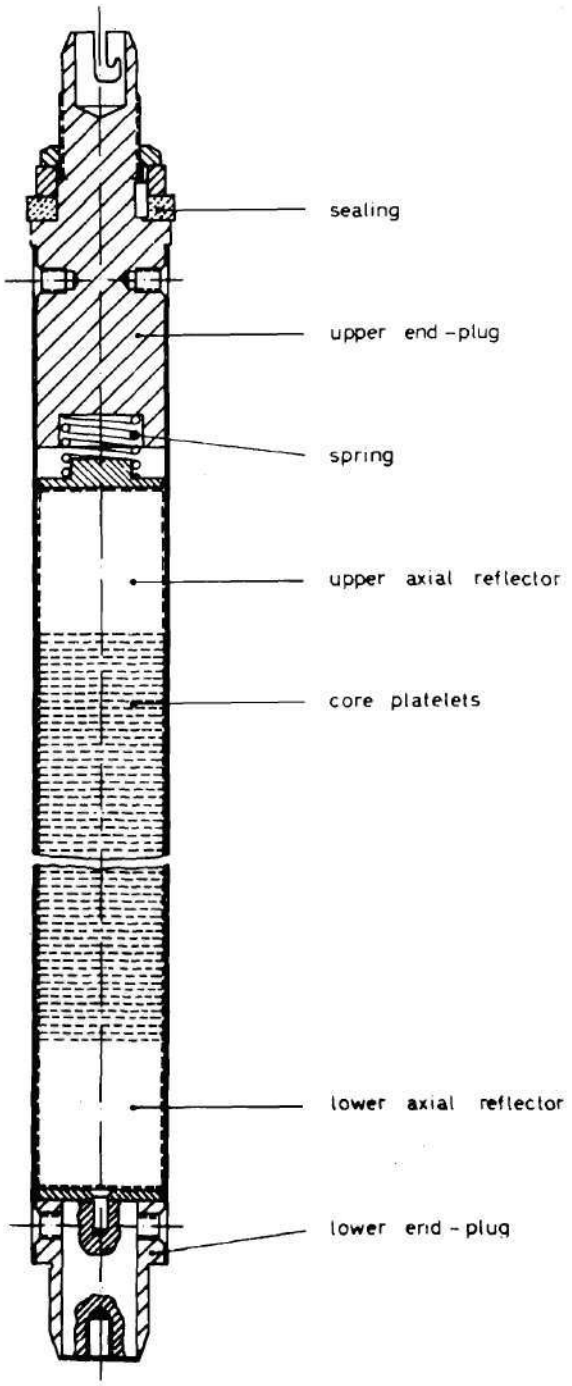

Figure 7. Vertical Section of Fast Assembly STARK

make up different types of fast fuel assemblies. The drawers are made of 0.1 cm thick stainless steel with inner dimensions of approximately 5.1 x 5.1 cm. The dimensions of the core platelets are 5.08 x 5.08 cm. The 37 fast assemblies make up the fast region with an average cylindrical diameter of 37.2 cm, and an active height of 61 cm.

2. Natural Uranium Blanket -- The fast region is surrounded by a natural uranium casing of an average thickness of 5.6 cm. The uranium casing is made up of smaller blocks, which fit around the fast assembly region. The main purpose of this blanket is to reduce power peaking at the outer edge of the fast region, due to the leakage of thermal neutrons into the fast region from the thermal driver zone, and subsequent high U-235 fission rate. This natural uranium blanket absorbs slow neutrons from the outer thermal Argonaut assemblies zone. Because of this blanket, the coupling between the fast assemblies and the thermal driver zone is accomplished mainly by fast neutrons.

3. Graphite Insert - Aluminum Tank Wall, Air Gap -- The fast assembly zone and the natural uranium blanket are surrounded by a five cm thick graphite annulus which fits into a cylindrical central aluminum tank, 56.4 cm ID. This tank also serves as a safety barrier in case of an accident. It prevents flow of water from the thermal Argonaut zone into the fast assembly region. This central aluminum tank is followed by an air gap, and an annular aluminum tank.

4. Thermal Driver Zone -- This core consists of up to 24 thermal Argonaut assemblies positioned in an annular fashion, with graphite wedges which are pushed in between them. Each assembly consists of up to 17 fuel plates immersed in light water. If fuel plates are removed, they

are usually replaced by carbon plates, with carbon wedges in between. The outer areas of the thermal Argonaut assemblies are, therefore, filled with graphite plates. Each fuel plate contains 124 grams U_3O_8 and the U-235 enrichment is 20 w/o of U. Each fuel plate therefore contains 20.83 grams U-235 and is composed of an U_3O_8-Al alloy. The distance between plates is approximately 0.63 cm. For the STARK configuration, each of the 24 Argonaut fuel assemblies contained from 7 to 15 fuel plates at the inner part of the annulus and graphite dummy plates at the outer part of the annulus.

5. The thermal core assemblies are enclosed in an annular tank, followed by thermal isolation, an air gap, and graphite.

6. The external graphite reflector is composed of graphite blocks. In the external graphite reflector there are several removable blocks in which neutron detectors can be placed, and there are 12 cadmium control plates at the outer boundary of the thermal zone around the aluminum annular tank. Those control plates are used for control and shutdown. The dimensions of absorber plates are 21 x 21 cm. Six control plates are used as safety control before water is pumped into the thermal zone. Three are used as safety control when water is present and three control plates are used as fine control. An additional safety rod is mounted in the fast zone at an eccentric position. That rod consists of a normal square drawer, filled with U platelets in its lower part and B_4C in its upper part. In the calculations, nine different regions were considered, for which for each one, appropriate cell spectrum-averaged and collapsed cross sections were generated.

Brief Description of the Fast Assemblies

Two different types of fast assemblies were considered in this numerical analysis.

Fast Assembly Type II Reactor Configuration

Each of the different 37 fast fuel assemblies contains a combination of horizontally stacked platelets (5.08 x 5.08 x 0.315 cm) consisting of

a) U(20) platelets containing 19.8 w/o U-235 enriched uranium metal, 38 platelets per assembly, 208.83 kgU in fast core

b) U(nat) platelets containing natural uranium metal, 38 platelets per assembly, 418.54 kgU in fast core

c) Al_2O_3 platelets containing Al_2O_3, 38 platelets per assembly

d) Al + $(CH_2)_n$ (polypropylene) platelets containing pure aluminum with an incorporated recessed polypropylene disk (see Figure 8). The polypropylene disks are placed in a 1.1 mm deep circular recess of the aluminum platelet. The disks are 1 mm thick with a diameter of 3.0 cm.

The configuration U(nat),U(20), Al_2O_3,U(nat),Al+CH_2 is repeated 38 times. The active height of Fast Assembly II is 59.9 cm. Each fast assembly contains an upper natural uranium blanket of 8.8 cm composed of three blocks of 5.08 x 5.08 x 2.5 cm and four platelets, and a lower natural uranium blanket composed of three blocks of 5.08 x 5.08 x 2.5 cm and three platelets. The upper blanket contains 159.0 kgU and the lower blanket 153.5 kgU. The fast assembly core contains, therefore, 44.59 kg of U-235 with a 7.06 w/o average U-235 enrichment. The purpose of the incorporation of CH_2 disks is to soften the spectrum slightly. The

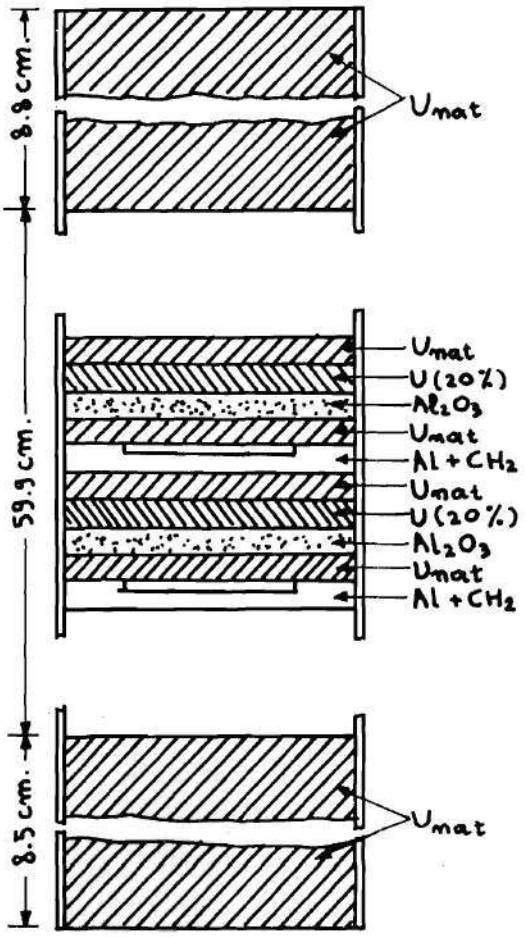

Figure 8. Fast Assembly Loading II

thermal core contains 6.53 kg of U-235. The power distribution of the fast core is 9.3%, natural uranium blanket 9.6%, and the thermal core 81%.[44]

The thermal region consists of 24 Argonaut type fuel assemblies. Each assembly contains 13 or 14 fuel plates with an average of 20.83 grams U-235 in each fuel plate. The plate distance is 6.3 mm and the outer region of each assembly is filled with graphite plates. The fuel plates are submerged in water which was kept at 80°C. The plate thickness is three mm and is an alloy mixture of U_3O_8 and Al. The enrichment in U-235 is 20 w/o of U. The critical experimental fuel mass of the thermal core was 6.53 kg U-235 for a cylindrical thermal core loading. The active height of the thermal driver zone is 61 cm. Kussmaul[44] reported that the critical calculated fuel mass of the thermal core was 6.911 kg U-235 based on a 26 ABN cross-section set and a 26 group diffusion theory calculation. However, in our power spectral density calculations, the experimental critical fuel mass of 6.53 kg U-235 was used. A 123 fine group cross-section set, the Nordheim integral method[118] for U-235 and U-238 resonance correction using a homogenized cell in the fast region and a one dimensional slab for the plate cell of the thermal fuel assemblies were used. An S_4P_3 cell collapse to 50 groups was subsequently performed. An S_4P_3 one dimensional transport calculation over the reactor was then performed to obtain a few broad-group, zone-averaged, cross-section sets for the different regions of the reactor.

While for the kinetic calculations a two dimensional configuration of the reactor core was chosen, a one dimensional representation of Assembly Type II core was chosen for the generation of the zone-dependent

cross sections. A detailed schematic of the two dimensional configuration is shown in Figure 5. The one dimensional schematic is shown in Figure 9. The homogenized number densities were taken from reference 44 and are tabulated in Table 1. The outer radius of the thermal zone blanket was calculated based on the experimentally determined critical mass of the thermal region. On a U-235 mass balance basis, we have that

$$R_2^2 = R_1^2 + \frac{M_{U\text{-}235}^{crit}}{N_{av}^{U\text{-}235}\ \pi\ H_{act}} \quad \frac{6.02252E\text{-}01}{235.044} \quad \frac{24}{N_{asbl}}$$

where

R_1 = inner radius thermal zone blanket (30.5 cm)

R_2 = outer radius thermal zone blanket

$M_{U\text{-}235}^{crit}$ = U-235 critical mass of thermal zone blanket

$N_{av}^{U\text{-}235}$ = U-235 homogenized number density thermal zone blanket

H_{act} = active height fuel

N_{asbl} = number of assemblies in thermal zone

For a critical mass of $M_{U\text{-}235}^{crit}$ = 6.53 kg, based on 20.83 grams U-235 per plate, we obtained a critical outer radius of 41.98 cm. This was subsequently used in the cross-section generation and the kinetic calculations of STARK loading II. It has to be observed that a mathematically $k_{eff} = 1$ reactor was obtained using those dimensions by adjusting the axial buckling (two dimensional poison search to $k_{eff} = 1.0$).

Fast Assembly Type IV Reactor Configuration

The type IV assembly experiment was performed in STARK in order to obtain a hard neutron spectrum, while still remaining within certain safeguard criteria. Each of the different 37 fast fuel assemblies contained

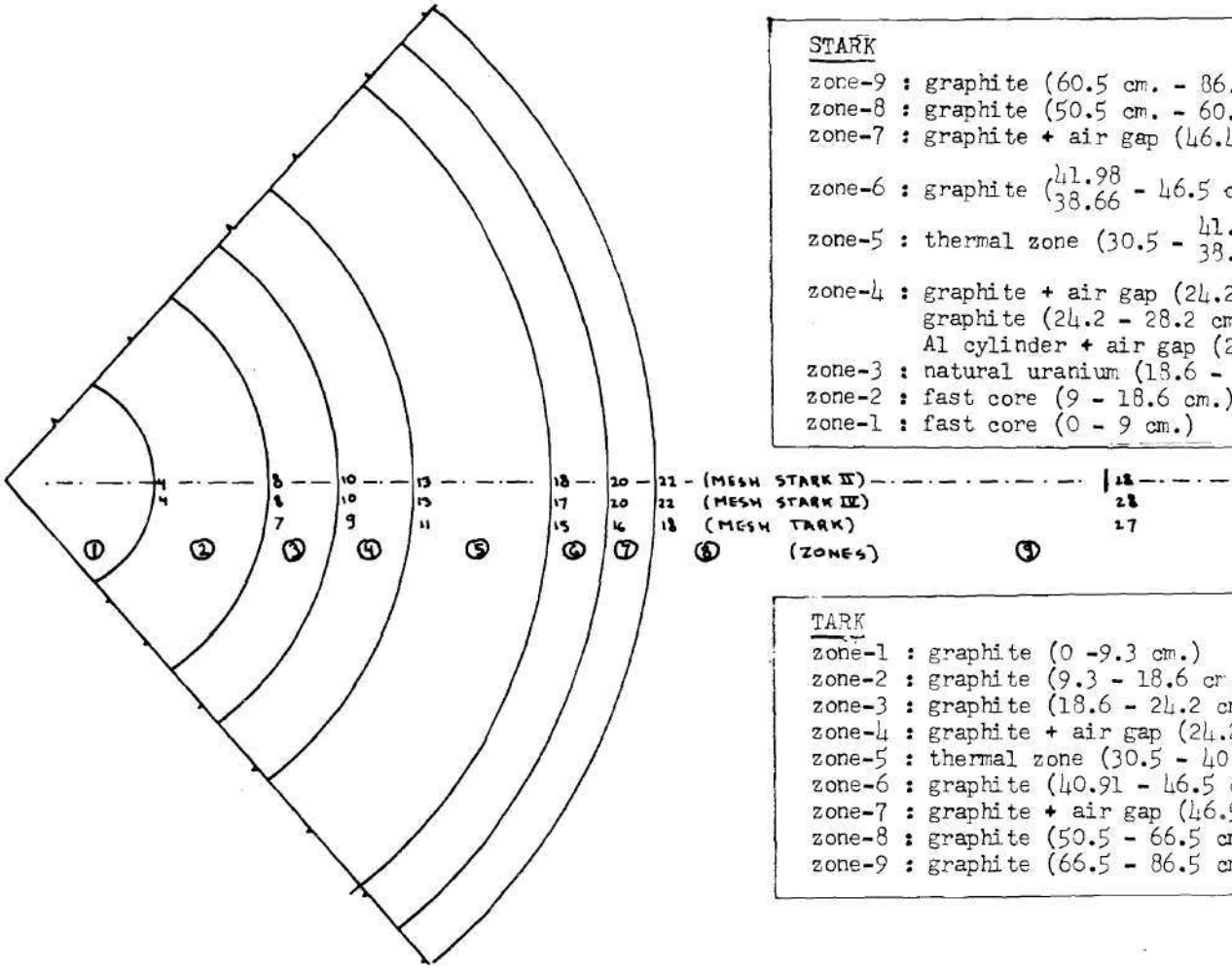

STARK

zone-9 : graphite (60.5 cm. - 86.5 cm.)
zone-8 : graphite (50.5 cm. - 60.5 cm.)
zone-7 : graphite + air gap (46.4 - 50.5 cm.)
zone-6 : graphite ($^{41.98}_{38.66}$ - 46.5 cm.) Asbl II / Asbl IV
zone-5 : thermal zone (30.5 - $^{41.98}_{38.66}$ cm.) Asbl II / Asbl IV
zone-4 : graphite + air gap (24.2 - 30.5 cm.)
graphite (24.2 - 28.2 cm.)
Al cylinder + air gap (28.2 - 30.5 cm.)
zone-3 : natural uranium (18.6 - 24.2 cm.)
zone-2 : fast core (9 - 18.6 cm.)
zone-1 : fast core (0 - 9 cm.)

TARK

zone-1 : graphite (0 -9.3 cm.)
zone-2 : graphite (9.3 - 18.6 cm.)
zone-3 : graphite (18.6 - 24.2 cm.)
zone-4 : graphite + air gap (24.2 - 30.5 cm.)
zone-5 : thermal zone (30.5 - 40.91 cm.)
zone-6 : graphite (40.91 - 46.5 cm.)
zone-7 : graphite + air gap (46.5 - 50.5 cm.)
zone-8 : graphite (50.5 - 66.5 cm.)
zone-9 : graphite (66.5 - 86.5 cm.)

Figure 9. One-Dimensional Cylindrical Representation Used in Cross Section Generations

Table 1. Homogenized Number Densities for STARK Loading II

Zone	1	2	3	4	5	6	7	8	9
	Fast Core	Fast Core	Natural Uranium Blanket	Graphite + Air Gap	Thermal Core	Graphite	Graphite + Air Gap	Graphite	Graphite
Outer Radius (cm)	9.0	18.6	24.2	30.5	41.98	46.5	50.5	60.5	86.5
Isotope									
H-1	1.3081-03	1.3081-03		3.680-04	3.726 -02		2.527-04		
C-12	6.706 -04	6.706 -04		4.922-02	1.468 -02	8.526-02	4.127-02	8.526-02	8.526-02
O-16	1.1637-02	1.1637-02			2.003 -02				
Al-27	1.700 -02	1.700 -02		9.264-03	1.343 -02		3.484-03		
Fe-56	6.042 -03	6.042 -03							
U-235	1.7659-03	1.7659-03	3.437-04		1.0495-04				
U-238	2.822-02	2.2822-02	4.739-02		4.193 -04				
Cr-52*	1.271 -03	1.271 -03							
Ni-59*	1.036 -03	1.036 -03							

*Added to the number density of Fe-56.

a combination of horizontally stacked platelets (5.08 x 5.08 x 0.315 cm) as described above. However, another configuration U(nat),Al_2O_3,U(20%) was repeated 46 times in each fast assembly. Each fast assembly contained an upper axial blanket composed of three blocks of natural uranium of dimensions 5.08 x 5.08 x 2.5 cm per block, three U(nat) platelets, and a U(20),Al,U(20) set of platelets, and a lower axial blanket composed of three blocks of natural uranium of dimensions 5.08 x 5.08 x 2.5 cm per block, three U(nat) platelets, and a U(nat),U(20),Al,U(20) set. The fast assembly core contained, therefore, 106.90 kg U-235 (average enrichment 13.50 w/o). The power distribution of the fast core was 31.1%, natural uranium blanket 11%, and the thermal zone 58%. The power fraction of the fast zone increases sharply as compared to assembly II, at the cost of the thermal zone, while the power fraction of the natural uranium zone remains nearly the same.

All the other zones were similar to Assembly Type II Reactor configuration, except that the U-235 loading in the thermal zone was 4.429 kg U-235. The critical outer radius of the thermal zone was determined from the experimentally determined critical loading to be R_2 = 38.66 cm, for a 24 assembly thermal zone. The number densities are listed in Table 2.

Brief Description of the TARK Coupled-Core Reactor

The TARK (Thermal Argonaut Reactor Karlsruhe) is basically similar to STARK, except that the fast assembly region and the natural uranium region were replaced by graphite blocks. The basic configuration is shown in Figure 16; it shows a two-slab thermal core configuration of TARK. In the two-slab TARK, the fast assembly region and the natural

Table 2. Homogenized Number Densities for STARK Loading IV

Zone	1	2	3	4	5	6	7	8	9
	Fast Core	Fast Core	Natural Uranium Blanket	Graphite + Air Gap	Thermal Zone Blanket	Graphite	Graphite + Air Gap	Graphite	Graphite
Outer Radius (cm)	9.0	18.6	24.2	30.5	38.66	46.5	50.5	60.5	86.5
Isotope									
H-1				3.680-04	3.726 -02		2.527-04		
C-12				4.922-02	1.468 -02	8.526-02	4.127-02	8.526-02	8.526-02
O-16	1.4428-02	1.4428-02			2.003 -02				
Al-27	9.619 -03	9.619 -03		9.264-03	1.343 -02		3.484-03		
Fe-56	6.042 -03	6.042 -03							
U-235	4.1597-03	4.1597-03	3.437-04		1.0495-04				
U-238	2.6330-02	2.6330-02	4.739-02		4.193 -04				
Cr-52*	1.271 -03	1.271 -03							
Ni-59*	1.140 -03	1.140 -03							

*Added to the number density of Fe-56.

uranium buffer zone were replaced by a graphite column a. The Argonaut fuel assemblies in the thermal zone are subdivided into two fuel regions each containing eight Argonaut assemblies. Seifritz and Albrecht[20-23] performed an experimental determination of the coherence function using two symmetrically located He^3 chambers. The He^3 chambers were positioned in channels by removing graphite blocks of the external graphite reflector. The reactor was brought to just critical with all control plates out, and by adding fuel plates to the Argonaut assemblies. The experimental determination of the coherence function was subsequently performed by using a total of 266 Argonaut fuel plates. This represents 5.541 kg U235 for the thermal zone based on 20.83 gr U235 per fuel plate. Comparison of the critical loading of the thermal zone of TARK with the STARK reactor showed only 5.541 kg U235 was needed for TARK, while 6.53 kg U235 was needed for STARK Assembly II, due to the harder neutron spectrum in STARK. The number densities are listed in Table 3.

Generation of Fifty Neutron Group Cross Sections Based on ENDF/B-II Data

The cross-section sets used in this study are based on the Evaluated Nuclear Data Files ENDF/B-II[119] through the use of DLC-16.[120] The fast group cross-sections for the DLC-16 library were generated using SUPERTOG[94] whereby point cross-sections from ENDF/B-II were structured into a standard 99 group GAM-II[121] set, using a 1/E weighting function. The thermal cross-sections were similarly processed with SUPERTOG into a standard 30 group THERMOS[122] energy structure. The fast and thermal sets thus generated were combined into a standard 123 neutron energy group structure (see Table 4) to be used in the one-dimensional multi-group

Table 3. Homogenized Number Densities for TARK Reactor

Zone	1	2	3	4	5	6	7	8	9
	Graphite	Graphite	Graphite	Graphite + Air Gap	Thermal Zone Two Slab	Graphite	Graphite + Air Gap	Graphite	Graphite
Outer Radius (cm)	9.3	18.6	24.2	30.5	40.91	46.5	50.5	66.5	86.5
Isotope									
H-1				3.680-04	3.726 -02		2.527-04		
C-12	8.526-02	8.526-02	8.526-02	4.922-02	1.468 -02	8.526-02	4.127-02	8.526-02	8.526-02
O-16					2.003 -02				
Al-27				9.264-03	1.343 -02		3.484-03		
U-235					1.0495-04				
U-238					4.193 -04				

Table 4. 123 Neutron Energy Group Boundaries and Fission Spectrum

GP	ENERGY BOUNDARIES (EV)	BROAD GP NUMBERS	LETHARGY BOUNDARIES	MID PT VELOCITIES (CM/SEC)	FISS SPEC
1	1.49182+07	1	+4.00000+01	5.21051+09	4.12166+05
2	1.34986+07	1	+3.00000+01	4.95620+09	1.13325+04
3	1.22140+07	1	+2.00000+01	4.71449+09	2.77033+04
4	1.10517+07	1	+1.00000+01	4.48456+09	6.09152+04
5	1.00000+07	2	0.00000	4.26586+09	1.21752+03
6	9.04837+06	2	1.00000+01	4.05780+09	2.23311+03
7	8.18731+06	2	2.00000+01	3.85990+09	3.79104+03
8	7.40818+06	2	3.00000+01	3.67165+09	6.00338+03
9	6.70320+06	2	4.00000+01	3.49258+09	8.93037+03
10	6.06531+06	2	5.00000+01	3.32224+09	1.25583+02
11	5.48812+06	2	6.00000+01	3.16022+09	1.67906+02
12	4.96585+06	3	7.00000+01	3.00609+09	2.14541+02
13	4.49329+06	3	8.00000+01	2.85948+09	2.63197+02
14	4.06570+06	3	9.00000+01	2.72002+09	3.11313+02
15	3.67879+06	3	1.00000+00	2.58737+09	3.56384+02
16	3.32871+06	3	1.10000+00	2.46118+09	3.96133+02
17	3.01194+06	4	1.20000+00	2.34114+09	4.28906+02
18	2.72532+06	4	1.30000+00	2.22697+09	4.53567+02
19	2.46597+06	5	1.40000+00	2.11836+09	4.69620+02
20	2.23130+06	5	1.50000+00	2.01500+09	4.77125+02
21	2.01897+06	6	1.60000+00	1.91677+09	4.78601+02
22	1.82684+06	6	1.70000+00	1.82329+09	4.68902+02
23	1.65299+06	7	1.80000+00	1.73436+09	4.55093+02
24	1.49569+06	7	1.90000+00	1.64978+09	4.36340+02
25	1.35335+06	8	2.00000+00	1.56932+09	4.13815+02
26	1.22456+06	8	2.10000+00	1.49278+09	3.88629+02
27	1.10803+06	9	2.20000+00	1.41998+09	3.61787+02
28	1.00259+06	9	2.30000+00	1.35072+09	3.34159+02
29	9.07180+05	10	2.40000+00	1.28485+09	3.06470+02
30	8.20850+05	10	2.50000+00	1.22218+09	2.79301+02
31	7.42736+05	11	2.60000+00	1.16258+09	2.53096+02
32	6.72055+05	11	2.70000+00	1.10588+09	2.28182+02
33	6.08101+05	12	2.80000+00	1.05194+09	2.04779+02
34	5.50232+05	12	2.90000+00	1.00064+09	1.83021+02
35	4.97871+05	13	3.00000+00	9.51839+08	1.62969+02
36	4.50492+05	13	3.10000+00	9.05417+08	1.44631+02
37	4.07622+05	14	3.20000+00	8.61259+08	1.27972+02
38	3.68832+05	14	3.30000+00	8.19255+08	1.12926+02
39	3.33733+05	15	3.40000+00	7.79299+08	9.94080+03
40	3.01974+05	15	3.50000+00	7.41293+08	8.73164+03
41	2.73237+05	16	3.60000+00	7.05139+08	7.65445+03
42	2.47235+05	16	3.70000+00	6.70749+08	6.69823+03
43	2.23708+05	17	3.80000+00	6.38036+08	5.85207+03
44	2.02419+05	17	3.90000+00	6.06919+08	5.10541+03
45	1.83156+05	18	4.00000+00	5.77319+08	4.44822+03
46	1.65727+05	18	4.10000+00	5.49163+08	3.87106+03
47	1.49956+05	19	4.20000+00	5.22380+08	3.36522+03
48	1.35686+05	19	4.30000+00	4.96903+08	2.92267+03
49	1.22773+05	19	4.40000+00	4.72669+08	2.53612+03
50	1.11090+05	20	4.50000+00	4.33066+08	4.95894+03
51	8.65170+04	20	4.75000+00	3.82181+08	3.45783+03
52	6.73795+04	21	5.00000+00	3.37274+08	2.40338+03
53	5.24752+04	21	5.25000+00	2.97643+08	1.66832+03
54	4.08677+04	21	5.50000+00	2.62669+08	1.15306+03
55	3.18278+04	22	5.75000+00	2.31805+08	7.96687+04
56	2.47875+04	23	6.00000+00	2.04567+08	5.49814+04
57	1.93045+04	24	6.25000+00	1.80530+08	3.79095+04
58	1.50344+04	24	6.50000+00	1.59317+08	0.00000
59	1.17088+04	24	6.75000+00	1.40597+08	0.00000
60	9.11882+03	24	7.00000+00	1.24076+08	0.00000
61	7.10175+03	24	7.25000+00	1.09497+08	0.00000
62	5.53085+03	25	7.50000+00	9.66306+07	0.00000
63	4.30743+03	25	7.75000+00	8.52762+07	0.00000
64	3.35463+03	26	8.00000+00	7.52560+07	0.00000
65	2.61259+03	26	8.25000+00	6.64132+07	0.00000
66	2.03468+03	26	8.50000+00	5.86094+07	0.00000
67	1.58461+03	26	8.75000+00	5.17226+07	0.00000
68	1.23410+03	27	9.00000+00	4.56451+07	0.00000
69	9.61117+02	27	9.25000+00	4.02816+07	0.00000
70	7.48519+02	27	9.50000+00	3.55484+07	0.00000
71	5.82947+02	28	9.75000+00	3.13714+07	0.00000
72	4.53999+02	28	1.00000+01	2.76851+07	0.00000
73	3.53575+02	28	1.02500+01	2.44320+07	0.00000
74	2.75365+02	29	1.05000+01	2.15612+07	0.00000
75	2.14454+02	29	1.07500+01	1.90277+07	0.00000
76	1.67017+02	29	1.10000+01	1.67919+07	0.00000
77	1.30073+02	29	1.12500+01	1.48188+07	0.00000
78	1.01301+02	30	1.15000+01	1.30775+07	0.00000
79	7.88933+01	30	1.17500+01	1.15409+07	0.00000
80	6.14421+01	30	1.20000+01	1.01848+07	0.00000
81	4.78512+01	30	1.22500+01	8.98805+06	0.00000
82	3.72665+01	30	1.25000+01	7.93192+06	0.00000
83	2.90232+01	31	1.27500+01	6.99990+06	0.00000
84	2.26033+01	31	1.30000+01	6.17739+06	0.00000
85	1.76035+01	31	1.32500+01	5.45153+06	0.00000
86	1.37096+01	31	1.35000+01	4.81095+06	0.00000
87	1.06770+01	32	1.37500+01	4.24565+06	0.00000
88	8.31529+00	32	1.40000+01	3.74677+06	0.00000
89	6.47595+00	32	1.42500+01	3.30652+06	0.00000
90	5.04348+00	32	1.45000+01	2.91799+06	0.00000
91	3.92786+00	32	1.47500+01	2.57512+06	0.00000
92	3.05902+00	33	1.50000+01	2.27253+06	0.00000
93	2.38237+00	33	1.52500+01	2.00671+06	0.00000
94	1.85985+00	34	1.54976+01	1.84701+06	0.00000
95	1.70986+00	34	1.55817+01	1.78755+06	0.00000
96	1.55986+00	34	1.56735+01	1.69320+06	0.00000
97	1.43985+00	34	1.57536+01	1.61465+06	0.00000
98	1.28988+00	35	1.58635+01	1.51804+06	0.00000
99	1.12489+00	36	1.60004+01	1.42439+06	0.00000
100	9.99923+01	37	1.61182+01	1.33803+06	0.00000
101	8.75930+01	38	1.62503+01	1.25583+06	0.00000
102	7.75918+01	38	1.63718+01	1.16555+06	0.00000
103	6.49938+01	39	1.65490+01	1.06945+06	0.00000
104	5.49902+01	39	1.67160+01	9.75525+05	0.00000
105	4.49954+01	40	1.69167+01	8.71291+05	0.00000
106	3.49965+01	41	1.71680+01	7.87293+05	0.00000
107	2.99970+01	42	1.73222+01	7.23772+05	0.00000
108	2.49980+01	43	1.75045+01	6.54012+05	0.00000
109	1.99979+01	43	1.77276+01	6.02448+05	0.00000
110	1.79979+01	44	1.78330+01	5.69752+05	0.00000
111	1.59987+01	44	1.79508+01	5.35058+05	0.00000
112	1.39991+01	45	1.80843+01	4.97938+05	0.00000
113	1.19992+01	45	1.82384+01	4.57763+05	0.00000
114	9.99889+02	46	1.84208+01	4.13632+05	0.00000
115	7.99900+02	46	1.86439+01	3.78352+05	0.00000
116	6.99950+02	47	1.87774+01	3.52095+05	0.00000
117	5.99949+02	47	1.89316+01	3.23687+05	0.00000
118	4.99942+02	48	1.91139+01	2.92481+05	0.00000
119	3.99961+02	48	1.93371+01	2.57411+05	0.00000
120	2.99948+02	49	1.96248+01	2.16453+05	0.00000
121	1.99972+02	49	2.00303+01	1.82017+05	0.00000
122	1.49985+02	50	2.03179+01	1.53059+05	0.00000
123	9.99884+03	50	2.07234+01	1.16303+05	0.00000
124	5.00028+03		2.14166+01		

transport code XSDRN.[123] The thermal cut-off of the 123 neutron group cross-section sets is at group 94 (1.859 eV). The 123 neutron group cross-section sets were subsequently collapsed, using cell spectrum weighting for the cross-sections of all the isotopes present, and resonance correction (resolved and unresolved) on U-235 and on U-238 for the different types of assemblies, into a 50 group structure (see Table 5). The thermal cut-off of the 50 neutron group collapsed sets was at neutron energy group 34 (1.859 eV). These 50 group sets were subsequently collapsed using zone weighting into two or three broad-group sets. Different cross-section sets were thus generated for the different zones of the reactor mockups.

The cell weighted cross-section collapses from 123 groups to 50 groups were performed using the XSDRN[123] code. The weighting for the cross-section generation was performed using the forward flux. The weighting using adjoint flux was not available in XSDRN. The capability of adjoint transport calculation in XSDRN was therefore implemented. Several cross-sections were also generated using adjoint flux weighting for comparison. However, it has been observed[124] that it is not obvious, that for a given problem the use of adjoint-weighted cross-sections is better than forward-weighted cross-sections. It was subsequently decided to use the standard weighting (forward flux) used in XSDRN for the generating of cross-sections. The adjoint weighting was used in the generation of the delayed neutron fractions and the group velocities, which were subsequently used in the PSD calculations.

The internal XSDRN cell-averaged cross-sections are calculated using

Table 5. Fifty Neutron Energy Group Boundaries and Fission Spectrum

GP	ENERGY BOUNDARIES (EV)	BROAD GP NUMBERS	LETHARGY BOUNDARIES	MID PT VELOCITIES (CM/SEC)	FISS SPEC
1	1.49182+07	1	-3.99997-01	4.83383+09	1.04073-03
2	1.00000+07	1	0.00000	3.67165+09	5.15243-02
3	4.96585+06	1	7.00000-01	2.72002+09	1.54155-01
4	3.01194+06	1	1.20000+00	2.28334+09	8.82472-02
5	2.46597+06	1	1.40000+00	2.06605+09	9.46745-02
6	2.01897+06	1	1.60000+00	1.86944+09	9.45503-02
7	1.65299+06	1	1.80000+00	1.69154+09	8.91433-02
8	1.35335+06	1	2.00000+00	1.53057+09	8.02444-02
9	1.10803+06	1	2.20000+00	1.38492+09	6.95946-02
10	9.07180+05	1	2.40000+00	1.25312+09	5.85771-02
11	7.42736+05	1	2.60000+00	1.13387+09	4.81278-02
12	6.08101+05	1	2.80000+00	1.02597+09	3.87800-02
13	4.97871+05	1	3.00000+00	9.28338+08	3.07600-02
14	4.07622+05	1	3.20000+00	8.39995+08	2.40898-02
15	3.33733+05	1	3.40000+00	7.60059+08	1.86724-02
16	2.73237+05	1	3.60000+00	6.87729+08	1.43527-02
17	2.23708+05	1	3.80000+00	6.22283+08	1.09575-02
18	1.83156+05	1	4.00000+00	5.63065+08	8.31927-03
19	1.49956+05	1	4.20000+00	4.96904+08	8.82401-03
20	1.11090+05	1	4.50000+00	4.06830+08	8.41677-03
21	6.73795+04	1	5.00000+00	2.97643+08	5.22276-03
22	3.18278+04	1	5.75000+00	2.31805+08	7.96687-04
23	2.47875+04	1	6.00000+00	2.04567+08	5.49814-04
24	1.93045+04	1	6.25000+00	1.40597+08	3.79095-04
25	5.53085+03	1	7.50000+00	9.07761+07	0.00000
26	3.35463+03	1	8.00000+00	6.23894+07	0.00000
27	1.23410+03	1	9.00000+00	4.02816+07	0.00000
28	5.82947+02	1	9.75000+00	2.76851+07	0.00000
29	2.75365+02	1	1.05000+01	1.78749+07	0.00000
30	1.01301+02	1	1.15000+01	1.01848+07	0.00000
31	2.90232+01	1	1.27500+01	5.60311+06	0.00000
32	1.06770+01	1	1.37500+01	3.30651+06	0.00000
33	3.05902+00	1	1.50000+01	2.13613+06	0.00000
34	1.85985+00	2	1.54976+01	1.72135+06	0.00000
35	1.28988+00	2	1.58635+01	1.51802+06	0.00000
36	1.12489+00	2	1.60004+01	1.42440+06	0.00000
37	9.99923-01	2	1.61182+01	1.33805+06	0.00000
38	8.75930-01	2	1.62506+01	1.20143+06	0.00000
39	6.49938-01	2	1.65490+01	1.01712+06	0.00000
40	4.49954-01	2	1.69167+01	8.71286+05	0.00000
41	3.49965-01	2	1.71680+01	7.87296+05	0.00000
42	2.99970-01	2	1.73222+01	7.23783+05	0.00000
43	2.49980-01	2	1.75045+01	6.37007+05	0.00000
44	1.79979-01	2	1.78330+01	5.51052+05	0.00000
45	1.39991-01	2	1.80843+01	4.75746+05	0.00000
46	9.99889-02	2	1.84208+01	4.00053+05	0.00000
47	6.99950-02	2	1.87774+01	3.36402+05	0.00000
48	4.99942-02	2	1.91139+01	2.72178+05	0.00000
49	2.99948-02	2	1.96248+01	2.01435+05	0.00000
50	1.49985-02	2	2.03179+01	1.28712+05	0.00000
51	5.00028-03		2.14164+01		0.00000

$$\overline{\sigma}_G^{cell} = \frac{\sum_{j=1}^{IZM} N_j \sum_{i \in j} \Delta V_i \sum_{g \in G} \phi_g^i \sigma_g^j}{\sum_{j=1}^{IZM} N_j \sum_{i \in j} \Delta V_i \quad \frac{1}{V} \sum_{i=1}^{IM} \Delta V_i \sum_{g \in G} \phi_g^i} \tag{91}$$

where N_j: number density of isotope in zone j

i: spatial interval at mesh i

ΔV_i: volume of interval i

V: cell volume

g: fine group index

G: broad group index

σ_g^j: microscopic cross-section of isotope in zone j at group g

IZM: total number of zones in the system

IM: total number of mesh intervals

The transport cross-sections were generated using "definition 2" of XSDRN[123]:

$$\overline{\sigma}_{tr_G}^{cell} = \frac{\sum_{g \in G} L_g \sigma_{tr}^g}{\sum_{g \in G} L_g} \tag{92}$$

where L_g: leakage spectrum, defined as

$$L_g = D_g B_j^2 \phi_g^{cell} V + \int_{E \in g} dE \int_{\text{outside boundary}} dA \int_0^{4\pi} d\Omega \, \Omega \cdot \phi(\bar{r} E \Omega)$$

dA: unit surface area on the outside of the system

$\phi(E\bar{r}\bar{\Omega})$: flux per unit energy, volume and solid angle at E, $\bar{r}$, $\bar{\Omega}$

$\bar{\phi}_g^{cell}$: average flux over cell at energy g

For the thermal zone, the collapse was performed on a typical fuel plate of an Argonaut assembly. The parameters/options used were:

a) One-dimensional slab geometry, with the boundaries of the cell midway in the water between the fuel plates. Five equally spaced meshes were taken inside the fuel plate section of the cell, and six equally spaced meshes in the water section of the cell. A typical fuel plate of an Argonaut assembly in the thermal zone was taken to be 0.3 cm thickness, with a distance between fuel plates of 6.3 mm, and plate width of 7.5 cm. A fuel plate contains typically 124 gr U_3O_8, or at an enrichment in U-235 of 20 w/o of U, 20.83 gr U-235. The following number densities were used (Note: for all number densities quoted, multiply by 10^{24}).

Fuel plate: $N^{U235} = 3.650\ -04\ \frac{\text{atoms U235}}{cc_{plate}}$

$N^{U238} = 1.441\ -03\ \frac{\text{atoms U238}}{cc_{plate}}$

$N^{016} = 4.817\ -03\ \frac{\text{atoms } O^{16}}{cc_{plate}}$

$N^{Al} = 4.67\ -02\ \frac{\text{atoms Al}}{cc_{plate}}$

Water: $N^{H1}_{H_2O} = 6.6767\text{-}02\ \frac{\text{atoms H1}}{cc_{H_2O}}$

$N^{016}_{H_2O} = 3.3383\text{-}02\ \frac{\text{atoms } O^{16}}{cc_{H_2O}}$

b) Reflective left boundary in the middle of the fuel plate, white/albedo right boundary in the water in between fuel plates.

c) S_4P_3 one-dimensional transport approximation (discrete ordinate diamond method) using 123 neutron energy group library based on ENDF/B-II cross-section data.

d) Overall convergence criterion: 0.001

Point convergence criterion: 0.001

e) Resonance correction (resolved and unresolved for U^{235} and U^{238} using

--slab geometry, with absorber lump dimension equal to thickness of fuel plate

--Nordheim's Integral Method (NIM)[118] for U^{235}, U^{238}, and NIM for 1st moderator O^{16} in the fuel plate, at a temperature of 294.6°K.

--Dancoff correction using Bell's[125] approximation for slabs. This factor corrects for the self-shielding effects in the resonance region due to the presence of more than one absorber lump. The surface correction factor for slabs is

$$1 - C = 1 - 2E_3(\Sigma_s d)$$

where: d = distance between fuel plates

Σ_s = scattering cross-section in the moderator

$$E_3(x) = \int_1^\infty e^{-xU} U^{-3}\, dU$$

We therefore obtain that C = 0.068.

--Effective moderator cross-section per absorber atom for U^{235}

$$\left(\sigma_m\right)_{eff}^{U235} = \sigma_{P_0}^{U235} + \frac{1}{N^{U235}}\left(N^{U238}\sigma_{P_0}^{U238} + N^{O16}\sigma_{P_0}^{O16}\right.$$

(continued)

$$+ N^{Al27}\sigma_{P_o}^{Al27}) + \frac{1}{\bar{\ell} N^{U235}}$$

where $\bar{\ell}$: means chord length in the lump

$\sigma_{P_o}^{Mat}$: potential scattering of material "Mat"

The following values were used for the potential scattering H-1: 20.36 barn, C-12: 4.65, O-16: 3.64, Al-27: 1.35, Fe-56: 11.39, U-235: 10.0, and U-238: 9.0.

As a first approximation we take $\bar{\ell} = 0.3$ cm for the mean chord length in the lump.

We obtain that:

$$(\sigma_m)_{eff}^{U235} = 9400$$

--Effective moderator cross-section per absorber atom for U-238:

$$(\sigma_m)_{eff}^{U238} = 2380$$

--For U-235, the moderator scattering cross section per absorber atom is defined for XSDRN as:

$$\sigma_s = \frac{N_1}{N_a}\sigma_{s_1}$$

where N_1: number density of moderator in the lump

N_a: number density of the absorber in the lump

For 1st moderator $\sigma_s^{O16} = 48.0$

For 2nd moderator $\sigma_s^{Al27} = 172.8$

--For U-238, the moderator scattering cross-section per absorber atom:

For 1st moderator $\sigma_s^{O16} = 12.17$

For 2nd moderator $\sigma_s^{A127} = 43.7$

f) k_{eff} calculation with no axial leakage

g) Collapsed 50 group cross-section sets were generated in XSDRN "magic-word" format. The scattering matrices were generated for P_0, P_1, P_2, and P_3 scattering. It has to be noted that the P_0 transfer matrix is composed of

--isotropic elastic scattering matrix

--inelastic transfer matrix

--(n,2n) transfer matrix

The P_1, P_2, P_3 transfer matrices contain the 1st, 2nd, 3rd order transfer coefficients of a Legendre expansion to the elastic scattering cross-section in the laboratory system. The P_1, P_2, P_3 account for anisotropic scattering and they are often negative over part of the angular range.

The 123 neutron group cross-sections were cell weighted and collapsed to 50 neutron groups for the isotopes H-1, C-12, O-16, Al-27, U-235, and U-238 in the fuel plates of the thermal zone, H-1 and O-16 in the water of the thermal zone. The C-12 isotope in the external graphite reflector, the H-1, C-12, O-16 isotopes in the external graphite + air gap, and the H-1, C-12, O-16 isotopes in the external graphite + air gap were reduced to a 50 group set by adding them into each mixture with a number density of 1.0×10^{-15}. No contribution (negligible) therefore was made to the actual macroscopic cross-section of the mixtures. As stated in XSDRN, when the cell weighting is performed, this will produce sets of

microscopic cross-sections averaged over the cell neutron spectrum of the thermal zone, but which have the homogenization and disadvantage factor effects cancelled out.

For the collapse from 123 to 50 groups of the cross-sections of the isotopes of the fast assembly region (Fast assembly Type II), the following parameters/options were used:

a) One-dimensional cylindrical geometry, with the outer radius of the cell boundary being the equivalent radius of the cell, based on the same surface as a fast assembly. Thus, the equivalent cell radius of the fuel platelets was taken based on a square dimension of 5.2 x 5.2 cm. The number densities of the isotopes of the different platelets were homogenized over the fuel volume, and are the same as in Table 1. Ten equally spaced meshes were used within the cell representing a fast fuel assembly.

b) Reflective left boundary in the middle of the equivalent cylinder, white/albedo right boundary at the outer radius of the fast assembly cell.

c) S_4P_3 one-dimensional transport approximation (discrete ordinate diamond method) using 123 neutron group library based on ENDF/B-II data.

d) Overall Convergence criterion: 0.001

Point Convergence criterion : 0.001

e) *Resonance correction* (resolved and unresolved) for U-235 in fast assembly II, U-238 in fast assembly II, U-238 in natural uranium blanket, at a temperature of 294.6°K, using:

--homogeneous geometry

--A value of 0.0 for the Dancoff correction was used (zero for a homogeneous resonance correction case)

--For U-235 in Fast assembly type II, we have that

the effective moderator cross-section per absorber atom:

$$(\sigma_m)_{eff}^{U235} = 219.1 \text{ barn}$$

the moderator scattering cross-section per absorber atom for:

1st moderator $\sigma_s^{O16} = 24.0$

2nd moderator $\sigma_s^{H1} = 15.1$

--For U-238 in the fast assembly II, we have that

the effective moderator cross-section per absorber atom:

$$(\sigma_m)_{eff}^{U238} = 16.95$$

the moderator scattering cross-section per absorber atom for:

1st moderator $\sigma_s^{O16} = 1.856$

2nd moderator $\sigma_s^{H1} = 1.167$

--For U-238 in the natural uranium blanket, we have that

the effective moderator cross-section per absorber atom:

$$(\sigma_m)_{eff}^{U238} = 9.1$$

f) Collapsed 50 group cross-section sets were generated, including P_0, P_1, P_2, and P_3 scattering matrices. The 123 neutron group cross-sections were cell-weighted over the fast assembly and collapsed to 50 groups for the isotopes H-1, C-12, O-16, Al-27, Fe-56, U-235, and U-238 of the fast assembly. The U-235 and U-238 cross-sections of the natural

uranium blanket were reduced to a 50 group set by adding them into each mixture with a number density of 1.0×10^{-15}. When the cell weighting over the fast assembly is performed, this will produce microscopic cross-section sets averaged over the fast assembly cell spectrum, but which have the homogenization and disadvantage factor effects cancelled out.

For the collapse from 123 to 50 groups of the cross-sections of the isotopes of fast Assembly type IV, the following parameters were used:

a) One-dimensional cylindrical geometry (see assembly type II). The number densities of the isotopes of the different platelets were homogenized over the fuel volume, and are the same as in Table 2. Ten equally spaced meshes were used within the cell of the fast fuel assembly.

e) Resonance correction (resolved and unresolved) for U-235 in fast assembly IV, U-238 in fast assembly IV, U-238 in natural uranium blanket, at a temperature of 294.6°K, using:

--homogeneous geometry

--a value of 0.0 was used for the Dancoff correction (zero for a homogeneous resonance correction case)

--For U-235 in the fast assembly IV, we have that

the effective moderator cross-section per absorber atom:

$$(\sigma_m)_{eff}^{U235} = 99.26 \text{ b.}$$

the moderator scattering cross-section per absorber atom for:

1st moderator $\sigma_s^{O16} = 12.6$ b.

2nd moderator $\sigma_s^{A127} = 3.1$ b.

--For U-238 in fast assembly IV, we have that:

the effective moderator cross-section per absorber atom:

$$(\sigma_m)_{eff}^{U238} = 15.7 \text{ b.}$$

the moderator scattering cross-section per absorber atom for:

1st moderator $\sigma_s^{O16} = 2.00$ b.

2nd moderator $\sigma_s^{Al27} = 0.49$ b.

--For U-238 in the natural uranium blanket, we have that:

the effective moderator cross-section per absorber atom:

$$(\sigma_m)_{eff}^{U238} = 9.1 \text{ b.}$$

f) Collapsed 50 neutron group cross-section sets were generated, including P_0, P_1, P_2, and P_3 scattering matrices. The 123 neutron group cross-sections were cell weighted over fast assembly IV spectrum and collapsed to 50 groups for the isotopes O-16, Al-27, Fe-56, U-235, and U-238. The U-235 and U-238 cross-sections of the natural uranium blanket were reduced to a 50 group set similarly to the case of assembly II type. In order to validate the method of cross sections generation using a cell weighted collapse from 123 to 50 neutron groups, and the cross-section sets themselves, benchmarks on experimental critical experiments were run (see Appendix B).

Generation of Broad Group Cross Sections

The fifty neutron group cross-section sets, generated by resonance corrections on U235 and U238, followed by cell spectrum-weighted collapses

to fifty neutron groups, were subsequently zone-weighting collapsed to broad group sets (two or three broad neutron groups) for use in the power spectral density calculations. Typically in the case of two broad groups, neutron groups 1 to 33 were zone-weighted to broad group one, neutron groups 34 to 50 were zone-weighted to broad group number two.

The zone-weighting was performed using the XSDRN code. The weighting was performed using forward flux weighting. The transport cross-sections were generated using "definition 2" of XSDRN[123]

$$\overline{\sigma}_{tr_G}^{zone} = \frac{\sum_{g \in G} L_g \sigma_{tr}^g}{\sum_{g \in G} L_g} \tag{94}$$

where L_g: leakage spectrum

$$L_g = D_g B_g^2 \bar{\Phi}_g^j V_j$$

The (n,2n) cross-sections were treated as fission (with a ν value of 2), and were added to the smooth fission cross-sections as follows:

$$\bar{\sigma}_f = \bar{\sigma}_f + \bar{\sigma}_{m,2m}$$

$$\bar{\nu} = \frac{\nu_f \bar{\sigma}_f + 2\bar{\sigma}_{m,2m}}{\bar{\sigma}_f + m,2m} \tag{95}$$

The same method was used for the three different reactors, namely TARK, Fast Argonaut Assembly II, and Fast Argonaut Assembly IV.

The parameters/options were:

a) One-dimensional cylindrical geometry, with the right boundary being the outer edge of the reactor. The mesh configuration and zone

numbering are shown in Figure 9. The number densities and material composition for each zone are shown in Tables 1, 2, and 3.

Number of zones:	TARK	9
	Assembly II core	9
	Assembly IV core	9
Number of mesh points:	TARK	27
	Assembly II core	28
	Assembly IV core	28

A buckling search for $k_{eff} = 1.0$ was performed in order to incorporate the effect of axial leakage on the neutron spectrum in the forward flux weighted cross-section collapses. The axial buckling was taken to be independent of the zones and of the neutron groups. The leakage was taken as $D_g B_g^2 \phi_g$

where

$B_g = \left(\frac{\pi}{DZ^*_g}\right)^2$: buckling

$D_g = \frac{1}{3\Sigma_{tr}}$: diffusion coefficient

ϕ_g: flux for group g

$DZ^*_g = DZ^\circ + 2\ f\ \lambda^g_{tr}$: cylinder height including extrapolation and was treated as an absorption term in the transport equation.

The factor f was taken to be 0.7104.

b) A reflective left boundary condition was taken in the center of the reactor; a vacuum right boundary (no reflection) was taken at the outer edge of the reactor.

c) S_4P_3 one-dimensional transport approximation (discrete ordinate diamond method) using the 50 group collapsed neutron cross-section sets

previously generated.

d) Overall Convergence criterion: 0.001

Point Convergence criterion: 0.001

e) Collapsed two or three group cross-section sets were generated. The scattering matrices were generated for P_0 and P_1 scattering.

The broad-group cross-sections were zone-spectrum weighted and collapsed using the forward flux, and they were generated for each of the isotopes in each zone.

The values of the microscopic cross-section, together with the macroscopic cross-sections for each zone are tabulated in Table 6 (broad-group cross-section TARK), Table 7 (broad-group cross-sections STARK Assembly II), and Table 8 (broad-group cross-sections STARK Assembly IV).

The 1/v broad group values are also tabulated. It has to be observed that no significant difference exists between the values obtained using adjoint flux weighting:

$$\overline{\left(\frac{1}{v}\right)} = \frac{\int_{\text{zone}\,j} dr \int_{g} \phi^* \frac{1}{v} \phi \, dE}{\int_{\text{zone}\,j} dr \int_{g} \phi^* \phi \, dE} \tag{96}$$

and forward flux weighting:

$$\overline{\left(\frac{1}{v}\right)} = \frac{\int_{\text{zone}\,j} dr \int_{g} \frac{1}{v} \phi \, dE}{\int_{\text{zone}\,j} dr \int_{g} \phi \, dE} \tag{97}$$

The adjoint weighted 1/v values were used in the calculation of the space- and energy-dependent power spectral densities and transfer functions. Different 1/v values were obtained for each zone of the reactors. For the TARK reactor the thermal group 1/v zone averaged values were not appreciably different from the reactor averaged values, while for the fast broad group zone averaged values, the highest values were found in the graphite coupling region, and the outside graphite reflector. It is precisely there that the spectrum is the most thermalized.

For the STARK reactor, the zone averaged, adjoint weighted 1/v values over the thermal broad-group vary approximately by a factor of four between the fast core zone and the reactor averaged values. This was expected since the spectrum in the fast core is harder than in the thermal core or the reflector zones.

We have seen that the cross-sections based on ENDF/B-II were obtained by a cell spectrum collapse from 123 to 50 groups, followed by a zone-dependent reactor spectrum collapse from 50 to two or three broad groups. In order to check how much difference there was between weighted 1/v values obtained this way and 1/v values obtained directly from a collapse from 123 to two or three broad groups, a zone-dependent S_4P_3 forward transport calculation was performed. The broad thermal group reactor averaged 1/v value was 3.2217-06, while the value obtained through cell collapse, followed by a reactor spectrum collapse with a critical buckling correction was 3.3996-06, a difference of approximately 5%.

Nagy and Danofsky[17] performed a study based on a one-dimensional, two-energy group representation of an Argonaut-type reactor. They performed a parametric study for the value of the first sink frequency versus

Table 6. Broad Group Cross Sections TARK

ZONE	MATERIAL	VOLUME	REGION	GROUP	σ_a	σ_f	σ_{tr}	ν	σ_{s_0}		$\bar{\mu}_1$	σ_{s_1}		
									1→2	2→1	1→2	1→2		
ZONE=1 (GRAPHITE)	C-12	4.526E+02	1		1.0872E-04	0.0000	4.0618E+00		4.7653E-02		-4.2202E-02	+1.4067E-02		
			2		2.5541E-03	0.0000	4.8955E+00			2.8018E-05				
	ZONE=1		1		(4.2490E-05)	(0.0000)	(9.6250E-01)		(4.0630E-03)		(-3.5980E-03)	(-1.1990E-03)	(8.0570E-04)	(8.2051E-08)
			2		(2.1740E-04)	(0.0000)	(7.9800E-01)			(2.3890E-06)			(1.0850E-06)	(3.4093E-06)
ZONE=2 (GRAPHITE)	C-12	4.526E+02	1		1.1300E-04	0.0000	3.9403E+00		4.0642E-02		-3.5998E-02	+1.1999E-02		
			2		2.5333E-03	0.0000	4.8938E+00			3.0067E-05				
	ZONE=2		1		(9.8800E-05)	(0.0000)	(8.9120E-01)		(3.4650E-03)		(-3.0690E-03)	(-1.0230E-03)	(7.1700E-04)	(7.1512E-08)
			2		(2.1600E-04)	(0.0000)	(7.9800E-01)			(2.5640E-06)			(1.0450E-06)	(1.9004E-06)
ZONE=3 (GRAPHITE)	C-12	4.526E+02	1		1.5145E-04	0.0000	3.7679E+00		3.3600E-02		-2.9768E-02	+9.9210E-03		
			2		2.4955E-03	0.0000	4.8907E+00			3.3030E-05				
	ZONE=3		1		(1.1220E-03)	(0.0000)	(1.0370E+00)		(2.4650E-03)		(-2.5360E-03)	(-8.4590E-04)	(6.1419E-06)	(5.9853E-08)
			2		(2.1280E-04)	(0.0000)	(7.9940E-01)			(2.8510E-06)			(1.3957E-06)	(3.4070E-06)
ZONE=4	H-1	3.480E+00	1		3.8644E-03	0.0000	4.6195E+00		7.9304E-01		1.0526E+00	3.5087E-01		
			2		2.4651E-01	0.0000	4.9076E+01			5.0430E-05				
(GRAPHITE + AIR GAP)	C-12	4.922E+02	1		1.4540E-04	0.0000	3.5082E+00		2.8567E-02		-2.5303E-02	-8.4343E-03		
			2		2.4977E-03	0.0000	4.8865E+00			3.7040E-05				
	AL	4.264E+03	1		4.4747E-03	2.5981E-04	2.4959E+00	2.0000E+00	3.7056E-03		-4.5209E-03	+1.1736E-03		
			2		1.6700E-01	0.0000	1.5943E+00			1.2585E-05				
	ZONE=4		1		(5.5680E-05)	(4.4400E-10)	(1.6711E+00)	(2.0000E+00)	(1.7320E-03)		(-1.9070E-04)	(-2.9690E-04)	(5.5267E-06)	(5.0694E-08)
			2		(1.7560E-03)	(0.0000)	(1.2351E+00)			(1.9580E-06)			(1.5225E-06)	(3.3403E-06)
ZONE=5	H-1	3.724E+02	1		3.2339E-03	0.0000	4.1435E+00		7.0259E-01		9.3374E-01	3.1125E-01		
			2		2.5339E-01	0.0000	5.4369E+01			5.5855E-05				
(THERMAL CONC)	C-12	1.488E+02	1		2.8600E-04	0.0000	3.5390E+00		2.5633E-02		-2.2713E-02	-7.5710E-02		
			2		2.3759E-03	0.0000	4.8799E+00			4.0876E-05				
	H-1H	2.403E+02	1		2.9879E-03	0.0000	3.1190E+00		1.5085E-02		+1.4159E-02	+4.7197E-03		
			2		1.2687E-04	0.0000	3.4391E+00			3.7376E-05				
	AL	1.343E+02	1		5.8198E-03	3.4753E-08	2.4571E+00	2.0000E+00	3.3250E-03		+3.1492E-03	+1.0531E-03		
			2		1.4209E-01	0.0000	1.5885E+00			1.3887E-05				

Table 6. Concluded

ZONE	ISOTOPE	NUMBER DENSITY	GROUP	σ_a (Σ_a)	σ_f ($\nu\Sigma_f$)	σ_{tr} ($1/3\Sigma_{tr}$)	ν	σ_s 1→2	σ_s 2→1	P_1 1→2	σ_{s_1} 1→2	$\int \phi^* \frac{1}{v} \phi \, dV$	$\int \frac{1}{v} \phi \, dV$
	U-235	1.044E-04	1	1.5404E+01	4.8979E+00	2.0793E+01	2.4365E+00	2.1013E-06		-2.0955E-06	-8.9850E-07		
			2	9.2582E+02	5.8264E+02	8.7179E+02	2.4230E+00		1.1108E-08				
	U-238	4.193E-02	1	1.6001E+00	1.1866E-01	1.5633E+01	2.7585E+00	1.0793E-06		-1.0758E-06	-5.5980E-07		
			2	1.9362E+00	0.0000	1.0872E+01			5.7061E-09				
	ZONE-5		1	(3.1580E-03)	(2.3590E-03)	(1.0818E+00)		(2.6910E-02)		(3.4130E-02)	(1.1348E-02)	(5.3252E-08)	(4.4475E-08)
			2	(5.8390E-02)	(9.2220E-02)	(2.0168E-01)			(3.6090E-06)			(3.2568E-06)	(3.2580E-06)
ZONE-6 (GRAPHITE)	C-12	8.528E-02	1	1.4121E-04	0.0000	3.5684E+00		2.8869E-02		-2.5571E-02	-8.5280E-03		
			2	2.4605E-03	0.0000	4.8877E+00			3.6694E-05				
	ZONE-6		1	(1.5450E-05)	(0.0000)	(1.0956E+00)		(2.4610E-03)		(-2.1400E-03)	(-7.2870E-04)	(5.0159E-06)	(5.1460E-08)
			2	(2.0940E-04)	(0.0000)	(7.9990E-01)			(3.1240E-06)			(3.3496E-06)	(3.3586E-06)
ZONE-7	H-1	2.527E-02	1	4.2300E-03	0.0000	5.1169E+00		9.1516E-01		1.2141E+00	4.0470E-01		
			2	2.4802E-01	0.0000	3.9631E+01			4.4862E-05				
(GRAPHITE + AIR GAP)	C-12	4.127E-02	1	1.3445E-04	0.0000	3.7521E+00		3.2827E-02		-2.9080E-02	-4.8438E-03		
			2	2.5034E-03	0.0000	4.4913E+00			3.2803E-05				
	AL	5.448E-03	1	4.9918E-03	1.3934E-04	2.5011E+00	2.0000E+00	4.2582E-03		-4.0854E-03	-1.3488E-03		
			2	1.7081E-01	0.0000	1.5987E+00			1.1148E-05				
	ZONE-7		1	(2.4810E-05)	(9.7113E-11)	(2.0220E+00)		(1.6010E-03)		(-9.0740E-04)	(-3.0250E-04)	(5.9369E-06)	(5.9823E-08)
			2	(7.6050E-04)	(0.0000)	(1.5329E+00)			(1.4040E-06)			(3.4098E-06)	(3.4188E-06)
ZONE-8 (GRAPHITE)	C-12	8.528E-02	1	1.1020E-04	0.0000	3.9815E+00		4.1152E-02		-3.6448E-02	-1.2149E-02		
			2	2.5491E-03	0.0000	4.6965E+00			2.6950E-05				
	ZONE-8		1	(9.7370E-06)	(0.0000)	(9.9190E-01)		(3.5090E-03)		(-3.1080E-03)	(-1.0360E-03)	(7.0937E-08)	(7.2120E-08)
			2	(2.1960E-04)	(0.0000)	(7.9650E-01)			(2.2960E-06)			(3.4995E-06)	(3.5032E-06)
ZONE-9 (GRAPHITE)	C-12	8.528E-02	1	1.1781E-04	0.0000	4.1809E+00		5.8210E-02		-5.1520E-02	-1.7173E-02		
			2	2.6281E-03	0.0000	4.9015E+00			2.0339E-05				
	ZONE-9		1	(1.0050E-05)	(0.0000)	(9.9410E-01)		(4.9830E-03)		(-4.5450E-03)	(-1.8840E-03)	(9.0452E-08)	(9.7327E-08)
			2	(2.2010E-04)	(0.0000)	(7.9760E-01)			(1.7300E-06)			(3.5917E-06)	(3.5923E-06)
REFLECTOR			1	(0.0000)	(0.0000)	(0.0000)						(5.0421E-08)	(5.9225E-08)
			2	(0.0000)	(0.0000)	(0.0000)						(3.1990E-06)	(3.4302E-06)

Table 7. Broad Group Cross Sections STARK Assembly II

ZONE	ISOTOPE	NUMBER DENSITY	ENERGY GROUP	σ_a (Σ_a)	σ_f $(\nu\Sigma_f)$	σ_{tr} $(1/3\Sigma_{tr})$	ν	σ_{s} $1\rightarrow 2$	P_1 $1\rightarrow 2$	σ_{s_1} $1\rightarrow 2$	$\int\phi^*_{\frac{1}{2}}\phi dV$	$\int_{\frac{1}{2}}\phi dV$
ZONE=1	M=1	1.30E=03	1	1.4717=04	0.0001	5.5317+00		7.8778=03	=.4524=05	2.8506=03		
			2	8.9175=02	0.0000	1.0161+01						
(EAST CORE)	C=12	8.70A=04	1	7.7A54=05	0.0000	3.5038+00		2.8294=04	=2.0981=04	=8.3270=05		
			2	7.09A2=04	0.0000	4.7A44+00						
	O=16	1.1A4=02	1	8.2421=04	0.0000	3.4742+00		1.7092=04	=1.5628=04	=5.2090=05		
			2	3.7767=04	0.0000	4.7714+00						
	AL	1.700=02	1	2.807A=03	1.3231=04	3.5957+00	2.0000+00	3.6702=05	=3.0872=05	=1.1624=05		
			2	8.A025=02	0.0000	1.0596+00						
	FE	8.042=03	1	1.4022=02	8.0805=06	4.A851+00	2.0000+00	9.1982=05	=9.2115=05	=3.0672=05		
			2	5.3404=01	0.0000	1.2260+01						
	U=235	1.7E8=03	1	2.A019+00	2.0223+00	9.A847+00	2.4545+00	2.3243=08	=2.317A=04	=7.7260=09		
			2	1.0436+02	A.A2A6+01	1.1936+02	2.4230+00					
	U=238	2.2A2=02	1	3.1038=01	4.017A=02	9.8112+00	2.7A80+00	1.1914=08	=1.1875=08	=3.9580=09		
			2	A.449A=01	0.0000	9.5760+00						
	ZONE=1		1	(1.1910=02)	(1.1290=02)	(A.7850=01)		(1.3680=05)	(2.0520=06)	(2.0640=06)	(3.8857=09)	(3.5395=09)
			2	(2.0320=011	(3.7760=011	(5.0630=01)					(9.5233=07)	(9.4704=07)
ZONE=2	M=1	1.57A=03	1	2.2853=04	0.0000	3.4459+00		3.7417=02	5.A571=02	1.9520=02		
			2	1.0043=01	0.0000	2.2009+01						
(EAST CORE)	C=12	8.70A=04	1	A.A05=05	0.0000	3.4971+00		2.1336=03	=1.AA3A=03	=8.2790=05		
			2	1.927=04	0.0000	4.7631+00						
	O=16	1.16=02	1	A.9025=04	0.0000	3.4A62+00		1.2A89=03	=1.1785=03	=5.9280=05		
			2	5.4756=05	0.0000	4.782=+00						
	AL	1.700=02	1	2.A817=03	1.4841=04	3.6022+00	2.0000+00	2.7670=04	=2.A24=04	=8.7A5=05		
			2	7.8091=02	0.0000	1.4839+00						
	FE	8.042=05	1	1.9443=02	8.7042=06	4.7242+00	2.0000+00	7.0869=04	=6.43A=04	=2.5129=04		
			2	7.7301=01	0.0000	1.2508+01						
	U=235	1.7E8=03	1	2.A187+00	2.0389+00	9.7309+00	2.4571+00	1.7494=07	=1.7044=07	=5.8150=08		
			2	1.6A37+02	1.4338+02	1.A337+02	2.4230+00					

Table 7. Continued

ZONE	ISOTOPE	NUMBER DENSITY	ENERGY GROUP	σ_a (Σ_a)	σ_f ($\nu\Sigma_f$)	σ_{tr} ($1/3\Sigma_{tr}$)	ν	$\sigma_{s,1\to2}$	$\sigma_{s,2\to1}$	$P_{1\to2}$	$\sigma_{s,1\to2}$	$\int\phi^* \frac{1}{v}\phi dV$	$\int \frac{1}{v}\phi dV$
	U-235	2.682E-02	1	5.0593E-01	9.3108E-02	9.5934E+00	2.7400E+00	8.9881E-08		-8.4500E-04	2.9000E-08		
			2	4.8484E-01	0.0000	9.8176E+00							
	ZONE-2		1	(1.1750E-02)	(1.1530E-02)	(8.9290E-01)		(7.0360E-05)		(5.2470E-05)	(1.7956E-04)	(5.5910E-09)	(6.6340E-09)
			2	(3.2350E-01)	(6.1550E-01)	(4.6000E-01)						(1.4940E-08)	(1.5800E-08)
ZONE-3	U-235	5.937E-04	1	5.2948E+00	5.0438E+00	1.2594E+01	2.4438E+00	8.1233E-07		-8.1010E-07	2.7000E-07		
			2	3.0347E+02	2.5795E+02	3.1846E+02	2.4230E+00		3.7873E-06				
(FAT=U HOPPER)	U-238	8.739E-02	1	5.3166E-01	5.1673E-02	1.0101E+01	2.7553E+00	6.1726E-07		-8.1588E-07	1.3463E-07		
			2	1.3891E+00	0.0000	1.0305E+01			1.9458E-06				
	ZONE-3		1	(1.7540E-02)	(9.7960E-03)	(6.9020E-01)		(2.0053E-07)		(-1.9990E-08)	(-8.8820E-09)	(1.6030E-08)	(1.5892E-08)
			2	(1.6920E-01)	(2.1448E-01)	(5.5760E-01)			(9.3490E-10)			(2.2804E-08)	(2.2401E-08)
ZONE-4	H-1	3.660E-04	1	2.5611E-05	0.0000	8.2395E-02		5.3894E-01		7.1410E-01	2.5803E-01		
			2	2.1038E-01	0.0000	1.5883E+01			9.6841E-05				
(SEAM-1TS + AIR GAP)	C-12	8.922E-02	1	1.4739E-04	0.0000	3.5252E-00		1.9136E-02		-1.8490E-02	-5.6310E-03		
			2	2.1432E-03	0.0000	4.8613E-00			7.0835E-05				
	AL	3.259E-03	1	4.3117E-04	0.0000	2.8390E-00	2.4000E-00	2.4418E-03		-2.3581E-03	-7.9400E-04		
			2	1.4819E-01	0.0000	1.5702E-00			2.4088E-05				
	ZONE-4		1	(4.9130E-05)	(4.3508E-10)	(1.6553E-01)		(1.1630E-03)		(-5.9060E-04)	(-1.9690E-03)	(4.0513E-08)	(3.8008E-08)
			2	(1.5370E-03)	(0.0000)	(1.2483E-00)			(3.7450E-06)			(2.9107E-06)	(2.9034E-06)
ZONE-5 (THERMAL	H-1	5.726E-02	1	3.2458E-03	0.0000	4.1988E-00		7.0363E-01		7.3346E-01	3.1150E-01		
			2	2.5847E-01	0.0000	5.8081E-01			5.9570E-05				
ZONE SCATTER)	C-12	1.484E-02	1	2.6598E-04	0.0000	1.3592E+00		2.5572E-02		-2.2580E-02	-7.5270E-03		
			2	2.5484E-03	0.0000	4.8777E-00			4.3752E-05				
	O-16	2.405E-02	1	2.4720E-03	0.0000	3.1284E+00		1.5446E-02		-1.4125E-02	-4.7080E-03		
			2	1.2590E-04	0.0000	3.8376E-00			8.0005-05				
	AL	1.343E-02	1	5.0401E-03	0.0000	2.4867E+00	0.0000	3.3172E-03		-3.1518E-03	-1.0590E-03		
			2	1.6021E-01	0.0000	1.5865E-00			1.4864E-05				
	U-235	1.049E-04	1	1.5183E-01	8.5835E-00	2.0626E-01	2.4340E-00	2.0963E-06		-2.0905E-06	-6.9680E-07		
			2	4.2017E-02	1.5798E-02	8.6599E-02	2.4230E-00		1.1890E-06				

Table 7. Concluded

ZONE	MATERIAL	NUMBER DENSITY	ENERGY GROUP	σ_a (Σ_a)	σ_f ($\nu\Sigma_f$)	σ_{tr} ($1/3\Sigma_{tr}$)	ν	σ_s 1→2	σ_s 2→1	P_1 1→2	σ_1 1→2	$\int \Phi^* \frac{1}{v} \Phi dV$	$\int \frac{1}{v} \Phi dV$
	H-2O	6.193E-02	1	3.6015E+00	1.1930E-01	1.4775E+01	2.7540E+00	1.0766E-06		+1.0732E-06	+3.5770E-07		
			2	1.9085E+00	0.0000	1.0850E+01			6.1075E-09				
	ZONE-5		1	(3.1580E-03)	(2.3210E-03)	(1.0758E+01)		(2.6950E-02)		(5.4120E-02)	(1.1370E-02)	(5.4031E-06)	(6.5143E-04)
			2	(5.5680E-02)	(9.1030E-02)	(2.0300E+01)			(3.8630E-06)			(3.2173E-06)	(3.2904E-06)
ZONE-6 (GRAPHITE)	C-12	8.52E-02	1	1.9631E-04	0.0000	5.5275E+00		2.8293E-02		+2.5960E-02	+8.3530E-03		
			2	2.0257E-03	0.0000	8.8408E+00		0.0000	3.9952E-05				
	ZONE-6		1	(1.6700E-05)	(0.0000)	(1.1083E+00)		(2.8120E-03)		(+2.1370E-03)	(+7.1220E-04)	(5.2814E-06)	(5.0669E-06)
			2	(2.0880E-04)	(0.0000)	(8.0040E-01)			(3.4060E-06)			(3.3021E-06)	(3.3998E-06)
ZONE-7	H-1	2.527E-02	1	5.9934E-03	0.0000	4.9290E+00		8.6431E-01		1.1430E+00	3.8100E-01		
			2	2.4205E-01	0.0000	3.9221E+01			4.9977E-05				
(GRAPHITE + AIR GAP)	C-12	4.127E-02	1	1.5211E-04	0.0000	3.6790E+00		3.1031E-02		-2.7490E-02	+9.1630E-03		
			2	2.4833E-03	0.0000	4.8840E+00			3.6707E-05				
	AL	5.480E-03	1	4.9153E-03	1.7545E-02	2.5188E+00	2.0000E+00	6.0252E-03		+3.8245E-03	+1.2748E-03		
			2	1.6880E-01	0.0000	1.5955E+00			1.2472E-05				
	ZONE-7		1	(2.4090E-05)	(1.2230E-10)	(2.0596E+00)		(1.5130E-03)		(+4.5900E-04)	(+2.8630E-04)	(5.6209E-06)	(5.5396E-06)
			2	(7.0880E-04)	(0.0000)	(1.5367E+00)			(1.5710E-06)			(3.3530E-06)	(3.3629E-06)
ZONE-8 (GRAPHITE)	C-12	8.52E-02	1	1.2116E-04	0.0000	3.8849E+00		3.8208E-02		+3.3881E-02	+1.1288E-02		
			2	2.5285E-03	0.0000	4.8934E+00			3.0441E-05				
	ZONE-8		1	(1.0330E-05)	(0.0000)	(1.0784E+00)		(3.2580E-03)		(+2.8850E-03)	(+9.6180E-04)	(6.5986E-06)	(6.7044E-06)
			2	(2.1560E-04)	(0.0000)	(7.9900E-01)			(2.5950E-06)			(3.4492E-06)	(3.4937E-06)
ZONE-9 (GRAPHITE)	C-12	8.52E-02	1	1.1853E-04	0.0000	4.1117E+00		5.4237E-02		+4.8048E-02	-1.6011E-02		
			2	2.5060E-03	0.0000	4.8991E+00			2.3097E-05				
	ZONE-9		1	(1.0110E-05)	(0.0000)	(9.5080E-01)		(4.6280E-03)		(+4.0960E-03)	(+1.3650E-03)	(8.8396E-06)	(9.1966E-06)
			2	(2.2180E-04)	(0.0000)	(7.9800E-01)			(1.9690E-05)			(3.5515E-06)	(3.5526E-06)
REACTOR			1									(5.5272E-06)	(4.6927E-06)
			2									(3.3220E-06)	(3.3628E-06)

Table 8. Broad Group Cross Sections STARK Assembly IV

ZONE	ISOTOPE	NUMBER DENSITY	BROAD GROUP	σ_a (Σ_a)	σ_f (Σ_f)	σ_{tr} $(1/3\Sigma_{tr})$	ν	$\sigma_{s_{1\to 2}}$	$P_{1\to 2}$	$\sigma_{s_{2\to 1}}$	$\int \Phi^* \frac{1}{v} \Phi dV$	$\int \frac{1}{v} \Phi dV$
ZONE-1	H-1	1.000E-15	1	1.9317E-05	0.0000	2.9885E+00		6.0610E-04				
			2	5.9812E-02	0.0000	7.8747E+00						
(FAST CORE)	C-12	1.000E-15	1	1.0378E-04	0.0000	3.3384E+00		3.0985E-05				
			2	8.1364E-04	0.0000	8.7609E+00						
	O-16	1.443E-02	1	1.1227E-03	0.0000	3.4404E+00		2.1135E-05	-1.9325E-05	-6.4028E-06		
			2	3.2655E-05	0.0000	3.7894E+00						
	AL	4.619E-03	1	2.7121E-05	1.7821E-08	3.7965E+00	2.0000E+00	8.5386E-06	-8.3120E-06	-1.0373E-06		
			2	4.1404E-02	0.0000	1.4529E+00						
	FE	8.642E-03	1	1.0512E-02	8.1632E-06	4.0194E+00	2.0000E+00	1.1821E-05	-1.1378E-05	-3.7930E-06		
			2	9.8188E-01	0.0000	1.2186E+01						
	U-235	4.160E-03	1	1.8210E+00	1.4947E+00	8.2905E+00	2.4781E+00	2.6824E-09	-2.6745E-09	-9.5520E-10		
			2	9.8896E+01	7.9719E+01	1.1190E+02	2.4230E+00					
	U-238	2.653E-02	1	2.4714E-01	5.1598E-02	8.5915E+00	2.7510E+00	1.4732E-09	-1.4865E-09	-8.8960E-10		
			2	5.7988E-01	0.0000	9.5106E+00						
	ZONE-1		1	(1.4190E-02)	(1.9290E-02)	(8.9810E-01)		(8.1890E-07)	(-3.8910E-07)	(-1.2970E-07)	(1.7690E-04)	(1.8070E-04)
			2	(9.2150E-01)	(8.0350E-01)	(3.8860E-01)					(8.2402E-07)	(8.1426E-07)
ZONE-2	H-1	1.000E-15	1	7.0440E-05	0.0000	3.4226E+00		1.6219E-02				
			2	9.7710E-02	0.0000	1.9817E+01						
(FAST CORE)	C-12	1.000E-15	1	1.0428E-04	0.0000	3.3462E+00		1.1501E-03				
			2	9.9990E-04	0.0000	8.7818E+00						
	O-16	1.443E-02	1	1.1160E-03	0.0000	3.4556E+00		6.9476E-04	-8.3526E-04	-2.1175E-04		
			2	5.5279E-05	0.0000	3.7816E+00						
	AL	9.619E-03	1	2.7622E-03	1.7919E-08	3.7867E+00	2.0000E+00	1.6918E-04	-1.6179E-04	-4.7250E-05		
			2	6.8205E-02	0.0000	1.4819E+00						
	FE	8.642E-03	1	1.1055E-02	8.2081E-06	4.0481E+00	2.0000E+00	3.8201E-04	-3.7401E-04	-1.2467E-04		
			2	7.5209E-01	0.0000	1.2487E+01						
	U-235	4.160E-03	1	1.9073E+00	1.5546E+00	8.4075E+00	2.4756E+00	9.4292E-08	-9.4033E-08	-3.1388E-08		
			2	1.0198E+02	1.5801E+02	1.7698E+02	2.4230E+00					

Table 8. Continued

ZONE	IDENTIFIER	NUMBER DENSITY	ENERGY GROUP	σ_a (Σ_a)	σ_f ($\nu\Sigma_f$)	σ_{tr} ($1/3\Sigma_{tr}$)	ν	$\sigma_{s_{1\to2}}$	$\sigma_{s_{2\to1}}$	$P_{1\to2}$	$\sigma_{s_{1\to2}}$	$\int \Phi^* \frac{1}{\alpha} \Phi dV$	$\int \frac{1}{\alpha} \Phi dV$
	H-2O	2.033-02	1	2.5101-01	5.2992-02	8.6443+00	2.7518+00	8.8027-08		-8.8267-08	-1.8049-08		
			2	8.6459-01	0.0000	9.7972+00							
	ZONE-2		1	(1.4850-02)	(1.9850-02)	(8.9290-01)		(1.3770-05)		(-1.2790-05)	(-8.2830-08)	(2.9313-04)	(2.5371-04)
			2	(7.0180-01)	(1.3910-03)	(2.9280-01)						(1.3543-06)	(1.3425-06)
ZONE-3	U-235	5.437-04	1	4.3624+00	3.8614+00	1.1524+01	2.4468+00	8.3072-07		-8.2900-07	-2.0967-07		
			2	5.0686+02	2.6049+02	3.2147+02	2.4210+00		3.7041-08				
(NaFe BUFFER)	U-238	4.734-02	1	3.0075-01	4.8695-02	9.7324+00	2.7467+00	3.2397-07		-3.2290-07	-1.0743-07		
			2	1.3801+00	0.0000	1.0516+01			1.9053-08				
	ZONE-3		1	(1.5750-02)	(8.5830-03)	(7.1670-01)		(1.5570-08)		(-1.5520-08)	(-5.1730-09)	(1.3465-04)	(1.2182-08)
			2	(1.7070-01)	(2.1690-01)	(5.5610-01)			(9.1570-10)			(2.2498-06)	(2.2594-06)
ZONE-4	H-1	5.688-02	1	2.3721-03	0.0000	8.2477+00		8.9637-01		8.5770-01	2.1923-01		
			2	2.1112-01	0.0000	3.5958+01			9.5524-05				
(CHARMIS + Al+ SAP)	C-12	4.422-02	1	1.4394-04	0.0000	3.5707+00		1.7600-02		-1.5581-02	-6.1800-03		
			2	2.1507-03	0.0000	8.8619+00			7.0161-05				
	AL	9.243-03	1	8.1520-03	1.9457-08	2.9631+00	2.0000+00	2.2830-03		-2.1692-03	-7.2310-04		
			2	1.4679-01	0.0000	1.5708+00			2.3839-05				
	ZONE-4		1	(8.6420-05)	(3.8980-10)	(1.6279+00)		(1.0700-03)		(-5.0300-04)	(-1.8100-04)	(3.4872-06)	(3.3496-05)
			2	(1.5430-03)	(0.0000)	(1.2480+00)			(3.7090-06)			(2.9248-06)	(2.9254-06)
ZONE-5 (TAPERMAT	H-1	5.726-02	1	3.1600-03	0.0000	8.3412+00		7.2569-01		9.6277-01	3.2092-01		
			2	2.3054-01	0.0000	3.8065+01			6.0050-05				
ZONE BLANKET)	C-12	1.466-02	1	2.4040-04	0.0000	3.4270+00		2.6283-02		-2.3208-02	-7.7360-03		
			2	2.3473-03	0.0000	8.8776+00			4.4104-05				
	O-16	2.003-02	1	2.2047-05	0.0000	3.1678+00		1.5877-02		-1.4518-02	-4.8390-03		
			2	1.2554-04	0.0000	4.8378+00			4.0327-05				
	AL	1.343-02	1	8.9919-03	3.5146-08	2.4819+00	2.0000+00	3.4093-03		-3.2393-03	-1.0798-03		
			2	1.6013-01	0.0000	1.5863+00			1.4980-05				
	U-235	1.049-04	1	1.3660-01	8.8809-00	2.1296+01	2.4369+00	2.1546-06		-2.1487-06	-7.1620-07		
			2	4.1996+02	5.8201+02	6.6576+02	2.4210+00		1.1986-08				

Table 8. Concluded

ZONE	ISOTOPE	NUMBER DENSITY	BROAD GROUP	σ_a (Σ_a)	σ_f ($\nu\Sigma_f$)	σ_{tr} ($1/3\Sigma_{tr}$)	ν	σ_{s_0} 1→2	σ_{s_0} 2→1	P_1 1→2	σ_{s_1} 1→2	$\int\Phi^*\frac{1}{r}\Phi dV$	$\int\frac{1}{r}\Phi dV$
	U-235	4.195E-04	1	1.7199E+00	1.8400E+01	1.5218E+01	2.7558E+00	1.1067E-06		-1.1030E-06	+3.6770E-07		
			2	1.9077E+00	0.0000	1.0849E+01			6.1567E-09				
	ZONE-5		1	(3.2330E-03)	(2.3900E-03)	(1.0500E+00)		(2.7790E-02)		(5.5200E-02)	(1.1730E-02)	(5.5963E-08)	(9.6718E-08)
			2	(5.5650E-02)	(9.0990E-02)	(2.0310E-01)			(5.8940E-06)			(3.2173E-06)	(3.1491E-06)
ZONE-6 (GRAPHITE)	C-12	4.526E-02	1	1.4664E-04	0.0000	5.6418E+00		3.1438E-02		-2.7841E-02	+9.2800E-03		
			2	2.4849E-03	0.0000	6.8881E+00			5.6181E-05				
	ZONE-6		1	(1.4210E-05)	(0.0000)	(1.0735E+00)		(2.6800E-03)		(-2.3740E-03)	(-7.9120E-04)	(5.8781E-08)	(5.5335E-08)
			2	(2.1020E-04)	(0.0000)	(7.9980E-01)			(3.0850E-06)			(3.3611E-06)	(3.3047E-06)
ZONE-7	H-1	2.527E-04	1	6.6566E-03	0.0000	5.3610E+00		1.0132E+00		1.3400E+00	6.4670E-01		
			2	2.4686E-01	0.0000	5.9122E+01			6.3359E-05				
(GRAPHITE + AIR GAP)	C-12	6.127E-02	1	1.2261E-04	0.0000	5.8428E+00		3.6503E-02		-5.2331E-02	+1.0777E-02		
			2	2.5119E-03	0.0000	6.8920E+00			5.1847E-05				
	AL	3.480E-05	1	5.1837E-03	1.1177E-04	2.4574E+00	2.0000E+00	6.7351E-03		-6.0991E-03	+1.0997E-03		
			2	1.7139E-01	0.0000	1.5994E+00			1.0821E-05				
	ZONE-7		1	(2.8300E-05)	(7.7880E-11)	(1.9781E+00)		(1.7790E-03)		(-1.0110E-03)	(-5.3710E-04)	(5.5495E-08)	(6.0432E-08)
			2	(7.6320E-04)	(0.0000)	(1.5525E+00)			(1.3630E-06)			(3.4270E-06)	(3.4304E-06)
ZONE-8 (GRAPHITE)	C-12	4.526E-02	1	1.1124E-04	0.0000	5.9943E+00		3.4586E-02		-5.9990E-02	+1.3163E-02		
			2	2.5630E-03	0.0000	6.8963E+00			2.6937E-05				
	ZONE-8		1	(9.4800E-06)	(0.0000)	(9.7860E-01)		(3.8010E-03)		(-5.3670E-03)	(-1.1223E-03)	(7.7247E-08)	(7.7199E-08)
			2	(2.1450E-04)	(0.0000)	(7.9850E-01)			(2.2970E-06)			(3.5038E-06)	(3.5014E-06)
ZONE-9 (GRAPHITE)	C-12	4.526E-02	1	1.1494E-04	0.0000	6.1682E+00		6.2050E-02		-5.4965E-02	+1.8322E-02		
			2	2.4252E-03	0.0000	6.9013E+00			2.0517E-05				
	ZONE-9		1	(1.0140E-05)	(0.0000)	(9.3600E-01)		(5.2910E-03)		(-4.6860E-03)	(-1.1562E-03)	(1.0228E-07)	(1.0238E-07)
			2	(2.2380E-04)	(0.0000)	(7.9770E-01)			(1.7040E-06)			(5.5952E-06)	(5.5884E-06)
REACTION			1									(5.2182E-08)	(6.2532E-08)
			2									(3.3905E-06)	(5.4086E-06)

the removal and absorption cross-sections of the coupling region. The coupling region was a 45 cm heavy water region. They showed that the sink frequency decreases with increasing removal and absorption cross-sections. They concluded that it was more sensitive to the removal cross-section than the absorption cross-section (2.0 $\Delta\Sigma_s$ - 1.7 Δ sink frequency, 10 $\Delta\Sigma_a$ - 1.7 Δ sink frequency). In the TARK reactor the main coupling region is made of graphite. Because of the sensitivity of the sink frequency upon the macroscopic scattering cross-section, the values for the macroscopic scattering cross-sections Σ_s for graphite, based on a number density of 8.526-02 are presented here. For the TARK reactor, the values range from 4.063-03 in zone 1, 3.465-03 in zone 2, 2.865-03 in zone 3, 2.436-03 in zone 4, 2.185-03 in zone 5, 2.461-03 in zone 6, 2.799-03 in zone 7, 3.108-03 in zone 8, 4.393-03 in zone 9. Because of the sensitivity of the value of the sink frequency not only on Σ_s, but even more on the dimensions of the coupling region, it is important that:

1. We use zone-dependent cross-sections
2. Multi-dimensional geometries for the description of the reactor core.

For the STARK reactor, the main coupling region was made up of the fast assembly region, and the natural uranium buffer zone. For such coupling regions, it is rather difficult to take conclusions out of a parametric study concerning the locations of sink frequencies.

In Figures 10 through 12, we have plotted $\int^{g} \phi(rE)dE$ for each neutron group, and for the different zones which were evaluated from S_4P_3 calculations using XSDRN. The values were zone-averaged. The values given by the different figures were arbitrarily normalized, so as to give

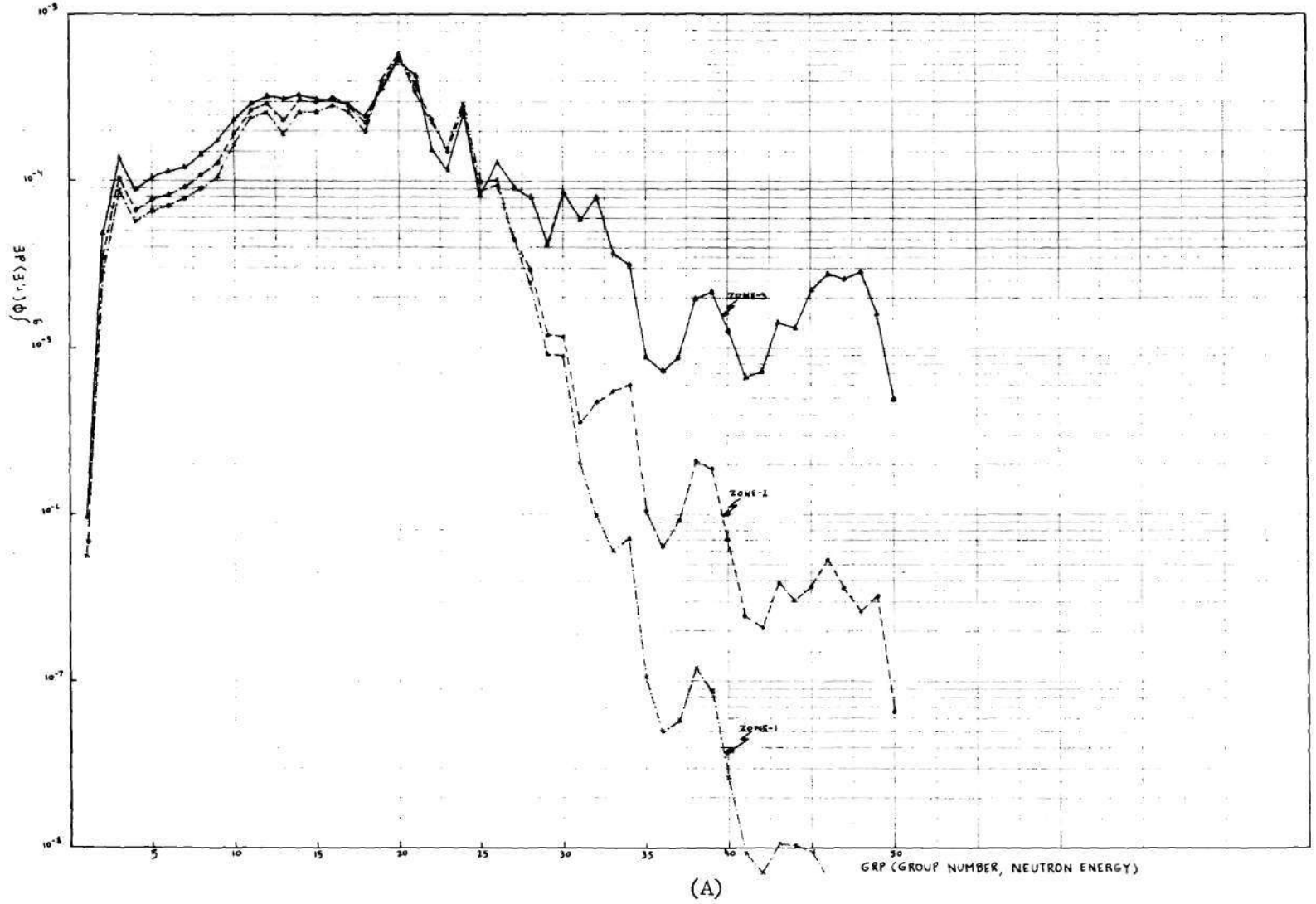

(A)

Figure 11. Neutron Flux vs Group Number for Stark Loading II

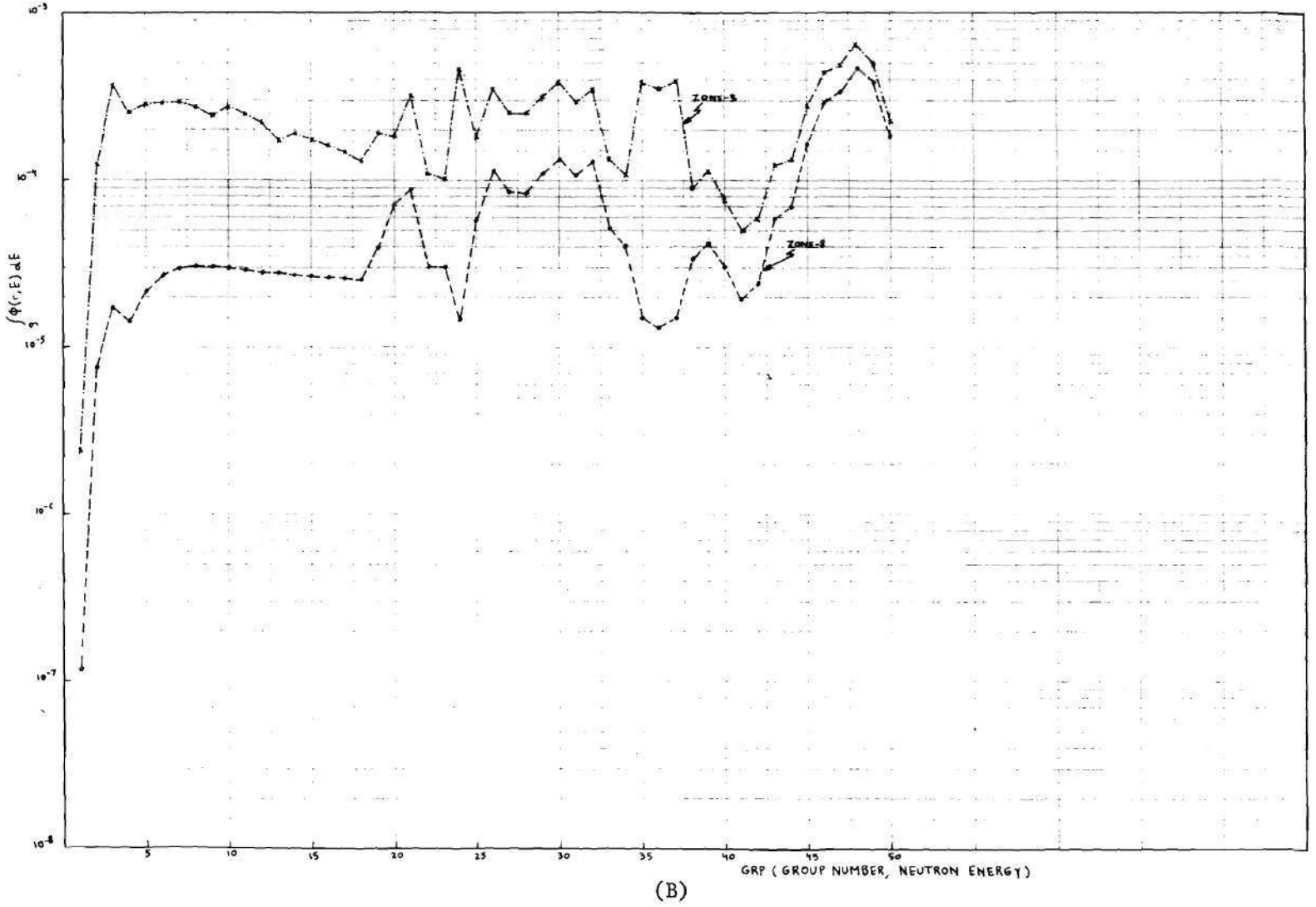

(B)

Figure 12. Concluded

a fission source density of unity, when integrated over the whole reactor. Comparison between the different curves show that not very much difference exists for zone 5 (20 w/o U235 thermal core) for the TARK, STARK loading II, and STARK loading IV reactors. As expected, significant differences exist in the neutron spectrum for the coupling region of the TARK and STARK reactors. In the internal region (zone 1 and zone 2) of the fast reactor STARK, the shape of the spectrum approaches the shape of the spectrum obtained from the S_4P_3 cell calculation on the fast assembly. Comparison of the spectrum of zone 1 for the STARK reactor (Assemblies Type II and Assemblies Type IV) reveals that the approach to the cell spectrum is much faster for loading IV than for loading II. This is due to the higher contribution of the fast core to the fast part of the spectrum in loading IV as compared to loading II.

In Figure 12a, the neutron spectrum of zone 1 of STARK loading IV readily shows that above group 30 (below 100 keV), a significant peak of slow neutrons exists. This overshoot of slow neutrons in the fast core was due to the penetration of fast neutrons, generated in the thermal core (zone 5), into the fast core zones. This peak is more pronounced for loading IV than for loading II, mainly because of the harder spectrum of STARK with loading IV, and therefore relatively more fast neutrons are available.

In Figures 13 through 15, we have plotted EØ(rE) versus energy for the different zones. Comparison of the spectrum readily shows that for zone 1, STARK loading IV has a much harder spectrum than loading II. For instance, at energy group 16 (273.2 to 223.7 keV) the flux is three times larger for loading IV than for loading II, when averaged over zone 1,

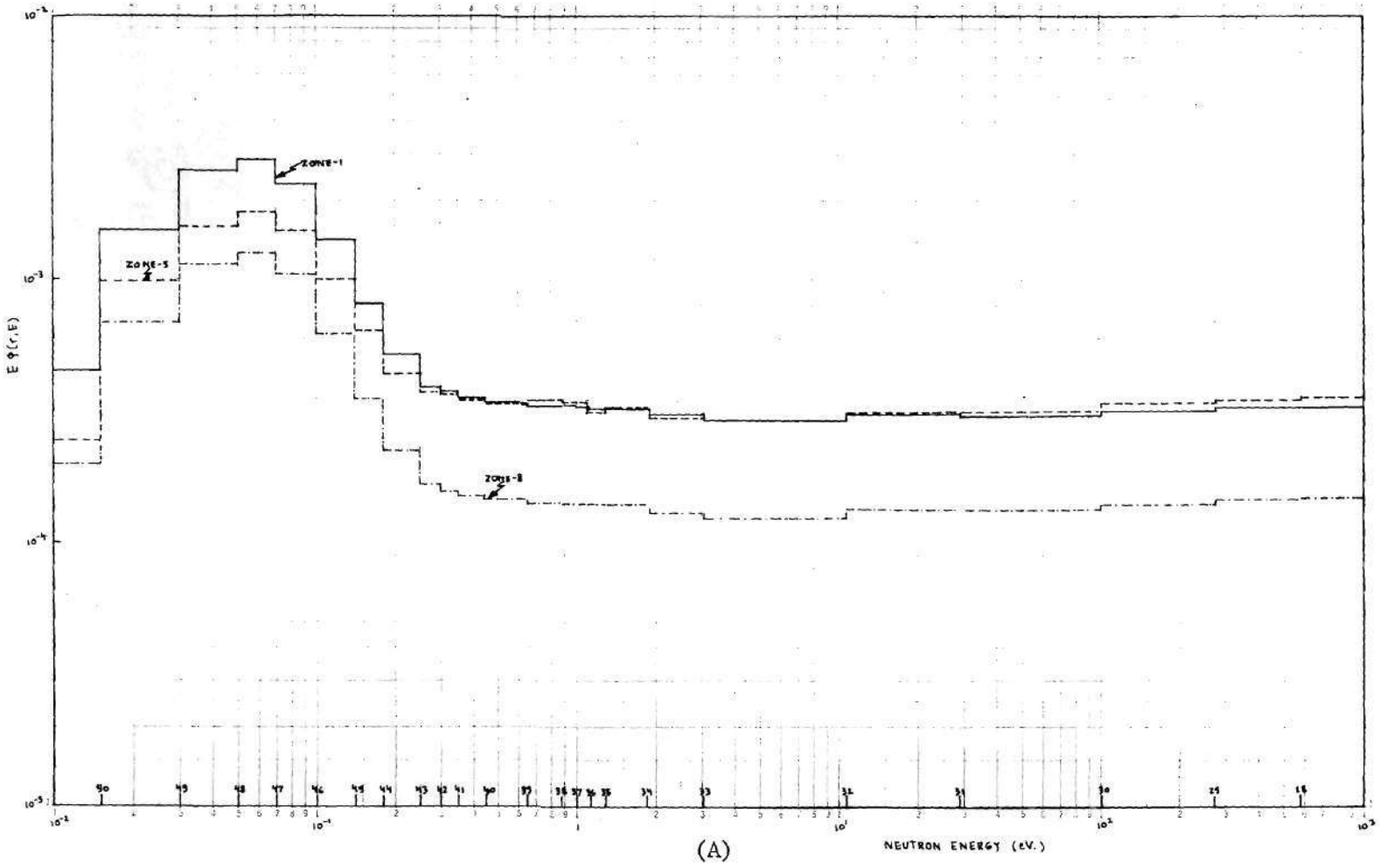

Figure 13. EØ(rE) vs Neutron Energy for TARK

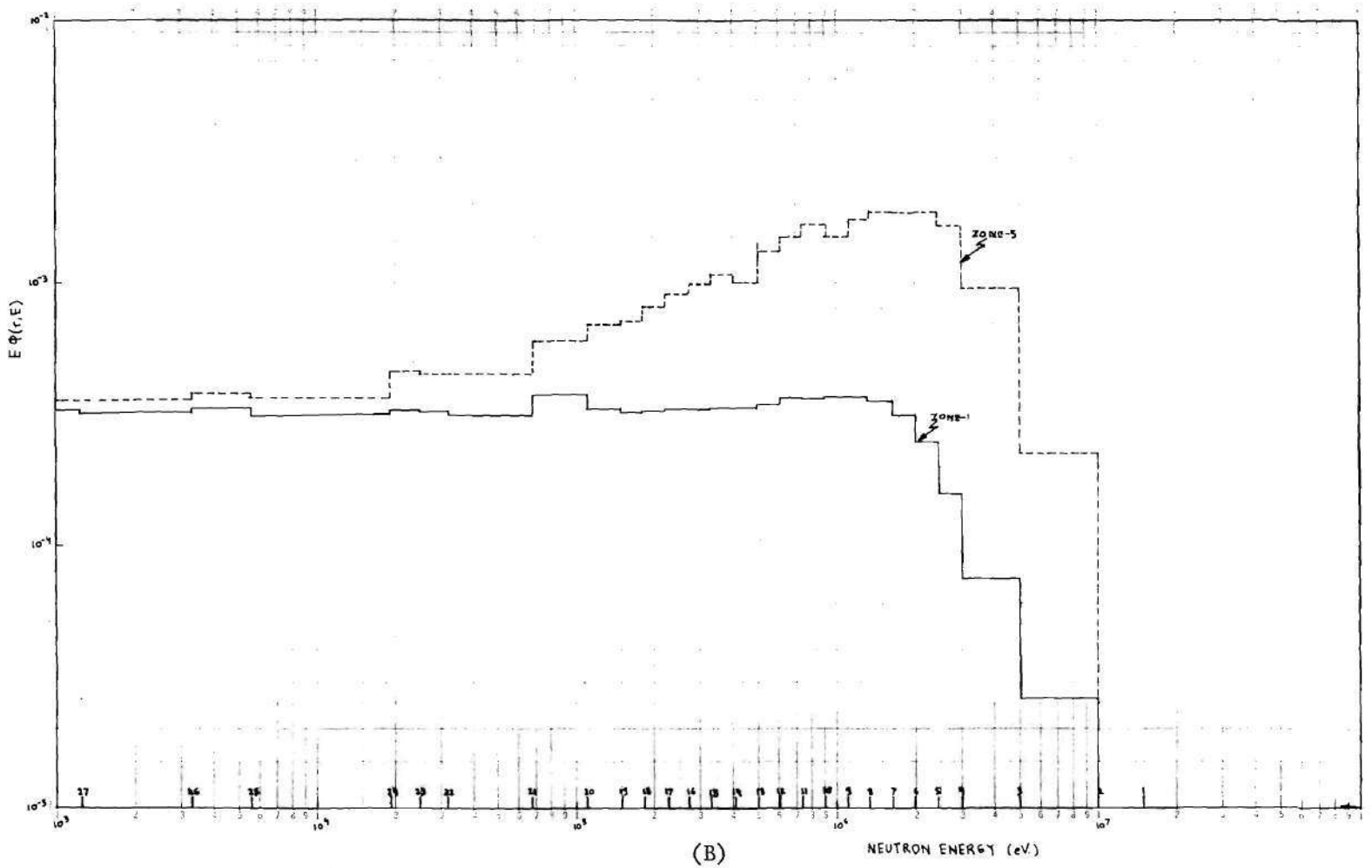

(B)

Figure 13. Concluded

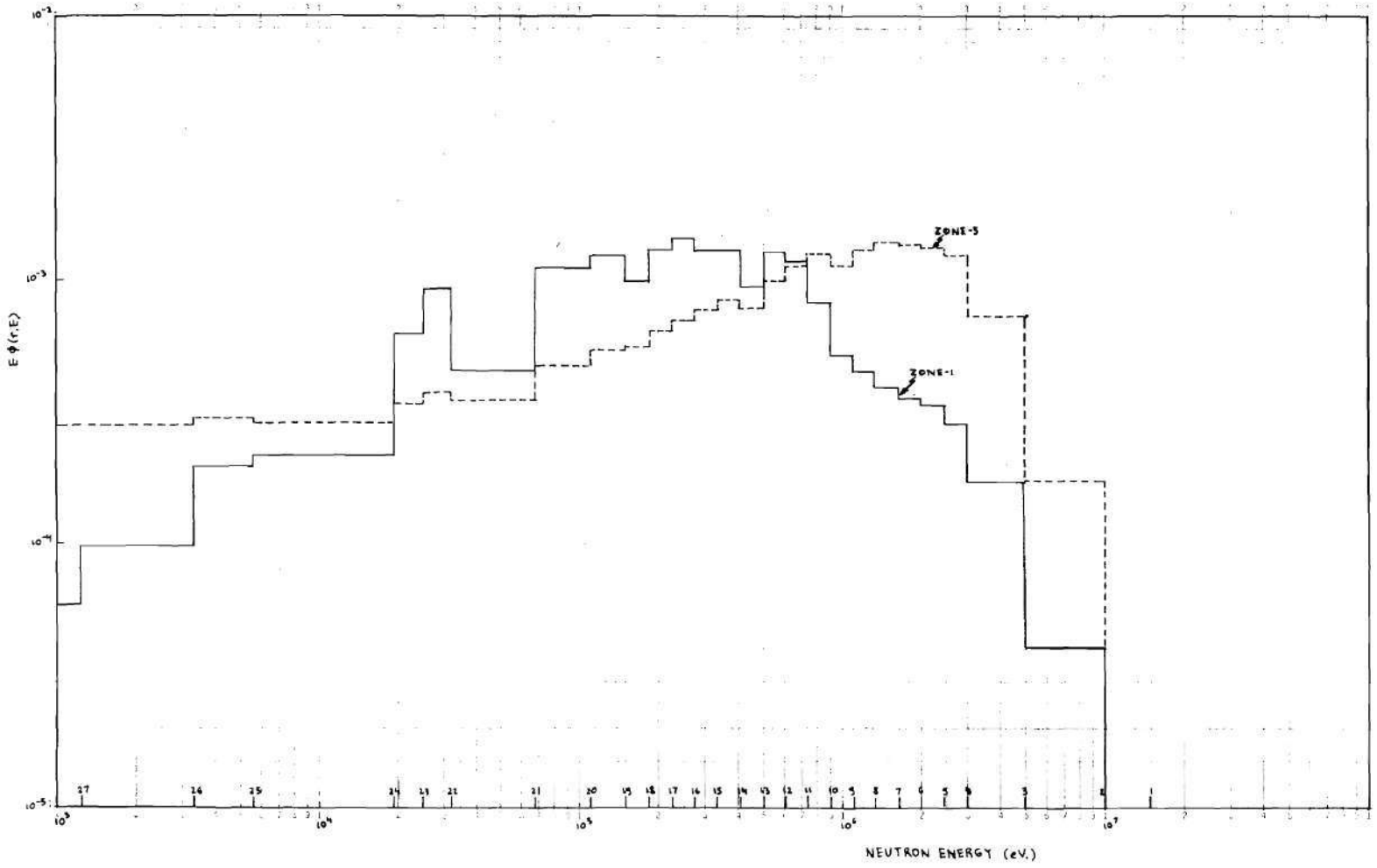

Figure 14. EØ(rE) vs Neutron Energy for STARK Loading II

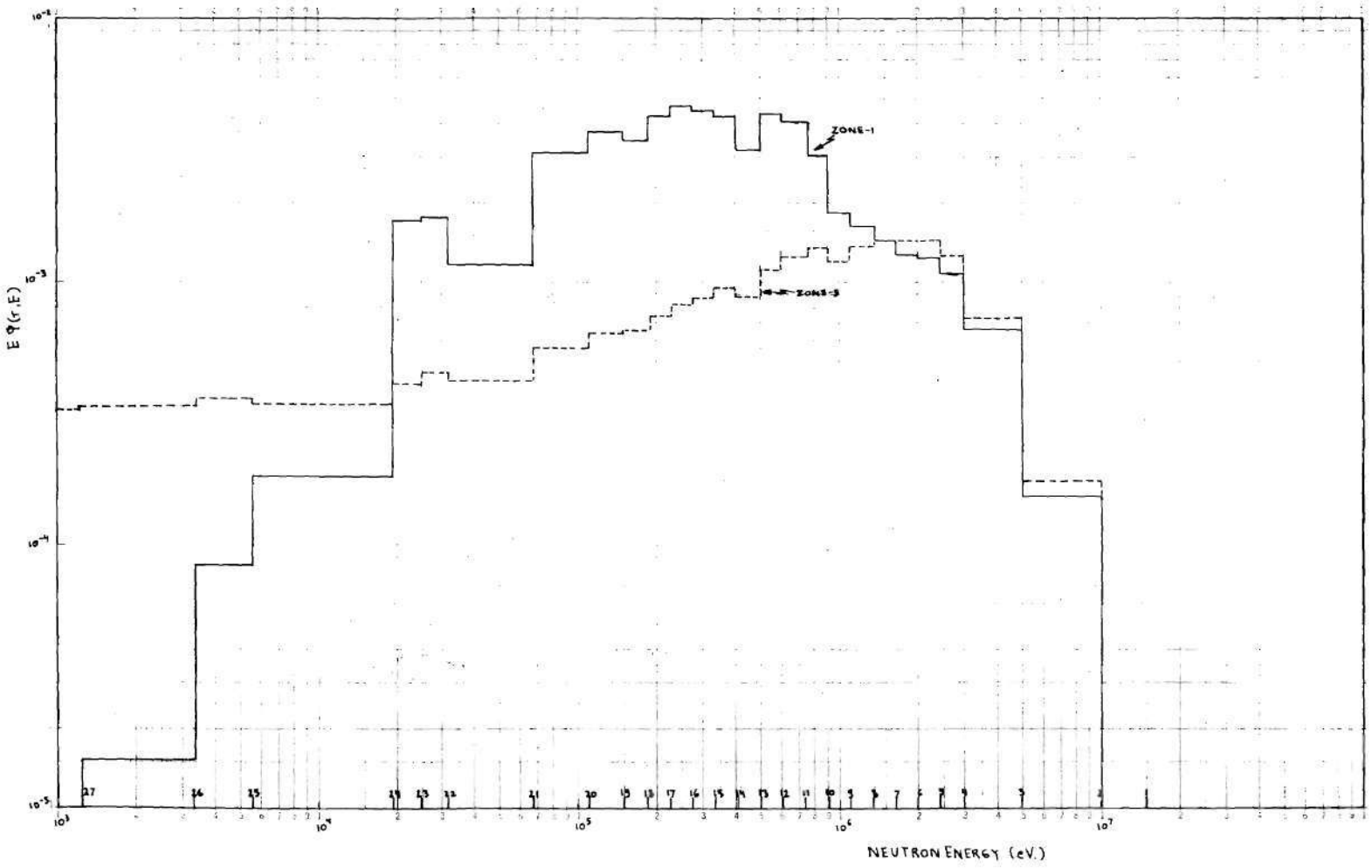

Figure 15. EØ(rE) vs Neutron Energy for STARK Loading IV

while the neutron fluxes in the fast spectrum region, averaged over zone 5, are very similar.

Determination of the Effective Delayed Neutron Fractions

First-order perturbation theory as presented in Citation[111] was used for the calculation of the effective delayed neutron fractions. No mixture-dependent or neutron-type-(prompt, delayed)-dependent fission spectra were used in the PSD calculation. Therefore, effective zone-averaged delayed neutron fractions $(\beta_{dg}^{Mat})_{eff}$ have to be used instead of β_{dg}^{Mat} (as obtained from small sample experiments), since the prompt fission spectrum χ_g is different from the delayed fission spectra $\chi_{g,dg}$. If only one fission spectrum is used, then the delayed fractions have to be adjusted because delayed neutrons are born in lower energy groups. Sloan and Woodruff,[126] Fieg,[127] and Batchelor and Hyder[128] performed extensive experiments in the determination of delayed neutron characteristics.

It can be shown[111] from first-order perturbation theory that the effective delayed neutron fraction of delayed group "dg" for material "Mat," averaged over zone j, is

$$\left(\beta_{dg}^{Mat}\right)_{eff} = \frac{\sum_{i\in j} V_i \sum_g \phi_g^* \chi_{g,dg} \sum_{g'} \nu\Sigma_{f g'}^{Mat} \phi_{g'}}{\sum_{i\in j} V_i \sum_g \phi_g^* \chi_g \sum_{g'} \nu\Sigma_{f g'} \phi_{g'}} \beta_{dg}^{Mat} \qquad (98)$$

where

β_{dg}^{Mat}: actual (as obtained from small sample experiment) delayed neutron fraction of delayed neutron group "dg," for material "Mat"

$\Sigma_{f_{g'}}^{Mat}$: macroscopic fission cross-section of material "Mat," for neutron group g'

$\Sigma_{f_{g'}}$: macroscopic fission cross-section of core material for neutron group g' (therefore, for U^{235}, U^{238}, and Pu^{239}, Pu^{240}, and Pu^{241})

$\chi_{g,dg}$: energy distribution of delayed fission neutrons for delayed neutron fraction group "dg"

χ_g: energy distribution of prompt fission neutrons for energy group "g"

V_i: volume of space element i

$\emptyset_g$: flux at neutron group "g"

$\emptyset_g^*$: adjoint flux at neutron group "g"

The delayed neutron energy spectra $\chi_{g,dg}$ were obtained from a report by Meister.[113] They were derived from experimental work by Batchelor and Hyder,[128] and put into a 26 group classification of the ABN set (see Table 9). Those values of $\chi_{g,dg}$ were subsequently "neutron energy width" adjusted to the fifty group set to which the 123 group ENDF-B/II sets were previously collapsed. The values of $\chi_{g,dg}$ that were used in the calculations of the effective delayed neutron fractions for the power spectral densities, are compiled in Table 10. The values of β_{dg}^{Mat} and λ_{dg}^{Mat} by Keepin[129] were used. The data tabulated for thermal fission in U^{235} and the data for fast fission in U^{238} were employed in the calculations of the effective delayed neutron fractions. Because of the differences of the decay constants λ_{dg}^{Mat} of the delayed neutron fractions for U^{235} and U^{238}, the calculations of the PSD's were always carried out with 12 delayed neutron groups. The forward fluxes obtained in the 50 group transport calculations were used in the calculations of the effective delayed

Table 9. Delayed Neutron Spectrum of the 26-Neutron Group ABN Set (taken from reference 128)

Neutron Group g	Energy Interval	g,dg				
		Delayed Group dg=1	Delayed Group dg=2	Delayed Group dg=3	Delayed Group dg=4	Delayed Group dg=5or6
4	1.4 - 2.5 MeV				0.07	0.04
5	0.8 - 1.4 MeV	0.06	0.14	0.09	0.16	0.14
6	0.4 - 0.8 MeV	0.17	0.37	0.36	0.30	0.36
7	0.2 - 0.4 MeV	0.23	0.28	0.25	0.22	0.26
8	0.1 - 0.2 MeV	0.27	0.11	0.16	0.15	0.14
9	46.5 - 100.0 keV	0.16	0.06	0.09	0.06	0.05
10	21.5 - 46.5 keV	0.08	0.03	0.04	0.03	0.01
11	10.0 - 21.5 keV	0.02	0.01	0.01	0.01	
12	4.65 - 10.0 keV	0.01				
		1.00	1.00	1.00	1.00	1.00

Table 10. Delayed Neutron Spectrum of the 50-Group Cross-Section Sets

Neutron Groups g	Energy Interval	Delayed Group dg=1	Delayed Group dg=2	Delayed Group dg=3	Delayed Group dg=4	Delayed Group dg=5or6
5,6,7	1.353 - 2.466 MeV		0.01		0.08	0.05
8,9,10	0.743 - 1.353 MeV	0.08	0.185	0.135	0.19	0.18
11,12,13	0.408 - 0.743 MeV	0.14	0.31	0.30	0.25	0.30
14,15,16	0.224 - 0.408 MeV	0.21	0.25	0.23	0.20	0.235
17,18,19	0.111 - 0.224 MeV	0.27	0.13	0.17	0.16	0.16
20	67.38 - 111.1 keV	0.13	0.05	0.075	0.055	0.045
21	31.83 - 67.98 keV	0.11	0.04	0.06	0.04	0.025
22,23,24, 25	5.53 - 31.83 keV	0.06	0.025	0.03	0.025	0.005
Total		1.00	1.00	1.00	1.00	1.00

neutron fractions. The version of XSDRN[123] that was used did not have the adjoint transport calculation available due to the lack of proper routines to adjoint the "magic word" packed cross-sections. The adjoint S_4P_3 transport calculation was therefore implemented. Proper care was taken to reverse all arrays which were a function of energy groups. Because the group order was reversed, the "lowest energy" group will be number 1. The packed cross-sections and the transfer routines were also adjointed. While the forward 50 group transport calculations for TARK, STARK loading II, and STARK loading IV were performed with an axial buckling search to $k_{eff} = 1.0$, the adjoint 50 group S_4P_3 transport calculations were performed with the axial critical buckling obtained by the forward search. The k_{eff} obtained by the adjoint calculations were:

TARK : $k_{eff} = 1.0119$

STARK loading II: $k_{eff} = 1.0064$

STARK loading IV: $k_{eff} = 1.0015$

The values of $(\beta_{dg}^{Mat})_{eff}$ were then computed for each zone containing U^{235} or U^{238} using the fifty neutron group values of the cross-sections, forward fluxes and adjoint fluxes. Table 11 tabulates the calculated delayed neutron characteristics for the TARK reactor. Tables 12 and 13 tabulate the zone-dependent and reactor averaged delayed neutron characteristics for the STARK reactor loadings II and IV. It is of interest to note that the values of the total effective fraction for U^{235} and the total effective fraction for U^{238} are not only zone-dependent but also loading-dependent. The $(\beta_{tot}^{U235})_{eff}$ calculated over the reactor spectrum is greater for loading II than for loading IV, while the content of U^{235} in loading II is smaller than in loading IV. The $(\beta_{tot}^{U238})_{eff}$ over the reactor spectrum is smaller

Table 11. Calculated Effective Delayed Neutron Fractions of TARK

	Isotope	Delayed Group	β_i ($\Sigma_i \beta_i$)	β_i^{eff} ($\Sigma \beta_i^{eff}$)	λ_i
Thermal Core Zone-5	^{235}U fast or thermal	1	2.067-04	2.415 -04	1.2400-02
		2	1.375-03	1.561 -03	3.0500-02
		3	1.232-03	1.412 -03	1.1100-01
		4	2.481-03	2.790 -03	3.0100-01
		5	7.235-04	8.150 -04	1.1300+00
		6	2.624-04	2.956 -04	3.0000+00
			(6.281-03)	(7.116 -03)	
	^{238}U fast	1	1.951-04	6.414 -07	1.3200-02
		2	2.038-03	6.509 -06	3.2100-02
		3	2.410-03	7.772 -06	1.3900-01
		4	5.778-03	1.829 -05	3.5800-01
		5	3.350-03	1.062 -05	1.4100+00
		6	1.117-03	3.539 -06	4.0200+00
			(1.489-02)	(4.737 -05)	
	Total U^{235} + U^{238}			(7.1634-03)	

Table 12. Calculated Effective Delayed Neutron Fractions of STARK Loading II

Isotope	Delayed Group	β_i ($\sum_i \beta_i$)	λ_i	β_i^{eff} ($\sum_i \beta_i^{eff}$)				
				Fast Core		ZONE-3 (Nat-U Buffer Zone)	ZONE-5 (Thermal Zone Blanket)	Total Reactor
				ZONE-1	ZONE-2			
U-235 thermal or fast	1	2.067-04	1.2400-02	1.199-04	1.208-04	1.080-04	2.433 -04	2.383 -04
	2	1.375-03	3.0500-02	8.492-04	8.680-04	7.569-04	1.566 -03	1.537 -03
	3	1.232-03	1.1100-01	7.466-04	7.610-04	6.687-04	1.418 -03	1.391 -03
	4	2.481-03	3.0100-01	1.561-03	1.591-03	1.380-03	2.798 -03	2.747 -03
	5	7.235-04	1.1300+00	4.541-04	4.652-04	4.044-04	8.169 -04	8.021 -04
	6	2.624-04	3.0000+00	1.647-04	1.687-04	1.467-04	2.963 -04	2.909 -04
		(6.281-03)		(3.896-03)	(3.975-03)	(3.465-03)	(7.138 -03	(7.005 -03)
U-238 fast	1	1.951-04	1.3200-02	3.139-05	2.986-05	5.658-05	6.870 -07	2.403 -06
	2	2.038-03	3.2100-02	3.490-04	3.368-04	6.224-04	6.940 -06	2.597 -05
	3	2.410-03	1.3900-01	4.050-04	3.897-04	7.258-04	8.298 -06	3.044 -05
	4	5.778-03	3.5800-01	1.009-03	9.708-04	1.784-03	1.950 -05	7.415 -05
	5	3.350-03	1.4100+00	5.831-04	5.641-04	1.038-03	1.132 -05	4.313 -05
	6	1.117-03	4.0200+00	1.944-04	1.880-04	3.464-04	3.772 -06	1.438 -05
		(1.489-02)		(2.571-03)	(2.479-03)	(4.574-03)	(5.051 -05)	(1.905 -04)
Total U-235 + U-238				(6.467-03)	(6.454-03)	(8.039-03)	(7.1885-03)	(7.1955-03)

Table 13. Calculated Effective Delayed Neutron Fractions of STARK Loading IV

Isotope	Delayed Group	β_i ($\sum_i \beta_i$)	λ_i	β_i^{eff} ($\sum_i \beta_i^{eff}$)				
				Fast Core		ZONE-3 (Nat-U Buffer Zone)	ZONE-5 (Thermal Zone Blanket)	Total Reactor
				ZONE-1	ZONE-2			
U-235 thermal and fast	1	2.067-04	1.2400-02	1.167-04	1.164-04	1.012-04	2.367 -04	2.131 -04
	2	1.375-03	3.0500-02	7.839-04	7.950-04	7.077-04	1.525 -03	1.382 -03
	3	1.232-03	1.1100-01	6.993-04	7.063-04	6.255-04	1.381 -03	1.249 -03
	4	2.481-03	3.0100-01	1.435-03	1.456-03	1.293-03	2.730 -03	2.480 -03
	5	7.235-04	1.1300+00	4.168-04	4.237-04	3.786-04	7.965 -04	7.235 -04
	6	2.624-04	3.0000+00	1.512-04	1.537-04	1.373-04	2.888 -04	2.624 -04
		(6.281-03)		(3.603-03)	(3.651-03)	(3.243-03)	(6.958 -03)	(6.311 -03)
U-238 fast	1	1.951-04	1.3200-02	5.491-05	4.992-05	6.055-05	5.966 -07	1.061 -05
	2	2.038-03	3.2100-02	5.792-04	5.350-04	6.645-04	6.034 -06	1.145 -04
	3	2.410-03	1.3900-01	6.820-04	6.274-04	7.752-04	7.210 -06	1.342 -04
	4	5.778-03	3.5800-01	1.667-03	1.540-03	1.908-03	1.698 -05	3.290 -04
	5	3.350-03	1.4100+00	9.623-04	8.910-04	1.111-03	9.845 -06	1.909 -04
	6	1.117-03	4.0200+00	3.208-04	2.970-04	3.703-04	3.282 -06	6.362 -05
		(1.489-02)		(4.266-03)	(3.940-03)	(4.889-03)	(4.395 -05)	(8.428 -04)
Total U-235 + U-238				(7.869-03)	(7.591-03)	(8.132-03)	(7.002 -03)	(7.154 -03)

for loading II than for loading IV. Those zone dependent values were subsequently used in the PSD calculations. In the XSDRN transport calculations only one fission spectrum χ_g can be allowed. The calculations could be improved by using the XSDRNPM[130] module of the AMPX[95] system, which allows mixture dependent fission spectra and takes into account the fission spectra of all fissionable nuclides in a problem.

CHAPTER VI

THEORETICAL STUDY OF THE TWO-DIMENSIONAL MULTI-GROUP COHERENCE FUNCTION OF THE THERMAL ARGONAUT REACTOR, AND COMPARISON WITH EXPERIMENTS

A detailed schematic of the TARK reactor (Thermal Argonaut Reactor Karlsruhe) has been presented earlier in Chapter V. In the two-slab core configuration, the thermal core was subdivided into two fuel regions containing each eight Argonaut assemblies. A total of 266 Argonaut fuel plates were used in the critical experimental configurations of the two-slab TARK reactor which represented a total loading of 5.541 kg U^{235}.

Two-Dimensional Coherence Function of the Coupled-Core TARK Reactor

The fuel (266 fuel plates) of the thermal zone was therefore spread over 16 Argonaut fuel positions, out of a possible 24. The outer radius of the thermal zone in the two dimensional calculations was calculated to be 44.0 cm based on a loading of 5.541 kg U^{235}, while the inner radius was 30.5 cm. The detailed schematic of the two-slab core configuration of TARK, which was used in the two dimensional multi-group calculation of the coherence function is presented in Figure 16. Calculations of the power spectral densities were performed using an r-θ mesh. The axial leakage in the third dimension was taken into account with the usual axial buckling correction factor. For the angular mesh a total of 28 radials (rows) were used. The radials were separated by 15 degrees,

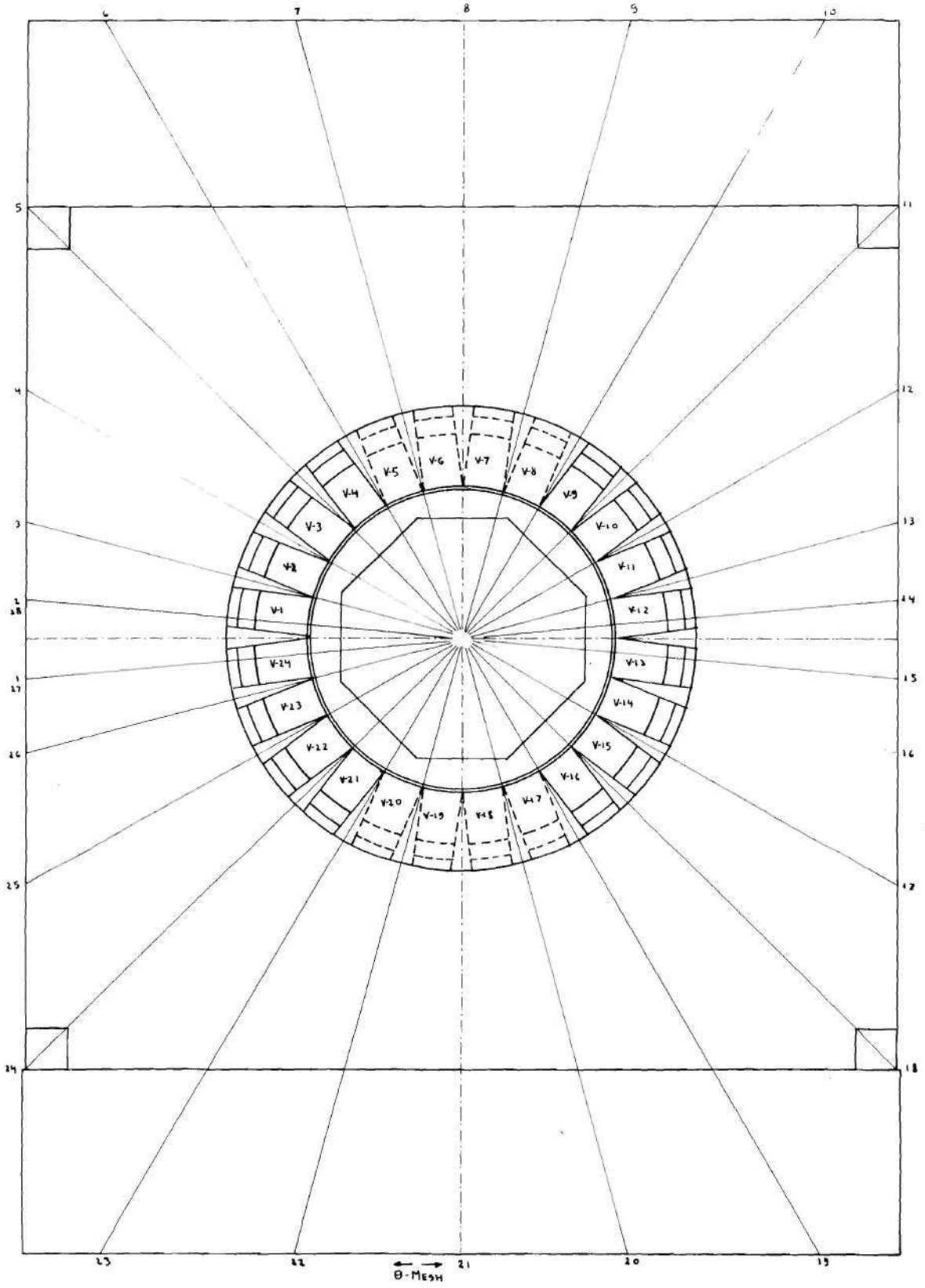

Figure 16. Two-Dimensional r-θ Mesh Layout of the TARK Coupled-Core Configuration

except radials 13-14, 14-15, 15-16, 1-2, 2-3, 26-27, which were separated by 10 degrees.

A periodic boundary condition was used for top and bottom rows. In this case, it specified that the fluxes along radial 2 were equal to the fluxes along radial 28. The total number of columns in the mesh was 48 (JMAX). The axis of the cylindrical geometry lay halfway between J = 1 and J = 2. The column numbers and correspondent r values are listed in Table 14. The boundaries were specified as defined in EXTERMINATOR-II.[82]

$$-\frac{D}{\phi}\frac{\partial \phi}{\partial x} = C \quad \text{with}$$

C = 0 for symmetry boundary

C = 1.0 + 15 (very large) for zero boundary

$$C = \frac{\lambda_{tr}/3}{d_{ext}} = \frac{\lambda_{tr}/3}{0.7104\ \lambda_{tr}} = 0.4692 \text{ for rod boundary}$$

d_{ext} = extrapolation distance rod boundary.

For the region surrounding the external graphite reflector, a rod group constant was specified in place of the macroscopic absorption cross section. An extrapolation distance of $0.7104\ \lambda_{tr}$ was specified at the outer boundary of the external graphite reflector by setting $\Sigma_a = 0.4692$ for all energy groups at the outer boundary.

The macroscopic broad-group cross sections obtained by S_4P_3 transport collapses from ENDF/B sets were used.

Since the material composition of the reactor was assumed to be homogeneous in the axial direction and in order to ensure that the calculations of the power spectral densities (PSD) were performed for a mathematically critical reactor ($k_{eff} = 1$), the axial height of the reactor was adjusted uniformly over the reactor. An axial buckling search using

Table 14. Column Numbers and Corresponding r Values in r-θ Mesh Layout for TARK Reactor

"J" Distribution (Column Number - "r" Value (cm))									
1	- 0.500	2	0.500	3	2.511	4	4.522	5	6.533
6	8.544	7	10.555	8	12.567	9	14.578	10	16.589
11	18.600	12	20.467	13	22.333	14	24.200	15	26.300
16	28.400	17	30.500	18	32.429	19	34.357	20	36.286
21	38.214	22	40.143	23	42.072	24	44.000	25	46.500
26	48.500	27	50.500	28	53.000	29	55.500	30	58.000
31	60.500	32	63.750	33	67.000	34	70.250	35	73.500
36	76.750	37	80.000	38	83.250	39	86.500	40	90.500
41	94.500	42	98.500	43	102.500	44	106.500	45	110.500
46	114.500	47	118.500	48	122.500				

a zone-dependent $D^g B_z^2 \phi^g$ correction factor for transverse leakage was thus performed using a modified version of EXTERMINATOR-II until a value of $k_{eff} = 1$ was satisfied for the steady state case. It must be noted that, for the steady state calculations, the normal version of EXTERMINATOR-II was modified in order to be able to solve the steady state equations as presented in Chapter III. The same mesh grid as for the TDPSD (Two Dimensional Power Spectral Density) code was used. A convergence criterion on the steady state fluxes and on k_{eff} of 1.0E-5 was used for the steady state calculation. An axial buckling $B_z^2 = 2.32048E-03$ was thus obtained, which represents a critical axial height of 65.22 cm. This is to be compared with the physical height of the fuel of 61 cm.

In Figure 17 are presented some of the steady state broad group fluxes. The steady state fluxes were used as weighting factors in the PSD calculations. The steady fluxes were normalized to give a value of 1.0 for the integral $\int_{\text{Reactor}} dV \sum_{g} \nu \Sigma_f^g \phi^g$.

In Figure 16 we observe that two symmetry axes are present. The presence of those was used in the PSD calculations in order to save computer time in the evaluation of the space integrals. The calculated values of the PSD's were obtained for all the space points, and for properly weighted stochastic fission sources in the space volumes that contain fuel. However, due to symmetry, only responses to the stochastic sources of the space volumes of the thermal fuel assemblies V-24 - V-1, V-1, V-2, V-3, and V-4 have to be performed. In order to get the space-, energy-, and frequency-dependent responses to the stochastic sources in the space volumes of the other assemblies, proper shifting of the mesh points was performed around the appropriate symmetry axes. A total of 126 volume

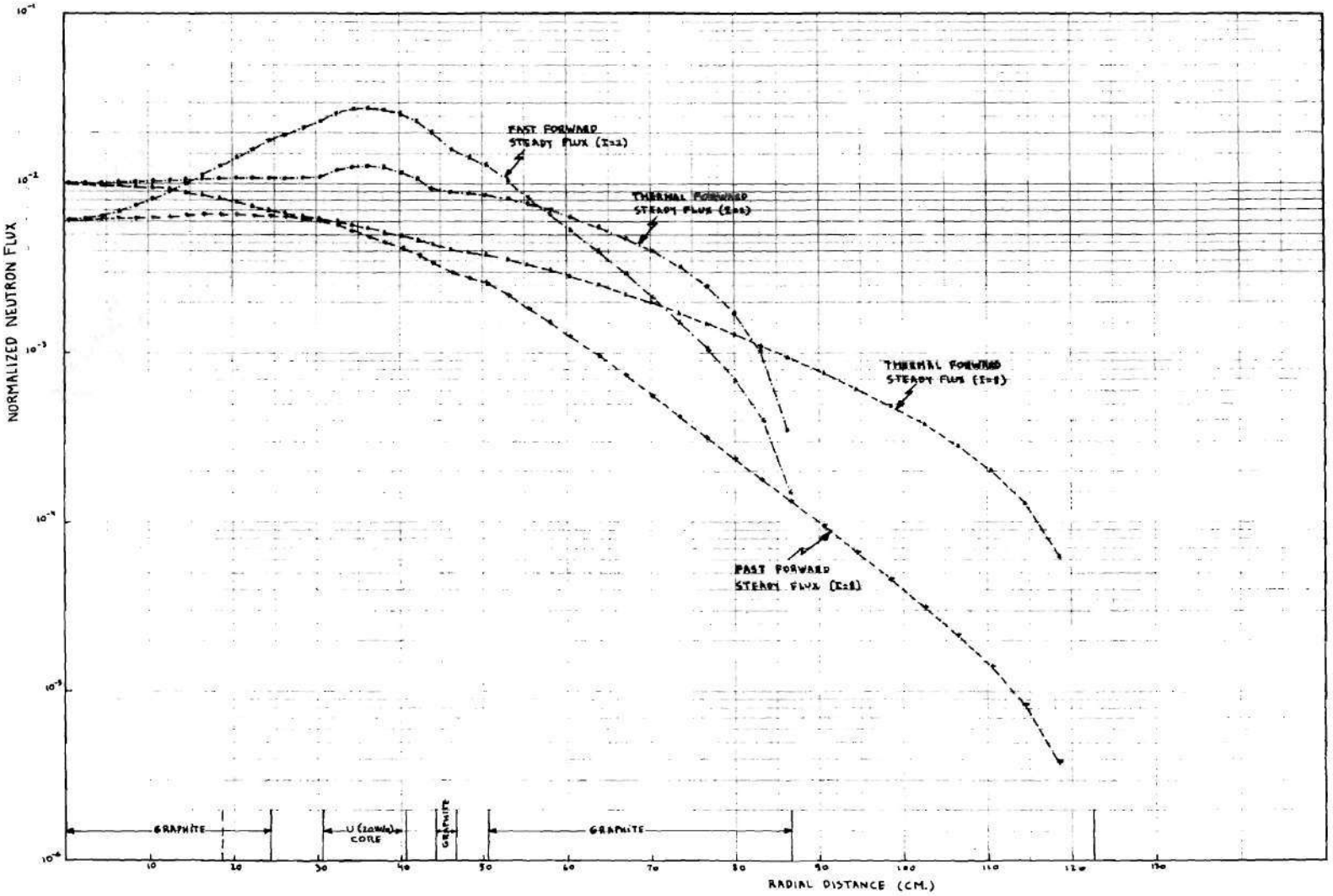

Figure 17. Steady-State Fluxes of the TARK Coupled-Core Configuration

elements with stochastic sources were present in the calculations of the PSD's for TARK. The presence of symmetry axes also enabled us to verify the accuracy of the numerical calculations of the PSD's. Indeed, we have seen in Chapter III that the phase of the CPSD between two detectors located at symmetrical locations inside a reactor with symmetry axes is zero or ± 180 degrees (which means they are real, and the imaginary component is zero). In addition, several space-, energy-, and frequency-dependent responses were calculated for stochastic sources in the space volumes of assembly V-9. They were compared with the values (amplitude and phase) of the responses to V-9 obtained by proper shifting of the mesh points around the appropriate symmetry axes for the responses to the stochastic sources in the space volumes of assembly V-4. The relative error on the amplitude and on the phase of the responses was less than 10^{-4}.

In addition, the CHF between the thermal response of detector 1 located at mesh (2-33) and the thermal response of detector 2 was calculated for external sources in volumes defined, respectively, by the θ-r mesh (02,03-15,16), (02,03-26,27), and (02,03-02,03). The location of detector 2 was swept along radial 2 for all values of J, and radial 14 for all values of J. Those values were stored for eventual later use in analyses of PSD's due to external sources.

By definition the phase of the cross-power spectral density (CPSD) is equal to the phase of the coherence function (CHF); therefore, Phase [CPSD ($\bar{r}_{det1}$,$\bar{r}_{det2}$,ω)] = Phase [CHF($\bar{r}_{det1}$$\bar{r}_{det2}$ω)] for all frequencies. This is easily proven since we have seen (Eq. 5) that the coherence function is defined by

$$CHF(\bar{r}_{det1},\bar{r}_{det2},\omega) = \frac{CPSD(\bar{r}_{det1},\bar{r}_{det2},\omega)}{\sqrt{APSD(\bar{r}_{det1},\omega)\cdot APSD(\bar{r}_{det2},\omega)}} \; ;$$

since the APSD's are real, they do not contribute to the phase.

In all the calculations, the proper values of the effective delayed neutron fractions for U-235 and U-238, as calculated previously in Chapter V, were used.

In Figures 18 and 19 the amplitude and the phase for the two dimensional CHF between the thermal broad group response of detector 1 and the thermal broad group response of detector 2 due to the inherent distributed stochastic fission sources have been plotted. While detector 1 was held at the position defined by mesh (2,33), detector 2 was moved into different positions of the reactor. Note that the amplitudes of the CHF exhibit a "waving" shape for positions of detector 2 inside the coupling region of TARK. They exhibit a minimum for positions starting at and defined by mesh (14,14), (14,15), and higher r's. For positions of detector 2 such as at mesh (14,15) (inside the coupling region) the minimum is shallow and is located at a frequency of approximately 105 cps. For positions of detector 2 in the external graphite reflector (outside the thermal fuel region, at the opposite side of the position of detector 1), we observe that the amplitude of the CHF goes through a sharp minimum at approximately a frequency of 87 cps with subsequent recovery at higher frequencies. The frequency at which this sharp minimum occurs is referred to as a "sink."

For the case of symmetrical locations of detector 1 and detector 2, it can be seen clearly in Figure 18 that the phase is zero below the sink,

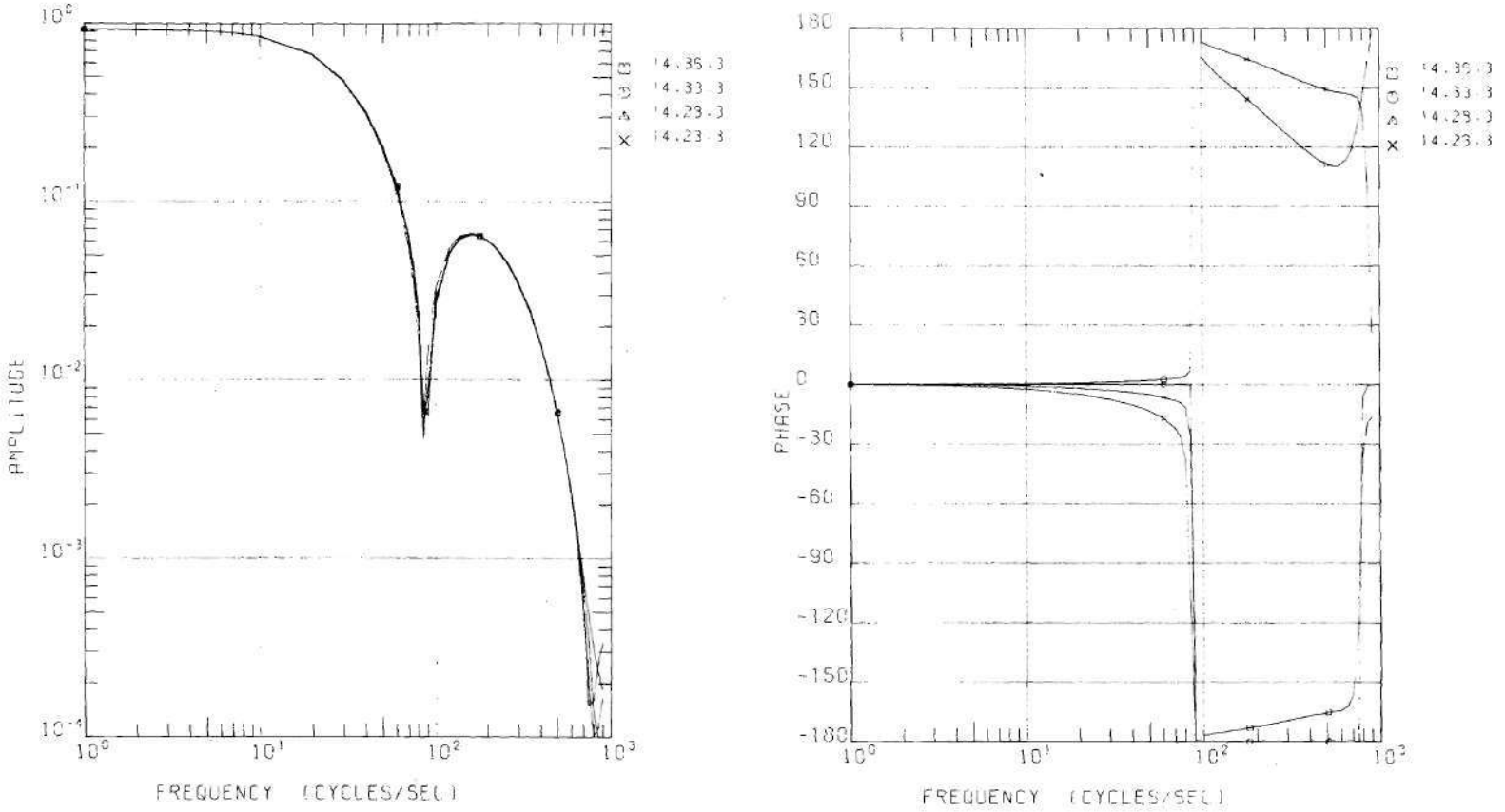

Figure 18. Calculated Amplitude and Phase of the Two-Dimensional Thermal-Thermal CHF, Detector 1 at Mesh (2,33), Detector 2 at Various Locations

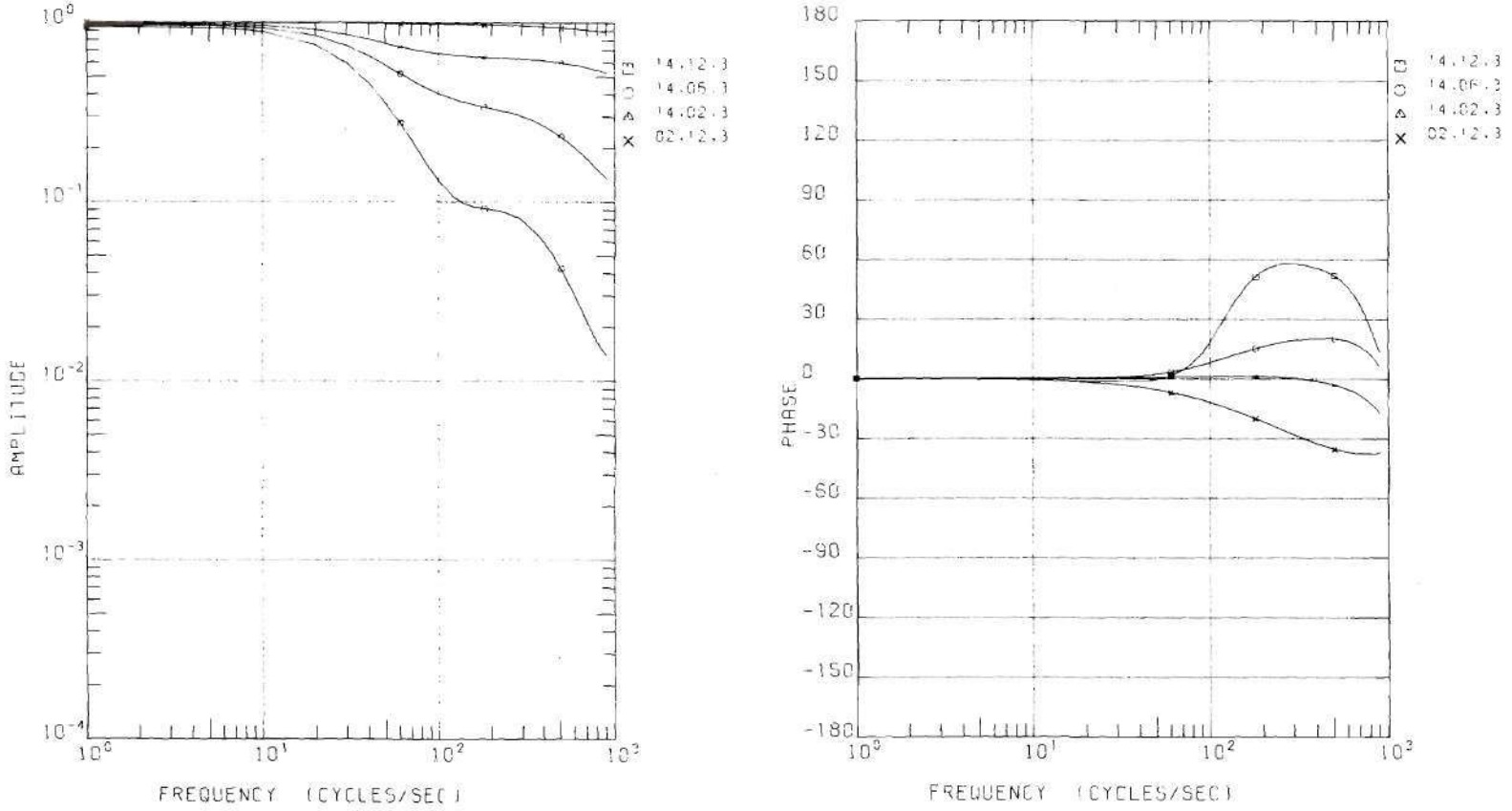

Figure 19. Calculated Amplitude and Phase of the Two-Dimensional Thermal-Thermal CHF, Detector 1 at Mesh (2,33), Detector 2 at Various Locations

and -180 degrees above the sink. We readily observe that the phase makes an abrupt jump from zero to -180 degrees at the sink frequency.

In the case of symmetrical positioned detectors, we observed from the numerical results that the imaginary part of the CHF was very small compared to the real part (theoretically it should be zero). We can therefore say that the passage of the real part of the CHF from positive to negative values indicates the position of the sink, and that it therefore goes through zero. The amplitude of the CHF is therefore zero at the sink frequency.

In the case of asymmetrical positions of the detectors, the real part of the CHF did not necessarily go through zero at the sink. Because in most cases in the TARK reactor the imaginary part of the CHF was small compared to the real part at the sink frequency, the minimum of the amplitude of the CHF at the sink was only a few cycles different from the frequency at which the real part of the CHF went through zero. The amplitude of the CHF at the sink in that case did not go to zero.

The frequency at which the sink or first sharp minimum in the amplitude of the coherence function occurs is quite insensitive to the spacing between the detectors. This was expected since the occurrence of a sink is due to certain neutron wave characteristics inside the reactor at particular frequencies and is therefore a reactor characteristic. This behavior in the CHF indicates that the neutron fluctuations at certain detector positions become uncorrelated at the sink frequency. We could therefore say that the coupling goes to a minimum at the sink, and subsequently recovers above the sink frequency.

The sink frequency corresponds to a 90 degree phase shift in the

neutronic coupling between fuel regions. This 90 degree phase shift causes an interference effect of neutronic waves from one fuel region to another. It has been shown by Nagy and Danofsky[17] that the frequency at which the *sink occurs is* dependent on the spacing between fuel regions, and the characteristics of the materials of the coupling region. For the same composition of the coupling region, the sink frequency decreases with increasing spacing. Seifritz and Albrecht[20-23] have shown that this 90 degree phase shift is the result of both the phase shift of the response of the coupled core to a perturbation and the phase shift due to time delay distribution function. We have seen that the introduction of a retardation time for the interaction between fuel assemblies comes from the transport approximation (P_1 and higher order). It is a well-known property that an instantaneous source immediately produces a disturbance at all points in space for the diffusion approximation. For the diffusion approximation, the propagation velocity of the disturbance is infinite. Using P_1 and higher order, we have previously seen that this approximation shows the phenomenon of retardation, which gives a wave-like behavior of the flux. The higher the frequency, the more this phenomenon of retardation will play a role in the determination of PSD's.

Since the space-dependent effects are small at low frequencies, we know that the APSD's and CPSD's contain similar information, but that at higher frequencies the presence of space-dependency causes the shape of the APSD's and CPSD's to differ. Albrecht and Seifritz[20-23] have pointed out the value of using the coherence function and showed that it is indicative of space-dependency. For pure fundamental mode behavior, the amplitude of the CHF is unity. Any departure from unity indicates

spatial dependence of the neutron waves caused by the stochastic sources, and it will therefore give an idea of the deviation from fundamental mode behavior, so that higher order effects can be studied.

In Figures 20 and 21 we have plotted the amplitude and phase of the CHF between the thermal response of detector 1 located at mesh (2,25) and the thermal response of detector 2, as a function of frequency, due to the presence of the inherent distributed stochastic fission sources. Comparison with the curves of Figures 18 and 19, which were calculated for detector 1 positioned at mesh (2,33), shows that the sink frequency is present at the same frequency and the shape of the different curves is similar.

From the results of the two dimensional calculations of the CHF for TARK, we observe that the very small deviation of the phase from zero degrees below the sink and from -180 degrees above the sink for symmetrically located detectors emphasizes the merit of the method used in this study over other approaches as the modal approach, the coupled core theory approach, etc. Ebert[131] has pointed out that, in his multimode, one dimensional approach, the results for the phase angles were very poor and that the phase angles for the CHF were difficult to predict with modal approximations, even for one dimensional and simplified approximations to the physical configuration of the TARK reactor. Ebert's calculations were performed for two identical parallel fuel slabs, separated by a graphite coupling region. However, the advantage of the modal approach lies in the fact that certain neutronic wave characteristics for simplified geometries could be more easily explained quantitatively than the difference approach taken in this dissertation.

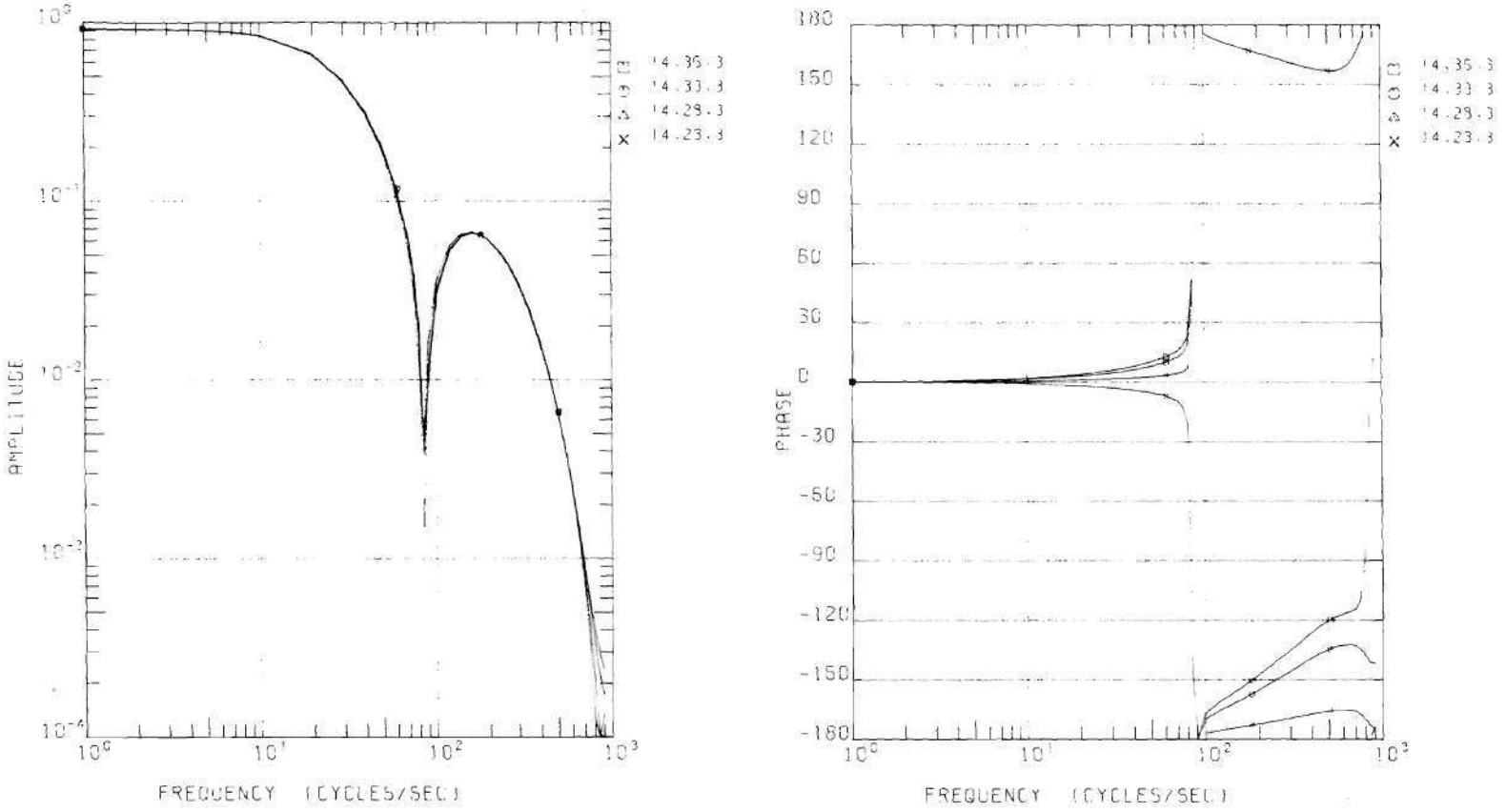

Figure 20. Calculated Amplitude and Phase of the Two-Dimensional Thermal-Thermal CHF, Detector 1 at Mesh (2,25), Detector 2 at Various Locations

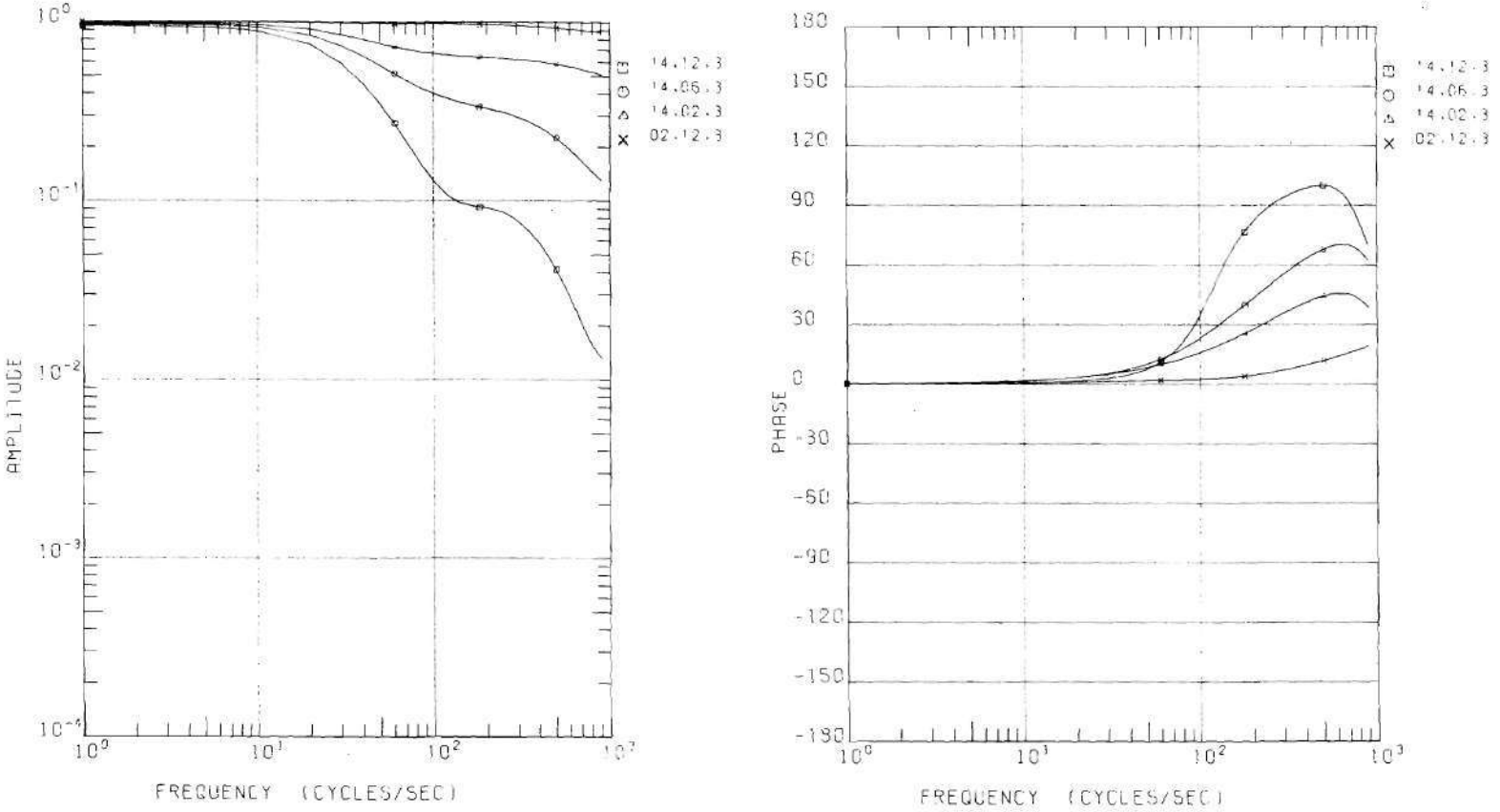

Figure 21. Calculated Amplitude and Phase of the Two-Dimensional Thermal-Thermal CHF, Detector 1 at Mesh (2,25), Detector 2 at Various Locations

The amplitude of the CHF between the fast response of detector 1 and the fast response of detector 2 also exhibited a sink at 87 cps. This was expected, since fast neutrons are born in the fissioning process, caused mainly by thermal neutrons, in contrast to fast reactor spectra.

Comparison with Experimentally Determined Coherence Functions for TARK and Discussion

An experimental determination of the coherence function, due to the stochastic fission sources, for the Thermal Argonaut Reactor Karlsruhe (TARK) was performed by Albrecht and Seifritz.[20-23] The characteristics of this reactor have been described earlier. A very brief description of the principal characteristics and results of the cylindrical slab configuration of the TARK experiment are:

1. internal diameter of coupling region 24 inches (61 cm);
2. two cylindrical slab core loading: 266 fuel plates (5.541 kg U-235) distributed over 16 Argonaut fuel assemblies;
3. two He^3 filled neutron detectors were positioned on each side of the reactor, inside the external graphite reflector, detectors (operated in current mode) were positioned inside the graphite reflector by removing graphite stringers;
4. the experimentally observed first sink was at 730 ± 50 rad/sec or 116 ± 8 cps;
5. the accuracy of the coherence function measurement and two possible detector arrangements with their respective accuracies were discussed by Seifritz and Albrecht[20-23]:

a) Two-detector experiment: One detector was located in each zone. The CPSD was obtained by cross correlating between the two detectors. The correlated part of the APSD was obtained by subtracting the white noise background. The typical total experimental error was 21.1%.

b) Four-detector experiment: One detector pair was located in each zone. The CPSD was determined by cross correlating the output of each detector pair, and the correlated part of the APSD by cross correlating between the output of each detector of a detector pair. The typical total experimental error was 9%.

In Figure 22 we have plotted: 1) the values of the amplitude of the coherence function (CHF) for TARK as determined experimentally by Seifritz and Albrecht[23] and 2) the values determined by two dimensional calculations using our TDPSD code with broad group cross sections based on ENDF/B-II sets. The agreement was found to be satisfactory within the experimental error band for frequencies below the sink frequency, while the agreement was poor above the sink frequency. It is seen that above the sink frequency, the two dimensional calculated amplitude was approximately an order of magnitude higher than the experimental values above the sink. It is not known if this is due to an experimental bias at the relatively high frequencies (above the sink). Another possible explanation of this discrepancy is that the assumption of a frequency-independent power spectrum for the stochastic fission sources is incorrect. As we mentioned before, all the calculations were performed based on this assumption. While the experimentally determined sink was at 116 ± 8 cps, the two dimensional calculated frequency of the first sink was at 87 cps for the TARK reactor, based on broad group ENDF/B-II data.

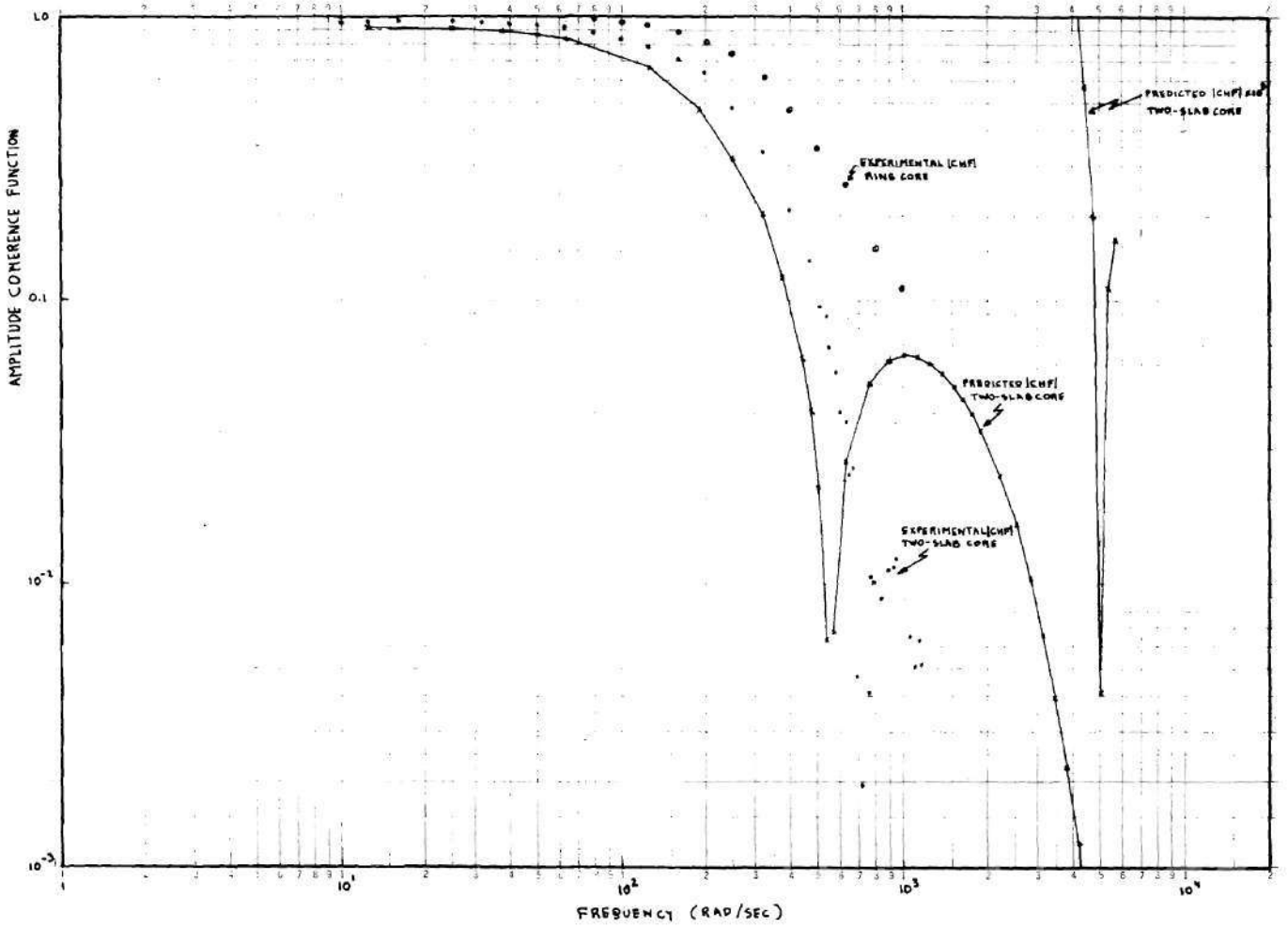

Figure 22. Comparison of the Calculated and Experimental Amplitude of the Thermal-Thermal CHF of the TARK Coupled-Core Configuration

The effect of limiting the anisotropy to a P_1 approximation is not known.

Before we continue with the comparison of the calculated results with the experimental values for TARK, let us point out that an experiment on the UTR-10 reactor (University Training Reactor-10 of Iowa State University) also demonstrated a sink. The UTR-10 reactor is a commercial version of the coupled-core Argonaut reactor and is very similar to the TARK reactor. The core of the UTR-10 consisted of two 5 by 20 by 24 inch fuel regions, each containing six fuel assemblies. The two regions were separated by approximately 18 inches (45 cm) of graphite. This 18 inch core separation of the UTR-10 falls between the value of the core separation distances of TARK of 24 inches (61 cm) and UFTR (University of Florida Training Reactor) of 12 inches (30.5 cm). For a detector configuration shown in Figure 23, Hendrickson and Murphy[19] observed a sink at 115 ± 5 cps for the CPSD between detectors 3 and 4 (see Figure 24 taken from reference 19). In the UTR-10 experiment, two BF_3 neutron detectors (one inch in diameter by four inches active length) were positioned at the midplane of the reactor.

Comparison between the experimentally determined first sink frequency for two similar reactors: 115 ± 5 cps for the UTR-10 with a spacing of 18 inches, and 116 ± 8 cps for the TARK reactor with a spacing of 24 inches, apparently could indicate a possible discrepancy between the experiments.

We know that, for identical or similar reactors, the sink frequency increases with decreasing spacing of the coupling region. We therefore can say that we would have expected the first sink for TARK at a lower frequency than for the UTR-10 reactor.

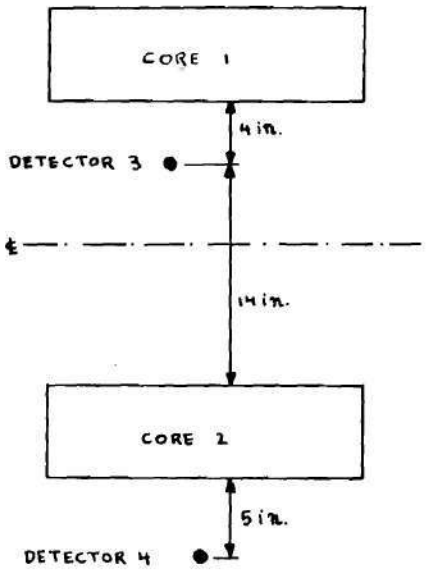

Figure 23. Detector Locations 3 and 4 in the UTR-10 Reactor[19]

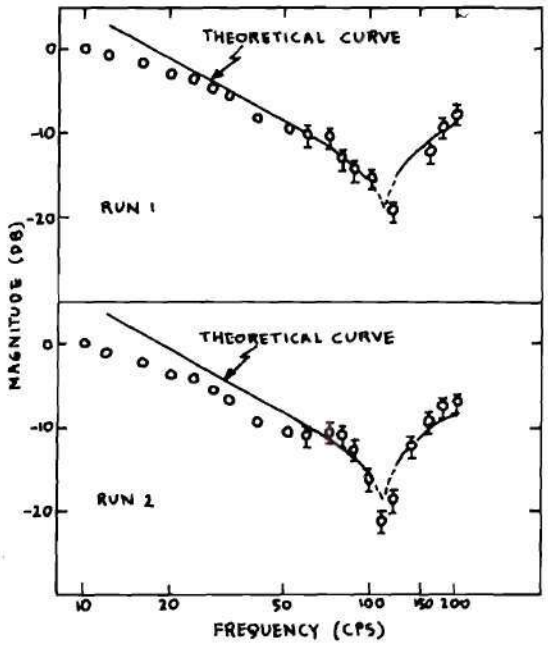

Figure 24. Cross-Power Spectral Density Function $\phi_{34}(\omega)$ between Detectors 3 and 4 for Two Experimental Runs[19]

Let us note that the experimental determination for the UTR-10 reactor was made between positions located at detector 3 inside the coupling region and close to the fuel region and detector 4 outside the fuel region in the external graphite reflector. We have seen that, for the two dimensional, multi-group calculations of the CHF for TARK, the minimum in the amplitude of the CHF was rather shallow when one detector was inside the coupling region, and that the frequency at which this shallow minimum occurred was at a somewhat higher frequency than the frequency at which a sharp minimum occurred when the two detectors were in the external reflector or fuel regions. The calculations of the CHF for TARK showed a sharp minimum at 87 cps for detector locations in the fuel regions or outside reflector, while a shallow minimum occurred at approximately 105 cps when one detector was inside the coupling region close to the fuel region. This would indicate that the sink frequency of the PSD between detectors located in the external reflector for UTR-10 would be lower than the experimental value of 115 ± 5 cps. The discrepancy between the UTR-10 and the TARK experiments would therefore be even greater.

We have seen that the calculational method used by Albrecht and Seifritz[23] was based on a two-node approach. When there is no flux tilt (therefore when the magnitude of the stochastic fission sources is identical in each fuel slab) and the stochastic sources are uncorrelated, they have shown that the coherence function can be approximated by

$$\mathrm{CHF}(\omega) = \frac{2\ \mathrm{Re}\ K}{1 + |K|^2}$$

where $K(\omega)$ is an arbitrary coupling function between the cores. The coupling function can therefore be implied from the coherence function. It should be noted, however, that this method can predict only the shape of the CHF, not the exact location of sink frequencies. While the experimentally determined first sink was at 730 ± 50 rad/sec or 116 ± 8 cps for TARK, a one dimensional calculated value of the sink frequency performed by Albrecht and Danofsky,[31] based on a theoretical model developed by Danofsky,[28] gave a calculated value of the sink at 550 rad/sec (87.5 cps). This method was based on a modal expansion approach.

Ebert, Clement, and Stacey[32-33] also used a modal approach for the one dimensional calculation of the CHF or TARK. We have seen that, in Ebert's work, the Argonaut cylindrical fuel shell was "squeezed" into two separate infinite slabs of 15 cm thickness, separated by a graphite coupling region. The distance between the slabs was varied to an equivalent thickness of the coupling region in that way, so that the value of his calculated sink frequency was the same as the measured sink of the TARK reactor coherence function experiment. The coupling region thickness thus obtained was 45 cm. The cross section set used in Ebert's work for TARK was obtained from the work of Danofsky,[28] which was performed for the 18 inch UTR-10 reactor. Ebert also pointed out that, in his multi-modal, one dimensional approach, the results for the phase angles of the CHF were very poor. The reason for this is not understood. As stated by Ebert,[131] it may have to do with the fact that the phase angles are difficult to predict with modal approximationa. If there were any appreciable error in the construction of the eigenfunctions of the modal expansions, the error would magnify itself into the phase calcula-

tions, since they are the results from differences of terms. This was certainly a deficiency of Ebert's one dimensional modal approach.

Although the application of modal expansions to one dimensional geometries could be useful to very simple geometries, their extension to actual configurations of cores is practically impossible, since too many modes would be required in two dimensional modal expansions. The situation would be even worse in complicated geometries.

Let us now perform two dimensional, multi-group calculations of the coherence function for TARK, based on the cross section set used by Ebert. This cross section set is tabulated in Table 15 and is taken from reference 28. The detailed schematic of the "two cylindrical slabs" configuration of TARK, which was used in the two dimensional, two-broad energy group calculations of the CHF is similar to the one used previously (see Figure 16). The calculations were performed using an r-θ mesh. For the angular mesh a total of 25 radials was used, each separated by 15 degrees, except radials 1-2, 12-13, 24-25, which were separated by 30 degrees. The total number of columns used in the mesh was 31. The mesh increments in the "r" direction were:

Mesh 01 to 08: 4.689 cm

Mesh 08 to 11: 5.0 cm

Mesh 11 to 31: 5.0 cm

An axial buckling search using a zone dependent $DB_z^2\phi$ correction factor for transverse leakage was performed using a modified version of EXTERMINATOR-II,[82] until a value of $k_{eff} = 1$ was obtained. The steady state fluxes thus obtained were used in the PSD calculations. An axial buckling of $B_z^2 = 1.42023E-03$ was obtained, which represents a critical

Table 15. UTR-10 Cross Section Set from Reference 28

Nuclear Constant	Definition	Fast Broad Group		Thermal Broad Group	
		Graphite Region	Fuel Region	Graphite Region	Fuel Region
D	Diffusion coefficient (cm)	1.016	1.23	0.84	0.189
$\Sigma_s^{1\rightarrow 2}$	Scattering cross section fast-to-thermal (cm^{-1})	0.00276	0.0267		
Σ_a	Absorption cross section (cm^{-1})			0.00024	0.0908
$\nu \Sigma_f$	ν x fission cross section (cm^{-1})			0.0	0.122
v	Group velocity (cm^2/sec)	4.36×10^8	4.36×10^8	2.2×10^5	2.2×10^5

axial height of 83.36 cm. A convergence criterion on the point fluxes for the two-dimensional CHF calculations of 1.0E-4 was used. Using the same approach as has been discussed earlier, the calculation of the CHF for TARK between the thermal responses of two neutron detectors was performed using the cross-section set of the UTR-10 reactor (same set that was used in the one-dimensional study of the 24in. TARK reactor performed by Ebert[131]). A total of 42 volume elements with stochastic fission sources were present in the calculations. In Figures 25 and 26 we have plotted some of the results of those calculations. The amplitude and phase of the CHF between the thermal response of detector 1 located at mesh(2, 23)(θ = 0, r = 107.8 cm), and the thermal response of detector 2 at several locations at the opposite side of the core are plotted (e.g., mesh(12,17) represents a detector position on radial 180° and r = 77.8 cm). For positions of detector 2 in the external graphite reflector (outside the thermal fuel regions, at the opposite side of the position of detector 1), we observe that the amplitude of the CHF goes through a sharp minimum at approximately 70 cps. It has to be noted again that the sink frequency is rather independent of the location of the detectors, as long as they are located in the fuel regions or outside them, in the external graphite reflector. For positions of detector 2 inside the coupling region close to the fuel region, we observe that the minimum is shallow and is located at a higher frequency, approximately at 80 cps. For positions of detector 2 inside the fuel region, at a radial of 180°, we observe that the minimum is shallow compared to the amplitude of the CHF for positions of detector 2 in the external graphite reflector; although it is a much more pronounced minimum than for detector 2 positions inside the coupling

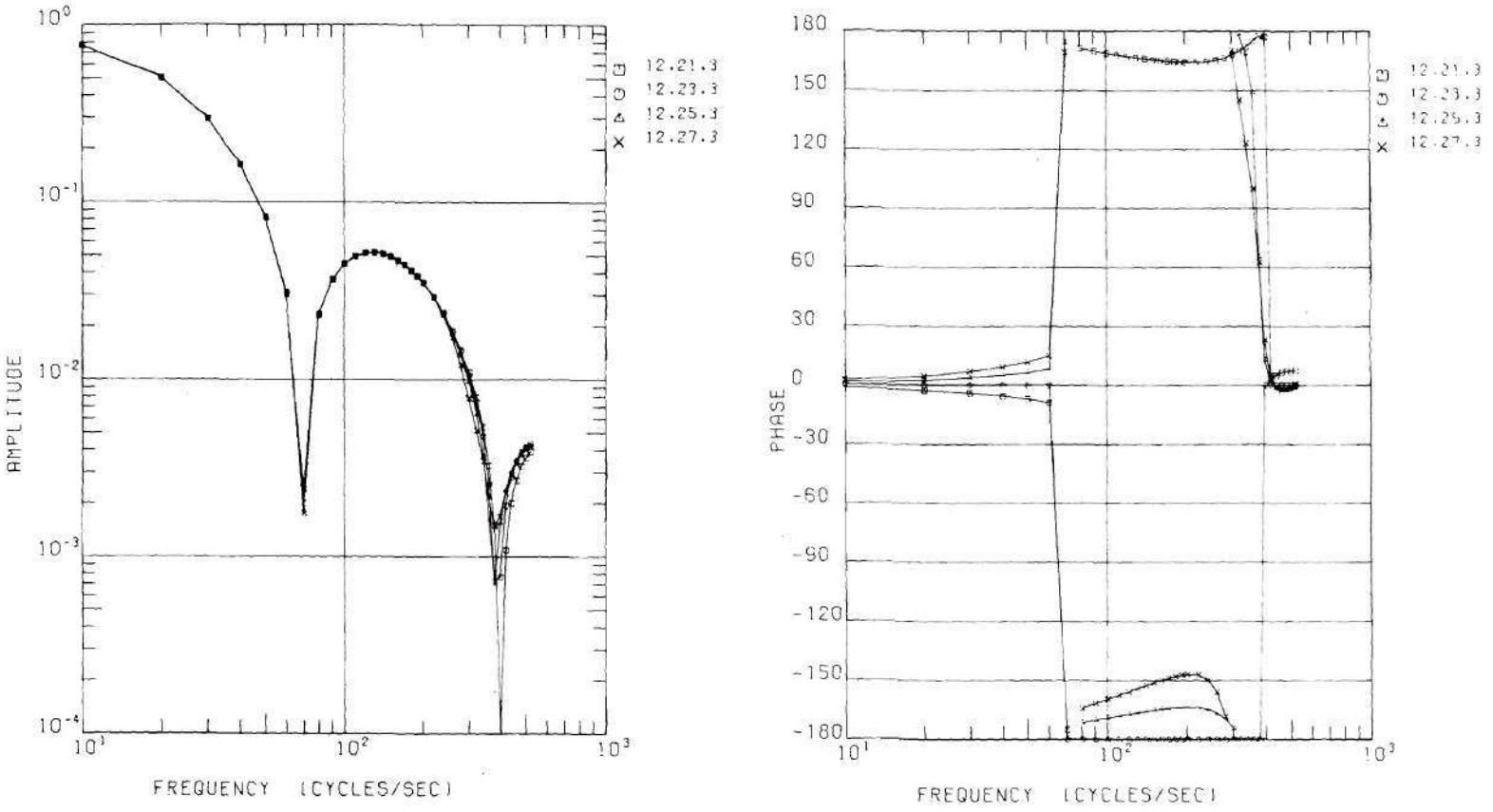

Figure 25. Calculated Amplitude and Phase of the Two-Dimensional Thermal-Thermal CHF for the TARK Coupled-Core Configuration, Detector 1 at Mesh (2,23), Detector 2 at Various Locations

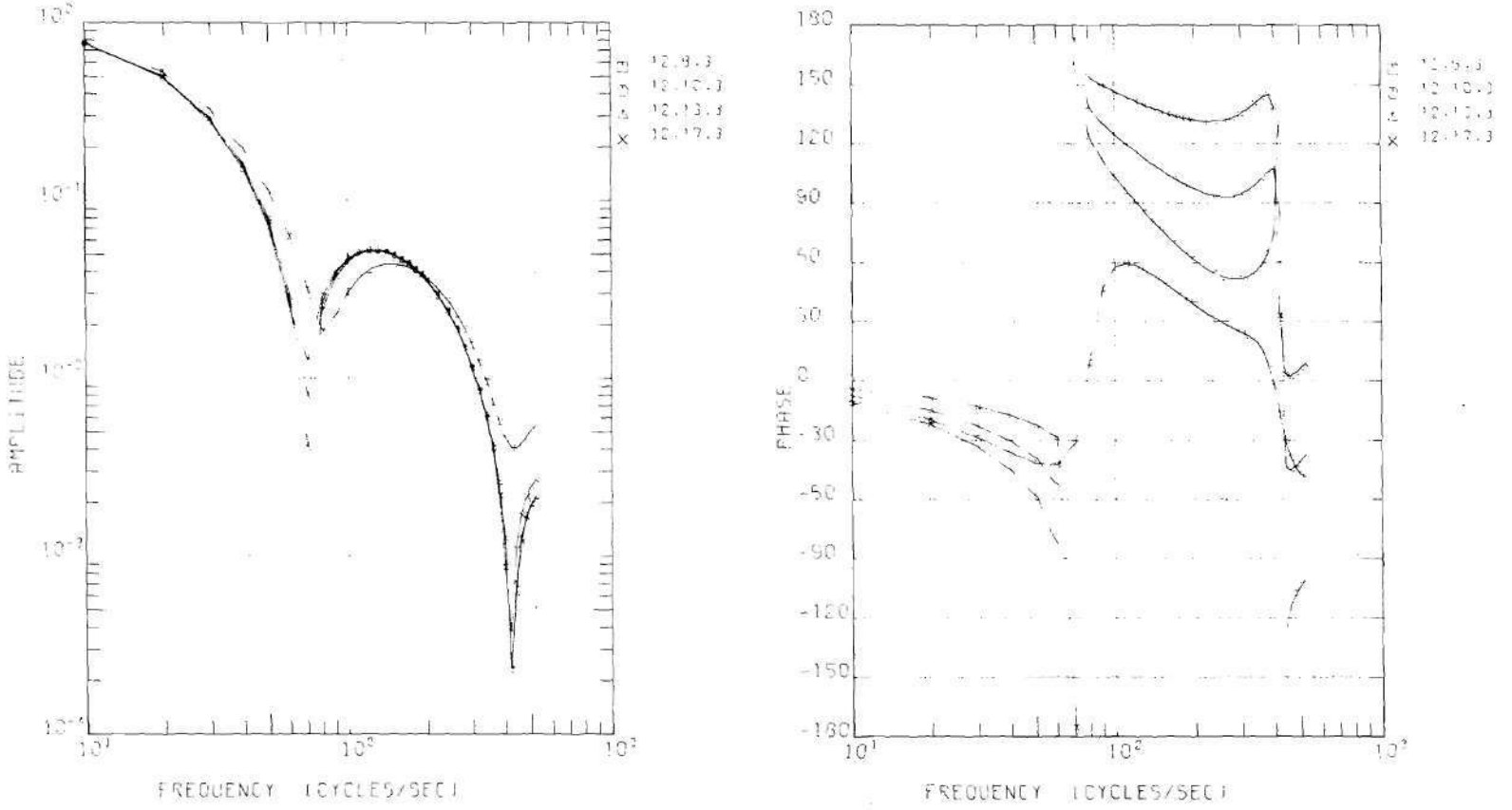

Figure 26. Calculated Amplitude and Phase of the Two-Dimensional Thermal-Thermal CHF for the TARK Coupled-Core Configuration, Detector 1 at Mesh (2,23), Detector 2 at Various Locations

region. For each case plotted, we also observe that the amplitude of the CHF goes through a second minimum at approximately 410 cps. For positions of detector 2 which are symmetrical to the position of detector 1, we observe that the phase of the CHF is zero below the first sink, - 180 degrees above this first sink, again zero above the second sink. The minimum in the amplitude becomes sharper as detector 2 is moved more to the outside, until it reaches a minimum value of zero for the position of detector 2, which is symmetrically located to the position of detector 1. In Figures 27a, b, c, d we have plotted the amplitude and in Figures 28a, b, c, d the phase of the CHF between the thermal response of detector 1 located at mesh(2,23)(θ = 0, r = 107.8), and the thermal response of detector 2, as a function of the position of detector 2. The position of detector 2 was swept throughout the reactor from r = 142.8 to 0 cm on radial 2, and from r = 0 to 142.8 cm on radial 12. As parameter of the curves, we have taken several frequencies. Again we can observe that the presence of a minimum in the amplitude of the CHF can be inferred from the crossing of the frequency curves. It can also be observed from the phase curves that the phase of the CHF goes through zero or ± 180 degrees for all frequencies at two distinct space points: a) position of detector 2 coincides with position of detector 1, and b) position of detector 2 coincides with the symmetrical location to detector 1. In order to compare the results of the two-dimensional calculations of the CHF using the UTR-10 cross-sections, with the one-dimensional calculational results determined by Ebert,[131] let us perform a two-dimensional analysis of the CHF for a two rectangular slab reactor. In Figure 29a we have superimposed two rectangular fuel slabs, separated by 45 cm of graphite coupling

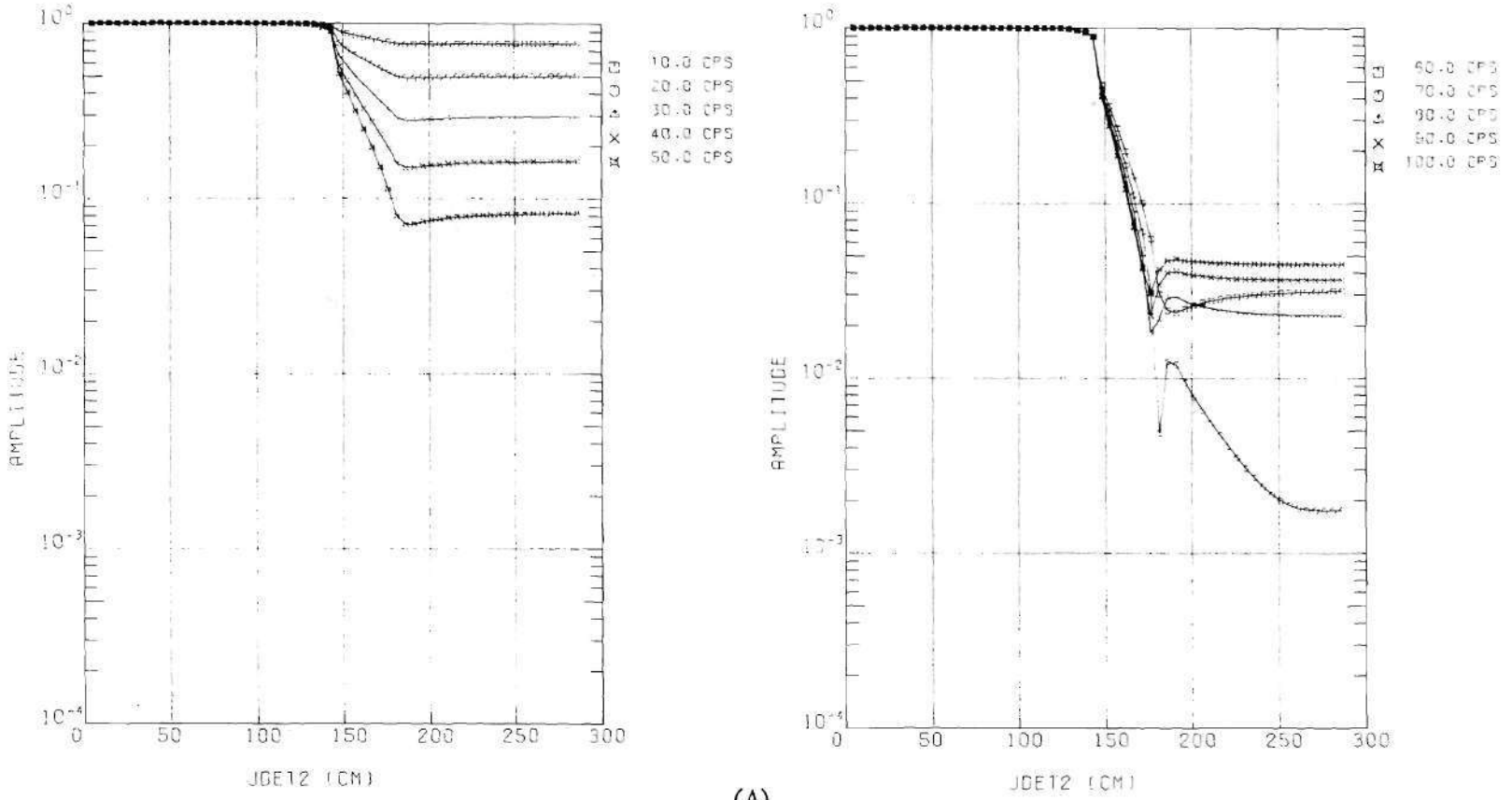

(A)

Figure 27. Calculated Amplitude vs Detector 2 Location, of the Two-Dimensional Thermal-Thermal CHF for the TARK Coupled-Core Configuration, Detector 1 at Mesh (2,23)

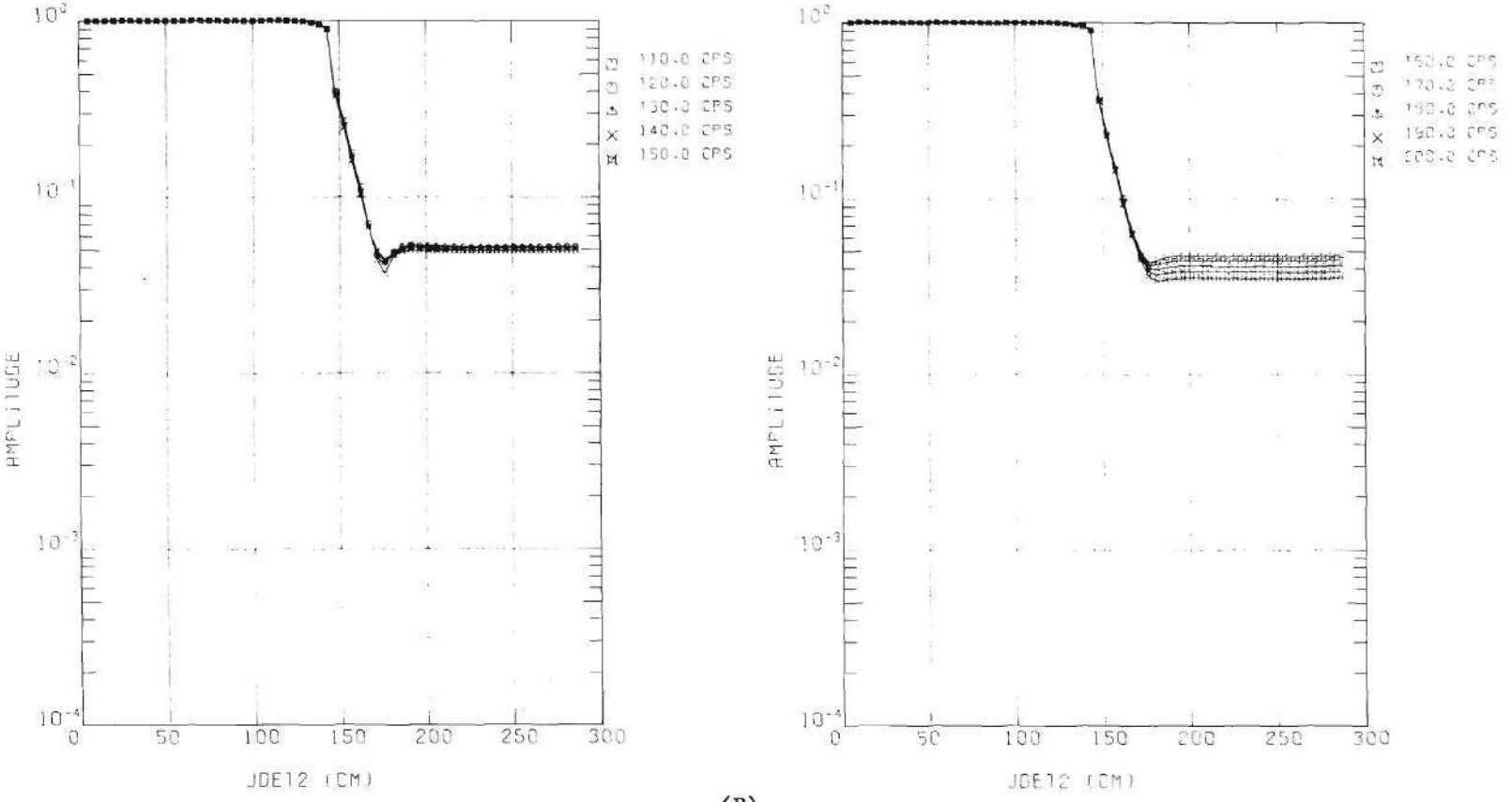

(B)

Figure 27. Continued

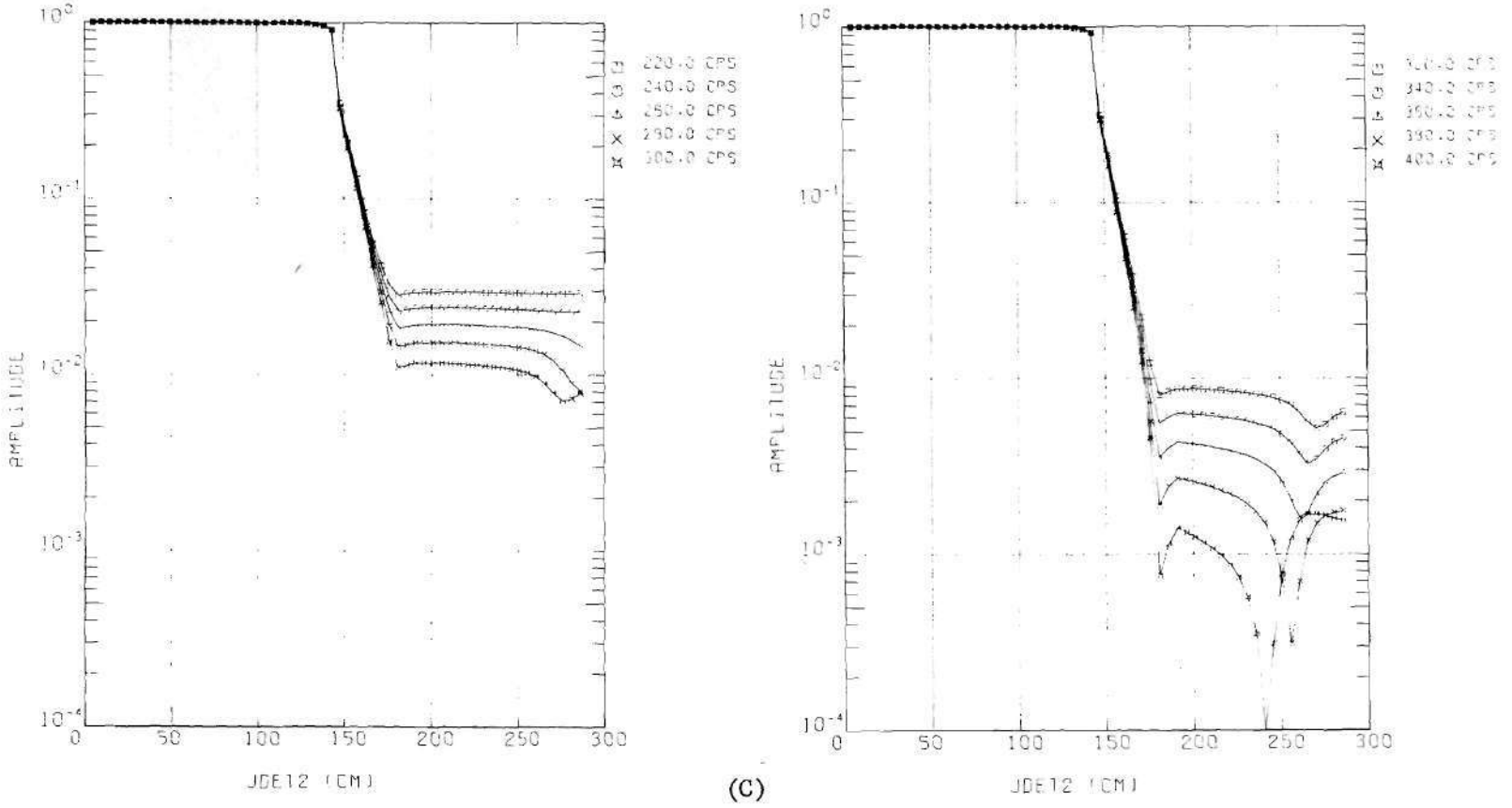

(C)

Figure 27. Continued

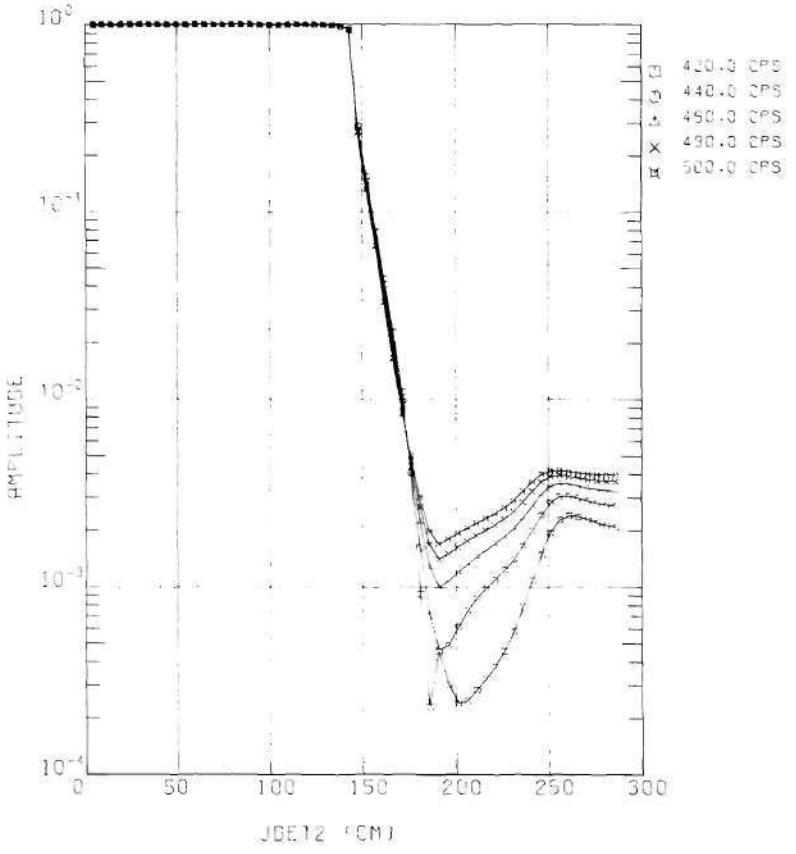

(D)

Figure 27. Concluded

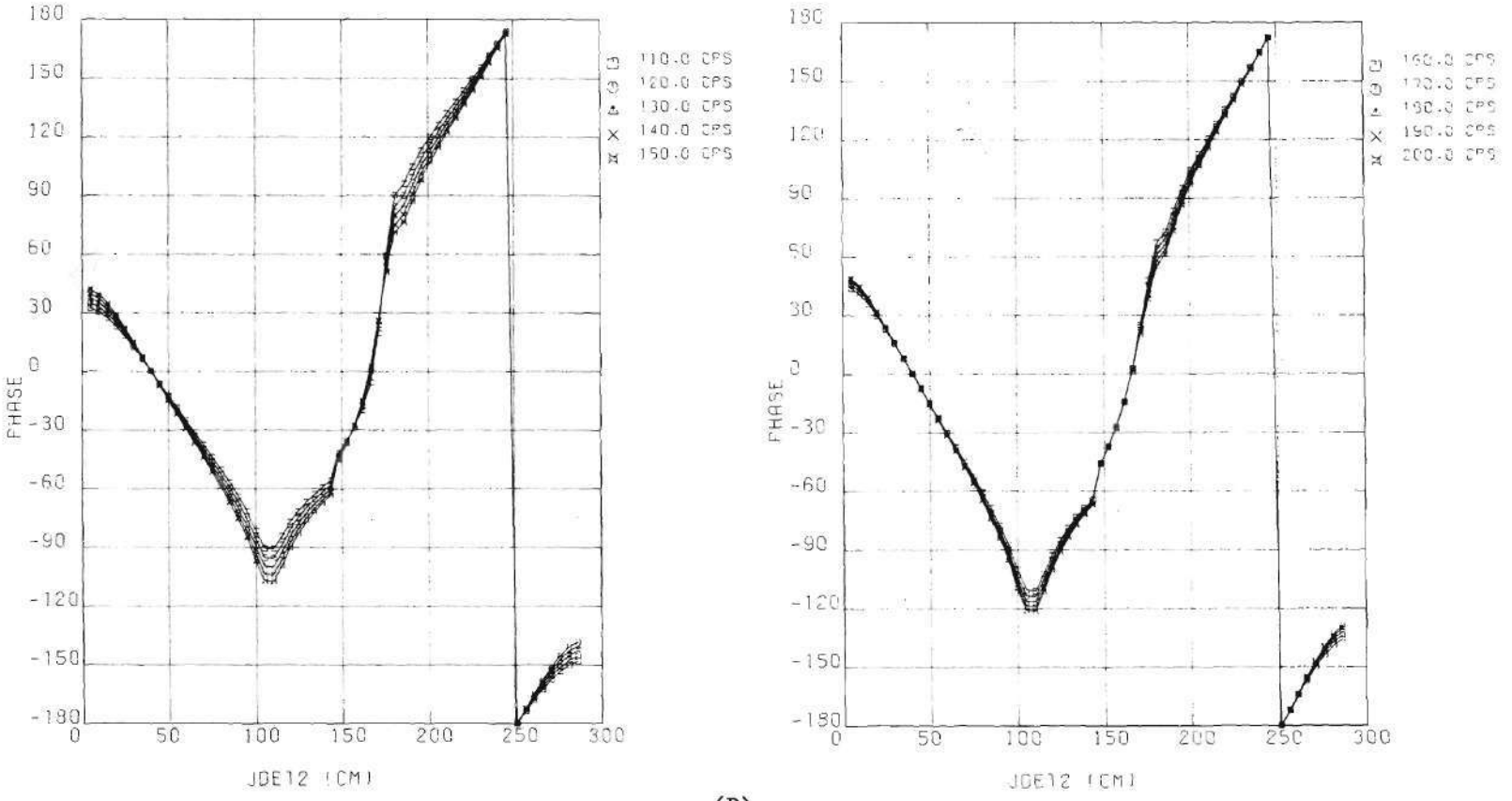

(B)

Figure 28. Continued

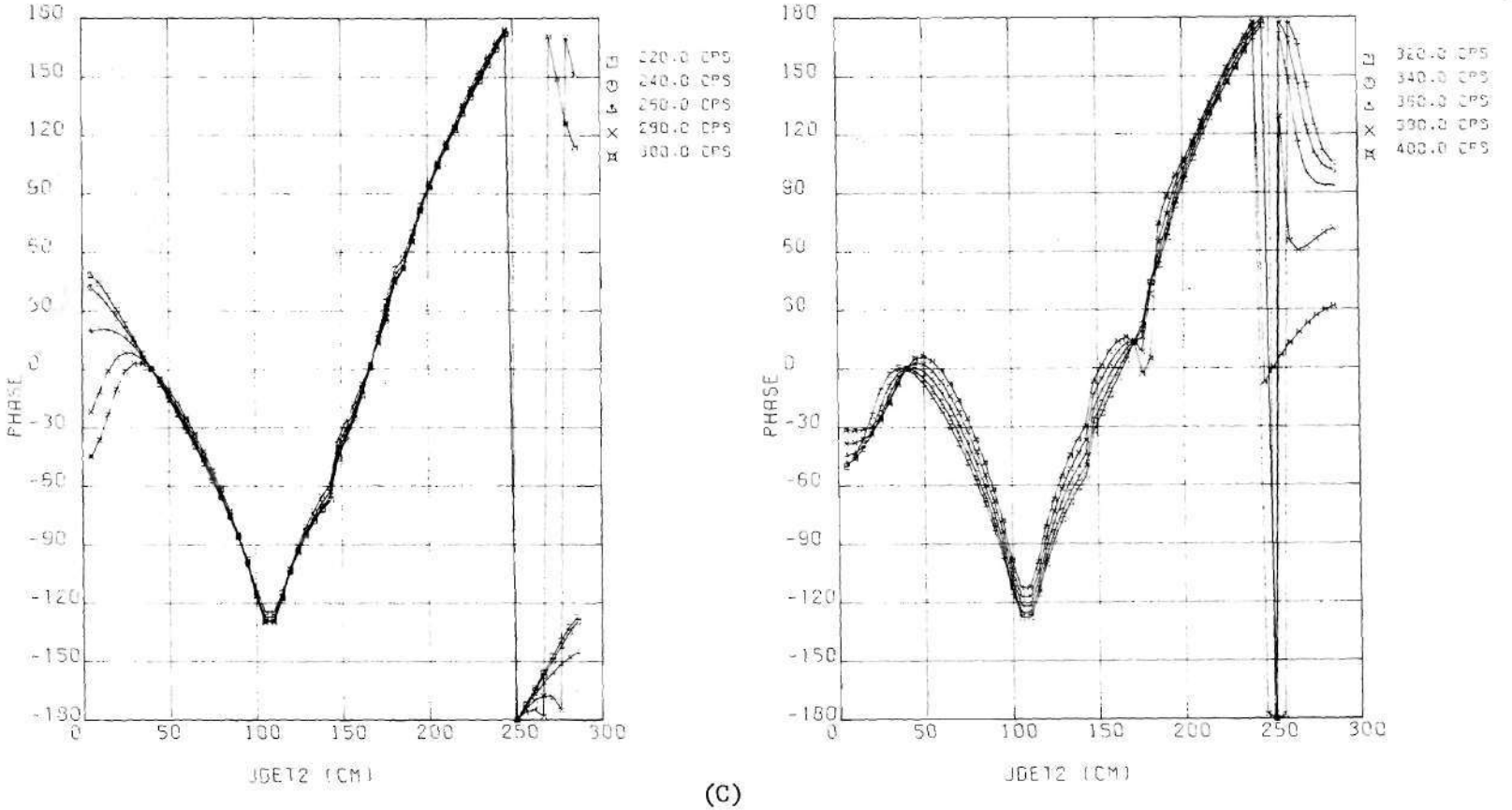

(C)

Figure 28. Continued

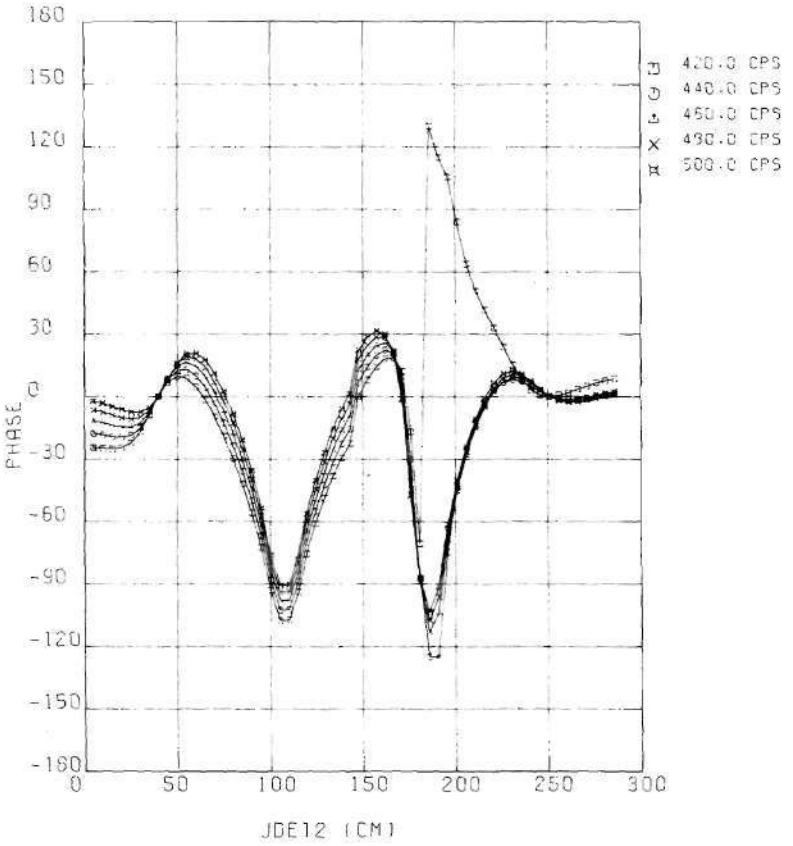

(D)

Figure 28. Concluded

region, onto the actual geometry of TARK. Each rectangular fuel slab contains eight "equivalent" Argonaut assemblies. A two-dimensional coherence function calculation was performed using a x-y mesh, with an axial buckling correction factor, for several selected frequencies. The UTR-10 cross-section set was used. The first sink frequency of the coherence function between the thermal response of detector 1, and the thermal response of detector 2 (each detector was located in the external graphite reflector, outside of the fuel region, in symmetrical locations) were found to be at a frequency of approximately 110 cps. In Figure 29b we have superimposed two rectangular fuel slabs, separated however by 61 cm of graphite coupling region, onto the actual geometry of TARK. The calculation of the CHF using a x-y mesh showed the first sink at approximately 65 cps. In order to ascertain that the analysis using r-θ geometry was equivalent to the use of x-y geometry, CHF calculations were performed for selected frequencies using the two-dimensional schematic presented in Figure 30 and the UTR-10 cross-section set. The difference in the value of the first sink frequency was less than five percent. If we calculate the number of pairs of interacting Argonaut assemblies of the two cylindrical-slab loading of TARK with their respective distances of the coupling region between them then (based on distances taken from the inside radius of 30.5 cm), we obtain that

Number of Pairs	Distance (cm)
2	37.13
4	43.13
6	48.39
8	52.83
10	56.36
12	58.92
14	60.48
8	61

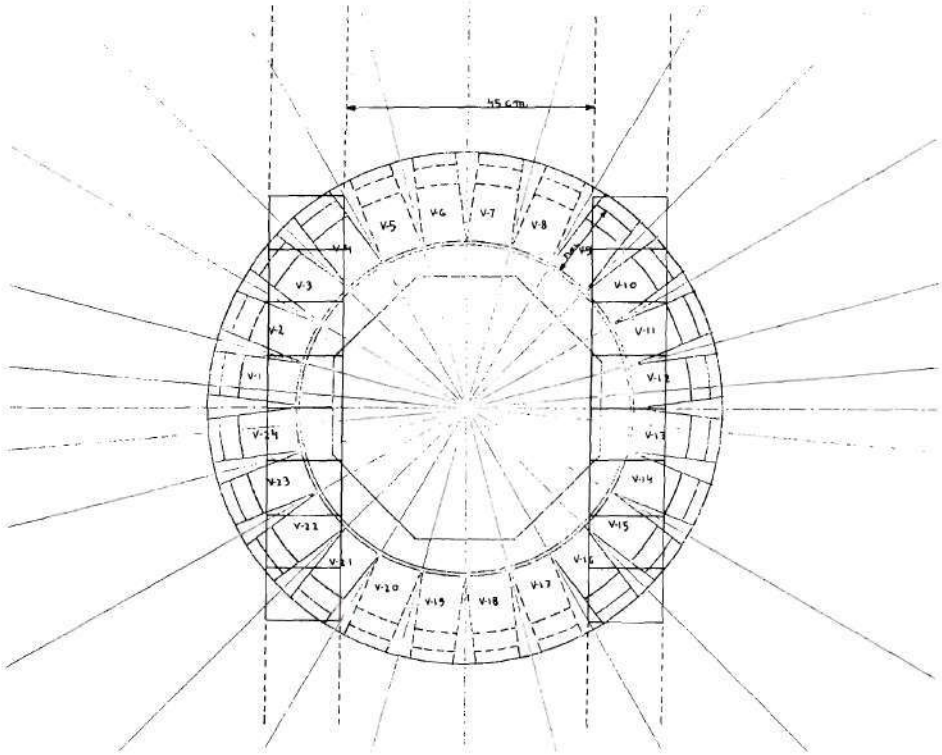

(A)

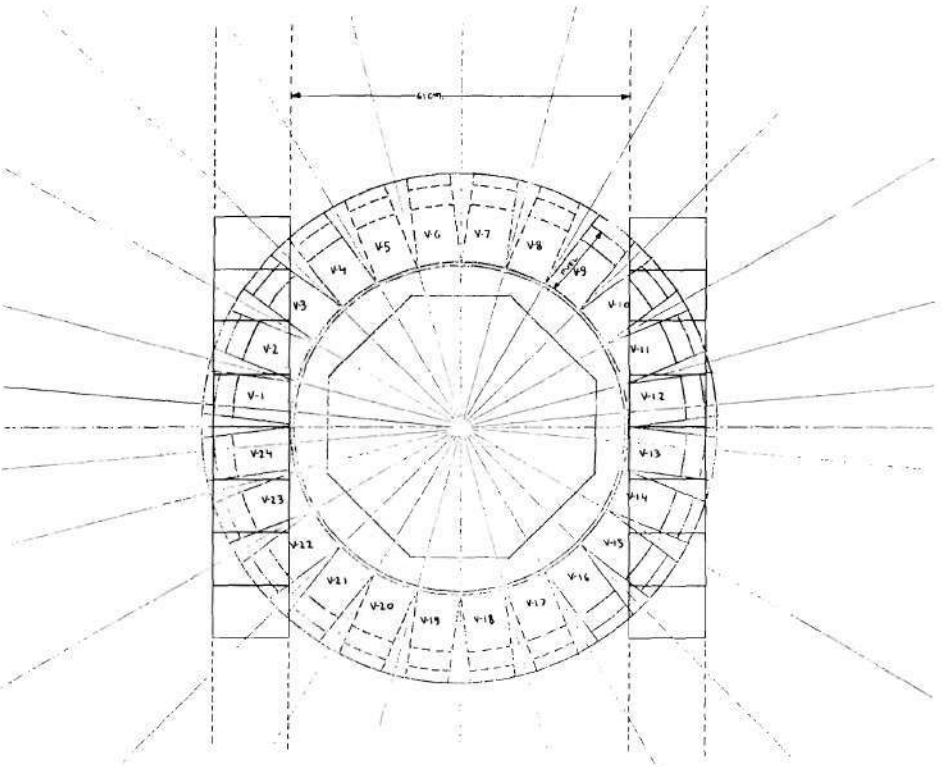

(B)

Figure 29. Two-Infinite Slab Configuration Superimposed on the Actual TARK Coupled-Core Configuration

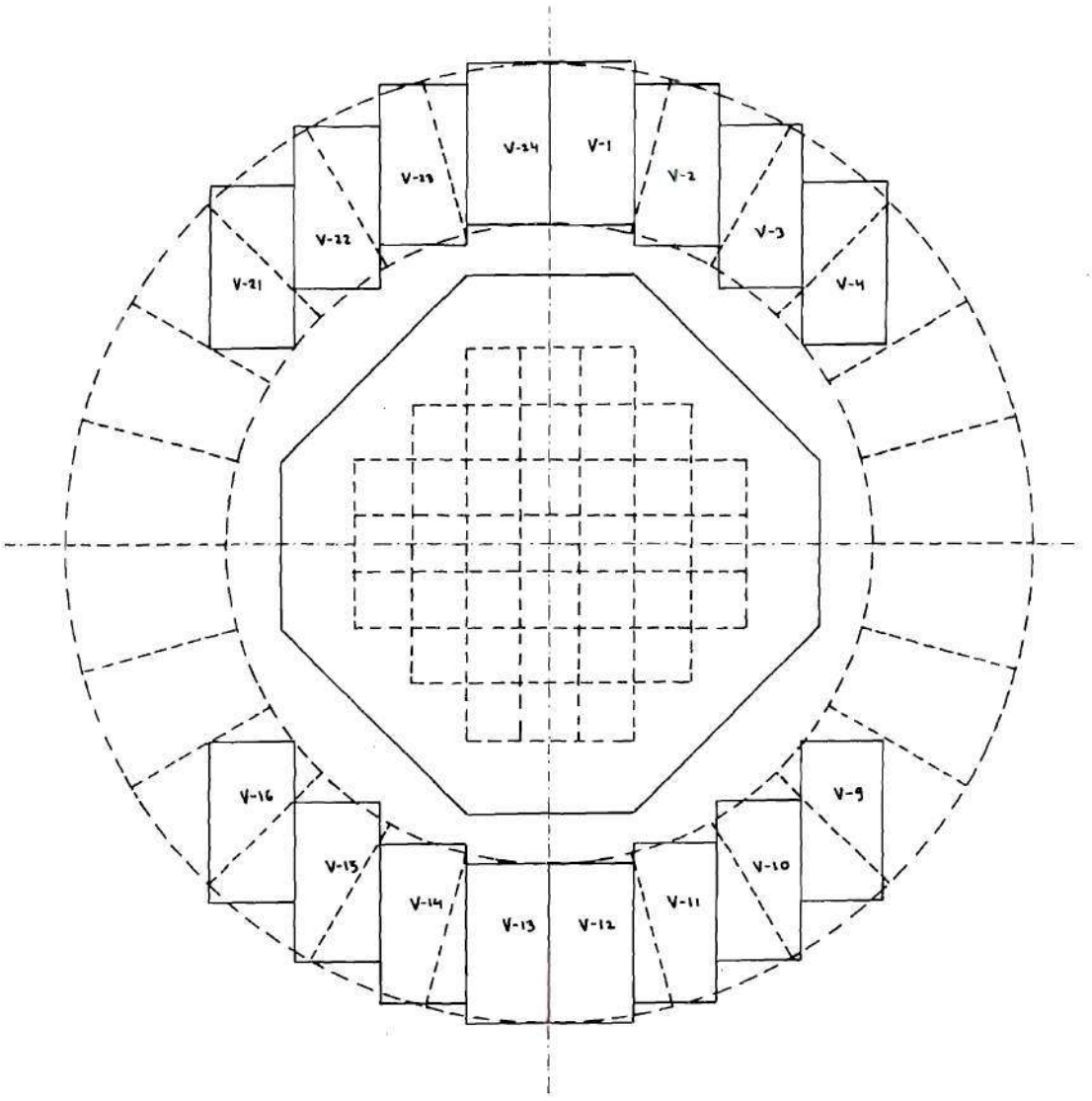

Figure 30. Two-Dimensional x-y Mesh Layout of the TARK Coupled-Core Configuration

Taking the geometrical mean, we obtain an average distance of 55.7 cm. It is evident that the one-dimensional calculation of the CHF for reactors such as TARK are inadequate to predict the precise position of a sink. However, multi-dimensional, multi-group calculations can be compared with experiments for the prediction of sinks. In one-dimensional calculations for multi-dimensional geometries, the location of the sink can only be predicted by proper variation of another parameter (e.g., coupling region thickness, coupling transfer function) in such a manner as to match calculated values of the sink frequency with the values determined by experiments.

CHAPTER VII

THEORETICAL STUDY OF THE TWO-DIMENSIONAL MULTI-GROUP STOCHASTIC CPSD AND CHF OF THE STARK REACTOR (LOADING II & IV), AND COMPARISON WITH EXPERIMENTS

Two-Dimensional Multi-group Power Spectral Density of STARK (Loading II & IV)

This part of the analysis will deal with the calculation of the cross-power spectral density (CPSD) and the coherence function (CHF) of the zero-power fast-thermal reactor STARK.

A detailed schematic of the STARK (Schnell Thermischen Argonaut Reaktor Karlsruhe) has been presented earlier. We have seen that STARK is an extension of the TARK reactor, where part of the coupling region was replaced by a fast region and a natural uranium intermediate blanket. The natural uranium blanket was used to reduce power peaking at the outer edge of the fast region due to leakage of slow neutrons into the fast region from the thermal Argonaut assembly region blanket.

For the configuration for which we performed the two-dimensional determination of the CHF, the fast region consisted of an array of 37 vertical square fuel assemblies, each fuel assembly being filled with a combination of different material platelets, as previously described. The thermal Argonaut region consisted of 24 Argonaut assemblies.

Two different loadings will be considered in the analyses:

--Loading II of the Fast Core Region: contained a total of 44.59 kg U^{235} in the fast region. For this configuration, a loading of 6.53 kg U^{235} in the thermal Argonaut core region was necessary in order to keep the reactor exactly critical with all control blades out.

--Loading IV of the Fast Core Region: contained a total of 106.90 kg U^{235} in the fast region. For this configuration, a loading of 4.429 kg U^{235} in the thermal Argonaut core region was necessary.

The detailed mesh schematic of STARK, which was used in the two-dimensional multi-group calculation of the PSD's, is presented in Figure 31. The calculations were performed using an r-θ mesh. The axial leakage in the third dimension was taken into account with the usual buckling correction factor. The outer radius of the Argonaut fuel region was calculated from the experimental loadings: 41.7 cm for loading II and 38.66 cm for loading IV.

For the angular mesh a total of 28 radials (rows) was used. Each radial was separated by 15 degrees, except radials 13-14, 14-15, 15-16, 1-2, 2-3, 26-27, 27-28, which were separated by 10 degrees.

A periodic boundary condition was used for top and bottom rows. The total number of columns in the mesh was 47 (JMAX). The axis of the cylindrical geometry lay halfway between mesh J=1 and J=2. The column numbers and correspondent "r" values are tabulated in Table 16.

The thermal Argonaut zone goes from r-mesh 17 (r=30.5 cm) to r-mesh 22 (r=41.7 cm) for loading II, and from r-mesh 17 (r=30.5 cm) to r-mesh 21 (r=38.66 cm) for loading IV.

The macroscopic broad-group cross sections, obtained by S_4P_3 transport calculations and collapses from ENDF/B-II sets (see Chapter V),

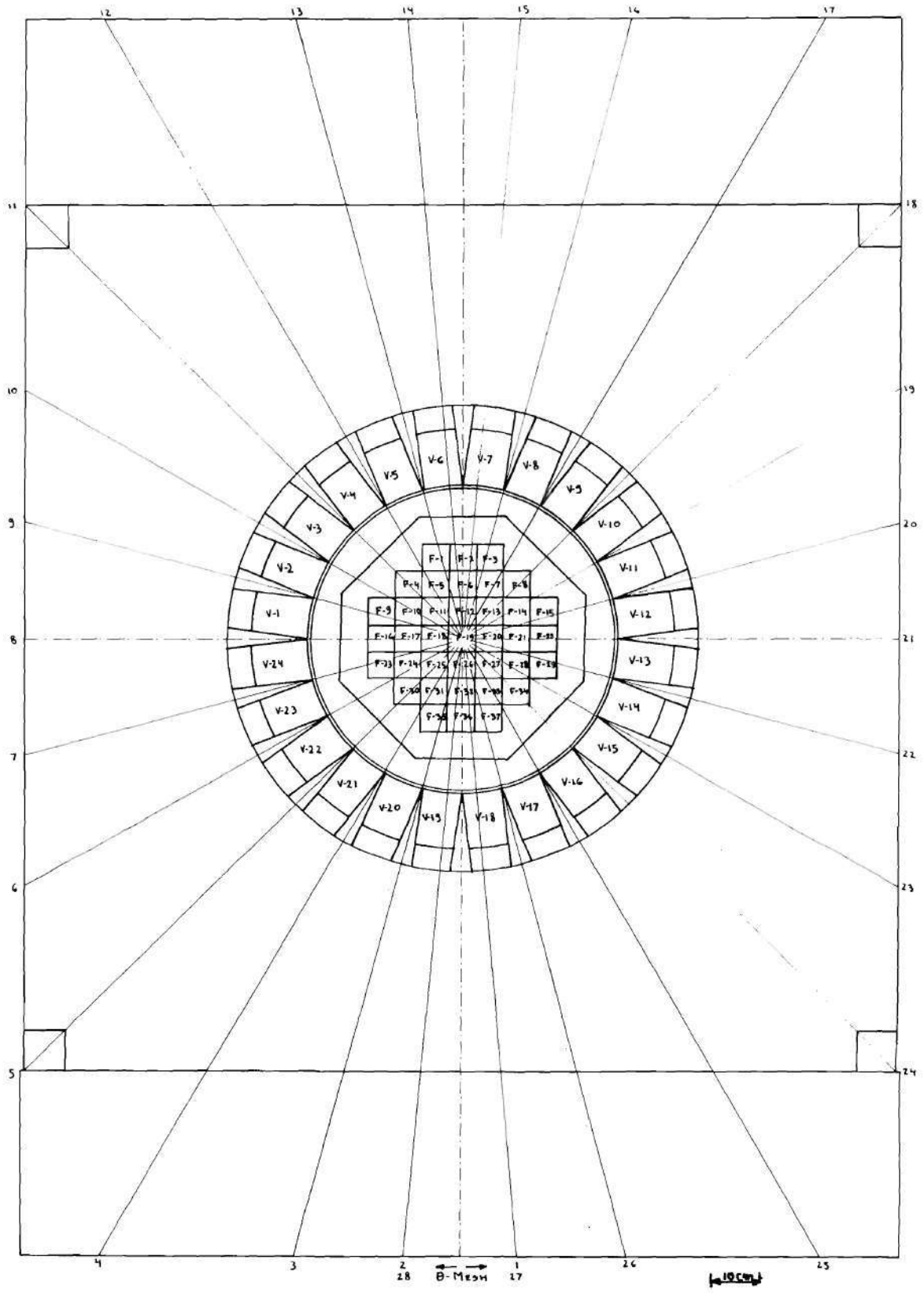

Figure 31. Two-Dimensional r-θ Mesh Layout STARK Loading II & IV

Table 16. Column Numbers and Correspondent "r" Values for STARK Loading II and Loading IV, r-θ Mesh Layout

STARK Loading II

"J" Distribution (Column Number - "r" Value (cm))

1	- 0.500	2	0.500	3	2.511	4	4.522	5	6.533	6	8.544	7	10.555
8	12.567	9	14.578	10	16.589	11	18.600	12	20.467	13	22.333	14	24.200
15	26.300	16	28.400	17	30.500	18	32.741	19	34.982	20	37.222	21	39.463
22	41.704	23	44.102	24	46.500	25	48.500	26	50.500	27	53.000	28	55.500
29	58.000	30	60.500	31	63.750	32	67.000	33	70.250	34	73.500	35	76.750
36	80.000	37	83.250	38	86.500	39	90.500	40	94.500	41	98.500	42	102.500
43	106.500	44	110.500	45	114.500	46	118.500	47	122.500				

STARK Loading IV

"J" Distribution (Column Number - "r" Value (cm))

1	- 0.500	2	0.500	3	2.511	4	4.522	5	6.533	6	8.544	7	10.555
8	12.567	9	14.578	10	16.589	11	18.600	12	20.467	13	22.333	14	24.200
15	26.300	16	28.400	17	30.500	18	32.540	19	34.580	20	36.620	21	38.660
22	41.273	23	43.887	24	46.500	25	48.500	26	50.500	27	53.000	28	55.500
29	58.000	30	60.500	31	63.750	32	67.000	33	70.250	34	73.500	35	76.750
36	80.000	37	83.250	38	86.500	39	90.500	40	94.500	41	98.500	42	102.500
43	106.500	44	110.500	45	114.500	46	118.500	47	122.500				

were used.

For the region surrounding the external graphite reflector, a rod group constant of 0.4692 was specified for all groups in place of the macroscopic absorption cross section.

An axial buckling search using a zone dependent $D^g B_z^2 \phi^g$ correction factor for transverse leakage was performed using a modified version of EXTERMINATOR-II,[82] until a value of $k_{eff} = 1$ was satisfied for the steady state case. The steady state fluxes and the axial buckling thus obtained were subsequently used in the PSD calculations using our TDPSD code.

In the steady state and axial buckling calculations, a convergence criterion (on the point steady state fluxes and on the value of $k_{eff} = 1$) of 1.0E-5 was used.

The same r-θ mesh grid as in the PSD calculations was used. In Figure 31 we observe that two symmetry axes are present. The presence of those symmetry axes was used in the PSD calculations in order to save computer time in the evaluation of space integrals.

An axial buckling of B_z^2 = 2.04619E-03 for loading II and B_z^2 = 1.79383E-03 for loading IV were thus obtained. They represent a critical axial height of, respectively, 27.343 inches and 29.203 inches.

In Figure 32 are presented the steady state broad group fluxes for STARK loading II along radial 2, and in Figure 33 the steady state broad-group fluxes for STARK loading IV along radial 2. Those steady state fluxes were normalized so to give a value of 1.0 for the integral, $\int_{\text{Reactor}} dV \sum_g \nu \Sigma_f^g \phi^g$. We observe that, in the center of the fast assembly

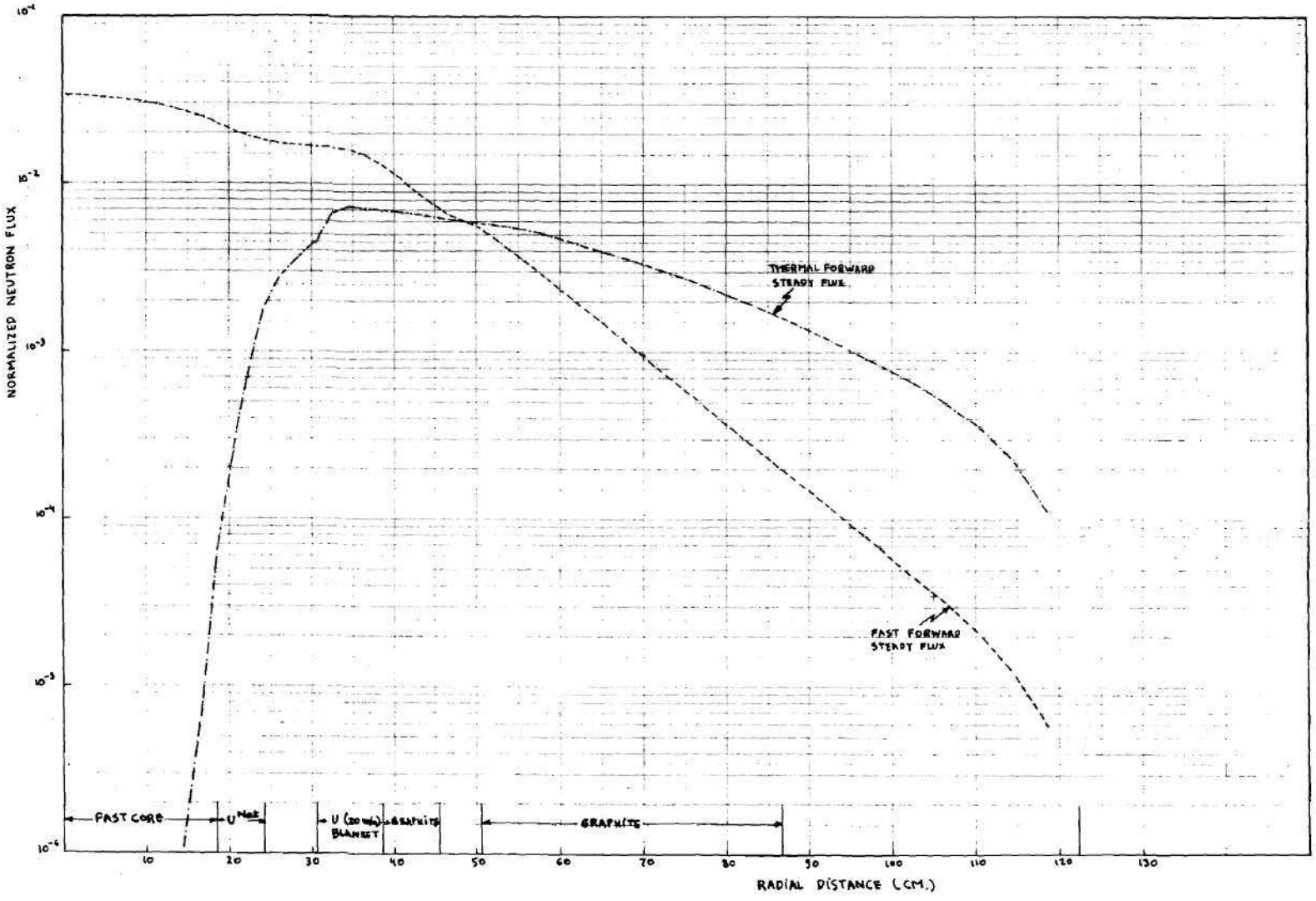

Figure 33. Steady State Fluxes of STARK Loading IV

region, the fast broad-group flux was 3.3 times greater for loading IV than loading II, while the thermal broad-group flux was 21 times greater for loading II than loading IV. The fast to thermal steady state flux ratio there was 1.38E+04 for loading II and 9.76E+05 for loading IV, as compared to the fast to thermal steady flux ratio of 0.61 for TARK. We therefore observe that the spectrum in the coupling region is quite different between TARK and STARK reactors. Since the coupling region between the Argonaut assemblies in TARK plays a major role in the characteristics of the power spectral densities, it will be interesting to observe the differences between the CHF of TARK and the CHF of different loadings of STARK.

In Tables 17a and 17b we have tabulated the relative volume fractions and power sources. For loading II, the calculated power fraction for the fast core and natural uranium blanket was 17.56%, for the thermal Argonaut zone 82.44%, while the experimentally determined power fractions were, respectively, 18.9 and 81.1%. For loading IV, the calculated power fraction for the fast core and natural uranium blanket was 42.5%, for the thermal Argonaut zone 57.5%, while the experimentally determined power fractions were, respectively, 42 and 58%.

The steady state spectra in the thermal Argonaut core zone and the outside graphite reflector are similar for loading II of STARK, loading IV of STARK, and TARK.

The calculated values of the PSD's were obtained for all space points in the mesh as well as properly weighted volume-distributed stochastic fission sources in the space volumes that contain fuel, using our TDPSD code. Let us repeat that the TDPSD (Two-Dimensional Power Spectral

Table 17a. Zone Fission Sources for STARK Loading II

Zone	Volume (cc)	Volume Fraction	Fission Source (2 Groups)	Calculated Power Fraction (%)	Experimental Power Fraction (%)
1	1.996+02	8.49-03	1.33 -02	7.46 / 17.56	9.3 / 18.9
2	8.872+02	3.77-02	6.13 -02		
3	7.530+02	3.20-02	1.008-01		
4	1.083+03	4.61-02	3.45 -09		
5	2.765+03	1.18-01	8.245-01	82.44	81.1
6	1.105+03	4.70-02	0.0		
7	1.219+03	5.19-02	5.74 -10		
8	5.643+03	2.40-01	0.0		
9	9.851+03	4.19-01	0.0		
$\sum$ Zones	2.351+04	1.00	1.00		

Table 17b. Zone Fission Sources for STARK Loading IV

Zone	Volume (cc)	Volume Fraction	Fission Source (2 Groups)	Calculated Power Fraction (%)	Experimental Power Fraction (%)
1	1.996+02	8.49-03	7.11-02	30.5 / 42.5	31.1 / 42
2	8.872+02	3.77-02	2.34-01		
3	7.530+02	3.20-02	1.20-01		
4	1.083+03	4.61-02	3.42-09		
5	1.773+03	7.54-02	5.75-01	57.5	58
6	2.097+03	8.92-02	0.0		
7	1.219+03	5.19-02	2.87-10		
8	5.643+03	2.40-01	0.0		
9	9.851+03	4.19-01	0.0		
$\sum$ Zones	2.351+04	1.0	1.00		

Density) code is based on theory and numerical approaches developed in Chapters III and IV. The weighting of the stochastic fission sources was performed using the broad-group steady state fluxes. Due to symmetry, only responses to the stochastic sources of the space volumes of the following assemblies must be performed:

1) Fast Assemblies -- F-16 to F-19, F-23 to F-26, F-30 to F-32 F-35 to F-36
2) Natural uranium blanket between radials 8 and 15
3) Thermal Argonaut fuel assemblies -- V-1, V-2, V-3, V-4, V-5, V-6, V-7.

To get the space-, energy-, and frequency-dependent responses to the stochastic sources in the space volumes of the other assemblies, proper shifting of the mesh points was performed around the appropriate symmetry axes.

A total of 486 volume elements with stochastic sources was therefore present in the PSD calculations for STARK loading II, and 459 volume elements for STARK loading IV.

In addition, the CPSD and the CHF between the thermal response of detector 1 located at various locations and the thermal response of detector 2 at various locations in the STARK reactor were calculated for externally controlled sources and stored for eventual later use. These PSD calculations were performed for each of the following separate external thermal unit sources in volumes defined by: (θ-r mesh 14,15-1,3) located in the fast core, (mesh 14,15-15,16) located at the outer boundary of the natural uranium blanket, and (mesh 14,15-26,27) located in the external graphite reflector just outside the thermal Argonaut zone. Those

external source calculations were performed for loading II and loading IV of STARK.

In all the PSD calculations, the proper values of the effective delayed neutron fractions for U-235 and U-238, as computed previously for STARK loading II and IV, were used.

In Figures 34a and 34b we have plotted the amplitude and the phase of the two-dimensional CHF for STARK loading II, between the thermal broad-group response of detector 1 and the thermal broad-group response of detector 2 due to the inherent distributed stochastic fission sources. While detector 1 was held at the position defined by mesh (2,32), detector 2 was moved into different positions of the reactor. In contrast to the behavior of the CHF for TARK, we do not observe a "waving" shape of the amplitude of the CHF in STARK loading II for any position of detector 2. The frequency range investigated extended from 1 to 500 cps. However, we observe a strong space-dependency for detector 2 locations inside the coupling region. For detector 2 positions outside of the thermal Argonaut fuel zone, no noticeable space-dependency can be observed in the amplitude of the CHF, except at higher frequencies (above 300 cps). The phase of the CHF behavior is more indicative of the presence of space-dependency.

For the case of symmetrical locations of detector 1 and detector 2 (mesh (2,32) and mesh (14,32)), we observe that the phase is nearly zero. The numerical values of the phase predicted for symmetrically located detectors were of the order of 10^{-2} degrees.

In Figures 35a,b,c we have plotted the amplitude and the phase of the CHF for STARK loading II, between the thermal response of detector 1

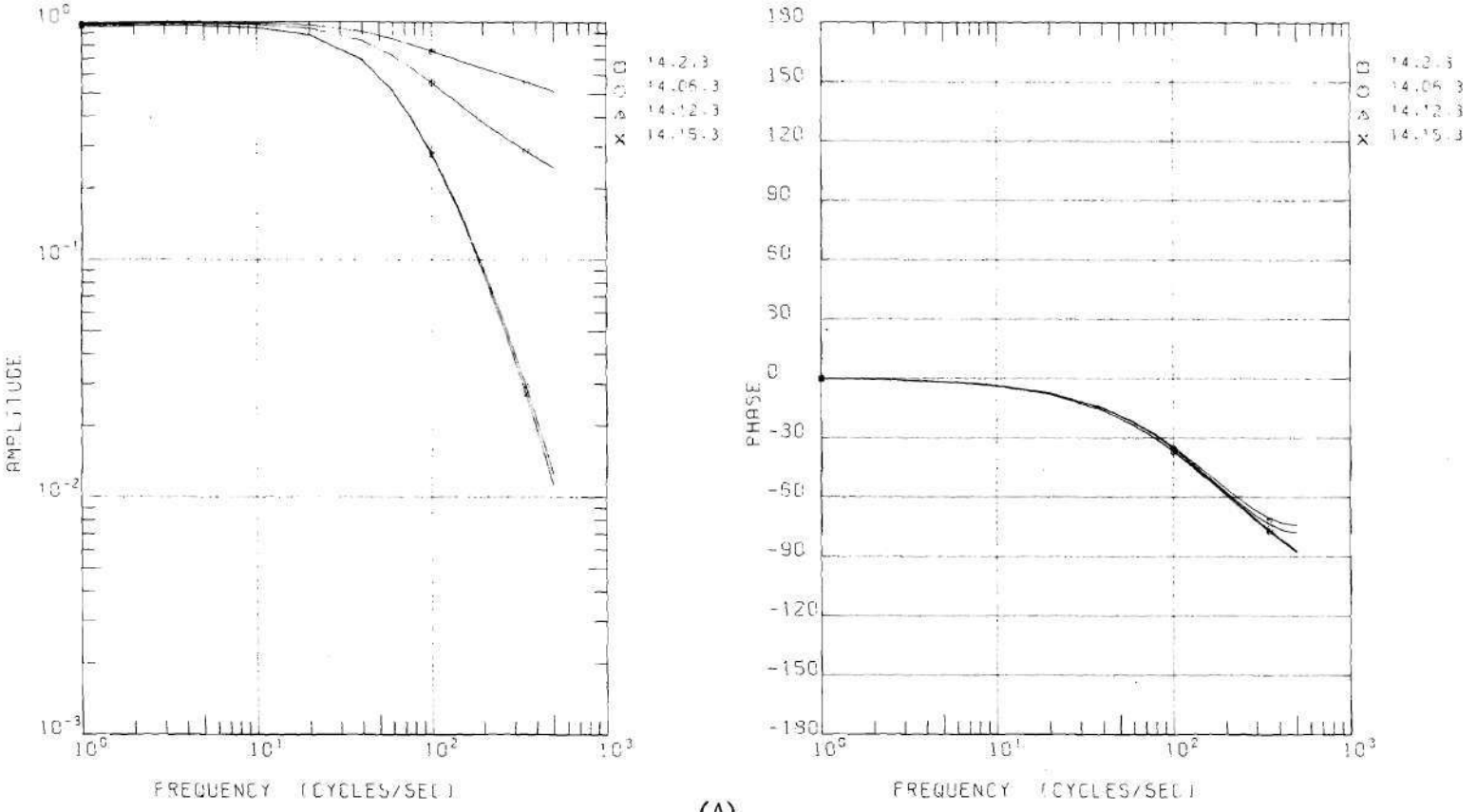

(A)

Figure 34. Calculated Amplitude and Phase of the Two-Dimensional Thermal-Thermal CHF for STARK Loading II, Detector 1 at Mesh (2,32), Detector 2 at Various Locations

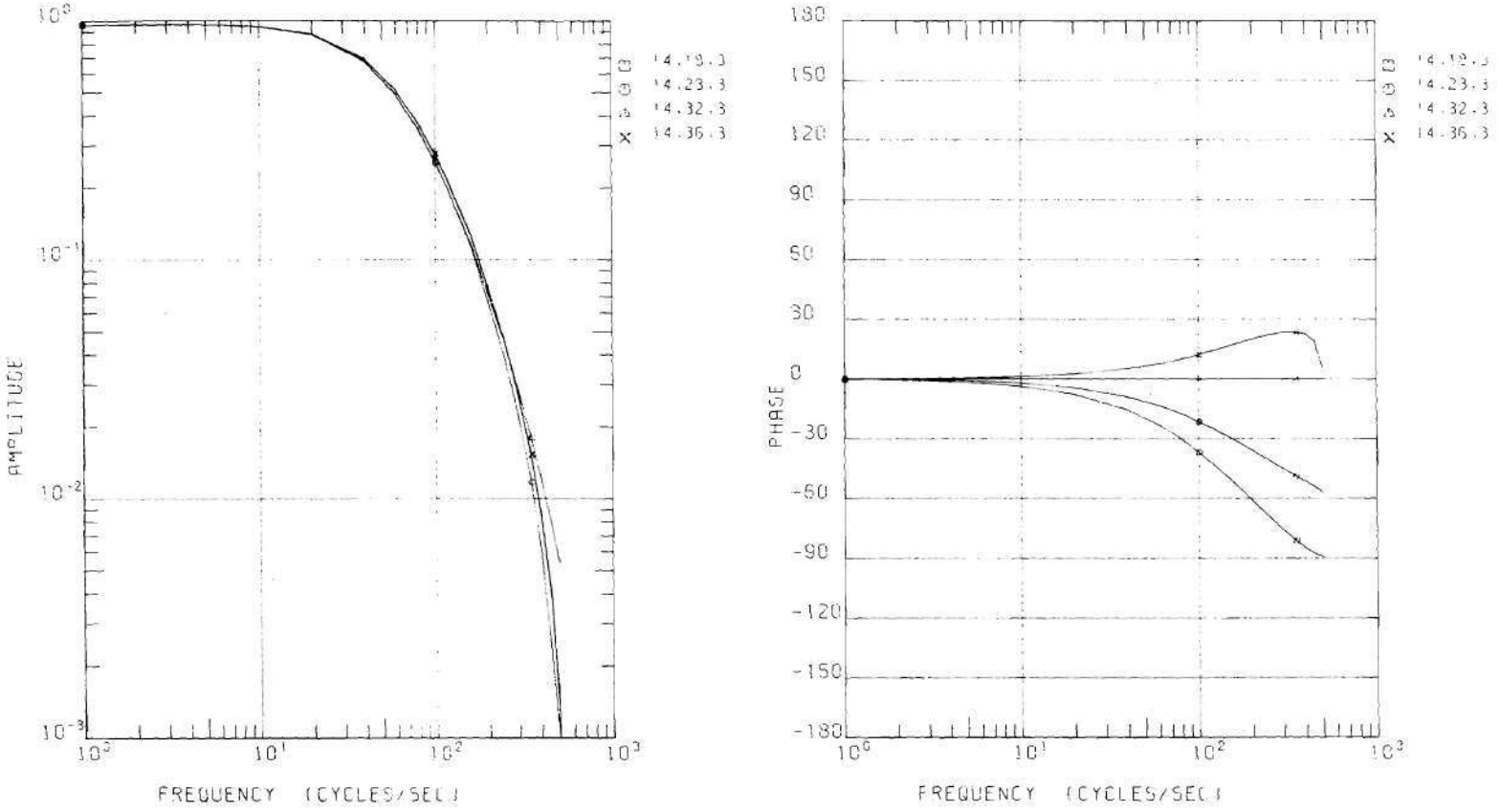

(B)

Figure 34. Concluded

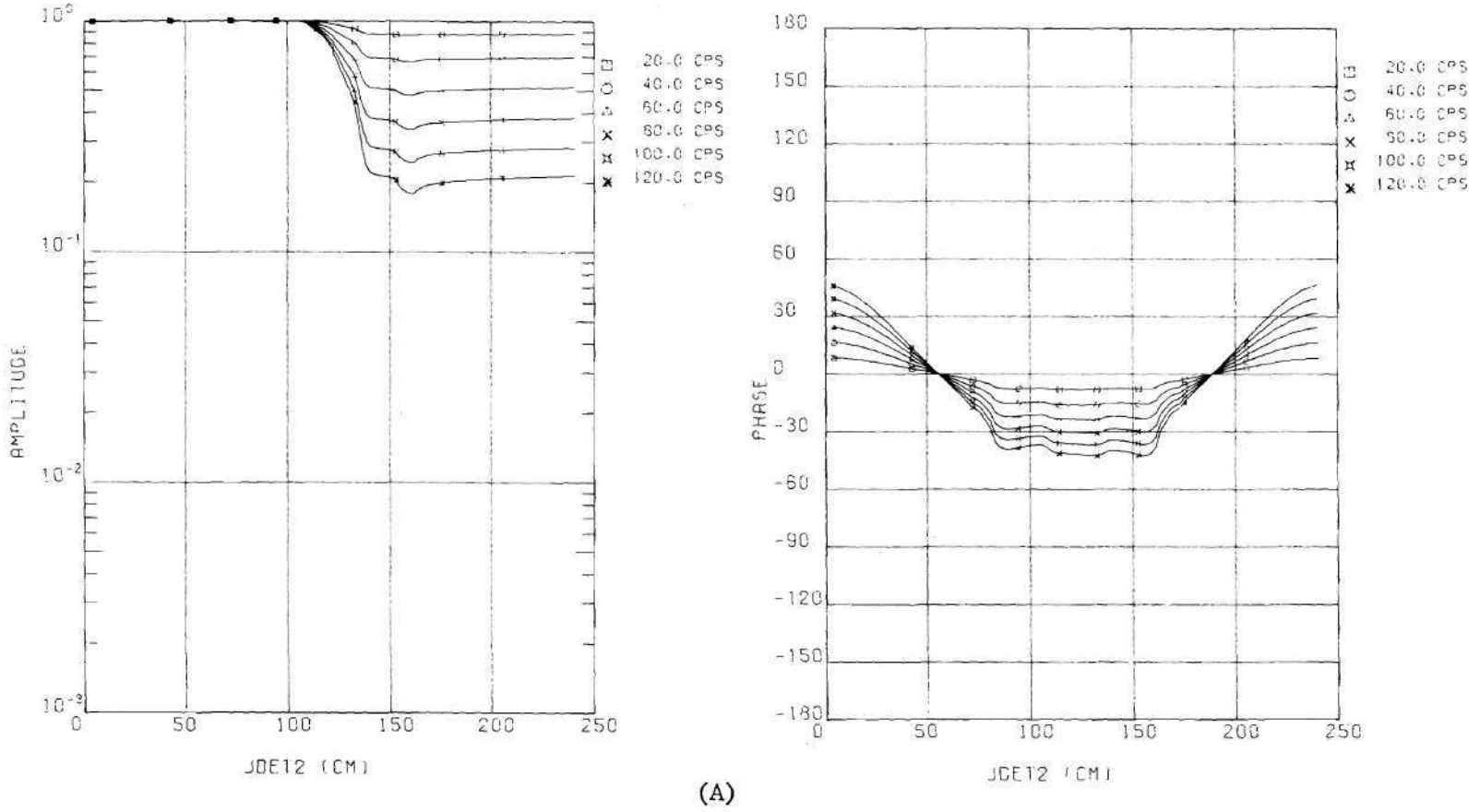

(A)

Figure 35. Calculated Amplitude and Phase vs Detector 2 Location of the Two-Dimensional Thermal-Thermal CHF for STARK Loading II, Detector 1 at Mesh (2,32)

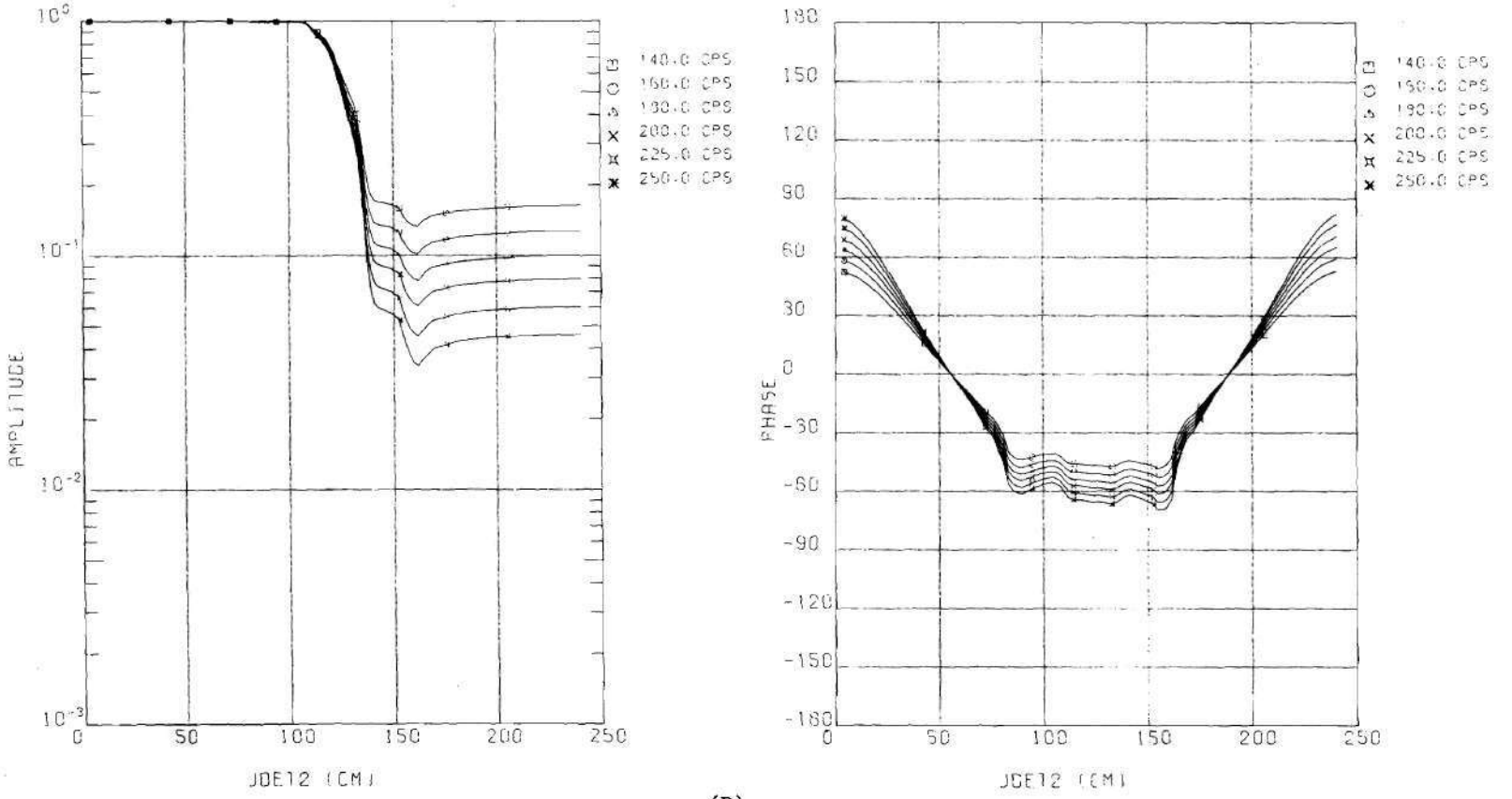

(B)

Figure 35. Continued

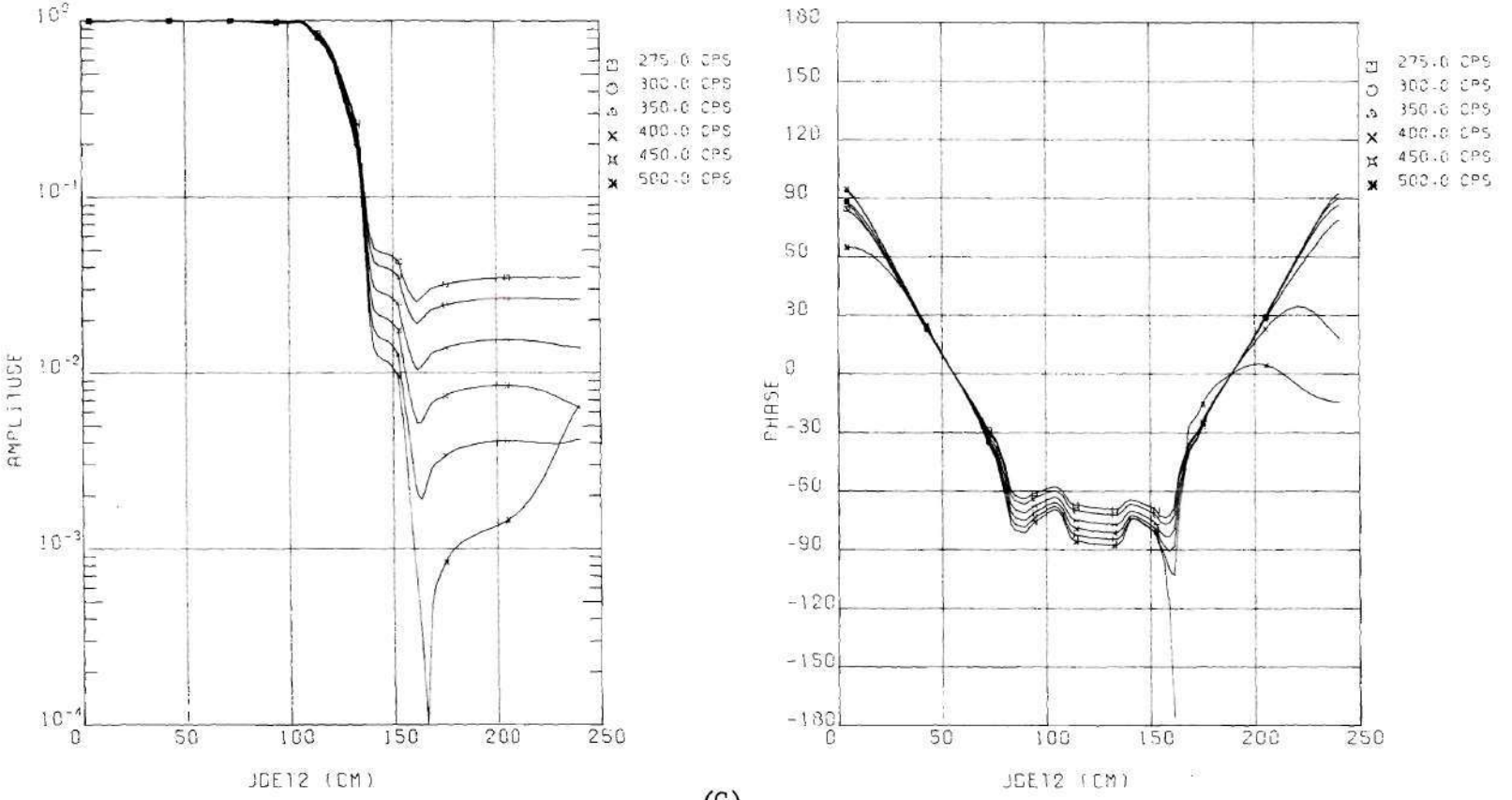

(C)

Figure 35. Concluded

at mesh (2,32) and the thermal response of detector 2, as a function of different positions of detector 2. The position of detector 2 was swept through STARK from r = 122.5 to r = 0 cm for radial 2, and from r = 0 to 122.5 cm for radial 14. As parameters of the family of the different curves we have used different frequencies. For frequencies below 300 cps, the amplitude and phase curves do not vary much in shape, but they vary in intensity. Above 300 cps, we observe that not only the magnitude, but also the shape of the amplitude and phase curves vary widely, especially for detector 2 positions in the external graphite reflector (at the opposite reactor side of where detector 1 was positioned). Comparison of those curves with the curves of Figures 27 and 28 for TARK indicates that neutron wave interferences are starting to be important at those frequencies. The presence of a minimum in the amplitude of the CHF is visible at 500 cps when detector 2 is located at approximately r = 100 cm on radial 14.

In Figures 36a and 36b we have plotted the amplitude and phase of the two-dimensional thermal-thermal CHF for STARK loading IV, due to the inherent distributed stochastic fission sources. While detector 1 was held at a position defined by mesh (2,32), detector 2 was moved into different positions of the reactor. The frequency range investigated extended from 1 to 300 cps. The amplitude of the CHF exhibits space-dependency for detector 2 locations inside the coupling region.

In Figure 37 we have plotted the thermal-fast CHF (between the thermal response of detector 1 at mesh (2,32) and the fast broad-group response of detector 2 at different reactor locations). The CHF exhibits space-dependency, and for the thermal response and for the fast response

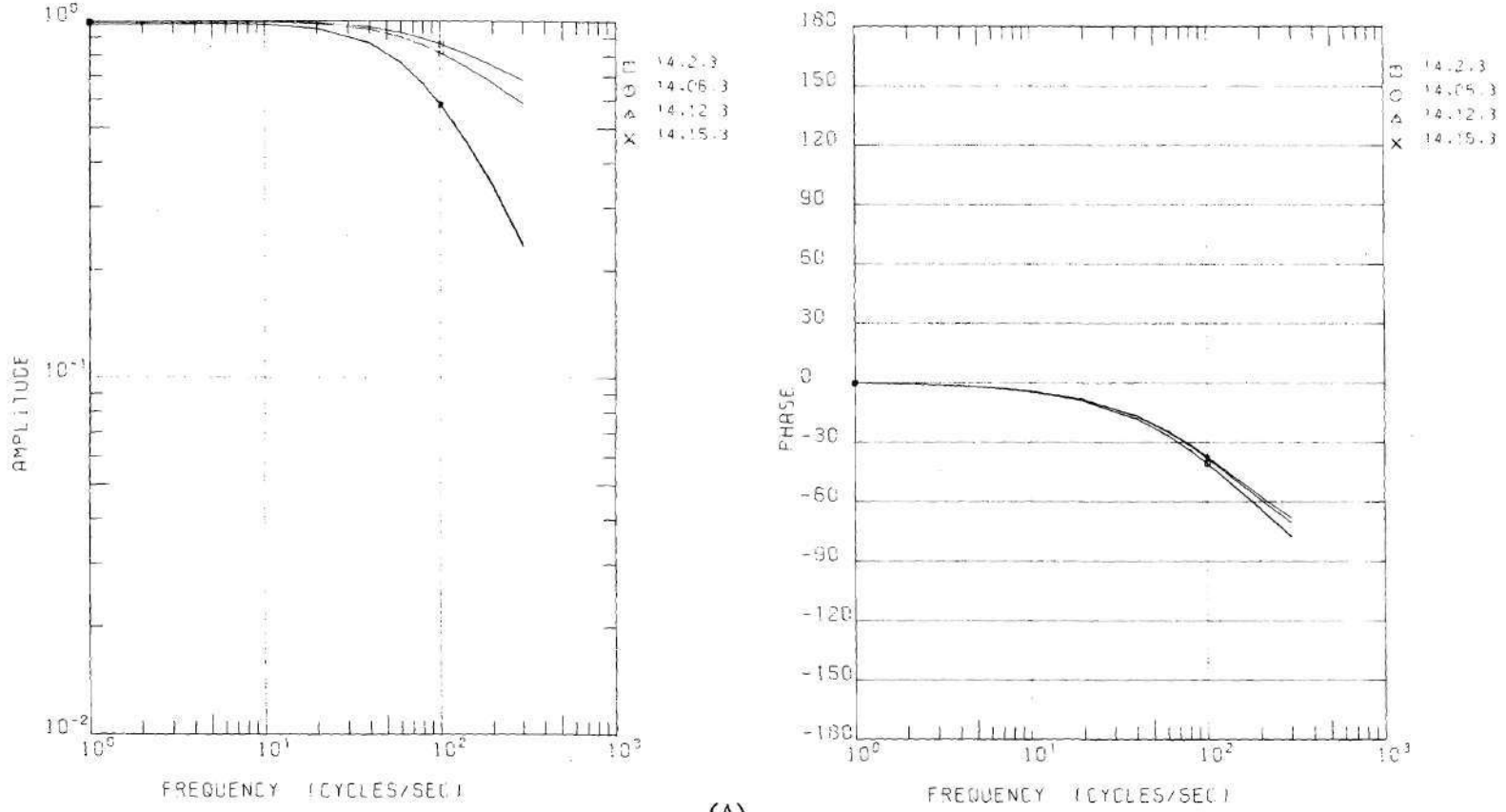

(A)

Figure 36. Calculated Amplitude and Phase of the Two-Dimensional Thermal-Thermal CHF for STARK Loading IV, Detector 1 at Mesh (2,32), Detector 2 at Various Locations

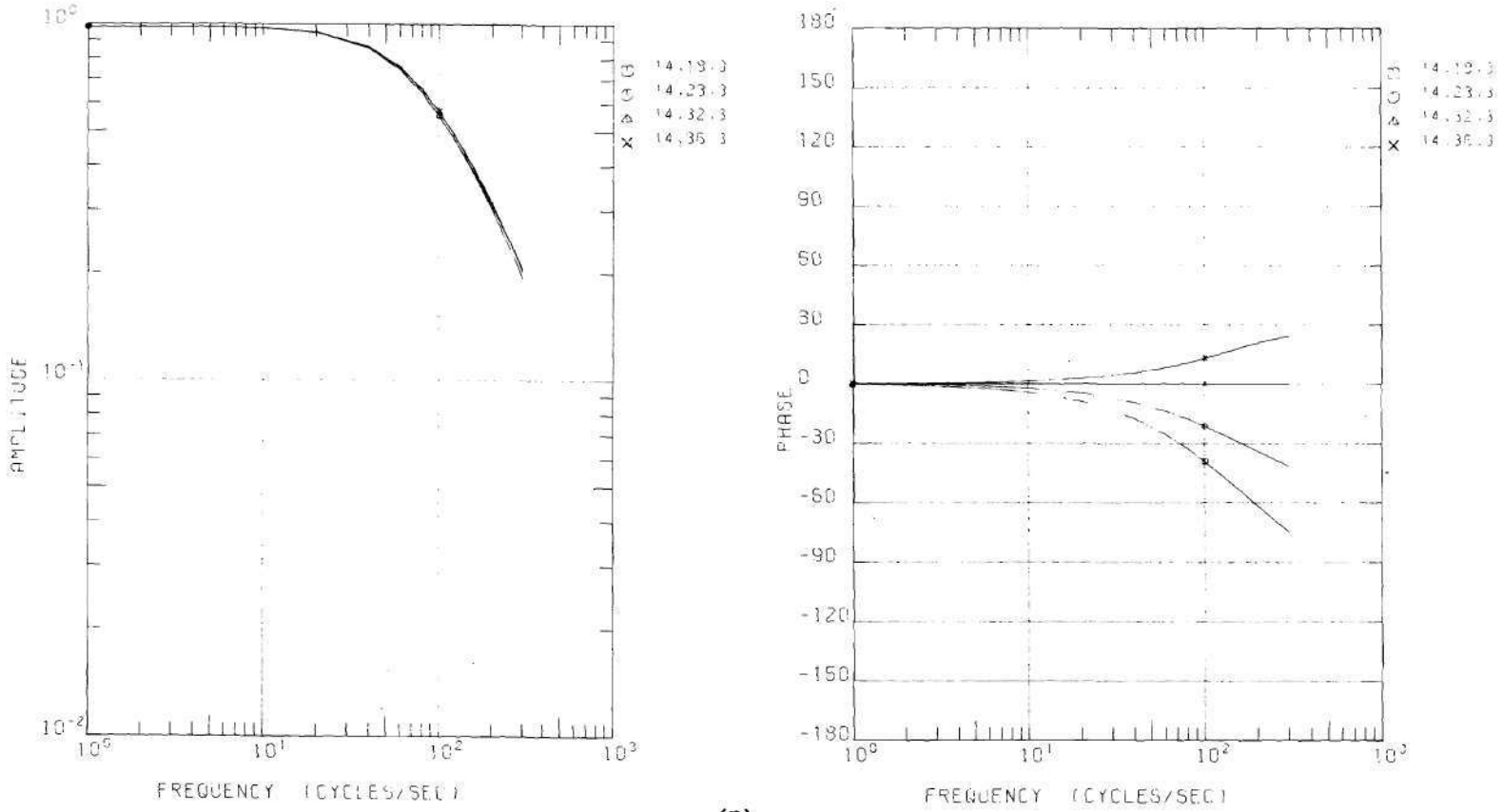

(B)

Figure 36. Concluded

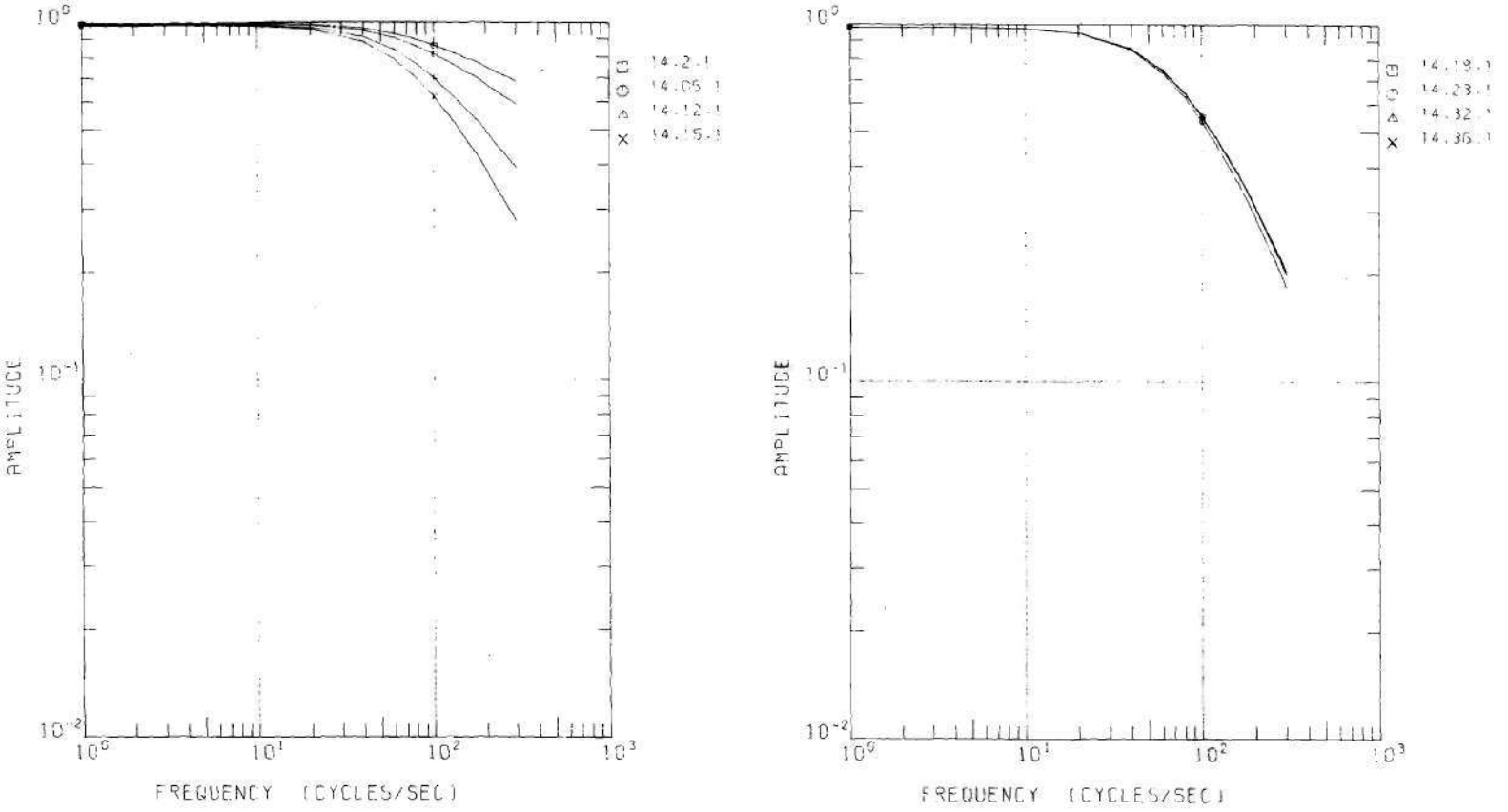

Figure 37. Calculated Amplitude of the Two-Dimensional Thermal-Fast CHF for STARK Loading IV, Detector 1 at Mesh (2,32), Detector 2 at Various Locations

of detector 2, when detector 2 is positioned inside the coupling region of STARK. Comparison between the thermal-fast and the thermal-thermal CHF indicates similar trends, except for detector 2 positions outside the fast assembly zone in the coupling region (refer to detector 2 position defined by mesh (14,12) and by mesh (14,15)).

For positions of detector 2 outside the thermal Argonaut zone, only small space-dependency of the CHF can be observed. This can be explained since the CHF depends primarily on the coupling between the regions being sampled by the neutron detectors.

Comparison between the thermal-thermal CHF of STARK loading II with loading IV, indicates that the amplitude is more frequency-dependent for loading II than for loading IV.

In Figures 38a and 38b we have plotted the amplitude and phase of the CHF for STARK loading IV as a function of the position of detector 2 for several frequencies. The thermal-thermal CHF exhibits strong dependence on the location of detector 2 within the coupling and fuel regions. The curves have similar shapes, but differ in amplitude, although less than for loading II.

In Figures 39a, 39b, 39c, and 40 we have displayed some of the results of the two-dimensional CPSD calculations for STARK loading II. While detector 1 was held in the reactor location defined by θ-r mesh (2,32), detector 2 was moved into several locations of the reactor.

The amplitudes of the CPSD's were normalized to a value of 1.0 at a frequency of 1 cps. The values are tabulated in Table 18.

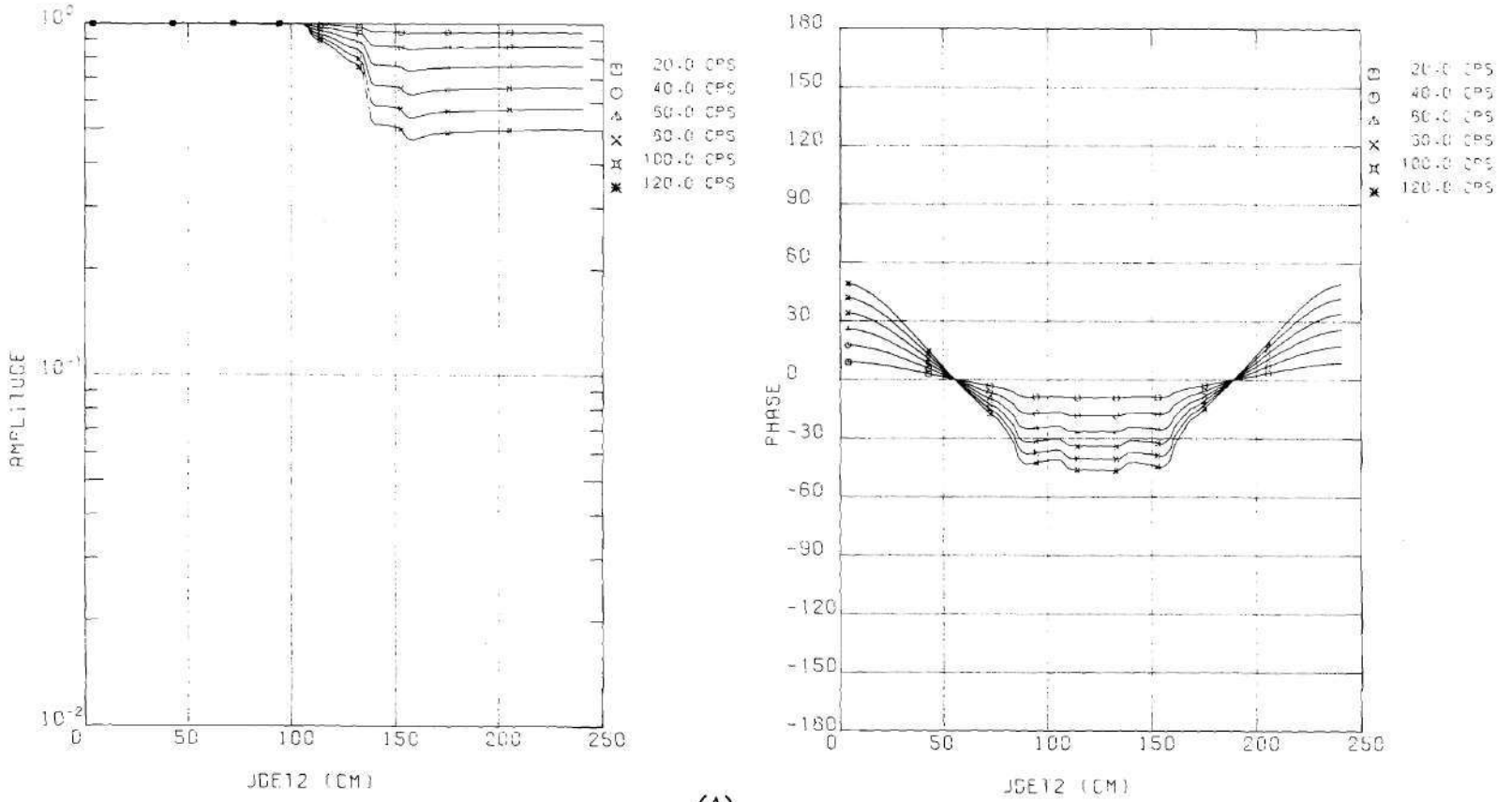

(A)

Figure 38. Calculated Amplitude and Phase vs Detector 2 Location of the Two-Dimensional Thermal-Thermal CHF for STARK Loading IV, Detector 1 at Mesh (2,32)

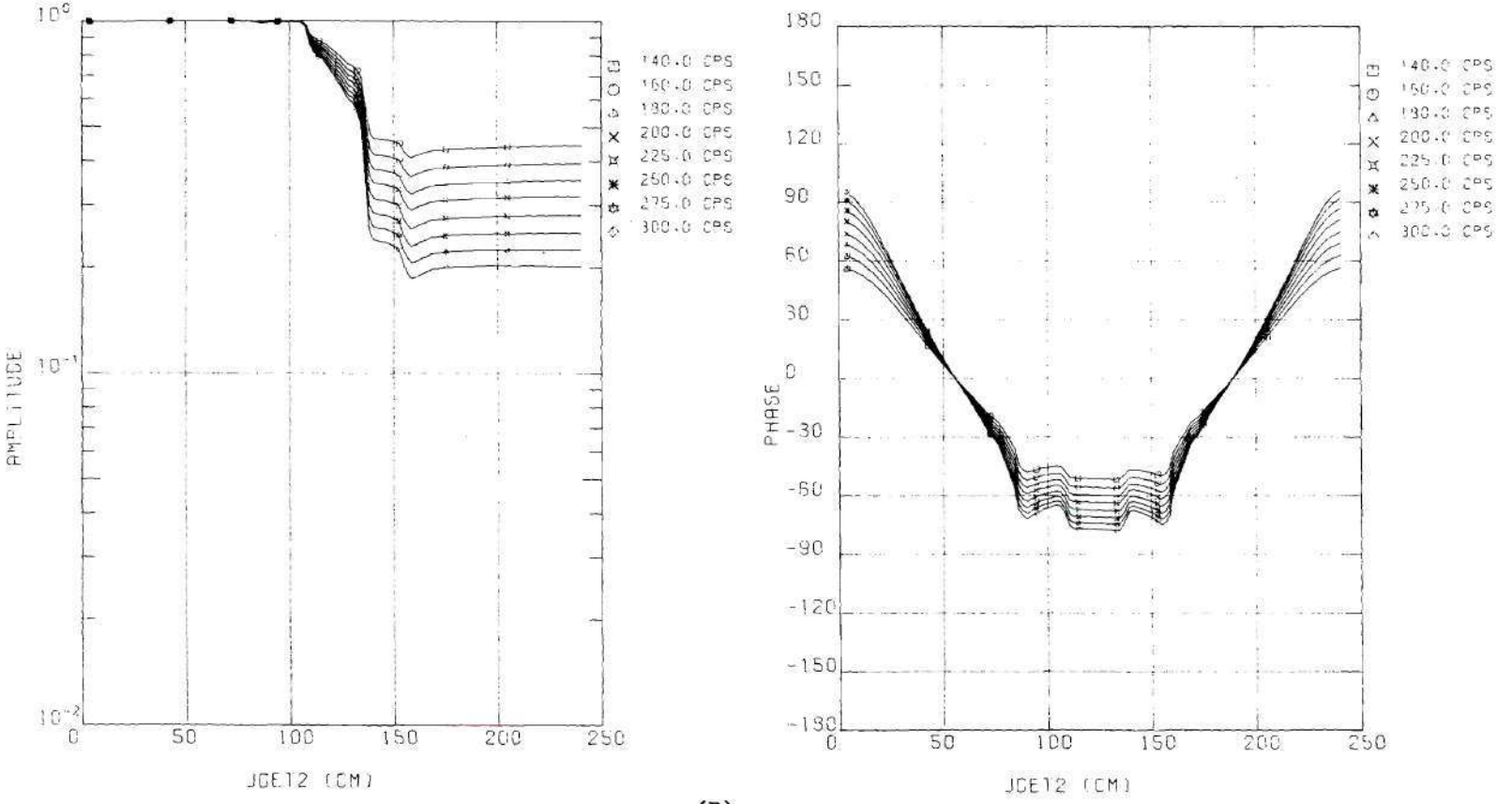

(B)

Figure 38. Concluded

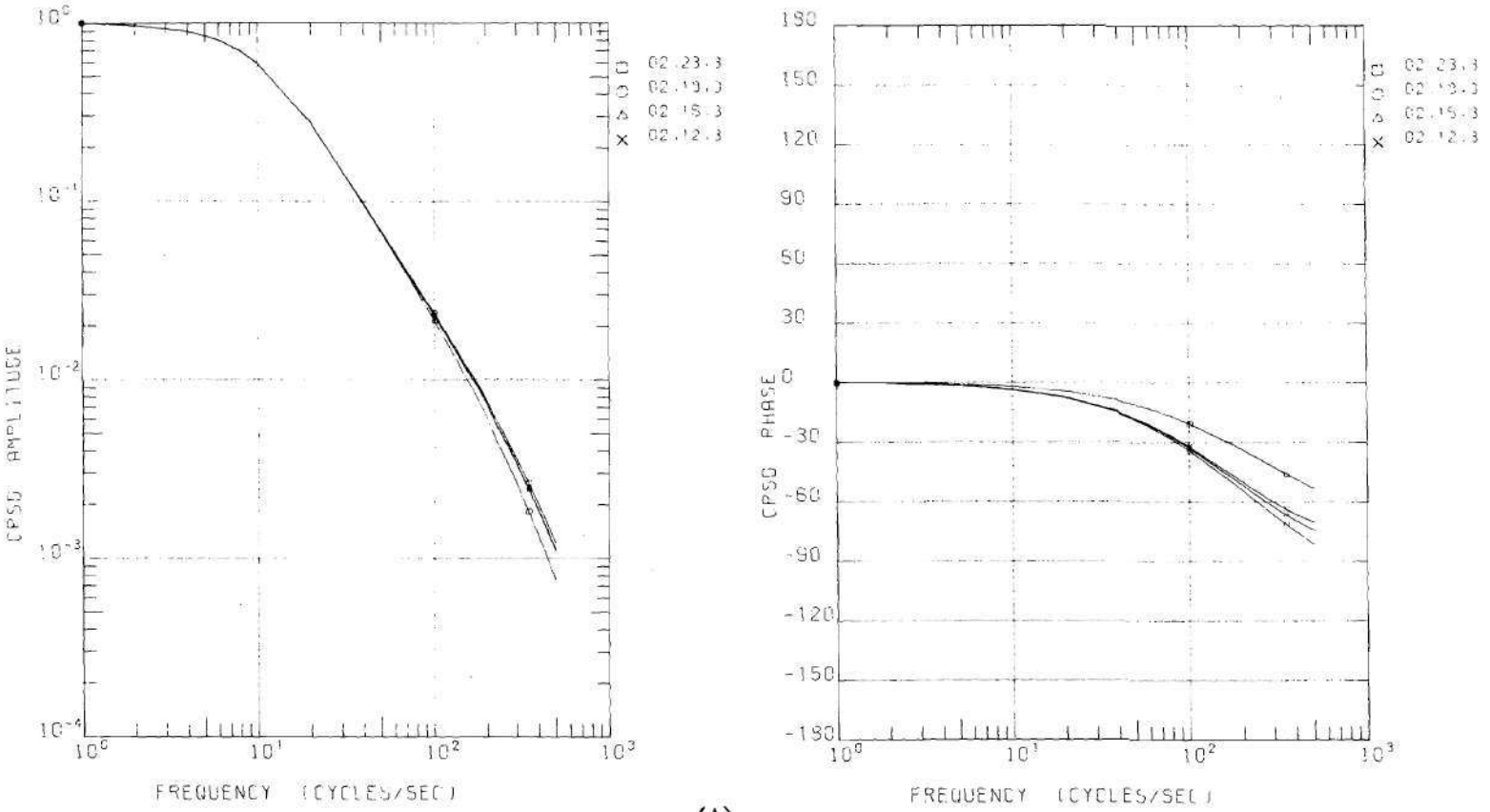

(A)

Figure 39. Calculated Amplitude and Phase of the Two-Dimensional Thermal-Thermal CPSD for STARK Loading II, Detector 1 at Mesh (2,32), Detector 2 at Various Locations

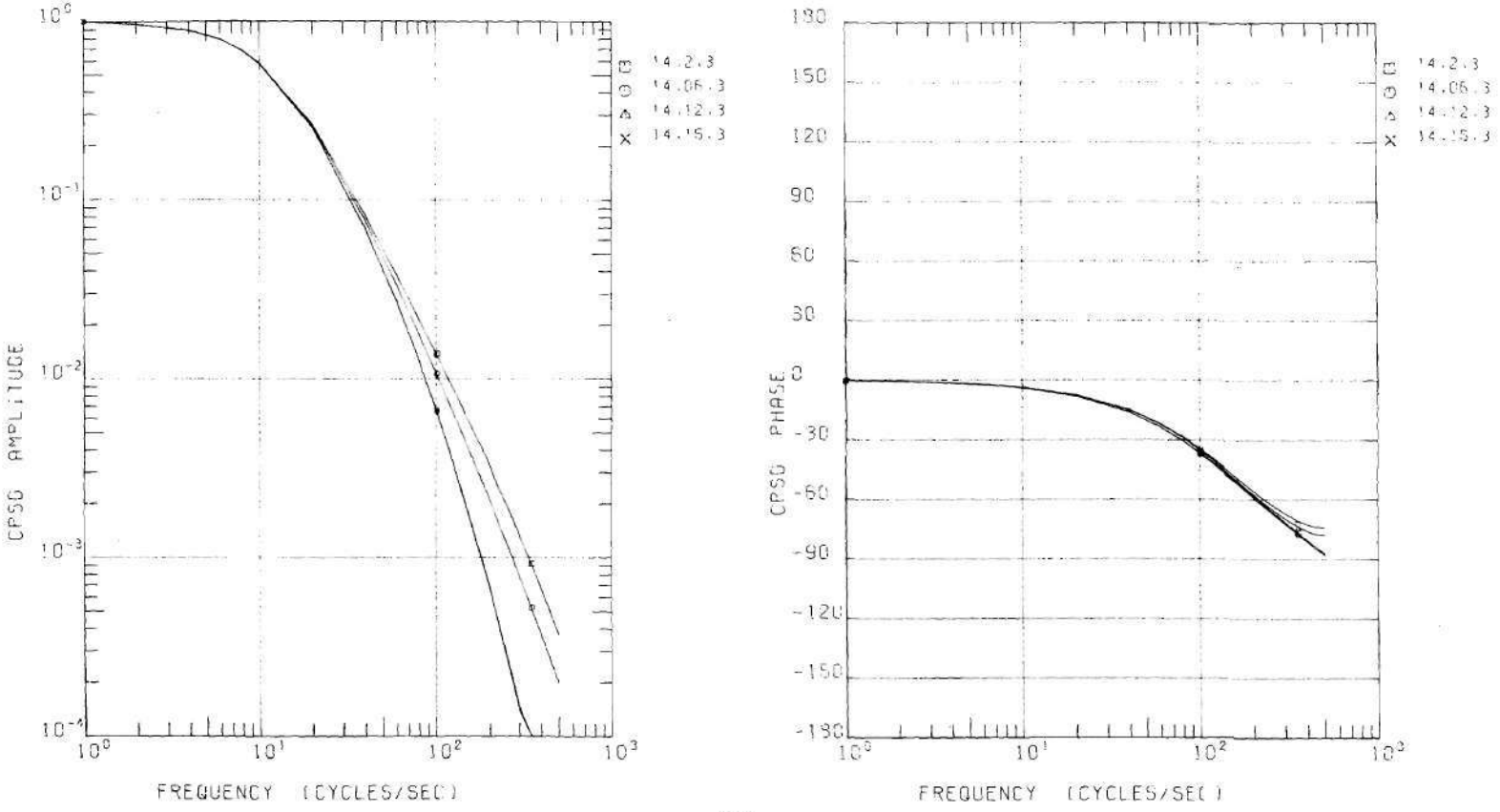

(B)

Figure 39. Continued

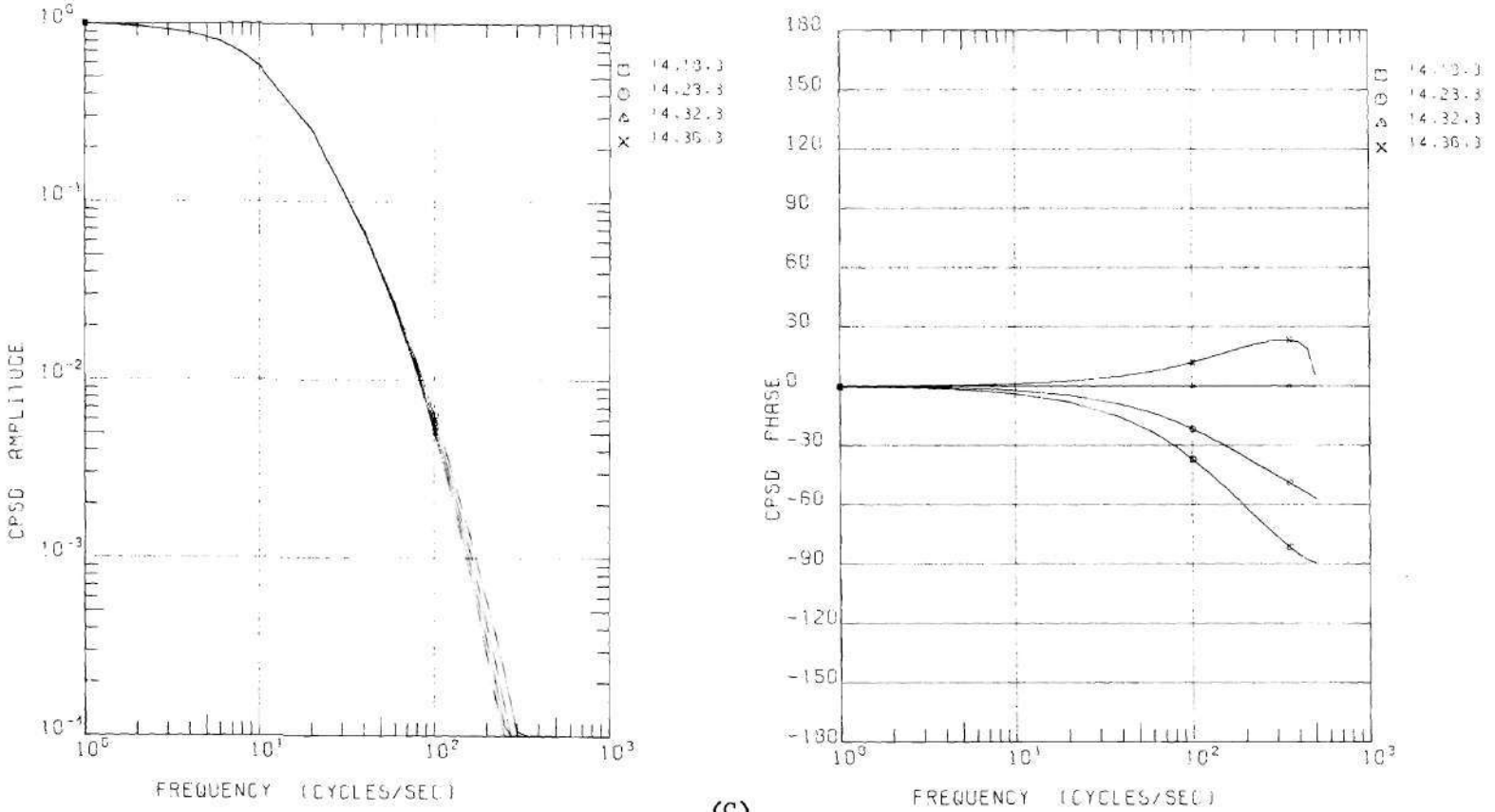

(C)

Figure 39. Concluded

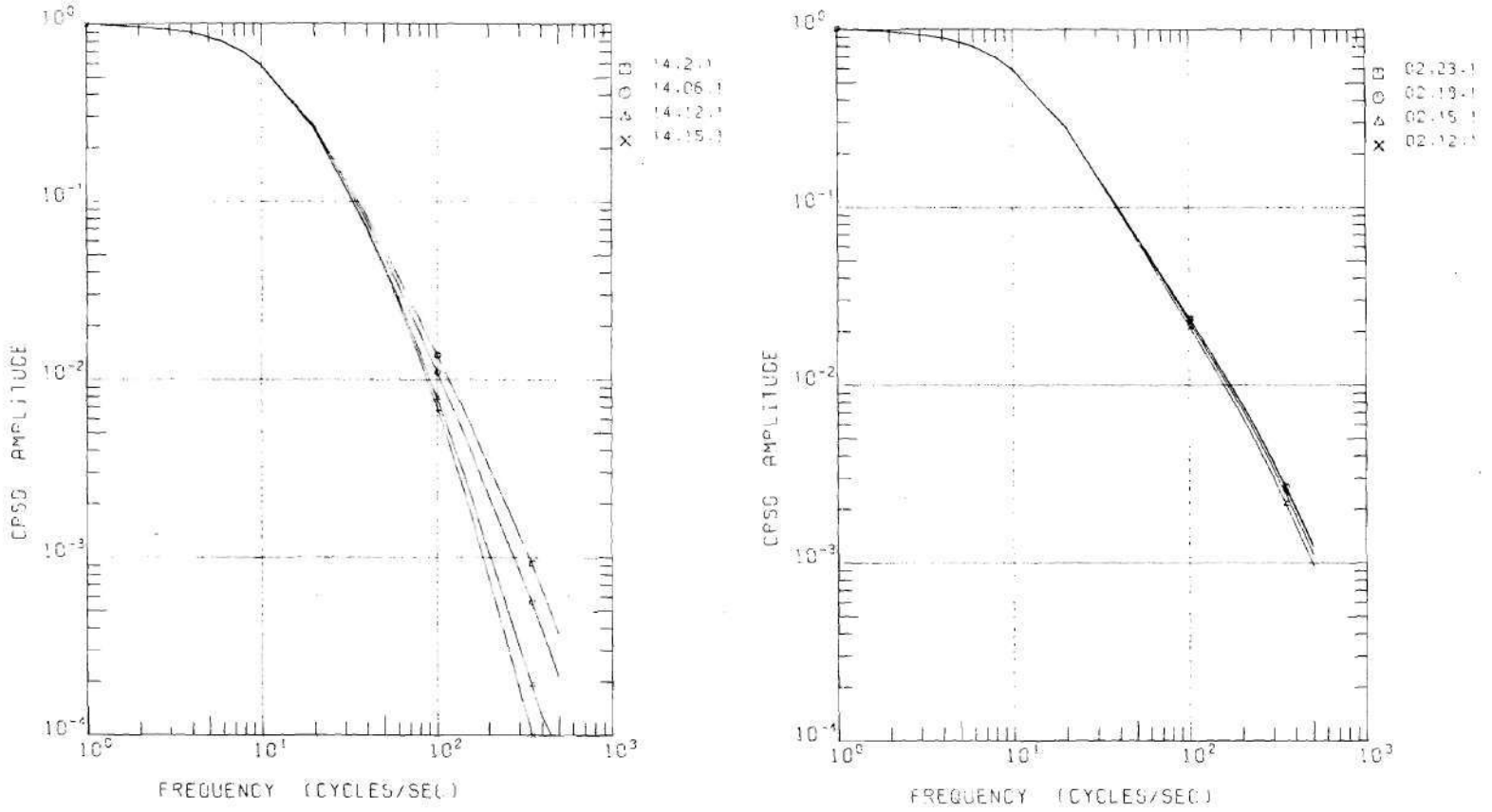

Figure 40. Calculated Amplitude of the Two-Dimensional Thermal-Fast CPSD for STARK Loading II, Detector 1 at Mesh (2,32), Detector 2 at Various Locations

Table 18. Thermal-Thermal and Thermal-Fast CPSD at 1 cps for STARK Loading II, Detector 1 at Mesh (2,32), Detector 2 at Various Reactor Locations

Detector 2 Location θ-r Mesh	Amplitude CPSD at 1 cps	
	Thermal-Thermal	Thermal-Fast
02,23	5.203+01	8.797+01
02,18	5.538+01	1.360+02
02,15	2.212+01	1.214+02
02,12	2.129+00	1.068+02
14,02	5.663-03	8.171+01
14,06	1.374-02	8.538+01
14,12	2.053+00	1.036+02
14,15	2.132+01	1.172+02
14,18	5.326+01	1.307+02
14,23	5.006+01	8.449+01
14,32	3.035+01	1.376+01
14,36	1.770+01	4.249+00

Those values of the amplitude of the CPSD's at 1 cps indicate that there is a strong space-dependency as a function of detector 2 locations. Comparison between the amplitudes of the thermal-thermal and thermal-fast cross-power spectral densities indicates the relatively higher correlation between the detectors, when detector 2 was positioned inside the fast assembly zone and is sensitive to the presence of fast neutrons. The steady state calculations have indeed shown that the fast to thermal flux ratio was there 1.38E+04 for loading II.

When we compare the normalized curves of the amplitudes of the CPSD's, we find that the values inside the coupling region are a factor of five higher at 100 cps, as compared to detector 2 positions in the thermal Argonaut fuel region and the external graphite zone, when taken on radial 14.

We observe that the amplitude of the thermal-thermal CPSD and the thermal-fast CPSD, when normalized to 1 cps, changes rapidly as a function of frequency, when detector 2 is swept throughout the fast core region.

Comparison of the CHF curves with the CPSD curves also shows that the latter are much more frequency-dependent than the CHF. It has been observed by Seifritz and Albrecht[23] in this regard that the CHF depends primarily on the coupling between regions being sampled by the neutron detectors, whereas the CPSD function depends also on the individual characteristics of the regions.

Looking back to the definition of the CHF between detectors, namely that:

$$\mathrm{CHF}(\mathrm{det}_1\ \mathrm{det}_2\omega) = \frac{\mathrm{CPSD}\ (\mathrm{det}_1\ \mathrm{det}_2\omega)}{\sqrt{\mathrm{APSD}\ (\mathrm{det}_1\omega)\ \mathrm{APSD}\ (\mathrm{det}_2\ \omega)}}$$

We realize why the amplitude of the coherence function is less frequency-dependent than the amplitude of the cross-power spectral density: both the APSD's and the amplitude of the CPSD's are decreasing functions of frequency. Their ratio, the amplitude of the CHF, will therefore be less frequency-dependent.

Comparison with STARK Loading II Experiments

The results of our calculational method will now be compared with experimental values for STARK loading II performed by Seifritz, Stegemann, and Väth.[132]

Several experimental determinations of power spectral densities (CPSD and CHF) on fast reactor cores are available in the literature, experiments for which numerical values obtained by our model and numerical approach could be compared [e.g. experimental investigations performed on the sodium-cooled fast reactor SNEAK[133-134] loaded with Pu-fuel, the coupled fast-thermal critical facility STEK[116], etc.].

It was, however, decided to perform the comparison with experimental investigations performed on STARK, because it is an extension of the TARK reactor, for which minima in the amplitude of the CHF were found experimentally and theoretically. The basic characteristics of STARK have been described earlier. The principal characteristics of STARK and the experimental setup by Seifritz, Stegemann, and Väth[132] were:

--Internal coupling region of TARK was replaced by 37 fast uranium assemblies, surrounded by a natural uranium blanket. The internal coupling region is 24 inches.

--The fast zone contained 44.59 kg U-235.[44]

--The thermal Argonaut zone contained 6.53 kg U-235 contained in 313 fuel plates (experimentally determined). (Note: The ABN 26 group set predicted[44] 6.911 kg U-235 contained in 332 fuel plates.) Those fuel plates were distributed over the 24 Argonaut assemblies of the thermal Argonaut zone (13 fuel plates per assembly). The moderator in the Argonaut zone was light water at 80°C.

--In the fast core, two He^3 filled detectors were used in the current mode (upper break frequency detector channel 132 cps).

--In the external graphite reflector, two B^{10} loaded compensated ion chambers were used (upper break frequency detector channel 33 cps).

--Experimental relative standard deviation of CPSD between He^3 detector 1, located in the center of the fast assembly region, and He^3 detector 2, at the boundary of the fast assembly region: 3.5%.

In Figure 41 we have plotted the values of the amplitude of the CPSD for STARK loading II as determined experimentally, and as determined by two-dimensional calculations using our model and numerical approach. Detector 1 (He^3) was positioned in the center of the fast assembly region, and detector 2 (He^3) was positioned at the outer boundary of this region.

The CPSD's were determined for the presence of the inherent distributed stochastic fission sources. Zone-dependent effective delayed neutron fractions for U-235 and U-238, as determined previously, were used in the calculations. The broad-group cross sections, determined from cell spectrum weighted collapses, followed by zone spectrum weighted collapses from ENDF/B-II sets, as explained previously, were used.

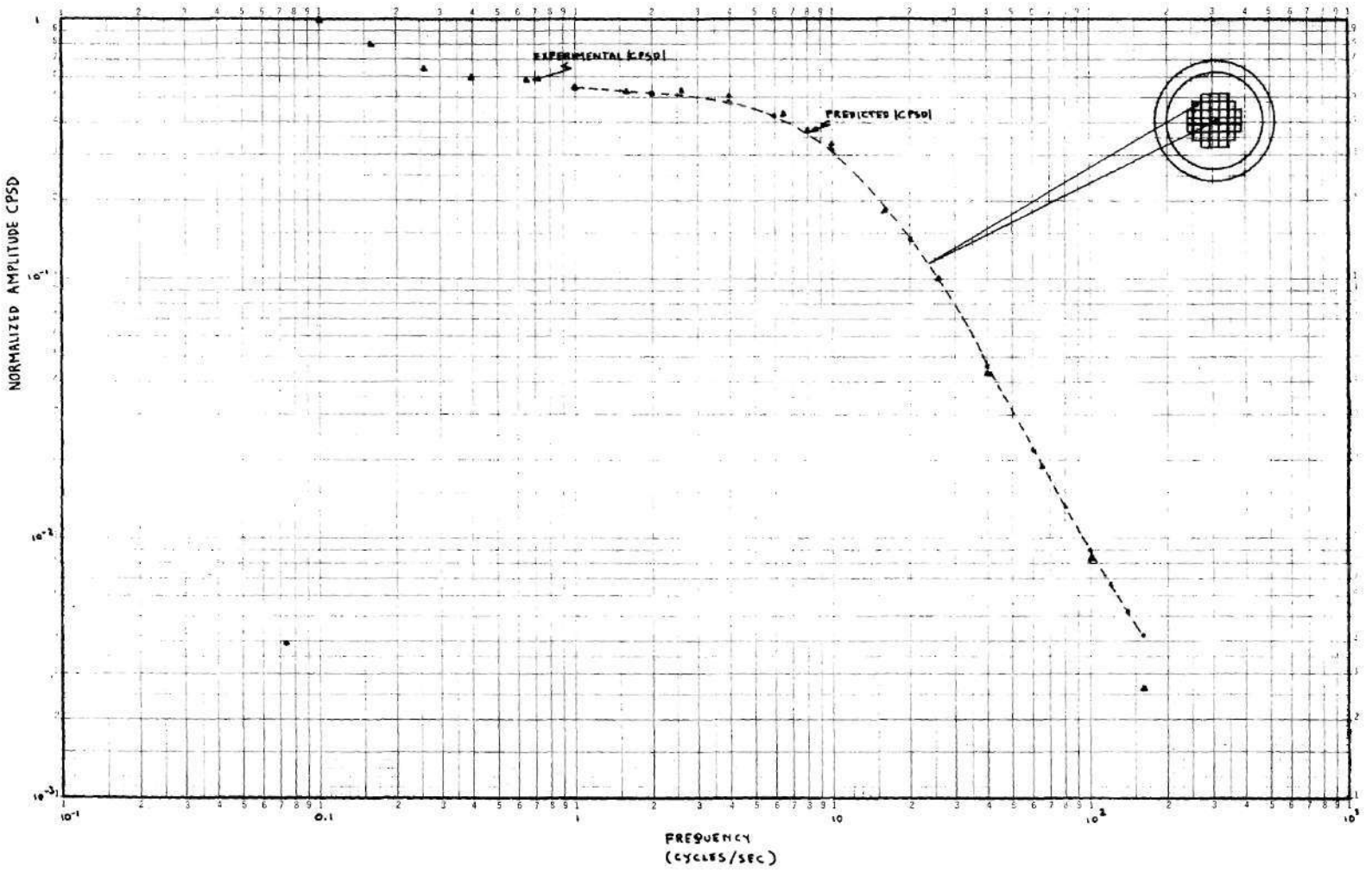

Figure 41. Comparison of Experimental and Calculated CPSD in the Fast Core of STARK Loading II

Comparison between the experimental and calculated values shows that the agreement is excellent for the frequency range investigated. However, above 100 cps, there exists some disagreement between the experimental point at 160 cps and the calculated value. It is not known if this is due to the presence of the upper break frequency of the He^3 detector channel at 132 cps. It is possible that proper correction of this experimental point at 160 cps would bring theoretical and experimental values closer together at 160 cps.

It must be noted that the use of the CHF, which is a normalization of the CPSD with the APSD's of each detector, removes the dependency of the measurement on the transfer properties of the measuring detector channel. The use of the CHF in the experiments would perhaps have been more appropriate.

In Figure 42 we have displayed some additional results of the two-dimensional CPSD calculations for STARK loading II, with detector 1 held in the center of the fast assembly region. On each amplitude plot, the amplitudes of the CPSD for different locations of detector 2 were normalized to a value of 1.0 at a frequency of 1 cps. The values of the amplitudes of the thermal-thermal CPSD's at 1 cps are listed in Table 19.

The thermal-thermal amplitude of the CPSD between detector locations close to the center of the fast assembly region was very small. This minimal decrease is even more accentuated in loading IV, because of the even lower values of the thermal broad-group fluxes in the fast assembly region. In contrast, the amplitude of the thermal-fast CPSD's between detector locations close to the center of the fast assembly show maximum values, many orders of magnitude higher than the amplitude of the thermal-

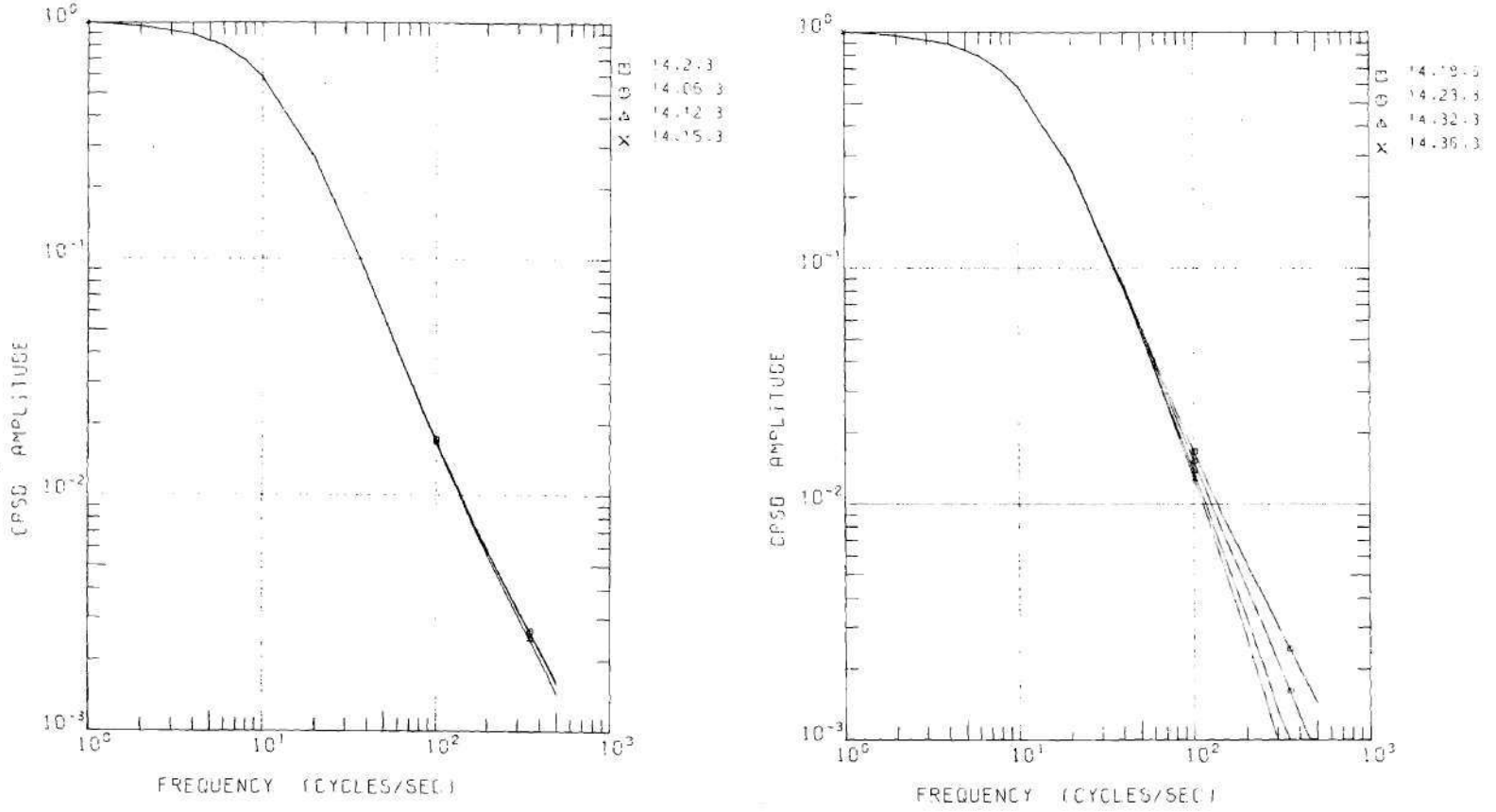

Figure 42. Calculated Amplitude of the Two-Dimensional Thermal-Thermal CPSD for STARK Loading II, Detector 1 at the Center of the Fast Core

Table 19. Thermal-Thermal CPSD at 1 cps for STARK Loadings II and IV, Detector 1 at the Center of the Fast Core, Detector 2 at Various Reactor Locations

Detector 2 Location (θ-r Mesh)	Amplitude CPSD at 1 cps Thermal-Thermal	
	Loading II	Loading IV
02,23	9.360-03	2.822-04
02,18	9.959-03	2.925-04
02,15	3.983-03	1.221-04
02,12	3.835-04	1.126-05
14,02	1.040-06	1.485-09
14,06	2.541-06	1.774-08
14,12	3.831-04	1.125-05
14,15	3.978-03	1.221-04
14,18	9.947-03	2.922-04
14,23	9.349-03	2.820-04
14,32	5.663-03	1.635-04
14,36	3.302-03	9.533-05

thermal CPSD's. This was even more accentuated for loading IV.

In conclusion, we can say that our theoretical model and numerical approach agree well with the experimental results with which they were compared. Some improvements, however, could have been introduced into the calculations such as the use of many more broad groups. However, due to the sizable increases in computer time that would have been entailed, this was not done.

CHAPTER VIII

STUDY OF THE POWER SPECTRAL DENSITY OF THE GTRR COUPLED-CORE AND FULL-CORE CONFIGURATIONS

The theoretical and experimental phase of the Power Spectral Density (PSD) studies reported in this chapter were performed on the Georgia Tech Research Reactor (hereafter referred to as GTRR), which is a heterogeneous, D_2O moderated and cooled, highly enriched reactor.

Brief Description of the Georgia Tech Research Reactor

For a full description of the reactor we refer to the GTRR Safety Analysis Reports.[135,136] A brief description of the GTRR follows. The reactor core configuration consists of fuel assemblies standing vertically in the plenum of the core tank and arranged on a 6.0 in. triangular pitch. The fuel assemblies are centrally located in a six ft diameter aluminum reactor vessel, which is filled with high quality heavy water (assumed approximately 99.77 w% D_2O). The fully loaded core contains 19 fuel assemblies as shown in Figure 43. Figure 43 is a horizontal section of the GTRR taken at the core mid-plane. The position of the horizontal beam tubes numbered H-1 through H-10, which are all centered at the core mid-plane, is also displayed. Those beam holes are plugged up with graphite stringers in normal operation. The six ft diameter aluminum vessel is surrounded by an additional two ft thick graphite reflector (on the sides and beneath the Al reactor vessel). A general view of the full assemblies, the semaphore control blades, and the beam tubes is displayed in Figure 44.

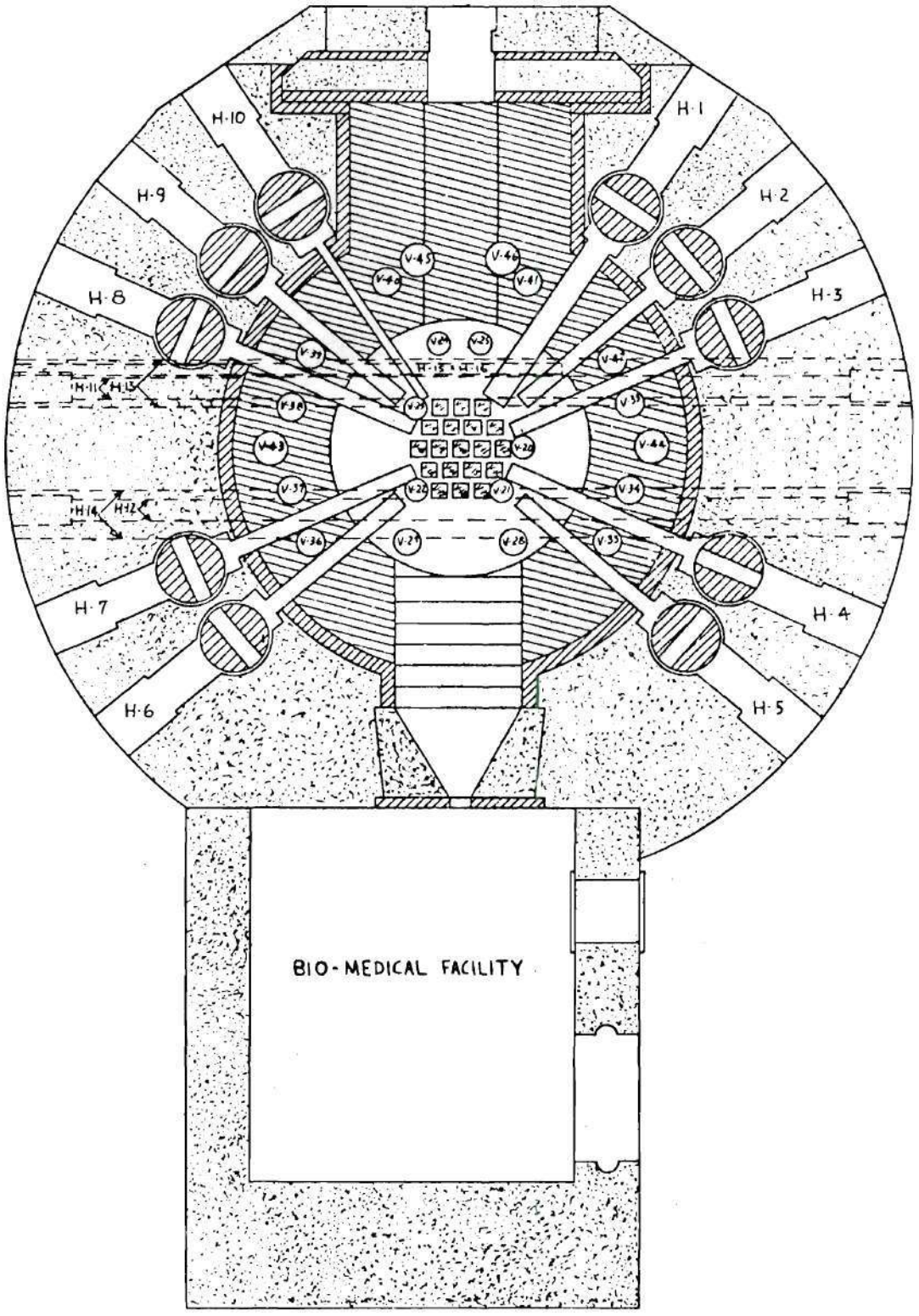

Figure 43. Horizontal Section of the GTRR Reactor at the Core Mid-Plane

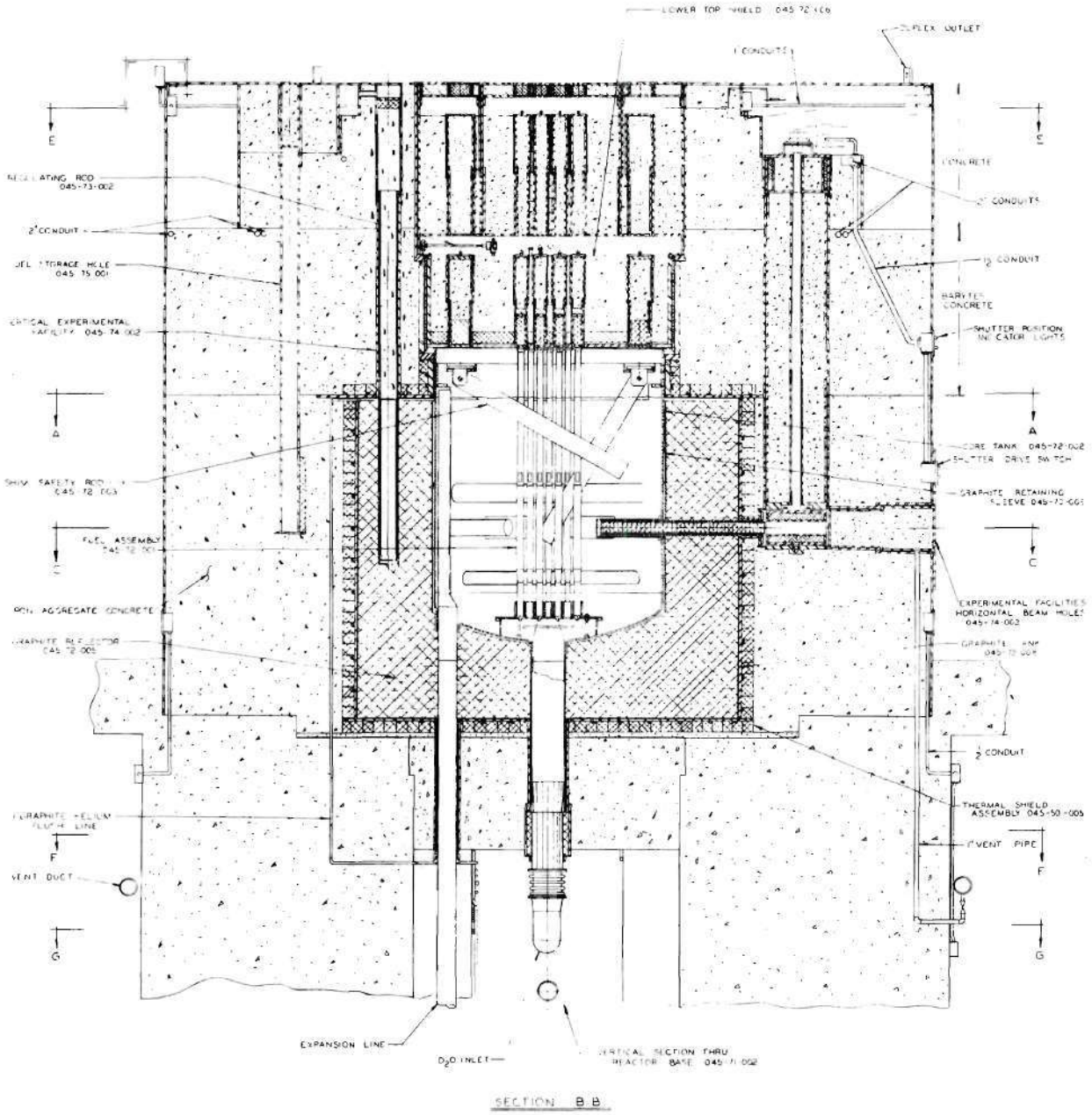

SECTION B-B

Figure 44. Vertical Section of the GTRR Reactor

The reactor is controlled with four semaphore control blades (Shim blades) and one fine control regulating rod. The shim blades are flat, hollow blades of cadmium metal 0.020 in. thick, clad inside and outside with 0.083 in. thick aluminum type 6061-T6. The blades are 5.5 in wide, one in. thick, cadmium length 45.5 in., total length from pivot point 60.75 in. The active fuel height of the reactor is 23.5 in. On top and bottom of this active fuel region, we have approximately two ft of D_2O axial reflector. Two different standard fuel assembly types are available in the GTRR, hereafter referred to as Mark I and Mark II fuel. The principal characteristics are:

Mark I Fuel (see Figure 45)

Contains ten individual curved Al-U alloy plates 0.020 in. thick and 23.5 in. in height, clad with 20 mill Al-1100 over the faces, and 0.205 in. over the edges. Coolant flow passages are nominally 0.183 in. thick by 2.620 in. wide.

The finished fuel plate is 0.060 in. thick, 2.886 in. wide, 25 in. long, 5.5 in. radius of curvature.

Each fuel plate contains approximately 14.2 ± 0.028 grams U235 (enrichment in U235 is 93.18 w/o of U).

On each side of the assembly of the ten curved fuel plates, we have a 60 mill thick aluminum dummy plate.

The fuel bearing section of the assemblies is a completely enclosed box 2.996 by 2.921 by 27.5 in. long.

Mark II Fuel

Contains 16 individual curved Al-U alloy plates 0.020 in. thick, and 23.5 in. in height, clad with 15 mill Al-1100. The fuel matrix is

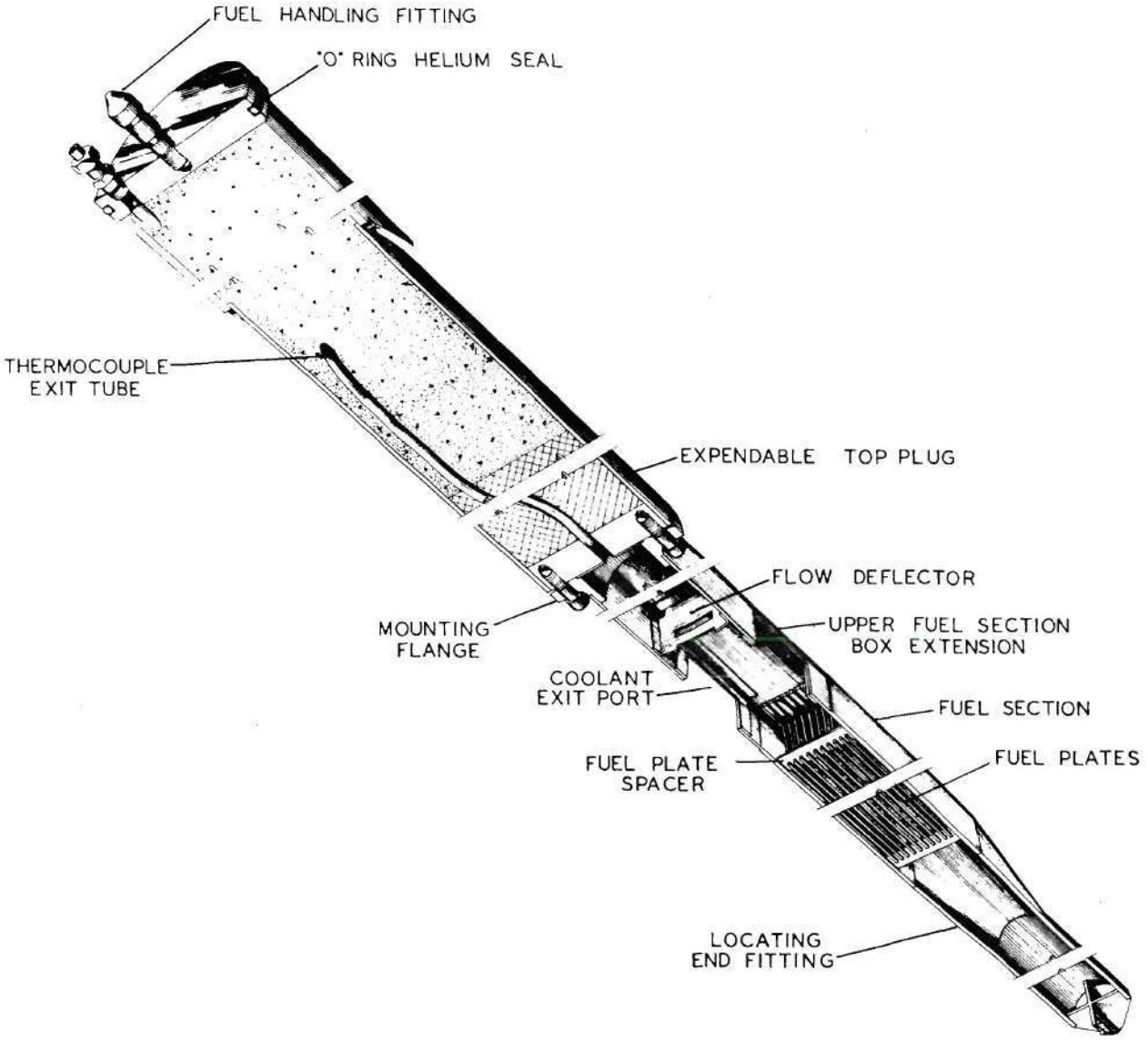

Figure 45. Perspective of GTRR Fuel Assembly Mark-I and Lower Shield Plug

2.5 in. wide, Coolant flow passage is nominally 0.106 in. thick by 2.583 in. wide. The finished fuel plate is 0.050 in. thick, 2.848 in. wide, 25 in. long, and 5.5 in. radius of curvature. Each fuel plate contains approximately 11.75 ± 0.024 grams U235. On each side of the assembly of 16 curved fuel plates, we have a 50 mill thick aluminum dummy plate.

The total fuel bearing section of the assembly is a completely enclosed box 2.959 by 2.772 by 27.5 in. long.

Generation of Neutron Cross Sections for the GTRR

In Figure 46 we have displayed a cross-sectional area of the GTRR core lattice, in which up to 19 standard fuel assembly positions are available. The number of fuel assemblies and their position within the core lattice can be changed. Each fuel assembly is kept from rotating by means of special slots in the lower shield plug located at the top of each assembly.

Calculations were performed for Mark-I type of GTRR fuel assemblies. The fuel plates of each fuel assembly were homogenized into a fuel bearing area which forms a rectangular box of 3.0 by 2.456 by 23.5 in. long.* The cross-sectional area is therefore 7.368 in^2. In the generation of the number densities, the following material characteristics were used:

*3.0 in. instead of 2.730 in. was used. This enables us reduction of the number of mesh points in the y-direction by a factor of five. In iterations based on difference schemes, it is mandatory that adjacent mesh intervals do not vary by more than a factor of two in order to obtain accurate solutions of the flux. This reduction in mesh points enabled us to keep the computer time down in the PSD calculations.

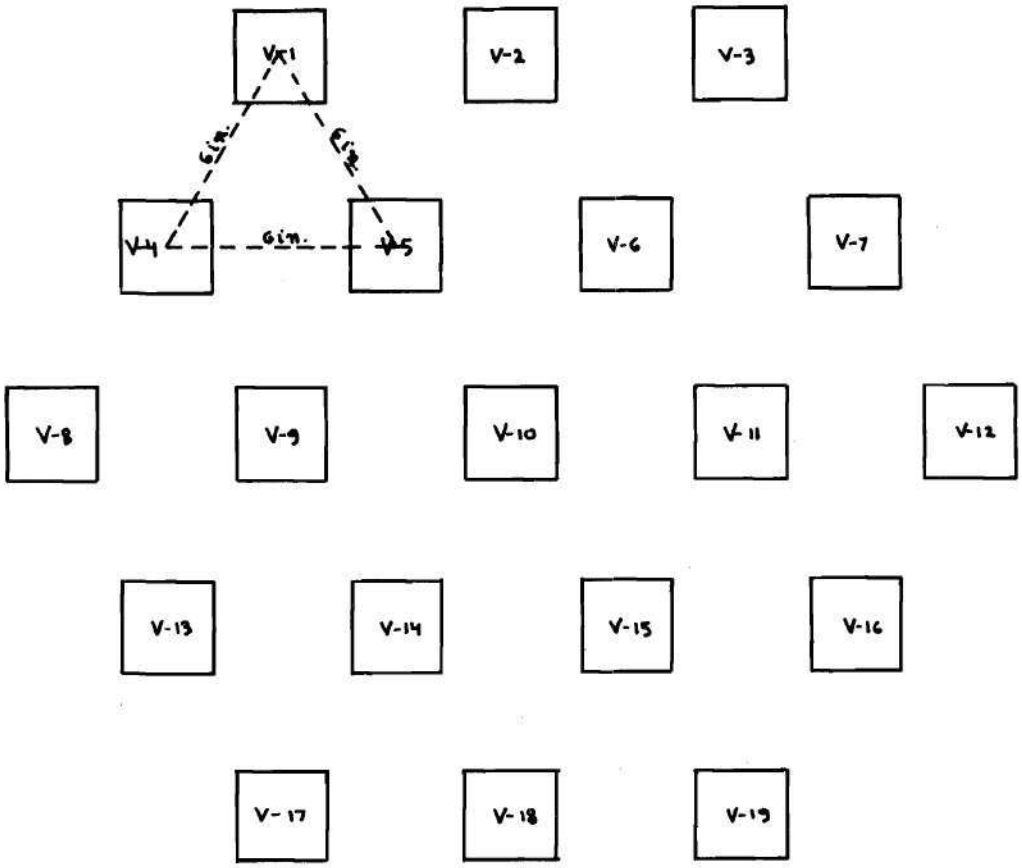

Figure 46. Nineteen Fuel Assembly Core Lattice GTRR

D_2O moderator: 99.77 w/o D_2O, 0.23 w/o H_2O

Enrichment in U235: 93.18 w/o of U

Fuel assembly loading: 142.19 grams U235 + 10.41 grams U238

Al-1100: 2.71 grams/cc, 26.98 at. wt.

C (Agot graphite): 1.70 grams/cc, 12.01 at. wt.

D_2O: 1.1049 grams/cc at 22°C, 20.028 at. wt.

H_2O: 0.9978 grams/cc at 22°C, 18.015 at. wt.

U: 19.05 grams/cc

Table 20 gives the number densities for the GTRR.

To take into account the effect of leakage on the spectrum, used in the generation of the broad group cross-sections, the following buckling correction factor was inputted into codes FORM[137] and TEMPEST[138]:

$$B^2 = B_z^2 + B_r^2 \quad \text{with} \quad B_z^2 = \left(\frac{\pi}{H + 2\delta}\right)^2 \quad \text{and} \quad B_r^2 = \left(\frac{2.405}{R + \delta}\right)^2$$

where H: height = 59.7 cm

δ: extrapolation distance 10.7 cm

R: radius core

We therefore obtain that $B^2 = 0.0015 + 0.0030 = 0.0045\ cm^{-2}$

The fast broad group cross-sections were generated with FORM,[137] which is a Fourier Transform Fast Spectrum Code. The FORM cross-section library tape used contains a 54 group microscopic cross-section set, including the resonance parameters, inelastic scattering matrices, and source spectra. The resonance self-shielding factor for U235 and U238 was taken to be 0.995. The following options were used:

B_1 approximation

Table 20. Number Densities for GTRR Mark-I Fuel

Mixture	Material	Number Density Nuclei/cc x 10^{24}
Fuel Assembly	U-235	1.2835-04
	U-238	9.2784-06
	Al	1.5458-02
	D	4.0926-02
	H	1.048-04
	O	2.051-02
D_2O Moderator	D	6.614-02
	H	1.700-04
	O	3.322-02
Graphite	C	8.524-02

the hydrogen slowing down was treated exactly

the self-consisting age option for the heavy element slowing down

broad energy breakpoints: a) Group 1 → 54

b) Groups 1 → 10, 11 → 25, 26 → 54

the complete U235 fission source was used

The results of the fast broad group cross-sections are tabulated in Table 21. The thermal broad-group cross-sections were generated with TEMPEST-II,[138] which is a neutron thermalization code based upon the Wigner-Wilkins approximation for light moderators, and the Wilkins approximation for heavy moderators. A standard library for TEMPEST was used. The thermal broad-group cross-sections thus obtained are:

Mixture	D (cm)	Σa (cm^{-1})	$\nu\Sigma f$ (cm^{-1})	Σtr (cm^{-1})
Homogenized Fuel	1.076	5.428-02	0.1067	0.3259
D_2O moderator	0.8374	8.118-05	0.0	0.4105
Graphite	0.8619	2.811-04	0.0	0.3867

Two-Dimensional Multi-Group Stochastic Coherence Function of the Coupled-Core GTRR

Different configurations of the GTRR fuel assemblies within the core lattice are possible. In Figure 46 we have displayed a 19 assemblies configuration, which is the maximum possible in the present core lattice. The excess reactivity is controlled by properly adjusting the four shim

Table 21. Fast Broad-Group Cross-Sections GTRR*

	Output	D (cm)	Σa (cm^{-1})	Σf (cm^{-1})	$\nu\Sigma f$ (cm^{-1})	Σr (cm^{-1})	ρ	τ (cm^2)
Homogenized Fuel	1 of 1	1.502	2.787-03	1.640-03	4.040-03	4.375-03	0.611	209.72
	1 of 3	2.279	1.097-03	0.170-03	0.470-03	6.667-02	0.984	25.17
	2 of 3	1.293	0.459-03	0.289-03	0.714-03	2.514-02	0.982	75.65
	3 of 3	1.458	5.215-03	3.188-03	7.837-03	9.277-03	0.640	176.23
Moderator D_2O	1 of 1	1.314	0.156-03	0.0	0.0	9.517-03	0.984	135.81
	1 of 3	2.239	1.276-03	0.0	0.0	8.468-02	0.985	19.49
	2 of 3	1.186	0.0	0.0	0.0	3.576-02	1.0	52.66
	3 of 3	1.186	0.0	0.0	0.0	1.786-02	1.0	119.04
Graphite	1 of 1	1.111	0.0	0.0	0.0	2.338-03	1.0	475.31
	1 of 3	2.173	0.0	0.0	0.0	2.730-02	1.0	59.55
	2 of 3	0.987	0.0	0.0	0.0	1.021-02	1.0	156.14
	3 of 3	0.873	0.0	0.0	0.0	5.195-03	1.0	324.24

*B^2 = 0.0045 cm^{-2} and 22°C.

control blades. The coupled-core configuration is obtained by removing assemblies Number V-8 through V-12 from the core. The core lattice is displayed in Figure 47. The coupled-core configuration contained two coupled cores, each containing seven GTRR assemblies. A crude investigation of the possible presence of minima in the PSD can be made by comparing the coupled core GTRR with a parametric one-dimensional study performed by Nagy and Danofsky[17] for two infinite fuel slabs separated by different thicknesses of heavy water coupling region. We observe that several D_2O coupling region thicknesses are present in the coupled-core GTRR. Basically let us identify three of them:

Coupling region between fuel assemblies as number V-4 and V-13, placed in the lattice on a pitch of 26.4 cm. From Figure 3 of reference (17) this would give a first minimum in the amplitude at approximately 200 cps.

Coupling region between fuel assemblies as number V-1 and V-13, placed on a pitch of 39.6 cm. This would give a minimum in the range of 95 cps.

Coupling region between fuel assemblies as number V-1 and V-17, placed on a pitch of 52.8 cm. Minimum would be in the range of 25 cps. Since the presence of a minimum in the PSD corresponds to the presence of interference effects of neutronic waves from one fuel assembly to another, we can say from this that the presence of minima in the PSD are likely in the coupled-core GTRR. Let us now investigate this more accurately using the model and numerical approach described in Chapters III and IV. Considering the reactor geometry in Figure 47 we observe that it would be impossible to locate the precise location of those minima for the coupled

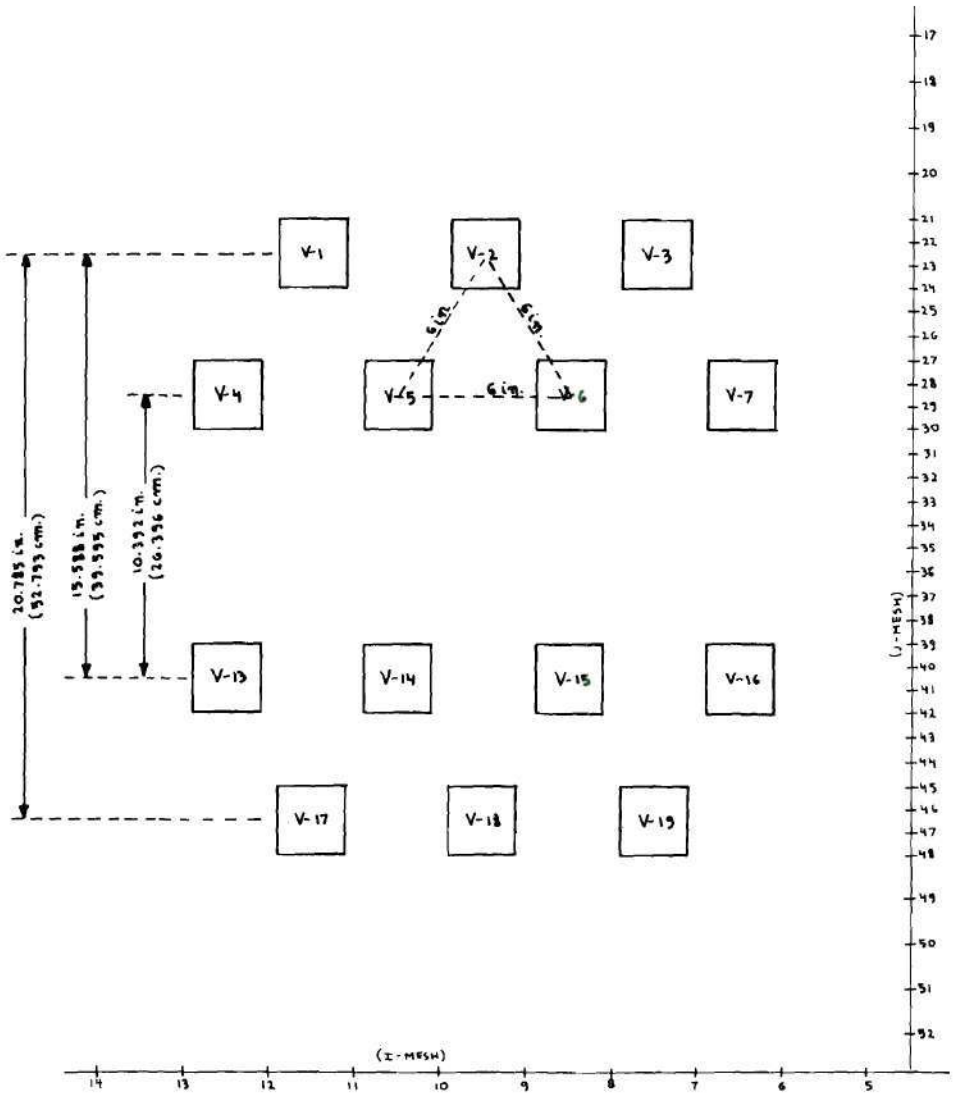

Figure 47. Fourteen Assembly GTRR Coupled-Core Configuration

core GTRR, unless we take into account in the analysis the true configuration of the core lattice. Let us observe that a one-dimensional analysis cannot take into account effects like interactions from couplings between assemblies V-4 - V-14, V-4 - V-15, and many others. Also the neutronic coupling from assembly V-1, through the heavy water region between assembly V-4 and V-5, to assembly V-13, is very much affected if it has to go through a solid one-dimensional fuel slab (that would be composed of assemblies V-4, V-5, V-6, and V-7). We have seen that a 90 degree phase shift in the neutronic coupling between fuel regions causes an interference effect of neutronic waves. This 90 degree phase shift is the result of both the phase shift of the response of the coupled cores to perturbations, and the phase shift due to neutron time delays. Because in the coupled-core GTRR there are a multitude of different types of couplings between assemblies, only a full blown two-dimensional analysis would be able to locate minima precisely. The coupled-core GTRR could be considered as a four "partial-slab" configuration. The schematic with an x-y mesh shown in Figure 48 was used in the two-dimensional multi-group calculations of the coherence function. In the numerical analysis the number of columns was 68 and the number of rows 18. The column and row numbers with their correspondent x- and y-values are listed in Table 22. The axial leakage in the third dimension was taken into account with the usual axial buckling correction. For the region surrounding the external graphite reflector, a rod group constant of 0.4692 was specified in place of the macroscopic absorption cross-section. Since the values of the steady-state fluxes are needed for the proper weighting of the distributed inherent stochastic fission sources, a steady-state flux distribution had to be

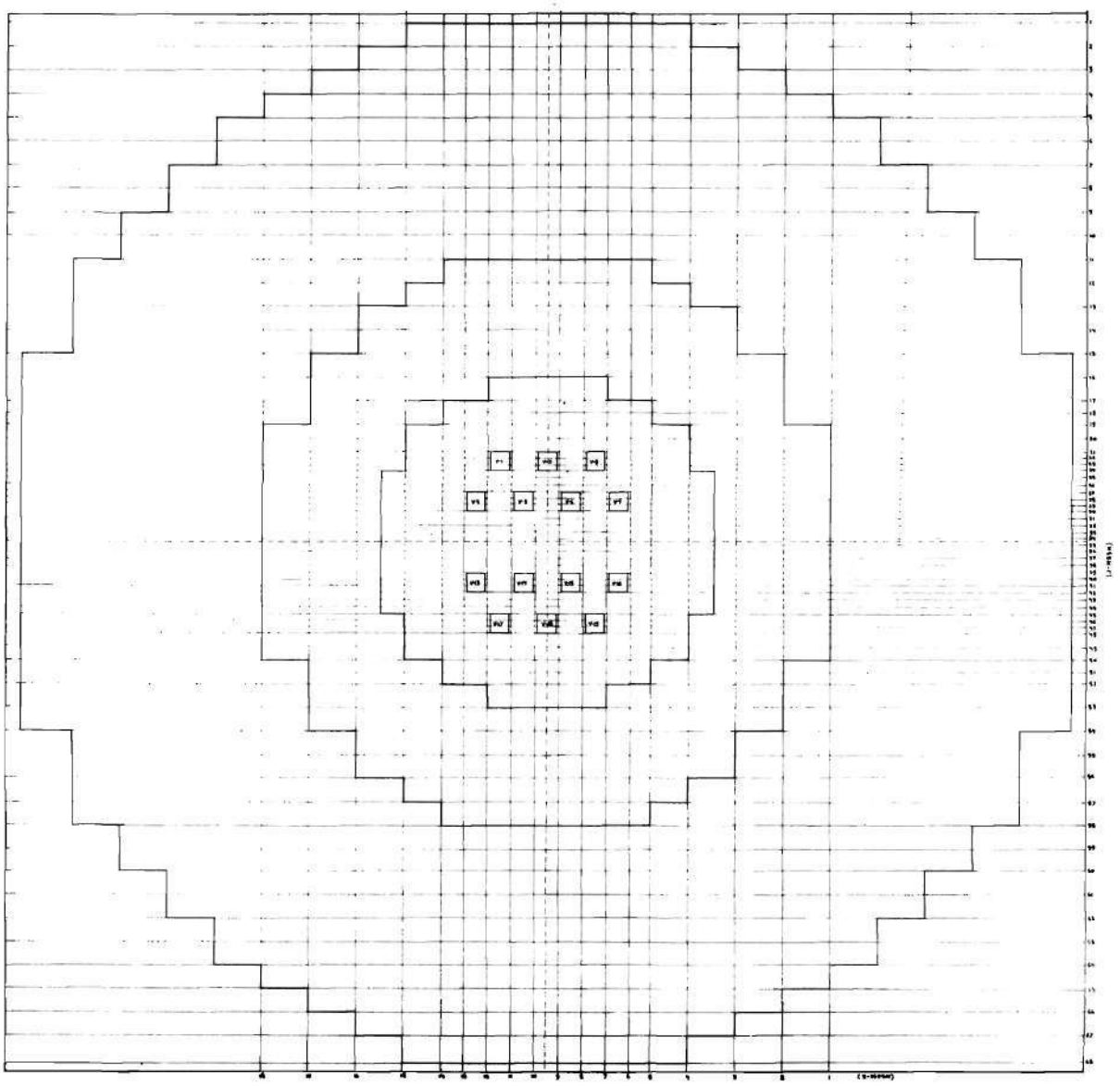

Figure 48. Fourteen Assembly Coupled-Core GTRR with x-y Mesh Layout

Table 22. Column and Row Numbers and Corresponding x- and y-Values for the GTRR Coupled-Core Configuration

"J" Distribution (Column Number - x-Value (cm))

1	0.0	2	7.620	3	15.240	4	22.860	5	30.480
6	38.100	7	45.720	8	53.340	9	60.960	10	68.580
11	76.200	12	83.820	13	91.440	14	99.060	15	106.680
16	114.300	17	121.920	18	125.971	19	130.023	20	134.074
21	138.125	22	140.205	23	142.284	24	144.363	25	146.683
26	149.003	27	151.323	28	153.402	29	155.482	30	157.561
31	159.881	32	162.201	33	164.521	34	166.600	35	168.680
36	170.759	37	173.079	38	175.399	39	177.719	40	179.798
41	181.878	42	183.957	43	186.277	44	188.597	45	190.917
46	192.996	47	195.075	48	197.155	49	201.206	50	205.257
51	209.309	52	213.360	53	220.980	54	228.600	55	236.220
56	243.840	57	251.460	58	259.080	59	266.700	60	274.320
61	281.940	62	289.560	63	297.180	64	304.800	65	312.420
66	320.040	67	327.660	68	335.280				

℄ 167.64 cm

"I" Distribution (Row Number - y-Value (cm))

1	0.0	2	15.240	3	30.480	4	45.720	5	57.498
6	65.118	7	72.738	8	80.358	9	87.978	10	95.598
11	103.218	12	110.838	13	118.458	14	126.078	15	137.856
16	153.096	17	168.336	18	183.576				

℄ 91.788 cm

obtained first. The material composition of the reactor was assumed homogeneous in the axial direction, and in order to ensure that the calculations of the PSD's were performed for a mathematically critical steady-state reactor ($k_{eff} = 1$), the axial height of the reactor was adjusted uniformly over the reactor. In order to obtain this critical axial height, a poison search was performed using a zone-dependent $D^g B_z^2 \phi^g$ correction factor for transverse leakage using a modified version of EXTERMINATOR-II,[82] until a value of $k_{eff} = 1$ was obtained for the steady-state core. A convergence criterion on the point fluxes and on k_{eff} of 1.0E-4 was used for the steady-state calculations. An axial buckling of $B_z^2 = 1.365465\text{-}03$ was thus obtained, which represents a critical height of 85.0 cm.

In Figure 49 we have plotted some of the steady state broad group fluxes. The steady state fluxes were normalized to give for the integral $\int_{\text{Reactor}} dv \sum_g \nu\Sigma f^g \phi^g$ a value of 1.0. In Figure 49 we observe that the value of the thermal flux in the D_2O coupling region between the coupled cores (each core composed of seven GTRR assemblies) was almost twice as high as the thermal flux in the adjoining assemblies. The fast flux, however, was twice as low in the adjoining assemblies. This is a characteristic behavior of a flux trap. The same mesh grid as was used in the steady state calculations (see Figure 48) was used for the calculation of the CHF. Our TDPSD (Two-Dimensional Power Spectral Density) code was used for the CHF calculations. In Figure 48 we see that two symmetry axes are present. They split the reactor into four quadrants. The presence of those symmetry axes was used in the PSD calculations to save computer time in the

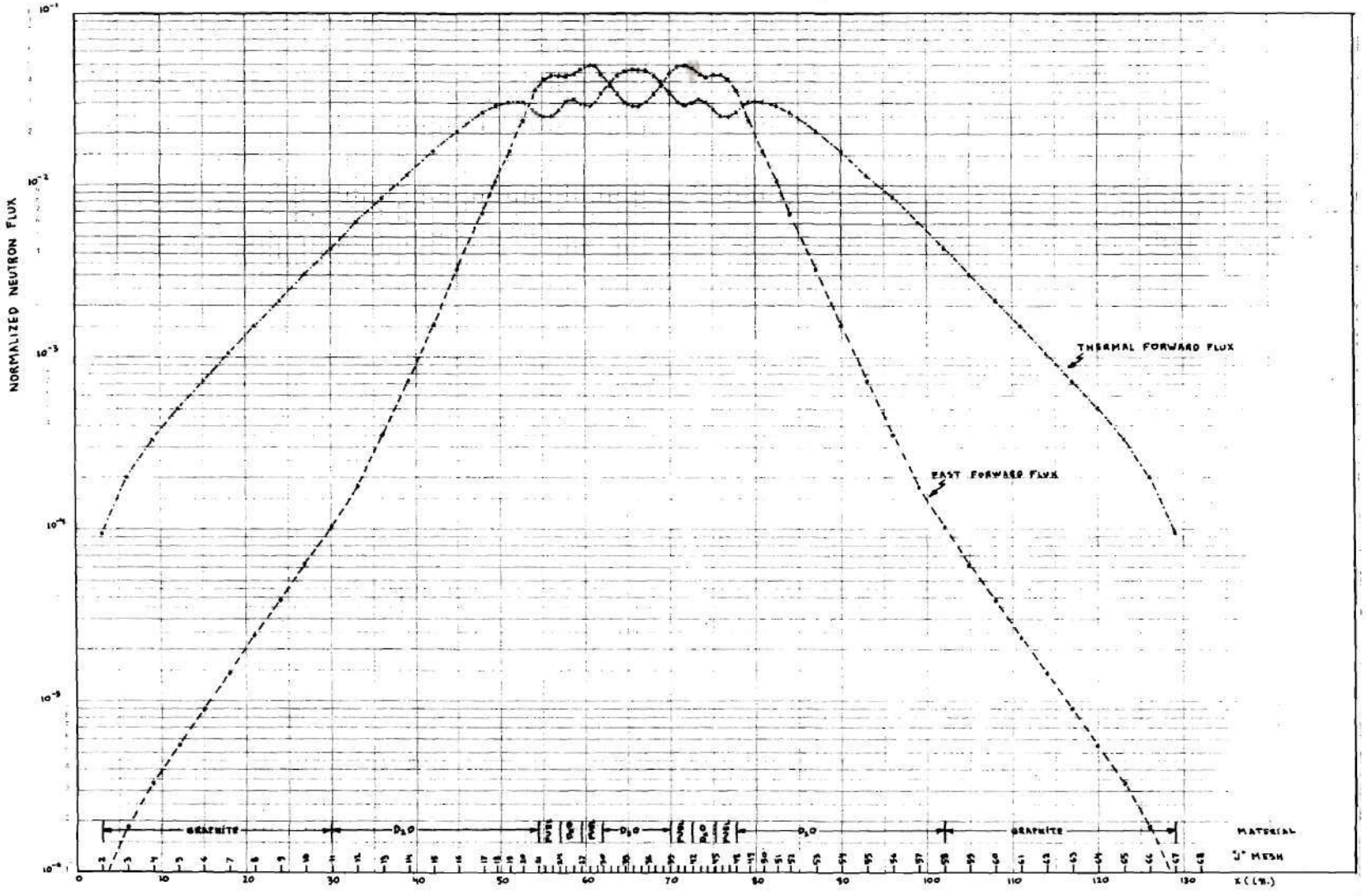

Figure 49. Broad Group Steady-State Fluxes of the GTRR Coupled-Core Configuration

evaluation of the space integrals of the PSD's. The calculated values of the PSD's were obtained for all the space points, and properly weighted stochastic fission sources were assumed in the space volumes that contain fuel. However, due to symmetry, only responses to the stochastic sources of the space volumes of the GTRR assemblies number V-2, V-3, V-6, and V-7 had to be performed. In order to get the space-, energy-, and frequency-dependent responses to the stochastic sources in the space volumes of the other GTRR assemblies namely numbers V-1, V-4, V-5, and V-13 through V-19, a shifting of the mesh points was performed around the appropriate symmetry axes. A total of 42 volume elements with stochastic sources were effectively present in the calculation of the PSD's for the coupled-core GTRR. The presence of symmetry axes also enabled one to verify the accuracy of the numerical calculations of the PSD's. We have seen in chapters III and IV that the CPSD is real (imaginary component is zero) between two detectors located at symmetrical locations inside a reactor with symmetry axes. The phase of the CPSD and the CHF will therefore be zero or ± 180 degrees. In addition, responses were determined for stochastic sources located in space volumes, which are symmetrically located to positions of space volumes in assemblies numbers V-2, V-3, V-6, and V-7. After proper shifting around the appropriate symmetry axes, the relative error of the amplitude and phase of the responses were determined. They were found to be of the order of less than 1.0E-5 degrees. In all the PSD calculations, the proper values of the effective delayed neutrons and photoneutron fractions were used. They had been experimentally determined by Graham[139] for the GTRR and are listed in Table 23. The CPSD between two neutron detectors and their respective APSD were subsequently calculated

Table 23. Delayed Neutron Constants for the GTRR[139]

Delayed Neutron Group	β_i eff	λ_i sec^{-1}
1	1.85×10^{-3}	1.96
2	6.12×10^{-4}	4.41×10^{-1}
3	2.06×10^{-3}	2.88×10^{-1}
4	1.21×10^{-3}	1.17×10^{-1}
5	1.50×10^{-3}	3.05×10^{-2}
6	2.54×10^{-4}	9.25×10^{-3}
7	2.33×10^{-5}	2.27×10^{-3}
8	1.51×10^{-5}	7.73×10^{-4}
9	1.07×10^{-5}	3.15×10^{-4}
10	1.70×10^{-5}	1.18×10^{-4}
11	3.79×10^{-6}	5.85×10^{-5}
12	2.10×10^{-7}	1.37×10^{-5}

$$\beta_{total} = 7.558 \times 10^{-3}$$

using our two-dimensional Power Spectral Density code, followed by the determination of the coherence function. The neutron velocities used in the analysis were 2.2E + 05 cm/sec for the thermal broad group and 4.0E + 08 cm/sec for the fast broad group. The frequency range investigated was ten cycles/sec to 700 cycles/sec.

In Figures 50 and 51 we have plotted the amplitudes and the phases of the two-dimensional CHF between the thermal group response of detector 1 and the thermal group response of detector 2. In Figures 50a and 50b detector 1 was held at the position defined by y-x mesh (9,14)(y = 87.98 cm, x = 99.06 cm) inside the external D_2O reflector. In Figures 51a and 51b detector 1 was held at position (9,7)(y = 87.98 cm, x = 45.72 cm) inside the external graphite reflector. While detector 1 was held in those respective locations, detector 2 was moved into different locations of the reactor around one of the symmetry axes. The curves show the following detector 2 locations around the axis I = 9 (y = 87.98 cm):

J = 25 (x = 146.68 cm) inside the D_2O between assemblies V-2, V-5, and V-6

J = 34 (x = 166.60 cm) inside the D_2O coupling region

J = 43 (x = 186.28 cm) inside the D_2O between assemblies V-14, V-15, and V-18

J = 51 (x = 209.31 cm) inside the D_2O external reflector, close to assembly V-18

J = 55 (x = 236.22 cm) inside the D_2O external reflector (symmetrical location to detector 1 in position J = 14)

J = 59 (x = 266.70 cm) inside the graphite external reflector

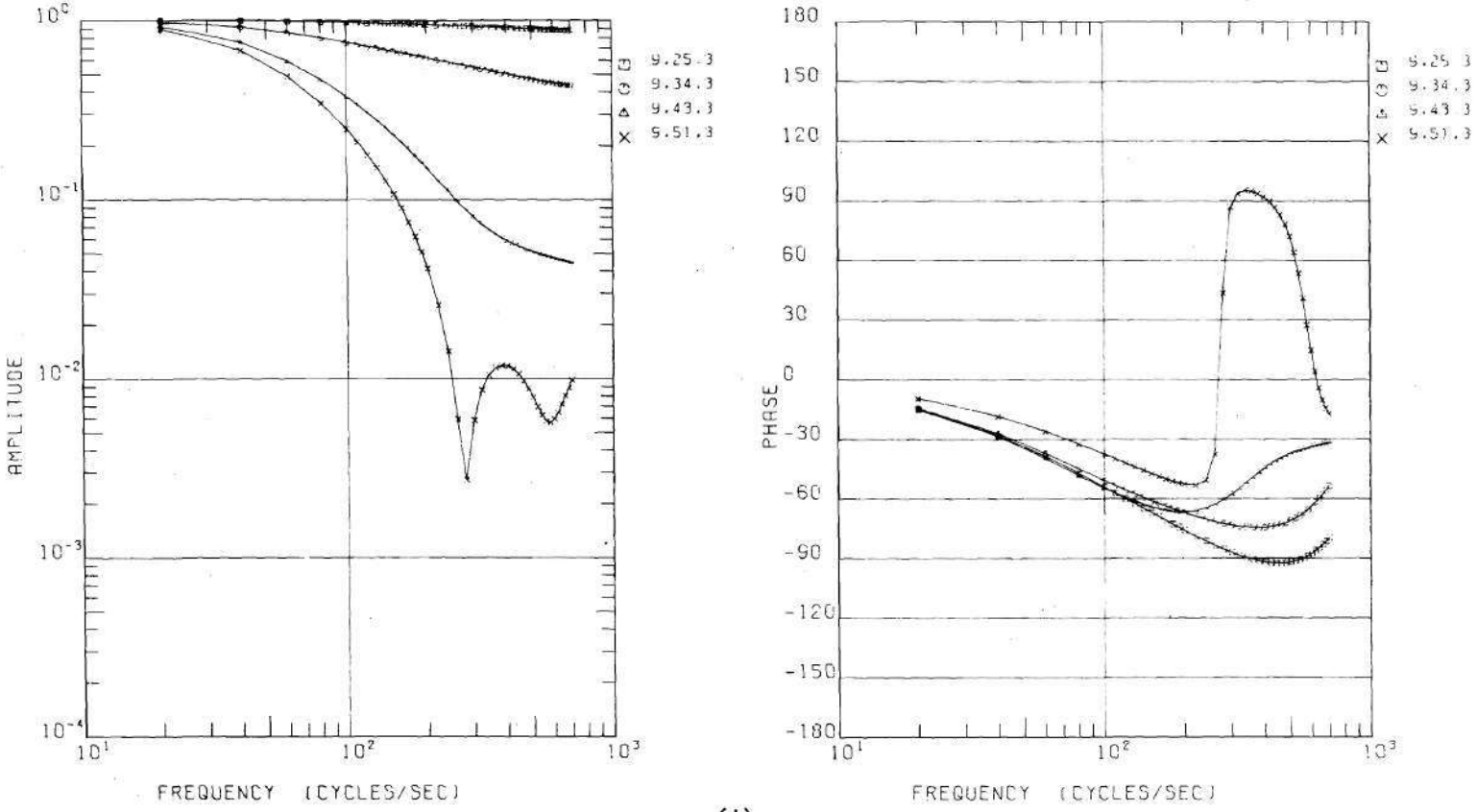

(A)

Figure 50. Amplitude and Phase of the Two-Dimensional Thermal-Thermal CHF for the GTRR Coupled-Core, Detector 1 at Mesh (9,14), Detector 2 at Various Locations

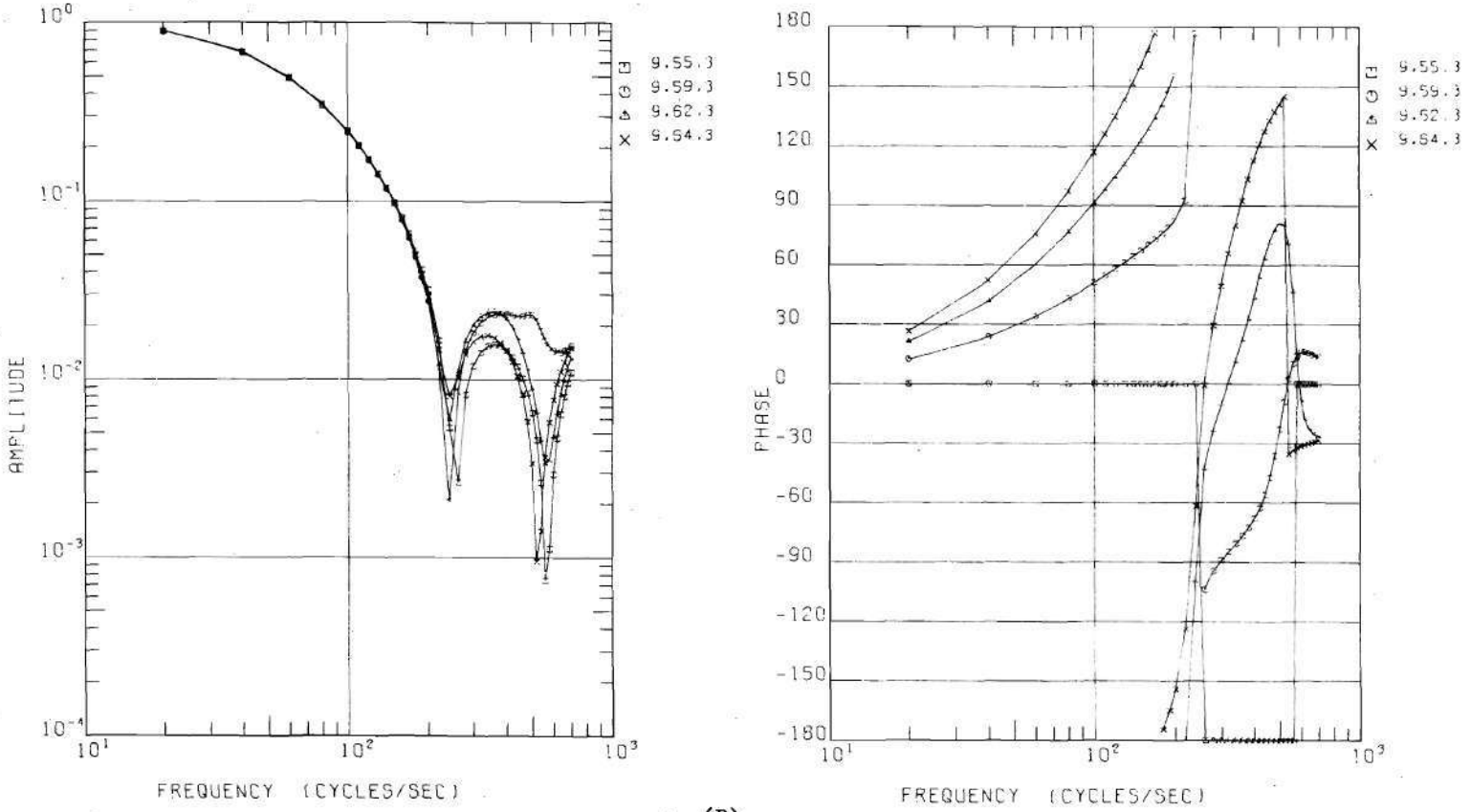

(B)

Figure 50. Concluded

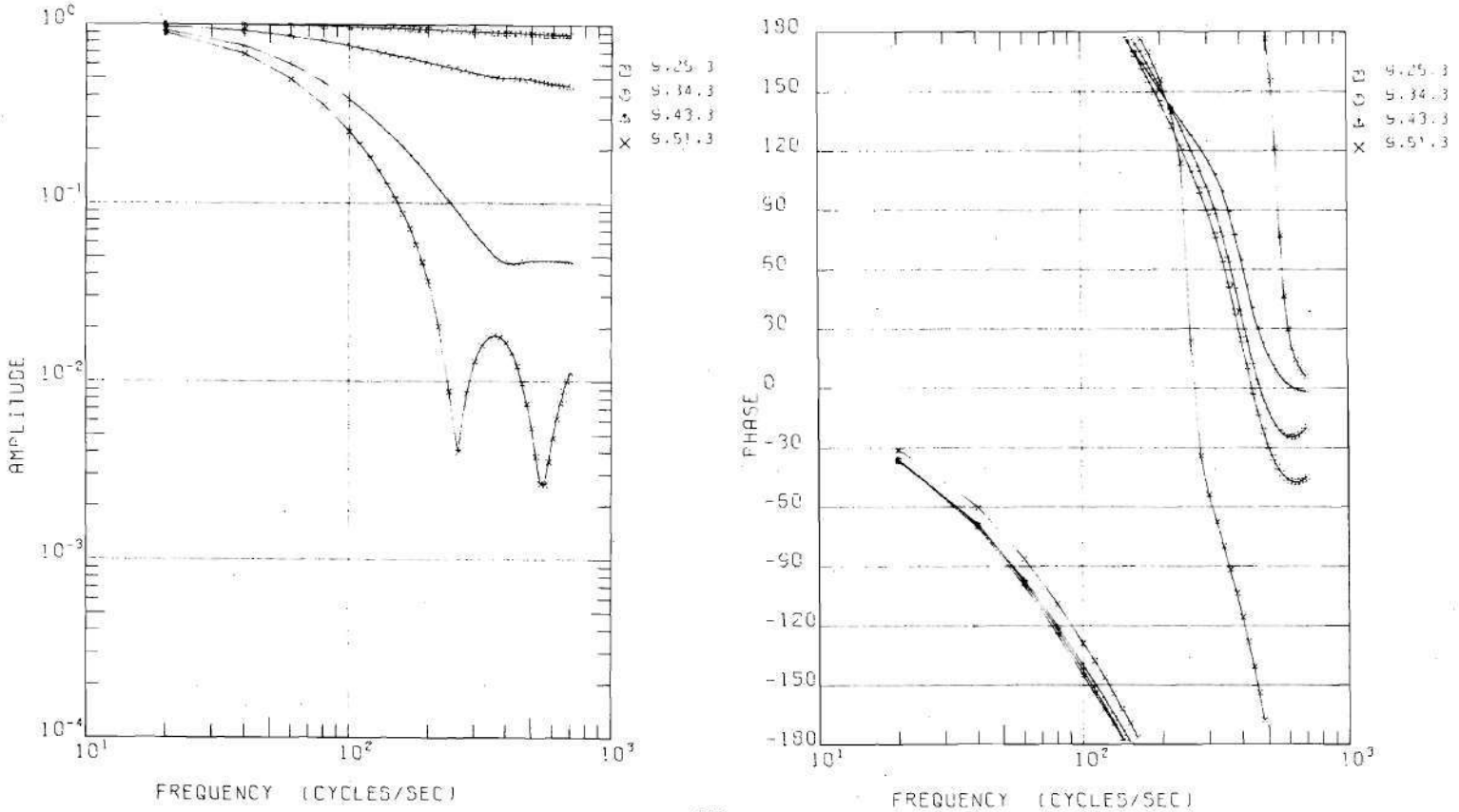

Figure 51. Amplitude and Phase of the Two-Dimensional Thermal-Thermal CHF for the GTRR Coupled-Core, Detector 1 at Mesh (9,7), Detector 2 at Various Locations

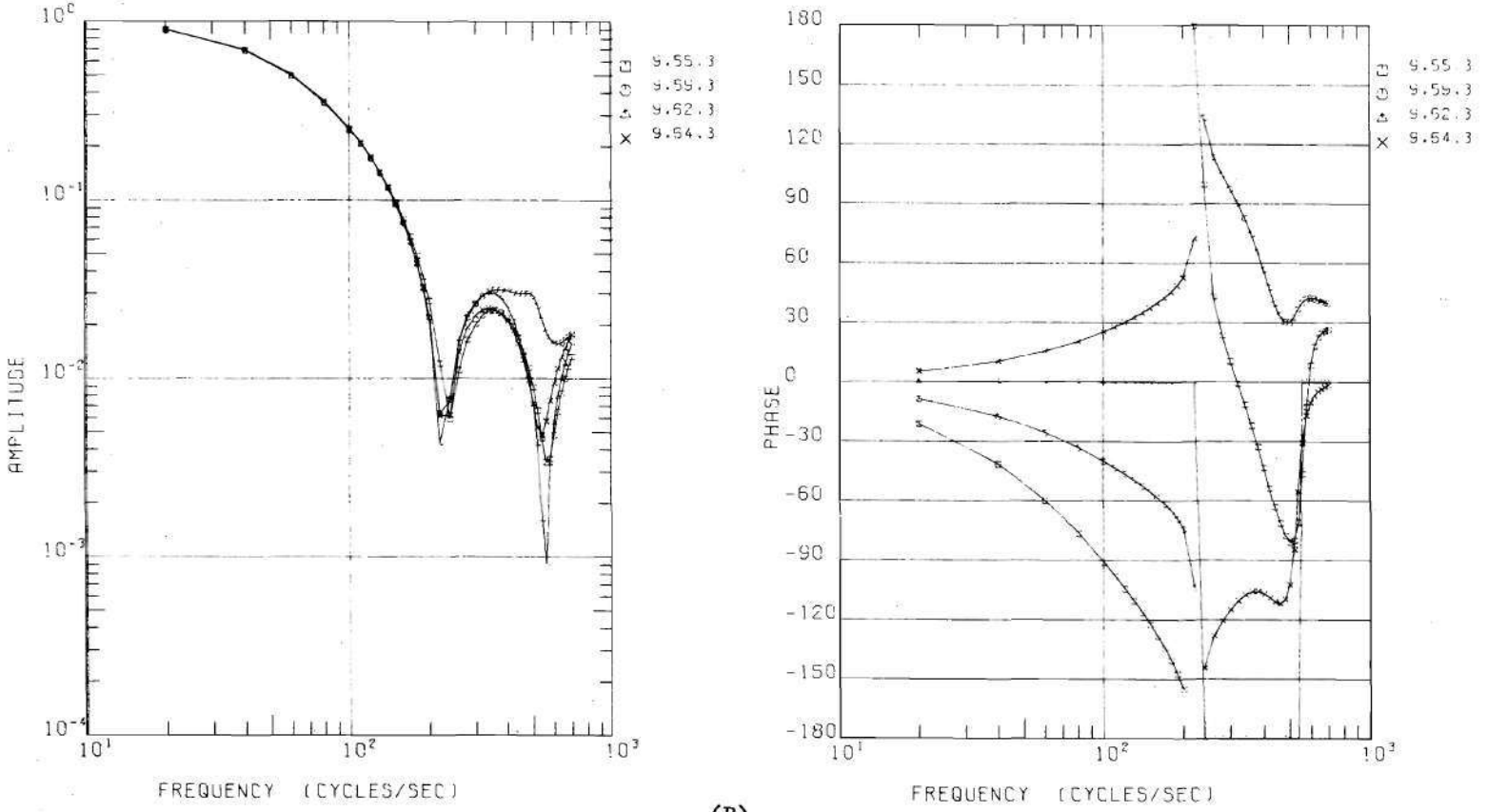

(B)

Figure 51. Concluded

J = 62 (x = 289.56 cm) inside the graphite external reflector (symmetrical location to detector 1 in position J = 7)

J = 64 (x = 304.80 cm) inside the graphite external reflector

Figures 50 and 51 show that the amplitudes of the CHF exhibit a "waving shape" starting with positions of detector 2 inside the D_2O coupling region. The amplitudes exhibit two minima in the frequency range investigated for positions starting at and defined by x-mesh J = 34. For positions inside the D_2O of the *core region lattice*, the minima were shallow. For positions of detector 2 in the external D_2O reflector, at the opposite side of the position of detector 1, we observe that the amplitudes of the CHF go through two sharp minima, the first one at a frequency of approximately 250 cycles/sec, with subsequent recovery at higher frequencies followed by another sharp minimum at approximately 560 cycles/sec, with another subsequent recovery at higher frequencies. Those frequencies at which the minima of the amplitude of PSD's or CHF's occur are usually referred to as "sinks."

In Table 24 we have tabulated the amplitudes and phases of the CHF's between two detectors, and in Table 25 the thermal APSD's of detector 1 and of detector 2. For the case of symmetrical locations of detector 1 and detector 2, it can be observed in Figures 50b (detector 1 at y-x mesh (9,14), detector 2 at mesh (9,55)) and 51b (detector 1 at mesh (9,7), detector 2 at mesh (9,62)) that the phase of the thermal-thermal CHF was zero degrees below the 250 cps sink, ± 180 degrees above this sink, and back to zero degrees above the 560 cps sink. We readily observe that the phase of the CHF between those symmetrical detector locations made an abrupt jump at the sink frequencies. In Chapters III and IV we have seen

Table 24. Coherence Function between Thermal Response Detector 1 and Thermal Response Detector 2

Y-X MESH	9,14		9,14		9,14		9,14		9,14		9,14		9,14	
DETECTOR 1	9,14		9,14		9,14		9,14		9,14		9,14		9,14	
DETECTOR 2	9,25		9,34		9,38		9,43		9,51		9,55		9,57	
FREQUENCY (CPS)	AMPLITUDE	PHASE (DEGREES)	AMPLITUDE	PHASE (DEGREES)	AMPLITUDE	PHASE (DEGREES)	AMPLITUDE	PHASE (DEGREES)	AMPLITUDE	PHASE (DEGREES)	AMPLITUDE	PHASE (DEGREES)	AMPLITUDE	PHASE (DEGREES)
10,0	9,992-01	-7,750+00	9,916-01	-7,538+00	9,857-01	-7,692+00	9,760-01	-7,849+00	9,681-01	-4,964+00	9,686-01	-1,350-06	9,689-01	3,062+00
20,0	9,971-01	-1,519+01	9,698-01	-1,477+01	9,488-01	-1,507+01	9,144-01	-1,543+01	8,874-01	-9,798+00	8,888-01	-2,854-06	8,898-01	6,059+00
40,0	9,905-01	-2,833+01	9,070-01	-2,748+01	8,430-01	-2,803-01	7,443-01	-2,901+01	6,718-01	-1,868+01	6,738-01	-5,630-06	6,760-01	1,166+01
60,0	9,830-01	-3,892+01	8,443-01	-3,746+01	7,387-01	-3,813-01	5,868-01	-3,997+01	4,825-01	-2,625-01	4,825-01	-8,432-06	4,845-01	1,657+01
80,0	9,759-01	-4,738-01	7,914-01	-4,510+01	6,527-01	-4,568+01	4,652-01	-4,842+01	3,445-01	-3,253+01	3,414-01	-1,147-05	3,426-01	2,078+01
100,0	9,693-01	-5,428+01	7,481-01	-5,102+01	5,840-01	-5,130+01	3,740-01	-5,483+01	2,469-01	-3,775+01	2,412-02	-1,499-05	2,412-01	2,439+01
110,0	9,662-01	-5,728+01	7,295-01	-5,348+01	5,549-01	-5,355+01	3,370-01	-5,739+01	2,092-01	-4,003+01	2,025-01	-1,704-05	2,019-01	2,601+01
120,0	9,632-01	-6,004+01	7,125-01	-5,569+01	5,288-01	-5,549+01	3,047-01	-5,958+01	1,773-01	-4,212+01	1,696-01	-1,936-05	1,686-01	2,753+01
130,0	9,604-01	-6,259+01	6,969-01	-5,768+01	5,051-01	-5,718+01	2,763-01	-6,143+01	1,500-01	-4,403+01	1,417-01	-2,201-05	1,403-01	2,896+01
140,0	9,577-01	-6,495+01	6,826-01	-5,947+01	4,836-01	-5,864+01	2,513-01	-6,296+01	1,267-01	-4,577+01	1,179-01	-2,511-05	1,161-01	3,032+01
150,0	9,550-01	-6,714+01	6,693-01	-6,109+01	4,641-01	-5,990+01	2,291-01	-6,421+01	1,067-01	-4,737+01	9,752-02	-2,878-05	9,540-02	3,161+01
160,0	9,525-01	-6,919+01	6,570-01	-6,256+01	4,462-01	-6,099+01	2,094-01	-6,519+01	8,946-02	-4,880+01	8,005-02	-3,322-05	7,767-02	3,285+01
170,0	9,500-01	-7,110+01	6,456-01	-6,391+01	4,298-01	-6,192+01	1,918-01	-6,591+01	7,459-02	-5,008+01	6,506-02	-3,873-05	6,245-02	3,408+01
180,0	9,476-01	-7,288+01	6,350-01	-6,513+01	4,148-01	-6,272+01	1,762-01	-6,638+01	6,175-02	-5,119+01	5,217-02	-4,574-05	4,937-02	3,525+01
190,0	9,453-01	-7,456+01	6,250-01	-6,625+01	4,009-01	-6,339+01	1,622-01	-6,662+01	5,064-02	-5,211+01	4,108-02	-5,499-05	3,813-02	3,644+01
200,0	9,431-01	-7,613+01	6,156-01	-6,727+01	3,881-01	-6,395+01	1,497-01	-6,664+01	4,104-02	-5,280+01	3,156-02	-6,776-05	2,849-02	3,768+01
220,0	9,387-01	-7,898+01	5,985-01	-6,906+01	3,652-01	-6,480+01	1,286-01	-6,605+01	2,556-02	-5,317+01	1,139-02	-1,169-04	1,312-02	4,078+01
240,0	9,346-01	-8,149+01	5,831-01	-7,054+01	3,455-01	-6,532+01	1,117-01	-6,473+01	1,411-02	-5,078+01	5,317-03	-3,228-04	1,985-03	5,610+01
260,0	9,306-01	-8,368+01	5,693-01	-7,176+01	3,283-01	-6,558+01	9,838-02	-6,279+01	5,920-03	-3,770+01	2,628-03	-1,800+02	6,143-03	-1,435+02
280,0	9,268-01	-8,560+01	5,567-01	-7,274+01	3,133-01	-6,562+01	8,784-02	-6,037+01	2,709-03	4,326+01	8,172-03	-1,800+02	1,172-02	-1,396+02
300,0	9,231-01	-8,726+01	5,452-01	-7,350+01	3,001-01	-6,548+01	7,956-02	-5,765+01	5,848-03	8,674+01	1,186-02	-1,800+02	1,542-02	-1,376+02
320,0	9,196-01	-8,867+01	5,346-01	-7,406+01	2,884-01	-6,518+01	7,309-02	-5,479+01	8,627-03	9,374+01	1,413-02	-1,800+02	1,766-02	-1,359+02
340,0	9,162-01	-8,985+01	5,247-01	-7,443+01	2,779-01	-6,474+01	6,805-02	-5,193+01	1,045-02	9,516+01	1,529-02	-1,800+02	1,877-02	-1,345+02
360,0	9,128-01	-9,082+01	5,156-01	-7,462+01	2,685-01	-6,417+01	6,410-02	-4,920+01	1,146-02	9,488+01	1,560-02	-1,800+02	1,900-02	-1,331+02
380,0	9,096-01	-9,157+01	5,070-01	-7,463+01	2,601-01	-6,349+01	6,099-02	-4,669+01	1,184-02	9,363+01	1,526-02	-1,800+02	1,855-02	-1,316+02
400,0	9,065-01	-9,213+01	4,990-01	-7,446+01	2,524-01	-6,269+01	5,851-02	-4,443+01	1,175-02	9,185+01	1,443-02	-1,800+02	1,756-02	-1,299+02
420,0	9,035-01	-9,248+01	4,915-01	-7,413+01	2,453-01	-6,179+01	5,648-02	-4,246+01	1,129-02	8,952+01	1,323-02	-1,800+02	1,616-02	-1,279+02
440,0	9,006-01	-9,265+01	4,845-01	-7,363+01	2,389-01	-6,078+01	5,480-02	-4,076+01	1,059-02	8,658+01	1,177-02	-1,800+02	1,444-02	-1,253+02
460,0	8,979-01	-9,262+01	4,779-01	-7,296+01	2,330-01	-5,967+01	5,338-02	-3,931+01	9,718-03	8,284+01	1,011-02	-1,800+02	1,250-02	-1,214+02
480,0	8,952-01	-9,242+01	4,718-01	-7,212+01	2,276-01	-5,845+01	5,214-02	-3,808+01	8,764-03	7,805+01	8,326-03	-1,800+02	1,044-02	-1,158+02
500,0	8,927-01	-9,203+01	4,660-01	-7,111+01	2,225-01	-5,713+01	5,105-02	-3,704+01	7,806-03	7,181+01	6,462-03	-1,800+02	8,453-03	-1,055+02
520,0	8,903-01	-9,147+01	4,607-01	-6,995+01	2,179-01	-5,571+01	5,008-02	-3,616+01	6,927-03	6,369+01	4,558-03	-1,800+02	6,881-03	-8,890+01
540,0	8,881-01	-9,074+01	4,559-01	-6,863+01	2,136-01	-5,418+01	4,920-02	-3,541+01	6,219-03	5,332+01	2,644-03	-1,800+02	6,271-03	-6,534+01
560,0	8,860-01	-8,984+01	4,514-01	-6,715+01	2,097-01	-5,256+01	4,840-02	-3,476+01	5,779-03	4,083+01	7,451-04	-1,800+02	6,917-03	-4,256+01
580,0	8,841-01	-8,879+01	4,475-01	-6,553+01	2,060-01	-5,084+01	4,767-02	-3,418+01	5,674-03	2,732+01	1,121-03	-2,243-04	8,395-03	-2,750+01
600,0	8,823-01	-8,759+01	4,439-01	-6,378+01	2,027-01	-4,904+01	4,701-02	-3,366+01	5,914-03	1,452+01	2,938-03	-7,701-05	1,012-02	-1,919+01
620,0	8,808-01	-8,624+01	4,409-01	-6,190+01	1,996-01	-4,716+01	4,641-02	-3,318+01	6,437-03	3,809+01	4,696-03	-4,360-05	1,177-02	-1,490+01
640,0	8,794-01	-8,477+01	4,383-01	-5,991+01	1,968-01	-4,522+01	4,587-02	-3,272+01	7,155-03	-4,403+01	6,385-03	-2,920-05	1,321-02	-1,286+01
660,0	8,783-01	-8,318+01	4,362-01	-5,784+01	1,942-01	-4,322+01	4,539-02	-3,227+01	7,990-03	-1,038+01	7,999-03	-2,139-05	1,443-02	-1,206+01
680,0	8,773-01	-8,149+01	4,345-01	-5,569+01	1,918-01	-4,118+01	4,496-02	-3,183+01	8,883-03	-1,460+01	9,533-03	-1,661-05	1,546-02	-1,193+01
700,0	8,765-01	-7,971+01	4,333-01	-5,349+01	1,897-01	-3,912+01	4,458-02	-3,139+01	9,795-03	-1,749+01	1,098-02	-1,347-05	1,636-02	-1,211+01

Table 25. APSD of the Thermal Response of Detector 1 and Detector 2

Y=X MESH	DETECTOR 1 9,14	DETECTOR 2 9,25	9,34	9,38	9,43	9,51	9,55	9,57
FREQUENCY (CPS)	AMPLITUDE	AMPLITUDE	AMPLITUDE	AMPLITUDE	AMPLITUDE	AMPLITUDE	AMPLITUDE	AMPLITUDE
10.0	1.816-01	1.265+00	2.953+00	2.128+00	1.334+00	1.132+00	1.816-01	4.921-02
20.0	4.713-02	3.406-01	7.773-01	5.623-01	3.581-01	3.033-01	4.713-02	1.254-02
40.0	1.201-02	9.946-02	2.125-01	1.577-01	1.038-01	8.639-02	1.201-02	2.995-03
60.0	5.228-03	5.237-02	1.047-01	7.778-02	5.433-02	4.354-02	5.228-03	1.192-03
80.0	2.788-03	3.451-02	6.508-02	4.904-02	3.564-02	2.719-02	2.788-03	5.738-04
100.0	1.654-03	2.540-02	4.557-02	3.479-02	2.615-02	1.891-02	1.654-03	3.061-04
110.0	1.309-03	2.236-02	3.921-02	3.013-02	2.300-02	1.618-02	1.309-03	2.295-04
120.0	1.050-03	1.993-02	3.420-02	2.644-02	2.048-02	1.402-02	1.050-03	1.745-04
130.0	8.522-04	1.795-02	3.017-02	2.346-02	1.842-02	1.228-02	8.522-04	1.342-04
140.0	6.985-04	1.630-02	2.685-02	2.101-02	1.671-02	1.085-02	6.985-04	1.042-04
150.0	5.775-04	1.490-02	2.409-02	1.896-02	1.527-02	9.665-03	5.775-04	8.101-05
160.0	4.811-04	1.371-02	2.175-02	1.722-02	1.404-02	8.662-03	4.811-04	6.440-05
170.0	4.034-04	1.268-02	1.975-02	1.573-02	1.298-02	7.808-03	4.034-04	5.116-05
180.0	3.404-04	1.178-02	1.803-02	1.443-02	1.205-02	7.074-03	3.404-04	4.087-05
190.0	2.887-04	1.099-02	1.652-02	1.331-02	1.123-02	6.437-03	2.887-04	3.283-05
200.0	2.461-04	1.029-02	1.521-02	1.231-02	1.051-02	5.882-03	2.461-04	2.648-05
220.0	1.811-04	9.102-03	1.301-02	1.065-02	9.287-03	4.964-03	1.811-04	1.744-05
240.0	1.352-04	8.136-03	1.126-02	9.324-03	8.293-03	4.240-03	1.352-04	1.164-05
260.0	1.023-04	7.336-03	9.837-03	8.237-03	7.471-03	3.659-03	1.023-04	7.851-06
280.0	7.827-05	6.662-03	8.665-03	7.336-03	6.779-03	3.185-03	7.827-05	5.339-06
300.0	6.046-05	6.088-03	7.686-03	6.580-03	6.190-03	2.794-03	6.046-05	3.655-06
320.0	4.711-05	5.594-03	6.860-03	5.937-03	5.683-03	2.468-03	4.711-05	2.515-06
340.0	3.700-05	5.164-03	6.156-03	5.386-03	5.243-03	2.120-03	3.700-05	1.738-06
360.0	2.927-05	4.786-03	5.551-03	4.910-03	4.856-03	1.980-03	2.927-05	1.205-06
380.0	2.331-05	4.453-03	5.028-03	4.495-03	4.515-03	1.757-03	2.331-05	8.369-07
400.0	1.868-05	4.156-03	4.571-03	4.131-03	4.212-03	1.583-03	1.868-05	5.830-07
420.0	1.505-05	3.890-03	4.171-03	3.810-03	3.941-03	1.432-03	1.505-05	4.072-07
440.0	1.220-05	3.651-03	3.819-03	3.525-03	3.697-03	1.300-03	1.220-05	2.857-07
460.0	9.945-06	3.435-03	3.507-03	3.271-03	3.477-03	1.185-03	9.945-06	2.018-07
480.0	8.151-06	3.239-03	3.229-03	3.044-03	3.277-03	1.082-03	8.151-06	1.440-07
500.0	6.716-06	3.061-03	2.981-03	2.839-03	3.095-03	9.919-04	6.716-06	1.046-07
520.0	5.565-06	2.897-03	2.759-03	2.655-03	2.929-03	9.113-04	5.565-06	7.777-08
540.0	4.636-06	2.748-03	2.559-03	2.488-03	2.776-03	8.394-04	4.636-06	5.978-08
560.0	3.884-06	2.610-03	2.379-03	2.336-03	2.636-03	7.749-04	3.884-06	4.788-08
580.0	3.274-06	2.482-03	2.216-03	2.198-03	2.507-03	7.170-04	3.274-06	4.015-08
600.0	2.776-06	2.364-03	2.068-03	2.072-03	2.387-03	6.647-04	2.776-06	3.526-08
620.0	2.369-06	2.255-03	1.933-03	1.956-03	2.276-03	6.174-04	2.369-06	3.226-08
640.0	2.034-06	2.153-03	1.810-03	1.849-03	2.173-03	5.746-04	2.034-08	3.050-08
660.0	1.759-06	2.059-03	1.698-03	1.752-03	2.077-03	5.357-04	1.759-06	2.954-08
680.0	1.531-06	1.970-03	1.595-03	1.661-03	1.987-03	5.002-04	1.531-06	2.906-08
700.0	1.342-06	1.888-03	1.500-03	1.578-03	1.903-03	4.678-04	1.342-06	2.885-08

that this was theoretically expected for symmetrical locations of neutron detectors.

In Table 24 the values of the phase of the thermal-thermal CHF (detector 2 at mesh (9,55)) show that the numerical values of this "theoretically zero" is of the order of 10^{-5}. This is an indicator of the quality and the success of the iteration schemes used in the PSD analyses. In the case of symmetrical positioned detectors, we therefore observe that the imaginary part of the CHF is very small compared to the real part (theoretically it should be exactly zero). We can therefore say that the passage of the real part of the CHF from positive to negative values indicates the position of sinks, and that it therefore goes through zero. We have seen earlier that the sink frequencies are defined as those frequencies where the amplitude of the PSD goes through a minimum. Since for symmetrically located detectors, the CHF is real, we can say that the frequency at which the real part of the CHF goes through zero coincides with the sink frequency. The amplitude, therefore, goes to zero at the sink frequency for symmetrically located detectors, which have identical energy sensitivities. In this case the minimum is sometimes referred to as a "null" frequency. In the case of asymmetrically located neutron detectors, the frequency at which the real part of the CHF changes sign does not coincide with the frequency at which the amplitude of the CHF goes through a minimum. The amplitude at the sink, therefore, does not go to zero. We also observe that the frequencies at which the minima in the amplitude of the coherence function occur are very insensitive to the spacing between detectors. We have seen that the sink frequency corresponds to a 90 degree phase shift in the neutronic coupling between fuel regions

and that this phase shift causes an interference effect of neutronic waves from one fuel region to another. While the sink at a frequency of 250 cycles/sec is due to this 90 degrees phase shift in the neutronic coupling, it is not known if the sink at 560 cycles/sec is due to a 270 degrees phase shift, or due to interactions between fuel regions whose coupling distances are smaller. If we refer back to Figure 3 of reference 17 we observe that a sink at 560 cps is possible for a D_2O coupling region distance between infinite fuel slabs of approximately 22 cm. Indeed the distance between GTRR assemblies as numbers V-2 and V-4 is 26.4 cm center to center, and the distance between their fuel boundaries is approximately 20 cm.

In the early burnup phase of the fuel of the GTRR, the excess reactivity enabled the reactor to go critical with only 11 assemblies in a compact lattice. Since there are 19 fuel positions available in the core lattice, many combinations of the reactor core configuration could be put together, although not all combinations would go critical. The coupled-core configuration that was analyzed above was shown to go critical by Graham.[140] Another interesting configuration is the one represented in Figure 52. This configuration is obtained by removing assemblies V-5, V-6, V-14, and V-15. This 15 fuel assemblies configuration should probably also give a sink in the neighborhood of 250 cycles/sec.

Experimental Determination of the PSD for the Full-Core GTRR

The power spectral density function was experimentally determined for a 17 fuel assemblies GTRR configuration. Neutronic disturbances were introduced due to inherent volume distributed stochastic fission sources.

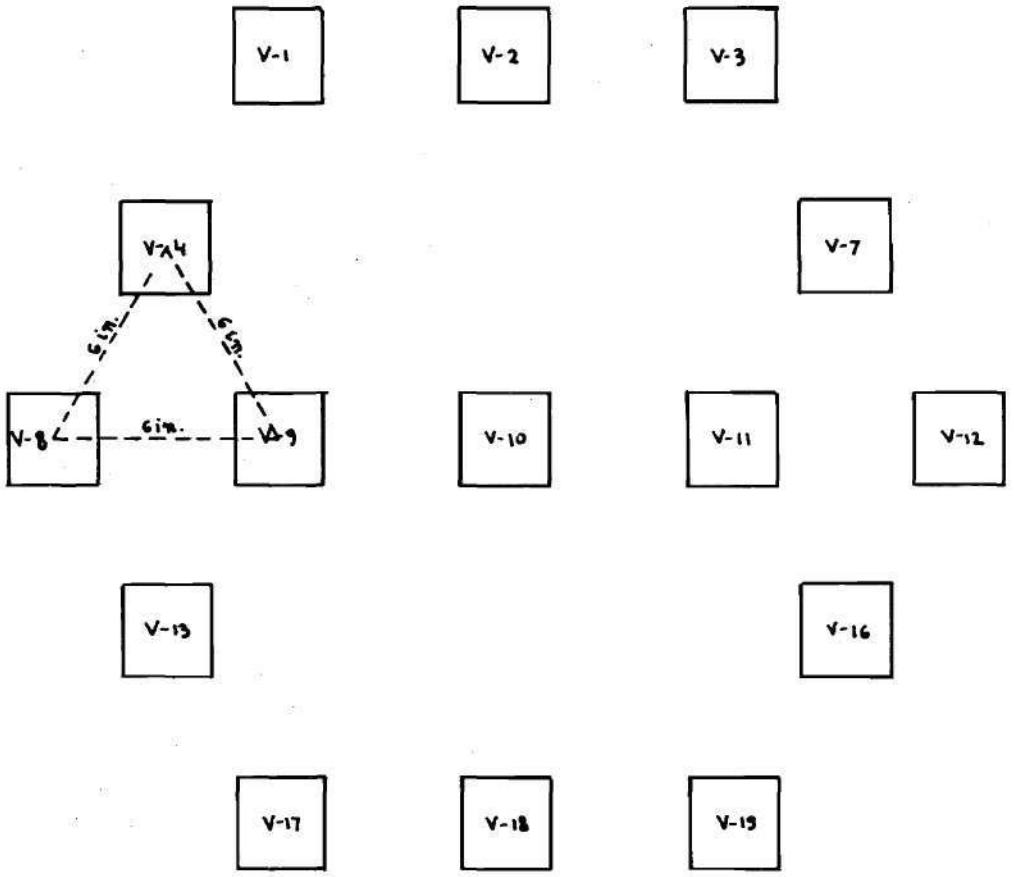

Figure 52. Fifteen Fuel Assembly GTRR Split-Core Configuration

All the measurements were performed at low reactor power, approximately one kW thermal.

A block diagram of the neutron detection system and the data reduction is shown in Figure 53.

Detection and Data Recording System

Detectors. The neutron detectors used for this investigation were B^{10} coated uncompensated ionization chambers of the type Reuter-Stokes Electronic Components, Inc. type RSN-76A. The operating characteristics of the RSN-76A detectors were:

thermal neutron sensitivity: 3×10^{-14} amp/n/cm^2-sec

gamma sensitivity: 2×10^{-11} amp/R/hr

thermal neutron flux range: 10^4 to 10^{11} n/cm^2-sec

signal electrode to shell capacitance: 115 picofarads and HV electrode to shell: 195 pF

sensitive length: 19.7 cm

The neutron detectors (minimum diameter: 5.24 cm, maximum overall length: 30.8 cm) were mounted inside a 20 mil thick Al-1100 cylindrical housing, 6.35 cm diameter and 34.6 cm long, held in place with Teflon rings. This aluminum housing was connected to a 3.66 m long Al-6061-T6 tube 1.27 cm OD, which served both as the housing of the HV and signal coaxial cables and as mechanical support of the detector. This detector system was positioned inside a horizontal beam hole of the GTRR. Special shielding plugs with a centrally located 2.5 cm diameter center hole through which the detector holder was placed, were installed in the outer section of the GTRR beam holes. The power supplies which provided high voltages to the ion chambers were highly stabilized type Hamner or Fluke units. No 60 or

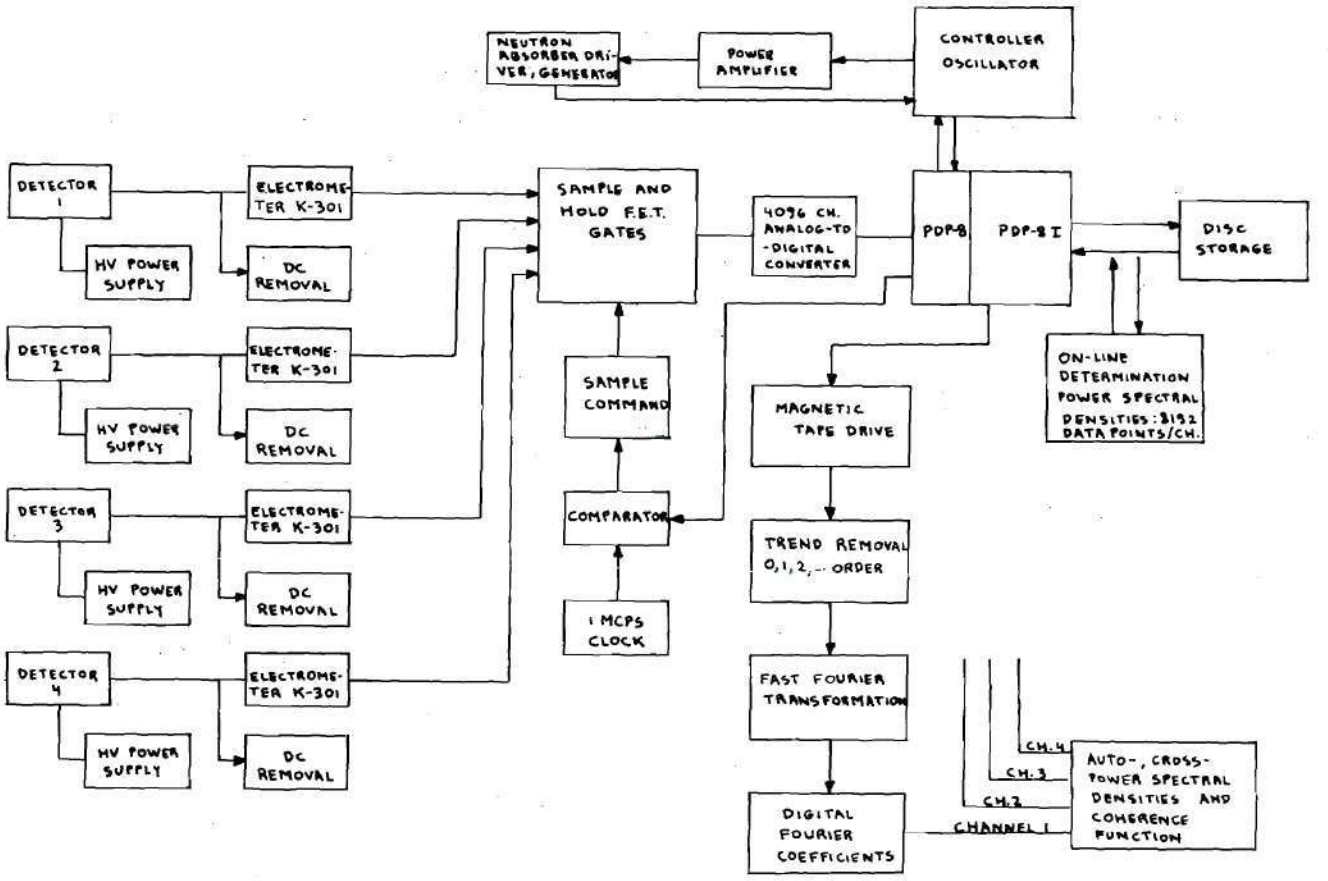

Figure 53. Block Diagram of the Neutron Detection and Experimental Data Acquisition System

120 cps ripple could be detected. Noise and ripple were less than 0.5 mV rms.

The electrometer module was designed in the DC suppressed mode, in order to accommodate noise analysis and other frequency domain experiments. The first requirement of the electrometer operation was the removal of the mean value (DC component) portion of the current, since the signal from the neutron detector results in an output which is indicative of the current fluctuation around some mean value. Since the mean value of the current is usually several orders of magnitude greater than the amplitude of the current fluctuation, removal of the DC component had to be performed before presenting the signal to the input of the amplification stage of the electrometer module. This was necessary to avoid saturation of the electronic circuits. The electrometer module can be considered as a very low-band pass filter, which had the advantage of removing DC and very low frequency components. In addition, it should be noted that the presence of DC or very slow frequency components was not only taken out electronically, but was also removed in our PSDDA (Power Spectral Density Data Analysis) program by least-squares fitting the digitized data.

It was found that, at high amplification levels of the detection system, the flexing of normal coaxial or triaxial cables was introducing spurious changes in the recorded voltage. The coupling between the neutron detectors and the electrometer modules was therefore done with the use of "Amphenol Noise-Free" coax cables of type RG-U/59. The reduction of inherent noise in these cables is achieved by the application of a semi-conductive coating over the dielectric. This coaxial cable will

remain electrically neutral under conditions of shock and vibration. The spurious signals generated by standard coaxial cable, due to flexing or distorting the cable, in certain cases may well be of a higher level than the useful signal being transmitted along the cable. No spurious changes in the output of the electrometer module were present with the use of those "Noise-Free" coax cables. The capacitance of the RG-U/59 coax was 21.5 pF/ft. The distance between the neutron detector and the electrometer was therefore kept to a minimum, approximately 15 ft and the electrometer module was located at the exit of the horizontal beam hole in which the detector was located.

A circuit diagram of the electrometer module is shown in Appendix C. The electrometer itself consisted of a Keithley Instruments Model 301 solid state electrometer operational amplifier, with built-in voltage regulators. The principal characteristics were:

input resistance greater than 5×10^{12} ohms

current offset less than 10^{-14} amp

current drift less than 10^{-15} amp/24 hours

current noise less than 5×10^{-15} amp peak to peak

electrostatically and magnetically shielded, Teflon insulated input connectors for minimum leakage.

These electrometers can provide extremely long time constants because of their low offset current. The Keithley 301 electrometers were powered by means of a Keithley Model 3012 power supply, which can be floated at up to 500 volts off chassis ground. Special low-leakage polystyrene capacitors and high quality resistors, type Keithley model R20, were used in the feedback loops.

After removing the DC and very slow varying components of the signal, we required that the output voltage range due to the AC components of the detector signal should not vary by more than 10 volts. The settings were accordingly set to meet those requirements. The output of the fluctuating signal from the electrometer module was then fed to a "sample-and-hold" module. At this point the signal contained high-frequency as well as low-frequency components. Some very low frequency components were introduced by slow drift in reactor power level and by moderator temperature feedback, especially at low flow rates of the coolant. Those drifts were removed by least-squares curve fitting of the data using the PSDDA program.

Sample-and-Hold Module. For each detector channel, an operational amplifier (with bias and gain control) sampled, at the command of a pulse from the PDP-8 minicomputer, the output of the electrometer module by charging up a capacitor. Each capacitor was subsequently discharged by another PDP-8 command pulse and the output presented to a 4096 channel ADC (analog to digital converter) module. A total of four input channels was available. While the sample command was performed simultaneously on the four input channels, the ADC was performed sequentially on pre-selected channels. The sampling was typically done every two msec for the inherent noise measurements. The whole data collection system was tested up to sample intervals of 0.5 msec on four channels. The bandwidth of the electrometer module and sample-and-hold module was determined between 0.1 cps and 400 cps and was found to be satisfactory.

PDP-8 Processor and Peripheral Equipment. A PDP-8 minicomputer was used for the on-line data handling and the complete control of the ex-

periment. The PDP-8 computer (4096 words core memory, 12 bits per word) was connected to a PDP-8I minicomputer (8192 words memory, 12 bits per word) via a special communication link, which had a capacity of eight bits per transmission. A magnetic tape drive and disk were connected to this PDP-8I minicomputer. Several small special purpose programs were written for the PDP-8 and PDP-8I minicomputers in the PALD language. (This language is very basic and quite similar to direct binary coding.) Special care had to be taken for proper synchronization between the different commands and signals of each minicomputer. Those programs controlled the PDP-8 sampling-time command to the sample-and-hold module, the ADC on the appropriate detection channels, and transmission to the PDP-8I. Since the signal from the ADC module has a 12 bit value, two transmissions via the communication line were necessary for each data word. The 12 bit data word was broken down into two separate 6 bit words for transmission and reconstructed at the PDP-8I site into a 12 bit data word. The data in the PDP-8I were buffered and the buffers were emptied onto a standard magnetic tape for subsequent power spectral density analysis on a U-1108 computer using our PSDDA package.

All electronic equipment was allowed to stabilize over a period of several hours. Before recording of the data started, the DC and very low frequency components of the signal were allowed to stabilize over a sufficient time span (usually 15 to 30 minutes).

Data Reduction and Analysis

The experimental data taken and stored on magnetic tape were analyzed on a Univac-1108 computer using our Power Spectral Data Analysis

(PSDDA) package. This program package was developed by the author to calculate the APSD, CPSD, and CHF from series of discrete time data. The basic output were the APSD, CPSD, and coherence function computed from a pair of time histories. The package can simultaneously analyze any number of pairs of time sequences of unlimited sample length.

The first part of the package was an interface between the PDP-8 and the U-1108 computer. Since the experimental data were recorded in sequential order of the neutron channels, proper unscrambling had to be performed, including the conversion of 12 bit integer words to 36 bit floating numbers. Typically, we obtained 65,536 data words per neutron channel.

The next phase was removal of second order trends with least-squares fitting to the data samples. This was performed for each channel. Any trend of a quadratic nature (DC, linear, second order) was subtracted. The third phase was a Discrete Fourier Transformation (DFT) processor. This processor performed a DFT of a series of data samples using a Fast Fourier Transformation (FFT) algorithm based on the classical method developed by Cooley and Tukey.[7,8] This processor computes the finite DFT of a complex time series for $N = 2^P$ data point sequences. The value of N can be unlimited in the PSDDA package, but has to be a power of 2. Our package has been tested for up to $N = 2^{19} = 524,288$ data points. In order to reduce round-off errors, most of the computations were performed in double precision arithmetic. Since for each data point a complex number is necessary, this would require over two million computer memory locations, larger than most computers. The option for unlimited complex time series was developed using sophisticated algorithms in order to

reduce the necessary computer memory storage and the IO handling. Some particular characteristics of the Cooley and Tukey[7] algorithm were taken into account in order to reduce the necessary core storage to less than 120K. All IO was done using UNIVAC's NTRAN random access capability.

It may be useful to point out that the FFT not only reduced the computation time, but also reduced substantially round-off errors in the calculation of the DFT. Both computation time and round-off errors were essentially reduced by a factor of $\log_2 N/N$ as compared to a standard Fourier Transformation Algorithm. In the case where $N = 2^{19} = 524,288$, this factor is 3.6-05. This algorithm can also be used for inverse discrete Fourier transformation if the coefficients are replaced by their complex conjugate and if the result of the computation is multiplied by 1/N. It can be shown that, in order for the result of an FFT algorithm to correspond to the DFT, it is required that half of the data points be zero. This can be done easily by adding a string of zeros to the discrete data point series and performing the FFT algorithm onto the whole series. The fourth phase of the experimental analysis consisted of determining the APSD, CPSD, or CHF from averages of the discrete Fourier transforms.

We have seen that the power spectral density between a variable x(t) and a variable y(t) defined by

$$\Phi_{xy}(\omega) = \lim_{T\to\infty} \int_{-T}^{+T} \phi_{xy}(\tau)\, e^{-j\omega\tau}\, d\tau$$

and

$$\phi_{xy}(\tau) = \lim_{T\to\infty} \frac{1}{2T} \int_{-T}^{+T} x(t)\, y(t-\tau)\, dt$$

calls for an infinitely long time of detection. However, in the actual

spectral analysis of a random signal, only a finite length record can be analyzed. We, therefore, only obtained an estimate of the true power spectral density. In determining the error of a PSD measurement due to finite time of detection, we need to look at two important parameters, namely the bandwidth and the record length of the measurement. It can be shown[141] that the theoretical probability distribution of the PSD estimate for a random signal with a Gaussian distribution of amplitudes and a uniform power spectrum within the bandwidth is

$$\frac{\chi^2}{df(m)}$$

where

$n = 2BT$ = degrees of freedom

B = bandwidth

T = record length of the measurement

χ = χ-distribution

Extending this to the estimate of a PSD with a confidence level α, it can be shown that[142]

$$\Phi_{xx}^{est}(\omega)\ \frac{df(m)}{\chi^2_{\left(\frac{1-\alpha}{2}\right)}} \leq \Phi_{xx}(\omega) \leq \Phi_{xx}^{est}(\omega)\ \frac{df(m)}{\chi^2_{\left(\frac{1+\alpha}{2}\right)}} \qquad (99)$$

where

$\phi_{xx}^{est}(\omega)$ = estimate of PSD

$\phi_{xx}(\omega)$ = true PSD

α = confidence level

$n = 2BT$ = degrees of freedom.

Data Collection and Procedure. The equipment used for the experiment has been described earlier. A block diagram for the equipment used is shown in Figure 53. The whole data collection system was thoroughly tested with known time series. This was done several ways.

First, a known mixture of up to fifty sinusoids of different frequencies and amplitudes was software generated by the PDP-8 processor. Appropriate DC, linear and quadratic biasing of the values was done in order to test the least-squares fit portion of the analysis package. Those time series were fed into a memory location where the values obtained by the ADC module are usually deposited. After transmission to the PDP-8I minicomputer and subsequent storage on magnetic tape, a complete analysis using our PSDDA package was performed on a U-1108 computer. For a time sequence of typically 65,536 data points per channel, an unscrambling followed by a least-squares fit was performed. This was followed by an FFT on 131,072 discrete data points, followed by a PSD determination with appropriate error analysis. It was found that the error between the amplitude of the different sinusoids (with phase lags between them) was typically less than 1%. The error was primarily due to round-off errors in the computation and limited number of degrees of freedom.

Second, a series of pure sine waves, generated by a Hewlett-Packard audio oscillator, was analyzed over a frequency range from 0.1 to 400 cps. Third, a background noise determination of the RSN-76A neutron detector and electrometer module was performed. The APSD was determined while the neutron detector was positioned inside a horizontal beam hole of the GTRR. The recording was started several hours after the GTRR was shut down and

the beam hole shutter closed. A white background noise was found to exist. The procedure followed to determine the transfer function of the detector channel is usually based on the fact that the APSD of the current of the neutron chamber is constant over the frequency range investigated, when the detector is exposed to a radioactive neutron source in a nonmultiplying medium or to a gamma source.

Experimental Procedure and Results. As pointed out in the description of the GTRR, there are 19 fuel assembly positions available in the core lattice. Due to the relatively high burnup of the Mark-I fuel, a fuel loading of 17 assemblies was necessary at that time (1970). After removal of the graphite stringers from the appropriate beam holes, the first neutron detector was placed inside the horizontal beam hole, H-1, and the second detector in horizontal beam hole, H-5. The exact position of the neutron detectors within the beam hole was determined by special markings on the 12 ft holders of the neutron detectors. Experimental measurements very close to the center of the core to the outer part of the external graphite reflector of the horizontal holes were possible.

Special beam hole shield plugs were installed in the beam holes, and the 12 ft detector holders were placed through a centrally located 2.5 cm hole in the shield plugs. After the neutron detectors were in position, the beam hole shutters were opened and the neutron detectors were pushed toward the center of the core. For most experiments, the detectors were located inside the D_2O external reflector. The sensitive length of 19.7 cm was located approximately 5 to 24.8 cm from the aluminum reactor vessel separating the D_2O from the external graphite reflector. Due to the high fuel burnup, the excess reactivity available with the 17

fuel assembly core was small, so that the semaphore control blades were nearly full out. Thus, any distortion of the neutron flux due to the presence of the control blades was small.

Before any movement of the detector holders, shutdown of the reactor was required by operational procedures. After movement of the detectors to the proper position, the reactor was allowed to come to equilibrium over a time span of approximately 15 to 30 minutes. During the entire experimental procedure, proper care had to be made to minimize radiation hazards. High radiation leakage and neutron streaming were recorded at the beam hole shield plugs, primarily around the centrally located opening. Special borated paraffin beam catchers were therefore constructed and put in place in front of the beam holes.

In Figure 54 we have plotted the APSD of detector 1. The reactor was at a power level of one kW and the core total coolant flow was 1,200 gpm (gallons of D_2O per minute). The sample time was two msec. After proper settling of the DC components, measurements were taken over a time span of typically 32.768 seconds. In this figure one can observe the presence of a 5.9 $\pm$ 0.05 cps mechanical resonance, and a harmonic at approximately 12 cps. Although the data collection and analysis package had sufficient resolution to cover a frequency band of several decades, the presence of this instability precluded the use of higher AC current amplifications of the detector signal. At relatively high frequencies, the correlated to uncorrelated signal ratio is rather small. Since the DC component was removed, sufficient amplification could have been obtained to detect higher frequency components, which were several orders of magnitude lower than the components at 5.9 cps. In addition, the

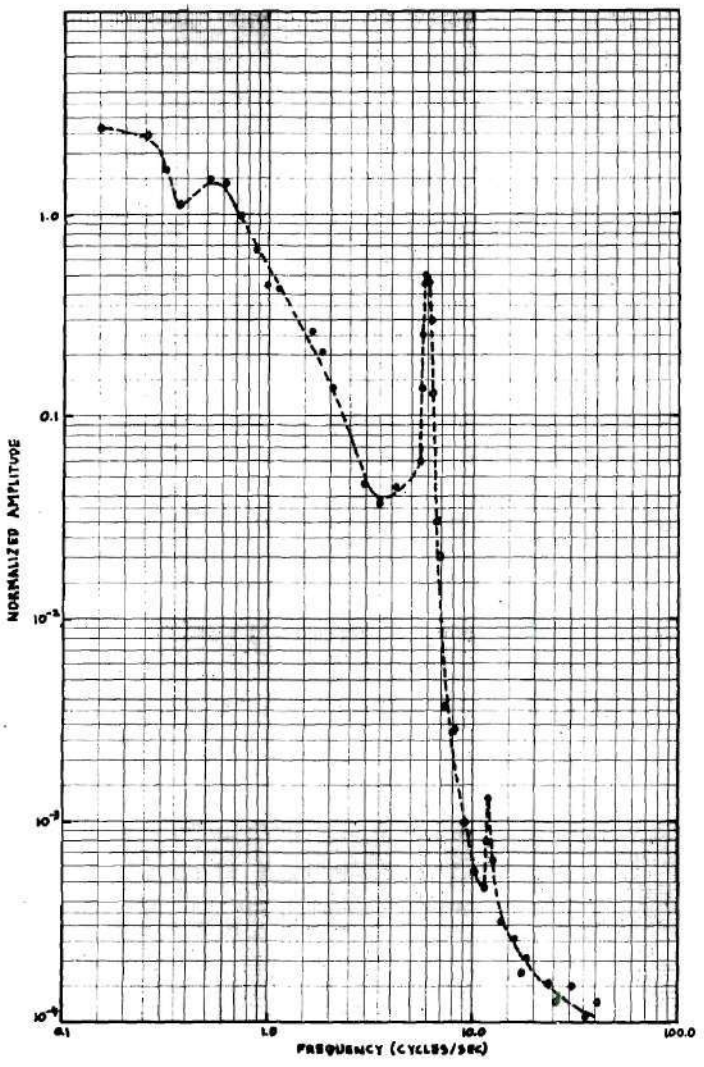

Figure 54. Amplitude of the GTRR Experimental Power Spectral Density, D_2O Coolant Flow Rate 1200 gpm

switching point error for a 4096 ADC was ± 0.025%. This mechanical instability introduced circuit saturation in the electrometer module and sample and hold circuits when a too high amplification was used. Another limitation on the bandwidth investigated was the high uncorrelation to correlation ratio due to the large size of the detector and the presence of high radiation levels caused by high yields of fission product (high burnup) inventories of the Mark-I fuel.

Since the gamma sensitivity of an ionization chamber is at a first approximation proportional to the sensitive volume of the detector, the quality of the measurements could be improved greatly by the use of smaller size detectors, while still maintaining an as high as possible neutron sensitivity. A great part of the uncorrelated noise is due to the presence of the radiation of the fission products; therefore, the quality and the bandwidth of the measurement could be improved by performing the measurements at higher flux levels. This was not possible, however, since the thermal neutron flux range of the RSN-76A detectors was 10^4 to 10^{11} n/cm^2-sec at 90% ion collection efficiency.

The error introduced by the finite data recording time spans was approximately 20% at one cps, 12% at 5.9 cps, and 9% at 10 cps for a 80% confidence level. It must be noted that the error band is not symmetrical around the PSD points. In order to ascertain the cause of the 5.9 cps resonance in the PSD at a coolant flow rate of 1,200 gpm, additional measurements were performed at lower coolant flow rates.

In Figure 55 we have plotted the APSD of detector 1, using variable discrete Fourier transform averages for a total coolant flow rate of 600 gpm, two msec sampling time, time span of 32.768 sec. Comparison of Fig-

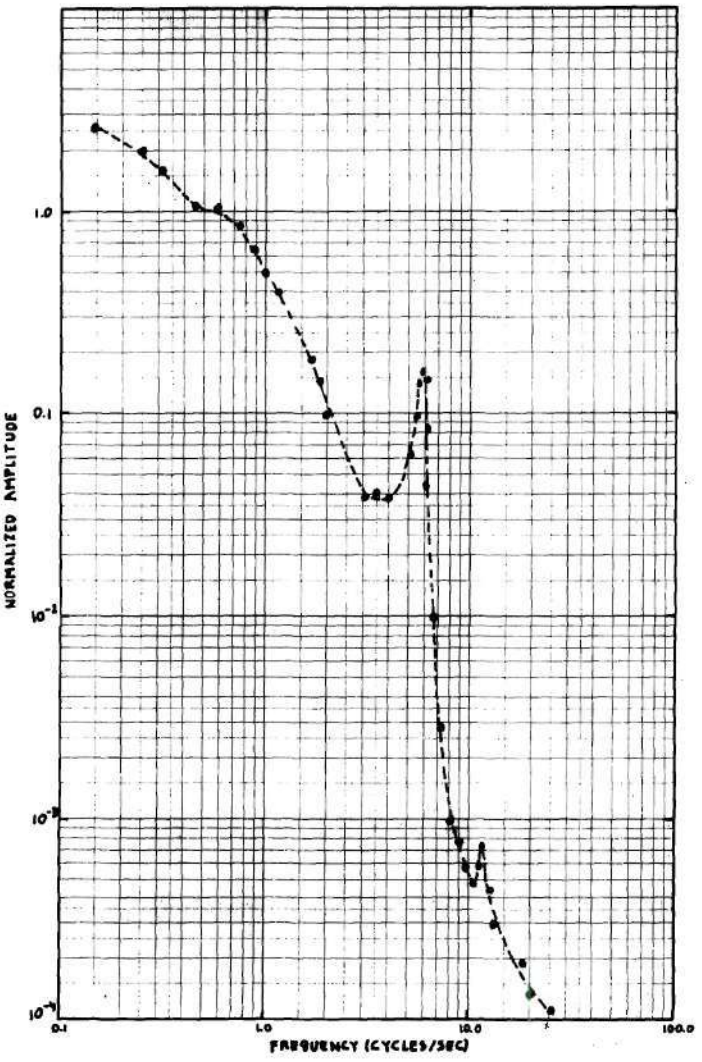

Figure 55. Amplitude of the GTRR Experimental Power Spectral Density, D_2O Coolant Flow Rate 600 gpm

ure 54 (flow rate of 1,200 gpm) with Figure 55 (600 gpm) clearly demonstrates that the power at the 5.9 cps resonance was related to the coolant flow rate. Subsequent measurements were performed at 100 gpm and with no coolant (see Figures 56 and 57). In the case of no coolant, the 5.9 cps resonance could not be detected. Since for the case of the experimental measurements with no coolant flow there were no high amplitude components of 5.9 cps and harmonics present, greater amplification of the AC components of the detector signal could be achieved without saturation of the electronic components. However, since in this case there was no coolant, a slow raise of the moderator temperature was observed, causing a negative reactivity feedback. This in turn caused a slow quadratic (almost linear) varying component to be superimposed on the detector signal.

With the high uniform amplification of the AC components of the neutron detector signal over a frequency band up to 300 cps, the output of the sample-and-hold module was slowly varying over a range of 10 volts in approximately three minutes. Stability of the DC component removal circuits required, however, several minutes. This stability was attained by starting the experiment with the regulating rod fully in, adjusting the shim blades so that a critical system was obtained, 1,200 gpm. After bringing the flow rate down from 1,200 gpm to 0 gpm, the data recording was started over a time span of 32.768 sec. The linear component due to moderator temperature feedback was determined by least-squares fit on the data and subsequently subtracted. This moderator reactivity feedback restricted the current AC amplification.

The presence of a 5.9 cps resonance and its harmonics was attributed directly to an excessive mechanical vibration of one of the semaphore

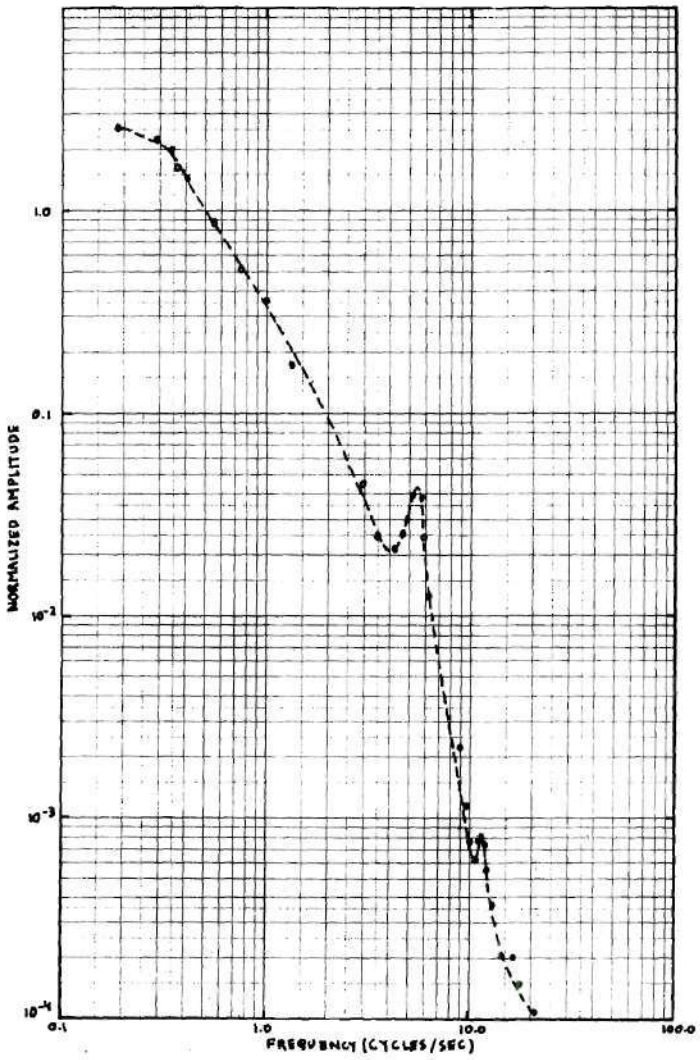

Figure 56. Amplitude of the GTRR Experimental Power Spectral Density, D_2O Coolant Flow Rate 100 gpm

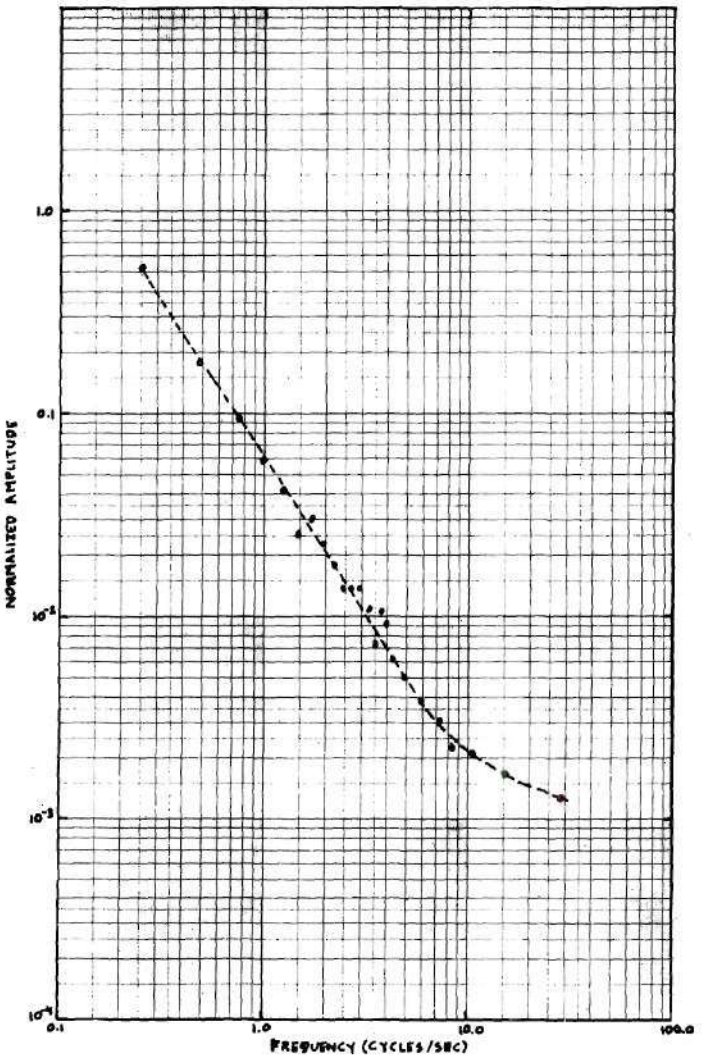

Figure 57. Amplitude of the GTRR Experimental Power Spectral Density, No D_2O Coolant Flow Rate

shim control blades, caused by the relatively fast moving D_2O coolant by the shim blade. The coolant velocity past the control blades was estimated at approximately 4.8 ft/sec for a 1,200 gpm flow rate. Since the semaphore control blades are 5.5 inches wide, 1 inch thick, with a total length from pivot point of 60.75 inches, vibration due to relatively high flow rates is possible. The presence of vibrations of one of the control blades was visually verified with a boroscope, which was installed in the reactor core. At shutdown, it was verified that the amplitude of the vibrations of the control blade was the highest at 1,200 gpm and lower at lower flow rates.

Several changes could be made to improve the quality of the power spectral density measurements at higher frequencies:

1. operation of the reactor at higher neutron flux levels, while still maintaining the assumption of "zero-power reactor" experiment. This would greatly improve the correlated to uncorrelated noise ratio. A large part of the uncorrelated noise was due to the presence of the long-life decay products. In the present experiment, it was not possible to go to higher neutron flux levels due to the limited neutron flux range of the RSN-76A neutron detectors.

2. selection of smaller size neutron detectors. This would increase the ratio of neutron to gamma sensitivity.

3. smaller decay product radiation. This could be partially attained by letting the GTRR, usually operated at one MW-thermal, cool down for longer times before performing those experiments.

4. removal of the mechanical vibration caused by a loose semaphore control blade.

Localized Absorber Perturbations of the GTRR Coupled-Core Configuration

We have seen that the presence of minima in the amplitude of the coherence function of the GTRR coupled-core configuration was due to interference effects of neutronic waves between fuel assemblies through the D_2O coupling region. In the frequency range 0 to 700 cps, two sink frequencies in the CHF of the coupled-core GTRR were observed for inherent spatially dependent stochastic fission sources, and they have been found to be dependent on the nature and the geometry of the coupling and fuel regions.

Let us now investigate the case of perturbing these coupling and fuel regions by means of localized absorber perturbations (e.g., pile oscillators). The most basic approach is the introduction of a known input as a sinusoidal disturbance into the system. However, since the net effect is a mixture of inherent fluctuations, such as the statistical behavior of reactor parameters due to the fission reaction and externally stimulated fluctuations, it would seem that the external input reactivity must be large enough so that the amplitude of the detector signals due to the external stimulation be much larger than the one due to the inherent fluctuations. However, since the theoretical approach was based on a linearization of the fluctuations, only valid for small perturbations, the amplitude of the external disturbance must be kept small. In addition, increasing the amplitude of the fluctuations greatly is undesirable, since we tend then to determine the describing function instead of the transfer function. Also, it may be unsafe to use large perturbations in the reactor.

Assuming that the uncorrelated noise spectrum is white, the output signal due to the external stimulated disturbance could be very much affected by the presence of the inherent sources, especially at the relatively higher frequencies of interest. However, the use of power spectral density data analyses would enable one to strip off the spectrum due to the statistical fluctuations in order to obtain the net response to the external sources.

The use of an external oscillator not only introduces a disturbance at one particular frequency, but also at its harmonics, since it is practically impossible to introduce a pure sinusoidal disturbance. Since the power spectrum of a sinusoid is theoretically a delta function of a certain area at the sinusoid frequency, the appropriate fundamental harmonic can be determined by power spectral density analyses.

For the proposed experiment, a special pile oscillator was designed and constructed (see Appendix C), which made it possible to introduce local disturbances in the core of the GTRR over a frequency band varying from 0 to approximately 700 cps. The pile oscillator was a rotor-stator type, which consisted of an aluminum coaxial tubular rotor and a similar stator with eight (or eighteen) cadmium strips of 20 mil (0.5 mm) thickness on the outer radial surface of each tube. This oscillator fitted into one of the GTRR fuel positions of the core lattice. The entire oscillator reactivity worth was estimated to be approximately 1.1% $\Delta k/k$. This was below the upper limit of 1.5% $\Delta k/k$ approved by the AEC for pile oscillator experiments of this type in the GTRR at that time.

The sampling time interval of the neutron detectors was selected based on the Nyquist frequency, f_N, which is the maximum frequency at

which frequencies are detected in the Fourier analysis. In our case, that limit was 700 cps, since

$$f_N = \frac{1}{2\,\Delta t} \quad , \quad \Delta t = \frac{1}{2 \times 700 \text{ cps}} = 714 \ \mu\text{sec} \ .$$

Since it is only possible to process a data record of finite length, only an estimate of the true power spectral density is therefore obtained. If we require that the power spectral density estimate is accurate to 10% at 5 cps, with a resolution of 2.5 cps at the 90% confidence level, then Schiesser[142] has shown that the degrees of freedom needed are $n = 2BT = 450$. The record length required is then $T = 450/(2 \times 2.5 \text{ cps}) = 90$ sec, and if we sample every 687 μsec, 131,072 (2^{17}) data samples are then required for each neutron detector channel.

The pile oscillator, controlled by a PDP-8 minicomputer, was checked out in the GTRR fuel assembly test stand. The data collection and data analysis procedures were similar to the ones described earlier in this chapter, and were checked out using software generated sinusoids. The discrete Fourier transforms (DFT) were obtained using a fast Fourier transform (FFT) on 262,144 samples for each neutron detector.

Due to the high burnup of the Mark-I fuel, at that time (1971) a GTRR coupled-core configuration with 14 fuel assemblies could not be made critical. The experimental verification of the predicted power spectral densities due to localized external perturbations could not be performed.

The PSD of the GTRR coupled-core was determined for two distinct configurations of the localized absorber perturbations:

1. One localized absorber perturbation, which excited primarily

the fundamental mode behavior of the flux.

2. Two symmetrically located absorbers, driven 180 degrees out of phase of each other, in order to excite primarily the higher modes and to minimize the contribution of the fundamental mode.

Power Spectral Density due to One Localized Absorber Perturbation

For the determination of the PSD due to a localized disturbance, we performed the analysis for the cases where the oscillator was located in the center of the core, in GTRR fuel assembly position V-10 (defined by y-mesh 9 to 10, x-mesh 33 to 36) and in the oustide D_2O reflector, adjacent to fuel assembly V-2.

For a one-point disturbance, the CPSD between detector 1 (d1) and detector 2 (d2) is:

$$CPSD_{d1,d2}(\omega) = H^{*}_{osc \rightarrow d1}(\omega) \cdot H_{osc \rightarrow d2}(\omega) \cdot PSD_{osc,osc}(\omega) \quad (100)$$

where

$H_{osc \rightarrow d1}(\omega)$ = space-, energy-, and frequency-dependent transfer function (or response function) between local disturbance (oscillator) and detector 1

$H^{*}_{osc \rightarrow d1}(\omega)$ = complex conjugate of $H_{osc \rightarrow d1}(\omega)$

$PSD_{osc,osc}(\omega)$ = power spectral density of oscillator (delta function at the sinusoidal frequency)

Since the CPSD between local absorber (osc) and detector 2 (d2) is $CPSD_{osc,d2}(\omega) = H_{osc \rightarrow d2}(\omega)\ PSD_{osc,osc}(\omega)$, the space- and energy-

dependent transfer function $H_{osc \rightarrow d2}(\omega)$ for a given linear reactor system is equal to the ratio of the CPSD between the input and output signals, and the PSD of the input signal.

Since by definition

$$CHF_{d_1,d_2}(\omega) = \frac{CPSD_{d_1,d_2}(\omega)}{\sqrt{APSD_{d_1}(\omega) \cdot APSD_{d_2}(\omega)}} \tag{101}$$

the coherence function between two points in a reactor system, for a one-point disturbance can be written as:

$$CHF_{d_1,d_2}(\omega) = \tag{102}$$

$$\frac{Tr^{*}_{osc \rightarrow d_1}(\omega) \cdot Tr_{osc \rightarrow d_2}(\omega) \cdot PSD_{osc,osc}(\omega)}{\left[\left(\left|Tr_{osc \rightarrow d_1}(\omega)\right|^2 \cdot PSD_{osc,osc}(\omega) + UPSD_{d_1}(\omega)\right)\left(\left|Tr_{osc \rightarrow d_2}(\omega)\right|^2 PSD_{osc,osc}(\omega) + UPSD_{d_2}(\omega)\right)\right]^{1/2}}$$

where

$UPSD_{d1}(\omega)$ = uncorrelated part of the power spectral density of detector 1

$UPSD_{d2}(\omega)$ = uncorrelated part of the power spectral density of detector 2

If the experiments are performed between two pairs of neutron detectors, namely a pair composed of detector 1 and detector 3, and a pair composed of detector 2 and detector 4, then the APSD of the detector pairs are obtained from the expressions $APSD_{d1}(\omega) = CPSD_{d1,d3}(\omega)$ and $APSD_{d2}(\omega) = CPSD_{d2,d4}(\omega)$. In this case we also have that $UPSD_{d1}(\omega) \equiv 0$ and $UPSD_{d2}(\omega) = 0$ for all frequencies.

For a four-detector system, we therefore have

$$CHF_{d_1,d_2}(\omega) = \frac{Tr^{*}_{osc\rightarrow d_1}(\omega)\cdot Tr_{osc\rightarrow d_2}(\omega)\cdot PSD_{osc,osc}(\omega)}{\left[\left|Tr_{osc\rightarrow d_1}(\omega)\right|^2 . PSD_{osc,osc}(\omega)\cdot\left|Tr_{osc\rightarrow d_2}(\omega)\right|^2 . PSD_{osc,osc}(\omega)\right]^{1/2}} \quad (103)$$

The amplitude of the CHF for a four-detector system is therefore 1.0 for all frequencies, and the phase is non-zero in the case of one localized absorber perturbation.

If the experiments are performed with a two-detector system, then we have that:

$$CHF_{d_1,d_2}(\omega) = \frac{Tr^{*}_{osc\rightarrow d_1}(\omega)\cdot Tr_{osc\rightarrow d_2}(\omega)\cdot PSD_{osc,osc}(\omega)}{Denom^{1/2}} \quad (104)$$

with Denom = $\left|Tr_{osc\rightarrow d_1}(\omega)\right|^2 . \left|Tr_{osc\rightarrow d_2}(\omega)\right|^2 . PSD^2_{osc,osc}(\omega)$

$+ \left|Tr_{osc\rightarrow d_1}(\omega)\right|^2 . PSD_{osc,osc}(\omega) . UPSD_{d_2}(\omega)$

$+ \left|Tr_{osc\rightarrow d_2}(\omega)\right|^2 . PSD_{osc,osc}(\omega) . UPSD_{d_1}(\omega)$

$+ UPSD_{d_1}(\omega) . UPSD_{d_2}(\omega)$

The amplitude of the CHF between the signals of a two-detector system is smaller than 1.0 and is frequency-dependent. The phase of the CHF is non-zero. The amplitude and phase are also dependent on the uncorrelated parts of the power spectral densities of the signals of detectors 1 and 2.

For the special case where the oscillator was placed in the center of the reactor core, the neutron detectors were located in symmetrical positions and since the reactor had material and geometrical geometry in that case, we can write that for a two-detector system:

$$CHF_{d_1,d_2}(\omega) = \frac{\left|Tr_{osc \rightarrow d_1}(\omega)\right|^2 . PSD_{osc,osc}(\omega)}{\left|Tr_{osc \rightarrow d_1}(\omega)\right|^2 . PSD_{osc,osc}(\omega) + UPSD_{d_1}(\omega)} \quad (105)$$

The amplitude of the CHF is frequency-dependent and the phase is zero.

In the experimental determination of the coherence function due to a local disturbance, the quality of the measurements can be checked for a four-detector experiment, since the amplitude should be 1.0 at all frequencies. Seifritz and Albrecht[21] have also pointed out that the experimental error for a four-detector system is smaller than for a two-detector system. It follows that a four-detector measurement is far superior to a two-detector one. In the analysis that follows we will assume that we have a four-detector system, so that $UPSD_{d1}(\omega) = 0$ and $UPSD_{d2}(\omega) = 0$.

Calculations of the power spectral densities, due to an externally driven localized disturbance, were performed using the TDPSD (Two-Dimensional Power Spectral Density) code described in Chapter IV. The same mesh grid was used as for the analyses of the GTRR coupled-core due to volume-distributed inherent stochastic sources. In the numerical analysis, the number of columns was 68 and the number of rows was 18. Note that, even in the case where the oscillator is positioned in the central position of the reactor, a one-dimensional approximation to the reactor geometry is insufficient.

The axial leakage (in the third dimension) was taken into account with the usual axial buckling correction factor. To ensure that the PSD calculations were performed for a mathematically critical steady-state reactor ($k_{eff} = 1$), the axial height of the reactor was adjusted uniformly over the reactor, until a value of $k_{eff} = 1$ was obtained for the steady state core. A value for the axial buckling of $B_z^2 = 1.365465\text{-}03\ cm^{-2}$ was obtained.

The local perturbance was assumed to be introduced uniformly over the whole axial direction. For a time-dependent thermal-neutron line absorber located at (x_{osc}, y_{osc}), we have that:

$$\Sigma_a(xyt) = \Sigma_a(xy) + \delta\Sigma_a(xy\omega)\, e^{j\omega t}$$

and for small perturbations

$$\Sigma_a(xyt)\cdot\Phi(xyt) = \Sigma_a(xy)\,\Phi(xy) + \Sigma_a(xy)\,\delta\Phi(xy\omega)\, e^{j\omega t}$$

$$+ \delta\Sigma_a(xy\omega)\,\Phi(xy)\, e^{j\omega t}$$

The spectrum of the disturbance $\delta\Sigma_a(xy\omega)\cdot\phi(xy)$ was arbitrarily chosen to be 1.0 for the power spectral density calculations.

In the PSD calculations, the proper values of the effective delayed neutron and photoneutron fractions were used. They were experimentally determined for the GTRR by Graham[139] and are listed in Table 23. The neutron velocities used in this analysis were 2.2E+5 cm/sec for the thermal-broad energy group and 4.0E+8 cm/sec for the fast-broad energy

group.

The frequency range investigated was 10 to 700 cps. While detector 1 (and detector 3) was held in a reactor location defined by mesh (9,14) (y = 87.98 cm, x = 99.06 cm, see Table 22) inside the external D_2O reflector, detector 2 (and detector 4) was located on an ordinate defined by y-mesh 9 (y = 87.98 cm), successively in locations defined by x-mesh 14 (x = 99.06 cm), 25 (x = 146.68 cm), 34 (x = 166.60 cm), 38 (x = 175.40 cm), 43 (x = 186.28 cm), 51 (x = 209.31 cm), 55 (x = 236.22 cm), and 57 (x = 251.46 cm).

In Table 26 we have displayed the results of the amplitude and phase of the CPSD between the thermal response of detector 1 and the thermal response of detector 2, due to a unity localized thermal perturbation at the center of the reactor core (see Figure 58). The amplitude of the CPSD's was normalized to 1.0 at a frequency of 10 cps.

The values of the amplitude of the CPSD's at 10 cps are also tabulated for the different detector 2 locations, normalized so that the amplitude of the CPSD between detector 1 located at mesh (9,14) and detector 2 at mesh (9,14) was 1.0.

The different curves representing the normalized amplitude and phase of the CPSD's exhibited large space-dependencies, when detector 2 was moved across the reactor core. For the cases that are tabulated, the amplitude changed by a factor of four at a frequency of 100 cps, and by a factor of 760 at 500 cps.

Table 26. Normalized CPSD between Thermal Response Detector 1 and Thermal Response Detector 2, External Source in Mesh Volume (9 to 10, 34 to 35)

X-Y MESH	9,14		9,14		9,14		9,14		9,14		9,14		9,14		9,14		9,14	
DETECTOR 1	9,14		9,25		9,34		9,38		9,43		9,51		9,55		9,57			
DETECTOR 2																		
FREQUENCY (CPS)	AMPLITUDE	PHASE (DEGREES)	AMPLITUDE	PHASE (DEGREES)	AMPLITUDE	PHASE (DEGREES)	AMPLITUDE	PHASE (DEGREES)	AMPLITUDE	PHASE (DEGREES)	AMPLITUDE	PHASE (DEGREES)	AMPLITUDE	PHASE (DEGREES)	AMPLITUDE	PHASE (DEGREES)		
10.0	1.000+00		2.674+00		4.591+00		3.643+00		2.758+00		2.495+00		1.000+00		5.205-01			
10.0	1.000+00	0.000	1.000+00	-1.033+01	1.000+00	-2.663+01	1.000+00	-1.839+01	1.000+00	-1.119+01	1.000+00	-5.126+00	1.000+00	7.752+06	1.000+00	3.072+00		
20.0	2.473+01	0.000	2.558+01	-2.031+01	2.913+01	-4.916+01	2.685+01	-3.542+01	2.565+01	-2.197+01	2.512+01	-1.010+01	2.473+01	+6.101+06	2.453+01	6.074+00		
40.0	5.447+02	0.000	6.304+02	-3.825+01	9.612+02	-8.094+01	7.597+02	-6.326+01	6.403+02	-4.124+01	5.839+02	-1.920+01	5.447+02	+2.309+05	5.239+02	1.165+01		
60.0	2.017+02	0.000	2.709+02	+5.305+01	5.179+02	-1.020+02	3.724+02	+8.371+01	2.790+02	+5.700+01	2.328+02	+2.686+01	2.017+02	+3.535+05	1.857+02	1.648+01		
80.0	9.224+03	0.000	1.453+02	+6.511+01	3.279+02	-1.177+02	2.225+02	+9.928+01	1.516+02	+6.976+01	1.153+02	+3.321+01	9.224+03	+5.512+05	8.075+03	2.056+01		
100.0	4.747+03	0.000	8.784+03	+7.512+01	2.246+02	-1.304+02	1.464+02	+1.118+02	9.250+03	+8.030+01	6.448+03	+3.852+01	4.747+03	+2.948+05	3.941+03	2.402+01		
110.0	3.512+03	0.000	7.006+03	+7.953+01	1.895+02	-1.380+02	1.216+02	+1.173+02	7.434+03	+8.493+01	4.970+03	+4.086+01	3.512+03	+1.846+05	2.837+03	2.556+01		
120.0	2.639+03	0.000	5.682+03	+8.382+01	1.614+02	-1.413+02	1.021+02	+1.228+02	6.060+03	+8.923+01	3.891+03	+4.303+01	2.639+03	+2.783+05	2.075+03	2.699+01		
130.0	2.011+03	0.000	4.666+03	+8.743+01	1.386+02	-1.462+02	8.650+03	+1.271+02	4.998+03	+9.323+01	3.086+03	+4.505+01	2.011+03	+2.594+05	1.539+03	2.832+01		
140.0	1.550+03	0.000	3.868+03	+9.099+01	1.198+02	-1.509+02	7.390+03	+1.315+02	4.165+03	+9.698+01	2.475+03	+4.693+01	1.550+03	+3.896+05	1.154+03	2.957+01		
150.0	1.207+03	0.000	3.236+03	+9.434+01	1.042+02	-1.553+02	6.356+03	+1.357+02	3.497+03	+1.005+02	2.004+03	+4.870+01	1.207+03	+3.785+05	8.740+04	3.075+01		
160.0	9.476+04	0.000	2.727+03	+9.709+01	9.106+03	-1.595+02	5.499+03	+1.397+02	2.980+03	+1.038+02	1.637+03	+5.036+01	9.476+04	+2.600+05	6.679+04	3.185+01		
170.0	7.501+04	0.000	2.314+03	+1.005+02	7.995+03	-1.636+02	4.781+03	+1.435+02	2.521+03	+1.069+02	1.386+03	+5.192+01	7.501+04	+3.466+05	5.143+04	3.290+01		
180.0	5.980+04	0.000	1.975+03	+1.033+02	7.047+03	-1.672+02	4.177+03	+1.470+02	2.159+03	+1.099+02	1.115+03	+5.338+01	5.980+04	+3.784+05	3.988+04	3.388+01		
190.0	4.796+04	0.000	1.696+03	+1.060+02	6.235+03	-1.712+02	3.663+03	+1.505+02	1.858+03	+1.127+02	9.289+04	+5.477+01	4.796+04	+2.468+05	3.111+04	3.481+01		
200.0	3.869+04	0.000	1.460+03	+1.085+02	5.534+03	-1.747+02	3.225+03	+1.538+02	1.607+03	+1.154+02	7.779+04	+5.608+01	3.869+04	+2.872+05	2.441+04	3.570+01		
220.0	2.556+04	0.000	1.097+03	+1.132+02	4.396+03	1.785+02	2.523+03	+1.599+02	1.216+03	+1.204+02	5.533+04	+5.848+01	2.556+04	+3.207+05	1.523+04	3.732+01		
240.0	1.717+04	0.000	8.364+04	+1.175+02	3.527+03	1.722+02	1.995+03	+1.656+02	9.323+04	+1.249+02	3.999+04	+6.062+01	1.717+04	+2.829+05	9.658+05	3.876+01		
260.0	1.171+04	0.000	6.450+04	+1.214+02	2.854+03	1.663+02	1.593+03	+1.709+02	7.229+04	+1.291+02	2.930+04	+6.253+01	1.171+04	+3.322+05	6.204+05	4.004+01		
280.0	8.079+05	0.000	5.024+04	+1.250+02	2.325+03	1.608+02	1.281+03	+1.758+02	5.660+04	+1.329+02	2.172+04	+6.422+01	8.079+05	+2.276+05	4.027+05	4.115+01		
300.0	5.635+05	0.000	3.946+04	+1.283+02	1.906+03	1.556+02	1.038+03	1.796+02	4.488+04	+1.363+02	1.626+04	+6.572+01	5.635+05	+3.852+05	2.636+05	4.209+01		
320.0	3.968+05	0.000	3.123+04	+1.312+02	1.571+03	1.507+02	8.457+04	1.754+02	3.553+04	+1.395+02	1.229+04	+6.702+01	3.968+05	+3.690+05	1.737+05	4.285+01		
340.0	2.816+05	0.000	2.487+04	+1.339+02	1.301+03	1.461+02	6.927+04	1.714+02	2.843+04	+1.424+02	9.356+05	+6.813+01	2.816+05	+3.836+05	1.150+05	4.342+01		
360.0	2.013+05	0.000	1.993+04	+1.363+02	1.082+03	1.418+02	5.699+04	1.678+02	2.287+04	+1.451+02	7.173+05	+6.907+01	2.013+05	+2.956+05	7.634+06	4.375+01		
380.0	1.448+05	0.000	1.604+04	+1.385+02	9.034+04	1.378+02	4.709+04	1.644+02	1.849+04	+1.475+02	5.533+05	+6.983+01	1.448+05	+2.702+05	5.078+06	4.382+01		
400.0	1.048+05	0.000	1.298+04	+1.405+02	7.566+04	1.340+02	3.905+04	1.612+02	1.502+04	+1.496+02	4.291+05	+7.042+01	1.048+05	+2.446+05	3.379+06	4.354+01		
420.0	7.619+06	0.000	1.054+04	+1.422+02	6.356+04	1.305+02	3.249+04	1.583+02	1.225+04	+1.515+02	3.345+05	+7.083+01	7.619+06	+2.391+05	2.245+06	4.284+01		
440.0	5.565+06	0.000	8.593+05	+1.437+02	5.353+04	1.272+02	2.711+04	1.557+02	1.002+04	+1.532+02	2.619+05	+7.106+01	5.565+06	+3.677+05	1.488+06	4.157+01		
460.0	4.081+06	0.000	7.029+05	+1.449+02	4.520+04	1.243+02	2.288+04	1.533+02	8.228+05	+1.546+02	2.060+05	+7.110+01	4.081+06	+2.126+05	9.833+07	3.955+01		
480.0	3.004+06	0.000	5.768+05	+1.459+02	3.825+04	1.215+02	1.903+04	1.512+02	6.776+05	+1.556+02	1.626+05	+7.095+01	3.004+06	+2.596+05	6.475+07	3.609+01		
500.0	2.220+06	0.000	4.747+05	+1.466+02	3.244+04	1.191+02	1.600+04	1.493+02	5.596+05	+1.567+02	1.288+05	+7.061+01	2.220+06	+2.852+05	4.256+07	3.201+01		
520.0	1.646+06	0.000	3.918+05	+1.471+02	2.757+04	1.169+02	1.348+04	1.477+02	4.635+05	+1.574+02	1.023+05	+7.005+01	1.646+06	+1.349+05	2.814+07	2.564+01		
540.0	1.224+06	0.000	3.242+05	+1.474+02	2.348+04	1.149+02	1.139+04	1.465+02	3.849+05	+1.578+02	8.160+06	+6.927+01	1.224+06	+1.311+05	1.893+07	1.693+01		
560.0	9.143+07	0.000	2.691+05	+1.473+02	2.004+04	1.133+02	9.640+05	1.453+02	3.204+05	+1.579+02	6.528+06	+6.826+01	9.143+07	+2.528+05	1.327+07	5.914+00		
580.0	6.854+07	0.000	2.239+05	+1.470+02	1.714+04	1.120+02	8.181+05	1.445+02	2.675+05	+1.578+02	5.239+06	+6.701+01	6.854+07	+8.831+06	9.910+08	+6.423+00		
600.0	5.160+07	0.000	1.869+05	+1.464+02	1.470+04	1.110+02	6.960+05	1.441+02	2.240+05	+1.573+02	4.219+06	+6.550+01	5.160+07	+2.408+05	7.951-08	-1.820+01		

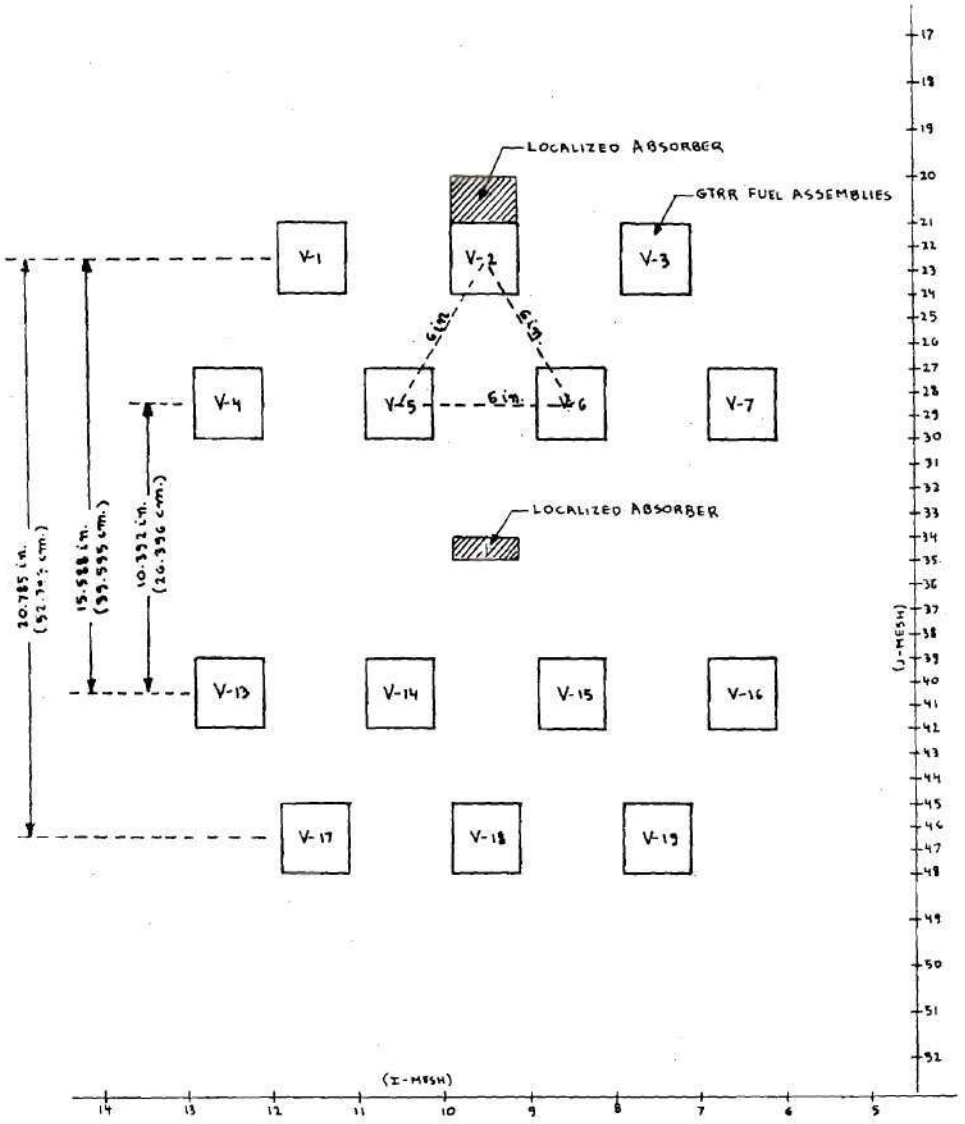

Figure 58. Fourteen Assembly Coupled-Core GTRR with a Localized Absorber Perturbation

For symmetrically located detectors (detector 1 at mesh (9,14) and detector 2 at mesh (9,55)), the phase was of the order of 10^{-5} degrees. In the cases where the reactor exhibited geometrical and material symmetry, the phase of the CPSD and the CHF was theoretically zero for symmetrically located detectors.

In Table 27 are tabulated the results of the APSD normalized to 1.0 at a frequency of 10 cps. The amplitude varies by a factor of 32 at 100 cps, and by a factor of 10^6 at 500 cps. The APSD's have the largest values when the detector location coincides with the localized perturbation.

No minima in the amplitude were detected either for the CPSD's or the APSD's when the localized absorber perturbation was in the center of the core.

Next, we have determined the PSD for the GTRR coupled-core configuration, when a localized thermal neutron absorber was located in the outside D_2O reflector, adjacent to GTRR assembly V-2 (see Figure 58), and defined by y-mesh 9 and 10 and by x-mesh 20 and 21. The calculational approach was similar to the case where the localized absorber was positioned in the center of the reactor core. In Table 28 are tabulated the amplitude and the phase of the CPSD's between the thermal responses of detector 1 and detector 2. The amplitudes were normalized to a value of 1.0 at a frequency of 10 cps. The amplitudes of the CPSD exhibited a strong space-dependency. In Table 29 are tabulated the results for the APSD due to the localized perturbation at y-mesh 9 to 10 and x-mesh 20 to 21. Again, we observe a strong space dependency. No minima or "sinks" were detected in the amplitude of the CPSD's or the APSD's for any

Table 27. Normalized APSD of Thermal Response Detector 2, External Source in Mesh Volume (9 to 10, 34 to 35)

Y-X MESH	9,14	9,25	9,34	9,38	9,43	9,51	9,55	9,57
FREQUENCY (CPS)	AMPLITUDE	AMPLITUDE	AMPLITUDE	AMPLITUDE	AMPLITUDE	AMPLITUDE	AMPLITUDE	AMPLITUDE
10.0	1.000+00	7.153+00	2.108+01	1.327+01	7.606+00	6.231+00	1.000+00	2.710-01
10.0	1.000+00	1.000+00	1.000+00	1.000+00	1.000+00	1.000+00	1.000+00	1.000+00
20.0	2.473-01	2.640-01	3.430-01	2.913-01	2.660-01	2.550-01	2.473-01	2.433-01
40.0	5.447-02	7.294-02	1.696-01	1.059-01	7.525-02	6.254-02	5.447-02	5.038-02
60.0	2.017-02	3.638-02	1.329-01	6.873-02	3.857-02	2.681-02	2.017-02	1.710-02
80.0	9.224-03	2.288-02	1.165-01	5.364-02	2.491-02	1.441-02	9.224-03	7.068-03
100.0	4.747-03	1.617-02	1.063-01	4.515-02	1.802-02	8.753-03	4.747-03	3.271-03
110.0	3.512-03	1.397-02	1.023-01	4.206-02	1.573-02	7.029-03	3.512-03	2.292-03
120.0	2.639-03	1.223-02	9.870-02	3.945-02	1.391-02	5.731-03	2.639-03	1.632-03
130.0	2.011-03	1.082-02	9.551-02	3.720-02	1.242-02	4.733-03	2.011-03	1.177-03
140.0	1.550-03	9.652-03	9.261-02	3.523-02	1.118-02	3.950-03	1.550-03	8.589-04
150.0	1.207-03	8.676-03	8.995-02	3.347-02	1.014-02	3.327-03	1.207-03	6.331-04
160.0	9.476-04	7.847-03	8.748-02	3.190-02	9.243-03	2.825-03	9.476-04	4.707-04
170.0	7.501-04	7.136-03	8.519-02	3.047-02	8.469-03	2.415-03	7.501-04	3.526-04
180.0	5.980-04	6.519-03	8.304-02	2.917-02	7.794-03	2.078-03	5.980-04	2.660-04
190.0	4.796-04	5.980-03	8.103-02	2.797-02	7.200-03	1.798-03	4.796-04	2.018-04
200.0	3.869-04	5.505-03	7.912-02	2.687-02	6.674-03	1.563-03	3.869-04	1.539-04
220.0	2.556-04	4.711-03	7.562-02	2.490-02	5.784-03	1.197-03	2.556-04	9.077-05
240.0	1.717-04	4.073-03	7.245-02	2.318-02	5.061-03	9.308-04	1.717-04	5.432-05
260.0	1.171-04	3.553-03	6.956-02	2.166-02	4.464-03	7.330-04	1.171-04	3.288-05
280.0	8.079-05	3.123-03	6.692-02	2.032-02	3.965-03	5.836-04	8.079-05	2.007-05
300.0	5.635-05	2.762-03	6.448-02	1.911-02	3.542-03	4.692-04	5.635-05	1.233-05
320.0	3.968-05	2.457-03	6.222-02	1.802-02	3.181-03	3.803-04	3.968-05	7.600-06
340.0	2.816-05	2.196-03	6.013-02	1.703-02	2.869-03	3.106-04	2.816-05	4.692-06
360.0	2.013-05	1.971-03	5.817-02	1.613-02	2.598-03	2.554-04	2.013-05	2.895-06
380.0	1.448-05	1.777-03	5.634-02	1.530-02	2.361-03	2.112-04	1.448-05	1.780-06
400.0	1.048-05	1.607-03	5.463-02	1.455-02	2.153-03	1.756-04	1.048-05	1.089-06
420.0	7.619-06	1.458-03	5.301-02	1.385-02	1.968-03	1.468-04	7.619-06	6.616-07
440.0	5.565-06	1.327-03	5.149-02	1.320-02	1.805-03	1.232-04	5.565-06	3.980-07
460.0	4.081-06	1.210-03	5.006-02	1.260-02	1.659-03	1.039-04	4.081-06	2.369-07
480.0	3.004-06	1.107-03	4.870-02	1.205-02	1.528-03	8.791-05	3.004-06	1.395-07
500.0	2.220-06	1.015-03	4.741-02	1.153-02	1.411-03	7.465-05	2.220-06	8.166-08
520.0	1.646-06	9.324-04	4.619-02	1.104-02	1.305-03	6.360-05	1.646-06	4.809-08
540.0	1.224-06	8.583-04	4.502-02	1.059-02	1.210-03	5.435-05	1.224-06	2.927-08
560.0	9.143-07	7.917-04	4.392-02	1.016-02	1.123-03	4.658-05	9.143-07	1.925-08
580.0	6.854-07	7.314-04	4.286-02	9.763-03	1.044-03	4.003-05	6.854-07	1.433-08
600.0	5.160-07	6.769-04	4.185-02	9.387-03	9.725-04	3.448-05	5.160-07	1.225-08

Table 28. Normalized CPSD between Thermal Response Detector 1 and Thermal Response Detector 2, External Source in Mesh Volume (9 to 10, 20 to 21)

Y-ax MESH		9,19		9,19		9,19		9,19		9,19		9,19		9,19		9,19	
DETECTOR 1		9,19		9,25		9,34		9,3A		9,43		9,51		9,55		9,57	
DETECTOR 2																	
FREQUENCY (CPS)	AMPLITUDE	PHASE (DEGREES)	AMPLITUDE	PHASE (DEGREES)	AMPLITUDE	PHASE (DEGREES)	AMPLITUDE	PHASE (DEGREES)	AMPLITUDE	PHASE (DEGREES)	AMPLITUDE	PHASE (DEGREES)	AMPLITUDE	PHASE (DEGREES)	AMPLITUDE	PHASE (DEGREES)
10.0	1.000+00		2.582+00		3.616+00		3.027+00		2.355+00		2.147+00		8.612+01		4.486+01	
10.0	1.000+00	0.000	1.000+00	-4.923+00	1.000+00	8.835+00	1.000+00	1.140+01	1.000+00	1.434+01	1.000+00	1.894+01	1.000+00	2.383+01	1.000+00	2.883+01
20.0	3.254+01	0.000	3.241+01	-1.063+01	2.910+01	1.392+01	2.874+01	1.885+01	2.841+01	2.459+01	2.801+01	3.303+01	2.763+01	4.328+01	2.741+01	4.922+01
30.0	1.304+01	0.000	1.344+01	-2.270+01	9.435+02	1.406+01	8.967+02	2.279+01	8.520+02	3.331+01	8.000+02	5.043+01	7.510+02	6.885+01	7.234+02	8.028+01
40.0	7.729+02	0.000	8.587+02	-3.332+01	4.964+02	9.155+00	4.517+02	2.047+01	4.086+02	3.460+01	3.593+02	5.850+01	3.149+02	8.842+01	2.909+02	1.006+02
50.0	5.076+02	0.000	6.167+02	-4.218+01	3.082+02	3.754+00	2.695+02	1.685+01	2.319+02	3.365+01	1.896+02	6.313+01	1.539+02	9.536+01	1.353+02	1.157+02
100.0	3.508+02	0.000	4.672+02	-4.968+01	2.083+02	-1.109+00	1.758+02	1.350+01	1.448+02	3.212+01	1.097+02	6.624+01	8.210+03	1.038+02	6.854+03	1.274+02
110.0	2.958+02	0.000	4.120+02	-5.304+01	1.749+02	-3.298+00	1.453+02	1.166+01	1.167+02	3.132+01	8.550+03	6.746+01	6.144+03	1.074+02	4.994+03	1.328+02
120.0	2.510+02	0.000	3.659+02	-5.620+01	1.484+02	-5.338+00	1.215+02	1.012+01	9.555+03	3.053+01	6.751+03	6.855+01	4.659+03	1.106+02	3.686+03	1.375+02
130.0	2.145+02	0.000	3.268+02	-5.917+01	1.271+02	-7.243+00	1.026+02	8.673+00	7.905+03	2.976+01	5.391+03	6.951+01	3.573+03	1.136+02	2.751+03	1.418+02
140.0	1.843+02	0.000	2.934+02	-6.198+01	1.097+02	-9.025+00	8.734+03	7.317+00	6.601+03	2.902+01	4.347+03	7.038+01	2.788+03	1.164+02	2.073+03	1.459+02
150.0	1.593+02	0.000	2.645+02	-6.466+01	9.530+03	-1.070+01	7.492+03	6.044+00	5.557+03	2.831+01	3.536+03	7.118+01	2.164+03	1.189+02	1.576+03	1.496+02
160.0	1.383+02	0.000	2.395+02	-6.721+01	8.327+03	-1.228+01	6.467+03	4.847+00	4.711+03	2.763+01	2.898+03	7.191+01	1.705+03	1.213+02	1.208+03	1.532+02
170.0	1.205+02	0.000	2.176+02	-6.965+01	7.314+03	-1.377+01	5.615+03	3.718+00	4.019+03	2.698+01	2.319+03	7.258+01	1.353+03	1.235+02	9.321+04	1.564+02
180.0	1.055+02	0.000	1.983+02	-7.198+01	6.455+03	-1.518+01	4.899+03	2.852+00	3.447+03	2.637+01	1.986+03	7.320+01	1.080+03	1.256+02	7.236+04	1.595+02
190.0	9.263+03	0.000	1.813+02	-7.423+01	5.719+03	-1.652+01	4.294+03	1.643+00	2.972+03	2.578+01	1.658+03	7.378+01	8.677+04	1.276+02	5.649+04	1.624+02
200.0	8.162+03	0.000	1.661+02	-7.639+01	5.087+03	-1.780+01	3.779+03	6.852+01	2.574+03	2.522+01	1.391+03	7.432+01	7.006+04	1.294+02	4.432+04	1.651+02
220.0	6.393+03	0.000	1.405+02	-8.048+01	4.084+03	-2.019+01	2.959+03	-1.094+00	1.954+03	2.416+01	9.921+04	7.528+01	4.630+04	1.327+02	2.763+04	1.701+02
240.0	5.059+03	0.000	1.198+02	-8.431+01	3.285+03	-2.238+01	2.346+03	-2.716+00	1.504+03	2.318+01	7.186+04	7.611+01	3.109+04	1.356+02	1.748+04	1.745+02
260.0	4.040+03	0.000	1.029+02	-8.792+01	2.681+03	-2.441+01	1.879+03	-4.206+00	1.171+03	2.227+01	5.272+04	7.683+01	2.116+04	1.381+02	1.118+04	1.783+02
280.0	3.252+03	0.000	8.894+03	-9.132+01	2.207+03	-2.630+01	1.519+03	-5.584+00	9.209+04	2.142+01	3.912+04	7.743+01	1.456+04	1.403+02	7.215+05	-1.783+02
300.0	2.636+03	0.000	7.727+03	-9.456+01	1.830+03	-2.867+01	1.238+03	-6.867+00	7.305+04	2.061+01	2.930+04	7.792+01	1.012+04	1.421+02	4.687+05	-1.755+02
320.0	2.150+03	0.000	6.745+03	-9.761+01	1.527+03	-2.973+01	1.016+03	-8.067+00	5.838+04	1.983+01	2.213+04	7.831+01	7.095+05	1.036+02	3.058+05	-1.732+02
340.0	1.764+03	0.000	5.913+03	-1.005+02	1.282+03	-3.129+01	8.386+04	-9.196+00	4.696+04	1.909+01	1.683+04	7.859+01	5.005+05	1.048+02	2.000+05	-1.715+02
360.0	1.454+03	0.000	5.204+03	-1.033+02	1.082+03	-3.277+01	6.961+04	-1.026+01	3.800+04	1.836+01	1.288+04	7.877+01	3.553+05	1.057+02	1.308+05	-1.703+02
380.0	1.204+03	0.000	4.595+03	-1.060+02	9.171+04	-3.418+01	5.806+04	-1.127+01	3.090+04	1.764+01	9.918+05	7.886+01	2.535+05	1.062+02	8.544+06	-1.698+02
400.0	1.001+03	0.000	4.070+03	-1.086+02	7.807+04	-3.551+01	4.884+04	-1.224+01	2.525+04	1.694+01	7.672+05	7.881+01	1.816+05	1.064+02	5.557+06	-1.701+02
420.0	8.358+04	0.000	3.616+03	-1.110+02	6.671+04	-3.679+01	4.091+04	-1.316+01	2.072+04	1.624+01	5.980+05	7.885+01	1.306+05	1.062+02	3.592+06	-1.714+02
440.0	6.998+04	0.000	3.220+03	-1.134+02	5.720+04	-3.801+01	3.453+04	-1.405+01	1.706+04	1.553+01	4.647+05	7.837+01	9.422+06	1.057+02	2.302+06	-1.739+02
460.0	5.880+04	0.000	2.875+03	-1.157+02	4.921+04	-3.917+01	2.925+01	-1.490+01	1.410+04	1.482+01	3.636+05	7.796+01	6.814+06	1.047+02	1.461+06	-1.783+02
480.0	4.954+04	0.000	2.572+03	-1.179+02	4.246+04	-4.029+01	2.485+04	-1.572+01	1.169+04	1.410+01	2.853+05	7.741+01	4.939+06	1.032+02	9.204+07	1.749+02
500.0	4.185+04	0.000	2.305+03	-1.201+02	3.673+04	-4.137+01	2.116+04	-1.652+01	9.715+05	1.336+01	2.244+05	7.671+01	3.588+06	1.013+02	5.821+07	1.648+02
520.0	3.545+04	0.000	2.071+03	-1.222+02	3.185+04	-4.241+01	1.807+04	-1.730+01	8.095+05	1.260+01	1.769+05	7.585+01	2.613+06	1.387+02	3.811+07	1.496+02
540.0	3.009+04	0.000	1.863+03	-1.242+02	2.768+04	-4.341+01	1.547+04	-1.806+01	6.761+05	1.182+01	1.398+05	7.480+01	1.908+06	1.355+02	2.717+07	1.310+02
560.0	2.559+04	0.000	1.679+03	-1.261+02	2.411+04	-4.437+01	1.327+04	-1.880+01	5.658+05	1.101+01	1.106+05	7.356+01	1.398+06	1.316+02	2.174+07	1.121+02
580.0	2.181+04	0.000	1.515+03	-1.280+02	2.104+04	-4.531+01	1.141+04	-1.952+01	4.745+05	1.017+01	8.772+06	7.211+01	1.030+06	1.269+02	1.846+07	9.631+01
600.0	1.862+04	0.000	1.369+03	-1.299+02	1.840+04	-4.621+01	9.820+05	-2.024+01	3.985+05	9.300+00	6.966+06	7.041+01	7.641+07	1.213+02	1.712+07	8.438+01

Table 29. Normalized APSD of Thermal Response Detector 2, External Source in Mesh Volume (9 to 10, 20 to 21)

Y-X MESH	9,14	9,25	9,34	9,38	9,43	9,51	9,55	9,57
FREQUENCY (CPS)	AMPLITUDE	AMPLITUDE	AMPLITUDE	AMPLITUDE	AMPLITUDE	AMPLITUDE	AMPLITUDE	AMPLITUDE
10.0	1.000+00	6.667+00	1.308+01	9.160+00	5.548+00	4.160+00	7.416-01	2.012-01
10.0	1.000+00	1.000+00	1.000+00	1.000+00	1.000+00	1.000+00	1.000+00	1.000+00
20.0	3.254-01	3.228-01	2.601-01	2.538-01	2.479-01	2.412-01	2.347-01	2.309-01
40.0	1.301-01	1.385-01	6.827-02	6.167-02	5.566-02	4.911-02	4.326-02	4.014-02
60.0	7.729-02	9.543-02	3.187-02	2.640-02	2.160-02	1.670-02	1.283-02	1.095-02
80.0	5.076-02	7.493-02	1.871-02	1.430-02	1.059-02	7.088-03	4.663-03	3.609-03
100.0	3.508-02	6.224-02	1.237-02	8.813-03	5.943-03	3.431-03	1.921-03	1.339-03
110.0	2.956-02	5.745-02	1.035-02	7.142-03	4.608-03	2.473-03	1.277-03	8.436-04
120.0	2.510-02	5.335-02	8.777-03	5.880-03	3.636-03	1.816-03	8.648-04	5.412-04
130.0	2.145-02	4.981-02	7.532-03	4.905-03	2.913-03	1.355-03	5.954-04	3.527-04
140.0	1.843-02	4.670-02	6.526-03	4.138-03	2.363-03	1.025-03	4.158-04	2.332-04
150.0	1.593-02	4.395-02	5.700-03	3.524-03	1.938-03	7.852-04	2.940-04	1.560-04
160.0	1.383-02	4.149-02	5.014-03	3.025-03	1.605-03	6.076-04	2.102-04	1.055-04
170.0	1.205-02	3.928-02	4.438-03	2.616-03	1.340-03	4.746-04	1.518-04	7.207-05
180.0	1.055-02	3.729-02	3.949-03	2.276-03	1.126-03	3.739-04	1.107-04	4.964-05
190.0	9.263-03	3.547-02	3.530-03	1.991-03	9.534-04	2.967-04	8.127-05	3.445-05
200.0	8.162-03	3.381-02	3.170-03	1.750-03	8.117-04	2.370-04	6.013-05	2.407-05
220.0	6.393-03	3.089-02	2.584-03	1.370-03	5.972-04	1.540-04	3.353-05	1.194-05
240.0	5.059-03	2.839-02	2.132-03	1.088-03	4.470-04	1.021-04	1.911-05	6.038-06
260.0	4.040-03	2.622-02	1.779-03	8.743-04	3.394-04	6.882-05	1.108-05	3.094-06
280.0	3.252-03	2.433-02	1.497-03	7.099-04	2.607-04	4.706-05	6.523-06	1.601-06
300.0	2.636-03	2.265-02	1.270-03	5.815-04	2.024-04	3.257-05	3.886-06	8.333-07
320.0	2.150-03	2.116-02	1.085-03	4.799-04	1.584-04	2.277-05	2.340-06	4.349-07
340.0	1.764-03	1.983-02	9.318-04	3.988-04	1.250-04	1.607-05	1.420-06	2.268-07
360.0	1.454-03	1.863-02	8.048-04	3.333-04	9.928-05	1.142-05	8.682-07	1.177-07
380.0	1.204-03	1.754-02	6.984-04	2.800-04	7.930-05	8.172-06	5.337-07	6.064-08
400.0	1.001-03	1.655-02	6.086-04	2.363-04	6.368-05	5.881-06	3.295-07	3.085-08
420.0	8.356-04	1.565-02	5.325-04	2.003-04	5.136-05	4.252-06	2.042-07	1.544-08
440.0	6.998-04	1.482-02	4.675-04	1.704-04	4.159-05	3.087-06	1.268-07	7.570-09
460.0	5.880-04	1.406-02	4.118-04	1.455-04	3.381-05	2.249-06	7.897-08	3.630-09
480.0	4.954-04	1.335-02	3.637-04	1.246-04	2.757-05	1.643-06	4.925-08	1.710-09
500.0	4.185-04	1.270-02	3.222-04	1.070-04	2.254-05	1.204-06	3.076-08	8.095-10
520.0	3.545-04	1.210-02	2.861-04	9.215-05	1.848-05	8.835-07	1.926-08	4.097-10
540.0	3.009-04	1.154-02	2.546-04	7.954-05	1.519-05	6.497-07	1.210-08	2.454-10
560.0	2.559-04	1.101-02	2.271-04	6.881-05	1.251-05	4.785-07	7.636-09	1.847-10
580.0	2.181-04	1.052-02	2.030-04	5.965-05	1.032-05	3.530-07	4.862-09	1.648-10
600.0	1.862-04	1.007-02	1.818-04	5.180-05	8.529-06	2.607-07	3.136-09	1.574-10

detector locations in the GTRR coupled-core configuration, when the localized perturbation was positioned in the outside D_2O reflector adjacent to fuel assembly V-2.

This is in contrast to the numerical calculations, based on one-dimensional modal expansions, performed by Danofsky[28] for the coupled-core UTR-10 reactor. In the numerical calculations, Danofsky used five and seven one-dimensional modes for a localized thermal neutron absorber located in a fuel region. Danofsky determined that the APSD exhibited a minimum at approximately 180 cps. This behavior of the APSD due to a localized absorber was found to be similar to the behavior of the CPSD's and the CHF's due to the volume distributed inherent fission sources. However, Danofsky pointed out that it was not known if the characteristics of the behavior of the APSD were due to a lack of convergence of the one-dimensional modal solution used in his numerical evaluations.

Power Spectral Density due to Two Localized Absorber Perturbations Driven 180 Degrees Out of Phase

In the introduction, it was shown that the modal method expresses the space-time dependence of the perturbed flux as

$$\phi(\bar{r}t) = \sum_{n=0}^{\infty} \psi_n(\bar{r})\, T_n(t) \tag{106}$$

where $T_n(t)$ = time-dependent function of the n^{th} mode

$\psi_n(\bar{r})$ = spatial function of the n^{th} mode.

For two-dimensional geometries, we have besides the fundamental mode ($n=0$) also the higher modes ($n>0$) as the azimuthal and radial modes in r-θ geometry, and the x- and y-modes in x-y geometry. In order to

minimize the excitation of the fundamental mode, two identical localized absorbers were located in symmetrical locations. The absorbers were driven 180 degrees out of phase, so that the total reactivity introduced in the system was zero. The higher modes were, therefore, preferentially excited and the contamination of the response through the high gain of the fundamental mode was minimized. Since space-dependency of transfer functions occurs primarily through the higher modes, excitations of those modes can be preferentially obtained through the use of several localized absorbers, each driven out of phase of one another.

The use of several localized perturbations, in order to excite preferentially higher modes, is not new. Serdula, Kendall, Cloutier, and Lawrence[143] performed modal calculations and experimental verification on the 250 Mwe Gentilly Nuclear Power Reactor (which is a CANDU boiling light water reactor),[144] using seven different localized control absorbers. The control absorbers were located in a region of constant flux, and their reactivity worths were the same. Dependent on the phase shift between the control absorbers, different higher modes were preferentially excited.

A similar experiment was performed by McDonnell et al.[145,146] on the heavy-water-moderated ZED-2 reactor. The experiments were carried out on a ZED-2 two coupled-core configuration, consisting each of natural uranium metal rods arranged in a square lattice with a 15 cm pitch. The coupling region was 90 cm wide.

The higher modes in the GTRR coupled-core configuration were excited through the use of two localized absorbers, located in symmetrical reactor locations and driven 180 degrees out of phase of each other. The

detectors were located in various regions of the GTRR to measure the resultant variation in the neutron flux. The reactor configuration with the two localized perturbations is shown in Figure 59. The localized absorbers were located in the outside D_2O reflector, adjacent to fuel assemblies V-2 and V-18 and defined by y-mesh 9 to 10, x-mesh 20 to 21, and y-mesh 9 to 10, x-mesh 48 to 49, respectively. The distance between the two coupled cores in the GTRR was 20.2 cm, and the distance between the two absorbers was 59 cm. The presence of the absorbers adjacent to assemblies V-2 and V-18 introduced externally controlled volume distributed stochastic sources in those assemblies. The calculations were performed in a similar fashion as in the case of one localized absorber. The frequency range investigated was 10 to 600 cps.

In Tables 30 and 31 are tabulated the results of this simulation. In Table 30 are shown the amplitude and phase of the CHF between the thermal response of detector 1, located at mesh (9,14) (in the outside D_2O reflector) and the thermal response of detector 2 at various reactor locations. We observe that the amplitude of the CHF's goes through a minimum at a frequency of approximately 75 cps for detector 2 locations in the outside D_2O reflector, at the opposite side of detector 1. The phase made an abrupt jump from 0 to -180° when detector 2 was located in a symmetrical position (defined by mesh (9,55)) to the position of detector 1 (defined by mesh (9,14)). The phase below this sink was of the order of 10^{-4} degrees (theoretically it should be zero), and the phase above this sink was -180°.

For detector 2 positions inside the D_2O region (between assemblies V-14, V-15, and V-18), defined by x-mesh 43, the amplitude of the CHF

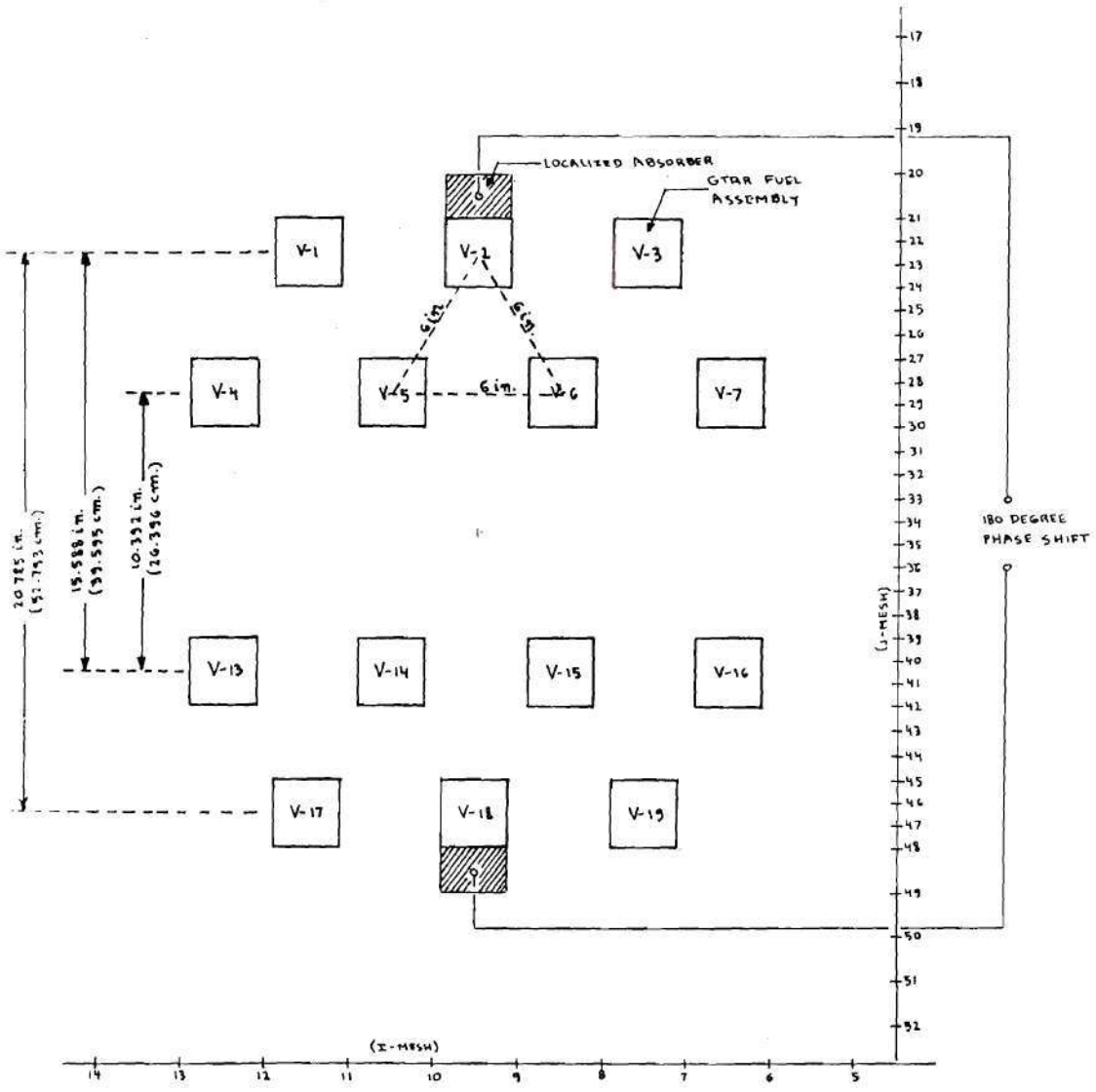

Figure 59. Fourteen Assembly Coupled-Core GTRR with Two Localized Absorber Perturbations, Driven 180 Degrees Out of Phase

Table 30. Coherence Function between Thermal Responses of Detector 1 and Detector 2, External Sources in Mesh Volumes (9 to 10, 20 to 21) and (9 to 10, 48 to 49) (180° Phase Shift), Detector 1 at Mesh (9,14), Detector 2 at Various Locations

Y-X MESH	9,14		9,14		9,14		9,14		9,14		9,14		9,14		9,14	
DETECTOR 1	9,14		9,25		9,34		9,38		9,43		9,51		9,55		9,57	
DETECTOR 2																
FREQUENCY (CPS)	AMPLITUDE	PHASE (DEGREES)	AMPLITUDE	PHASE (DEGREES)	AMPLITUDE	PHASE (DEGREES)	AMPLITUDE	PHASE (DEGREES)	AMPLITUDE	PHASE (DEGREES)	AMPLITUDE	PHASE (DEGREES)	AMPLITUDE	PHASE (DEGREES)	AMPLITUDE	PHASE (DEGREES)
10,0	1,000+00	0,000	9,993-01	-6,679+00	9,775-01	-1,850+00	9,644-01	-2,232+00	9,312-01	-5,353+00	8,751-01	-9,217+00	9,047-01	-5,960-06	9,087-01	3,609+00
20,0	1,000+00	0,000	9,978-01	-1,319+01	9,247-01	-3,600+00	8,810-01	-4,107+00	7,725-01	-1,014+01	6,217-01	-1,908+01	6,938-01	-1,271-05	7,049-01	7,224+00
40,0	1,000+00	0,000	9,957-01	-2,508+01	8,163-01	-6,496+00	6,963-01	-5,891+00	4,362-01	-1,575+01	2,123-01	-4,723+01	2,873-01	-3,489-05	3,038-01	1,478+01
60,0	1,000+00	0,000	9,951-01	-3,509+01	7,462-01	-8,660+00	5,717-01	-5,227+00	2,277-01	-1,175+01	7,804-02	-1,264+02	6,072-02	-1,382-04	7,495-02	2,714+01
80,0	1,000+00	0,000	9,953-01	-4,345+01	7,126-01	-1,047+01	5,026-01	-3,476+00	1,333-01	6,851+00	1,091-01	1,770+02	4,568-02	1,800+02	3,810-02	-1,749+02
100,0	1,000+00	0,000	9,957-01	-5,060+01	6,981-01	-1,220+01	4,658-01	-1,833+00	1,106-01	3,120+01	1,293-01	1,583+02	9,231-02	1,800+02	8,840-02	-1,804+02
110,0	1,000+00	0,000	9,959-01	-5,383+01	6,949-01	-1,307+01	4,544-01	-1,228+00	1,114-01	3,969+01	1,324-01	1,524+02	1,035-01	1,800+02	9,845-02	-1,575+02
120,0	1,000+00	0,000	9,962-01	-5,687+01	6,934-01	-1,396+01	4,458-01	-7,896-01	1,146-01	4,527+01	1,325-01	1,476+02	1,098-01	1,800+02	1,054-01	-1,551+02
130,0	1,000+00	0,000	9,964-01	-5,975+01	6,931-01	-1,486+01	4,393-01	-5,117-01	1,181-01	4,886+01	1,304-01	1,434+02	1,127-01	1,800+02	1,087-01	-1,531+02
140,0	1,000+00	0,000	9,967-01	-6,248+01	6,937-01	-1,576+01	4,341-01	-3,791-01	1,211-01	5,056+01	1,270-01	1,397+02	1,130-01	1,800+02	1,094-01	-1,513+02
150,0	1,000+00	0,000	9,969-01	-6,509+01	6,949-01	-1,666+01	4,299-01	-3,731-01	1,233-01	5,147+01	1,227-01	1,364+02	1,117-01	1,800+02	1,082-01	-1,496+02
160,0	1,000+00	0,000	9,971-01	-6,758+01	6,964-01	-1,757+01	4,264-01	-4,752-01	1,248-01	5,171+01	1,178-01	1,334+02	1,092-01	1,800+02	1,059-01	-1,481+02
170,0	1,000+00	0,000	9,973-01	-6,997+01	6,983-01	-1,848+01	4,232-01	-6,678-01	1,251-01	5,150+01	1,126-01	1,306+02	1,058-01	1,800+02	1,026-01	-1,466+02
180,0	1,000+00	0,000	9,975-01	-7,226+01	7,003-01	-1,937+01	4,203-01	-9,552-01	1,249-01	5,100+01	1,072-01	1,281+02	1,019-01	1,800+02	9,872-02	-1,453+02
190,0	1,000+00	0,000	9,977-01	-7,447+01	7,024-01	-2,027+01	4,175-01	-1,284+00	1,241-01	5,029+01	1,018-01	1,256+02	9,769-02	1,800+02	9,449-02	-1,440+02
200,0	1,000+00	0,000	9,978-01	-7,660+01	7,048-01	-2,115+01	4,148-01	-1,662+00	1,229-01	4,943+01	9,646-02	1,234+02	9,328-02	1,800+02	9,003-02	-1,428+02
220,0	1,000+00	0,000	9,981-01	-8,064+01	7,091-01	-2,288+01	4,095-01	-2,511+00	1,192-01	4,748+01	8,611-02	1,192+02	8,423-02	1,800+02	8,089-02	-1,405+02
240,0	1,000+00	0,000	9,984-01	-8,444+01	7,134-01	-2,458+01	4,039-01	-3,480+00	1,144-01	4,537+01	7,646-02	1,155+02	7,537-02	1,800+02	7,189-02	-1,384+02
260,0	1,000+00	0,000	9,986-01	-8,801+01	7,176-01	-2,619+01	3,981-01	-4,507+00	1,090-01	4,321+01	6,763-02	1,121+02	6,699-02	1,800+02	6,336-02	-1,364+02
280,0	1,000+00	0,000	9,987-01	-9,139+01	7,215-01	-2,776+01	3,920-01	-5,564+00	1,032-01	4,108+01	5,968-02	1,090+02	5,922-02	1,800+02	5,543-02	-1,345+02
300,0	1,000+00	0,000	9,989-01	-9,459+01	7,252-01	-2,927+01	3,857-01	-6,630+00	9,737-02	3,900+01	5,250-02	1,062+02	5,213-02	1,800+02	4,818-02	-1,327+02
320,0	1,000+00	0,000	9,990-01	-9,765+01	7,286-01	-3,072+01	3,791-01	-7,693+00	9,151-02	3,709+01	4,612-02	1,037+02	4,570-02	1,800+02	4,160-02	-1,310+02
340,0	1,000+00	0,000	9,992-01	-1,006+02	7,318-01	-3,213+01	3,722-01	-8,742+00	8,577-02	3,507+01	4,046-02	1,013+02	3,992-02	1,800+02	3,588-08	-1,293+02
360,0	1,000+00	0,000	9,993-01	-1,033+02	7,348-01	-3,348+01	3,653-01	-9,773+00	8,020-02	3,322+01	3,544-02	9,927+01	3,475-02	1,800+02	3,038-02	-1,277+02
380,0	1,000+00	0,000	9,994-01	-1,060+02	7,376-01	-3,477+01	3,582-01	-1,078+01	7,488-02	3,145+01	3,100-02	9,741+01	3,013-02	1,800+02	2,565-02	-1,260+02
400,0	1,000+00	0,000	9,994-01	-1,086+02	7,401-01	-3,602+01	3,511-01	-1,176+01	6,977-02	2,975+01	2,709-02	9,576+01	2,602-02	1,800+02	2,143-02	-1,242+02
420,0	1,000+00	0,000	9,995-01	-1,110+02	7,426-01	-3,723+01	3,439-01	-1,272+01	6,494-02	2,812+01	2,365-02	9,432+01	2,238-02	1,800+02	1,769-02	-1,224+02
440,0	1,000+00	0,000	9,996-01	-1,134+02	7,449-01	-3,839+01	3,366-01	-1,366+01	6,038-02	2,654+01	2,061-02	9,310+01	1,915-02	1,800+02	1,437-02	-1,203+02
460,0	1,000+00	0,000	9,996-01	-1,157+02	7,470-01	-3,951+01	3,294-01	-1,456+01	5,609-02	2,502+01	1,795-02	9,210+01	1,629-02	1,800+02	1,194-02	-1,178+02
480,0	1,000+00	0,000	9,997-01	-1,179+02	7,490-01	-4,059+01	3,223-01	-1,545+01	5,207-02	2,355+01	1,561-02	9,132+01	1,378-02	1,800+02	8,842-03	-1,146+02
500,0	1,000+00	0,000	9,997-01	-1,201+02	7,509-01	-4,163+01	3,151-01	-1,631+01	4,830-02	2,210+01	1,356-02	9,078+01	1,152-02	1,800+02	6,563-03	-1,101+02
520,0	1,000+00	0,000	9,997-01	-1,222+02	7,528-01	-4,264+01	3,081-01	-1,715+01	4,478-02	2,069+01	1,175-02	9,048+01	9,541-03	1,800+02	4,587-03	-1,028+02
540,0	1,000+00	0,000	9,998-01	-1,242+02	7,545-01	-4,362+01	3,011-01	-1,797+01	4,150-02	1,929+01	1,018-02	9,044+01	7,792-03	1,800+02	2,952-03	-8,684+01
560,0	1,000+00	0,000	9,998-01	-1,261+02	7,562-01	-4,456+01	2,942-01	-1,877+01	3,843-02	1,789+01	8,792-03	9,070+01	6,247-03	1,800+02	1,876-03	-5,754+01
580,0	1,000+00	0,000	9,998-01	-1,280+02	7,578-01	-4,548+01	2,874-01	-1,956+01	3,558-02	1,649+01	7,580-03	9,127+01	4,881-03	1,800+02	1,882-03	-1,087+01
600,0	1,000+00	0,000	9,998-01	-1,299+02	7,594-01	-4,637+01	2,807-01	-2,033+01	3,293-02	1,508+01	6,519-03	9,220+01	3,672-03	1,800+02	2,710-03	1,600+01

Table 31. Coherence Function between Thermal Responses of Detector 1 and Detector 2, External Sources in Mesh Volumes (9 to 10, 20 to 21) and (9 to 10, 48 to 49) (180° Phase Shift), Detector 1 at Mesh (9,25), Detector 2 at Various Locations

Y-X MESH	9,25		9,25		9,25		9,25		9,25		9,25		9,25		9,25	
DETECTOR 1	9,14		9,25		9,34		9,38		9,44		9,51		9,55		9,57	
DETECTOR 2																
FREQUENCY (CPS)	AMPLITUDE	PHASE (DEGREES)	AMPLITUDE	PHASE (DEGREES)	AMPLITUDE	PHASE (DEGREES)	AMPLITUDE	PHASE (DEGREES)	AMPLITUDE	PHASE (DEGREES)	AMPLITUDE	PHASE (DEGREES)	AMPLITUDE	PHASE (DEGREES)	AMPLITUDE	PHASE (DEGREES)
10,0	9,993E-01	6,679E+00	1,000E+00	0,000	9,845E-01	4,806E+00	9,737E-01	4,409E+00	9,342E-01	-4,850E-06	8,928E-01	-2,563E+00	9,201E-01	6,626E+00	9,238E-01	1,023E+01
20,0	9,978E-01	1,319E+01	1,000E+00	0,000	9,478E-01	9,426E+00	9,099E-01	8,806E+00	7,816E-01	-9,876E-06	6,717E-01	-6,031E+00	7,393E-01	1,278E+01	7,496E-01	1,998E+01
40,0	9,957E-01	2,508E+01	1,000E+00	0,000	8,629E-01	1,771E+01	7,561E-01	1,751E+01	4,526E-01	-2,147E-05	3,013E-01	-2,055E+01	3,722E-01	2,158E+01	3,876E-01	3,611E+01
60,0	9,951E-01	3,509E+01	1,000E+00	0,000	8,031E-01	2,456E+01	6,375E-01	2,580E+01	2,370E-01	-3,799E-05	1,489E-01	-5,474E+01	1,552E-01	1,970E+01	1,654E-01	4,297E+01
80,0	9,953E-01	4,345E+01	1,000E+00	0,000	7,672E-01	3,021E+01	5,586E-01	3,345E+01	1,134E-01	-6,869E-05	1,275E-01	-9,220E+01	6,498E-02	-1,496E+01	6,178E-02	2,052E+01
100,0	9,957E-01	5,060E+01	1,000E+00	0,000	7,457E-01	3,499E+01	5,058E-01	4,043E+01	4,075E-02	-1,635E-04	1,360E-01	-1,106E+02	6,949E-02	-6,127E+01	5,792E-02	-3,276E+01
110,0	9,959E-01	5,383E+01	1,000E+00	0,000	7,384E-01	3,713E+01	4,858E-01	4,367E+01	1,577E-02	-3,910E-04	1,394E-01	-1,154E+02	8,051E-02	-6,935E+01	6,988E-02	-4,177E+01
120,0	9,962E-01	5,687E+01	1,000E+00	0,000	7,327E-01	3,913E+01	4,689E-01	4,676E+01	6,051E-03	-1,800E+02	1,413E-01	-1,188E+02	8,985E-02	-7,264E+01	8,045E-02	-4,432E+01
130,0	9,964E-01	5,975E+01	1,000E+00	0,000	7,281E-01	4,101E+01	4,544E-01	4,971E+01	1,991E-02	-1,800E+02	1,418E-01	-1,212E+02	9,690E-02	-7,361E+01	8,858E-02	-4,401E+01
140,0	9,967E-01	6,248E+01	1,000E+00	0,000	7,246E-01	4,279E+01	4,419E-01	5,252E+01	3,267E-02	-1,800E+02	1,412E-01	-1,231E+02	1,018E-01	-7,339E+01	9,441E-02	-4,238E+01
150,0	9,969E-01	6,509E+01	1,000E+00	0,000	7,218E-01	4,447E+01	4,311E-01	5,521E+01	4,297E-02	-1,800E+02	1,398E-01	-1,245E+02	1,050E-01	-7,252E+01	9,832E-02	-4,007E+01
160,0	9,971E-01	6,758E+01	1,000E+00	0,000	7,197E-01	4,608E+01	4,216E-01	5,778E+01	5,128E-02	-1,800E+02	1,374E-01	-1,256E+02	1,068E-01	-7,129E+01	1,007E-01	-3,744E+01
170,0	9,973E-01	6,997E+01	1,000E+00	0,000	7,181E-01	4,760E+01	4,131E-01	6,023E+01	5,798E-02	-1,800E+02	1,348E-01	-1,265E+02	1,075E-01	-6,987E+01	1,018E-01	-3,464E+01
180,0	9,975E-01	7,226E+01	1,000E+00	0,000	7,169E-01	4,906E+01	4,056E-01	6,257E+01	6,335E-02	-1,800E+02	1,315E-01	-1,273E+02	1,072E-01	-6,833E+01	1,019E-01	-3,178E+01
190,0	9,977E-01	7,447E+01	1,000E+00	0,000	7,160E-01	5,046E+01	3,988E-01	6,481E+01	6,763E-02	-1,800E+02	1,281E-01	-1,279E+02	1,063E-01	-6,674E+01	1,013E-01	-2,891E+01
200,0	9,978E-01	7,660E+01	1,000E+00	0,000	7,155E-01	5,180E+01	3,926E-01	6,696E+01	7,098E-02	-1,800E+02	1,244E-01	-1,285E+02	1,048E-01	-6,513E+01	1,001E-01	-2,607E+01
220,0	9,981E-01	8,064E+01	1,000E+00	0,000	7,152E-01	5,432E+01	3,818E-01	7,097E+01	7,550E-02	-1,800E+02	1,168E-01	-1,295E+02	1,008E-01	-6,193E+01	9,634E-02	-2,052E+01
240,0	9,984E-01	8,444E+01	1,000E+00	0,000	7,156E-01	5,666E+01	3,725E-01	7,466E+01	7,781E-02	-1,800E+02	1,091E-01	-1,303E+02	9,570E-02	-5,885E+01	9,151E-02	-1,522E+01
260,0	9,986E-01	8,801E+01	1,000E+00	0,000	7,165E-01	5,886E+01	3,643E-01	7,805E+01	7,851E-02	-1,800E+02	1,015E-01	-1,311E+02	9,014E-02	-5,591E+01	8,608E-02	-1,018E+01
280,0	9,987E-01	9,139E+01	1,000E+00	0,000	7,178E-01	6,088E+01	3,569E-01	8,118E+01	7,804E-02	-1,800E+02	9,409E-02	-1,318E+02	8,438E-02	-5,314E+01	8,040E-02	-5,393E+00
300,0	9,989E-01	9,459E+01	1,000E+00	0,000	7,193E-01	6,280E+01	3,501E-01	8,408E+01	7,672E-02	-1,800E+02	8,705E-02	-1,324E+02	7,862E-02	-5,052E+01	7,468E-02	-8,383E+01
320,0	9,990E-01	9,765E+01	1,000E+00	0,000	7,211E-01	6,462E+01	3,436E-01	8,677E+01	7,478E-02	-1,800E+02	8,040E-02	-1,331E+02	7,298E-02	-4,807E+01	6,906E-02	3,505E+00
340,0	9,992E-01	1,006E+02	1,000E+00	0,000	7,230E-01	6,633E+01	3,374E-01	8,926E+01	7,241E-02	-1,800E+02	7,416E-02	-1,338E+02	6,755E-02	-4,576E+01	6,363E-02	7,662E+00
360,0	9,993E-01	1,033E+02	1,000E+00	0,000	7,250E-01	6,796E+01	3,314E-01	9,159E+01	6,973E-02	-1,800E+02	6,834E-02	-1,345E+02	6,237E-02	-4,359E+01	5,845E-02	1,186E+01
380,0	9,994E-01	1,060E+02	1,000E+00	0,000	7,271E-01	6,951E+01	3,256E-01	9,377E+01	6,684E-02	-1,800E+02	6,292E-02	-1,352E+02	5,768E-02	-4,155E+01	5,355E-02	1,552E+01
400,0	9,994E-01	1,086E+02	1,000E+00	0,000	7,292E-01	7,099E+01	3,199E-01	9,581E+01	6,383E-02	-1,800E+02	5,789E-02	-1,359E+02	5,289E-02	-3,963E+01	4,894E-02	1,928E+01
420,0	9,995E-01	1,110E+02	1,000E+00	0,000	7,314E-01	7,240E+01	3,142E-01	9,772E+01	6,076E-02	-1,800E+02	5,324E-02	-1,366E+02	4,859E-02	-3,781E+01	4,466E-02	2,297E+01
440,0	9,996E-01	1,134E+02	1,000E+00	0,000	7,335E-01	7,376E+01	3,085E-01	9,953E+01	5,767E-02	-1,800E+02	4,895E-02	-1,373E+02	4,459E-02	-3,609E+01	4,064E-02	2,661E+01
460,0	9,996E-01	1,157E+02	1,000E+00	0,000	7,356E-01	7,506E+01	3,029E-01	1,012E+02	5,460E-02	-1,800E+02	4,499E-02	-1,380E+02	4,087E-02	-3,445E+01	3,693E-02	3,026E+01
480,0	9,997E-01	1,179E+02	1,000E+00	0,000	7,378E-01	7,630E+01	2,973E-01	1,028E+02	5,157E-02	-1,800E+02	4,135E-02	-1,387E+02	3,743E-02	-3,288E+01	3,351E-02	3,394E+01
500,0	9,997E-01	1,201E+02	1,000E+00	0,000	7,398E-01	7,751E+01	2,917E-01	1,043E+02	4,862E-02	-1,800E+02	3,799E-02	-1,394E+02	3,424E-02	-3,137E+01	3,037E-02	3,771E+01
520,0	9,997E-01	1,222E+02	1,000E+00	0,000	7,419E-01	7,867E+01	2,862E-01	1,058E+02	4,574E-02	-1,800E+02	3,491E-02	-1,401E+02	3,130E-02	-2,991E+01	2,748E-02	4,163E+01
540,0	9,998E-01	1,242E+02	1,000E+00	0,000	7,439E-01	7,979E+01	2,806E-01	1,071E+02	4,297E-02	-1,800E+02	3,208E-02	-1,408E+02	2,858E-02	-2,848E+01	2,485E-02	4,577E+01
560,0	9,998E-01	1,261E+02	1,000E+00	0,000	7,459E-01	8,087E+01	2,751E-01	1,084E+02	4,030E-02	-1,800E+02	2,948E-02	-1,414E+02	2,608E-02	-2,707E+01	2,247E-02	5,020E+01
580,0	9,998E-01	1,280E+02	1,000E+00	0,000	7,479E-01	8,192E+01	2,698E-01	1,097E+02	3,773E-02	-1,800E+02	2,710E-02	-1,421E+02	2,377E-02	-2,567E+01	2,033E-02	5,501E+01
600,0	9,998E-01	1,299E+02	1,000E+00	0,000	7,498E-01	8,293E+01	2,641E-01	1,108E+02	3,528E-02	-1,800E+02	2,491E-02	-1,427E+02	2,165E-02	-2,425E+01	1,843E-02	6,032E+01

exhibited a minimum at a frequency of approximately 105 cps, which is slightly higher than the minimum at 75 cps, which occurred when detector 2 was in the outside D_2O reflector (x-mesh greater than 48).

This behavior, namely the presence of a minimum for the amplitude of the CHF due to two localized externally driven perturbations, each driven 180° out of phase, is similar to the one that occurred in the CHF due to volume distributed inherent stochastic fission sources.

We have previously seen that the frequency, at which the first minimum occurred in the amplitude of the CHF or the CPSD, was approximately 250 cps for the GTRR coupled-core configuration, when the perturbations were due to the volume distributed inherent stochastic fission sources. This is to be compared with the location of the first sink at approximately 75 cps when the perturbations were introduced by two localized absorbers, 180° out of phase. The occurrence of the minima in the amplitude of the CHF's was due to interference effects between neutronic waves inside the reactor. Those interference effects arise from the different couplings between the GTRR fuel assemblies through heavy water coupling regions. Let us consider two different couplings: the coupling between assemblies V-2 and V-14, V-15 and between assemblies V-18 and V-5, V-6. The distance between the assemblies is approximately 38 cm center to center. In a parametric numerical study based on a one-dimensional modal expansion method, Nagy and Danofsky[17] obtained for a two fuel slab coupled-core reactor, separated by approximately 38 cm of heavy water coupling region, a sink at a frequency of approximately 90 cps. Based on this parametric study, it seems most likely that the interference effects are due to the interactions between the above mentioned couplings.

In Table 31 are tabulated the results of the amplitude and phase of the coherence functions between the thermal response of detector 1, located inside the GTRR heavy water coupling media, at a position defined by mesh (9,25), and the thermal response of detector 2, located in various positions of the GTRR coupled-core configuration. The driving forces were the two localized absorber perturbations located at y-mesh 9 to 10, and x-mesh 20 to 21 and 48 to 49, respectively (see Figure 59).

For symmetrical locations of detector 1 (at mesh (9,25)) and detector 2 (at mesh (9,44)) the amplitude went through a minimum at a frequency of approximately 115 cps, and the phase was of the order of 10^{-4} degrees below the sink and -180° above the sink frequency. We observed that the frequency, at which the amplitude of the CHF went through a minimum and the phase made an abrupt jump from 0 to -180°, was at a slightly higher frequency (115 cps) when detector 1 and detector 2 were located in between the two localized perturbations than when detector 1 was located outside the fuel region (75 cps).

For detector 2 locations outside of the fuel region and for x-mesh greater than 48, the minimum in the amplitude of the CHF was at approximately 80 cps.

Note that an advantage of our method over the modal analysis was that the possible inaccuracies in the corrections for fundamental mode contamination into the higher modes were not existent, since our method automatically included those contaminations in the results obtained.

CHAPTER IX

CONCLUSIONS

The purpose of this dissertation was to develop and apply a general method to be used in investigations of two-dimensional and multigroup power spectral densities without any restraint on the geometry or heterogeneity of the neutronic system. The method and numerical approach which were developed in Chapters III and IV, and applied in this research to several reactors which had widely different neutron spectra (reactors containing a hard spectrum and reactors in which a thermal spectrum predominated), were very effective in the calculations of two-dimensional multigroup PSD's and transfer functions. No restraint was imposed on the space dimensionality and the frequency range. The usefulness of the method was not limited by slow convergence or divergence of the iterative process in the solution of the frequency-dependent equations describing the two-dimensional space-dependent multigroup PSD's and transfer functions within a reactor. The method was applied over a fairly wide range of frequencies (typically 1 to 900 cycles per second). The starting point was the three-dimensional space-, energy-, and time-dependent P_1 approximation to the Boltzmann equations.

In the derivation of the equations of the model, starting from the Boltzmann equation through the P_1 approximation, several terms appeared in the frequency-dependent P_1 equations which were derived, terms which were not present when the derivation was made directly from the time-

dependent diffusion equations or the telegraphist[3,96] equations. The coefficient ω/v^g appeared in all the terms that did not show up in the frequency-dependent diffusion equations. Also several additional complex leakage terms were present in the frequency-dependent multigroup P_1 equations. Those P_1 equations were subsequently used in the space-, energy-, and frequency-dependent power spectral densities and transfer function studies. Note that the frequency dependence came through the Fourier transform of the time-derivatives of the P_1 approximation.

A major problem that was initially encountered in this study was the very slow convergence rate of the iterative methods used. At relatively high frequencies of the power spectral densities (typically above 50 cps) no convergence could be attained, i.e., the iterative methods with which we experimented were divergent for the two-dimensional multigroup solutions to the PSD's sought, even with the use of various rebalancing accelerations.

New iteration techniques were developed that not only improved the convergence rate at low frequencies of the iterative methods to the solution of the equations of our model describing the PSD's in a reactor, but that also gave a convergent solution to the PSD's over the whole frequency range investigated (typically 1 to 900 cycles/sec). In addition, the introduction of a complex constraint overrelaxation correction to the frequency-dependent responses during the outer iterations enhanced the convergence rate of the iterative methods.

When applying standard iterative methods such as the one-line, one-energy-group overrelaxation technique or the alternating direction overrelaxation, major problems were encountered in the convergence rate

of the iterations. In addition no convergence of the solution could be obtained even for a single space- and energy-dependent and -weighted transfer function above frequencies of typically 50 cps. In a case where a normal time-independent problem iterated in less than 100 iterations at a point flux relative error of 10^{-4}, attempts to obtain a convergent solution to the time-dependent problems failed even after 5000 iterations. Failure was also encountered when all computer arithmetic was done in double precision. As mentioned previously, a standard scheme did not prove successful at higher frequencies, mainly because of the neutron imbalance during the course of an outer iteration. The imbalance at a certain energy group and at a line propagated itself through all the following line iterations of the outer iteration, and this caused instabilities at higher frequencies, where sharp gradients (energy and/or space) of the frequency-dependent responses were present.

Extensive experimentation using space- and group-dependent scale factors on the frequency-dependent fluxes was performed in the calculations of the two-dimensional multigroup power spectral densities using a standard one-line one-energy overrelaxation technique. Faster convergence was attained at higher frequencies than was the case with group-dependent, space-independent rebalancing or no balancing accelerations. However, at higher frequencies, no stability of the iteration scheme could be attained.

The use of an iterative method in which all energy groups were solved simultaneously within an outer iteration along all space points at a certain row proved to be much more effective in accelerating convergence. Convergence was speeded up either by solving the block-tridiagonal

matrices directly, or by the use of inner iterations. The module iterative method was a further step to achieve convergence. In this method, several adjacent or all energy groups were solved simultaneously within an outer iteration, along with all space points of several adjacent rows. This was followed by a complex constraint overrelaxation correction to the frequency-dependent responses.

The frequency-dependent correlations between several neutron detectors, positioned at different locations inside a reactor, were determined using this method, and they were compared with available results of several existing experiments. The studies were performed for three different types of perturbations: (1) the inherent volume distributed binary fission noise, (2) one externally controlled localized absorber perturbation, and (3) two externally controlled localized absorber perturbations driven 180 degrees out of phase of each other to minimize the excitation of the fundamental mode.

The model and numerical approach that was used in the determination of the power spectral densities was applied to three neutronic systems with widely different neutron spectra: the TARK coupled-core configuration and the 14 assembly GTRR coupled-core configuration with predominant thermal spectra, the STARK reactor loadings II and IV with a fast spectrum in the central fast core surrounded by a natural uranium blanket and by a thermal driver zone with a thermal spectrum.

In each case, the agreement between the results of the power spectral densities predicted by our model and numerical approach and existing experimental results was good, with the exception perhaps of the frequency range above the first minimum in the amplitude of the coherence function

of the TARK coupled-core configuration. This could be attributed to several causes, among them the validity of the assumption that the power spectrum of the inherent binary noise is white, a possible experimental systematic error above the first sink, the effect of phase interferences between the modes of propagation of the neutron waves in the axial direction of heterogeneous media, as shown by Quddus[13] or the effect of limiting the anisotropy to a P_1 approximation.

Some interesting characteristics of the power spectral density between the responses of two neutron detectors were determined for the TARK and GTRR coupled-core configurations, when the perturbation was introduced by the inherent volume distributed binary noise. We have seen that the amplitude of the CHF between two neutron detectors went through a minimum (called sink) when the detectors were located outside of the coupling regions. In the case where one of the detectors was located inside the coupling region, the amplitude displayed a shallow minimum or an inflection point.

When the reactor exhibited a material symmetry, and the detectors were located in symmetrical locations, the amplitude of the CHF went to zero at the sink frequency. For this configuration, the phase was zero below the sink, -180 degrees above the first sink, and back to zero above the second sink. The phase made an abrupt jump at the sink frequencies. The minima were due to interference effects of the neutronic waves, and the phase shift was the result of the response of the reactor to a perturbance (residual disturbance) and the time-delay (wavelike) behavior. For symmetrically located detectors, we have seen that the phase was theoretically zero or $\pm$ 180 degrees. The two-dimensional multigroup

numerical calculations of the CHF showed that the relative deviation of the phase from zero or ± 180 degrees was less than 10^{-4}. This is in contrast to the one-dimensional calculations of the CHF by Ebert.[131] Ebert's multi-mode computations of the various phase angles were very poor, and the agreement between the exact and modal approximations of the phase angles of the thermal-thermal and fast-thermal coherence function was very poor in both his reactor models. In his method the one-dimensional eigenvector and eigenvalue computations were based on the critical determinate method. The method that was used in our work avoided the problem of round-off errors on the zero-crossing of the determinate.

The goals of this dissertation in the area of theoretical modeling and numerical methods were achieved. A numerical technique was developed which determined the multi-dimensional and multigroup power spectral densities between neutron detectors, when the disturbances were due to inherent volume distributed binary noise or externally driven localized absorber perturbations. The model was based on the three-dimensional P_1 approximation to the Boltzmann equation. The presence of inherent binary noise or several externally driven localized absorber perturbations, driven out of phase of one another, induced minima in the coherence functions.

In the area of the experimental determination of the power spectral densities of the GTRR, the goals were only partially achieved. The PSD of the full core GTRR, when the driving source was the inherent binary noise, was determined, but the value of the upper limit of the frequency was limited due to the presence of large mechanical vibrations of a safety control blade. They were induced by the D_2O coolant flow past the control

blade. The coolant flow induced peaks in the power spectrum were observed at 5.9 cps and its harmonics. The discrete Fourier transforms of the discrete data samples were obtained using a fast Fourier transformation (FFT) algorithm. Due to the upper limit of the frequency range in the experimental PSD determination, no comparisons could be made with the calculated PSD's in the Georgia Tech Research Reactor (GTRR). Removal of the mechanical vibration caused by a loose semaphore control blade was not possible at the time of the experiments.

A high frequency absorber oscillator was built and extensively tested. The oscillator fitted into a GTRR fuel lattice position. However, due to the high burnup of the GTRR Mark-I fuel assemblies, the GTRR coupled-core configuration with 14 fuel assemblies could not be made critical at the time of the experiments.

It has also been shown during this investigation that the model and numerical approach developed in this dissertation can be applied to complicated neutronic systems perturbed by several localized absorbers. We have seen that, to minimize the excitation of the fundamental mode, two identical localized absorbers were located in symmetrical reactor locations and were driven 180 degrees out of phase, so that the total reactivity introduced in the system was zero. The higher modes were, therefore, preferentially excited. A minimum at 75 cps in the amplitude of the CHF of the GTRR coupled-core configuration was predicted in the frequency range 1 to 600 cps and was caused by interference effects of the neutronic waves. Note that an advantage of our method over the modal analysis was that the possible inaccuracies in the corrections for fundamental mode contamination into the higher modes were not existent, since

our method automatically included those contaminations in the results obtained.

The results of this work have demonstrated that solutions to multigroup space-dependent PSD's and transfer functions for two-dimensional representations of neutronic systems can be attained without any restrictions on the material configuration, number of energy groups, frequency range, or neutron spectrum. The usefulness of the method was not limited by slow convergence or divergence of the iterative process.

We have seen that the solution of a two-dimensional multigroup PSD at a given frequency required that a successful converged iterative process be performed for several transfer functions. In particular, when the perturbances were introduced by the inherent binary noise, STARK Loading II required the convergent solution of 486 different space-, energy-, and frequency-dependent transfer functions per frequency point. However, as we have shown in Chapter IV, substantial amounts of computer time were saved by the need of only having to compute once the partial inverses of the block-tridiagonal matrices at each frequency point. Even in the case where 486 different convergent solutions were required per frequency, the solution took typically only a few minutes CPU per frequency on a U-1108 computer for two-dimensional, two broad-energy-group PSD calculations.

The PSD calculations were also performed for up to five broad-groups for selected frequencies, and no problems were encountered with the convergence of the iterations.

The following recommendations should be made:

1. Incorporation of power feedback into the model--The model and the numerical iterative methods that were developed and used in this work could be extended easily to include power feedback with the incorporation in our model of a theoretical approach developed by Bridges, Clement, and Renier.[85]

2. Cross-section sets and calculational methods are often tested with a static critical experiment as was done in Appendix B. The cross sections based on ENDF/B-II data which were used in the TARK and STARK Loading II and IV PSD calculations were tested against the $k_{eff} = 1$ of Pu- and U-fueled critical experiments. The sensitivity of cross sections on the k_{eff} is also routinely done. Similarly, a study of the sensitivity of the variation of nuclear parameters onto certain frequency-dependent kinetic characteristics of a neutronic system, as the minima in the amplitude of coherence functions between detectors, could be performed. It is not known if the variation of a nuclear parameter has a higher sensitivity on kinetic characteristics as compared to static experiments. This needs further work.

3. Since the time delay of the coupling between fuel regions is due to several different contributions, among them the time-delay introduced by the delayed neutron fraction half-lives, and time-delay introduced by the finite travel time of neutrons in a reactor system with finite dimensions, it would be of interest to determine the PSD's between neutron detectors for a system with a lower total effective delayed neutron fraction, as a Pu-fueled core. Several experimental determinations of PSD's on Pu-fueled fast and thermal cores have been described in the literature, experiments with which numerical values obtained by our model

and numerical approach could be compared (e.g., experimental investigations performed on the sodium-cooled fast reactor SNEAK[133,134] loaded with Pu-fuel, kinetic parameters obtained on plutonium-enriched lattices of PuO_2 rods bathing in water.[147]

4. With the use of neutron-gamma coupled cross-section sets, the effect of photoneutrons on the space-, energy-, and frequency-dependent transfer function and PSD calculations could be incorporated. The effect of photoneutrons on kinetic parameters could be important in cases of low power levels, for subcritical systems, for D_2O moderated neutronic systems as the GTRR.

5. The effect of the inclusion of phase interference in the axial direction should be determined. If we refer back to modal expansions, one sees that propagation of neutron waves in a heterogeneous medium is different from that in a homogeneous medium. In a heterogeneous system a number of modes of propagation may occur. Quddus[13] has shown that phase interference between the modes of propagation in the axial direction may give rise to resonances in the frequency response of the flux. It is not known what the influence of incorporating the third dimension would be on the calculations of the CHF (instead of an axial buckling correction).

6. PSD analysis using many broad groups--The model and numerical approach developed in this dissertation can be used with an arbitrary number of energy groups in the frequency-dependent P_1 transport approximation. In most of the power spectral density calculations performed in this dissertation, only a few broad-energy-groups were used due to limited amounts of allocated computer time available. It is, however, recognized

that the fast broad group, as well as the thermal broad group, cover a fairly wide energy span and, therefore, a wide range of neutron velocities. We know that the mean time delays are sensitive to the neutron spectra. Analyses of the CHF using more broad energy groups were therefore performed by the author for several selected frequencies, using the theoretical model and numerical approach described previously. However, due to the increased computer time necessary and the limit on the allocated funds, it was decided to perform the analysis with only two broad groups. The computer time and the speed of convergence of methods based on difference schemes of the transport equations are very dependent on the number of energy groups, even for two-dimensional geometries. Extension to three-dimensional geometries, where an axial buckling correction factor would not be required, is even more time consuming and it is difficult to obtain convergence.

It has to be noted that the use of a Monte Carlo approach would perhaps be more appropriate in the calculation of power spectra. The number of neutron histories required to obtain a certain minimum variance at a preset confidence level is only slightly dependent[148] on the number of energy groups used in Monte Carlo calculations. A more expeditious approach would be to solve the CHF between two detectors by way of a neutronic Monte Carlo approach. Proper modification of widely used codes as KENO[149] or MORSE[150] using Fourier transformation could be performed. An added benefit would be that a Monte Carlo approach enables one to obtain a solution for very complicated geometries in three dimensions. The solution of problems for three-dimensional complicated geometries is very time consuming and difficult to represent with the use of difference

schemes. The use of KENO or MORSE enables one to describe any geometry in three dimensions with the use of special options (e.g., GENERAL geometry option or the combinatorial geometry option). TARK and STARK reactors could be described precisely by them, while a r-θ or x-y mesh description of the GTRR, TARK and STARK reactors are only approximate.

7. The effect of using higher order anisotropy with S_nP_ℓ transport approximations on the results of PSD and transfer function calculations, especially at higher frequencies, should be determined. The effect of limiting the anisotropy to a P_1 approximation is not known as far as the PSD calculations is concerned. A generalized frequency-dependent S_nP_ℓ transport model could be derived and the effects of higher transport on the computed PSD's determined. The effects could be important at higher frequencies for which the kinetic fluxes exhibit higher anisotropy. Codes such as ANISN[108] or XSDRN[123] could be used as the starting point for the development of a one-dimensional S_nP_ℓ transport power spectral density and transfer function model, while DOT-III[110] could be used as the basis for a two-dimensional S_nP_ℓ transport PSD model.

While in the P_1 approximation, only one expansion was used over all angles, in the double-P_1 or Yvon's[151] method a separate expansion is used over each region within which the angular distribution is smoothly and slowly varying. When a plane wave hits an interface, it becomes split into transmitted and reflected components. Using the double-P_1 approximation would enable us to follow the incoming, transmitted and reflected neutron waves in heterogeneous media. A better understanding of neutron wave interferences could then be achieved.

APPENDIX A

THREE-DIMENSIONAL DERIVATION OF STOCHASTIC P_1 EQUATIONS

The forward space-, time-, and energy-dependent P_1 equations, which will be taken as the basis of the mathematical approach, are derived from the Boltzmann equation.

$$\frac{1}{v}\frac{\partial}{\partial t}\phi(\bar{r}E\Omega t) + \Omega\cdot\nabla\phi(\bar{r}E\Omega t) + \Sigma_t(\bar{r}E\Omega t)\,\phi(\bar{r}E\Omega t) = \tag{107}$$

$$S(\bar{r}E\Omega t) + \int dE' \int d\Omega'\, \Sigma_s(\bar{r}, E'\rightarrow E, \Omega'\rightarrow\Omega, t)\,\phi(\bar{r}E\Omega t)$$

where

$\Sigma_t(\bar{r}E\Omega t) = \Sigma_a(\bar{r}E\Omega t) + \Sigma_s(\bar{r}E\Omega t)$ = the macroscopic total cross section of the media (cm^{-1}) at position $\bar{r}$, energy E, direction Ω, and time t

$\Sigma_s(\bar{r}E'\rightarrow E\ \Omega'\rightarrow\Omega t)$ = the transfer scattering matrix

$\phi(\bar{r}E\Omega t)$ = the neutron flux

$v(\bar{r}E)$ = the neutron velocity corresponding to energy E

$S(\bar{r}E\Omega t)$ = the source term (fission, delayed, external source)

Parts of the following derivation are similar to the one given by Meghreblian and Holmes[3]

As in reference (3), we expand the vector flux $\phi(\bar{r}E\Omega t)$ and the source term $S(\bar{r}E\Omega t)$ into associated spherical harmonics. The differential cross section for scattering events in dE and $d\Omega$, which result in neutrons in dE' and $d\Omega'$, is expressed as a Legendre polynomial expansion

$$\phi(\bar{r}E\Omega t) = \sum_{\ell=0}^{\infty} \sum_{m=-\ell}^{+\ell} \phi_{\ell,m}(\bar{r}Et)\, Y_\ell^m(\Omega)$$

$$S(\bar{r}E\Omega t) = \sum_{\ell=0}^{\infty} \sum_{m=-\ell}^{+\ell} S_{\ell,m}(\bar{r}Et)\, Y_\ell^m(\Omega)$$

$$\Sigma_s(\bar{r}, E' \to E, \Omega' \to \Omega, t) = \sum_{\ell} \sigma_\ell(\bar{r}, E' \to E, t)\, P_\ell(\Omega \cdot \Omega')$$

$$= \sum_{\ell} \sigma_\ell(\bar{r}, E' \to E, t)\, Y_\ell^m(\Omega)\, Y_\ell^m(\Omega')^*$$

$$= \sum_{\ell} (2\ell+1)\, \Sigma_{s_\ell}(\bar{r}, E' \to E, t)\, P_\ell(\Omega \cdot \Omega')$$

where

$Y_\ell^m(\Omega)$ = associated spherical harmonics

$Y_\ell^m(\Omega)^*$ = complex conjugate of the associated spherical harmonics

$\int Y_{\ell'}^{m'}(\Omega)\, Y_\ell^m(\Omega)^*\, d\Omega = \frac{4\pi}{2\ell+1}\, \delta_\ell^{\ell'} \delta_m^{m'}$ = orthogonality property

$\delta_\ell^{\ell'}$ = Kronecker delta

It can be shown that

$$\phi_{\ell,m}(\bar{r}Et) = \frac{2\ell+1}{4\pi} \int_\Omega \phi(\bar{r}E\Omega t)\, Y_\ell^{m*}(\Omega)\, d\Omega$$

$$S_{\ell,m}(\bar{r}Et) = \frac{2\ell+1}{4\pi} \int_\Omega S(\bar{r}E\Omega t)\, Y_\ell^{m*}(\Omega)\, d\Omega$$

$$\mathcal{S}_\ell(\bar{r}, E' \to E, t) = \frac{2\ell+1}{4\pi} \int \Sigma_s(\bar{r}, E' \to E, \Omega' \to \Omega, t) \cdot P_\ell(\Omega \cdot \Omega')\, d(\Omega \cdot \Omega')$$

By the use of spherical harmonics, Meghreblian and Holmes[3] have shown that the time-dependent, three-dimensional P_1 equations can be written as

$$-\left(\frac{1}{v(\bar{r}E)}\frac{\partial}{\partial t} + \Sigma_t(\bar{r}Et)\right)\Phi_{0,0}(\bar{r}Et) + S_{0,0}(\bar{r}Et) \tag{108}$$

$$+\int \Sigma_{s_0}(\bar{r}, E' \to E, t)\,\Phi_{0,0}(\bar{r}E't)\,dE' = \frac{1}{\sqrt{3}}\frac{\partial}{\partial x}\Phi_{1,0}(\bar{r}Et) - \frac{1}{\sqrt{6}}\left(\frac{\partial}{\partial y} - i\frac{\partial}{\partial z}\right)\Phi_{1,-1}(\bar{r}Et)$$

$$+\frac{1}{\sqrt{6}}\left(\frac{\partial}{\partial y} + i\frac{\partial}{\partial z}\right)\Phi_{1,1}(\bar{r}Et)\Big| - \left(\frac{1}{v(\bar{r}E)}\frac{\partial}{\partial t} + \Sigma_t(\bar{r}Et)\right)\Phi_{1,-1}(\bar{r}Et) + S_{1,-1}(\bar{r}Et)$$

$$+\int \Sigma_{s_1}(\bar{r}, E' \to E, t)\,\Phi_{1,-1}(\bar{r}E't)\,dE' = -\frac{1}{\sqrt{6}}\left(\frac{\partial}{\partial y} + i\frac{\partial}{\partial z}\right)\Phi_{0,0}(\bar{r}Et)\Big|$$

$$-\left(\frac{1}{v(\bar{r}E)}\frac{\partial}{\partial t} + \Sigma_t(\bar{r}Et)\right)\Phi_{1,0}(\bar{r}Et) + S_{1,0}(\bar{r}Et)$$

$$+\int \Sigma_{s_1}(\bar{r}, E' \to E, t)\,\Phi_{1,0}(\bar{r}E't)\,dE' = \frac{1}{\sqrt{3}}\frac{\partial}{\partial x}\Phi_{0,0}(\bar{r}Et)\Big|$$

$$-\left(\frac{1}{v(\bar{r}E)}\frac{\partial}{\partial t} + \Sigma_t(\bar{r}Et)\right)\Phi_{1,1}(\bar{r}Et) + S_{1,1}(\bar{r}Et)$$

$$+\int \Sigma_{s_1}(\bar{r}, E' \to E, t)\,\Phi_{1,1}(\bar{r}E't)\,dE' = \frac{1}{\sqrt{6}}\left(\frac{\partial}{\partial y} - i\frac{\partial}{\partial z}\right)\Phi_{0,0}(\bar{r}Et)$$

Those three-dimensional P_1 equations can be related to the one-dimensional equations by the use of the relations:

$$\Phi(\bar{r}Et) = \frac{\Phi_{\ell,o}(\bar{r}Et)}{H_\ell^o} \qquad \text{where} \quad H_\ell^m = \left|\frac{(2\ell+1)(\ell-m)!}{4\pi(\ell+m)!}\right|^{1/2}$$

$$H_\ell^{-m} = \frac{(\ell+m)!}{(\ell-m)!} H_\ell^m$$

Therefore:

$$\Phi_o(rEt) = \Phi_{o,o}(rEt)$$

$$\Phi_1(rEt) = \frac{\Phi_{1,o}(rEt)}{\sqrt{3}}$$

Using those relations, the following one-dimensional P_1 equations are derived as

$$-\left(\frac{1}{v(xE)}\frac{\partial}{\partial t} + \Sigma_t(xEt)\right)\Phi_o(xEt) + S_o(xEt) \tag{109}$$

$$+ \int dE' \, \Sigma_{s_o}(x, E' \to E, t) \, \Phi_o(xE't) = \frac{\partial}{\partial x}\Phi_1(xEt)$$

$$-\left(\frac{1}{v(xE)}\frac{\partial}{\partial t} + \Sigma_t(xEt)\right)\Phi_1(xEt) + S_1(xEt)$$

$$+ \int dE' \, \Sigma_{s_1}(x, E' \to E, t) \, \Phi_1(xE't) = \frac{1}{3}\frac{\partial}{\partial x}\Phi_o(xEt)$$

To develop the multigroup equations, we write

$$\Phi_{\ell,m}(\bar{r}Et) = \Phi^{g}_{\ell,m}(\bar{r}t)\,\Psi^{g}_{\ell,m}(\bar{r}Et) \quad \text{for } E_g < E \leq E_{g+1}$$

Neglecting the time and space dependency of the energy weighting function, we have

$$\Phi_{\ell,m}(\bar{r}Et) = \Phi^{g}_{\ell,m}(\bar{r}t)\,.\,\delta(E_g < E \leq E_{g+1})$$

The forward multi-group, time-dependent, three-dimensional P_1 equations become

(110)

$$-\left(\frac{1}{v^g(\bar{r})}\frac{\partial}{\partial t} + \Sigma^g_t(\bar{r}t)\right)\Phi^g_{0,0}(\bar{r}t) + S^g_{0,0}(\bar{r}t) + \sum_{g'}\Sigma^{g'\to g}_{s_0}(\bar{r}t)\,\Phi^{g'}_{0,0}(\bar{r}t)$$

$$= \frac{1}{\sqrt{3}}\frac{\partial}{\partial x}\Phi^g_{1,0}(\bar{r}t) - \frac{1}{\sqrt{6}}\left(\frac{\partial}{\partial y} - i\frac{\partial}{\partial z}\right)\Phi^g_{1,-1}(\bar{r}t) + \frac{1}{\sqrt{6}}\left(\frac{\partial}{\partial y} + i\frac{\partial}{\partial z}\right)\Phi^g_{1,1}(\bar{r}t)$$

$$-\left(\frac{1}{v^g(\bar{r})}\frac{\partial}{\partial t} + \Sigma^g_t(\bar{r}t)\right)\Phi^g_{1,-1}(\bar{r}t) + S^g_{1,-1}(\bar{r}t) + \sum_{g'}\Sigma^{g'\to g}_{s_1}(\bar{r}t)\,\Phi^{g'}_{1,-1}(\bar{r}t)$$

$$= -\frac{1}{\sqrt{6}}\left(\frac{\partial}{\partial y} + i\frac{\partial}{\partial z}\right)\Phi^g_{0,0}(\bar{r}t)$$

$$-\left(\frac{1}{v^g(\bar{r})}\frac{\partial}{\partial t} + \Sigma^g_t(\bar{r}t)\right)\Phi^g_{1,0}(\bar{r}t) + S^g_{1,0}(\bar{r}t) + \sum_{g'}\Sigma^{g'\to g}_{s_1}(\bar{r}t)\,\Phi^{g'}_{1,0}(\bar{r}t)$$

$$= \frac{1}{\sqrt{3}}\frac{\partial}{\partial x}\Phi^g_{0,0}(\bar{r}t)$$

$$-\left(\frac{1}{v^g(\bar{r})}\frac{\partial}{\partial t} + \Sigma^g_t(\bar{r}t)\right)\Phi^g_{1,1}(\bar{r}t) + S^g_{1,1}(\bar{r}t) + \sum_{g'}\Sigma^{g'\to g}_{s_1}(\bar{r}t)\,\Phi^{g'}_{1,1}(\bar{r}t)$$

$$= \frac{1}{\sqrt{6}}\left(\frac{\partial}{\partial y} - i\frac{\partial}{\partial z}\right)\Phi^{g}_{0,0}(\bar{r}t)$$

In order to follow the different terms, we rewrite the three-dimensional equations as follows:

$$-\left(\alpha_5 \frac{1}{v^g(\bar{r})}\frac{\partial}{\partial t} + \alpha_2 \Sigma^g_t(\bar{r}t)\right)\Phi^g_{0,0}(\bar{r}t) + \alpha_4 S^g_{0,0}(\bar{r}t) \qquad (111)$$

$$+\alpha_3 \sum_{g'} \Sigma^{g'\to g}_{s_0}(\bar{r}t)\,\Phi^{g'}_{0,0}(\bar{r}t) = \alpha_1 \frac{1}{\sqrt{3}}\frac{\partial}{\partial x}\Phi^g_{1,0}(\bar{r}t) - \alpha_6 \frac{1}{\sqrt{6}}\left(\frac{\partial}{\partial y} - i\frac{\partial}{\partial z}\right)\Phi^g_{1,-1}(\bar{r}t)$$

$$+\alpha_7 \frac{1}{\sqrt{6}}\left(\frac{\partial}{\partial y} + i\frac{\partial}{\partial z}\right)\Phi^g_{1,1}(\bar{r}t)\Big| - \left(\eta_4 \frac{1}{v^g(\bar{r})}\frac{\partial}{\partial t} + \eta_2 \Sigma^g_t(\bar{r}t)\right)\Phi^g_{1,-1}(\bar{r}t)$$

$$+\eta S^g_{1,-1}(\bar{r}t) + \eta_3 \sum_{g'} \Sigma^{g'\to g}_{s_1}(\bar{r}t)\,\Phi^{g'}_{1,-1}(\bar{r}t) = -\eta_1 \frac{1}{\sqrt{6}}\left(\frac{\partial}{\partial y} + i\frac{\partial}{\partial z}\right)\Phi^g_{0,0}(\bar{r}t)\Big|$$

$$-\left(\varepsilon_4 \frac{1}{v^g(\bar{r})}\frac{\partial}{\partial t} + \varepsilon_2 \Sigma^g_t(\bar{r}t)\right)\Phi^g_{1,0}(\bar{r}t) + \varepsilon S^g_{1,0}(\bar{r}t) + \varepsilon_3 \sum_{g'} \Sigma^{g'\to g}_{s_1}(\bar{r}t)\,\Phi^{g'}_{1,0}(\bar{r}t)$$

$$= \varepsilon_1 \frac{1}{\sqrt{3}}\frac{\partial}{\partial x}\Phi^g_{0,0}(\bar{r}t)\Big|$$

$$-\left(\gamma_4 \frac{1}{v^g(\bar{r})}\frac{\partial}{\partial t} + \gamma_2 \Sigma^g_t(\bar{r}t)\right)\Phi^g_{1,1}(\bar{r}t) + \gamma S^g_{1,1}(\bar{r}t) + \gamma_3 \sum_{g'} \Sigma^{g'\to g}_{s_1}(\bar{r}t)\,\Phi^{g'}_{1,1}(\bar{r}t)$$

$$= \gamma_1 \frac{1}{\sqrt{6}}\left(\frac{\partial}{\partial y} - i\frac{\partial}{\partial z}\right)\Phi^g_{0,0}(\bar{r}t)$$

We assume that the source term (prompt and delayed fission sources, external sources) are isotropic. Since stochastic processes introduce small variations of the flux around the mean, we can write (by converting from the time domain to the frequency (ω) domain

$$\Phi^{g}_{\ell,m}(\bar{r}t) = \Phi^{g}_{\ell,m}(\bar{r}) + \delta\Phi^{g}_{\ell,m}(\bar{r}\omega)\, e^{j\omega t}$$

$$S^{g}_{\ell,m}(\bar{r}t) = S^{g}_{\ell,m}(\bar{r}) + \delta S^{g}_{\ell,m}(\bar{r}\omega)\, e^{j\omega t}$$

The derivations will be made for a zero power reactor. Converting from the time domain to the frequency domain, and separating steady and stochastic parts gives

$$-\alpha_2 \Sigma^{g}_{t}(\bar{r})\, \Phi^{g}_{0,0}(\bar{r}) + \alpha_4 S^{g}_{0,0}(\bar{r}) + \alpha_3 \sum_{g'} \Sigma^{g'\to g}_{s_0}(\bar{r})\, \Phi^{g'}_{0,0}(\bar{r}) \qquad (112)$$

$$= \alpha_1 \frac{1}{\sqrt{3}} \frac{\partial}{\partial x} \Phi^{g}_{1,0}(\bar{r}) - \alpha_6 \frac{1}{\sqrt{6}} \left(\frac{\partial}{\partial y} - i \frac{\partial}{\partial z} \right) \Phi^{g}_{1,-1}(\bar{r}) + \alpha_7 \frac{1}{\sqrt{6}} \left(\frac{\partial}{\partial y} + i \frac{\partial}{\partial z} \right) \Phi^{g}_{1,1}(\bar{r})$$

$$-\eta_2 \Sigma^{g}_{t}(\bar{r})\, \Phi^{g}_{1,-1}(\bar{r}) + \eta_3 \sum_{g'} \Sigma^{g'\to g}_{s_1}(\bar{r})\, \Phi^{g'}_{1,-1}(r) = -\eta_1 \frac{1}{\sqrt{6}} \left(\frac{\partial}{\partial y} + i \frac{\partial}{\partial z} \right) \Phi^{g}_{0,0}(\bar{r})$$

$$-\varepsilon_2 \Sigma^{g}_{t}(\bar{r})\, \Phi^{g}_{1,0}(\bar{r}) + \varepsilon_3 \sum_{g'} \Sigma^{g'\to g}_{s_1}(\bar{r})\, \Phi^{g'}_{1,0}(\bar{r}) = \varepsilon_1 \frac{1}{\sqrt{3}} \frac{\partial}{\partial x} \Phi^{g}_{0,0}(\bar{r})$$

$$-\gamma_2 \Sigma^{g}_{t}(\bar{r})\, \Phi^{g}_{1,1}(\bar{r}) + \gamma_3 \sum_{g'} \Sigma^{g'\to g}_{s_1}(\bar{r})\, \Phi^{g'}_{1,1}(\bar{r}) =$$

$$\gamma_1 \frac{1}{\sqrt{6}} \left(\frac{\partial}{\partial y} - i \frac{\partial}{\partial z} \right) \Phi^{g}_{0,0}(\bar{r})$$

$$-\left(\alpha_5 \frac{J\omega}{v^g(\bar{r})} + \alpha_2 \Sigma_t^g(\bar{r})\right) \delta\phi_{0,0}^g(\bar{r}\omega) + \alpha_4 \delta S_{0,0}^g(\bar{r}\omega) \tag{113}$$

$$+ \alpha_3 \sum_{g'} \Sigma_{s_0}^{g'\to g}(\bar{r})\, \delta\phi_{0,0}^{g'}(\bar{r}\omega) = \alpha_1 \frac{1}{\sqrt{3}} \frac{\partial}{\partial x} \delta\phi_{1,0}^g(\bar{r}\omega)$$

$$- \alpha_6 \frac{1}{\sqrt{6}}\left(\frac{\partial}{\partial y} - i\frac{\partial}{\partial z}\right) \delta\phi_{1,-1}^g(\bar{r}\omega) + \alpha_7 \frac{1}{\sqrt{6}}\left(\frac{\partial}{\partial y} + i\frac{\partial}{\partial z}\right) \delta\phi_{1,1}^g(\bar{r}\omega)$$

$$-\left(\eta_4 \frac{J\omega}{v^g(\bar{r})} + \eta_2 \Sigma_t^g(\bar{r})\right) \delta\phi_{1,-1}^g(\bar{r}\omega) + \eta_3 \sum_{g'} \Sigma_{s_1}^{g'\to g}(\bar{r})\, \delta\phi_{1,-1}^{g'}(\bar{r}\omega)$$

$$= -\eta_1 \frac{1}{\sqrt{6}}\left(\frac{\partial}{\partial y} + i\frac{\partial}{\partial z}\right) \delta\phi_{0,0}^g(\bar{r}\omega)$$

$$-\left(\varepsilon_4 \frac{J\omega}{v^g(\bar{r})} + \varepsilon_2 \Sigma_t^g(\bar{r})\right) \delta\phi_{1,0}^g(\bar{r}\omega) + \varepsilon_3 \sum_{g'} \Sigma_{s_1}^{g'\to g}(\bar{r})\, \delta\phi_{1,0}^{g'}(\bar{r}\omega)$$

$$= \varepsilon_1 \frac{1}{\sqrt{3}} \frac{\partial}{\partial x} \delta\phi_{0,0}^g(\bar{r}\omega)$$

$$-\left(\gamma_4 \frac{J\omega}{v^g(\bar{r})} + \gamma_2 \Sigma_t^g(\bar{r})\right) \delta\phi_{1,1}^g(\bar{r}\omega) + \gamma_3 \sum_{g'} \Sigma_{s_1}^{g'\to g}(\bar{r})\, \delta\phi_{1,1}^{g'}(\bar{r}\omega)$$

$$= \gamma_1 \frac{1}{\sqrt{6}}\left(\frac{\partial}{\partial y} - i\frac{\partial}{\partial z}\right) \delta\phi_{0,0}^g(\bar{r}\omega)$$

To obtain the P_1 equations, only the first two terms (i.e. ℓ=0 and ℓ=1) were used in the scattering source. As we have seen in Chapter III, two

different approaches can be taken, depending on the approximation:

1. $$\int dE' \Sigma_{s_1}(\bar{r}, E' \rightarrow E)\ \Phi_{1,m}(\bar{r}E't) =$$

$$\int dE' \Sigma_{s_1}(\bar{r}, E \rightarrow E')\ \Phi_{1,m}(\bar{r}Et) \quad \text{for } m = 0, 1$$

The integral is therefore independent of energy. In group form we have

$$\sum_{g'} \Sigma_{s_1}^{g' \rightarrow g}(\bar{r})\ \Phi_{1,m}^{g'}(\bar{r}t) = \sum_{g'} \Sigma_{s_1}^{g \rightarrow g'}(\bar{r})\ \Phi_{1,m}^{g}(\bar{r}t) \tag{114}$$

We also know that $\sum_{g'} \Sigma_{s_1}^{g \rightarrow g'}(\bar{r}) = \Sigma_{s_1}^{g}(\bar{r})$ where the g' are the sink groups for g.

2. Approximation based on the assumption that $|\Sigma_{s_1}^{g' \rightarrow g}| \ll |\Sigma_t^g|$ for any g' and g, except g = g'.

If we apply assumption 1 to the three-dimensional steady state, P_1 equations, we obtain

$$\Phi_{1,-1}^{g}(\bar{r}) = \frac{\eta_1 \frac{1}{\sqrt{6}}\left(\frac{\partial}{\partial y} + i\frac{\partial}{\partial z}\right) \Phi_{0,0}^{g}(\bar{r})}{\eta_2 \Sigma_t^g(\bar{r}) - \eta_3 \Sigma_{s_1}^g(\bar{r})}$$

$$\Phi_{1,1}^{g}(\bar{r}) = \frac{-\gamma_1 \frac{1}{\sqrt{6}}\left(\frac{\partial}{\partial y} - i\frac{\partial}{\partial z}\right) \Phi_{0,0}^{g}(\bar{r})}{\gamma_2 \Sigma_t^g(\bar{r}) - \gamma_3 \Sigma_{s_1}^g(\bar{r})}$$

$$\Phi_{1,0}^{g}(\bar{r}) = \frac{-\varepsilon_1 \frac{1}{\sqrt{3}} \frac{\partial}{\partial x} \Phi_{0,0}^{g}(\bar{r})}{\varepsilon_2 \Sigma_t^g(\bar{r}) - \varepsilon_3 \Sigma_{s_1}^g(\bar{r})}$$

We insert those expressions into the steady state P_1 equations (112) and we obtain, after a few manipulations, the steady state *diffusion equation*

$$-\alpha_2 \Sigma_t^g(\bar{r})\, \phi_{0,0}^g(\bar{r}) + \alpha_4 S_{0,0}^g(\bar{r}) + \alpha_3 \sum_{g'} \Sigma_{s_0}^{g' \to g}(\bar{r})\, \phi_{0,0}^{g'}(\bar{r})$$

$$= -\alpha_1 \frac{1}{3} \nabla \frac{1}{\varepsilon_2 \Sigma_t^g(\bar{r}) - \varepsilon_3 \Sigma_{s_1}^g(\bar{r})} \nabla \phi_{0,0}^g(\bar{r})$$

The stochastic part of the three-dimensional P_1 equations becomes

$$\mathcal{J}\phi_{1,0}^g(\bar{r}\omega) = -\frac{1}{\varepsilon_2 \Sigma_t^g(\bar{r}) - \varepsilon_3 \Sigma_{s_1}^g(\bar{r}) + \varepsilon_4 \frac{j\omega}{v^g(\bar{r})}} \varepsilon_1 \frac{1}{\sqrt{3}} \frac{\partial}{\partial x} \mathcal{J}\phi_{0,0}^g(\bar{r}\omega)$$

If we define

$$D^g(\bar{r}) = \frac{1}{3\left(\varepsilon_2 \Sigma_t^g(\bar{r}) - \varepsilon_3 \Sigma_{s_1}^g(\bar{r})\right)} \tag{115}$$

then it is easily shown that

$$D^g(\bar{r}\omega) = D^{Rg}(\bar{r}\omega) + j\, D^{Ig}(\bar{r}\omega)$$

with

$$D^g(\bar{r}\omega) = \frac{D^g(\bar{r})}{1 + \varepsilon_4 \frac{3j\omega}{v^g(\bar{r})} D^g(\bar{r})} \tag{116}$$

$$D^{Rg}(\bar{r}\omega) = \frac{D^g(\bar{r})}{1 + \left(\varepsilon_4 \frac{3\omega}{v^g(\bar{r})} D^g(\bar{r})\right)^2}$$

$$D^{Ig}(\bar{r}\omega) = \frac{-\varepsilon_4 \frac{3\omega}{v^g(\bar{r})} D^g(\bar{r})^2}{1 + \left(\varepsilon_4 \frac{3\omega}{v^g(\bar{r})} D^g(\bar{r})\right)^2}$$

After elimination of $\delta\phi^g_{1,0}(\bar{r}\omega)$, $\delta\phi^g_{1,1}(\bar{r}\omega)$, $\delta\phi^g_{1,-1}(\bar{r}\omega)$ between the P_1 equations (113), we obtain

$$\alpha_1\varepsilon_1\nabla\frac{D^g(\bar{r})}{1+\varepsilon_4\frac{3j\omega}{v^g(\bar{r})}D^g(\bar{r})}\nabla\delta\phi^g_{0,0}(\bar{r}\omega)-\alpha_2\Sigma^g_t(\bar{r})\delta\phi^g_{0,0}(\bar{r}\omega)+\alpha_3\sum_{g'}\Sigma^{g'\to g}_{s_0}(\bar{r})\delta\phi^{g'}_{0,0}(\bar{r}\omega)+\alpha_4\delta S^g_{0,0}(\bar{r}\omega)=\alpha_5\frac{j\omega}{v^g(\bar{r})}\delta\phi^g_{0,0}(\bar{r}\omega) \quad (117)$$

After splitting this complex equation into its real and imaginary components, we get

$$\alpha_1\varepsilon_1\nabla\frac{D^g(\bar{r})}{1+\left(\varepsilon_4\frac{3\omega}{v^g(\bar{r})}D^g(\bar{r})\right)^2}\nabla\delta\phi^{Rg}_{0,0}(\bar{r}\omega)-\alpha_2\Sigma^g_t(\bar{r})\delta\phi^{Rg}_{0,0}(\bar{r}\omega)+\alpha_3\sum_{g'}\Sigma^{g'\to g}_{s_0}(\bar{r})\delta\phi^{Rg'}_{0,0}(\bar{r}\omega)+\alpha_4\delta S^g_{0,0}(\bar{r}\omega)+\alpha_1\varepsilon_1\nabla\frac{\varepsilon_4\frac{3\omega}{v^g(\bar{r})}D^g(\bar{r})^2}{1+\left(\varepsilon_4\frac{3\omega}{v^g(\bar{r})}D^g(\bar{r})\right)^2}\nabla\delta\phi^{Ig}_{0,0}(\bar{r}\omega)+\alpha_5\frac{\omega}{v^g(\bar{r})}\delta\phi^{Ig}_{0,0}(\bar{r}\omega)=0 \quad (118)$$

and

$$\alpha_1\varepsilon_1\nabla\frac{D^g(\bar{r})}{1+\left(\varepsilon_4\frac{3\omega}{v^g(\bar{r})}D^g(\bar{r})\right)^2}\nabla\delta\phi^{Ig}_{0,0}(\bar{r}\omega)-\alpha_2\Sigma^g_t(\bar{r})\delta\phi^{Ig}_{0,0}(\bar{r}\omega)+\alpha_3\sum_{g'}\Sigma^{g'\to g}_{s_0}(\bar{r})\delta\phi^{Ig'}_{0,0}(\bar{r}\omega)+\alpha_4\delta S^g_{0,0}(\bar{r}\omega)-\alpha_1\varepsilon_1\nabla\frac{\varepsilon_4\frac{3\omega}{v^g(\bar{r})}D^g(\bar{r})^2}{1+\left(\varepsilon_4\frac{3\omega}{v^g(\bar{r})}D^g(\bar{r})\right)^2}\nabla\delta\phi^{Rg}_{0,0}(\bar{r}\omega)-\alpha_5\frac{\omega}{v^g(\bar{r})}\delta\phi^{Rg}_{0,0}(\bar{r}\omega)=0 \quad (119)$$

where

$$\int\phi^{g}_{0,0}(\bar{r}\omega) = \int\phi^{Rg}_{0,0}(\bar{r}\omega) + j\int\phi^{Ig}_{0,0}(\bar{r}\omega).$$

These three-dimensional equations are formally similar to the one-dimensional P_1 equations (41 and 42) obtained in Chapter III, except that $\nabla D^{g}(\bar{r}\omega)\nabla$ represents the three-dimensional Laplacian.

Let us now apply assumption 2 to the P_1 three-dimensional set of equations. We define

$$D^{g}(\bar{r}) = \frac{1}{3\left(\Sigma^{g}_{t}(\bar{r}) - \Sigma^{g\to g}_{s_1}(\bar{r})\right)}$$

Therefore

$$\frac{1}{\Sigma^{g}_{t}(\bar{r}) - \Sigma^{g\to g}_{s_1}(\bar{r}) + \varepsilon_4 \frac{j\omega}{v^{g}(\bar{r})}} = \frac{3\,D^{g}(\bar{r})}{1 + D^{g}(\bar{r})\,\varepsilon_4 \frac{3j\omega}{v^{g}(\bar{r})}}$$

The stochastic equations therefore give

$$\int\phi^{g}_{1,0}(\bar{r}\omega) = \frac{3\,D^{g}(\bar{r})}{1 + \varepsilon_4 \frac{3j\omega}{v^{g}(\bar{r})} D^{g}(\bar{r})}\left[-\varepsilon_1 \frac{1}{\sqrt{3}} \frac{\partial}{\partial x} \int\phi^{g}_{0,0}(\bar{r}\omega) + \varepsilon_3 \sum_{\substack{g' \\ g'\neq g}} \Sigma^{g'\to g}_{s_1}(\bar{r})\int\phi^{g'}_{1,0}(\bar{r}\omega)\right]$$

We also know that

$$\int\phi^{g'}_{1,0}(\bar{r}\omega) = \frac{3\,D^{g'}(\bar{r})}{1 + \varepsilon_4 \frac{3j\omega}{v^{g'}(\bar{r})} D^{g'}(\bar{r})}\left[-\varepsilon_1 \frac{1}{\sqrt{3}} \frac{\partial}{\partial x} \int\phi^{g'}_{0,0}(\bar{r}\omega) + \varepsilon_3 \sum_{\substack{g'' \\ g''\neq g'}} \Sigma^{g''\to g'}_{s_1}(\bar{r})\int\phi^{g''}_{1,0}(\bar{r}\omega)\right]$$

Assuming that $\left|\Sigma_{s_1}^{g'\to g}\right|^2 \ll \left|\Sigma_t^g\right|^2$ for all g' and g except g' = g, it is easily shown that

$$\delta\phi_{1,0}^g(\bar{r}\omega) = \frac{3\,D^g(\bar{r})}{1+\varepsilon_4\frac{3J\omega}{v^g(\bar{r})}D^g(\bar{r})}\left[-\varepsilon_1\frac{1}{\sqrt{3}}\frac{\partial}{\partial x}\delta\phi_{0,0}^g(\bar{r}\omega)\right.$$
$$\left.-\varepsilon_3\sum_{g'}\Sigma_{s_1}^{g'\to g}(\bar{r})\,\frac{3\,D^{g'}(\bar{r})}{1+\varepsilon_4\frac{3J\omega}{v^{g'}(\bar{r})}D^{g'}(\bar{r})}\varepsilon_1\frac{1}{\sqrt{3}}\frac{\partial}{\partial x}\delta\phi_{0,0}^{g'}(\bar{r}\omega)\right]$$

$$\delta\phi_{1,-1}^g(\bar{r}\omega) = \frac{3\,D^g(\bar{r})}{1+\varepsilon_4\frac{3J\omega}{v^g(\bar{r})}D^g(\bar{r})}\left[\eta_1\frac{1}{\sqrt{6}}\left(\frac{\partial}{\partial y}+i\frac{\partial}{\partial z}\right)\delta\phi_{0,0}^g(\bar{r}\omega)\right.$$
$$\left.+\eta_3\sum_{g'}\Sigma_{s_1}^{g'\to g}(\bar{r})\,\frac{3\,D^{g'}(\bar{r})}{1+\varepsilon_4\frac{3J\omega}{v^{g'}(\bar{r})}D^{g'}(\bar{r})}\eta_1\frac{1}{\sqrt{6}}\left(\frac{\partial}{\partial y}+i\frac{\partial}{\partial z}\right)\delta\phi_{0,0}^{g'}(\bar{r}\omega)\right]$$

$$\delta\phi_{1,1}^g(\bar{r}\omega) = \frac{3\,D^g(\bar{r})}{1+\varepsilon_4\frac{3J\omega}{v^g(\bar{r})}D^g(\bar{r})}\left[-\gamma_1\frac{1}{\sqrt{6}}\left(\frac{\partial}{\partial y}-i\frac{\partial}{\partial z}\right)\delta\phi_{0,0}^g(\bar{r}\omega)\right.$$
$$\left.-\gamma_3\sum_{g'}\Sigma_{s_1}^{g'\to g}(\bar{r})\,\frac{3\,D^{g'}(\bar{r})}{1+\varepsilon_4\frac{3J\omega}{v^{g'}(\bar{r})}D^{g'}(\bar{r})}\gamma_1\frac{1}{\sqrt{6}}\left(\frac{\partial}{\partial y}-i\frac{\partial}{\partial z}\right)\delta\phi_{0,0}^{g'}(\bar{r}\omega)\right]$$

After a few manipulations, we get

$$-\left(\alpha_5\frac{J\omega}{v^g(\bar{r})}+\alpha_2\Sigma_t^g(\bar{r})\right)\delta\phi_{0,0}^g(\bar{r}\omega)+\alpha_4\delta S_{0,0}^g(\bar{r}\omega) \tag{120}$$
$$+\alpha_3\sum_{g'}\Sigma_{s_0}^{g'\to g}(\bar{r})\,\delta\phi_{0,0}^{g'}(\bar{r}\omega) = \alpha_1\frac{1}{\sqrt{3}}\frac{\partial}{\partial x}3\,D^g(\bar{r}\omega)$$
$$\cdot\left(-\varepsilon_1\frac{1}{\sqrt{3}}\frac{\partial}{\partial x}\delta\phi_{0,0}^g(\bar{r}\omega)-\varepsilon_3\sum_{g'}\Sigma_{s_1}^{g'\to g}(\bar{r})\,3\,D^{g'}(\bar{r}\omega)\,\varepsilon_1\frac{1}{\sqrt{3}}\frac{\partial}{\partial x}\delta\phi_{0,0}^{g'}(\bar{r}\omega)\right)$$
$$-\alpha_6\frac{1}{\sqrt{6}}\left(\frac{\partial}{\partial y}-i\frac{\partial}{\partial z}\right)3\,D^g(\bar{r}\omega)\left(\eta_1\frac{1}{\sqrt{6}}\left(\frac{\partial}{\partial y}+i\frac{\partial}{\partial z}\right)\delta\phi_{0,0}^g(\bar{r}\omega)\right.$$

$$+\eta_3 \sum_{g'} \Sigma_{s_1}^{g'\to g}(\bar{r})\; 3\, D^{g'}(\bar{r}\omega)\, \eta_1 \frac{1}{\sqrt{2}}\left(\frac{\partial}{\partial y} + i\frac{\partial}{\partial z}\right) \delta\phi_{0,0}^{g'}(\bar{r}\omega)\Bigg) \tag{121}$$

$$+\alpha_7 \frac{1}{\sqrt{2}}\left(\frac{\partial}{\partial y} + i\frac{\partial}{\partial z}\right) 3\, D^{g}(\bar{r}\omega)\left(-\gamma_1 \frac{1}{\sqrt{2}}\left(\frac{\partial}{\partial y} - i\frac{\partial}{\partial z}\right) \delta\phi_{0,0}^{g}(\bar{r}\omega)\right.$$

$$\left.-\gamma_3 \sum_{g'} \Sigma_{s_1}^{g'\to g}(\bar{r})\; 3\, D^{g'}(\bar{r}\omega)\, \gamma_1 \frac{1}{\sqrt{2}}\left(\frac{\partial}{\partial y} - i\frac{\partial}{\partial z}\right) \delta\phi_{0,0}^{g'}(\bar{r}\omega)\right)$$

with

$$D^{g}(\bar{r}\omega) = \frac{D^{g}(\bar{r})}{1 + \varepsilon_4 \frac{3\lambda\omega}{v^{g}(\bar{r})}\, D^{g}(\bar{r})} \tag{122}$$

or

$$\alpha_1 \varepsilon_1 \nabla D^{g}(\bar{r}\omega)\, \nabla \delta\phi_{0,0}^{g}(\bar{r}\omega) \tag{123}$$

$$+ 3\alpha_1 \varepsilon_1 \varepsilon_3 \sum_{g'} \nabla D^{g}(\bar{r}\omega)\, \Sigma_{s_1}^{g'\to g}(\bar{r})\, D^{g'}(\bar{r}\omega)\, \nabla \delta\phi_{0,0}^{g'}(\bar{r}\omega)$$

$$-\left(\alpha_5 \frac{\lambda\omega}{v^{g}(\bar{r})} + \alpha_2 \Sigma_t^{g}(\bar{r})\right) \delta\phi_{0,0}^{g}(\bar{r}\omega) + \alpha_3 \sum_{g'} \Sigma_{s_0}^{g'\to g}(\bar{r})\, \delta\phi_{0,0}^{g'}(\bar{r}\omega) + \alpha_4\, \delta S_{0,0}^{g}(\bar{r}\omega) = 0$$

Those three-dimensional equations are formally similar to the one-dimensional equations obtained in Chapter III (Equation 48).

APPENDIX B

BENCHMARK AND VALIDATION OF THE FIFTY GROUP CROSS SECTION GENERATION BASED ON ENDF/B-II DATA

In order to validate the method of cross section generation using cell-weighted collapses from 123 to 50 neutron energy-groups, and the cross section sets themselves, several critical experiments were considered, with which calculated values of k_{eff} can be compared. All the calculations were performed on a U-1108 computer with 262,000 decimal memory locations. The first critical experiment considered is a PuO_2-UO_2 experiment. This experiment was performed under the Plutonium Utilization Program (PUP)[152] and is described by Uotinen.[147] The experiment was conducted in the Critical Approach Facility (CAF) and consisted of a certain number of Zircaloy clad rods submersed in water.

The major characteristics of a fuel rod were:

1) PuO_2 mixed in natural UO_2

2) 1084.5 grams of PuO_2-UO_2 mixture per rod and 3.98 wt % PuO_2 of total mixture

3) Isotopics: U-235 w/o : natural 0.711 of total U
Atomic % Pu-238 of total Pu : 0.28
Atomic % Pu-239 of total Pu : 75.38
Atomic % Pu-240 of total Pu : 18.10
Atomic % Pu-241 of total Pu : 5.08
Atomic % Pu-242 of total Pu : 1.13

4) Pellet density: 9.46 g/cc (86% TD)

5) Pellet OD: 1.264 cm, and diametrical gap was assumed to be zero

6) Clad: Zircaloy-2, clad OD: 1.435 cm, clad thickness: 0.086 cm

7) Active fuel height: 91.4 cm.

The major characteristics of the critical experiment with PuO_2-UO_2 fuel rods bathed in H_2O (average temperature of 25°C) were:

1) Lattice spacing: 2.16 cm on a triangular pitch

2) Approach-to-critical critical size: 252.6 ± 0.5 rods

3) H/Pu Atom Ratio: 152.8 and H_2O/Rod Volume Ratio: 1.500

The cell weighted cross section collapses from 123 groups to 50 groups were performed using the XSDRN[123] code. The parameters/options used were:

a) one-dimensional cylindrical geometry, with the equivalent radius of the cell (rod surrounded by water) being the outer radius boundary. The area of one cell for a triangular pitch: $\sqrt{3}/2 \times \overline{\text{pitch}}^2$. We therefore have $R_{cell} = \sqrt{\sqrt{3}/(2\pi)} \times$ pitch = 1.1336 cm. Six equally spaced meshed in the "r" direction were taken in the fuel, two in the Zircaloy-2 clad, four in the water of the cell.

The critical radius of the critical experiment, based on uniform cylindrical distribution of the fuel rods is

$$R_{crit} = \sqrt{252.6 \times \sqrt{3}/(2\pi)} \times \text{pitch} = 18.016 \text{ cm.}$$

The following number densities were used for the cell:

PuO_2-UO_2 oxide:	N^{U-235}	= 1.4568-04
	N^{U-238}	= 2.0087-02
	N^{Pu-239}	= 6.2988-04
	N^{Pu-240}	= 1.6319-04
	N^{Pu-241}	= 4.2449-05
	N^{O-16}	= 4.2136-02

where Pu-242 was added into Pu-240

Zircaloy-2 clad:	N^{Zr}	= 4.3232-02
H_2O surrounding rod:	N^{H1}	= 6.6767-02
	N^{O-16}	= 3.3383-02

b) Reflective left boundary at the center of the cell, white/albedo right boundary at the equivalent radius boundary of the cell

c) S_4P_3 one-dimensional transport approximation (discrete ordinate diamond method) using a 123 neutron group cross section library based on ENDF/B-II data

d) Overall convergence criterion: 0.001

Point convergence criterion: 0.001

e) Resonance correction (resolved and unresolved) for U-238 using

i) cylindrical geometry with absorber lump dimension equal to the radius of the pellet

ii) Nordheim's Integral Method (NIM)[118] for U-238 and NIM for first moderator 016 in the oxide, at a temperature of 294.6°K

iii) Dancoff correction using Sauer's[153] approximation.

This factor corrects for the self-shielding effects in the resonance region due to the presence of the other fuel rods

$$1\text{-}C = \frac{e^{-\tau\Sigma\bar{\ell}}}{1+(1-\tau)\Sigma\bar{\ell}}$$

where

τ = geometric index

$\bar{\ell}$ = moderator mean chord length

Σ = total moderator cross section of H_2O

Sauer has shown that, for a square lattice, the geometric index can be approximated by

$$\tau = \frac{\sqrt{\frac{\pi}{4}}\ \sqrt{1 + \frac{V_1}{V_0}} - 1}{\frac{V_1}{V_0}} - 0.08$$

where

V_0 = fuel volume in the cell

V_1 = moderator volume in the cell

It has been shown[153] that, for a wide range of lattices, this approximation agreed satisfactorily with Monte Carlo results.

The following values were calculated and used in the resonance calculation.

Mean chord length in moderator: 2.8032

Geometric index: 0.1859

Total moderator cross section: 1.4889

Dancoff correction: 0.1047

iv) Effective moderator cross section per absorber atom for U-235: 56.58

v) For U-238, the first moderator scattering cross section per absorber atom for O-16 in UO_2: 7.636

f) Collapsed fifty group cross sections, with a group energy structure as in Table 5, were generated in standard ANISN[108] format. The P_0, P_1, P_2, P_3 scattering matrices were also generated. The total cross section table length was 17, with σ_t in position 3. The 123 neutron group cross sections were cell-weighted over a fuel rod cell and collapsed to fifty groups for U-235, U-238, Pu-239, Pu-240, Pu-241, O-16 in UO_2, Zr in clad, H-1, O-16 in water moderator.

The Al cross sections were obtained by adding them into each mixture with a number density of 1.0×10^{-15}.

The k_{eff} calculation was performed using the KENO[149] code. This code performs multi-group neutron transport Monte Carlo calculations in three-dimensional geometry.

In the KENO run, the scattering was represented by P_0 and P_1 Legendre polynomials and the P_2 and P_3 matrices were stripped off. The Russian roulette and splitting techniques to minimize the variance of k_{eff} were used. Weighting was taken to be 0.5. Homogenized number densities were used over the UO_2-PuO_2 rods - Zr-H_2O cell. This approximation is accurate because the fifty group cross sections were generated using a cell-weighted spectrum collapse.

The equivalent radius of the active region was calculated as: 18.016 cm.

In the z-direction, the active region was topped and bottomed

by an H_2O + Zr mixture of 0.825 cm thickness. This represented the homogenization of the Zircaloy fuel end-plugs and the water between fuel rods.

The fuel was supported by a 1.27 cm aluminum plate.

The whole system was surrounded in the r and z directions by two feet of water.

The homogenized number densities used were:

Active fuel region:	N^{U-235}	= 4.526-05
	N^{U-238}	= 6.2406-03
	N^{Pu-239}	= 1.9742-04
	N^{Pu-240}	= 5.1148-05
	N^{Pu-241}	= 1.3304-05
	N^{H1}	= 4.0013-02
	N^{O16}	= 3.310 -02
	N^{Zr}	= 3.8865-03
Reflector:	N^{H1}	= 6.6767-02
	N^{O16}	= 3.3383-02
Al support plate:	N^{Al}	= 6.0200-02
Water + Zr region:	N^{H1}	= 4.0018-02
	N^{O16}	= 2.0009-02
	N^{Zr}	= 1.732 -02

The calculation of k_{eff} for the mockup was obtained using 15,000 neutron histories. The neutron histories were subdivided into 50 generations of 300 neutron histories each. Discarding the first nine generations in order to obtain a more or less settled source, we obtained a value of $k_{eff} = 1.00927 \pm 0.00915$ at a 67% confidence level.

In order to give some estimate of the normality of the distribution of k_{eff}, the Shapiro-Wilk[154] test was performed and found to be satisfactory. From the results of the benchmark, it can be seen that the cross section sets and the cell spectrum-weighted collapses gave results which were in good agreement with the critical experiments.

Although the calculation of just one critical experiment gives insight as to the ability of a computational method to calculate certain parameters of that experiment, it is not necessarily a proof of the accuracy of that method. However, many other critical experiments were calculated by the author using a similar computational approach and in all cases the agreement was good.

APPENDIX C

INSTRUMENTATION AND EQUIPMENT

A local perturbation of the coupling region in the GTRR can be introduced by varying the degree of neutron absorption within the reactor with a predetermined movement of 20-mil thick cadmium strips. The device constructed for this task was a pile oscillator, which was designed to operate in the active core region of the GTRR, in a fuel assembly position V-1 to V-19.

The basic requirements for the design were: 1) the total reactivity worth of the oscillator should be as small as possible; 2) the magnitude of the perturbance at a certain frequency should be sufficient in order to dominate all other noise sources, especially in the high frequency range; and 3) the frequency range of the perturbance should be from 0 to 1000 cycles per second.

The basic design of the pile oscillator used the "cadmium shading" principle. Since 20-mil thick cadmium is almost totally black to thermal neutrons, it can be assumed as a first approximation that the amount of absorption is proportional to the exposed surface area rather than the amount of cadmium present. Thus, if two cadmium sheets shadow one another in the reactor, the same amount of absorption would ideally occur as if only one sheet had been present.

To implement this principle, 8 or 18 cadmium strips, 0.85 or 0.38 cm wide by 2.5 cm long by 20 mils thick were positioned into 8 or 18

equally spaced 25-mil deep grooves of a 50-mil thick hollow aluminum cylinder (see Figures 60 and 61). The cadmium strips were held in place by a 60-mil thick aluminum cylindrical sleeve. The outside diameter of this rotor was 4.84 cm. Similarly, 8 or 18 cadmium strips 1.06 or 0.47 cm wide by 4 cm long by 20 mils thick were positioned into 25-mil deep grooves of a 50-mil thick hollow aluminum cylinder and kept in place by a 60-mil thick aluminum cylindrical sleeve. The inside diameter of this stator was 5.397 cm.

In the rotor position where its Cd leaves coincide with the position of the Cd leaves of the stator, the shadowed leaves absorb almost no additional neutrons. When the rotor turns, its Cd leaves are exposed and the absorption of the stator-rotor system increases by an amount proportional to the Cd area exposed by the rotor. However, since the radius of curvature of the Cd leaves of the rotor is not the same as the one of the stator, and due to the angular distribution of the neutron flux, we will have a rotor-stator absorption change smaller than two. In order to determine the reactivity change as compared to the total reactivity introduced by the stator-rotor, reactivity calibrations were made with the rotor-stator system positioned with the most Cd exposed, and with the least Cd exposed. The stator-rotor was positioned inside a special dummy fuel assembly and placed in position V-10 at the midplane of the GTRR reactor core. The relative reactivity change was approximately 40% of the total Cd reactivity worth for the eight Cd-strip system, and 15% for the 18 Cd-strip system, as measured from regulating rod and shim blades calibrations. An accurate determination of the total reactivity introduced by the pile oscillator, and the range of the reactivity change

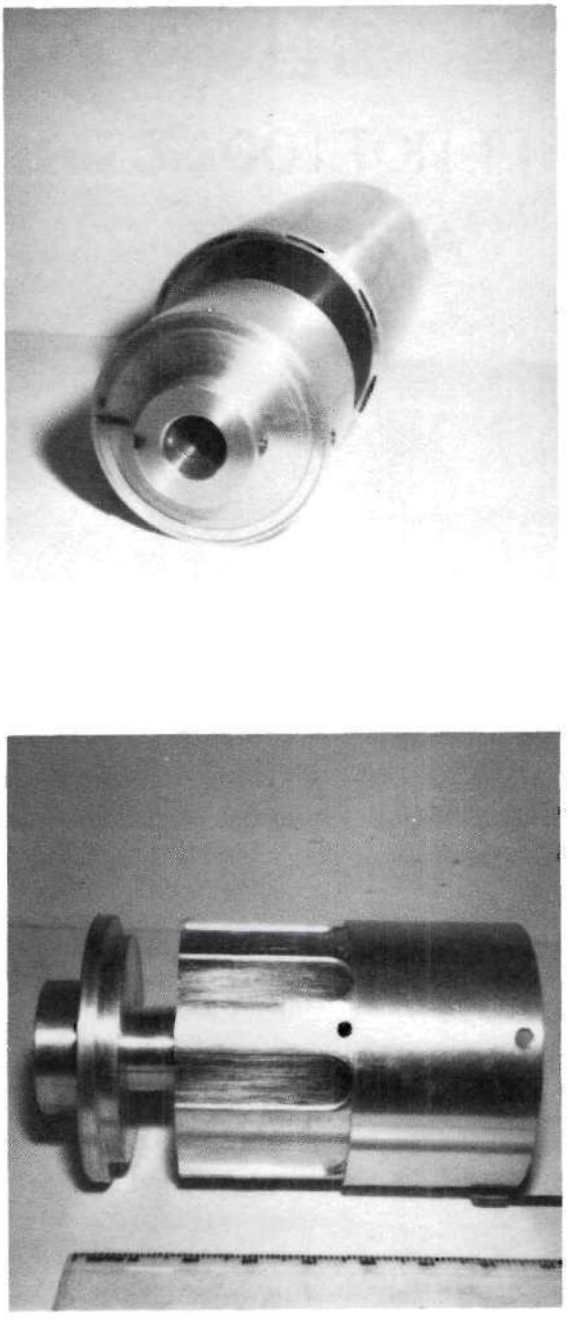

Figure 60. Rotor-Stator Assembly GTRR In-Core Pile Oscillator

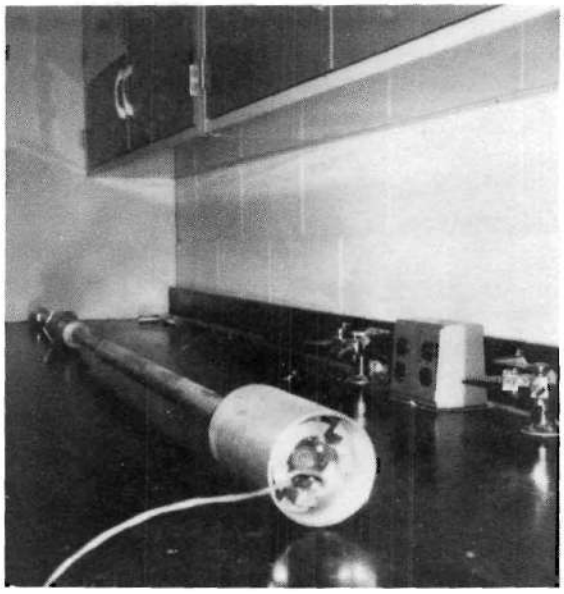

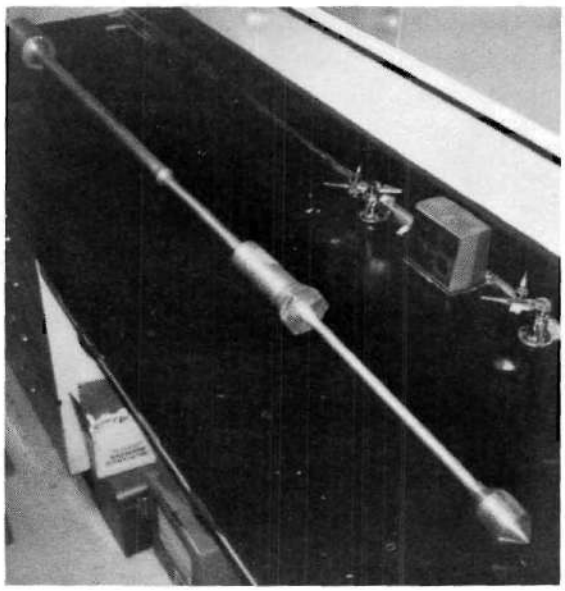

Figure 61. GTRR In-Core Pile Oscillator

introduced by the movement of the rotor could be performed by three-dimensional Monte Carlo calculations with P_0 and P_1 scattering.

The oscillator was housed inside a 6.35 cm OD by 17.8 cm long aluminum tube. All the aluminum materials of the pile oscillator were of type 6061-T6. The leaves on the rotor thus provide 8 or 18 perturbation cycles per one revolution of the drive shaft. The drive shaft was driven by a high precision Electro-Craft Corporation type E550MG DC servo motor-generator, controlled by an E550S controller. This system offered a precise speed control even in the presence of changing load conditions with a special low drift amplifier. The speed control was better than 0.1% variation over 10 minute time spans, and the speed could be varied from 0 to 5000 rpm.

The motor was housed inside an aluminum tube, 10.2 cm OD and 17.8 cm length, with Boral* neutron shielding. The housing was located above the D_2O upper axial reflector. The motor was connected to the rotor by way of a 0.5 inch OD aluminum shaft and kept in place with stainless steel ball bearings of type Fafnir. The total oscillator assembly is shown in Figure 61. In normal operation the oscillator was connected to a fuel assembly lower shield plug in an identical manner as a GTRR fuel assembly.

In the eight Cd-strip system, the frequency of the perturbation had a range from 0 to 660 ± 6 cps and for the 18 Cd-strip system from 0 to 1500 ± 15 cps. The speed stability was extensively checked in the GTRR fuel assembly test stand over the whole frequency range by means

*Brooks & Perkins, Inc., 1/4 inch Boral.

of a high precision stroboscope and a photocell system, and was found to be adequate. The speed was controlled by a "ten turn" helipot and by a PDP-8 computer.

BIBLIOGRAPHY

1. A. F. Henry and J. D. Germann, "Oscillations in the Power Distribution Within a Reactor," Nucl. Sci. Eng., 2, 469 (1957).

2. J. B. Yasinsky and A. F. Henry, "Some Numerical Experiments Concerning Space-Time Reactor Kinetics Behavior," Nucl. Sci. Eng., 22, 171 (1965).

3. R. V. Meghreblian and D. K. Holmes, Reactor Analysis, McGraw-Hill Book Company, Inc., New York, 1960.

4. A. Ozembre, "Sur l'Approximation P_1 de l'Equation de Transport Dépendent du Temps et ses Conséquences," Nukleonik, 7, Heft 1 (1965).

5. "Proceedings of the Conference on the Computational Methods in Nuclear Engineering," Charleston, S. C., Vol. I and II, CONF-750413, *Savannah River Lab. E. I.* du Pont de Nemours, and Co., Aiken, S.C., 1975.

6. D. N. Bridges, J. D. Clement, and J. P. Renier, "A Method for Calculating Space-Dependent Reactor Source Transfer Functions With Feedback," Nucl. Sci. Eng., 36 (1), 122 (1969).

7. J. W. Cooley and J. W. Tukey, "An Algorithm for the Machine Calculation of Complex Fourier Series," Mathematics of Computations, 19, 297 (1965).

8. "Special Issue of Fast Fourier Transform and Its Application to Digital Filtering and Spectral Analysis," IEEE Trans. on Audio and Electroacoustics, AU-15, No. 2 (1967).

9. N. Pacilio, "Reactor-Noise Analysis in the Time Domain," TID-24512, AEC Critical Review Series, U.S. Govt. Printing Off., Washington, D.C., 1969.

10. R. E. Uhrig, Random Noise Techniques in Nuclear Reactor Systems, The Ronald Press Company, New York, 1970.

11. R. E. Uhrig, "Neutron Noise, Waves, and Pulse Propagation," CONF-660206, Proceedings of a Symposium, USAEC Symposium Series 9 (1967).

12. J. D. Balcomb, H. B. Demuth, and E. P. Gyftopoulos, "A Cross-correlation Method for Measuring the Impulse Response of Reactor Systems," Nucl. Sci. Eng., 11(2), 159 (1961).

13. M. A. Quddus, R. G. Cochran, and D. E. Emon, "Axial Propagation of Neutron Waves in Heterogeneous Media," Nucl. Sci. Eng., 35, 342 (1969).

14. S. M. Feinberg, "Heterogeneous Methods for Calculating Reactors: Survey of Results and Comparison with Experiment," in Proc. Intern. Conf. Peaceful Uses of Atomic Energy, Vol. 5, P/669, IAEA, Geneva, 1955, p. 484.

15. A. D. Galanin, "Critical Size of Heterogeneous Reactor with Small Number of Rods," Proc. Intern. Conf. Peaceful Uses of Atomic Energy, Vol. 5, P/663, IAEA, Geneva, 1955, p. 462.

16. P. M. Morse and H. Feshbach, Methods of Theoretical Physics, McGraw-Hill Book Company, Inc., New York, 1953.

17. M. Nagy and R. A. Danofsky, "Cross-Spectral-Density Sink Frequency Behavior for Coupled-Core Argonaut Reactors," Nucl. Sci. Eng., 42, 419 (1970).

18. J. P. Renier, H. Genz, K. W. D. Ledingham, and R. W. Fink, "M/L Orbital-Electron-Capture Ratio in Ar^{37} Decay and the Fraction of k_α X-Rays in the K Series of Chlorine," The Physical Review, 166, No. 4, 935 (1968).

19. R. A. Hendrickson and G. Murphy, "Cross-Spectral Density Measurements in a Coupled-Core Reactor," Nucl. Sci. Eng., 31, 215 (1968).

20. R. W. Albrecht and W. Seifritz, "Fundamental Properties of the Coherence Function in Symmetrical Two-Node Systems," Nukleonik, 11, 143 (1968).

21. W. Seifritz and R. W. Albrecht, "Measurement and Analysis of the Coupled Core Coherence Function in a Two Node Symmetrical Reactor," Nukleonik, 11, 149 (1968).

22. W. Seifritz and D. Stegemann, "Reactor-Noise Analysis," Journal of the International Atomic Energy Agency, 9, 1 (1971).

23. R. W. Albrecht and W. Seifritz, "The Coherence Function: A Measure of Spatially Dependent Nuclear Reactor Properties," Preprints of the Japan-U.S. Seminar on Nuclear Reactor Noise Analysis, 285 (1968).

24. G. C. Baldwin, "Kinetics of a Reactor Composed of Two Loosely Coupled Cores," Nucl. Sci. Eng., 6, 320 (1959).

25. P. G. Johnson, "Coupled Reactors in Nuclear Rocket Applications," in Proceedings of the American Nuclear Society National Topical Meeting on Coupled Reactor Kinetics, Texas A & M University Press, College Station, Texas (1967).

26. A. L. Mowery, Jr. and H. C. Romesburg, "Calculations of Interactions Between Clustered NERVA Reactors," in Proceedings of the American Nuclear Society National Topical Meeting on Coupled Reactor Kinetics, Texas A & M University Press, College Station, Texas, 1967 .

27. J. S. Woyski, "Neutronic Coupling and Its Effects in Clustered Nuclear Engines," in Proceedings of the American Nuclear Society National Topical Meeting on Coupled Reactor Kinetics, Texas A & M University Press, College Station, Texas, 1967 .

28. R. A. Danofsky, "A Space-Dependent Reactor-Noise Formulation Utilizing Modal Expansions," Nucl. Sci. Eng., 36, 28 (1969).

29. R. W. Albrecht, "Comments on 'A Space-Dependent Reactor-Noise Formulation Utilizing Modal Expansions'," Nucl. Sci. Eng., 37, 322 (1969); R. A. Danofsky, "Further Comment on 'A Space-Dependent Reactor-Noise Formulation Utilizing Modal Expansions'," Nucl. Sci. Eng., 37, 322 (1969).

30. J. M. Betancourt and R. A. Danofsky, "A Space-Dependent Reactor-Noise Formulation Based on the Natural Mode Approximation," Nucl. Sci. Eng., 38, 77 (1969).

31. R. W. Albrecht and R. A. Danofsky, "Analytical-Experimental Correlations in Space-Dependent Coherences," Trans. Am. Nucl. Soc., 12, 708 (1969).

32. D. D. Ebert, J. D. Clement, and W. M. Stacey, "Investigation of the Space-and Energy-Dependent Coherence Function in Zero-Power Coupled-Core Reactors," Nucl. Sci. Eng., 55, 368 (1974).

33. D. D. Ebert, J. D. Clement, and W. M. Stacey, "Interpretation of Coherence Function Measurements in Zero-Power Coupled Core Reactors," Nucl. Sci. Eng., 55, 380 (1974).

34. N. Carter and R. Danofsky, "The Application of the Calculus of Variations and the Method of Green's Functions to the Solution of Coupled Core Kinetics Equations," in Proceedings of the American Nuclear Society National Topical Meeting on Coupled Reactor Kinetics, Texas A & M University Press, College Station, Texas, 1967.

35. D. E. Dougherty and C. N. Shen, "The Space-Time Neutron Kinetic Equations Obtained by the Semidirect Variational Method," Nucl. Sci. Eng., 13, 141 (1962).

36. R. A. Rydin, J. A. Burke, W. E. Moore, and K. W. Seemann, "Noise and Transient Kinetics Experiments and Calculations for Loosely Coupled Cores," Nucl. Sci. Eng., 46, 179 (1971); R. A. Rydin, J. A. Burke, W. E. Moore, and K. W. Seemann, "Space-Time Kinetics Experiments and Calculations for a Loosely Coupled Core," Trans. Am. Nucl. Soc., 13, 698 (1970).

37. "An Evaluation of Four Design Studies of a 1000 MWe Ceramic Fueled Fast Breeder Reactor," COO-279, Reactor Engineering Division, Chicago Operations Office, Chicago, Illinois, U.S. Atomic Energy Commission (1964).

38. "An Evaluation of the Atomics International 1000 MWe Fast Breeder Reactor," COO-285, Reactor Engineering Division, Chicago Operations Office, Chicago, Illinois, U.S. Atomic Energy Commission (1966).

39. "Liquid Metal Fast Breeder Reactor Design Study," WCAP-3251, Westinghouse Electric Corporation (1969).

40. W. E. Gunson, F. M. Heck, and R. S. Daleas, "Transient Response of Coupled Fast Reactor Cores," ANL-7120, Proceedings of the Conference on Safety, Fuels, and Core Design in Large Fast Power Reactors, Argonne National Laboratory, Argonne, Illinois (1965).

41. F. M. Heck, M. W. Dyos, and W. E. Gunson, "The Inherent Neutronic Safety Characteristics of the Fast Modular Reactor Concept," in Proceedings of the American Nuclear Society National Topical Meeting on Coupled Reactor Kinetics, Texas A & M University Press, College Station, Texas, 1967.

42. D. Eggen, "Enhanced Safety Characteristics of a Sodium-Cooled Coupled Reactor," Proceedings of the Conference on Safety, Fuels, and Core Design in Large Fast Power Reactors, ANL-7120, Argonne National Laboratory, Argonne, Illinois (1965), p. 789.

43. R. Avery, "Coupled Fast-Thermal Power Breeder Critical Experiment," Proceedings of the Second United Nations International Conference on the Peaceful Uses of Atomic Energy, Geneva, Vol. 12, 1958, p. 2160.

44. L. Barleon, A. Bayer, C. Brückner, K. Burkart, G. Fieg, D. Kuhn, G. Kussmaul, H. Meister, H. Seufert, D. Stegemann, and H. Werle, "Evaluation of Reactor Physics Experiments on the Coupled Fast-Thermal Argonaut Reactor STARK," International Conference on Fast Critical Experiments and Their Analysis, ANL-7320, Argonne, Illinois (1966), p. 137.

45. P. R. Pluta, W. G. Hubschmann, and G. W. Lill, "Kinetics of Coupled Thermal-Fast Spectrum Power Reactors," in Proceedings of the American Nuclear Society National Topical Meeting on Coupled Reactor Kinetics, Texas A & M University Press, College Station, Texas, 1967, p. 361.

46. P. R. Kasten, "Space-Dependent Reactor Kinetics," Nuclear Safety, 7(2), 162 (Winter 1965-1966).

47. B. R. Leonard, "A Review of Fusion-Fission (Hybrid) Concepts," Nucl. Technol., 20, 161 (1973).

48. A. F. Henry, "Neutron Kinetics," Sec. 5.2 in Naval Reactors Physics Handbook, Vol. I, Naval Reactors, Division of Reactor Development USAEC, U.S. Government Printing Office, Washington, D.C., 1964, p. 855.

49. A. F. Henry and N. J. Curlee, "Verification of a Method for Treating Neutron Space-Time Problems," Nucl. Sci. Eng., 4(6), 727 (1958).

50. R. Avery, "Theory of Coupled Reactors," Second United Nations International Conference on the Peaceful Uses of Atomic Energy, Geneva, Vol. 12, 1958, p. 1858.

51. M. Komata, "On the Derivation of Avery's Coupled Reactor Kinetics Equations," Nucl. Sci. Eng., 38, 193 (1969).

52. B. V. Koen, "Calculation of Reactor Coupling Coefficients," CSR-T-68-1 Center for Space Research, Massachusetts Institute of Technology (1968).

53. R. G. Cockrell and R. B. Perez, "Kinetic Theory of Spatial and Spectral Coupling of the Reactor Neutron Field," CONF-650413, Symp. 7, Proc. Conf. on Neutron Dynamics and Control, USAEC, 323 (1966).

54. G. C. Hopkins, "Analysis of Neutron Response in Pulsed Coupled-Core Reactors," Trans. Am. Nucl. Soc., 10, 2, 629 (1967); G. C. Hopkins, "Pulsed Neutron Analysis in Coupled-Core Nuclear Reactors," Ph.D. Thesis, Purdue University, LaFayette, Indiana, 1967.

55. A. Belleni-Morante, "The Kinetic Behavior of a Reactor Composed of Two Loosely Coupled Cores with Time-Dependent Coupling Coefficients," Nukleonik, 8, Heft 5 (1966).

56. A. Belleni-Morante, "The Kinetic Behavior of a Reactor Composed of G Loosely Coupled Cores: Integral Formulation," Journal of Nucl. Energy Part A/B, 18, 547 (1964).

57. R. L. Seale, "Coupled Core Reactors," LAMS-2967, Los Alamos Scientific Laboratory, Los Alamos, New Mexico (1964).

58. D. Schwalm, "On a Derivation of the Multigroup Kinetic Equations of Coupled Reactors," EUR-2416e EURATOM, Ispra, Italy (1965).

59. G. E. Hansen, "Kinetics Equations for a Cluster of Rover Reactors," N-2-7967, Los Alamos Scientific Laboratory, Los Alamos, New Mexico (1965).

60. H. Plaza and W. H. Köhler, "Coupled-Reactor Kinetics Equations," Nucl. Sci. Eng., 26, 419 (1966).

61. R. G. Cockrell and R. B. Perez, "Kinetic Theory of Spatial and Spectral Coupling of the Reactor Neutron Field," CONF-630413, Proceedings of the Symposium on Neutron Dynamics and Control, 323 (1966).

62. A. Belleni-Morante, "Neutron Transport and Kinetics in a Reactor Composed of Two Loosely Coupled Cores," in Proceedings of the American Nuclear Society National Topical Meeting on Coupled Reactor Kinetics, Texas A & M University Press, College Station, Texas, 1967, p. 176.

63. S. G. Raju and R. S. Stone, "Dynamics of Coupled Core Reactors," Nucl. Safety, 9(2) (1968).

64. W. H. Köhler, "Summary of Derivations of Coupled Point Reactor Kinetics Equations, in Proceedings of the American Nuclear Society National Topical Meeting on Coupled Reactor Kinetics, Texas A & M University Press, College Station, Texas, 1967, p. 192.

65. M. W. Dyos and F. M. Heck, "The Current Status of Analytical Methods for Calculating the Kinetic Behavior of Loosely Coupled Fast Reactors," International Conference on La Sûrete des Reacteurs à Neutrons Rapides, Aix en Provence, (1967).

66. A. F. Henry, "The Application of Inhour Modes to the Description of Nonseparable Reactor Transients," Nucl. Sci. Eng., 20(3), 338 (1964).

67. E. R. Cohen, "Some Topics in Reactor Kinetics," in Proceedings of the Second United Nations International Conference on the Peaceful Uses of Atomic Energy, Vol. 11, IAEA, Geneva, 1958, p. 302.

68. S. Kaplan, "The Property of Finality and the Analysis of Problems in Reactor Space-Time Kinetics by Various Modal Expansions," Nucl. Sci. Eng., 9(3), 357 (1961).

69. D. R. Harris and P. S. Lacy, "A Simple Approximate Test for Spatial Xenon Stability," Trans. Am. Nucl. Soc., 8(2), 437 (1960).

70. D. E. Dougherty, "The Space-Time Neutron Kinetics by a Variational Method with Application to Power Reactor Dynamics," KAPL-2217, Knolls Atomic Power Laboratory, (1962).

71. A. M. Weinberg and E. P. Wagner, The Physical Theory of Neutron Chain Reactors, The University of Chicago Press, Chicago, 1958.

72. J. Wakabayashi, H. Yoshikawa, and T. Hoshino, "Analysis of Space-Dependent Reactor Kinetics by Modified Helmholtz Modal Expansion Method," Preprints of the Japan-U.S. Seminar on Nuclear Reactor Noise Analysis, (1968).

73. W. M. Stacey, Jr., "A General Modal Expansion Method for Obtaining Approximate Equations for Linear Systems," Nucl. Sci. Eng., 28, 438 (1967); Modal Approximations: Theory and an Application to Reactor Physics, M.I.T. Press, Cambridge, Mass., 1967; Space-Time Nuclear Reactor Kinetics, Academic Press, New York, 1969.

74. A. M. Weinberg and H. C. Schweinler, "Theory of Oscillating Absorber in a Chain Reactor," Physical Review, 74, 851 (1948).

75. T. Nomura, "Some Aspects of Zero Power Reactor Transfer Functions," J. Nucl. Sci. Technol. (Tokyo), 1(2), 41 (1964).

76. R. L. Seale, "Coupled Core Reactors," LAMS-2967, Los Alamos Scientific Laboratory, Los Alamos, New Mexico (1964).

77. W. E. Loewe, "Space-Dependent Effects in the Response of a Nuclear Reactor to Forced Oscillations," Nucl. Sci. Eng., 21, 536 (1965).

78. C. D. Kylstra and R. E. Uhrig, "Spatially Dependent Transfer Function for Nuclear System," Nucl. Sci. Eng., 22, 191 (1965).

79. C. G. Chezem and H. H. Helmick, "Pulsed Neutron Analysis in the Los Alamos Coupled Reactor Experiment," LA-3263-MS, Los Alamos Scientific Laboratory, Los Alamos, New Mexico; H. H. Helmick and C. G. Chezem, "Summary of Coupled Kiwi Experience," in Proceedings of the American Nuclear Society National Topical Meeting on Coupled Reactor Kinetics, Texas A & M University Press, College Station, Texas, 1967, p. 29.

80. R. B. Perez, R. S. Booth, R. S. Denning, and R. H. Harley, "Propagation of Neutron Waves in Subcritical Assemblies," Trans. Am. Nucl. Soc., 7,49 (1964).

81. C. E. Cohn, R. J. Johnson, and R. N. MacDonald, "Calculating Space-Dependent Reactor Transfer Functions Using Statics Techniques," Nucl. Sci. Eng., 26, 198 (1966).

82. T. B. Fowler, M. L. Tobias, and D. R. Vondy, "EXTERMINATOR-I--A Multigroup Code for Solving Neutron Diffusion Equations in One and Two Dimensions," ORNL-TM-842, Oak Ridge National Laboratory, Oak Ridge, Tennessee (1966); T. B. Fowler, M. L. Tobias, and D. R. Vondy, "EXTERMINATOR-II: A Fortran-IV Code for Solving Multi-Group Neutron Diffusion Equations in Two-Dimensions," ORNL-4078, Oak Ridge National Laboratory, Oak Ridge, Tennessee, (1967); and, M. L. Tobias, T. B. Fowler, and D. R. Vondy, "First-Order Perturbation Theory As Used in the Multigroup Diffusion Code EXTERMINATOR-II," ORNL-TM-1741, Oak Ridge National Laboratory, Oak Ridge, Tennessee (1967).

83. P. T. Hansson and L. R. Foulke, "Investigations in Spatial Reactor Kinetics," KR-43, Institutt for Atomenergi, Kjeller Research Establishment, Kjeller, Norway (1963).

84. C. G. Poncelet, "Space Dependent Reactor Transfer Functions," WCAP-2873, Westinghouse Electric Corporation (1966).

85. D. N. Bridges, J. D. Clement, and J. P. Renier, "A Method for Calculating Space-Dependent Reactor Source Transfer Functions With Feedback," Nucl. Sci. Eng., 36(1), 122 (1969).

86. Chun Hsu and T. P. Mulcahey, "Methods for Studying Space-Dependent Reactor Dynamics," Reactor and Fuel-Processing Tech., 11(4) (1968).

87. Proceedings of the National Topical Meeting on New Developments in Reactor Physics and Shielding, CONF-720901, Reactor Technology TID-4500, USAEC Technical Information Center, 1972 .

88. C. G. Chezem and W. H. Köhler, Proceedings of the American Nuclear Society National Topical Meeting on Coupled Reactor Kinetics, Texas A & M University Press, College Station, Texas, 1967.

89. Proceedings of a Symposium on Statistical Methods in Experimental Reactor Kinetics, and Related Techniques, RCN-98, Reactor Centrum Nederland (1968).

90. K. Saito, "On the Noise-Equivalent Source in a Zero-Power Reactor," Nucl. Sci. Eng., 28(3), 452 (1967); K. Saito, "Temperature Noise in Low-Power Reactors," Nucl. Sci. Eng., 37(2), 316 (1969).

91. K. Saito, "Noise-Equivalent Source in Nuclear Reactors," Nucl. Sci. Eng., 28, 384 (1967).

92. W. Stacey, "General Multi-group and Spectral Synthesis Equations," Nucl. Sci. Eng., 73 (1970).

93. G. I. Bell and S. Glasstone, Nuclear Reactor Theory, Van Nostrand Reinhold Company (1970).

94. R. L. Wright, N. M. Greene, J. L. Lucius, and C. W. Craven, Jr., "SUPERTOG: A Program to Generate Fine Group Constants and Pn Scattering Matrices from ENDF/B," ORNL-TM-2679, Oak Ridge National Laboratory, Oak Ridge, Tennessee (1969).

95. N. M. Greene, J. L. Lucius, L. M. Petrie, W. E. Ford, J. E. White, and R. Q. Wright, "AMPX--A Modular Code System for Generating Coupled Multigroup Neutron-Gamma Libraries from ENDF/B," ORNL-TM-3706 (AMPX-1), Oak Ridge National Laboratory, Oak Ridge, Tennessee, (1975).

96. G. F. Niederauer, "Solution of the Telegrapher's Equation for an Arbitrary Infinite Plane Source," Nucl. Sci. Eng., 38(1), 70 (1969); G. F. Niederauer, "Neutron Kinetics Based on the Equation of Telegraphy," Ph.D. Thesis, Iowa State University, Ames, Iowa (1967).

97. G. A. Mortenson and H. P. Smith, "Neutron-Wave Propagation Using the P_1 Approximation," Nucl. Sci. Eng., 22, 321 (1965).

98. K.H. Beckurts and K. Wirtz, Neutron Physics, Springer-Verlag, New York, 1964.

99. D. D. Ebert, "Space- and Energy-Dependent Noise Analysis Using Modal Expansions," Ph.D. Thesis, Georgia Institute of Technology, Atlanta (1971).

100. N. J Ackermann, J. M. Nieto, and P. Akhtar, "Two-Group Reactor Noise Analysis by Langevin's Technique," J. Nucl. Energy, 22, 675 (1968).

101. D. N. Bridges, "An Investigation of the Spatially Dependent Reactor Source Transfer Function with Temperature Feedback," Ph.D. Thesis, Georgia Institute of Technology, Atlanta (1970).

102. D. N. Bridges and J. D. Clement, "An Investigation of Space-Dependent Reactor Transfer Functions with Temperature Feedback," Nucl. Sci. Eng., 47, 421 (1972).

103. M. L. Tobias and T. B. Fowler, "Equipoise--AN IBM-704 Code for the Solution of Two-Group, Two-Dimensional, Neutron Diffusion Equations in Cylindrical Geometry," ORNL-2967, Oak Ridge National Laboratory, Oak Ridge, Tennessee (1960); "Equipoise 3A," ORNL-3199, Oak Ridge National Laboratory, Oak Ridge, Tennessee (1962).

104. M. L. Tobias and T. B. Fowler, "The Twenty Grand Program for the Numerical Solution of Few-Group Neutron Diffusion Equations in Two Dimensions," ORNL-3200, Oak Ridge National Laboratory, Oak Ridge, Tennessee (1962).

105. H. Greenspan, C. N. Kelber, and D. Okrent, Computing Methods in Reactor Physics, Gordon and Breach Science Publishers, New York, 1968.

106. M. Tobias, D. R. Vondy, and T. B. Fowler, "A Note on a Simple Method for Acceleration of Finite Difference Group-Diffusion Calculations," Nucl. Sci. Eng., 15, 98 (1963).

107. K. D. Lathrop, "DTF-IV, A Fortran-IV Program for Solving the Multi-Group Transport Equation with Anisotropic Scattering," LA-3373, Los Alamos Scientific Laboratory, Los Alamos, New Mexico (1965).

108. W. W. Engle, Jr., "ANISN, A One Dimensional Discrete Ordinates Transport Code with Anisotropic Scattering," K-1693 (1967); ANISN-W, CCC-82, Radiation Shielding Information Center; "ANISN-W, A One-Dimensional Discrete Ordinates Transport Code," WANL-PR-(LL)-034, Westinghouse Astronuclear Laboratory (1970).

109. W. W. Engle and F. R. Mynatt, "A Comparison of Two Methods of Inner Iteration Convergence Acceleration in Discrete Ordinates Codes," Trans. Am. Nucl. Soc., 193 (1968).

110. F. R. Mynatt, F. J. Muckenthaler, and P. N. Stevens, "Development of Two-Dimensional Discrete Ordinates Transport Theory for Radiation Shielding," CTC-INF-952, Computing Technology Center, Oak Ridge National Laboratory, Oak Ridge, Tennessee (1969).; F. R. Mynatt, W. W. Engle, M. L. Gritzner, W. A. Rhoades, and R. J. Rodgers, "The DOT-III Two-Dimensional Discrete Ordinates Transport Code," ORNL-TM-4280, CCC-209, Oak Ridge National Laboratory, Oak Ridge, Tennessee (1973).

111. T. B. Fowler, D. R. Vondy, and G. W. Cunningham, "Nuclear Reactor Core Analysis Code: CITATION," ORNL-TM-2496, Oak Ridge National Laboratory, Oak Ridge, Tennessee (1971).

112. M. T. Beyens-Henry, "Characteristics of Fast Neutron Power Reactors," EUR-2766e, European Atomic Energy Community-Euratom (1966).

113. H. Meister, L. Barleon, A. Bayer, C. Brückner, K. Burkart, D. Kuhn, G. Kussmaul, and D. Stegemann, "Untersuchungen an der Ladung 2 des Schnell-Thermischen Argonaut-Reactor STARK," KFK-592, Kernforschungszentrum Karlsruhe (1967); "Studies at Charge 2 of the Fast Thermal Argonaut Reactor STARK," EURFNR-352, United States-Euratom Fast Reactor Exchange Program (1967).

114. L. Barleon, C. Brückner, K. Burkart, G. Fieg, D. Kuhn, G. Kussmaul, H. Meister, H. Saufert, D. Stegemann, and H. Werle, "Investigations on Loads 3 and 4 of STARK, the Fast Thermal Argonaut Reactor," EURFNR-424, United States-Euratom Fast Reactor Exchange Program (1967); "Investigation on the 3rd and 4th Loadings of the Fast-Thermal Argonaut Reactor STARK," KFK-668, Kernforschungszentrum Karlsruhe (1967).

115. C. Brückner, Kinetic Reactor Investigations by means of a Cross-Correlation with Pseudostochastic Reactivity Modulation, KFK-1622, Kernforschungszentrum Karlsruhe (1972).

116. H. T. Klippel and J. Smit, "Complex Fast-Thermal Critical Facility STEK," RCN-209, Stichting Reactor Centrum Nederland, Petten (1974).

117. S. D. Conte, Elementary Numerical Analysis, McGraw-Hill Book Company, New York, 1965 ; S. D. Conte and C. DeBoor, Elementary Numerical Analysis, Second Edition, McGraw-Hill Book Company, New York, 1972 .

118. L. W. Nordheim, "A Program of Research and Calculations of Resonance Absorption," GA-2527, General Atomics (1961); L. W. Nordheim, "The Theory of Resonance Absorption," in Symposium on Applied Mathematics, Vol. XI (1961).

119. M. K. Drake, Editor, "Data Formats and Procedures for the ENDF Neutron Cross Section Library," BNL-50279 (1970); H. C. Honeck, "ENDF/B, Specifications for an Evaluated Nuclear Data File for Reactor Applications," BNL-50066, Brookhaven National Laboratory (1966).

120. "RSIC-DLC-16: 123 Group Neutron Cross-Section Data Generated From ENDF/B Data for Use in the XSDRN Discrete Ordinate Spectral Averaging Code," DLC-16, Radiation Shielding Information Center, Oak Ridge National Laboratory, Oak Ridge, Tennessee

121. G. D. Joanou and J. S. Dudek, "GAM-II: A B_3 Code for the Calculation of Fast-Neutron Spectra and Associated Multigroup Constants," GA-4265, General Atomics (1965).

122. H. C. Honeck, "THERMOS: A Thermalization Transport Theory Code for Reactor Lattice Calculations," BNL-5826, Brookhaven National Laboratory (1961).

123. N. M. Greene and C. W. Craven, Jr., "XSDRN: A Discrete Ordinates Spectral Averaging Code," ORNL-TM-2500 (RSIC-CCC-123), Oak Ridge National Laboratory, Oak Ridge, Tennessee (1969).

124. R. W. Roussin, "Group Averaging of Cross-Sections with ANISN Using Results of Adjoint Discrete Ordinates Calculations," CCC-82/ANISN-W Code Package, Radiation Shielding Information Center, Oak Ridge National Laboratory, Oak Ridge, Tennessee

125. "Reactor Physics Constants," ANL-5800 Argonne National Laboratory, Argonne, Illinois, 281 (1963); G. I. Bell, "A Simple Treatment for Effective Resonance Absorption Cross-Section in Dense Lattices," Nucl. Sci. Eng., 5(2), 138 (1959).

126. W. R. Sloan and G. L. Woodruff, "Spectrum of Delayed Neutrons from the Thermal-Neutron Fission of Uranium-235," Nucl. Sci. Eng., 53, 28 (1974).

127. G. Fieg, "Measurements of Delayed Fission Neutron Spectra of U^{235}, U^{238}, and Pu^{239} with Proton Recoil Proportional Counters," J. Nucl. Energy, 26, 585 (1972).

128. R. Batchelor and H. R. Hyder, "The Energy of Delayed Neutrons from Fission," J. Nucl. Energy, 3, 7 (1956).

129. G. R. Keepin, Physics of Nuclear Kinetics, Addison-Wesley Publishing Company, Inc., Reading, Mass., 1965.

130. L. M. Petrie and N. M. Greene, "XSDRNPM-AMPX Module with One-Dimensional Sn Capability for Spatial Weighting," ORNL-TM-3706, Oak Ridge National Laboratory, Oak Ridge, Tennessee (1975).

131. D. D. Ebert, "Space- and Energy-Dependent Noise Analysis Using Modal Expansions," Ph.D. Thesis, Georgia Institute of Technology, Atlanta (1971).

132. W. Seifritz, D. Stegemann, and W. Váth, "Two Detector Cross-Correlation Experiments in the Fast-Thermal Argonaut Reactor STARK," CONF-660206, Proceedings of a Symposium on Neutron Noise, Waves, and Pulse Propagation, AEC Symposium Series, 9, 195 (1967); W. W. Seifritz and D. Stegemann, "Ein Zwei-Detektor-Kreuzkorrelationsexperiment zur Bestimmung von Reaktorparametern aus dem Neutronenrauschen, Nukleonik, 9, Heft 4, 169 (1967).

133. G. Jourdan, F. Plum, and M. Reichel, "Physics Investigations of Sodium Cooled Fast Reactors SNEAK-Assemblies 6A/6B," KFK-1612, EURFNR-1029, Kernforschungszentrum Karlsruhe (1972).

134. W. Váth, "Measurement of the β/sub eff/of the SNEAK-7A and 7B Assemblies and Masurca R2 by the Frequency Analysis of Reactor Noise, EURFNR-1170, United States-Euratom Fast Reactor Exchange Program; KFK-1883, Kernforschungszentrum Karlsruhe (1974).

135. "Final Safeguards Report for the Georgia Tech Research Reactor," Georgia Institute of Technology and General Nuclear Engineering Corporation, Atlanta, Georgia (1963).

136. W. W. Graham and D. M. Walker, "Safety Analysis Report for the 5 MW Georgia Tech Research Reactor," GT-NE-7, Georgia Institute of Technology Nuclear Engineering Series (1967).

137. D. J. McGaff, "FORM--A Fourier Transform Fast Spectrum Code for the IBM-709," NAA-SR-Memo-5766, North American Aviation.

138. R. Shudde and J. Dyer, "TEMPEST--A Neutron Thermalization Code," AMTD-11, Atomics International (1962).

139. W. W. Graham, III, "The Determination of Effective Delayed Neutron and Photoneutron Kinetics Parameters in a Highly Enriched Heavy-Water Reactor," Ph.D. Thesis, Georgia Institute of Technology, Atlanta, Georgia (1965).

140. W. W. Graham, III, personal communication.

141. R. B. Blackman and J. W. Tukey, The Measurement of Power Spectra, Dover Publications, Inc., New York, 1958, pp. 21-25.

142. W. E. Schiesser, "Statistical Uncertainty of Frequency Response Determined from Random Signals," TM-711-C-2, Weston-Boonshaft and Fuchs, Inc.; W. E. Schiesser, "Statistical Uncertainty of Power Spectral Estimates," TM-711-C-1, Weston-Boonshaft and Fuchs, Inc.

143. K. J. Serdula, J. D. Kendall, P. M. Cloutier, and C. B. Lawrence, "Frequency Response Measurements of the Gentilly Nuclear Reactor Dynamics," Proceedings of a Symposium on Nuclear Power Plant Control and Instrumentation, STI/PUB/341, IAEA, Geneva, 1973, pp. 373-395.

144. P. A. Leger and L. F. Monier, "Etat de la Centrale Nucléaire de Gentilly," 72-CNA-304, Proc-1972 Annual Canadian Nuclear Association Conference, Ottawa (1972).

145. F. N. McDonnell, H. W. Hinds, P. M. Garvey, and D. H. Walker, "Kinetics Measurements on Coupled Cores in the ZED-2 Reactor," Trans. Am. Nucl. Soc., 16, 293 (1973).

146. H. W. Hinds, F. N. McDonnell, and D. H. Walker, "Kinetics Experiments on Coupled Cores in the ZED-2 Reactor," AECL-4267, Atomic Energy of Canada Limited (1972).

147. V. O. Uotinen, W. P. Stinson, and S. P. Singh, "Lattices of Plutonium-Enriched Rods in Light Water--Part 1: Experimental Results," Nucl. Tech., 15, 257 (1972).

148. G. E. Whitesides and L. M. Petrie, private communication, Oak Ridge National Laboratory, Oak Ridge, Tennessee.

149. G. E. Whitesides and N. F. Cross, "KENO--A Multigroup Monte Carlo Criticality Program," CTC-5, Computing Technology Center, Union Carbide Corp., Oak Ridge, Tennessee; L. M. Petrie and N. F. Cross, "KENO-IV--An Improved Monte Carlo Criticality Program," ORNL-4938, Oak Ridge National Laboratory, Oak Ridge, Tennessee (1975).

150. E. A. Straker, P. N. Stevens, D. C. Irving, and V. R. Cain, "The MORSE Code--A Multigroup Neutron and Gamma-Ray Monte Carlo Transport Code," ORNL-4585, Oak Ridge National Laboratory, Oak Ridge, Tennessee (1970).

151. J. Yvon, "La Diffusion Macroscopique des Neutrons, Une Méthode d'Approximation," J. Nucl. Energy, I, 4, 305 (1957).

152. F. G. Dawson, "Program Analysis and Plans, Plutonium Utilization Program," BNWL-298, Pacific Northwest Laboratories (1966).

153. A. Sauer, "Appropriate Escape Probabilities," Nucl. Sci. Eng., 16, 329 (1963).

154. G. L. Burrows and D. B. MacMillan, "Confidence Limits for Monte Carlo Calculations," Nucl. Sci. Eng., 22, 384 (1965).

VITA

Jean-Paul A. Renier was born in Anderlecht, Belgium, on July 19, 1940. He attended both grammar and high school in Brussels, Belgium, where he completed high school in 1959.

He entered the Engineering Division of the University of Louvain, Belgium, and received the "Ingénieur Civil Electrotechnique" degree with thesis in 1964. In 1962 he also entered the special program in Nuclear Science of the University of Louvain and obtained the Diploma in Nuclear Sciences in 1965. During 1965 he was a Research Associate in Nuclear Spectroscopy at the Institute of Nuclear Physics in Louvain, Belgium.

Mr. Renier entered the Graduate Division of the Georgia Institute of Technology and graduated with a Master of Science in Nuclear Engineering degree in 1967. His thesis was "Studies of the M/L Orbital Electron Capture Ratio in Ar^{37} Decay." During 1966 and 1967 he was a Graduate Research Assistant and performed research at the Frank H. Neely Nuclear Research Center at Georgia Tech and was, subsequently, a consultant to the Nuclear Spectroscopy Group for two and one half years. During this latter period, financial support was provided by the U.S. Atomic Energy Commission. During 1968 and 1969 he was a data processing consultant to two industrial companies as well as a Graduate Research Assistant in the School of Nuclear Engineering while beginning his doctoral program.

In 1969 Mr. Renier joined the Nuclear Assurance Corporation, where he managed the design of numerous applications programs in the field of

power reactor nuclear fuel cycles. As a technical manager he was also in charge of the implementation of a worldwide nuclear fuel requirements computer model and data base. From 1974 to 1976 he was in charge of criticality and shielding calculations at the Nuclear Assurance Corporation. In 1972, Mr. Renier returned to the Georgia Institute of Technology, School of Nuclear Engineering to complete his Ph.D. dissertation. He is presently self employed as a Nuclear Consultant.

Mr. Renier is a member of the Society of the Sigma Xi (honorary), the American Physical Society, and is a former associate member of the American Nuclear Society.

Mr. Renier is married to the former Carolyn Ruth Merritt of Atlanta and they have one eight month old son, Mark Christian.